Transactions of the ASME

HEAT TRANSFER DIVISION
Chairman, **R. K. SHAH**
Secretary, **A. S. ADORJAN**
Senior Technical Editor, **G. M. FAETH**
Technical Editor, **I. CATTON**
Technical Editor, **R. GREIF**
Technical Editor, **P. J. MARTO**
Technical Editor, **R. H. PLETCHER**
Technical Editor, **R. VISKANTA**
Technical Editor, **M. M. YOVANOVICH**

BOARD ON COMMUNICATIONS
Chairman and Vice President
K. N. REID, JR.

Members-at-Large
W. BEGELL
J. T. COKONIS
W. G. GOTTENBERG
F. LANDIS
J. R. LLOYD
R. E. NICKELL
J. E. ORTLOFF
C. F. PHILLIPS
R. E. REDER
F. W. SCHMIDT

President, **L. S. FLETCHER**
Executive Director,
PAUL ALLMENDINGER
Treasurer,
ROBERT A. BENNETT

PUBLISHING STAFF
Mng. Dir., Publ., **J. J. FREY**
Dep. Mng. Dir., Pub.,
JOS. SANSONE
Managing Editor,
CORNELIA MONAHAN
Production Editor,
VALERIE WINTERS
Editorial Prod. Asst.,
MARISOL ANDINO

The Journal of Heat Transfer (ISSN 0022-1481) is published quarterly for $100 per year by The American Society of Mechanical Engineers, 345 East 47th Street, New York, N Y 10017. Second class postage paid at New York, NY and additional mailing offices. POSTMASTER: Send address changes to The Journal of Heat Transfer, c/o THE AMERICAN SOCIETY OF MECHANICAL ENGINEERS, 22 Law Drive, Box 2300, Fairfield, NJ 07007-2300.
CHANGES OF ADDRESS must be received at Society headquarters seven weeks before they are to be effective. Please send old label and new address.
PRICES: To members, $24.00, annually; to nonmembers, $100.00.
Add $6.00 for postage to countries outside the United States and Canada.
STATEMENT from By-Laws. The Society shall not be responsible for statements or opinions advanced in papers or . . . printed in its publications (B7.1, para. 3).
COPYRIGHT © **1986** by the American Society of Mechanical Engineers. Reprints from this publication may be made on condition that full credit be given the TRANSACTIONS OF THE ASME, JOURNAL OF HEAT TRANSFER, and the author, and date of publication be stated.
INDEXED by Engineering Information

Journal of Heat Transfer

Published Quarterly by The American Society of Mechanical Engineers

VOLUME 108 • NUMBER 1 • FEBRUARY 1986

ANNOUNCEMENTS

TECHNICAL PAPERS

Downloaded 04 Feb 2011 to 194.85.80.107. Redistribution subject to ASME license or copyright; see http://www.asme.org/terms/Terms_Use.cfm

(Contents continued)

TECHNICAL NOTES

T. Kumada
Associate Professor.
Hokkaido University

T. Hirota
Engineer.
Toshiba Corporation

N. Tamura
Engineer.
Mitsui Engineering and
Shipbuilding Corporation

R. Ishiguro
Professor.
Hokkaido University

Heat and Mass Transfer With Liquid Evaporation Into a Turbulent Air Stream

Some of the previously reported heat transfer coefficients with evaporation are fairly large as compared with those of a dry body under similar hydrodynamic conditions. In order to clarify this curious enhancement of heat transfer, a method of error evaluation was developed and applied to correct the experimental errors in the recently reported results. An experimental study was also made on turbulent heat and mass transfer of air flowing over a water surface. The present and the previously reported experimental results revealed that the heat transfer coefficient with evaporation agrees with that of a dry body without evaporation, within experimental error, if the erroneous heat inputs into the liquid are properly corrected according to the proposed method.

Introduction

Heat transfer with evaporation from a free surface of a liquid or a wet porous plate is not only of theoretical interest but is also of practical importance in engineering. Theoretical analysis [1] and experiments [2] for a laminar boundary layer with mass injection confirm that the heat transfer coefficient is reduced with increasing blowing parameter. For the turbulent boundary layer with mass injection, many studies [3, 4] show the same effect. However, for a turbulent boundary layer with evaporation, present-day opinion is divided on the subject of the physical mechanism of heat transfer, and also on the qualitative effect of evaporation upon heat transfer. Many studies report that if a transverse mass flow is in a direction opposite to heat flow, then the thickness of a boundary layer increases with evaporation thus leading to a decrease in heat transfer. However, other experiments [5-13] have revealed that the heat transfer coefficient increases with increasing evaporation rate.

Smolsky et al. [7] intensively studied heat and mass transfer from free surfaces of various liquids into a heated turbulent air stream. They obtained the following empirical equations from the treatment of their experimental data

$$\mathrm{Nu}_e = 0.086\mathrm{Re}^{0.8}\mathrm{Pr}^{0.33}\mathrm{Gu}^{0.2} \quad \text{for heat transfer} \tag{1}$$

$$\mathrm{Sh}_e = 0.094\mathrm{Re}^{0.8}\mathrm{Sc}^{0.33}\mathrm{Gu}^{0.2} \quad \text{for mass transfer} \tag{2}$$

The heat transfer coefficient of a dry body was also measured at the same thermal, hydrodynamic, and other equivalent conditions. Their experimental points characterizing heat transfer of a dry body lie on a straight line of the well-known critical relation with a scattering of ±5 percent

$$\mathrm{Nu} = 0.037\mathrm{Re}^{0.8}\mathrm{Pr}^{0.33} \tag{3}$$

$$\mathrm{Sh} = 0.037\mathrm{Re}^{0.8}\mathrm{Sc}^{0.33} \tag{4}$$

They concluded that the absolute values of Nu_e and Sh_e increase with increasing evaporation rate, other conditions being equal.

Luikov [13] suggested that increased heat and mass transfer is due to the evaporation of fine drops, which are carried away by the air flow from the surface of the liquid into the boundary layer. Smolsky et al. [7] also agreed with this idea. On the other hand, Katto et al. [11] obtained an increased heat transfer coefficient with evaporation for the case of a mirrorlike smooth surface of water, and concluded that the hypothesis of volumetric evaporation is not always valid.

Typical examples of measured Nusselt numbers as a function of Reynolds number are presented in Fig. 1. Values of Nu_e from Smolsky et al. [7] and Katto et al. [11, 12] are 30 to 100 percent larger than the values of a dry body and vary linearly with Re.

Measurements of heat and mass transfer with evaporation are usually carried out under adiabatic conditions except for the surface of a liquid which retains convective heat transfer. However, an exact adiabatic condition at the walls of a liquid pan is not easily achieved. Therefore, Nu_e might include some errors resulting from heat gains and losses to the walls of the liquid pan used in the recent reports [5-13]. Using this evaporation rate $\dot{m}$, Nu_e is readily expressed as

$$\mathrm{Nu}_e = \frac{\dot{m}L_w l}{\lambda(T_\infty - T_w)} \tag{5}$$

where the transport properties are evaluated at a reference temperature. In the treatment of experimental data, the Sherwood number Sh_e can also be expressed as

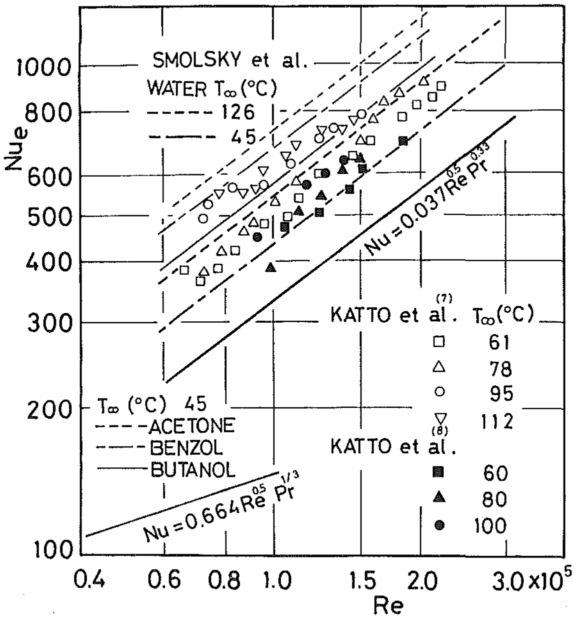

Fig. 1 Previously reported mean Nusselt number of a flat plate

---

Contributed by the Heat Transfer Division for publication in the JOURNAL OF HEAT TRANSFER. Manuscript received by the Heat Transfer Division January 2, 1985.

$$\mathrm{Sh}_e = \frac{\dot{m}l}{D\rho_M(w_w - w_\infty)} \tag{6}$$

where D and ρ_M are the values determined at a film temperature $(T_w + T_\infty)/2$. The errors from undesired heat gains and losses into the liquid pan are not included in Sh_e in principle. Combining equation (5) and (6) gives

$$\mathrm{Sh}_e = \frac{\mathrm{Nu}_e(T_\infty - T_w)\lambda}{L_w D\rho_M(w_w - w_\infty)} \tag{7}$$

If Nu_e, T_∞, $T_w(w_w)$, and w_∞ are given in the prior reports, Sh_e can be calculated using equation (7). The blowing factor in the previously reported experiments [7, 11, 12] is so small its effect on Nu_e and Sh_e can be neglected. If the condition of adiabatic evaporation is satisfied in these experiments, the analogy between Nu_e and Sh_e obtained in those experiments must be valid, because of the small blowing parameter.

Theoretical

Corrected Nusselt and Sherwood Numbers. The solution, satisfying the conditions that $T = T_w$ at the interface, where $y = 0$, and T_∞, at the bulk-gas boundary of the stagnant film, is

$$T = T_w + (T_\infty - T_w)\frac{e^{c_w y/\delta_H} - 1}{e^{c_w} - 1} \tag{8}$$

where $c_w = \dot{m}c_{pv}\delta_H/\lambda$ [14]. The conduction flux of heat at the interface is easily found using equation (8)

$$q_c = \lambda\left(\frac{dT}{dy}\right)_w = h_{H0}(T_\infty - T_w)\frac{c_w}{e^{c_w} - 1} \tag{9}$$

where $c_w/(e^{c_w} - 1)$ appearing in equation (9) is often called the "Ackermann correction" for mass transfer. The total heat input q_t into a liquid pan is expressed as

$$q_t = Ch_{H0}(T_\infty - T_w)\frac{c_w}{e^{c_w} - 1} \tag{10}$$

where

$$C = 1 + \frac{q_s}{h_{H0}(T_\infty - T_w)\dfrac{c_w}{e^{c_w} - 1}} \tag{11}$$

Combining equations (9) and (10), the corrected Nusselt number without mass injection can be expressed as

$$\mathrm{Nu}_{e0} = \frac{\dot{m}L_w l}{C\lambda(T_\infty - T_w)}\,\frac{e^{c_w} - 1}{c_w} \tag{12}$$

The corrected Sherwood number can be derived by a similar process to that used for the Nusselt number. The mass flux at the interface, on the basis of the stagnant film model, becomes

$$\dot{m} = h_D\left(\frac{PM_v}{R_0 T}\right)\ln\left(\frac{1 - Y_\infty}{1 - Y_w}\right) \tag{13}$$

where $h_D = \beta_w h_{D0}$ and β_w is a correction factor by Bedingfield and Drew [15] to account for differences in the transport equations for heat and mass other than the replacement of mole fraction by temperature and Sc by Pr. The Sherwood number can be expressed as

$$\mathrm{Sh}_e = \frac{\dot{m}l}{D\left(\dfrac{PM_v}{R_0 T}\right)(Y_w - Y_\infty)} = \frac{\beta_w h_{D0} l}{DY_{BM}} = \beta_w \mathrm{Sh}_{e0}/Y_{BM} \tag{14}$$

where T in the term PM_v/R_0T is a film temperature $(T_w + T_\infty)/2$ and h_{D0} is the mass transfer coefficient at the limiting of $\dot{m} \to 0$. Then, the corrected Sherwood number Sh_{e0} can be obtained as

$$\mathrm{Sh}_{e0} = \mathrm{Sh}_e \cdot Y_{BM}/\beta_w \tag{15}$$

where Y_{BM} is as follows

$$Y_{BM} = (Y_w - Y_\infty)/\ln[(1 - Y_\infty)/(1 - Y_w)] \tag{16}$$

Wet-Bulb Temperature and Correction Factor C. In the case of adiabatic evaporation, the inward flux of heat is just equal to the enthalpy requirement for evaporation of liquid at steady state. The heat balance can be represented by the following relationship [14]

$$h_{H0}(T_\infty - T_{wb})\frac{c_{wb}}{e^{c_{wb}} - 1} = \beta_{wb} h_{D0} L_{wb}\left(\frac{PM_v}{R_0 T}\right)\ln\left(\frac{1 - Y_\infty}{1 - Y_{wb}}\right) \tag{17}$$

Nomenclature

a = thermal diffusivity, m^2/s
C = correction factor of heat input
c_w = thermal blowing parameter = $\dot{m}c_{pv}\delta_H/\lambda$
c_p = specific heat, kJ/kg•K
D = diffusion coefficient, m^2/s
h_{D0} = average mass transfer coefficient at the limit of $\dot{m} \to 0$, m/s
h_D = average mass transfer coefficient, m/s
h_{H0} = average heat transfer coefficient at the limit of $\dot{m} \to 0$, kW/m^2•K
h_H = average heat transfer coefficient, kW/m^2•K
l = characteristic length, m
L = latent heat, kJ/kg
$\dot{m}$ = mass flux, kg/m^2•s
M = molecular weight
P = total pressure, kg/m^2
q_c = convective heat input, kW/m^2
q_s = nonconvective heat input, kW/m^2
q_t = $q_c + q_s$, kW/m^2
R_0 = universal gas constant, kJ/kmol•K
T = temperature, K
u = velocity, m
w = mass fraction
Y = mole fraction of vapor
y = coordinate perpendicular to a surface, m
β = correction factor defined by equation (19)
δ_D = diffusion thickness, m
δ_H = thermal conduction thickness, m
ρ = density, kg/m^3
λ = thermal conductivity, kW/m•K
$\mathrm{Gu}[(T_\infty - T_w)/T_\infty]$ = Guhmann number
$\mathrm{Le}(a/D)$ = Lewis number
$\mathrm{Nu}(h_H l/\lambda)$ = Nusselt number
$\mathrm{Pr}(\nu/a)$ = Prandtl number
$\mathrm{Re}(ul/\nu)$ = Reynolds number
$\mathrm{Sc}(\nu/D)$ = Schmidt number
$\mathrm{Sh}(h_D l/D)$ = Sherwood number

Subscripts

e = measured value
g = gas
M = mixture of gases
0 = corrected value
v = vapor
w = wall or surface of liquid
wb = wet-bulb temperature
∞ = mainstream

where c_{PM} is the heat capacity of the mixture, and β_{wb} is a factor defined by Bedingfield and Drew [15]. Within the limit of small driving force, $Y_{wb} - Y_\infty$, β_{wb} becomes approximately

$$(T_\infty - T_{wb})\frac{c_{wb}}{e^{c_{wb}}-1} = L_{wb}\left(\frac{\beta_{wb}}{c_{PM}}\right)\mathrm{Le}_{wb}^{2/3}\ln\left(\frac{1-Y_\infty}{1-Y_{wb}}\right) \quad (18)$$

where c_{PM} is the heat capacity of the mixture, and β_{wb} is a factor defined by Bedingfield and Drew [15]. Within the limit of small driving force, $Y_{wb} - Y_\infty$, β_{wb} becomes approximately

$$\beta_{wb} = 1 - \frac{1}{2}\left(\frac{M_v - M_g}{M_M} + \frac{1}{1-Y_{wb}}\right)(Y_{wb} - Y_\infty) \quad (19)$$

Figure 2 shows a comparison between the wet-bulb temperature calculated using equation (18) and values for water surfaces measured by Smolsky et al. [7] and Katto et al. [11, 12]. If the temperature of the liquid surface is higher than the wet-bulb temperature, then the liquid pan must have received radiative and conductive heat transfer. Figure 2 suggests that adiabatic evaporation was not realized in the experiments of Smolsky et al. [7] and Katto et al. [11, 12].

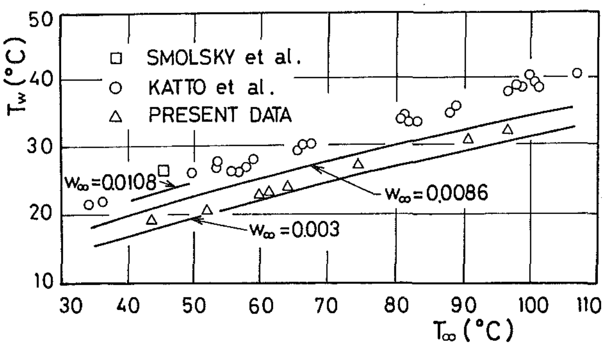

Fig. 2 Comparisons between wet-bulb and water surface temperatures: Solid lines are the predictions of equation (18)

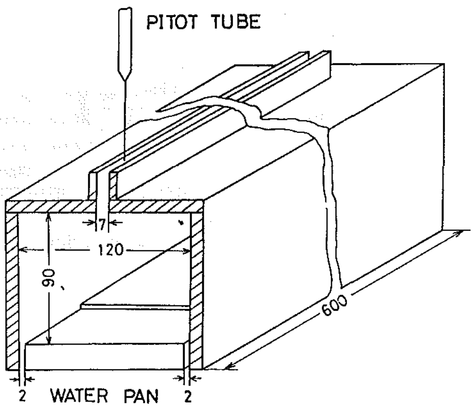

Fig. 3 Details of the test section of the tunnel I

If there is heat input q_c per unit area of liquid surface and unit time, except convective heat from the liquid surface, equation (17) becomes

$$Ch_{H0}(T_\infty - T_w)\frac{c_w}{e^{c_w}-1} = \beta_w h_{D0} L_w\left(\frac{PM_v}{R_0 T}\right)\ln\left(\frac{1-Y_\infty}{1-Y_w}\right) \quad (20)$$

Taking the ratio of equations (17) and (20), C is expressed by the following relation

$$C = \left(\frac{\beta_w}{\beta_{wb}}\right)\left(\frac{c_{wb}}{c_w}\right)\left(\frac{e^{c_w}-1}{e^{c_{wb}}-1}\right)\frac{L_w}{L_{wb}} \cdot \left(\frac{T_\infty - T_{wb}}{T_\infty - T_w}\right)\ln\left(\frac{1-Y_\infty}{1-Y_w}\right)\Big/\ln\left(\frac{1-Y_\infty}{1-Y_{wb}}\right) \quad (21)$$

If $\dot{m}$ is small, as in the experiments of both Smolsky et al. [7] and Katto et al. [11, 12], in the above equation, it can be assumed that $\beta_w = \beta_{wb}$, $L_w = L_{wb}$, and $(c_{wb}/c_w)(e^{c_w} - 1)/(e^{c_{wb}} - 1) = 1$. Then equation (21) becomes

$$C = \left(\frac{T_\infty - T_{wb}}{T_\infty - T_w}\right)\ln\left(\frac{1-Y_\infty}{1-Y_w}\right)\Big/\ln\left(\frac{1-Y_\infty}{1-Y_{wb}}\right) \quad (22)$$

Experimental

Two wind tunnels were used in order to clarify the universality of the measured results.

Tunnel *A*. The exit cross section of the tunnel A is 50 mm high and 120 mm wide. Air flow supplied by a blower is discharged into an electric heater chamber, passed through a stilling chamber, which contained a layer of 100 mm mesh screen, and then passed into an evaporation test section. A flexible duct is used to mechanically isolate the blower from the heater chamber.

Details of the evaporation test section, which is made of acrylic resin, are shown in Fig. 3. The rectangular duct (120 mm wide, 500 mm long, and 120 mm high) is provided with a slit (7 mm wide) at the top, to permit measurement of temperature and velocity profiles from above. The probes are supported by a rack and pinion, equipped with a vernier, and can be moved along the metal track attached to the instrument platform. Turbulent intensity was measured using a linearized-output hot wire anemometer. A single wire probe with the wire mounted horizontally and oriented perpendicularly to the air stream was used to measure the longitudinal components of turbulence velocity. The velocity distribution across the duct was measured with a pitot tube (outside dimensions of 1.2 mm × 0.4 mm).

The bottom of the duct is a liquid pan which is isolated from the lateral walls of the duct to prevent surface waves due to the mechanical vibration induced by turbulent flow. Several liquid pans were constructed; the details of the designs

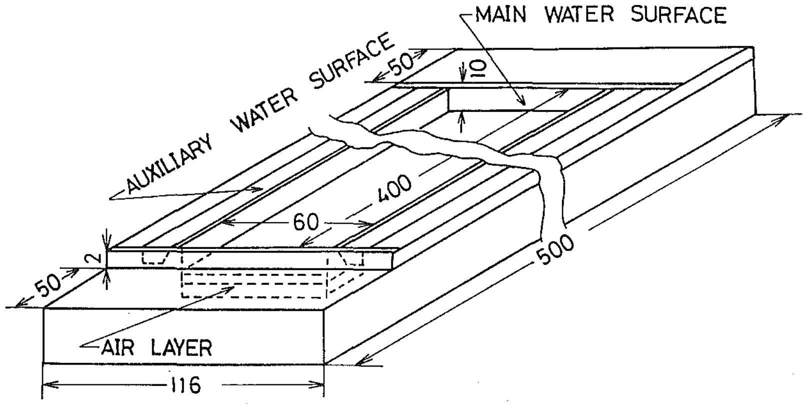

Fig. 4 Details of the water pan

are shown in Fig. 4. Water filling the pan formed a free surface on its floor occupying a rectangle 60 mm wide and 400 mm long, beginning from a point 50 mm downstream of the entrance of the duct floor. The temperatures of the surface of liquid and beneath were measured with a thermocouple probe supported by the rack. The evaporation surface of the other pans was covered by a sheet of smooth, thin silk cloth which was completely wetted by capillary forces. The temperature of the evaporation surface was measured with thermocouples embedded between the silk cloth and the acrylic resin plates.

Tunnel B. In order to obtain data at different conditions, the equipment setup was varied. Turbulence intensity and waves on a liquid surface may differ depending on the type of equipment used, and thus a change in the heat and mass transfer coefficients may occur. For example, heat gains and losses may be dependent on the structure and size of the water pan. The purpose of this measurement was to check whether the data changed depending on the equipment used. In this experiment, the exit cross section of the duct is 300 × 300 (mm) and is set 1700 (mm) downstream from the suction end of the tunnel. The water pan is placed in front of the exit of the tunnel.

The bottom of the duct is a liquid pan which is isolated from the lateral walls of the test section. The liquid surface forms a rectangle 120 mm wide and 500 mm long beginning from a point 50 mm downstream of the exit of the duct. Auxiliary water surfaces are provided on the side walls of the duct.

Equipment for Measuring Surface Waves. An optical system based on Moire fringes is used to measure the amplitude and lengths of traveling waves. This technique was applied for amplitudes below 0.3 mm. When the amplitudes were larger than 0.3 mm, the conductive-probe technique was used to measure the amplitude and frequency of the surface waves. A probe, which is insulated apart from its tip, is set on the surface waves.

Measurement of Evaluation Rate. During the experiment, water was supplied to the water pan from a water container to keep the water level at a nearly constant height. The total weight of both the water pan and the water supply container was measured before and after the experiment. In the measurements with the first wind tunnel, the water on all auxiliary surfaces was wiped off at the moment of measuring the weight. In the measurements with the second wind tunnel, however, the water on these surfaces was left because it adhered to the side walls of the duct.

Results and Discussions

Property Evaluation. The physical properties c_p, D, λ, ρ, and ν, used in the present calculation, are evaluated using the film temperature as a reference temperature. The effect of vapor concentration on mixture specific heat and density is weighted by mole fraction. The diffusion coefficient is assumed to be independent of vapor concentration. Thermal conductivity and viscosity are evaluated by the methods by Lindsay and Bromley [16] and Bromley and Wilke [17], respectively. Latent heat is evaluated at the temperature of the wetted surface.

Surface Temperature of Water. The temperature distributions were measured along the center line of the water surface in the longitudinal direction. The temperature of a water body is nonuniform in both lateral or longitudinal directions due to the erroneous heat inputs except convective heat into the water pan. If the temperature of a water body is significantly nonuniform, it is very difficult to determine exactly the mean temperature of its water surface. The previously reported temperature T_w includes an error caused by the uneven distribution of surface temperature because the erroneous heat inputs are large. As shown in Fig. 2 the present data obtained using tunnel A do not deviate as much from the wet-bulb temperature as those by Smolsky et al. [7] and Katto et al. [11, 12].

Waves on Water Surface. The level change due to the variation of static pressure leads to errors in determining the wave amplitudes. In the ceiling wall of a duct, a long narrow slit of 7 mm in width was made along the central line in the direction of air flow. The static pressure in the duct was maintained by this slit at a value almost equal to atmospheric pressure except for the region within 50 mm from the leading edge. This was confirmed by measuring the static pressure along the bottom plate. The amplitude of surface waves was measured by means of the Moire interferometric method and the contact probe method in wind tunnel II for water depths of 1.5, 6, and 12 mm. Irregular waves were observed in the range of about 50 mm from the leading edge. Regular waves were observed in the region downstream of 50 mm from the leading edge. Figure 6 shows the amplitude of the surface waves as a function of the velocity of main stream u_∞.

Heat Transfer Coefficient for a Copper Plate. Heat transfer coefficients were measured using a copper plate for u_∞ of 3 m/s to 6 m/s. The air flow was adjusted to almost room temperature, and the copper plate was heated to a temperature of about 40°C. The average Nusselt number Nu was determined after the equipment had reached a stationary temperature. The results shown in Figs. 6 and 7 agree exceptionally well with the theoretical values given by equation (3).

***Correction Factor** C.* Heat inputs, except for heat convection, were calculated using the measured temperature distribution of the water pans. The water surface receives radiative heat from the surroundings, mainly the walls of the duct. The water pan receives conductive and radiative heat from its bottom and side walls. These heat inputs were calculated along with the temperatures of each part of the water pan. The difference between temperature at the surface of the water and within the water was within 1°C. It was assumed that the interior surfaces of the bottom and side walls were equal to the surface temperature of the water. The outside and auxiliary surfaces of the water were measured and used for the above calculation. The temperatures of each part of the pan were assumed to be nearly independent of the velocity of the main stream because they did not change greatly under the present experimental conditions.

Figure 5 shows the correction factor calculated by both equation (22) and the model based on the temperatures measured in each part of the pan. The results found using equation (22) are not consistent with each other due to the different conditions of the experiment, not due to experimental error. The values of C calculated by equation (22) agree qualitatively and quantitatively with the values calculated with the temperature distribution of the pans.

Sherwood and Nusselt Numbers Sh_e, Nu_e. For the case of no correction of the effect of erroneous heat inputs and blowing, Sh_e and Nu_e are presented against Re in Fig. 6. The figure reveals, notably, that the values of Sh_e agree with the value calculated from equation (4), except in the range of $1.5 \times 10^5 \sim 2.0 \times 10^5$, where transfer coefficients are enhanced due to the production of surface waves. Sh_e obtained from the surface of the wet cloth are also in fairly good agreement with the predicted values given by equations (4). The large difference between Nu_e for $T_\infty = 30°\mathrm{C}$ and Nu_e for $T_\infty = 65°\mathrm{C}$ comes from the different design of the water pans and the different equilibrium temperature of the water surfaces. The blowing factor is so small that its effect on Sh_e and Nu_e can be neglected. The factor $\rho_{v,w} v_m / \rho_\infty u_\infty$ is only on the order of

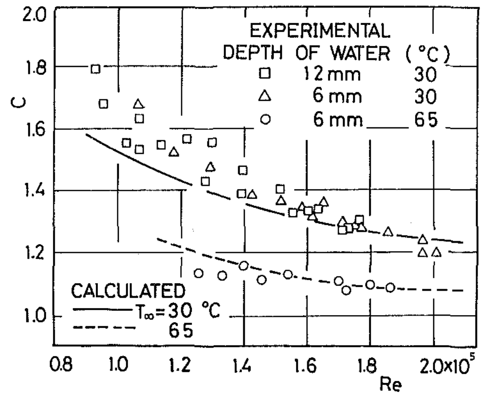

Fig. 5 Comparisons between measured and calculated correction factors

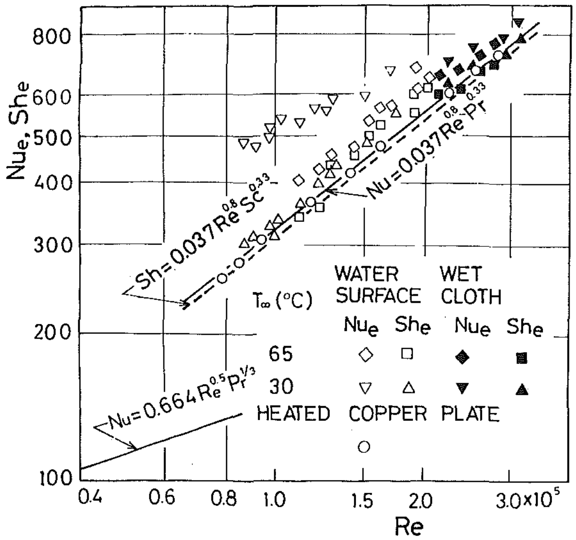

Fig. 6 Sherwood and Nusselt numbers with no correction

0.001, so the correction of Sh_e and Nu_e is within 3 percent, based on the stagnant film model.

Correct Nusselt Number. Figure 7 shows Nusselt number, which is corrected for the effect of blowing and erroneous heat inputs. The results of the present experiment demonstrate clearly that the curious enhancement of Nusselt number did not occur in this experiment.

Conclusions

The overall results are summarized as follows:

1 The enhancement of Nusselt number Nu_e is small if a well-insulated liquid pan is used.

2 This enhancement is most likely caused by conductive and radiative heat inputs from the surroundings into the pan because of the lack of enhancement in Sherwood number Sh_e.

3 If Nu_e is corrected according to the method proposed in this paper, then there is no enhancement of the corrected Nusselt number Nu_{e0}.

4 Heat inputs calculated by the proposed method quantitatively and qualitatively agree with those calculated using the temperature distribution of two pans.

5 Nusselt and Sherwood numbers are not greatly enhanced by waves produced on the surface of water, if their amplitudes are less than 1 mm.

6 The condition of perfect adiabatic evaporation is hard to achieve in experiments of this type.

It is very curious that the problem of abnormal enhancement of heat transfer has not been solved up to now.

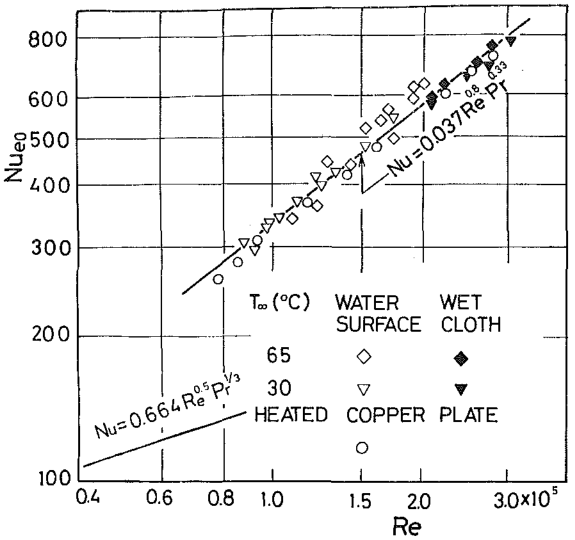

Fig. 7 Comparisons between measured and calculated Nusselt number Nu_{e0}

This problem may be caused by the relatively small heat input by convection as compared with heat inputs by conduction and radiation through the walls of a liquid pan.

The abovementioned curiosity is, interestingly, not encountered in basic research on the wet-bulb hygrometer for the measurement of air humidity. Erroneous inputs are mainly caused by radiation from surroundings and partly by heat conduction through a stem, because most of the experiments are performed for bluff objects.

References

1 Hartnett, J. P., and Eckert, E. R. G., "Mass Transfer Cooling in a Laminar Boundary Layer With Constant Fluid Properties," *Trans. ASME*, Vol. 79, 1957, pp. 247-254.

2 Hirata, M., and Yamazaki, S., "Experimental Study of Heat Transfer in a Laminar Boundary Layer on a Porous Flat Plate With Fluid Injection," *J. Appl. Mech.*, 1957, pp. 297-301.

3 Rannie, W. D., "A Simplified Theory of Porous Wall Cooling," C. I. T. Propul. Lab. Progress Rept., No. 4-50, 1947.

4 Dorrance, W. H., and Dore, F. J., "The Effect of Mass Transfer on the Compressible Turbulent Boundary Layer Skin Friction and Heat Transfer," *J. Aero. Sci.*, Vol. 21, 1954, pp. 404—410.

5 Sergeyev, G. T., "Investigation of External Heat and Mass Transfer With Liquid Evaporation From a Capillary Porous Body," *Inzh. Fiz. Zh.*, No. 5, 1961, pp. 33-37.

6 Nesterenko, A. V., "Heat and Mass Transfer With Liquid Evaporation a Free Surface," *Zh. Tekh. Fiz.*, Vol. 24, 1957, pp. 729-737.

7 Smolsky, B. M., and Sergeyev, G. T., "Heat and Mass Transfer With Liquid Evaporation," *Int. J. Heat and Mass Transfer*, Vol. 5, 1962, pp. 1011-1021.

8 Luikov, A. V., *Advances in Heat Transfer*, Vol. 1, Academic Press, New York, 1964, pp. 123-164.

9 Kikkawa, S., and Nakatani, Y., "The Experimental Investigation on the Transpiration Cooling," *Bulletin of JSME*, Vol. 8, 1965, pp. 677-682.

10 Mawatari, K., Hiramoto, M., and Okazaki, T., "Measurements of the Concentration Boundary Layer in Heat and Mass Transfer," *JSME 1967 Semi-Int. Symp. Papers, Heat and Mass Transfer, Thermal Stress*, Vol. 1, 1967, pp. 249-257.

11 Katto, Y., and Aoki, H., "Peculiarity of Evaporating Liquid-Surface With Reference to Turbulent Heat Transfer," *Bulletin of JSME*, Vol. 12, 1969, pp. 79-86.

12 Katto, Y., and Koizumi, H., "Turbulent Heat Transfer of a Gas Flow on an Evaporation Liquid Surface," *Bulletin of JSME*, Vol. 18, 1975, pp. 866-873.

13 Luikov, A. V., "Heat and Mass Transfer With Transpiration Cooling," *Int. J. Heat Mass Transfer*, Vol. 6, 1963, pp. 559-577.

14 Sherwood, T. K., Pigford, R. L., and Wilke, C. R., *Mass Transfer*, Intl. Student edn., McGraw-Hill Kogakusha, LTD, 1975, pp. 56-57.

15 Bedingfield, C. H., and Drew, T. B., "Analogy Between Heat Transfer—A Psychrometric Study," *Ind. Eng. Chem.*, Vol. 42, 1950, pp. 1164-1173.

16 Lindsay, A. L., and Bromley, L. A., "Thermal Conductivity of Gas Mixtures," *Ind. Eng. Chem.*, Vol. 42, 1951, pp. 1508-1513.

17 Bromley, L., and Wilke, C. R., "Viscosity Behavior of Gases," *Ind. Eng. Chem.*, Vol. 43, 1951, pp. 1641-1648.

R. N. Meroney
Professor.

D. E. Neff
Research Associate.

Fluids Mechanics and Wind Engineering,
Civil Engineering Department,
Colorado State University,
Fort Collins, CO 80523

Heat Transfer Effects During Cold Dense Gas Dispersion: Wind-Tunnel Simulation of Cold Gas Spills

Wind-tunnel concentration data were obtained for continuous area releases of ambient temperature Freon-air mixtures, cold N_2, cold CO_2, and cold CH_4 clouds. Heat transfer and humidity effects on model concentration distributions were significant for methane plumes when surface Richardson numbers Ri_* were large (i.e., low wind speed and high boiloff rate conditions). At field scales heat transfer and humidity will still play a role in the dispersion of methane spill cases, but plume dilution and liftoff are not expected to be as exaggerated as for the model cases.

1.0 Introduction

Storage and transport of flammable hydrocarbon fuels with subambient boiling points have potential hazards associated with inadvertent release into the atmosphere. Fuels in this category include liquefied natural gas (LNG), ethane, propane, and butane (LPG). At ambient temperature, these liquids boil rapidly and form cold gas clouds that are negatively buoyant often until the cloud dilutes below its lower flammability limit (LFL). Previous analyses of laboratory experiments modeling dense gas plumes have not discussed thermal effects on plume mixing behavior, so new model experiments were performed to study the effect of heat transfer on cold dense cloud dispersion.

Wind-tunnel tests were performed at model scale to determine heat transfer effects on a LNG plume. Since a LNG plume is heavier than air at boiloff conditions, it is expected to disperse as a negatively buoyant cloud. Negatively buoyant plumes were simulated in the wind tunnel by ambient temperature heavy gas or cooled lighter gases, such that the specific gravity of the source gas is equal to that of LNG vapor at boiloff.

The measured concentrations were scaled to account for differences in moles of cold methane gas versus the source moles of alternative model source gas. Heavy gases were introduced into the wind tunnel via a constant-area source mounted flush with the wind-tunnel floor. Mean gas concentrations and mean temperatures were evaluated at various locations both downwind and upwind of the source. Concentration samples were analyzed using a gas chromatograph. Temperatures were evaluated throughout the plume with a thermocouple multiplexer system. Plume structure was determined from the concentration and temperature profiles.

1.1 Dense Gas Kinematics. Continuous source plumes arise in situations such as pipeline ruptures without valve closedown or releases of very large quantities of cryogenic liquid gas onto land or water in the presence of wind. Puttock et al. [10] describe a number of field tests which produced continuous dense gas plumes.

Initially, continuous cold plumes exhibit rapid horizontal spreading caused by the excess hydrostatic head of the cloud. The result is a low wide plume, the effect being more pronounced at low wind speeds. In instances of low and moderate wind speed, the plume will even extend upwind, although the gas will eventually lose its initial upwind momentum and be rolled back over or around the source. A consequence of the velocity reversal of gas upwind from the source is the generation of a horseshoe-shaped vortex, which bounds the laterally parabolic gas cloud.

The initial gravitationally induced collapse of the cloud converts potential energy into kinetic energy, part of which is in turn transmitted to the surrounding ambient fluid, where it is dissipated by turbulence. The energy transfer primarily occurs at the head of the spreading cloud and in its wake. The cloud will reach a point where the gravitational spreading velocity is small compared to the mean ambient wind velocity. Presumably, significant amounts of air will be entrained due to mixing, and the cloud will be advected downwind at ambient air speeds. Hence, the cloud takes on a parabolic shape with plume depth being symmetric about the center line.

Surface heating of the plume and heat from condensation of water vapor entrained with the air reduce the plume's negative buoyancy. The result is a decrease in the instantaneous Richardson number thereby enhancing both dispersion by atmospheric turbulence and the subsequent downwind advection of the plume. As the buoyancy becomes positive and the plume less stably stratified, it may actually lift off the ground surface. For large spills of LNG under moderate wind conditions significant liftoff does not seem to occur before the lower flammability limit is attained.

For small field spills or laboratory-scale spills surface heating effects will be exaggerated. When a large Rayleigh number condition exists (i.e., large temperature differences or large cloud depth) it is hypothesized that surface heat transfer will be proportional to $h_s L^3/U$, where L is the characteristic length scale of the plume, U is the characteristic velocity scale, and h_s is the convection heat transfer coefficient, which is not a strong function of the length scale. The thermal capacity of a gas cloud will vary as $\rho C_p L^3$, where ρ is plume density and C_p is specific heat capacity. The ratio of surface heat transport to thermal capacitance (the Stanton number St) is $h_s/(\rho C_p U)$. Since the wind speed for stratified flows is scaled by the ratio of buoyancy to inertial forces or a Froude number, $U^2/g'L$, and the surface heat transfer is likely to include a free convection component small model-scale plumes will see a temperature increase (or density decrease) which does not scale to the field equivalent. Cold model plumes will entrain air faster and lift off before the comparable field situation [1].

1.2 Simulation of Dense Cloud Motion. The structure of the adiabatic atmospheric boundary layer may be adequately simulated in the laboratory if a minimum Reynolds number, $\mathrm{Re} = u_* z_0/\nu$, exceeds 2.5, where u_* is friction velocity, z_0 is surface roughness, and ν is kinematic viscosity; otherwise the

---

Contributed by the Heat Transfer Division for publication in the JOURNAL OF HEAT TRANSFER. Manuscript received by the Heat Transfer Division December 7, 1984. Paper No. 84-WA/HT-78.

boundary layer grows over an unrealistically smooth surface. In addition similarity between approach wind and turbulence profiles is generally necessary. Simulation of heavy cloud motion additionally requires that various plume mass ratios, force ratios, energy ratios, and property ratios be equal for both model and prototype. Neff and Meroney [8] considered various scaling arguments for isothermal dense gas plumes, and they concluded that equivalence of specific gravity ratio, SG = ρ_0/ρ_a; flux Froude number, Fr = $U_a^3 L/(g'_0 Q)$; and volume flux ratio, $Q/(U_a L^2)$ are sufficient to assure similarity.

The scaling considerations mentioned above are equally applicable to the scaling of cold heavy clouds. However, in the case of thermal plumes additional considerations must be made to insure that the model plume's specific gravity history is similar to that of its full-scale counterpart. Processes which affect specific gravity history include:

- thermal expansion or contraction of the plume due to differences in the molar specific heat capacity of the plume source gas and air
- release of latent heat during the entrainment of humid air
- heat transfer by conduction, convection, or radiation across plume boundaries

For the case of a thermal plume whose molar specific heat capacity is different from air, such as an LNG vapor plume, the modeling of the density history variation within the plume can only be approximate. For a given molar dilution the specific gravity after adiabatic mixing of the LNG plume will slightly exceed that for isothermal modeling, and the plume cross section will be slightly smaller. The release of latent heat through the entrainment of humid air can also have a very significant effect on the density history of a thermal plume. Latent heat will reduce the plume's negative buoyancy during its initial mixing period, but the plume density may increase later as the moisture re-evaporates, when the plume temperature exceeds the atmospheric dew point.

2.0 Data Acquisition and Analysis

The cold gas experiments were modeled in the Environmental Wind Tunnel (EWT) at Colorado State University. This atmospheric boundary-layer wind tunnel has a test section 3.66 m wide, 2.28 m tall, and 17.0 m long. Vortex generators and a wall trip at the test-section entrance produced a boundary layer about 1 m deep at the experiment location 10.0 m downwind of the entrance.

A constant area source (Fig. 1*a*) was mounted flush with the floor of the EWT. Two heavy isothermal and three cooled gases were released continuously from the source. A heat exchanger (Fig. 1*b*) was used to establish the proper thermal conditions of the source gases. The heat exchanger used nitrogen as the cooling fluid both in gaseous and in liquid form. A pool of liquid nitrogen was maintained around the source gas plenum, so that little if any source gas heating would occur until the gas became exposed to the ambient atmosphere. The source gas was cooled in a gas-to-gas counterflow heat exchanger. Temperatures were regulated by adjusting coolant gas temperatures and flow rate, and release temperatures were set within ±5 K. All source gases contained a known percentage of a hydrocarbon tracer. An oil smoke was used to visually define ambient temperature gas

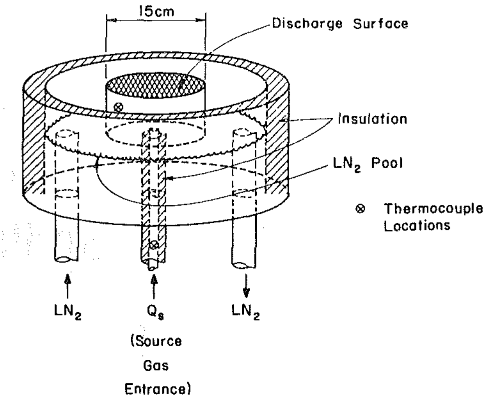

Fig. 1(*a*) Source plenum construction details

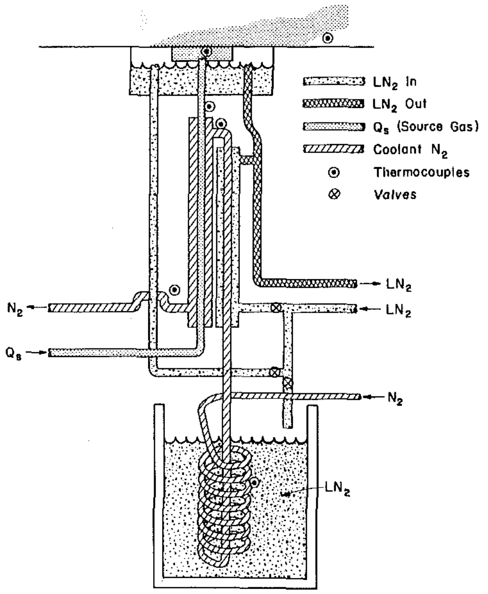

Fig. 1(*b*) Schematic diagram cryogenic heat exchanger to cool source gases and plenum

Nomenclature

C = concentration
C_f = skin friction coefficient
C_p = specific heat capacity (mass)
C_p^* = specific heat capacity (molar)
E = entrainment ratio = w_e/u_*
g' = modified gravitational constant = $g(\Delta\rho/\rho)$
Gr = Grashof number
H = cloud depth
h_s = surface heat transfer coefficient
K = dimensionless concentration coefficient
L = characteristic length scale
l_b = buoyancy length scale = $g'Q/U_R^3$
MW = molecular weight
Nu = Nusselt number
Q = source strength
R = universal gas constant
Re = Reynolds number
Ri_* = Richardson number
SG = specific gravity
St = Stanton number
T = temperature
U = wind speed
u_* = friction velocity
w_e = entrainment velocity
z_0 = surface roughness length
ρ = density
ν = kinematic viscosity
Δ = temperature difference
ϕ = humidity

Subscripts

0 = source conditions
a = ambient conditions
m = model conditions
p = prototype conditions
R, ref = reference conditions

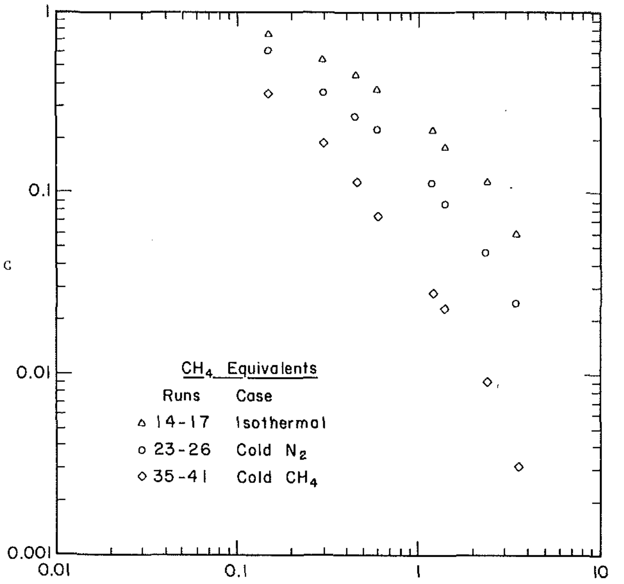

Fig. 2 Surface centerline concentration variation with distance, l_b ~4.0, $Q = 130$ ccs, $u_* = 1.85$ cm/s

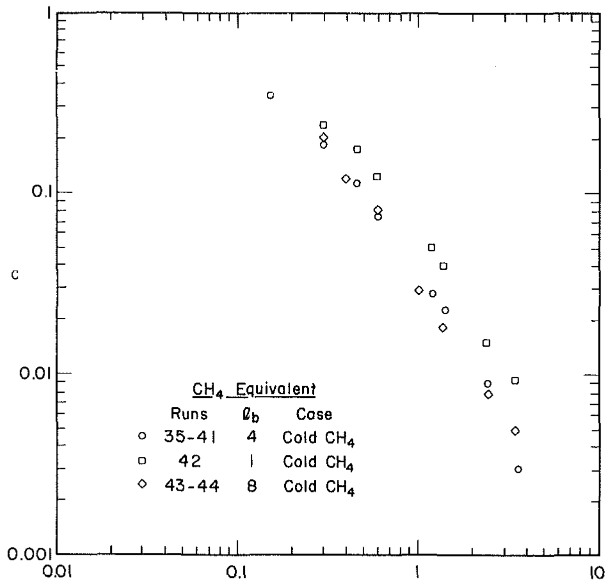

Fig. 4 Surface centerline concentration variation with distance, methane runs, l_b = 1, 4, and 8

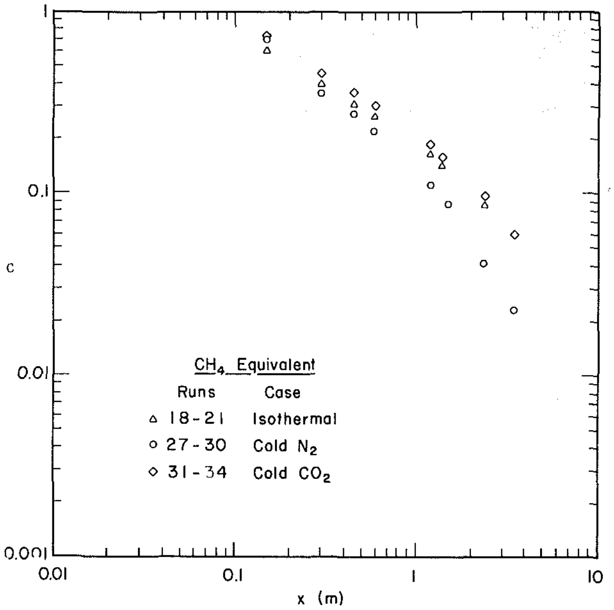

Fig. 3 Surface centerline concentration variation with distance, l_b ~4.0, $Q = 223$ ccs, $u_* = 3.20$ cm/s

plume behavior, while cold gas plume boundaries could be observed as a result of background humidity condensation within the plume. Correlations of plume outlines with concentration isopleths suggest the smoke edges reflect a concentration near 0.1 percent.

The approach wind velocity profile, reference wind speed conditions, and turbulence were measured with a Thermo-Systems 1050 anemometer and 1210 hot-film probe. Multipoint calibration procedures suggest that velocities were measured within 5-10 percent of their actual values. A thermocouple multiplexer (Model Digitrend 22) monitored up to 45 copper/constantan thermocouples once each minute during each experiment. In addition one fast response (0.025 mm diameter) thermocouple was placed 15 cm downwind of the source and 0.5 cm above the ground and monitored continuously.

Average concentrations were measured at 81 stations for each simulated spill. The floor in the vicinity of the plumes was always flat and smooth with no obstacles to cause wake effects. Runs 1-12 were performed to determine the reaction of plume behavior to a range of initial conditions. Sample tubes for vertical and surface concentrations were arranged above the floor and may have produced wakes which caused additional dilution. In later tests, Runs 13-44, sampling tubes were mounted flush with the surface and connected to the sampler via a hollow chamber beneath the wind-tunnel floor. To obtain a series of vertical profiles, experiments were replicated up to five times, and only data at or upwind of any concentration probe rake should be considered accurate. The replications provided redundant data that defined concentration variability between test runs. Samples were drawn from the tunnel in 50 sample sets over a period of 5 min at a rate of about 6 cc/min. Such sampling times are equivalent to 10-20-min averages at field scales. Individual samples were then evaluated for tracer gas concentration by a flame-ionization detector in a gas chromatograph (Hewlett Packard Model 5710A). The error in measured concentration is imposed by the detector sensitivity, source strength and sampling uncertainties, and the background concentration of tracer within the wind tunnel. Background concentrations were measured and subtracted from all data; hence, final model concentrations are accurate to ±10 percent over most of the detection range.

3.0 Test Program and Data

The cold dense plume measurement program was designed to provide a basis for the analysis of heat transfer effects on plume dispersion, the evaluation of plume scaling laws, and to assist in the development of and verification of numerical models. Source gas mixtures were prepared to provide gases which were all initially heavy; but they were either ambient temperature, cold with molar specific heat capacity ratio $(C_p^*)_0/(C_p^*)_a = 1.0$, or cold with $(C_p^*)_0/(C_p^*)_a > 1.0$. Thus one could evaluate whether dilution and plume dimensions resulted from adiabatic entrainment, heat transfer effects, or unbalanced thermal expansion. Since wind-tunnel velocity and heat-exchanger temperatures sometimes drifted from the ideal set points, the actual conditions examined are noted in Table 1. Detailed data tables are available in the report by Andriev et al. [1].

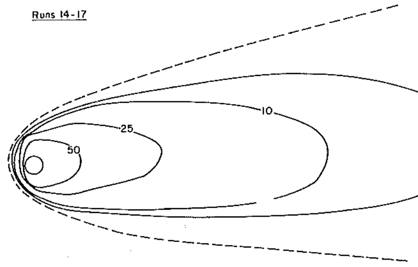

Fig. 5(*a*) Surface concentration isopleths, runs 14-17, isothermal gas, l_b = 4.0, Q = 130 ccs, u_* = 1.85 cm/s

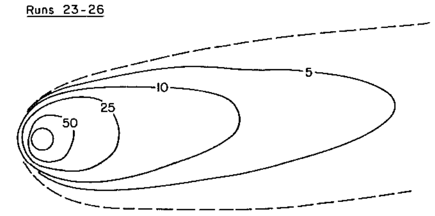

Fig. 5(*b*) Surface concentration isopleths, runs 23-26, cold nitrogen, l_b = 4.0, Q = 130 ccs, u_* = 1.85 cm/s

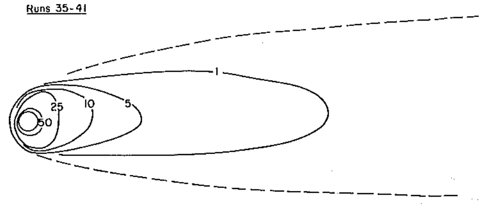

Fig. 5(*c*) Surface concentration isopleths, runs 35-41, cold methane, $l_b \simeq 2.9$, Q = 130 ccs, u_* = 1.85 cm/s

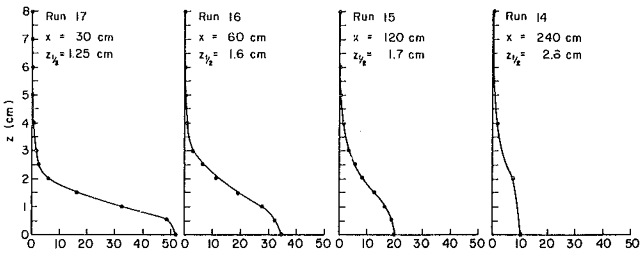

Fig. 6 Vertical concentration profiles, runs 14-17, isothermal gas, l_b = 4.0, Q = 130 ccs, u_* = 1.85 cm/s

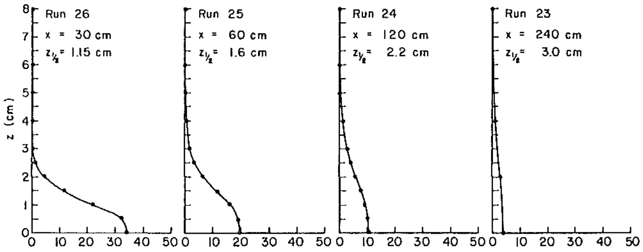

Fig. 7 Vertical concentration profiles, runs 23-26, cold nitrogen, l_b = 4.0, Q = 130 ccs, u_* = 1.85 cm/s

Since gravity effects should be a function of buoyancy length scale l_b (or Richardson number), two buoyancy conditions were selected, $l_b = 1$ cm and $l_b = 5$ cm, which were expected to produce small and significant buoyancy effects respectively. Under the first condition background turbulence was expected to dominate entrainment very quickly, but under the latter condition gravity spreading and suppression of vertical mixing was expected to persist. Two combinations of initial molecular weight and initial temperatures were arranged for each buoyancy length scale, and wind speeds were selected to produce equal buoyancy length scales (or equal Richardson numbers) under quite different conditions. If equality of Richardson number alone were adequate for proper plume scaling, then in the absence of heat transfer such experiments should produce identical concentration isopleths. If thermal expansion effects are also minimal then the isothermal and cold nitrogen releases could produce coincident concentration isopleths. If heat transfer effects are minimal then the combined cold methane runs could produce coincident dimensionless concentration isopleths K.

3.1 Velocity and Turbulence Environment. Wind tunnel entrance and floor geometries were identical to those examined by Neff and Meroney [8]. Their conclusions concerning the reasonable similarity of the tunnel boundary layer to the atmospheric boundary remain relevant. The mean wind speed profile was found to fit a logarithmic relationship between heights of 1 to 40 cm. Over a wide range of velocities (0.2 to 1.0 m/s) the surface friction coefficient, $C_f/2 = (u_*/U_{\text{ref}})^2 = 0.075$, and the surface roughness z_0 was 0.0001 m. Profiles of longitudinal turbulence intensity decay with height from values near 0.25 at the ground. Magnitudes fall off at upper levels faster than equivalent atmospheric profiles; nonetheless, turbulence levels at heights of 1 to 5 cm are comparable to empirical expressions for field measurements for scale ratios between 1:1000 to 1:2000. Turbulence spectra and integral scales measured by Neff and Meroney [8] suggest equivalent field values ranging from 100 to 150 m at a height of 10 m for model scale ratios near 1:1000. (Although the apparent scale ratio for the wind tunnel to atmospheric boundary layer at low velocities is near 1:1000, this need not severely constrain model scales for smaller scale ratio experiments with heavy plumes. Earlier dense gas plume measurements in a similar boundary layer revealed that 1:85 simulations reproduced field measurements reasonably well [7].)

3.2 Visual Appearance of the Cold Gas Plumes. For the $l_b = 5$ cm cases the plume gases moved upwind against the wind field several centimeters until they were turned back and around the main body of the plume. These gases produced a horseshoe vortex which bent downwind around the source. For the $l_b = 1$ cm situation upwind motion was minimal, but some significant initial lateral spreading still occurred. Ambient temperature Freon-air mixtures, cold nitrogen, and cold carbon dioxide plumes always remained negatively buoyant; thus, the maximum visual extent of the plume rarely exceeded $z = 3$ cm at $x = 3$ m. The stable stratification in the plumes suppressed vertical mixing, so vertical growth followed the character of a Pasquill-Gifford F category plume [9].

The cold methane plumes became positively buoyant after contact with the warm wooden wind-tunnel floor increased plume temperatures. Thus for the $l_b = 5$ cm cases the plume height grew rapidly within 20 cm of the source. Vertical growth rates appeared to approach Pasquill-Gifford A category rates (unstable atmosphere), and the cloud was 20 cm deep by $x = 3$ m. In addition the plume lofted above the floor. The vertical rise of the cloud resulted in a narrow ground-level plume width and a very dilute wispy plume. The $l_b = 1$ cm plume encountered higher wind speeds which suppressed lofting; nonetheless, vertical plume growth exceeded the heavier isothermal and cold nitrogen counterpart plumes.

3.3 Concentration Results. Heat transfer effects may be observed in the relative mixing rates of the various plumes, the resultant variation in centerline concentration with distance, ground level plume isopleths, and vertical concentration profiles. Concentration data were tabulated in terms of model values, equivalent methane values, and K (dimensionless concentration) values in Appendix D of Andriev et al. [1]. Figures 2–4 show surface centerline methane-equivalent concentrations C versus downwind distance x for selected runs. The isothermal runs 14–17 and 18–21 are essentially coincident; thus, for cases where source vertical momentum is small, buoyancy scale equality is sufficient to assure similarity. Cases where $l_b = 1$ cm also produce similar ambient temperature plume growth.

Cold plumes at $l_b = 1$ or 4 cm do not produce similar behavior. They generally arrange themselves in order of initial temperature, where a lower source temperature subsequently leads to faster dilution rates. An interesting exception is cold carbon dioxide, where the relatively small initial temperature differences from ambient levels and the large specific heat capacity ratio result in centerline concentrations slightly above any isothermal counterpart. The high specific heat capacity of carbon dioxide causes the local specific gravity to remain larger than that of an isothermal counterpart plume of equivalent dilution. This higher density slightly inhibits vertical mixing (see Fig. 3). Methane concentrations displayed in Fig. 4 do not display systematic behavior with buoyancy scale because they involve different source flow conditions. These data will be discussed later in the form of K isopleths.

Typical surface concentration isopleths are plotted in Figs. 5–7 for isothermal, cold nitrogen, and cold methane gases when $l_b = 4$ cm. On each curve the visual extent of the cloud associated with smoke or water droplets is indicated by a dashed line. Visual definition seems to fall off near molar concentrations of one percent. This figure displays upwind plume motion and rapid lateral spreading. The methane plume is comparatively quite narrow, but the concentrations reflect the effects of a buoyant plume rapidly lofting into the air. The plumes continue to grow laterally even after the hydrostatically driven spread velocity $\sqrt{g'H}$ is nearly zero. The growth rate for $x > 2$ m approaches values associated with mixing due to background ambient turbulence.

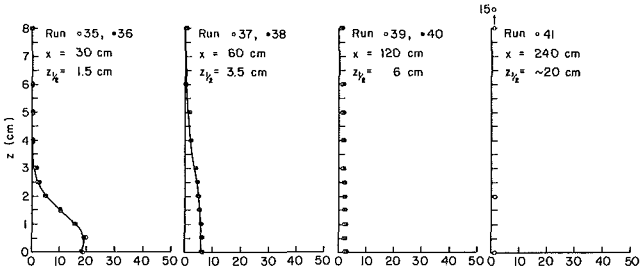

Fig. 8 Vertical concentration profiles, runs 35–41, cold methane, l_b = 2.9, Q = 130 ccs, u_* = 1.85 cm/s

Vertical concentration profiles were made at $x = 0.3$ to 2.4 m downwind of the source on plume centerline. In no case do we see that the flat, well-mixed regions within the plumes proposed by several authors result from thermal convection. Instead the profiles decay in either a Gaussian or exponential manner. The profiles reported for LNG spills at China Lake showed similar vertical behavior [2].

Cold methane plumes were released under three shear flow conditions (l_b = 1, 4, and 8). Figure 4 displays the dilution of these plumes parallel to wind surface. An alternative data presentation is provided in Fig. 8, where a dimensionless concentration $K = [T_0/T_a]\ [C/(1-C)]\ [U_R L_R^2/Q]$, suggested by Neff and Meroney [8], is plotted versus downwind distance x. This plot automatically normalizes for source variations in volume flow rate or temperature. A band of data associated with isothermal experiments falls above the methane data. Model methane plumes would produce such values if heat transfer effects were absent. The cold methane plumes dilute faster as buoyancy length scale l_b increases. Isothermal data scatter due to sampling tube wake induced turbulence during Runs 1–12. They also vary among Runs 14–17 and 18–21 due to specific gravity effects.

3.4 Temperature Results.

During the cold gas runs thermocouples monitored the gas temperatures at selected surface and elevated locations. Temperatures measured are tabulated in Appendix E of Andriev et al. [1]. Local plume temperatures are compared to local concentrations for cold methane plume in Fig. 9. Predicted variations for dry adiabatic and humid adiabatic mixing are noted. These curves are independent of any entrainment model and assume only adiabatic mixing of constant property ideal gases. Predicted

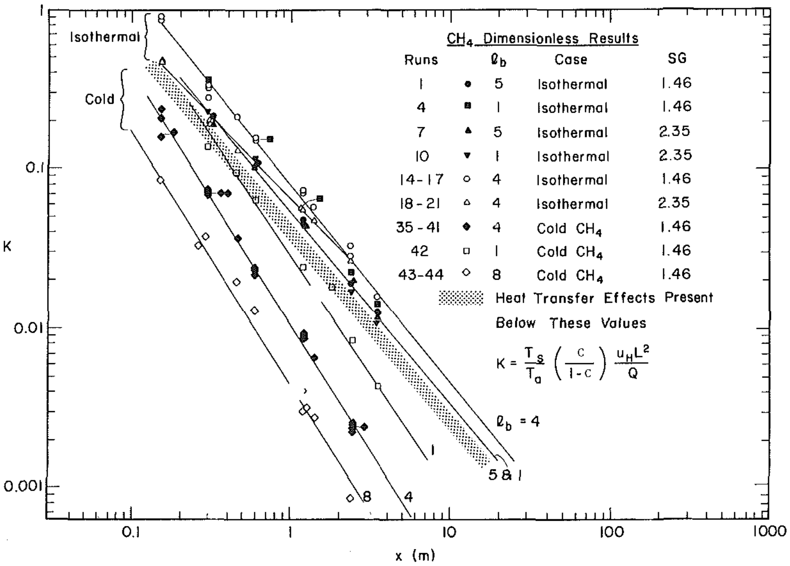

Fig. 9 Dimensionless concentration coefficient variation with distance, isothermal and methane runs; during runs 1–13 the wakes of sampling tube suspended over the cloud artificially reduced plume concentrations

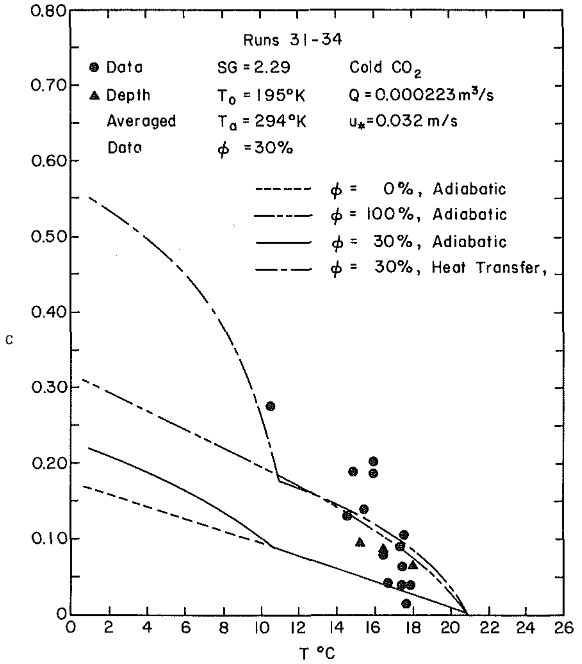

Fig. 10 Concentration against temperature measurements for vertical profile stations, runs 31-34, cold carbon dioxide, I_b = 3.9, Q = 223 ccs, u_* = 3.20 cm/s

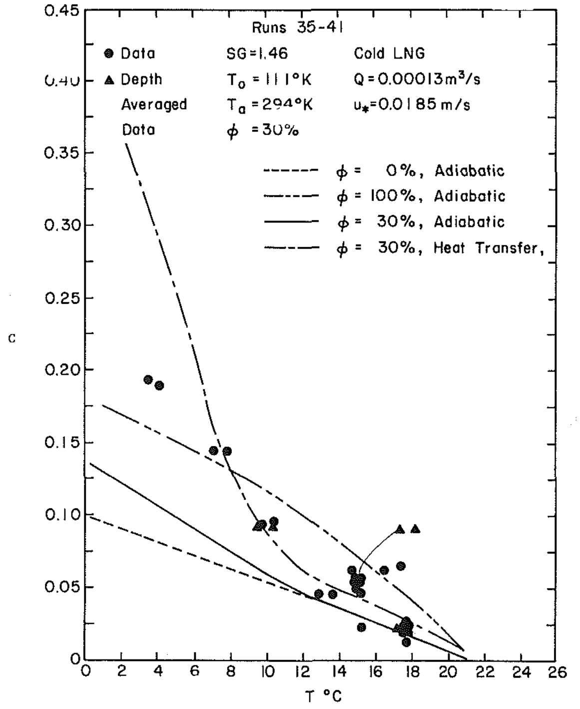

Fig. 11 Concentration against temperature measurements for vertical profile stations, runs 35-41, cold methane, I_b = 2.9, Q = 130 ccs, u_* = 1.85 cm/s

variations including heat transfer effects are provided by a simple depth-averaged numerical box model previously described in Meroney and Lohmeyer [5] and Meroney [3]. Re-evaporation of condensed water vapor results in the sudden change in slope or kinks observed on the figure. Surface heat transfer generally produces higher temperatures at lower dilution levels.

4.0 Discussion of Cold Gas Plume Behavior

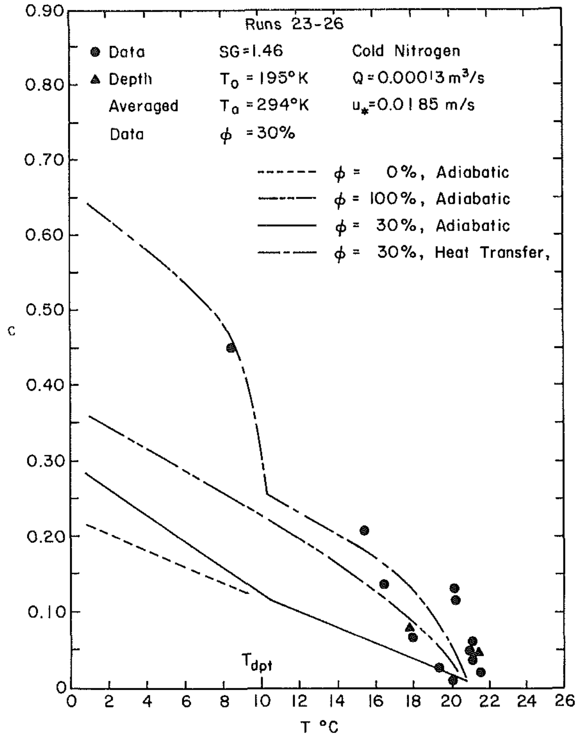

Fig. 12 Concentration against temperature measurements for vertical profile stations, runs 23-26, cold nitrogen, I_b = 4.0, Q = 130 ccs, u_* = 1.85 cm/s

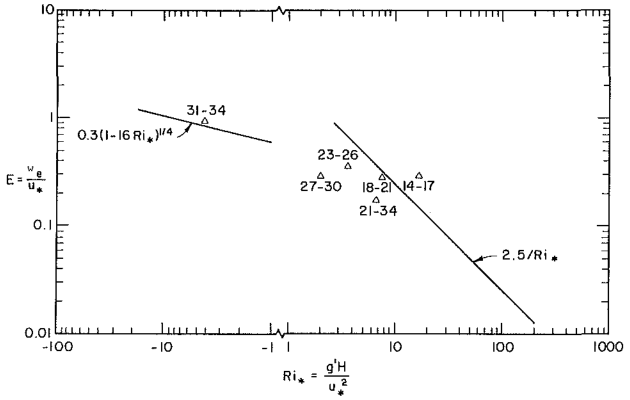

Fig. 13 Entrainment rate versus Richardson number

The number of analytic and numerical models often seems to exceed the sets of data to evaluate them. Most of these models do contain a common physical foundation, but differ on the entrainment mechanisms or constants recommended. A generalized box model was used by Andriev et al. [1] to compare such assumptions with the experimental data, and molar balances of gas species were performed across downwind cloud sections to estimate entrainment rates.

A critical element in all integral type plume models is the relationship between expected air entrainment rate and local plume stability. Most authors assume that entrainment rate behaves as $w_e/u_* = \text{const}\ \mathrm{Ri}_*^{-n}$, where the constant is of order one and n equals one. Since very few model or field data are available to estimate these coefficients for dense gas dispersion, the new cold gas data were evaluated by a molar balance analysis over successive plume sections. Entrainment velocities calculated from the molar balance are plotted versus measured local Richardson numbers in Fig. 10. The data generally fall close to expected values of const = 2.5 and n = 1; however, due to measurement and evaluation inaccuracies the scatter is large, and the sections examined did not exhibit the more interesting high Richardson number magnitudes. Picknett [11] and Meroney and Lohmeyer [6] found that dense cloud structure was also influenced by the existence of gravity waves which tend to increase mixing. Perhaps such waves explain the exhibited uncertainties in the measured entrainment rates.

5.0 Conclusions

A large data base detailing heavy gas plume temperatures and concentrations was obtained in an atmospheric boundary layer wind tunnel. Releases included ambient temperature Freon-air mixtures, cold nitrogen, cold carbon dioxide, and cold methane plumes. Heat transfer and humidity effects on model concentration distributions are significant for methane plumes when buoyancy length ratio l_b/L or surface Richardson number Ri_* are large (i.e., low wind speed and high boiloff rate conditions). Ambient temperature mixtures and heavier molecular weight cold simulants always produced higher surface concentrations than the buoyant methane plumes. At field scales heat transfer and humidity are expected to still play a role in the dispersion of methane spill cases, but plume dilution and liftoff will not be as exaggerated as for the model cases.

Cold nitrogen plumes at $l_b = 4$ cm displayed the effects of heat transfer without the complication of specific heat capacity variations between source gas and ambient air. The carbon dioxide plumes, however, required proportionately larger heat transfer to reduce the local buoyancy flux; hence, the cold carbon dioxide plumes resisted mixing even longer than the ambient temperature plume mixtures.

Cold plumes at different buoyancy scales did not display similar patterns of concentration decay. The profiles generally arranged themselves in order of initial temperature, where lower source temperatures resulted in faster dilution rates. (Note exception of carbon dioxide run due to specific heat capacity effects.)

Vertical concentration profiles decay in a Gaussian manner in the vertical for both ambient temperature and cold plumes. The cold plumes mixed vertically more rapidly, since heat transfer destroyed the negative buoyancy and permitted unstable mixing and liftoff.

Acknowledgments

The authors wish to acknowledge support from the Gas Research Institute, Chicago, IL, through Contract No. 5014-352-0203. Mr. George Andriev assisted during measurements and data analysis.

References

1 Andriev, G., Neff, D. E., and Meroney, R. N., "Heat Transfer Effects During Cold Dense Gas Dispersion," Report to Gas Research Institute GRI-83/0082, Chicago, IL, Contract No. 5014-352-0203 to Colorado State University, Fort Collins, CO, 1983.

2 Ermak, D. L., Chan, S. T., Mrogan, D. L., and Morris, L. K., "A Comparison of Dense Gas Dispersion Model Simulations With Burro Series LNG Spill Test Results," *J. Hazardous Materials*, Vol. 6, Nos. 1 & 2, 1982, pp. 129–160.

3 Meroney, R. N., "Transient Characteristics of Dense Gas Dispersion, Part I: A Depth-Averaged Numerical Model," accepted by *J. Hazardous Materials*, 1984.

4 Meroney, R. N., "Transient Characteristics of Dense Gas Dispersion, Part II: Numerical Experiments on Dense Cloud Physics," accepted by *J. Hazardous Materials*, 1984.

5 Meroney, R. N., and Lohmeyer, A., "Prediction of Propane Cloud Dispersion by a Wind-Tunnel-Data Calibrated Box Model," accepted by *J. Hazardous Materials*, 1984.

6 Meroney, R. N., and Lohmeyer, A., "Gravity Spreading and Dispersion of Dense Gas Clouds Released Suddently into a Turbulent Boundary Layer," Report to Gas Research Institute GRI-82/0025, Chicago, IL, Contract No. 5014-352-0203 to Colorado State University, Fort Collins, CO, 1982.

7 Neff, D. E., and Meroney, R. N., "The Behavior of LNG Vapor Clouds: Wind-Tunnel Simulations of 40 m^3 LNG Spill Tests at China Lake Naval Weapons Center, California," Report to Gas Research Institute GRI-80/0094, Chicago, IL, Contract No. 5014-352-0203 to Colorado State University, Fort Collins, CO, 1981.

8 Neff, D. E., and Meroney, R. N., "The Behavior of LNG Vapor Clouds: Wind-Tunnel Tests on the Modeling of Heavy Plume Dispersion," Report to Gas Research Institute GRI-80/0145, Chicago, IL, Contract No. 5014-352-0203 to Colorado State University, Fort Collins, CO, 1982.

9 Pasquill, F., *Atmospheric Diffusion*, Wiley, New York, 1974.

10 Puttock, J. S., Blackmore, D. R., and Colenbrander, G. W., "Field Experiments on Dense Gas Dispersion," *J. Hazardous Materials*, Vol. 6, Nos. 1 & 2, 1982, pp. 13–42.

11 Picknett, R. G., "Field Experiments on the Behavior of Dense Clouds," Report PTN IL 1154/78/1, Chemical Defence Establishment, Porton Down, Wilts., Contract report to the Health & Safety Exec., Sheffield, 1978.

Numerical and Experimental Study of Turbulent Heat Transfer and Fluid Flow in Longitudinal Fin Arrays

D. S. Kadle

E. M. Sparrow
Fellow ASME

Department of Mechanical Engineering,
University of Minnesota,
Minneapolis, MN 55455

Heat transfer from an array of parallel longitudinal fins to a turbulent air stream passing through the interfin spaces has been investigated both analytically/numerically and experimentally. The fins were integrally attached to a heated base plate, while the fin tips were shrouded to avoid leakage. In the analytical/numerical work, a conjugate problem was solved which encompassed turbulent flow and heat transfer in the air stream and heat conduction in the fins and in the base plate. The turbulence model and computational scheme were verified by comparison with experiment. It was found that the local heat transfer coefficients varied along the fins and along the surface of the base plate, with the lowest values in the corners formed by the fin/base plate intersections and the fin/shroud intersections. The numerically determined fin efficiencies did not differ appreciably from those calculated from the conventional pure-conduction fin model. Average Nusselt numbers, evaluated from the experimental data in conjunction with the numerically determined fin efficiencies (for derating the fin surface area), agreed well with those for fully developed heat transfer in a uniformly heated circular tube.

Introduction

Fins are the most commonly used technique for enhancing the rate of heat transfer between a surface and a flowing fluid. In general, fins are treated as a heat conduction problem, while the complex convective heat transfer and fluid mechanic processes in the flow adjacent to the fin and base surfaces have rarely been investigated. The role of convection in fin theory is confined to the introduction of an assumed spatially uniform heat transfer coefficient into the conduction analysis. The assumed uniformity of the heat transfer coefficient is known to be at odds with reality, and the magnitude of the coefficient needed to evaluate the end result of the conduction analysis is often obtained by an educated estimate.

The research described here is a fundamentals-level study of fins which deals both with fin heat conduction and with the turbulent fluid flow and convective heat transfer which occurs in the spaces between the fins. The work includes both experiments and analysis/computation, with the latter encompassing both turbulence modeling and the interactive numerical solution of the fins, the flowing fluid, and the wall to which the fins are attached. Comparisons between the experimental and numerical results are used to establish the validity of the adopted turbulence model and the numerical scheme.

A schematic diagram of the physical situation investigated in both the experimental and the analytical portions of the work is presented in Fig. 1. The figure is a cross-sectional view showing an array of parallel longitudinal fins of rectangular cross section which are integrally attached to a heated wall (hereafter referred to as the base plate). An insulated wall in contact with the fin tips serves to confine the fluid flow to the interfin spaces and, thereby, to create an array of parallel flow passages of rectangular cross section. The experiments were performed for two aspect ratios of the interfin flow passages, namely, $H/W = 3.75$ and 7.5. Air was the heat transfer fluid, and the Reynolds numbers of the airflow ranged from about 5000 to 35,000. In order to facilitate comparisons with the experimental results, the numerical solutions were carried out for the same parametric conditions.

The analytical work was performed for hydrodynamically and thermally developed conditions. The adopted turbulence model took account of the fact that the interfin flow passage was a finite-aspect-ratio rectangular duct rather than a parallel-plate channel, with the resulting velocity distribution being dependent on both cross-sectional coordinates and including corner effects. In the heat transfer portion of the analysis, the energy conservation equations for the fins, the fluid, and the heated base plate were all solved simultaneously. The fundamental nature of this type of analysis eliminates the use of the heat transfer coefficient and thus avoids the aforementioned uncertainties which are related to it. The fin, in common with the fluid and the base plate, was treated on a two-dimensional basis, in contrast to the one-dimensional approach used in the conventional heat conduction analysis of fins.

The results obtained from the combined numerical-experimental study performed here include fin efficiencies, fin temperature distributions, local Nusselt numbers at the surfaces of the fins and the base plate, overall heat transfer rates and Nusselt numbers, and friction factors. The comparisons between the experimental and numerical results will be supplemented by comparisons with literature information for ductflow Nusselt numbers and friction factors.

A survey of the published literature did not reveal any prior work which overlaps with that performed here. In [1], the turbulent flow and heat transfer processes in the fluid passing through an internally finned circular tube were solved numerically, but without simultaneous solution of the fins and the tube wall, which had been assumed to be isothermal. No experimental work was reported in [1]. In [2], a laminar flow analysis, without complementary experiments, was made of a system similar to that of Fig. 1, with the fins being treated by a one-dimensional model.

Contributed by the Heat Transfer Division for publication in the JOURNAL OF HEAT TRANSFER. Manuscript received by the Heat Transfer Division March 13, 1985.

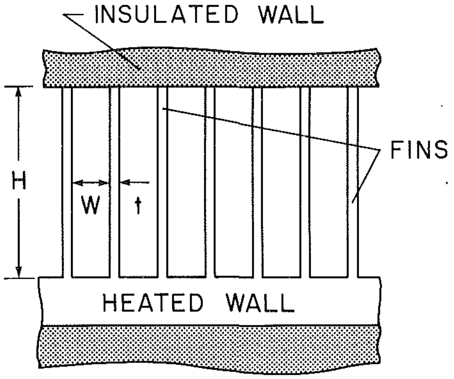

Fig. 1 Cross-sectional view of a longitudinal fin array

Analysis

The analysis is facilitated by the symmetry that is inherent in the spanwise periodicity of the fin array. Because of the periodicity, it is only necessary to consider the region between the adjacent vertical symmetry lines which respectively bisect the thickness t of the fin and the width W of the interfin region. The resulting solution domain is displayed in Figs. 2(*a*) and 2(*b*). Figure 2(*a*) conveys the dimensions relevant to the domain and the coordinates used in the analysis, while Fig. 2(*b*) illustrates the fluid and solid regions. The numerical values of the dimensions were chosen to match those of the experimental apparatus, which will be described later. Note that in Fig. 2(*b*), AB and CDE are the symmetry lines, while AE and BC are adiabatic boundaries.

In the approach to be used here, the fluid and solid regions of the solution domain will be regarded as being occupied by a single substance whose molecular and turbulent viscosities (μ and μ_t) and thermal conductivities (k and k_t) change abruptly at the fluid–solid interface (FGD in Fig. 2(*b*)). In particular, the specification $\mu = \infty$ totally suppresses motion in the solid region.[1] This approach allows the conservation laws to be expressed by differential equations (and, subsequently, by difference equations) which apply throughout the entire solution domain. Furthermore, the continuity conditions (e.g., temperature, heat flux) at the fluid–solid interface are automatically satisfied.

The first step in the analysis is to solve the velocity problem, after which the heat transfer problem is solved using the already-obtained velocity field as input.

Velocity Problem. In the fully developed regime, the inertia terms vanish, and the streamwise momentum equation for turbulent flow can be written as

$$(\partial/\partial x)[(\mu+\mu_t)(\partial w/\partial x)] + (\partial/\partial y)[(\mu+\mu_t)(\partial w/\partial y)] = dp/dz \qquad (1)$$

As already noted, μ is equal to infinity in the solid region. The major task in implementing equation (1) is the specification of the turbulent viscosity μ_t in the fluid region, taking account of the interaction of the fluid turbulence with both the long and short bounding walls (FG and GD, EF in Fig. 2(*b*)).

At any point (x, y) in the fluid region, the turbulent viscosity μ_t can be modeled as

$$\mu_t = \rho l^2[(\partial w/\partial x)^2 + (\partial w/\partial y)^2]^{1/2} \qquad (2)$$

which reduces to the conventional representation when one of the derivatives is dominant. In principle, the mixing length l at (x, y) will be influenced by all of the walls of the flow passage, but the closer the point is to one of the walls, the greater will be the effect of that wall. In particular, when (x, y) is in very close proximity to any wall, $l \cong 0$ regardless of the distance of the point from the other walls.

It is proposed to represent l as a combination of the one-dimensional mixing lengths l_x and l_y. Here, l_x will be assumed to depend on the perpendicular distance between the point (x, y) and the nearest vertical wall which, according to Fig. 2(*a*), is x itself. Similarly, l_y will depend on the distance between the point and the nearest horizontal wall, which, depending on whether the point is in the lower or upper half of the flow passage, is y or y'. Since l_x and l_y respectively increase with x and y (or y'), it follows that a reciprocal combination of l_x and l_y will yield the characteristics noted in the preceding paragraph.

In view of the foregoing, it is postulated that

$$(1/l)^m = (1/l_x)^m + (1/l_y)^m \qquad (3)$$

where the exponent m is a constant whose value will be fixed on the basis of subsequent comparisons with experimental data. The one-dimensional mixing lengths l_x and l_y will each be represented as a product of a Nikuradse-type mixing length L and the Van Driest damping factor D, so that

$$l_x = L_x D_x,\ l_y = L_y D_y \qquad (4)$$

For L_x and L_y, a direct adaptation of Nikuradse's formula for the mixing length in a circular tube ([3], p. 605) to the present rectangular geometry yields

Nomenclature

A' = surface area per unit axial length
c_p = specific heat
D = Van Driest damping factor, equation (6)
D_h = hydraulic diameter = $4HW/2(H+W)$
f = friction factor, equation (13)
H = fin height
h = average heat transfer coefficient, equation (18)
h_{loc} = local heat transfer coefficient, equation (19)
k = thermal conductivity
k_t = turbulent thermal conductivity
L = Nikuradse-type mixing length, equation (5)
l = mixing length
l_x = x-direction mixing length
l_y = y-direction mixing length
m = exponent in mixing-length superposition, equation (3)
Nu = average Nusselt number = hD_h/k
$\mathrm{Nu_{loc}}$ = local Nusselt number = $h_{\mathrm{loc}}D_h/k$
p = pressure
Q' = rate of heat transfer per unit axial length
q = local rate of heat transfer per unit area
$\bar{q}$ = average rate of heat transfer per unit area
Re = Reynolds number = $\rho\bar{w}D_h/\mu$
T = temperature
T_b = fluid bulk temperature
T_{fin} = fin temperature
T_w = temperature of base plate
t = fin thickness
W = width of flow passage
w = axial velocity
$\bar{w}$ = mean axial velocity
x, y = cross-sectional coordinates, Fig. 2(*a*)
z = axial coordinate
η = fin efficiency
μ = viscosity
μ_t = turbulent viscosity
ρ = density

---

[1] It was much more convenient to set $\mu = \infty$ than to set the velocities equal to zero in the solid region. This is because the μ values at internal grid points are inputs to the user section of the computer program, while the velocity values are not.

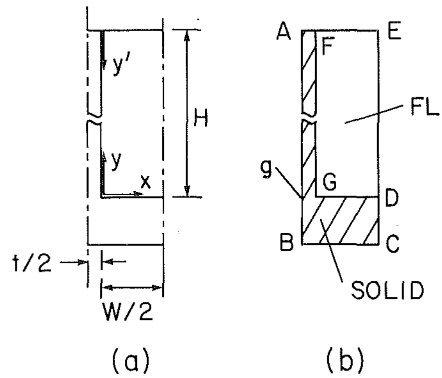

Fig. 2 Solution domain

$$L_i/L_{\mathrm{ref}} = 0.14 - 0.08(1-\eta)^2 - 0.06(1-\eta)^4 \tag{5}$$

where, for $i = x$,

$$L_{\mathrm{ref}} = W/2, \ \eta = x/(W/2) \tag{5a}$$

and for $i = y$,

$$L_{\mathrm{ref}} = H/2, \ \eta = y/(H/2) \text{ or } y'/(H/2) \tag{5b}$$

in which the first form for η is used when $0 \le y \le H/2$, while the second form is used for $H/2 < y \le H$.

The Van Driest damping factors D_x and D_y are expressed in standard form [4]

$$D_x = 1 - \exp(-x^+/A^+), \ D_y = 1 - \exp(-y^+/A^+) \tag{6}$$

The quantities x^+ and y^+ appearing in equations (6) (the so-called wall coordinates) are given by

$$x^+ = x(\tau_w\rho)^{1/2}/\mu, \ y^+ = y(\tau_w\rho)^{1/2}/\mu \text{ or } y'(\tau_w\rho)^{1/2}/\mu \tag{6a}$$

in which τ_w is the local wall shear stress corresponding to the point where the perpendicular from (x, y) intersects the wall. In particular, for the evaluation of x^+ at point (x, y), τ_w corresponds to the wall location $(0, y)$; for y^+, τ_w corresponds either to wall locations $(x, 0)$ or (x, H), respectively, when (x, y) is in the lower half of the channel or in the upper half. The damping constant A^+ was set equal to 26, which is the value most commonly found in the literature.

The foregoing discussion provides a complete specification of the turbulent viscosity μ_t needed for the solution of the streamwise momentum equation (1). The velocity boundary conditions, when specified in terms of Fig. 2(*b*), are that $w = 0$ on lines AB, BC, and EA, and that $\partial w/\partial x = 0$ on lines CD and DE.

The solution of the velocity problem was obtained numerically by adapting the elliptic finite-difference scheme of [5]. A total of 1050 grid points was deployed throughout the solution domain, 21 in the x-direction and 50 in the y-direction, with a higher concentration of points adjacent to the bounding walls of the fluid region.

The solutions were performed iteratively. At the conclusion of each cycle of the iteration, the velocity field $w(x, y)$ was known, enabling $\partial w/\partial x$ and $\partial w/\partial y$ to be evaluated at each grid point and τ_w to be evaluated locally on the bounding walls FG, GD, and EF of the flow passage. Then, by successive application of equations (6), (5), (4), and (3), the mixing length l at each grid point was determined. With l and with the aforementioned derivative values $\partial w/\partial x$ and $\partial w/\partial y$, the turbulent viscosity μ_t at each grid point followed from equation (2). The discretized form of equation (1) was then solved to yield a new distribution for $w(x, y)$, and the iterative process was continued to convergence.

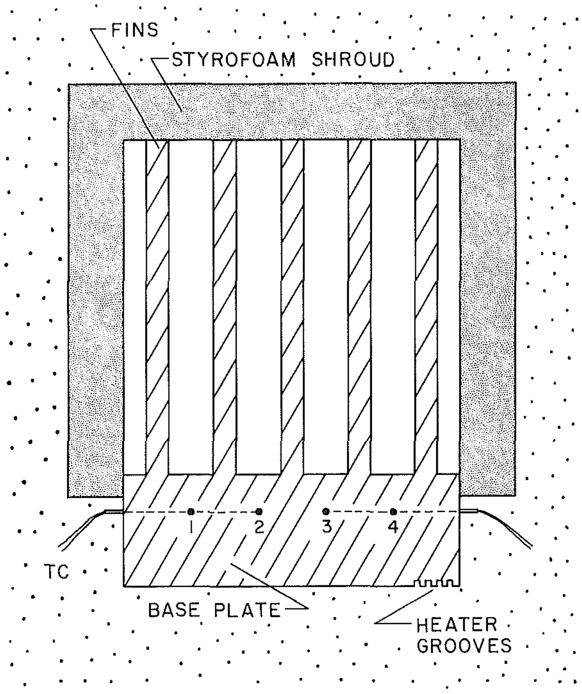

Fig. 3 Cross-sectional view of one of the test sections

In addition to the velocity field needed as input to the heat transfer problem, the solution of equation (1) yielded results for the friction factor which will be presented later and compared with literature information. The velocity solutions, the friction factors, and the subsequent heat transfer results were parameterized by the conventional rectangular-duct Reynolds number Re

$$\mathrm{Re} = \rho\bar{w}D_h/\mu \tag{7}$$

where D_h is the hydraulic diameter

$$D_h = 4HW/2(H+W) \tag{8}$$

Heat Transfer Problem. The conservation of energy principle can be expressed by the same differential equation in both the fluid and solid regions of the solution domain

$$(\partial/\partial x)[(k+k_t)(\partial T/\partial x)] + (\partial/\partial y)[(k+k_t)(\partial T/\partial y)] = \rho c_p w(\partial T/\partial z) \tag{9}$$

where k_t is the turbulent conductivity. A relation between k_t and μ_t is provided by the turbulent Prandtl number Pr_t

$$k_t = (c_p/\mathrm{Pr}_t)\mu_t \tag{10}$$

The widely used value of 0.9 for Pr_t will also be employed here.

In the solid region of the solution domain, the velocity field solution automatically yields $w = 0$ and $\mu_t = 0$ (so that $k_t = 0$), which reduces (9) to a heat conduction equation. Therefore, the only special attention that need be given to the solid is to set

$$k = k_{\mathrm{solid}} \tag{11}$$

As noted earlier, consideration is given here to the thermally developed regime. Thermal development was attained in the experimental portion of the work in the presence of a uniform rate of heat addition per unit axial length, and the same heating condition will be used in the analysis. In this regard, let Q'_{sd} denote the rate at which heat is added per unit axial length to the solution domain shown in Fig. 2. Then, from an energy balance and noting that $\partial T/\partial z = dT_b/dz$ (T_b = bulk temperature) in the thermally developed regime, it follows that

$$\partial T/\partial z = Q'_{sd}/\rho c_p \bar{w}(HW/2) \tag{12}$$

which enables $\partial T/\partial z$ to be eliminated from the right-hand side of equation (9).

With the information conveyed by equations (10)–(12) and with the availability of the velocity distribution, the energy equation (9) is ready for numerical solution, pending specification of the thermal boundary conditions.

Two sets of boundary conditions were employed. The first set was chosen to closely correspond to the conditions of the experiments, while the second set was more idealized in order to better relate to conventional fin models.

With regard to the first set of boundary conditions, it may be noted that in the experimental apparatus, fine-diameter electrical resistance wires were embedded in closely spaced longitudinal grooves that had been milled into the lower face of the heated wall. This arrangement provided a spanwise-uniform heat flux along the lower face of the wall. Furthermore, the lower face of the wall was very well insulated. For the analysis, these conditions were modeled by making BC in Fig. 2(*b*) an adiabatic surface (i.e., $\partial T/\partial y = 0$) and by introducing a heat source into each finite-difference control volume situated in the row of control volumes sitting atop BC. The source strengths were adjusted to give a spanwise uniform heat input and a total rate of heat addition equal to Q'_{sd}.

In addition, in the experimental apparatus, the wall which closed the flow passage at the fin tips was made of an insulating material which, in turn, was backed by a powder insulation. For the analysis, this was reflected by $\partial T/\partial y = 0$ along the line AE. The other boundaries of the solution domain, AB and CDE, are symmetry lines, at which the appropriate boundary condition is $\partial T/\partial x = 0$.

For the second set of boundary conditions, the zero derivative specification for the lines AE, AB, and CDE continues in force. However, the line gGD is now assigned a spanwise-uniform temperature T_w. This corresponds to the textbook model of fins attached to an isothermal base surface. When the temperature on line gGD is assigned, the solid region gBCDGg no longer plays a role in the heat transfer processes in the fin and in the flow passage.

The solutions of the energy equation were obtained iteratively. These solutions yielded fin efficiencies, fin temperature distributions, local Nusselt numbers along the fin and the base surface, and overall heat transfer/temperature difference characteristics. These results will be presented later, where they will be compared, wherever possible, with data from the present experiments and with the literature.

Experimental Apparatus

Test Section. The description of the experimental apparatus is facilitated by reference to Fig. 3, which is a cross-sectional view of one of the two test section configurations used during the course of the research. As seen there, the test section consisted of an array of parallel longitudinal fins, a heated base plate, and a shroud.

The fins were integral with the base plate, made of aluminum because of its high thermal conductivity, easy machinability, and low radiative emissivity. The fin/base plate assembly was fabricated by milling longitudinal grooves (i.e., the interfin gaps) into one of the faces of a long rectangular bar whose external dimensions, 3.81 × 5.08 × 50.8 cm, had been established by prior machining operations. Special techniques were used to ensure that the fins were straight and parallel and that warping did not occur as the successive interfin gaps were cut [6]. Shallow grooves were also milled into the rear face of the bar to accommodate electrical resistance wire which served to heat the test section. The heater wire grooves were anodized to provide a thin insulating layer which functioned as a second line of defense against possible shorts between the thinly clad wire and the aluminum.

The closure of the interfin flow passages was accomplished by the use of an inverted-U-shaped shroud which was attached to the fin/base plate assembly at the outboard edges of the base plate. In selecting the shroud material, the main considerations were to minimize extraneous heat conduction from the base plate through the shroud and to maintain close dimensional tolerances. The low thermal conductivity and the structural stiffness required to fulfill these objectives are inherent properties of closed-pore, extruded polystyrene insulation (Styrofoam). Furthermore, Styrofoam can be machined to close tolerances and with a smooth surface finish. To guarantee hydrodynamic smoothness, the Styrofoam surfaces which interfaced with the airflow were covered with plasticized, self-adhering contact paper (the contact paper was applied after the surfaces were sealed to ensure impermeability). The shroud was fixed in place against the respective outboard edges of the base plate by silicone rubber, which also served to prevent leakage.

As can be seen in Fig. 3, there was a total of five fins. The interfin spaces formed four parallel flow passages, flanked at either side by a passage bounded by the outboard fin and the adjacent shroud wall. Note that the shroud-adjacent passages are half as wide as the interior passages. This arrangement was employed to more closely model an infinite array of fins.

Figure 3 is to scale, and the key test section dimensions are (in cm):

flow passage width $W = 0.508$
fin thickness $t = 0.254$
fin height $H = 1.905$ and 3.810
thickness of base plate = 1.27
thickness of shroud = 0.635
streamwise length of test section = 50.8

Note that two distinct fin heights, $H = 1.905$ and 3.810 cm, were used in the experiments, giving rise to the two test section configurations alluded to earlier. The configuration pictured in Fig. 3 corresponds to the $H = 3.810$ cm fin height. Once the experiments for this configuration had been completed, the fin height was reduced to 1.905 cm by a milling operation, with special techniques used to maintain straightness and parallelism. A new shroud suitable for the shorter fins was also fabricated.

From the foregoing dimension list, it is also seen that the streamwise length of the test section is 100 times the channel width. This length was chosen to ensure the attainment of the thermally developed regime. In the actual experiments, thermally developed conditions prevailed along a substantial portion of the test section.

Other Apparatus Components. The test section was preceded by a hydrodynamic development section and followed by an exit length. Both of these were rectangular ducts fabricated from insulating materials in order to minimize extraneous axial conduction losses from the test section.

The development section, the test section, and the exit length were all situated within a large, closed, wooden-walled container (52.5 × 52.5 cm in cross section and 91.5 cm long) filled with silica aerogel powder insulation. The thermal conductivity of the aerogel is 20 percent smaller than that of air. As a further defense against extraneous losses, the aforementioned components were suspended in the insulation enclosure by nylon lines instead of being supported by rigid structural members. A finite-difference analysis of the conduction heat losses through the insulation demonstrated that they were entirely negligible [6]. Owing to the large volume of the insulation, about 8–10 hr was required to attain steady-state conditions during a data run.

The experimental apparatus was operated in the open-circuit mode and in suction. Air from the laboratory room

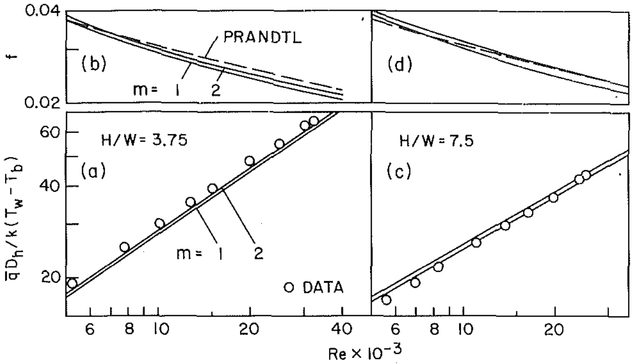

Fig. 4 Comparisons of numerical and experimental heat transfer and friction factor results

was drawn through a flowmeter (a calibrated rotameter) into a plenum chamber, from which it passed successively through the hydrodynamic development length, the heated test section, and the exit length. From there, the air entered a circular pipe which contained a control valve and terminated at the blower inlet. The hot discharge from the blower was ducted out of the building.

Heating Arrangement and Instrumentation. As was mentioned earlier and illustrated in Fig. 3, shallow, closely spaced, longitudinal grooves were milled into the lower surface of the base plate. All told, there were 33 such grooves uniformly deployed across the 3.81 cm width of the plate. The heating circuit was subdivided into three independently controlled sections. One was the main heater, the wiring for which occupied the central 23 grooves. The main heater was flanked on each side by a guard heater, each occupying five grooves. The guards provided a means to compensate for possible end effects associated with the finiteness of the array.

Fine-gage, Teflon-clad thermocouple wire was used as the resistance wire for the winding of the heaters. Power was supplied by a regulated a-c source, with an individual autotransformer to control the voltage for each circuit. The heater voltage drops and the associated shunt voltage drops (which yielded the heater currents) were measured with a true rms voltmeter.

The voltage settings for the heaters were guided by the test section thermocouples. There were 52 such thermocouples, two in each of 26 cross sections. The thermocouple installation in a typical cross section is illustrated in Fig. 3. As seen there, the thermocouples were brought in from the sides, and the lead wires were laid along the dashed lines, which were expected to be (and were) isothermal. In any cross section, the junctions were positioned either at points 1 and 3 or at points 2 and 4. The 1-3 and 2-4 positioning alternated in consecutive cross sections. The thermocouples were made from 30-gage, Teflon-coated, chromel and constantan wire which had been calibrated specifically for these experiments.

During the course of the experiments, it was found that if the heater voltages were set so as to achieve a spanwise uniform heat input, the two thermocouples in each cross section read the same to within the 1 μV resolving power of the instrumentation. This indicates that any end effects were too small to be detected.

To facilitate the determination of the bulk temperature, measurements were made of the temperature of the air entering the test section. To this end, three thermocouples were installed in the air stream in the hydrodynamic development duct just upstream of the test section inlet. During any data run, the three thermocouples indicated the same value.

The test section and inlet-bulk thermocouples were read and recorded by a programmable data logger with a 1 μV resolution.

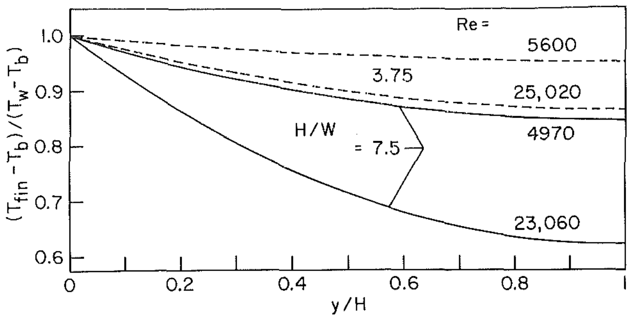

Fig. 5 Fin temperature distributions

Results and Discussion

Numerical-Experimental Comparisons. Comparisons of fully developed heat transfer and friction factor results from the numerical solutions with corresponding experimental results are made in Fig. 4. The figure includes four graphs, of which (*a*) and (*b*) pertain to the $H/W = 3.75$ fin configuration while (*c*) and (*d*) are for the $H/W = 7.5$ configuration. The two graphs for each configuration are stacked one above the other, with the friction factor plotted in the upper and the heat transfer plotted in the lower.

The friction factor results presented in the figure correspond to the conventional definition

$$f = (-dp/dz)D_h/\tfrac{1}{2}\rho\bar{w}^2 \tag{13}$$

In the plotted heat transfer group, $\bar{q}$ is the average rate of heat transfer per unit surface area of the fins and the base plate, T_w is the base plate temperature, and T_b is the bulk temperature of the air. Note that in the evaluation of the heat transfer group using the numerical solutions, T_w was taken at the grid point which corresponds to the thermocouple location in the experiments. The geometry and the thermal boundary conditions for the computations and for the experiments were identical.

The solid lines labeled $m = 1$ and 2 in the figure respectively represent the predictions from the numerical solutions which correspond to the indicated values of the exponent m in the mixing length superposition (3). Results corresponding to $m > 2$ were hardly distinguishable from those for $m = 2$. The exponent m was the only adjusted parameter in the turbulence model.

The numerically determined friction factors will be compared with those of the Prandtl equation

$$f^{-1/2} = 2\log(f^{1/2}\mathrm{Re}) - 0.8 \tag{14}$$

which is the most widely accepted experimental correlation. As seen in Figs. 4(*b*) and 4(*d*), the deviations between the f values coresponding to $m = 2$ and those from the Prandtl equation are less than four percent for Re ≥ 10,000, where the flow is fully turbulent and where, therefore, the turbulence model can be fairly tested. For the smaller aspect ratio ($H/W = 3.75$), equally good agreement continues to prevail to the lowest investigated Reynolds number (Re = 5000), while for the larger aspect ratio ($H/W = 7.5$), slightly greater deviations occur as the Reynolds number decreases. The agreement between the f values corresponding to $m = 1$ and the Prandtl f values is almost as good as the aforementioned agreement for the $m = 2$ results.

The heat transfer predictions from the numerical solutions are compared with the present experimental results in Figs. 4(*a*) and 4(*c*). The qualitative outcome of the comparison is very similar to that for the friction factor results. For Re ≥ 10,000, the deviations between the data and the $m = 2$ predictions do not exceed five percent, a level of agreement which persists over the entire Reynolds number range for $H/W = 3.75$. With the data as a standard, the $m = 2$

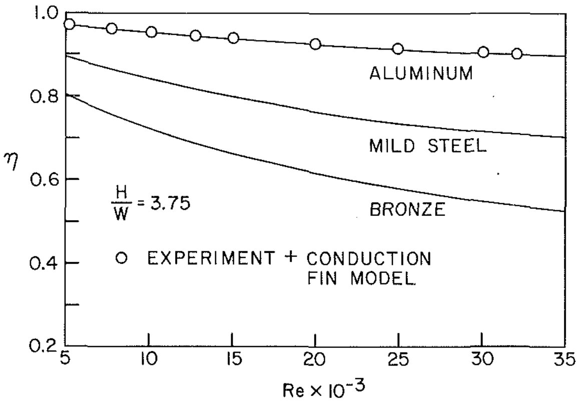

Fig. 6 Fin efficiencies, $H/W = 3.75$

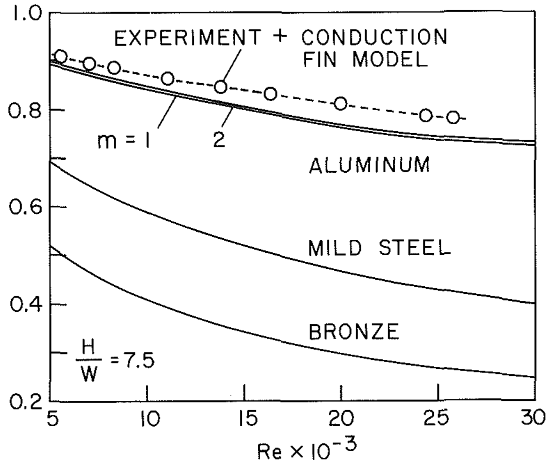

Fig. 7 Fin efficiencies, $H/W = 7.5$

predictions are slightly better than the $m = 1$ predictions for the $H/W = 3.75$ aspect ratio, with the opposite relation for the $H/W = 7.5$ aspect ratio. Over all, the $m = 2$ predictions appear slightly better.

If account is taken of the general quality level of analytical/numerical turbulent heat transfer predictions, the comparisons conveyed in Fig. 4 lend strong support to the utility of the turbulence model used here as a tool for providing results suitable for applications. The friction factor comparisons are also strongly supportive. Since the $m = 2$ exponent in the mixing length superposition appears to yield results that agree best with those of experiment, it will be used as the basis for all the subsequent numerical results to be presented here.

Fin Temperature Distributions and Efficiencies. The standard approach for dealing with the base-to-tip temperature drop along a fin is to use the efficiency η to derate the fin surface area. Fin efficiencies will be evaluated here from the numerical solutions, but first, representative fin temperature distributions will be displayed to provide perspective for the subsequent presentation of the efficiency results.

To give greater generality to the results, the numerical solutions were performed for thermal boundary conditions which are less closely tied to the experiments than those used for the numerical results of Fig. 4. The uniform heat addition per unit axial length was retained as before, but now, the surface temperature of the base plate is assigned to be uniform in each cross section. This condition was already alluded to earlier and, with regard to Fig. 2(*b*), it corresponds to temperature uniformity along the line gGD.

Figure 5 conveys the numerically determined fin temperature distributions, which are plotted in the ratio form $(T_{\text{fin}} - T_b)/(T_w - T_b)$ as a function of the dimensionless distance y/H along the fin (the y coordinate is illustrated in Fig. 2(*a*)). In the ratio, T_{fin} is the fin temperature at y/H, T_w is the uniform surface temperature of the base plate, and T_b is the bulk temperature of the air in the flow passage. With regard to T_{fin}, it is relevant to note that the temperature variations across the thickness of the fin were much too small to be represented in Fig. 5.

The dashed and solid lines in the figure correspond respectively to the $H/W = 3.75$ and 7.5 fin configurations. For each configuration, results are presented for a low and a moderately high Reynolds number. The fins are of aluminum (204 W/m – °C) with a thickness t equal to $\frac{1}{2}W$, as in the experiments.

The dropoff of the temperature along the fin is seen to be quite regular, with the rate of decrease becoming more gradual with increasing distance from the base. The extent of the fin temperature drop increases with both the fin height, as expressed by H/W, and the Reynolds number. For $\text{Re} \cong 23{,}000$ and $H/W = 7.5$ ($H/t = 15$), which is by no means an extreme case, the tip value of $(T_{\text{fin}} - T_b)/(T_w - T_b) \cong 0.62$, which reflects a substantial temperature drop.

The greater the base-to-tip temperature drop, the lower is the fin efficiency. Fin efficiencies were evaluated from the numerical solutions in accordance with the standard definition

$$\eta = Q_f'/Q_{f,\text{ideal}}' \tag{15}$$

where Q_f' and $Q_{f,\text{ideal}}'$ denote fin heat transfer rates per unit axial length. Q_f' and $Q_{f,\text{ideal}}'$ differ in that the former corresponds to the actual fin thermal conductivity, while the latter is for infinite thermal conductivity. Accordingly, to evaluate equation (15), separate numerical solutions were carried out to obtain Q_f' and $Q_{f,\text{ideal}}'$. Note also that in the definition of η, both Q_f' and $Q_{f,\text{ideal}}'$ correspond to the same value of $(T_w - T_b)$. The implementation of this condition is described in [6].

The η values determined from equation (15) are plotted as a function of the Reynolds number in Figs. 6 and 7, respectively, for the $H/W = 3.75$ and 7.5 fin configurations. In each figure, the primary results for aluminum (204 W/m – °C) are supplemented by results for lesser conducting metals to illustrate the sensitivity of the efficiency to the fin thermal conductivity. The supplementary results correspond to mild steel and bronze (respectively, 54 and 26 W/m – °C).

From the figures, it is seen that the efficiency decreases with the Reynolds number, reflecting the Reynolds-number-related increase in the heat transfer coefficient. The rate at which η drops off with Re is markedly accentuated with increasing fin height and with decreasing fin thermal conductivity. Special care (i.e., materials selection, fin height) is, therefore, required in the design of fins for use at higher Reynolds numbers.

For the aluminum fins employed in the present experiments, the efficiency for the $H/W = 3.75$ configuration varied from 0.97 to 0.90 over the investigated Reynolds number range, with a corresponding variation from 0.91 to 0.78 for the $H/W = 7.5$ configuration. The superposition exponent m (= 1 or 2) of equation (3) had no discernible effect on η in Fig. 6 and only a slight effect in Fig. 7, as documented there.

It is relevant to compare these efficiency results with those from the conventional pure-conduction fin model. For the latter, from any heat transfer textbook,

$$\eta = [\tanh(\lambda H)]/\lambda H \tag{16}$$

where

$$\lambda = (2h/k_{\text{fin}}t)^{1/2} \tag{17}$$

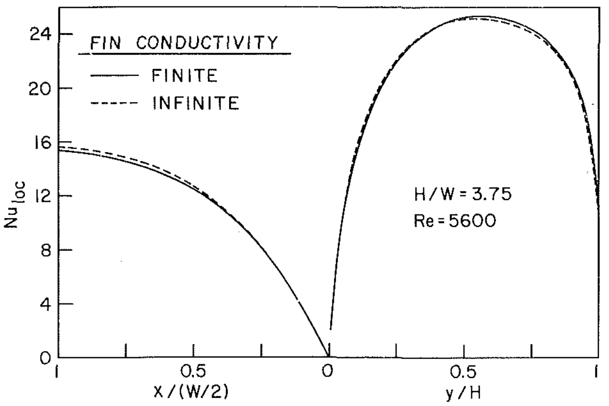

Fig. 8 Local Nusselt number distributions along a fin and along the base plate, H/W = 3.75, Re = 5600

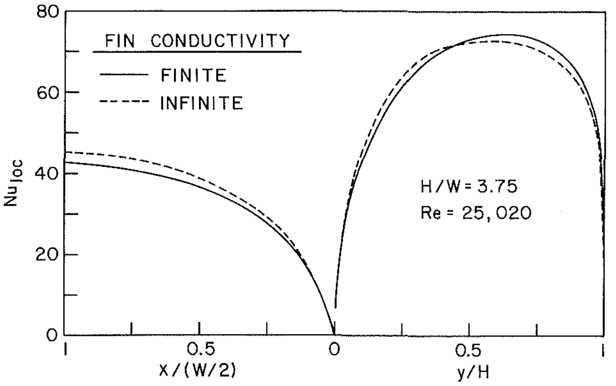

Fig. 9 Local Nusselt number distributions along a fin and along the base plate, H/W = 3.75, Re = 25,020

To avoid the uncertainties inherent in using handbook or textbook values of h as input to equation (17), they were determined iteratively from the experimental data.

To this end, h was expressed as

$$h = Q' / (A'_{bp} + \eta A'_f)(T_w - T_b) \tag{18}$$

which is a standard equation in the design of finned heat exchangers. Here, A'_{bp} and A'_f are, respectively, the base plate and fin surface areas per unit axial length. Then, with $\eta = 1$, the experimental data were used to evaluate h from equation (18). This h value enabled η to be calculated from equations (17) and (16), and, in turn, the η value was introduced into equation (18) along with the data to find a new h. This process was continued until convergence, yielding both h and η.

The thus-determined η values are plotted as the circle data symbols in Figs. 6 and 7. For the shorter fins (Fig. 6), the η values from the conduction model are in virtually precise agreement with those from the numerical solutions, whereas for the longer fins (Fig. 7), the greatest deviation is 0.74 versus 0.78. In view of the gross assumptions embodied in the pure conduction model, the quality of its predictions, relative to those of the numerical solutions, is remarkable. Evidently, the averaging which is inherent in the efficiency has mitigated the effects of the simplifying assumptions.

Local Nusselt Number Distributions. Local heat transfer coefficients h_{loc} were evaluated from the numerical solutions as a function of position along the fin and along the surface of the base plate, where

$$h_{loc,fin} = q(y) / [T_{fin}(y) - T_b], \quad h_{loc,bp} = q(x) / (T_w - T_b) \tag{19}$$

These local coefficients were recast in dimensionless form as

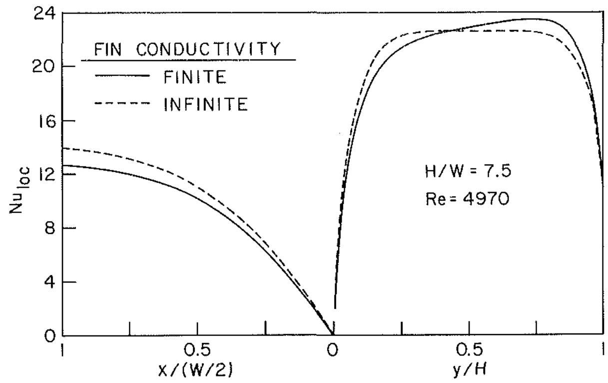

Fig. 10 Local Nusselt number distributions along a fin and along the base plate, H/W = 7.5, Re = 4970

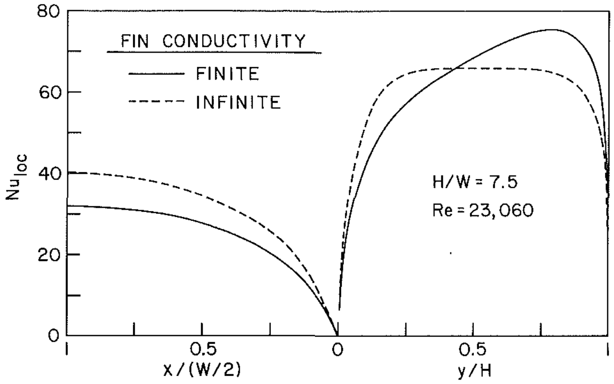

Fig. 11 Local Nusselt number distributions along a fin and along the base plate, H/W = 7.5, Re = 23,060

$$\mathrm{Nu}_{loc} = h_{loc} D_h / k \tag{20}$$

and plotted in Figs. 8-11. The first two figures are for the H/W = 3.75 fin configuration, respectively, for Re = 5600 and 25,020, while the last two are for H/W = 7.5 with Re = 4970 and 23,060. These are the same H/W, Re combinations for which fin temperature distributions were presented in Fig. 5.

The Nu_{loc} results for the fin are plotted in the right-hand half of each figure, extending over the abscissa range from $y/H = 0$ to 1, while the Nu_{loc} for the base plate are plotted in the left half over the abscissa range from $x/(W/2) = 0$ to 1. Note that the point $x/(W/2) = 0$, $y/H = 0$ on the abscissa corresponds to the point of intersection of the fin and the base plate (see Fig. 2(*a*) for coordinates).

The solid and dashed lines in each figure respectively convey results for aluminum fins (finite conductivity) and for ideal fins having infinite conductivity. For the latter, the fin temperature is uniform and equal to the base temperature T_w.

An overall inspection of the figures reveals a pattern in the variation of the fin heat transfer coefficient that is common to all the investigated cases; similarly, the base-plate heat transfer coefficients also display a common pattern. For the fin, the coefficient, which is virtually zero at the intersection of the fin and the base plate, rises sharply at small distances from the base and then more slowly as it approaches a maximum. After the maximum, the coefficient begins to decrease – a dropoff which becomes very sharp in the neighborhood of the intersection of the fin tip and the shroud wall. In the central region of the fin, the coefficient is relatively uniform, especially for the longer fins (H/W = 7.5).

The general shape of the distribution of the fin heat transfer coefficient reflects the shape of the velocity distribution, with

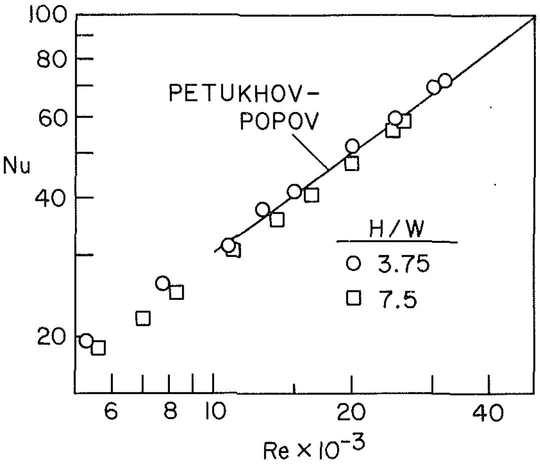

Fig. 12 Average Nusselt numbers

temperature effects being responsible for specific details. For example, the fact that the coefficient at the intersection of the fin and the base plate is different from that at the intersection of the fin and the shroud is due to the different heating conditions at the two corners. In particular, for the former, the heating at the two walls which form the corner gives rise to local temperature saturation which, in turn, is responsible for the $h_{loc} \cong 0$ result. Also, the different degrees of symmetry of the distributions corresponding to the infinite- and finite-conductivity fins can be rationalized in terms of the degree of uniformity of the fin temperature distribution.

The base-plate heat transfer coefficient is also virtually zero at the corner where the fin and the base plate intersect. The coefficient increases smoothly along the base plate in the direction away from the corner, attaining a maximum at the interfin midpoint, $x/(W/2) = 1$.

As seen in the figures, the results for the infinite- and finite-conductivity-fin cases are not very different, especially for the shorter ($H/W = 3.75$) fins. Of particular note is the fact that the heat transfer coefficients for the base plate respond to differences in the fin thermal conductivity. This response is a result of changes in the temperature distribution in the air flow which accompany the changes in fin conductivity.

Average Nusselt Numbers. By complementary use of the experimental and numerical results, average Nusselt numbers were evaluated for comparison with standard literature information. First, average heat transfer coefficients were found from equation (18) using values of Q', T_w, and T_b from the experiments in conjunction with the numerically determined η values. These average coefficients were then recast in terms of

$$\mathrm{Nu} = hD_h/k \qquad (21)$$

and plotted in Fig. 12. The solid line in the figure represents the widely used Petukhov-Popov equation (e.g., [7], equations (6-7) and (6-8) with $n = 0$) for fully developed turbulent flow in a uniformly heated circular tube for $\mathrm{Re} \geq 10{,}000$.

The specified accuracy of the Petukhov-Popov equation is ±6 percent, and all of the data fall within that band. This level of agreement is noteworthy, not only because of differences in flow passage geometry (circular tube versus rectangular duct), but also because of differences in the thermal boundary conditions (circumferential uniform versus circumferential nonuniform wall temperature). The good agreement suggests that the hydraulic diameter adequately rationalizes the geometry issue and that the fin efficiency resolves the issue of the circumferential temperature variation.

Concluding Remarks

Fully developed heat transfer from a longitudinally finned base plate to a turbulent air stream passing through the interfin spaces has been investigated here both analytically/numerically and experimentally. In the analytical/numerical work, a conjugate problem was solved which encompassed turbulent flow and heat transfer in the air stream and heat conduction in the fins and in the base plate. The turbulence model and the numerical scheme were shown to be valid by comparisons with heat transfer data measured here and with friction factors from the literature.

In addition, the computations yielded fin temperature distributions, fin efficiencies, and distributions of the local Nusselt numbers along the fins and along the base surface. The efficiency results were compared with those given by the conventional pure-conduction fin model and, despite the simplifying assumptions inherent in that model, good agreement was found to prevail. This suggests that the averaging inherent in the efficiency mitigates the effects of the simplifying assumptions.

The local heat transfer coefficient was found to vary along the fins and along the surface of the base plate. In particular, low values were found to prevail in the corners formed by the intersection of a fin with the base plate and by the intersection of the fin tip and a shroud wall.

Average heat transfer coefficients, evaluated from the experimental data in conjunction with the numerically determined fin efficiencies, agreed well with the standard literature correlation for fully developed heat transfer in a uniformly heated circular tube. The good agreement suggests that the hydraulic diameter effectively rationalizes the differences in flow passage geometry (circular tube versus rectangular duct) and that the fin efficiency resolves differences in the thermal boundary conditions (circumferential uniform versus circumferential nonuniform wall temperature).

References

1 Patankar, S. V., Ivanovic, M., and Sparrow, E. M., "Analysis of Turbulent Flow and Heat Transfer in Internally Finned Tubes and Annuli," ASME Journal of Heat Transfer, Vol. 101, 1979, pp. 29-37.

2 Sparrow, E. M., Baliga, B. R., and Patankar, S. V., "Forced Convection Heat Transfer From a Shrouded Fin Array With and Without Tip Clearance," ASME Journal of Heat Transfer, Vol. 100, 1978, pp. 572-579.

3 Schlichting, H., *Boundary Layer Theory*, 7th edn., McGraw-Hill, New York, 1979.

4 Van Driest, E. R., "On Turbulent Flow Near a Wall," *Journal of the Aeronautical Sciences*, Vol. 23, 1956, pp. 1007-1011.

5 Patankar, S. V., *Numerical Heat Transfer and Fluid Flow*, Hemisphere, Washington, 1980.

6 Kadle, D. S., "Effect of Tip Clearance on Turbulent Heat Transfer From a Shrouded, Longitudinal Fin Array," Ph.D. thesis, Department of Mechanical Engineering, University of Minnesota, Minneapolis, MN, 1984.

7 Holman, J. P., *Heat Transfer*, 5th edn., McGraw-Hill, New York, 1981.

B. R. Baliga
Associate Professor.
Mem. ASME

R. R. Azrak
Former Graduate Student.

Department of Mechanical Engineering,
McGill University,
Montreal, Quebec H3A 2K6, Canada

Laminar Fully Developed Flow and Heat Transfer in Triangular Plate-Fin Ducts

This paper presents a numerical investigation of fully developed flow and heat transfer in triangular cross section plate-fin ducts encountered in compact heat exchangers. Heat conduction in the fin and convection in the fluid are analyzed simultaneously as a conjugate problem. Overall and local results are presented for representative values of the duct aspect ratio and a fin conductance parameter.

Introduction

Compact heat exchangers are characterized by a high ratio of heat transfer area to core volume, usually in excess of 700 m^2/m^3 [1]. Fins are commonly used between the plates in such heat exchangers to increase their compactness, and this practice often results in plate-fin flow passages of triangular cross section, as shown in Fig. 1. The heat transfer problem posed by such plate-fin ducts requires a simultaneous analysis of conduction in the fin and forced convection in the flow passage [2]. A numerical investigation of this conjugate problem is presented in this paper.

The plate-fin passages encountered in compact heat exchangers usually have small hydraulic diameters. This results in high area densities and high heat transfer coefficients, and the Reynolds number range for such passages, particularly for gases, usually falls well within the laminar flow regime [2]. Furthermore, with highly compact continuous plate-fin passages, such as those encountered in vehicular gas turbines, fully developed conditions can prevail over a substantial portion of the flow length [2]. In this paper, attention is limited to laminar fully developed flow and heat transfer in triangular plate-fin passages.

Laminar fully developed flow and heat transfer in ducts of triangular cross section have been analyzed by Kays [3], Schmidt and Newell [4], Nakamura et al. [5], Sparrow and Haji-Sheikh [6], Shah [7], Schneider and LeDain [8], and others. A comprehensive review of many of these investigations is available in a monograph by Shah and London [2]. The results of these investigations are useful in the design of plate-fin ducts, but they are strictly applicable only to fins of very high, or infinite, thermal conductance. In this investigation, fins of finite thermal conductance are considered. Thus the results presented in this paper complement and extend those in [2-8].

The importance of solving the conjugate problem in the analysis of heat transfer in finned ducts has been discussed by Shah and London [2], and demonstrated by Sparrow et al. [9] and Soliman et al. [10]. The mathematical model of the conjugate plate-fin duct problem presented in this paper is similar to that proposed in [9]. It is assumed in this model that longitudinal heat conduction (in the flow direction) is negligible in the plates, fins, and fluid. The influence of longitudinal conduction in a heat exchanger is to reduce its effectiveness for a given number of transfer units [1]. This reduction may be quite serious in heat exchangers with short flow lengths, but it is not expected to be serious in the fully developed flow regime analyzed in this paper. An analysis of this effect is available in [1].

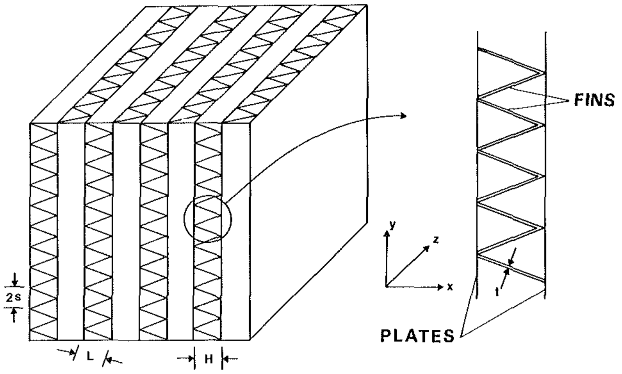

Fig. 1 Triangular plate-fin ducts encountered in compact heat exchangers

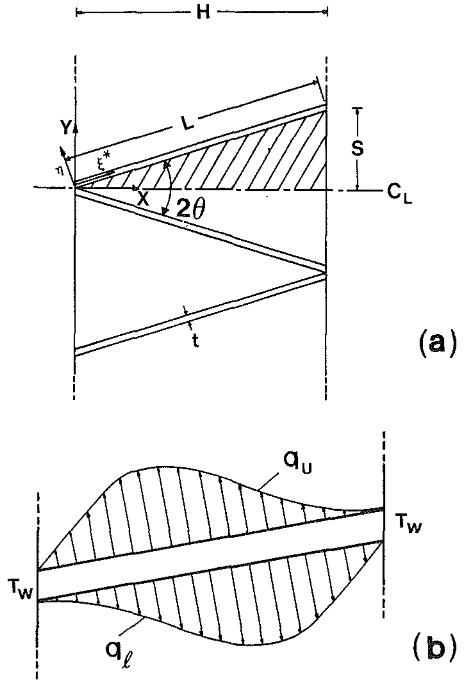

Fig. 2(*a*) Typical plate-fin duct cross section, showing the calculation domain and related nomenclature; (*b*) skew-symmetric heat flux distributions on the upper and lower fin-fluid interfaces

Spatially averaged, or overall, and local results are presented in this paper. The overall results include friction factor–Reynolds number products and mean Nusselt numbers. The local results include velocity distribution in the fluid, and temperature and heat flux distributions along the plates and fins. The results depend on the duct aspect ratio and a fin conductance parameter. These parameters are assigned values that are representative of triangular plate-fin ducts commonly encountered in compact heat exchangers.

Contributed by the Heat Transfer Division for publication in the JOURNAL OF HEAT TRANSFER. Manuscript received by the Heat Transfer Division May 9, 1984. Paper No. 84-HT-55.

Problem Formulation

In a majority of compact heat exchangers, the plate-fin flow passages are very small compared to the overall core dimensions [1, 2]. In this analysis, therefore, it is assumed that the core is an infinite matrix of similar plate-fin passages, as shown in Fig. 1. Numerous symmetry surfaces exist in such a matrix. Furthermore, for any given fin in the central region of such a core, the fluid flow in the passages adjacent to its upper and lower surfaces is skew-symmetric; therefore, the heat flux distributions on its two surfaces are skew-symmetric, as is qualitatively illustrated in Fig. 2(*b*). Advantage is taken of these features to limit the calculation domain to only 1/4 of the total cross-sectional area between two similar fins, as shown by the shaded region in Fig. 2(*a*).

Two types of thermal boundary conditions are considered in this analysis. In one, the temperature of the plates T_w is assumed to be constant, both in the streamwise direction and in any cross section: The symbol Ⓣ will be used to denote this boundary condition. In the other, a uniform rate of heat input per unit length Q' is prescribed, and the plates are regarded as being highly conductive, or sufficiently thick, so that their temperature T_w is uniform in any cross section but varies axially: This boundary condition will be denoted by the symbol (H1). In both these categories of the problem of interest, the fin temperature distribution T_f is determined by conduction within the fin and convection in the fluid. At the fin-plate interface, it is assumed that $T_f = T_w$. In practice, however, because the rate of heat transfer at the plate-fin interface is usually much greater than that passing through a comparable area on the unfinned portion of the plate, the temperature at the plate-fin interface may be depressed relative to that of the surrounding plate material. Sparrow and Lee [11] have shown that this base temperature depression could result in a significant decrease in the fin heat transfer relative to that predicted by a model which neglects this base temperature depression, but its influence on the total (fin + plate) rate of heat transfer is not as serious. Furthermore, for a fixed plate area, as the number of fins increases, the effect of the base temperature depression becomes progressively less important [11]. Heggs and Stones [12] have also investigated this problem, using a two-dimensional model of heat conduction in the fin. It should also be noted that the Ⓣ and (H1) boundary conditions imposed on the plates may not correspond to those encountered in practice, but they represent extreme or bounding cases of the actual conditions in compact heat exchangers [1, 2, 13].

As shown in Fig. 2(*a*), the spacing between the plates is denoted by H, s is half the distance between adjacent fin attachment points on any given plate, L is the length of the fin, and the fin thickness is denoted by t. Two Cartesian coordinate systems, (x, y) and (ξ^*, η^*), are used in the analysis: The x axis is aligned along the centerline between two adjacent fins, and the ξ^* axis is oriented along the fin. Mathematical descriptions of the fluid flow and heat transfer problems of interest are presented in the remainder of this section in terms of the following dimensionless coordinates and geometrical parameters

$$X=x/H;\ Y=y/H;\ \xi=\xi^*/H;\ \eta=\eta^*/H$$
$$Z=(z/H)/(\bar{w}H/\alpha);\ \zeta=H/s \tag{1}$$

where α is the thermal diffusivity of the fluid ($\alpha=k/\rho c_p$), and ζ is the aspect ratio of the plate-fin duct.

Fluid Flow. In the fully developed region, $u=v=0$, $w=w(x, y)$, p is uniform in any given cross section, dp/dz is constant, and for a constant-property Newtonian fluid flow, the z-momentum equation reduces to

$$\partial^2 W/\partial X^2 + \partial^2 W/\partial Y^2 + 1 = 0 \tag{2}$$

where W is a nondimensional axial velocity

$$W=\frac{w}{(H^2/\mu)(-dp/dz)} \tag{3}$$

The boundary conditions on W are the following: At $X=1$, or along the plate, $W=0$; along the centerline, or $Y=0$, $\partial W/\partial Y=0$; and along the fin, or $X=\zeta Y$, $W=0$.

Heat Transfer: Ⓣ Boundary Condition. In this category of problems, the thermally fully developed region is characterized by a dimensionless temperature distribution that remains invariant with the streamwise coordinate [2, 3]

$$(T_W-T)/(T_W-T_b)=\theta(X, Y) \tag{4a}$$

where T_b is the fluid bulk temperature. In the thermally fully developed region, the difference between T_b and T_w decays exponentially with z, so that

$$\{d(T_w-T_b)/dZ\}/(T_w-T_b)=\text{const}=-\lambda \tag{4b}$$

Nomenclature

a, b = constants in interpolation function for ϕ_f, equation (23)
A, B, C = constants in interpolation function for ϕ, equation (22)
a_i, a_n, b_i = constants in discretization equation, equation (24)
c_i, d_i, e_i, f_i = constants in discretization equation, equation (25)
c_p = specific heat at constant pressure, J/kg•K
D_H = hydraulic diameter, equation (27), m
f = Darcy friction factor, equation (26)
h = heat transfer coefficient, equation (28), W/m^2•K
H = spacing between plates, Fig. 2(*a*), m
i = index in fin node numbering scheme, Fig. 4(*b*)
I, J = indices in node numbering scheme, Fig. 3
k = thermal conductivity, for fluid if no subscript, W/m•K
L = length of the fin, Fig. 2(*a*), m
$\mathcal{L}$ = nondimensional fin length $=L/H$
M = total number of nodes along the centerline, $Y=0$
N = total number of nodes along the plate, $X=1$
Nu = Nusselt number, equation (28)
p = pressure, N/m^2
q = heat flux, W/m^2
q_u = heat flux on the upper fin-fluid interface, Fig. 2(*b*), W/m^2
q_l = heat flux on the lower fin-fluid interface, Fig. 2(*b*), W/m^2
q_p = heat flux to the fluid at the plate–fluid interface, W/m^2
$\bar{q}_l, \bar{q}_p$ = mean values of q_l and q_p, respectively, W/m^2
Q = total surface-integrated heat loss over the fin and the plate, W/m
Q_f = surface-integrated heat loss over the fin, W/m
Q' = constant rate of heat transfer to the fluid per unit axial length, equation (15), W/m
Re = Reynolds number, equation (26)
s = half-distance along the plate between successive plate-fin junctions, Fig. 2(*a*), m

Noting that $u=v=0$, and neglecting longitudinal heat conduction and viscous dissipation, the energy equation in the fluid reduces to the following

$$\rho w c_p \frac{\partial T}{\partial z} = k\left(\frac{\partial^2 T}{\partial x^2} + \frac{\partial^2 T}{\partial y}\right) \tag{5a}$$

In terms of θ, λ, and the dimensionless variables defined in equation (1), it can be shown that

$$\rho w c_p (\partial T/\partial z) = k(T_w - T_b)(W/\bar{W})\lambda\theta/H^2$$
$$(\partial^2 T/\partial x^2) = -(T_w - T_b)(\partial^2\theta/\partial X^2)/H^2;$$
$$(\partial^2 T/y^2) = -(T_w - T_b)(\partial^2\theta/\partial Y^2)/H^2 \tag{5b}$$

and equation (5a) can be rewritten as follows

$$\partial^2\theta/\partial X^2 + \partial^2\theta/\partial Y^2 + \lambda(W/\bar{W})\theta = 0 \tag{6}$$

At $X=1$, or along the plate, $\theta=0$; and along the centerline, or $Y=0$, $(\partial\theta/\partial Y)=0$. The normalized velocity distribution $(W/\bar{W})$ in equation (6) is obtained from the fluid flow analysis.

At any location ξ^* along the fin, there is a balance between the net conduction along the fin and the heat transfer from the surface of the fin to the fluid. In the context of a one-dimensional model of the fin, this energy balance can be expressed as

$$k_f t(d^2T_f/d\xi^{*2}) = q_u + q_l \tag{7}$$

where the subscript f refers to the fin, and q_u and q_l are the heat fluxes on the upper and lower surfaces of the fin, respectively

$$q_u = -k(\partial T/\partial\eta^*)_u; \; q_l = k(\partial T/\partial\eta^*)_l \tag{8}$$

In this equation, the temperature gradients correspond to those on the fluid side of the fin-fluid interfaces, and k is the thermal conductivity of the fluid. With reference to the skew-symmetric heat flux distributions shown in Fig. 2(b), it can be established that q_u and q_l are related by the following equation

$$q_u\Big|_{\xi^*} = q_l\Big|_{L-\xi^*} \tag{9}$$

Advantage is taken of this relationship between q_u and q_l to limit the calculation domain to the shaded region shown in Fig. 2(a). In dimensionless terms, equations (7-9) can be combined and expressed as follows

$$\Omega(d^2\theta_f/d\xi^2) = [(\partial\theta/\partial\eta)_{\xi} + (\partial\theta/\partial\eta)_{£-\xi}] \tag{10}$$

where $(\partial\theta/\partial\eta)$ is the normal gradient of θ in the fluid on the lower surface of the fin, the subscript l has been dropped for compactness in the presentation; $£ = (L/H) = [1+(1/\zeta)^2]^{1/2}$; and Ω is the fin conductance parameter, given by

$$\Omega = (k_f t)/(kH) \tag{11}$$

At $\xi=0$ and at $\xi=£$, $\theta_f=0$.

For any given set of ζ and Ω, equations (6) and (10), along with the aforementioned boundary conditions, pose an eigenvalue problem. The eigenvalue λ has to be found so that the solution satisfies the following requirement, which follows from the definition of the bulk temperature

$$2\zeta\iint(W/\bar{W})\theta dXdY = 1 \tag{12}$$

where the integration is carried out over the shaded region in Fig. 2(a).

In the solution of this eigenvalue problem, it is convenient to define a variable ψ as follows

$$\psi = \theta/\lambda; \; \phi_f = \psi_f/\lambda \tag{13}$$

In terms of ϕ, equations (6) and (10), and the associated boundary conditions, remain unchanged, and equation (12) yields

$$\lambda = 1/\{2\zeta\iint(W/\bar{W})\psi dXdY\} \tag{14}$$

An iterative numerical method is used to solve this conjugate heat transfer problem. Details of this method are presented later in this paper.

Heat Transfer: Ⓗ① Boundary Condition. In this problem, a uniform rate of heat input per unit axial length Q' is prescribed, and the plate temperature T_w is assumed to be uniform in each cross section but varies axially. With this boundary condition, and assuming that viscous dissipation is negligible, all temperatures vary linearly with axial distance in the thermally developed region, and an overall energy balance yields the following

$$\partial T/\partial z = dT_b/dz = dT_w/dz = 2Q'/(\rho\bar{w}Hsc_p) \tag{15}$$

Furthermore, in the thermally developed regime, the following dimensionless temperature remains invariant with the streamwise coordinate [2, 3]

$$(T_w - T)/(Q'/k) = \tau(X, Y) \tag{16}$$

Nomenclature (cont.)

S = volumetric source term, equation (19)
t = fin thickness, Fig. 2(a), m
T = temperature, K
T_b = fluid bulk temperature, K
T_f = temperature inside the fin, K
T_w = plate temperature, K
u, v, w = fluid velocity components in the x, y, and z directions, respectively, m/s
W = dimensionless axial velocity of the fluid, equation (3)
$\bar{w}$, $\bar{W}$ = mean values of w and W, respectively
x, y, z = Cartesian coordinates, Figs. 1 and 2(a), m
X, Y, Z = nondimensional coordinates, equation (1)
α = thermal diffusivity = $k/\rho c_p$, m^2/s
ζ = aspect ratio = H/s
$\eta_{0,\text{prop}}$ = total (fin + plate) surface efficiency obtained using the proposed conjugate analysis, equation (33)
$\eta_{0,\text{conv}}$ = total (fin + plate) surface efficiency obtained using conventional analysis, equation (31)
θ = nondimensional temperature, equation (4)
Θ = half-angle between adjacent fins, Fig. 2(a), deg
λ = eigenvalue, equations (4a) and (14)
μ = dynamic viscosity of the fluid, kg/m•s
ξ^*, η^* = Cartesian coordinates, Fig. 2(a), m
ξ, η = nondimensional coordinates, equation (1)
ρ = mass density of the fluid, kg/m^3
τ = dimensionless temperature, equation (16)
ψ = dimensionless temperature = θ/λ
ϕ = general scalar dependent variable, equation (19)
Ω = fin conductance parameter, equation (11)

Subscripts

$a, b, c, 0$ = values pertaining to specific locations in the domain discretization, Fig. 4(a)
e, w = control volume face locations in the fin discretization, Fig. 4(b)
f = values or variables pertaining to the fin
H1 = pertaining to the thermal boundary condition of prescribed Q'
T = pertaining to the thermal boundary condition of prescribed T_w

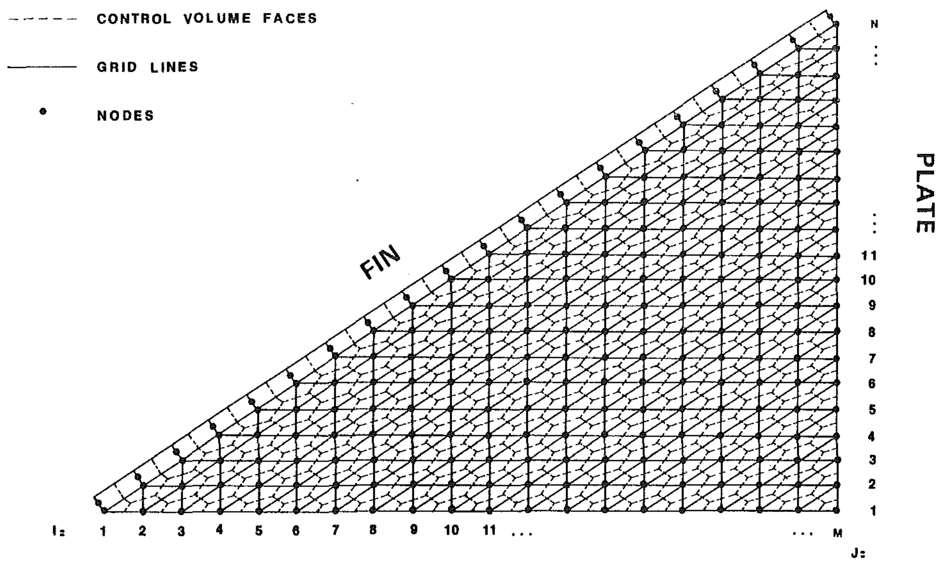

Fig. 3 Domain discretization scheme

Using equations (15) and (16), the energy equation (5*a*) in the fluid can be written in the following dimensionless form

$$\partial^2\tau/\partial X^2 + \partial^2\tau/dY^2 + 2\zeta(W/\bar{W}) = 0 \tag{17}$$

At $X=1$, or along the plate, $\tau=0$; and along the centerline, or $Y=0$, $\partial\tau/\partial Y=0$. The normalized velocity distribution $(W/\bar{W})$ in equation (17) is obtained from the fluid flow analysis.

The thermal analysis of the fin is similar to that presented in the previous section, and the governing equation for τ_f is the following

$$\Omega(d^2\tau_f/d\xi^2) = [(\partial\tau/\partial\eta)_\xi + (\partial\tau/\partial\eta)_{\pounds-\xi}] \tag{18}$$

where Ω is the fin conductance parameter given by equation (11), and $(\partial\tau/\partial\eta)$ is the normal gradient of τ in the fluid on the lower surface of the fin; the right side of equation (18) reflects the skew-symmetric distributions of the heat flux at the upper and lower fin-fluid interfaces, as shown in Fig. 2(*b*). At $\xi=0$ and at $\xi=\pounds$, $\tau_f=0$.

Equations (17) and (18), subject to the aforementioned boundary conditions, were solved by an iterative numerical method described in the next section.

Numerical Method

A control volume finite element method was used to solve the mathematical models described in the previous section. This method is briefly described in this section; a detailed description of the method is available in [14].

Domain Discretization. The shaded region in Fig. 2(*a*) is first discretized into three-node triangular elements. Then the centroids of the elements are joined to the midpoints of the corresponding sides to create polygonal control volumes surrounding each node in the calculation domain. A sample domain discretization is shown in Fig. 3; the solid lines denote the domain and element boundaries, and the dashed lines represent the control volume faces. The nodes along the centerline, $Y=0$, are numbered $I=1, 2, 3, \ldots, M$; and along the plate, $X=1$, the nodes are numbered $J=1, 2, 3, \ldots, N$. In all discretizations used in this investigation, the same number of nodes was used along the centerline, the plate and the fin boundary: $M=N$ in all cases. Thus the nodes in the proposed discretization scheme are arranged in a line-by-line pattern, with the lines parallel to the sides of the triangular calculation domain. This arrangement of nodes facilitates the storage, assembly, and solution of the discretization equations.

The fin is discretized into control volumes and nodes which are compatible with the discretization of the flow passage, as illustrated in Fig. 3.

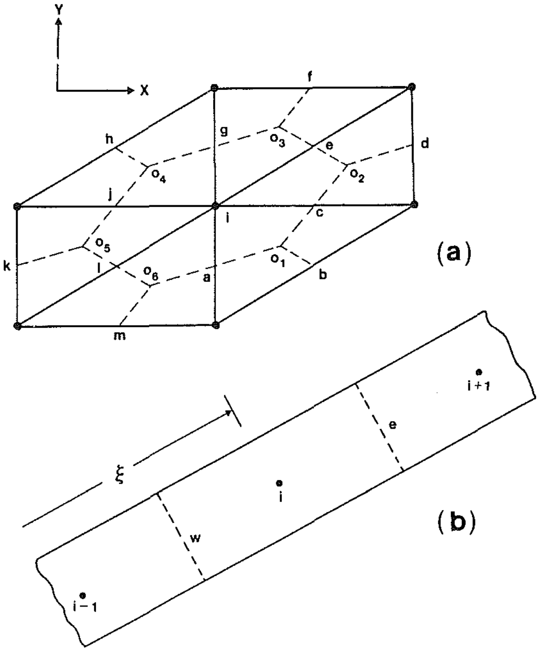

Fig. 4 Details of the discretization of (*a*) the flow passage, and (*b*) the fin

Conservation Equation for a Control Volume. Equations (2), (6), and (17) can be integrated over a control volume V and cast in the following general form

$$\int_{\partial V} \nabla\phi \cdot \mathbf{n} ds + \int_V S dV = 0 \tag{19}$$

where ϕ is a general scalar dependent variable, S is interpreted as a volumetric source term, ∂V is the surface of the control volume, and **n** is a unit outward normal to the differential area element ds. The fluid flow problem can be modeled by setting $\phi=W$ and $S=1$; the Ⓣ heat transfer problem can be simulated by setting $\phi=\psi$ and $S=\lambda(W/\bar{W})\psi$; and by setting $\phi=\tau$ and $S=2\zeta(W/\bar{W})$, the (H1) heat transfer problem can be modeled.

When applied to the polygonal control volume associated with a typical node i, such as the one shown in Fig. 4(*a*), equation (19) can be written as follows

Table 1 Overall fluid flow results

ζ	Angle ∢ 2θ	f.Re [Present]	f.Re [2]	f.Re [8]
11.430	10°	50.188	49.90	50.044
3.732	30°	52.520	52.26	52.346
1.732	60°	53.744	53.33	53.360
1.000	90°	52.936	52.61	52.645
0.577	120°	51.224	50.98	50.970

Table 2 Comparison of average Nusselt numbers for $\Omega = \infty$

ζ	Nu_T [Present]	Nu_T [8]	Nu_{H1} [Present]	Nu_{H1} [8]
11.430	1.726	1.700	2.467	2.437
3.732	2.284	2.274	2.921	2.910
1.732	2.500	2.497	3.110	3.111
1.000	2.359	2.358	2.979	2.983
0.577	2.031	2.029	2.681	2.684

$$\left[\int_a^{0_1} \nabla \phi \cdot \mathbf{n} ds + \int_{0_1}^{c} \nabla \phi \cdot \mathbf{n} ds - \int_{ia0_1c} S dV\right] \tag{20}$$

\+ [Similar contributions from other elements associated with node *i*]

\+ [Boundary contributions, if applicable] = 0

This form of the conservation equation emphasizes that it can be assembled using an element-by-element procedure.

Similarly, the fin equations (10) and (18) can be integrated over the control volume associated with a typical fin node *i*, such as the one shown in Fig. 4(*b*), and cast in the following general form

$$\Omega[(d\phi_f/d\xi)_e - (d\phi_f/d\xi)_w] = \left[\int_w^e (\partial\phi/\partial\eta)_\xi d\xi + \int_w^e (\partial\phi/d\eta)_{\pounds-\xi} d\xi\right] \tag{21}$$

Interpolation Functions. In the flow passage, all dependent variables are interpolated linearly in each three-node triangular element

$$\phi = AX + BY + C \tag{22}$$

the constants A, B, and C in this interpolation function can be uniquely determined in terms of the nodal coordinates and the corresponding values of ϕ.

In the fin, the dependent variables are interpolated by piecewise linear functions in ξ. Thus between any two adjacent nodes

$$\phi_f = a\xi + b \tag{23}$$

where a and b are unique functions of the nodal values of ξ and ϕ_f.

Discretization Equations. The interpolation functions given by equations (22) and (23) are used to obtain algebraic approximations to the integrals and derivatives in equations (20) and (21). The area and line integrals involved in this derivation are quite straightforward [14, 15], so the details will not be presented here.

In a general form, the discretization equation for a node *i* in the flow passage can be expressed as follows

$$a_i\phi_i = \sum_n a_n\phi_n + b_i \tag{24}$$

where the summation is taken over all neighbors of node *i*. Similarly, a general representation of the discretization equation for a node *i* in the fin is

$$c_i(\phi_f)_i = d_i(\phi_f)_{i+1} + e_i(\phi_f)_{i-1} + f_i \tag{25}$$

Solution of the Discretization Equations

Fluid Flow. In the fluid flow problem, $\phi = W$ and $S = 1$, and equation (24) represents a set of simultaneous, linear algebraic equations. In this investigation, these equations were solved by a line-by-line iterative method based on the *T*ri-*D*iagonal-*M*atrix-*A*lgorithm (TDMA). Details of this method are available in [16]. It should be noted here that this scheme can be used because the proposed domain discretization scheme provides a line-by-line arrangement of the nodes. In all cases considered in this analysis, the iterations were terminated when all values of W had converged to at least five significant figures.

Heat Transfer: Ⓣ *Problem.* In this case, $\phi = \psi$, $S = \lambda(W/\bar{W})\psi$, and $\phi_f = \psi_f$. The normalized velocity distribution $(W/\bar{W})$ in this problem is obtained by solving the aforementioned fluid flow problem first. Equations (24) and (25) represent a coupled set of simultaneous linear algebraic equations which, together with equation (14), pose an eigenvalue problem. The following iterative procedure was used to solve this problem: (1) guess all unknown nodal values of ϕ; (2) using this ϕ distribution, calculate the coefficients in equation (25), and solve this set of equations, using TDMA, to obtain the fin temperature distribution ϕ_f; (3) with the available ϕ distribution, calculate λ using equation (14); (4) with this value of λ, and using the available ϕ_f values as boundary conditions at the fluid-fin interface, solve equation (24), using a line-by-line iterative method, to obtain a new ϕ distribution; (5) return to step 2, and repeat until all ϕ values and the value of λ have converged to at least five significant figures; and (6) calculate the θ distribution, using $\theta = \lambda\phi$.

Heat Transfer: (H1) *Problem.* In this problem, $\phi = \tau$, $S = 2\zeta(W/\bar{W})$, and $\phi_f = \tau_f$. Again $(W/\bar{W})$ is obtained from the fluid flow analysis, and equations (24) and (25) represent a coupled set of simultaneous linear algebraic equations. The following iterative procedure was used to solve this set of equations: (1) Guess all unknown nodal values of ϕ; (2) using this ϕ distribution, calculate the coefficients in equation (25) and solve this set of equations, using TDMA, to obtain the fin temperature distribution ϕ_f; (3) using the available ϕ_f values as boundary conditions at the fluid-fin interface, solve equation (24), using a line-by-line iterative method, to obtain

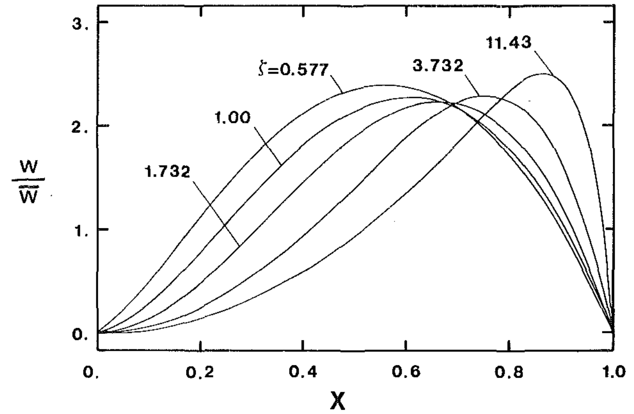

Fig. 5 Normalized velocity distributions along the symmetry boundary ($Y=0$) for different aspect ratios

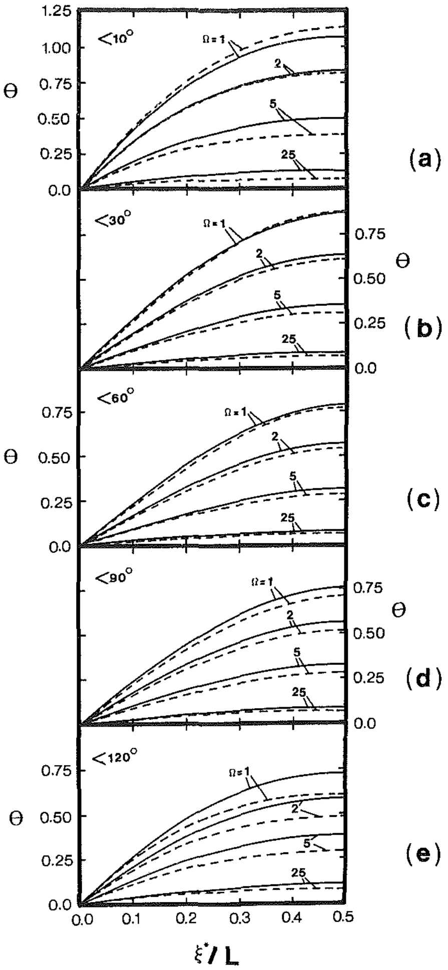

Fig. 6 Nondimensional fin temperature distribution (——— (H1); -------- (T)): (a) $\zeta=11.43$; (b) $\zeta=3.732$; (c) $\zeta=1.732$; (d) $\zeta=1.00$; (e) $\zeta=0.577$

a new ϕ distribution; (4) return to step 2 and repeat until all ϕ values have converged to at least five significant figures.

Results

The numerical method described in the previous section was used to study fully developed flow and heat transfer in a total of thirty different triangular plate-fin ducts; five values of the aspect ratio were considered, $\zeta=11.43$, 3.732, 1.732, 1.0, and 0.577; for each of these aspect ratios, six values of the fin conductance parameter were investigated, $\Omega=\infty$, 25, 10, 5, 2, and 1. These values of ζ and Ω are characteristic of air flows in commonly encountered triangular plate-fin passages.

Numerous preliminary runs were undertaken to (1) establish the validity of the computer implementation of the proposed numerical method, and (2) obtain grid configurations that provide a satisfactory balance between the accuracy and the computational cost of the results. The final choice for $\zeta>1.732$ was a 325-node (625-element) grid with a moderate stacking of nodes adjacent to the solid boundaries: the spacing of successive grid points along $Y=0$, moving away from the point $X=0$ toward the centroid of the triangular flow passage, was given by $(X_{i+1}/X_i) = \{(i+1)/i\}^{1.2}$, and similar grid spacing was used in the vicinity of other solid boundaries. For $\zeta \leqq 1.732$ a 190-node (361-element) uniform grid was used.

The results of this study can be grouped into two main categories: overall results and local results. These two categories of results are presented and discussed next in this section. Following that, the results of this study are used to evaluate the validity of the conventional approach to the design of plate-fin ducts.

Overall Results

Fluid Flow: Overall fluid flow results will be presented in terms of the product of the Darcy friction factor and the Reynolds number

$$f\cdot\mathrm{Re}=\left\{\frac{(-dp/dz)D_h}{\rho\bar{w}^2/2}\right\}\left(\frac{\rho\bar{w}D_h}{\mu}\right)=\frac{8}{[(\zeta^2+1)^{1/2}+1]^2\bar{W}} \tag{26}$$

where D_h is the hydraulic diameter

$$D_h=(2Hs)/[(H^2+s^2)^{1/2}+s] \tag{27}$$

The values of $f\cdot\mathrm{Re}$ obtained in this study and those reported in [2, 8] are presented in Table 1. Good agreement between the results is evident in all cases.

Heat Transfer Results: The overall heat transfer characteristics of the triangular plate-fin ducts will be presented in terms of the average Nusselt number Nu and the ratio Q_f/Q; with reference to Fig. 2, Q_f is the surface-integrated heat loss from the lower surface of the fin to the fluid, and Q is the sum of Q_f and the heat loss from the plate to the fluid over the range $0 \leqq y \leqq s$. The average Nusselt number was evaluated as follows

$$h=\frac{Q/(T_w-T_b)}{(H^2+s^2)^{1/2}+s};\quad \mathrm{Nu}=\frac{hD_h}{k} \tag{28}$$

In Table 2, the values of Nu_T and Nu_{H1} for $\Omega=\infty$ are compared with those reported in [8]. In all cases, the agreement between the results is good.

All overall heat transfer results are presented in Table 3. For all aspect ratios, Nu_T and Nu_{H1} decrease monotonically as the fin conductance parameter Ω decreases. This indicates that for a fixed plate-fin geometry, a decrease in fin thermal conductivity lowers the average heat transfer coefficient h defined in equation (28). The ratio Q_f/Q decreases as Ω decreases for a fixed aspect ratio. This is because low fin thermal conductivities lead to low values of Q_f. For a fixed value of Ω, Q_f/Q increases with aspect ratio. The reason for this is that for high aspect ratios, the fin surface area constitutes the major part of the overall heat transfer area. It is to be noted that the Nu values for the (T) problem are consistently lower than the corresponding values for the (H1) problem; this is consistent with the results for $\Omega=\infty$ reported in [2, 8].

Local Results

Nondimensional Velocity Distribution: Dimensionless velocity distributions ($W/\bar{W}$) along the symmetry boundary ($Y=0$) between two adjacent fins are presented in Fig. 5. These distributions are strongly influenced by the aspect ratio

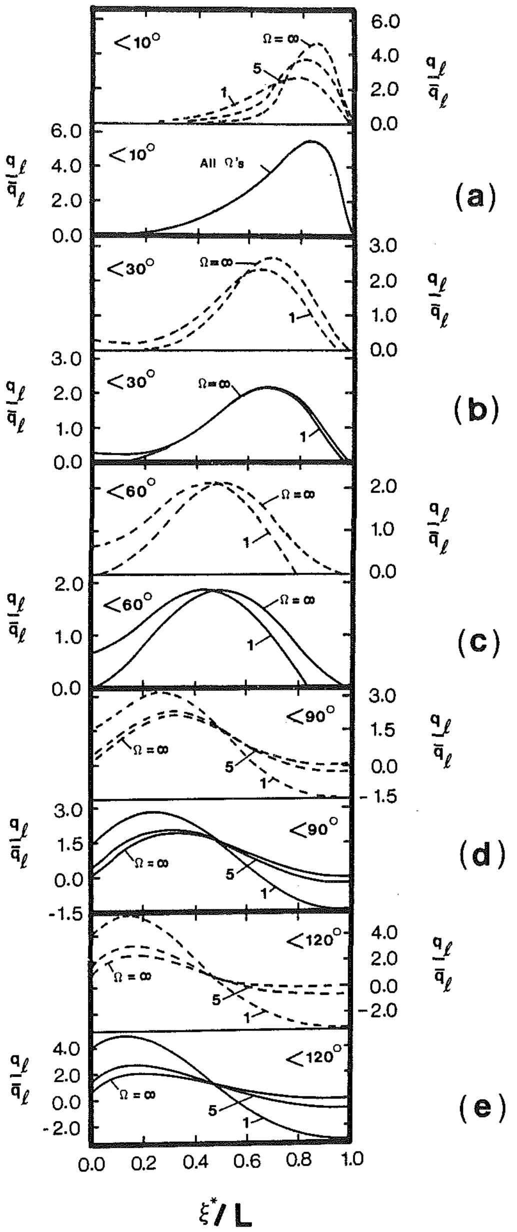

Fig. 7 Nondimensional heat flux distribution on the lower fin-fluid interface (——— (H1) ; ········ (T)): (*a*) $\zeta = 11.43$; (*b*) $\zeta = 3.732$; (*c*) $\zeta = 1.732$; (*d*) $\zeta = 1.00$; (*e*) $\zeta = 0.577$

ζ. Furthermore, the maxima do not occur at the centroids of the triangular plate-fin passages, except when the passage is equilateral ($\zeta = 1.732$). The location of the maximum velocity point shifts toward the plate ($X = 1$) as the aspect ratio is increased. This is because the fluid flow seeks the path of least resistance; it is to be noted that the location of the maxima in Fig. 5 agree well with the corresponding results in [2]. Another interesting feature of the plots in Fig. 5 is that the maximum value of $(W/\bar{W})$ for the equilateral passage ($\zeta = 1.732$) is lower than that of other ducts. This indicates that for $\zeta = 1.732$, the W distribution over the cross section of the duct is not as nonuniform as that for other values of ζ.

Nondimensional Fin Temperature: Distributions of $(T_w - T_f)/(T_w - T_b)$ are presented in Figs. 6(*a*–*e*). Results for both the (T) and (H1) thermal boundary conditions are plotted on the same graphs, the former being shown by dashed lines and the latter by solid lines. Each graph corresponds to a particular value of ζ and is parametrized by values of Ω. It is to be noted that for all cases, the two end temperatures of the fin are T_w, and the heat flux distributions on the upper and lower fin-fluid interfaces are skew-symmetric. Therefore, the total surface heat flux $(q_u + q_l)$ and the fin temperature distribution are symmetric about the center point of the fin; thus the range of the abscissa in Fig. 6 is $0 \leqq \xi^*/L \leqq 0.5$.

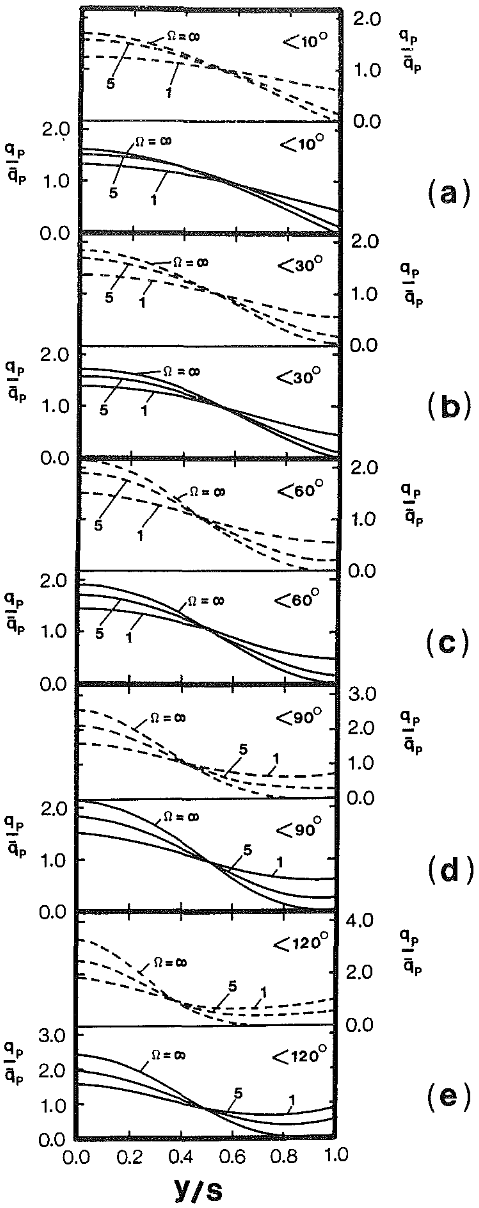

Fig. 8 Dimensionless heat flux distribution on the plate-fluid interface (——— (H1) ; ········ (T)): (*a*) $\zeta = 11.43$; (*b*) $\zeta = 3.732$; (*c*) $\zeta = 1.732$; (*d*) $\zeta = 1.00$; (*e*) $\zeta = 0.577$

The curves corresponding to $\Omega = \infty$ coincide with the abscissa in all graphs. For a finite Ω, T_f drops from T_w at the ends of the fin to its lowest value at the midpoint. This causes $(T_w - T_f)/(T_w - T_b)$ to increase from zero at $(\xi^*/L) = 0$ to its maximum value at $(\xi^*/L) = 0.5$. For a given aspect ratio, this increase in $(T_w - T_f)/(T_w - T_b)$ gets more pronounced as Ω is decreased; this implies that for a fixed T_w, or a given axial location along the duct, as Ω decreases, the drop in T_f exceeds that in T_b. Another feature of the plots in Fig. 6 is that the temperature drop along the fin increases, consistently, with an increase in the aspect ratio. This may be explained by noting that an increase in aspect ratio ζ can be viewed as an increase in the fin length L for a fixed value of s; hence a larger temperature drop at its center, which is now farther from the plates, is to be expected.

For $\zeta = 11.43$ and $\Omega = 1$, it is seen that $\{(T_w - T_f)/(T_w -$

Table 3 Overall heat transfer results

ζ	Ω	Nu_T	Nu_{H1}	$(Q_f/Q)_T$	$(Q_f/Q)_{H1}$
11.430	∞	1.726	2.467	0.88	0.905
	25	1.676	2.254	0.88	0.902
	10	1.594	1.997	0.88	0.898
	5	1.450	1.682	0.88	0.890
	2	1.065	1.154	0.88	0.869
	1	0.710	0.774	0.87	0.836
3.732	∞	2.284	2.921	0.770	0.781
	25	2.210	2.761	0.768	0.773
	10	2.105	2.555	0.765	0.762
	5	1.944	2.283	0.758	0.744
	2	1.575	1.770	0.726	0.695
	1	1.218	1.348	0.666	0.627
1.732	∞	2.500	3.110	0.668	0.668
	25	2.424	2.972	0.658	0.654
	10	2.322	2.797	0.643	0.634
	5	2.174	2.564	0.619	0.605
	2	1.862	2.124	0.552	0.530
	1	1.574	1.762	0.464	0.441
1.000	∞	2.359	2.979	0.600	0.595
	25	2.299	2.859	0.581	0.573
	10	2.220	2.711	0.555	0.544
	5	2.110	2.521	0.515	0.501
	2	1.890	2.184	0.424	0.407
	1	1.701	1.924	0.328	0.312
0.577	∞	2.301	2.681	0.553	0.545
	25	1.987	2.563	0.519	0.507
	10	1.931	2.431	0.475	0.459
	5	1.861	2.280	0.417	0.398
	2	1.738	2.053	0.309	0.289
	1	1.647	1.907	0.221	0.204

Table 4 Total surface efficiencies obtained with the conventional and the proposed analyses

		Ⓣ			(H1)		
ζ	Ω	$\eta_{o,conv}$	$\eta_{o,prop}$	% Error	$\eta_{o,conv}$	$\eta_{o,prop}$	% Error
11.430	∞	1.000	1.000	0.00	1.000	1.000	0.00
	25	0.939	0.971	- 3.30	0.915	0.914	0.11
	10	0.863	0.924	- 6.60	0.818	0.809	1.11
	5	0.768	0.840	- 8.57	0.706	0.682	3.52
	2	0.599	0.617	- 2.92	0.530	0.468	13.25
	1	0.468	0.411	13.87	0.408	0.314	29.94
3.732	∞	1.000	1.000	0.00	1.000	1.000	0.00
	25	0.970	0.968	0.21	0.962	0.945	1.80
	10	0.930	0.922	0.87	0.912	0.875	4.23
	5	0.873	0.851	2.59	0.845	0.782	8.06
	2	0.752	0.690	8.99	0.713	0.606	17.66
	1	0.638	0.533	19.70	0.597	0.461	29.50
1.732	∞	1.000	1.000	0.00	1.000	1.000	0.00
	25	0.979	0.970	0.93	0.974	0.956	1.88
	10	0.949	0.929	2.15	0.939	0.899	4.45
	5	0.907	0.870	4.25	0.889	0.824	7.89
	2	0.814	0.745	9.26	0.786	0.683	15.08
	1	0.721	0.630	14.44	0.690	0.567	21.69
1.000	∞	1.000	1.000	0.00	1.000	1.000	0.00
	25	0.979	0.975	0.41	0.973	0.960	1.35
	10	0.950	0.941	0.96	0.939	0.910	3.19
	5	0.909	0.894	1.68	0.891	0.846	5.32
	2	0.822	0.801	2.62	0.795	0.733	8.46
	1	0.738	0.721	2.36	0.710	0.646	9.91
0.577	∞	1.000	1.000	0.00	1.000	1.000	0.00
	25	0.967	0.864	11.92	0.962	0.956	0.63
	10	0.926	0.839	10.37	0.916	0.907	0.99
	5	0.873	0.809	7.91	0.859	0.850	1.06
	2	0.776	0.755	2.78	0.759	0.766	-0.91
	1	0.699	0.716	-2.37	0.683	0.711	-3.94

$T_b)\} > 1$ in the vicinity of the midpoint of the fin; this indicates that in the central region of the fin, its temperature falls below the fluid bulk temperature. The plots in Fig. 6 also indicate that the dimensionless fin temperatures for the Ⓣ and (H1) boundary conditions differ only slightly.

Dimensionless Fin Heat Flux: Distributions of $q_l/\bar{q}_l$ are presented in Figs. 7($a-e$), for both the Ⓣ (dashed lines) and the (H1) (solid lines) boundary conditions. For each of the aspect ratios considered, the plots in Fig. 7 are parametrized by the fin conductance parameter Ω; to avoid excessive crowding, however, the results for certain values of Ω have been omitted.

In all cases, the $q_l/\bar{q}_l$ distribution varies markedly along the fin. All $q_l/\bar{q}_l$ plots are significantly affected by the values of ζ and Ω. For fixed values of Ω, as ζ decreases, the location of the maxima of $q_l/\bar{q}_l$ shifts away from the vicinity of the plate at $X=1$, and moves toward the end at $X=0$. This is in response to similar changes in the location of the maxima of the fluid velocity distribution. For a fixed aspect ratio, it is expected that as Ω decreases, q_l decreases. In Fig. 7, however, it is seen that for $\zeta < 1.732$, the maxima in $q_l/\bar{q}_l$ increase as Ω decreases; this indicates that the decrease in $\bar{q}_l$ is faster than that in the maximum value of q_l.

In Fig. 2(b), the heat flux distributions on the lower and upper surfaces of the fin are shown to be skew-symmetric and positive. From the plots in Fig. 7, however, it is seen that $q_l/\bar{q}_l$ takes on negative values in the region adjacent to the plate at $(\xi^*/L)=1$, for $\zeta < 11.43$ and small values of Ω. This phenomenon, which may appear surprising at first, is physically meaningful. Using the information in Fig. 7 and noting that q_u and q_l are skew-symmetric, it can be deduced that the algebraic sum (q_u+q_l) is always positive. Thus the net heat transfer is always from the fin to the fluid. The negative part of the heat flux distribution on the individual fin surfaces implies, therefore, that the hot fluid in the corners formed by the fins and the plates transfers energy, *via the fin*, to the relatively less hot fluid in the corners formed by adjacent fins. In the context of compact heat exchanger design, therefore, it may be concluded that combinations of ζ and Ω, which give rise to negative values of $q_l/\bar{q}_l$, are not thermally efficient.

Nondimensional Plate Heat Flux: Distributions of $q_p/\bar{q}_p$ are given in Figs. 8(a–e), for the Ⓣ (dashed lines) and (H1) (solid lines) boundary conditions. In all plots, $q_p/\bar{q}_p$ achieves its maximum value at $Y=0$, and decreases monotonically along the plate toward the corner of the duct. In the vicinity of the duct corners, the fluid velocity is lower than that in the region adjacent to the center of the plate ($Y=0$); on the other hand, the fluid temperature in the corners is higher than that in the region adjacent to the center of the plate. Both these phenomena adversely influence the convective heat transfer in the corners, in relation to that at the center of the plate; the plots in Fig. 8 reflect this reasoning.

From Figs. 8(a–e), it is evident that for a fixed aspect ratio, the variation in $q_p/\bar{q}_p$ along the plate for high values of Ω is larger than for low values of Ω. This is because plate-fin ducts with high Ω values, or high fin conductivity, have higher fin temperatures, and hence higher corner fluid temperatures, than those with low Ω values; the closer the fluid temperature is to T_w, the less receptive it is to heat transfer from the plate. Furthermore, the fluid velocity distribution in the region adjacent to the plate is less nonuniform along the plate for high aspect ratio ducts ($\zeta=11.43$ and 3.732) than that for low aspect ratio ducts ($\zeta=0.577$ and 1). Thus, for a fixed value of

Ω, the variation in $q_p/\bar{q}_p$ along the plate for high aspect ratio ducts is somewhat lower than that for low aspect ratio ducts.

Evaluation of the Conventional Approach to the Design of Plate-Fin Ducts. In the conventional approach to the design of plate-fin ducts [1], the less than 100 percent effectiveness of the fin surface is accounted for by using a fin efficiency η_f, and a total surface (plate + fin) efficiency η_0

$$\eta_f = \frac{\text{Actual rate of heat transfer from the fin}}{\text{Rate of heat transfer from the fin when } \Omega = \infty} \tag{29}$$

$$\eta_0 = \frac{\text{Actual rate of heat transfer from the (plate + fin)}}{\text{Rate of heat transfer from the (plate + fin) when } \Omega = \infty} \tag{30}$$

In the conventional approach, these efficiencies are obtained using standard fin theory, in which the surface heat transfer coefficient is assumed to be a constant. For the plate-fin ducts analyzed in this paper, the conventional approach yields

$$\eta_{f,\text{conv}} = \frac{\tanh\,(mL/2)}{(mL/2)}; \quad m = \left(\frac{2h_{\Omega=\infty}}{k_f t}\right)^{1/2} \tag{31}$$

$$\eta_{0,\text{conv}} = 1 - \{L/(L+s)\}(1-\eta_{f,\text{conv}})$$

In terms of the dimensionless parameters used in this analysis, it can be shown that:

$$\frac{mL}{2} = \left[\frac{\{(\zeta^2+1)^{1/2}+1\}(\zeta^2+1)\text{Nu}_{\Omega=\infty}}{4\zeta^2\Omega}\right]^{1/2} \tag{32}$$

$$\{L/(L+s)\} = (\zeta^2+1)^{1/2}/\{(\zeta^2+1)^{1/2}+1\}$$

The results of the proposed conjugate analysis of plate-fin ducts can be used to calculate the total surface efficiency η_0 as follows

$$\eta_{0,\text{prop}} = \text{Nu}/\text{Nu}_{\Omega=\infty} \tag{33}$$

For laminar fully developed flow and heat transfer, with a given thermal boundary condition and fixed values of ζ and Ω, the average heat transfer coefficient and the corresponding value of η_0 are constant, independent of the Reynolds and Prandtl numbers. Values of $\eta_{0,\text{conv}}$ and $\eta_{0,\text{prop}}$ for all the plate-fin ducts considered in this study, for both the Ⓣ and (H1) boundary conditions, are presented in Table 4. These results show that the conventional approach, for the parameters investigated, can lead to errors in the values of η_0 that range from -8.57 to 29.94 percent.

Concluding Remarks

In this investigation, the heat transfer characteristics of triangular cross section plate-fin ducts have been determined by analyzing conduction in the fin and convection in the fluid, simultaneously, as a conjugate problem. This approach obviates the need for arbitrary assumptions about the heat transfer from the fin surface. The overall and local results presented in this paper highlight the importance of including the fin conductance parameter Ω in the thermal analysis of triangular plate-fin ducts. In addition, they illustrate that the conventional approach to the design of plate-fin ducts, based on the standard fin theory, can lead to significant errors.

Using the data in [1, 2], it may be established that the values of H and t characteristic of plate-fin ducts encountered in compact heat exchangers lie in the following ranges: 2.54 mm $\leq H \leq 20.9$ mm, and 0.025 mm $\leq t \leq 0.254$ mm. These values of H and t yield the following ranges of Ω $(= k_f t/kH)$: with copper fins ($k_f \simeq 400$ W/m − °C) and air ($k \simeq 0.0263$ W/m − °C), $18.2 \leq \Omega \leq 1521$; with aluminum fins ($k_f \simeq 237$ W/m − °C) and air, $10.8 \leq \Omega \leq 901$; with carbon steel fins ($k_f \simeq 60.5$ W/m − °C) and air, $2.75 \leq \Omega \leq 230$; and with 304 stainless steel ($k_f \simeq 14.9$ W/m − °C) and air, $0.68 \leq \Omega \leq 56.7$. For air-to-air compact heat exchangers, therefore, the results presented in this paper may be used to draw the following conclusions: With copper fins, $T_f \simeq T_w$ throughout the fin, and the results for $\Omega = \infty$ apply; with aluminum, carbon steel, and stainless steel fins, and for fins with $k_f < 200$ W/m − °C, however, it could be erroneous to assume that $T_f \simeq T_w$ throughout the fin, and the results of the conjugate problem analyzed in this paper should be used.

Only triangular plate-fin ducts were investigated in this study. It should be noted, however, that the control-volume numerical method presented in this paper can be easily adapted for the analysis of other plate-fin ducts, such as trapezoidal plate-fin ducts, encountered in compact heat exchangers.

It has been assumed in this work that the triangular plate-fin ducts have sharp corners. In practice, however, soldering, brazing, or welding processes are used to attach the fins to the plates, and the fins may be formed by rolling or cold forging a continuous metal sheet. Thus rounded corners, and imperfect thermal contact between the fins and the plates, could result [1, 2]. An investigation of these effects would be a useful extension of this work. Another interesting and worthwhile extension of this study would be an analysis of developing flow and heat transfer in plate-fin ducts, accounting for axial heat conduction in the fins and the plates. An investigation of turbulent flows and complementary experiments to verify the numerical predictions are also desirable.

Acknowledgments

Financial support from the Natural Sciences and Engineering Research Council of Canada is gratefully acknowledged. Constructive criticism of this work by Dr. R. K. Shah is appreciated.

References

1 Kays, W. M., and London, A. L., *Compact Heat Exchangers*, 3rd ed., McGraw-Hill, New York, 1984.

2 Shah, R. K., and London, A. L., *Laminar Flow Forced Convection in Ducts*, Supplement 1, *Advances in Heat Transfer*, Academic Press, 1978.

3 Kays, W. M., and Crawford, M. E., *Convective Heat and Mass Transfer*, 2nd ed., McGraw-Hill, New York, 1980.

4 Schmidt, F. W., and Newell, M. E., "Heat Transfer in Fully Developed Laminar Flow Through Rectangular and Isosceles Triangular Ducts," *Int. J. Heat Mass Transfer*, Vol. 10, 1967, pp. 1121–1123.

5 Nakamura, H., Hiraoka, S., and Yamada, I., "Laminar Forced Convection Flow and Heat Transfer in Arbitrary Triangular Ducts," *Heat Transfer—Japanese Research*, Vol. 1, 1972, pp. 120–122.

6 Sparrow, E., and Haji-Sheikh, A., "Laminar Heat Transfer and Pressure Drop in Isosceles Triangular, Right Triangular, and Circular Sector Ducts," ASME JOURNAL OF HEAT TRANSFER, Vol. 87, 1965, pp. 426–427.

7 Shah, R. K., "Laminar Flow Friction and Forced Convection Heat Transfer in Ducts of Arbitrary Geometry," *Int. J. Heat Mass Transfer*, Vol. 18, 1975, pp. 849–862.

8 Schneider, G. E., and LeDain, B. L., "Fully Developed Laminar Heat Transfer in Triangular Passages," *J. Energy*, Vol. 5, 1981, pp. 15–21.

9 Sparrow, E. M., Baliga, B. R., and Patankar, S. V., "Forced Convection Heat Transfer From a Shrouded Fin Array With and Without Tip Clearance," ASME JOURNAL OF HEAT TRANSFER, Vol. 100, 1978, pp. 572–579.

10 Soliman, H. M., Chau, T. S., and Trupp, A. C., "Analysis of Laminar Heat Transfer in Internally Finned Tubes With Uniform Outside Wall Temperature," ASME JOURNAL OF HEAT TRANSFER, Vol. 102, 1980, pp. 598–604.

11 Sparrow, E. M., and Lee, L., "Effects of Fin Base-Temperature Depression in a Multifin Array," ASME JOURNAL OF HEAT TRANSFER, Vol. 97, 1975, pp. 463–465.

12 Heggs, P. J., and Stones, P. R., "The Effects of Dimensions on the Heat Flowrate Through Extended Surfaces," ASME JOURNAL OF HEAT TRANSFER, Vol. 102, 1980, pp. 180–182.

13 Sparrow, E. M., and Patankar, S. V., "Relationships Among Boundary Conditions and Nusselt Numbers for Thermally Developed Duct Flows," ASME JOURNAL OF HEAT TRANSFER, Vol. 99, 1977, pp. 483=485.

14 Baliga, B. R., and Patankar, S. V., "A New Finite-Element Formulation for Convection-Diffusion Problems," *Numerical Heat Transfer*, Vol. 3, 1980, pp. 393–409.

15 Segerlind, L. J., *Applied Finite Element Analysis*, Wiley, New York, 1976.

16 Patankar, S. V., *Numerical Heat Transfer and Fluid Flow*, Hemisphere, Washington, D.C., 1980.

On the Convective Heat Transfer in a Tube of Elliptic Cross Section Maintained Under Constant Wall Temperature

M. A. Ebadian
Mem. ASME

H. C. Topakoglu

Department of Mechanical Engineering,
Southern University,
Baton Rouge, LA 70813

O. A. Arnas
Department of Mechanical Engineering,
California State University,
Chico, CA 95929
Mem. ASME

The convective heat transfer problem along the portion of a tube of elliptic cross section maintained under a constant wall temperature where hydrodynamically and thermally fully developed flow conditions prevail is solved in this paper. The successive approximation method is used for the solution utilizing elliptic coordinates. Analytical expressions for temperature distribution and Nusselt number corresponding to the first cycle of approximation are obtained in terms of the ellipticity of the cross section. In the case of a circular section, the first cycle approximation of the Nusselt number is obtained as 3.7288 compared to the exact value of 3.6568. Representative temperature distribution curves are plotted and compared to those corresponding with constant wall heat flux conditions.

Introduction

An inspection of literature [1-5] indicates that in the area of convective heat transfer for laminar flows in tubes of elliptic cross sections, the main important studies are [6, 7]. Reference [6] deals with convective heat transfer in tubes of elliptic cross section maintained under constant heat flux and the problem is analyzed by using rectangular coordinates. However, the differential equation of the problem considered in this paper requires a temperature distribution expression expressed in elliptic coordinates. For this reason, the temperature distribution of [6] is obtained again in elliptic coordinates.

Reference [7] deals with the convection heat transfer problem with constant wall temperature conditions. The results of the problem are obtained by following the approach of Graetz and, as a result, no analytical formula is obtained.

A straightforward approach to solving the convective heat transfer problem under constant wall temperature conditions is the successive approximation method [3-5] where the temperature distribution for constant heat flux is used to start the perturbation. Noting that a starting temperature distribution expressed in a system of orthogonal coordinates fitting the boundary of the section would facilitate the solution of the problem considered, a temperature distribution corresponding to constant heat flux conditions is first obtained in elliptic coordinates.

Energy Equation

The energy equation suitable for constant wall temperature conditions, neglecting axial heat conduction, and corresponding to first-order successive approximation is

$$\left(\frac{T_0-T}{T_0-T_m}\right) W\frac{dT_m}{dZ}=\alpha\left(\frac{\partial^2 \bar{T}}{\partial X^2}+\frac{\partial^2 \bar{T}}{\partial Y^2}\right) \qquad (1)$$

where

X, Y are the rectangular coordinates in the cross section of the tube
Z is the longitudinal coordinate along the pipe
$\bar{T}$ is the temperature under constant wall temperature conditions
T is the temperature under constant wall heat flux conditions
T_0 is the wall temperature
T_m is the mixed mean temperature
α is the thermal diffusivity
W is the velocity distribution.

Denoting the semi-major and semi-minor axes of the elliptic section by A and B, respectively, and selecting the mean semi-axis

$$L=\frac{1}{2}(A+B) \qquad (2)$$

as the reference length, the following dimensionless variables are introduced

$$X=Lx, \qquad Y=Ly, \qquad Z=Lz, \qquad W=\frac{\nu}{L}w \qquad (3)$$

The dimensionless velocity in an elliptic pipe expressed in elliptic coordinates is

$$w=(\mathrm{Re})(w_0-w_2\cos 2\eta) \qquad (4a)$$

with

$$w_0=1+m^4-\xi^2-\frac{m^4}{\xi^2} \qquad (4b)$$

$$w_2=\frac{2m^2}{1+m^4}w_0$$

where m is the ellipticity of the section and is

$$m=\left[\left(1-\frac{B}{A}\right)\Big/\left(1+\frac{B}{A}\right)\right]^{1/2} \qquad (4c)$$

The Reynolds number Re is defined as the Reynolds number in a simple circular pipe of radius L maintained under the same pressure gradient as that of the elliptic pipe [8].

Temperature for Constant Wall Heat Flux Condition

Following the procedure of [8], define a dimensionless excess temperature e by the relation

$$e=\frac{k}{LF}E \qquad (5)$$

where k is the thermal conductivity, F is a reference heat flux, and E is the dimensional excess temperature.

The energy equation to be satisfied by e in elliptic coordinates is [8]

Contributed by the Heat Transfer Division for publication in the JOURNAL OF HEAT TRANSFER. Manuscript received by the Heat Transfer Division January 14, 1985.

$$\left(\frac{\partial^2}{\partial t^2}+\frac{\partial^2}{\partial \eta^2}\right)e=G(E_0-E_2\cos 2\eta+E_4\cos 4\eta) \tag{6a}$$

where t ($=\ln \xi$) and η are isometric elliptic coordinates and

$$\begin{aligned} G&=c(\mathrm{Pe})\\ E_0&=x_2w_0+m^2w_2\\ E_2&=2m^2w_0+x_2w_2\\ E_4&=m^2w_2\\ x_2&=\xi^2+\frac{m^4}{\xi^2} \end{aligned} \tag{6b}$$

The solution of the differential equation (6*a*), satisfying the boundary condition $e=0$ for $\xi=1$, is obtained as

$$e=G(e_0+e_2\cos 2\eta+e_4\cos 4\eta) \tag{7a}$$

where

$$\begin{aligned} e_0&=-\frac{1}{16}\left[3(1+m^8)-4\frac{1+m^8}{1+m^4}x_2+x_4\right]\\ e_2&=-\frac{8}{3}\frac{m^2}{1+m^4}e_0\\ e_4&=\frac{2}{3}\frac{m^4}{1+m^8}e_0\\ x_4&=\xi^4+\frac{m^8}{\xi^4} \end{aligned} \tag{7b}$$

The mixed mean excess temperature corresponding to equation (6*a*) is obtained from

$$E_m=(T_m-T_o)=\frac{\rho}{Q}\int_S W\,E\,dS \tag{8}$$

where ρ is the density, Q is the mass rate of flow, and S and dS are the full and elemental cross-sectional areas, respectively.

After some calculations

$$E_m=-\frac{FL}{k}\frac{J}{I_{00}} \tag{9a}$$

where

$$\begin{aligned} J&=G\bar{J}\\ I_{00}&=\frac{1}{4}\frac{(1-m^4)^3}{1+m^4}\\ \bar{J}&=\frac{1}{32}\frac{1-m^4}{1+m^4}(1+m^8)^2+\frac{5}{96}\frac{1-m^4}{1+m^4}(1+m^8)(1+4m^4+m^8)\\ &-\frac{7}{128}(1-m^{16})+\frac{m^4}{(1+m^4)^2}\left[-\frac{1}{3}\frac{1-m^4}{1+m^4}(1+m^8)^2\right.\\ &\left.-\frac{5}{48}(1-m^{16})+\frac{1}{9}\frac{1+m^8}{1+m^4}(1-3m^8+3m^4-m^{12})\right]\\ &-\frac{7}{48}\frac{1-m^4}{1+m^4}m^8+\frac{1}{96}\frac{1-m^8}{1+m^8}m^8+\frac{1}{24}\frac{1-m^8}{(1+m^4)^2}m^8\\ &-\frac{1}{144}\frac{1-m^4}{1+m^4}\frac{m^8}{1+m^8}(1+4m^4+m^8) \end{aligned} \tag{9b}$$

Temperature for Constant Wall Temperature Condition

Defining the following dimensionless temperatures

$$\bar{e}=\frac{k}{LF}\bar{T} \quad \text{and} \quad e_m=\frac{k}{LF}E_m \tag{10a}$$

the energy equation (1) changes into a dimensionless form, expressed in elliptic coordinates, as

Nomenclature

A = semi-major axis of elliptic pipe, equation (2)
a_0 = function defined by equation (A1)
a_2 = function defined by equation (A3)
a_4 = function defined by equation (A5)
a_6 = function defined by equation (A7)
a_8 = function defined by equation (A9)
B = semi-minor axis of elliptic pipe, equation (2)
C = dimensional temperature gradient along the pipe
c = dimensionless temperature gradient along the pipe
dS = elemental cross-sectional area of elliptic pipe
E = dimensional excess temperature
E_1 = elliptic integral of second kind
E_m = mixed mean excess temperature
E_0, E_2, E_4 = factors defined by equation (6*b*)
e_0, e_2, e_4 = factors defined by equation (7*b*)
F = characteristic heat flux
G = dimensionless factor defined by equation (6*b*)
I_{00} = function defined by equation (9*b*)
$J, \bar{J}$ = functions defined by equation (9*b*)
J_{01}, J_{21}, J_{41} = functions defined by equation (B1)
k = thermal conductivity
L = average of axes of the elliptic pipe, equation (2)
m = ellipticity parameter
Nu = Nusselt number
Pe = Peclet number = Re • Pr
Re = Reynolds number
S = full area of elliptic pipe
T = temperature for constant wall heat flux conditions
$\bar{T}$ = temperature for constant wall temperature conditions
T_m = mixed mean temperature
T_o = outer wall temperature
t = dimensionless elliptic coordinate
U_{01} = function defined by equation (B2)
U_{21} = function defined by equation (B4)
U_{41} = function defined by equation (B7)
V_{01} = function defined by equation (B3)
V_{21} = function defined by equation (B5)
V_{41} = function defined by equation (B7)
w = dimensionless velocity, equation (4*a*)
w_0, w_2 = functions defined by equation (4*b*)
X = dimensional transverse coordinate, equation (3)
x = dimensionless transverse coordinate, equation (3)
x_2 = function defined by equation (6*b*)
x_4 = function defined by equation (7*b*)
x_6 = function defined by equation (A1)
x_8 = function defined by equation (A1)
Y = dimensional transverse coordinate
y = dimensionless transverse coordinate
Z = dimensional longitudinal coordinate
z = dimensionless longitudinal coordinate
α = thermal diffusivity
η = dimensionless elliptical coordinate
ν = kinematic viscosity
ξ = dimensionless elliptical coordinate
ρ = density

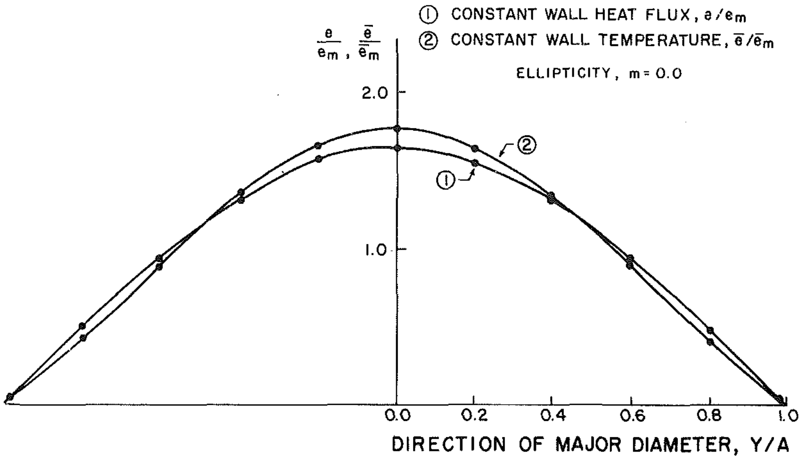

Fig. 1 Temperature distribution versus major diameter for $m=0$, circular tube

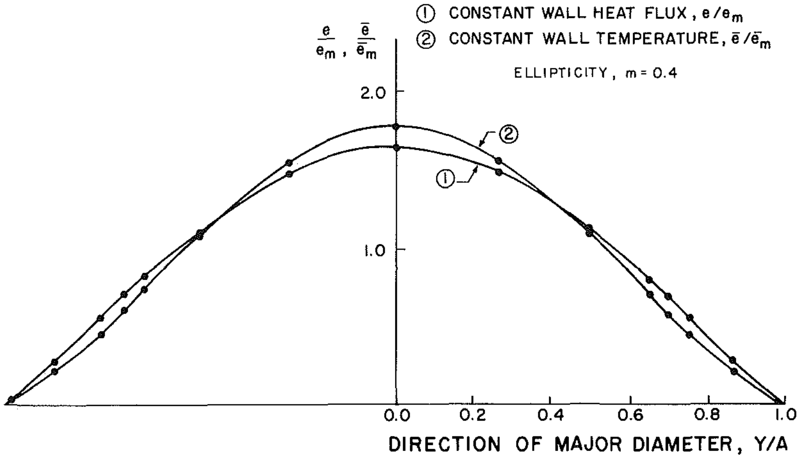

Fig. 2 Temperature distribution versus major diameter for ellipticity, $m=0.4$

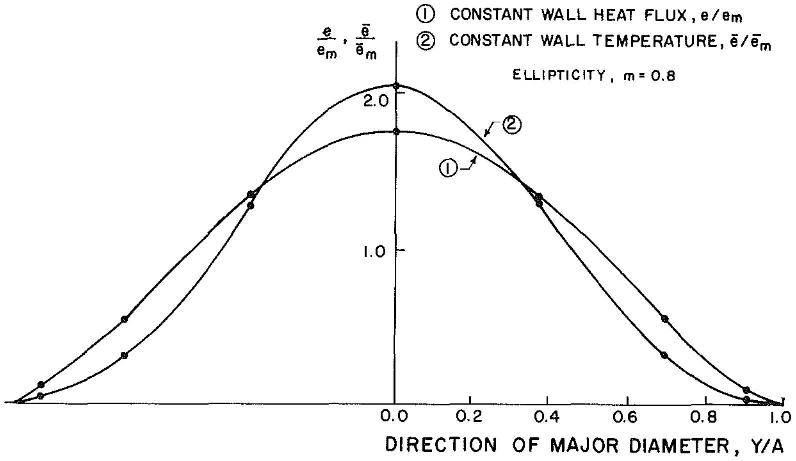

Fig. 3 Temperature distribution versus major diameter for ellipticity, $m=0.8$

$$\left(\frac{\partial^2}{\partial t^2}+\frac{\partial^2}{\partial \eta^2}\right)\bar{e}=\frac{G^2}{e_m}\left[\left(E_0e_0-\frac{1}{2}E_2e_2+\frac{1}{2}E_4e_4\right)\right.$$
$$+\left(E_0e_2-E_2e_0-\frac{1}{2}E_2e_4+\frac{1}{2}E_4e_2\right)\cos 2\eta$$
$$+\left(E_0e_4-\frac{1}{2}E_2e_2+E_4e_0\right)\cos 4\eta$$
$$\left.+\frac{1}{2}\left(E_4e_2-E_2e_4\right)\cos 6\eta+\frac{1}{2}E_4e_4\cos 8\eta\right] \qquad (10b)$$

The solution satisfying the boundary condition

$$\bar{e}=0 \text{ for } \xi=1 \qquad (11)$$

is obtained as

$$\bar{e}=\frac{G^2}{e_m}\left(a_0+a_2\cos 2\eta+a_4\cos 4\eta\right.$$
$$\left.+a_6\cos 6\eta+a_8\cos 8\eta\right) \qquad (12)$$

where a_0, a_2, a_4, a_6, a_8 are given in Appendix A.

The mixed mean temperature for $\bar{e}$ is calculated from

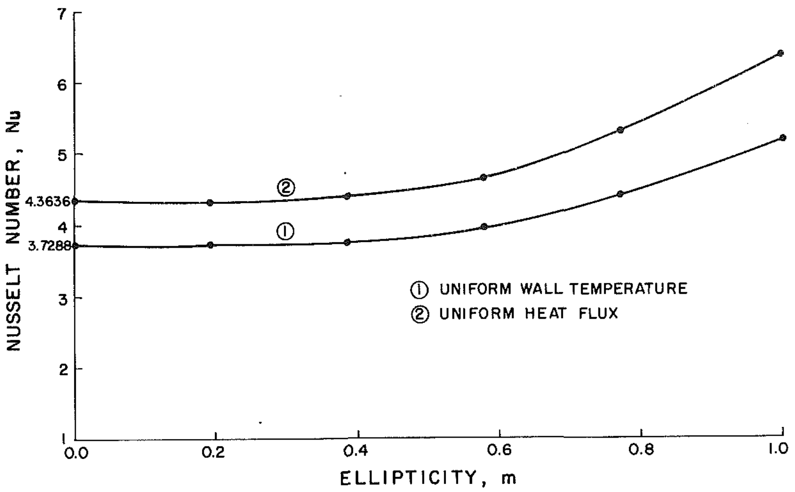

Fig. 4 Nusselt number versus ellipticity

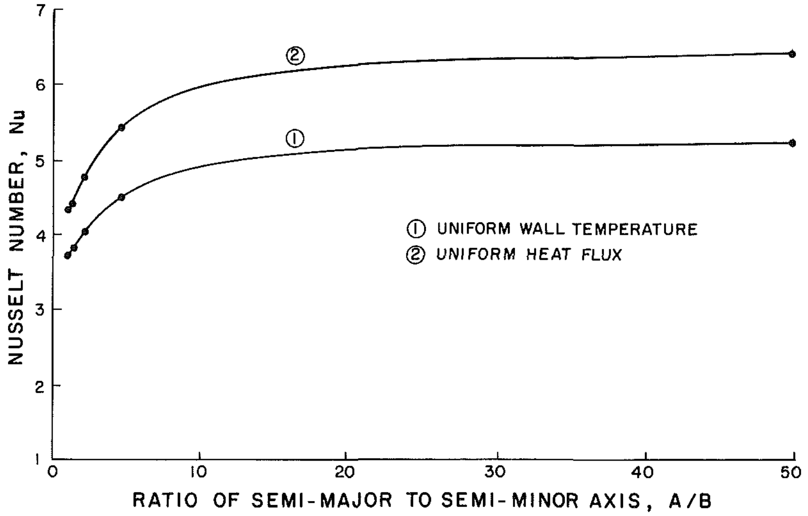

Fig. 5 Nusselt number versus the ratio of semi-major to semi-minor axis

$$\bar{T}_m = \frac{\rho}{Q}\int_S W\bar{T}dS \tag{13}$$

which after substituting $\bar{T}$ from (10*a*) and (12) can be written as

$$\bar{T}_m = -\frac{FL}{k}\frac{J_1}{I_{00}} \tag{14}$$

where

$$J_1 = -\frac{1}{2\pi(\mathrm{Re})}\int_0^{2\pi}\int_m^1 \xi j^2 w\bar{e}d\xi d\eta$$

$$j^2 = \frac{1}{\xi^2}(x_2 - 2m^2\cos 2\eta) \tag{15}$$

After some calculations and grouping the similar terms, one obtains

$$\frac{J_1}{G} = \frac{G}{e_m}(J_{01} + J_{21} + J_{41}) \tag{16}$$

for which the factors J_{01}, J_{21}, J_{41} are expressions depending only on the ellipticity ratio of the elliptic cross section. The expressions of these factors are given in Appendix B.

Considering the dimensionless mixed mean temperature for $\bar{T}_m$

$$\bar{e}_m = \frac{k}{LF}\bar{T}_m \tag{17}$$

the dimensionless temperatures can now be expressed by

$$\left(\frac{T - T_0}{T_m - T_0}\right)_{\text{constant heat flux}} = \frac{e}{e_m}$$

$$\left(\frac{\bar{T} - T_0}{\bar{T}_m - T_0}\right)_{\text{constant wall temperature}} = \frac{\bar{e}}{\bar{e}_m} \tag{18}$$

The distribution of these dimensionless temperatures along the major axis of the section for the values of ellipticity $m = 0.0$, 0.4, and 0.8 are plotted in Figs. 1-3. It must be noted that each temperature refers to its own bulk temperature; therefore, the curves show only the variation of each particular distribution.

The Nusselt number expression based on the hydraulic diameter of the elliptic section is obtained as

$$\mathrm{Nu} = \frac{\pi^2(1 - m^2)}{2(1 + m^2)E_1^2}\frac{I_{00}}{J_{01} + J_{21} + J_{41}}a_0'(1) \tag{19}$$

where E_1 is the complete elliptic integral of the second kind which is a function of the eccentricity, $2m(1 + m^2)$, of the elliptic periphery, and

$$a_0'(1) = \frac{1}{8}[2\bar{A}_{10} + \bar{B}_{10}(1+m^8) + 2\bar{E}_{10}](1-m^8)$$

$$- \frac{1}{2}(m^4\bar{C}_{10} + \bar{D}_{10})(1-m^4) - \frac{1}{6}\bar{C}_{10}(1-m^{12}) \qquad (20)$$

The factors $\bar{A}_{10}$, $\bar{B}_{10}$, $\bar{C}_{10}$, $\bar{D}_{10}$, $\bar{E}_{10}$ involved in the above are given in Appendix A.

The Nusselt number expression for the uniform heat flux case is given by

$$\mathrm{Nu} = \frac{\pi^2(1-m^2)}{2(1+m^2)E_1^2}\,\frac{I_{00}}{\bar{J}}\,e_0'(1) \qquad (21)$$

where I_{00} and $\bar{J}$ are given by equation (9*b*) and

$$e_0'(1) = \frac{1}{4}\,\frac{(1-m^4)^3}{(1+m^4)} \qquad (22)$$

Equation (21) is used in plotting Figs. 4 and 5.

The expression of Nusselt number given in equation (19) corresponds to the result of the first cycle of the successive approximation. However, a check of Nusselt number for the circular case is found as 3.7288 as opposed to its exact value of 3.6568. This is assumed a satisfactory agreement and the values of Nusselt numbers from equation (19) are plotted against the ellipticity ratio m and presented in Fig. 4. Higher order successive approximations are not presented since they are straightforward extensions of the method developed here.

Discussion

It is to be noted again that the dimensionless temperature for each case is with reference to its own bulk temperature. Therefore, the two temperature distribution curves cannot be compared with each other. However, an inspection of Figs. 1-3 reveals that a definite shape distinction exists between the two temperature distributions and this distinction is maintained for circular and for elliptic sections of any ellipticity.

A second point to be mentioned is that the calculation of the Nusselt number in this paper follows an analysis parallel to [8]; that is, the wall heat transfer coefficient is based on the averaged heat flux around the periphery. This makes it impossible to obtain a well-known Nusselt number in the case of $m = 1$. Therefore the limiting value of Nusselt number in Fig. 4, for $m = 1$, cannot approach any established value.

Also, the numerically obtained results of [7] use Nusselt numbers that are based on an equal area diameter rather than a hydraulic diameter. To correlate with these values, the Nusselt numbers obtained in this paper are transformed to a form corresponding to that of [7]. These are plotted against the axial ratio of the cross section (the ratio between major and minor axes). By comparing this curve with that of [7], a satisfactory agreement has been found (Fig. 5).

It is to be noted that no substantial increase in Nusselt number is obtained for values of $m < 0.4$ or ratio of the axes $A/B > 10.0$. This characteristic is depicted for both the constant wall heat flux as well as the constant wall temperature cases, Figs. 4 and 5. For purposes of design, therefore, one should consider these characteristics.

Acknowledgments

The results presented in this paper were obtained in the course of research sponsored by the National Science Foundation, Washington, D.C. under Grant No. (R11-8305297) to Southern University and its precursors.

The authors appreciate the contribution made by Chiang Lee for the calculations involved in this paper.

References

1 Shah, R. K., and London, A. L., *Laminar Flow Forced Convection in Ducts*, Academic Press, New York, 1978.

2 Eckert, E. R. G., et al., "A Review of the 1982 Literature," *Int. J. Heat Mass Transfer*, Vol. 26, No. 12, 1983, pp. 1733-1770.

3 Bejan, A., *Convection Heat Transfer*, Wiley-Interscience, New York, 1984.

4 Kays, W. M., and Crawford, M. E., *Convective Heat and Mass Transfer*, McGraw-Hill, New York, 1980.

5 Arpaci, V. S., and Larsen, P. S., *Convection Heat Transfer*, Prentice-Hall, New York, 1984.

6 Tao, L. N., "On Some Laminar Forced-Convection Problems," ASME JOURNAL OF HEAT TRANSFER, Vol. 83, 1961, pp. 466-472.

7 Schenk, J., and Han, B. S., "Heat Transfer From Laminar Flow in Ducts With Elliptic Cross Section," *App. Sci. Res.*, Vol. 17, 1967, pp. 96-114.

8 Topakoglu, H. C., and Arnas, O. A., "Convective Heat Transfer for Steady Laminar Flow Between Two Confocal Elliptic Pipes With Longitudinal Uniform Wall Temperature Gradient," *Int. J. Heat Mass Transfer*, Vol. 17, 1974, pp. 1487-1498.

APPENDIX A

The functions involved in (12) are:

The function a_0

$$a_0 = K_2x_2 + K_4x_4 + K_6x_6 + K_8x_8 + K_0 \qquad (A1)$$

where

$$x_6 = \xi^6 + \frac{m^{12}}{\xi^6}, \qquad x_8 = \xi^8 + \frac{m^{16}}{\xi^8}$$

$$K_2 = -\frac{1}{4}(m^4\bar{C}_{10} + \bar{D}_{10})$$

$$K_4 = \frac{1}{16}(\bar{A}_{10} + \bar{E}_{10})$$

$$K_6 = -\frac{1}{36}\bar{C}_{10}$$

$$K_8 = \frac{1}{64}\bar{B}_{10}$$

$$K_0 = -\frac{1}{16}(\bar{A}_{10} + \bar{E}_{10})(1+m^8)$$

$$+ \frac{1}{4}(\bar{C}_{10}m^4 + \bar{D}_{10})(1+m^4) \qquad (A2)$$

$$+ \frac{1}{36}\bar{C}_{10}(1+m^{12}) - \frac{1}{64}\bar{B}_{10}(1+m^{16})$$

$$\bar{A}_{10} = \frac{1}{(1+m^4)^2}\left[\frac{1}{4}(1+m^{16}) + \frac{1}{3}m^8\right]$$

$$\bar{B}_{10} = \frac{1}{16} + \frac{1}{6}\,\frac{m^4}{(1+m^4)^2}$$

$$\bar{C}_{10} = \frac{1}{48}\,\frac{1}{1+m^4}\left[15(1+m^8) + 32m^4\frac{1+m^8}{(1+m^4)^2} - 2\frac{m^8}{1+m^8}\right]$$

$$\bar{D}_{10} = \frac{1}{48}\,\frac{1}{1+m^4}\left[9(1+m^8)^2 - 32m^4\frac{(1+m^8)^2}{(1+m^4)^2} - 14m^8\right]$$

$$\bar{E}_{10} = \frac{1}{3}m^4\frac{1+m^8}{(1+m^4)^2} + \frac{3}{16}(1+m^8) - \frac{1}{24}\,\frac{m^8}{1+m^8}$$

The function a_2

$$a_2 = C_1x_2 + \frac{1}{12}(\bar{A}_{12} + \bar{E}_{12})x_4 + \frac{1}{32}\bar{C}_{12}x_6 - \frac{1}{60}\bar{B}_{12}x_8$$

$$+ \frac{1}{2}m^4(m^4\bar{B}_{12} - \bar{A}_{12}) - \frac{1}{4}\bar{F}_{12} \qquad (A3)$$

where

$$\bar{A}_{12} = -\frac{2}{3}m^2\frac{1+m^8}{(1+m^4)^3}(1-m^4+m^8)$$

$$\bar{B}_{12} = \frac{1}{24}\frac{m^2}{1+m^4}\left(7+\frac{m^4}{1+m^8}\right)$$

$$\bar{C}_{12} = \frac{4}{3}m^2\frac{1+m^8}{(1+m^4)^2}$$

$$\bar{D}_{12} = -\frac{4}{3}m^6\frac{1+m^8}{(1+m^4)^2} \tag{A4}$$

$$\bar{E}_{12} = \frac{1}{12}\frac{m^2}{1+m^4}[m^4-9(1+m^8)]$$

$$\bar{F}_{12} = \frac{1}{8}m^2\frac{1+m^8}{1+m^4}[3(1+m^8)+5m^4]$$

$$C_1 = -\frac{1}{1+m^4}\Big[\frac{1}{12}\bar{A}_{12}(1-6m^4+m^8)$$

$$-\frac{1}{60}\bar{B}_{12}(1-30m^8+m^{16})$$

$$+\frac{1}{32}\bar{C}_{12}(1+m^{12})+\frac{1}{12}\bar{E}_{12}(1+m^8)-\frac{1}{4}\bar{F}_{12}\Big]$$

The function a_4

$$a_4 = \frac{1}{12}(\bar{D}_{14}+m^4\bar{C}_{14})x_2+C_2x_4-\frac{1}{20}\bar{C}_{14}x_6+\frac{1}{48}\bar{B}_{14}x_8$$

$$-\frac{1}{8}m^4(\bar{A}_{14}+m^4\bar{B}_{14})+\frac{1}{16}\bar{F}_{14} \tag{A5}$$

where

$$\bar{A}_{14} = -\frac{1}{3}m^4\frac{1+m^8}{(1+m^4)^2}$$

$$\bar{B}_{14} = \frac{1}{24}m^4\left[\frac{1}{1+m^8}+4\frac{1}{(1+m^4)^2}\right]$$

$$\bar{C}_{14} = \frac{1}{12}\frac{m^4}{1+m^4}\left[1+8\frac{1+m^8}{(1+m^4)^2}\right]$$

$$\bar{D}_{14} = -\frac{1}{12}m^4\frac{1+m^8}{1+m^4}\left[9+8\frac{1+m^8}{(1+m^4)^2}\right] \tag{A6}$$

$$\bar{F}_{14} = \frac{1}{8}m^4(1+m^8)\left[4\frac{1+m^8}{(1+m^4)^2}+3\right]$$

$$C_2 = \frac{1}{1+m^8}\Big[\frac{1}{8}\bar{A}_{14}m^4-\frac{1}{48}\bar{B}_{14}(1-6m^8+m^{16})$$

$$+\frac{1}{60}\bar{C}_{14}(3-5m^4-5m^8+3m^{12})$$

$$-\frac{1}{12}\bar{D}_{14}(1+m^4)-\frac{1}{16}\bar{F}_{14}\Big]$$

The function a_6

$$a_6 = \frac{1}{64}\bar{D}_{16}x_2-\frac{1}{40}(\bar{A}_{16}+\bar{E}_{16})x_4+C_3x_6-\frac{1}{56}\bar{B}_{16}x_8$$

$$+\frac{1}{72}(2m^2\bar{B}_{16}-2m^4\bar{A}_{16}-\bar{F}_{16}) \tag{A7}$$

where

$$\bar{A}_{16} = \frac{4}{3}m^6\frac{1+m^8}{(1+m^4)^3}$$

$$\bar{B}_{16} = \frac{1}{12}\frac{m^6}{(1+m^4)(1+m^8)}$$

$$\bar{D}_{16} = \frac{8}{3}m^6\frac{1+m^8}{(1+m^4)^2}$$

$$\bar{E}_{16} = \frac{1}{6}\frac{m^6}{1+m^4} \tag{A8}$$

$$\bar{F}_{16} = \frac{5}{4}m^6\frac{1+m^8}{1+m^4}$$

$$C_3 = \frac{1}{2}\left(\frac{1}{1+m^{12}}\right)\Big[\frac{1}{180}\bar{A}_{16}(9+10m^4+9m^8)+\bar{B}_{16}\Big(\frac{1}{28}$$

$$-\frac{1}{18}m^8+\frac{1}{28}m^{16}\Big)-\frac{1}{32}\bar{D}_{16}(1+m^4)+\frac{1}{20}\bar{E}_{16}(1+m^8)$$

$$+\frac{1}{36}\bar{F}_{16}\Big]$$

The function a_8

$$a_8 = -\frac{1}{120}(\bar{C}_{18}+m^4\bar{B}_{18})x_2+\frac{1}{96}(\bar{A}_{18}+\bar{D}_{18})x_4$$

$$-\frac{1}{56}\bar{B}_{18}x_6+C_4x_8+\frac{1}{128}(2m^4\bar{A}_{18}+\bar{E}_{18}) \tag{A9}$$

where

$$\bar{A}_{18} = \frac{1}{3}\frac{m^8}{(1+m^4)^2}$$

$$\bar{B}_{18} = \frac{1}{12}\frac{m^8}{(1+m^4)(1+m^8)}$$

$$\bar{C}_{18} = \frac{7}{12}\frac{m^8}{1+m^4} \tag{A10}$$

$$\bar{D}_{18} = \frac{1}{12}\frac{m^8}{1+m^8}$$

$$\bar{E}_{18} = \frac{1}{4}m^8$$

$$C_4 = -\frac{1}{2}\left(\frac{1}{1+m^{16}}\right)\Big[\frac{1}{192}\bar{A}_{18}(4+6m^4+4m^8)$$

$$-\frac{1}{420}\bar{B}_{18}(15+7m^4+7m^8+15m^{12})$$

$$-\frac{1}{60}\bar{C}_{18}(1+m^4)+\frac{1}{48}\bar{D}_{18}(1+m^8)+\frac{1}{64}\bar{E}_{18}\Big]$$

APPENDIX B

The functions involved in equation (16) are

$$J_{01}+J_{21}+J_{41} = U_{01}+V_{01}+U_{21}+V_{21}+U_{41}+V_{41} \tag{B1}$$

where

$$U_{01} = -\frac{1+m^8}{1+m^4}\Big\{\frac{1}{96}(\bar{A}_{10}+\bar{E}_{10})(1+3m^4-3m^8-m^{12})$$

$$+\frac{1}{1920}\bar{B}_{10}(3+5m^4-5m^{16}-3m^{20})-\frac{1}{288}\bar{C}_{10}(1+20m^4$$

$$-20m^{12}-m^{16})-\frac{1}{16}[\bar{D}_{10}(1-m^8)-8K_0(1-m^4)]\Big\} \tag{B2}$$

$$\begin{aligned} V_{01} = \Big\{ & \frac{1}{128}\bar{A}_{10}(1-m^{16}) + \frac{1}{768}\bar{B}_{10}(1+3m^8-3m^{16}-m^{24}) \\ & + \frac{1}{360}\bar{C}_{10}(1+15m^4+50m^8+40m^2+15m^{16}-m^{20}) \\ & - \frac{1}{24}\bar{D}_{10}(1+3m^4-3m^8-m^{12}) + \frac{1}{128}[\bar{E}_{10}(1-m^{16}) \\ & + 32K_0(1-m^8)]\Big\} \end{aligned} \tag{B3}$$

$$\begin{aligned} U_{21} = m^2\frac{1+m^8}{1+m^4}\Big\{ & \frac{1}{2}C_1(1-m^4) + \frac{1}{48}(\bar{A}_{12}+\bar{E}_{12})(1-m^8) \\ & + \frac{1}{192}\bar{C}_{12}(1-m^{12}) - \frac{1}{480}\bar{B}_{12}(1-m^{16})\Big\} \end{aligned} \tag{B4}$$

$$\begin{aligned} V_{21} = -\frac{m^2}{1+m^4}\Big\{ & \frac{1}{96}\bar{A}_{12}(1+12m^{12}-m^{16}-12m^4) \\ & - \frac{1}{720}\bar{B}_{12}(1-87m^8+87m^{16}-m^{24}) + \frac{1}{320}\bar{C}_{12}(1+5m^8 \\ & - 5m^{12}-m^{20}) + \frac{1}{96}[\bar{E}_{12}(1-m^{16})-6\bar{F}_{12}(1-m^8)] \\ & + \frac{1}{6}C_1(1+3m^4-3m^8-m^{12})\Big\} \end{aligned} \tag{B5}$$

$$\begin{aligned} V_{41} = \frac{m^4}{1+m^4}\Big\{ & -\frac{1}{16}\bar{A}_{14}m^4(1-m^4) + \frac{1}{1440}\bar{B}_{14}(3+5m^4 \\ & - 90m^8+90m^{12}-5m^{16}-3m^{20}) - \frac{1}{480}\bar{C}_{14}(3-4m^4+4m^{12} \\ & - 3m^{16}) + \frac{1}{96}[2\bar{D}_{14}(1-m^8)+3\bar{F}_{14}(1-m^4)] \\ & + \frac{1}{6}C_2(1+3m^4-3m^8-m^{12})\Big\} \end{aligned} \tag{B6}$$

$$\begin{aligned} U_{41} = -m^4\Big\{ & \frac{1}{384}\bar{B}_{14}(1-m^{16}) - \frac{1}{120}\bar{C}_{14}(1-5m^4 \\ & + 5m^8-m^{12}) + \frac{1}{24}\bar{D}_{14}(1-m^4) + \frac{1}{4}C_2(1-m^8)\Big\} \end{aligned} \tag{B7}$$

The factors with bars above are already defined in Appendix A.

Turbulent Flow and Heat Transfer in Bends of Circular Cross Section: I—Heat Transfer Experiments

E. M. Sparrow
Fellow ASME

G. M. Chrysler
Assoc. Mem. ASME

Department of Mechanical Engineering,
University of Minnesota,
Minneapolis, MN 55455

Experiments were performed to determine the local heat transfer characteristics of bends of circular cross section to which fluid was delivered either via a sharp-edged inlet or via a hydrodynamic development tube. The naphthalene sublimation technique, a mass transfer method, was used to facilitate the experiments. Bends subtending turning angles of 30, 60, and 90 deg were investigated, and the Reynolds number was varied between 5000 and 100,000. It was found that the local heat transfer coefficients at the outside of the bend were, for the most part, larger than those at the inside of the bend, but the deviations decreased as the Reynolds number increased. The streamwise distributions of the local transfer coefficient were markedly affected by the inlet condition; those for the sharp-edged inlet exhibited a universal shape, while the shapes of those for the tube-fed inlet depended both on the Reynolds number and on whether the distribution corresponded to the inside or the outside of the bend. In addition, the distributions for the case of the sharp-edged inlet exhibited higher local maxima and approached the fully developed regime more rapidly than did those for the tube-fed inlet. The heat transfer results were supplemented by flow visualization.

Introduction

Fluid flow in bends and curved ducts is encountered in a diverse range of applications including, for example, piping systems, heat exchangers, and the coolant passages of turbomachinery. The turning of the flow as it passes through the bend gives rise to cross-stream fluid motions which are superimposed on the streamwise mainflow. These secondary flows are responsible for the departures of the heat transfer and pressure drop characteristics of bends from those of straight ducts.

This paper is the first part of a two-part experimental study of turbulent flow and heat transfer in bends of circular cross section. The heat transfer experiments are reported here, while complementary pressure distribution experiments are described in [1]. In addition, flow visualization studies were performed here using the oil-lampblack technique. Identical bend geometries were used in all parts of the research, thereby providing continuity. Bends which subtend turning angles of 30, 60, and 90 deg were used in the experiments and, for each, the effects of two different hydrodynamic inlet conditions were investigated. In one, the flow was ducted to the inlet via a hydrodynamic development tube, while in the other, fluid from a large upstream plenum chamber was drawn into the bend through a sharp-edged inlet. For each bend and each inlet condition, the Reynolds number was varied from 5000 to 100,000.

Local heat transfer coefficients were determined as a function of the streamwise coordinate along the bend, with separate coefficient values obtained for the portions of the wall at the inside of the bend and at the outside of the bend. The heat transfer coefficients were deduced from mass transfer coefficients measured by the use of the naphthalene sublimation technique. In dimensionless terms, streamwise distributions of the Nusselt (Sherwood) number are presented

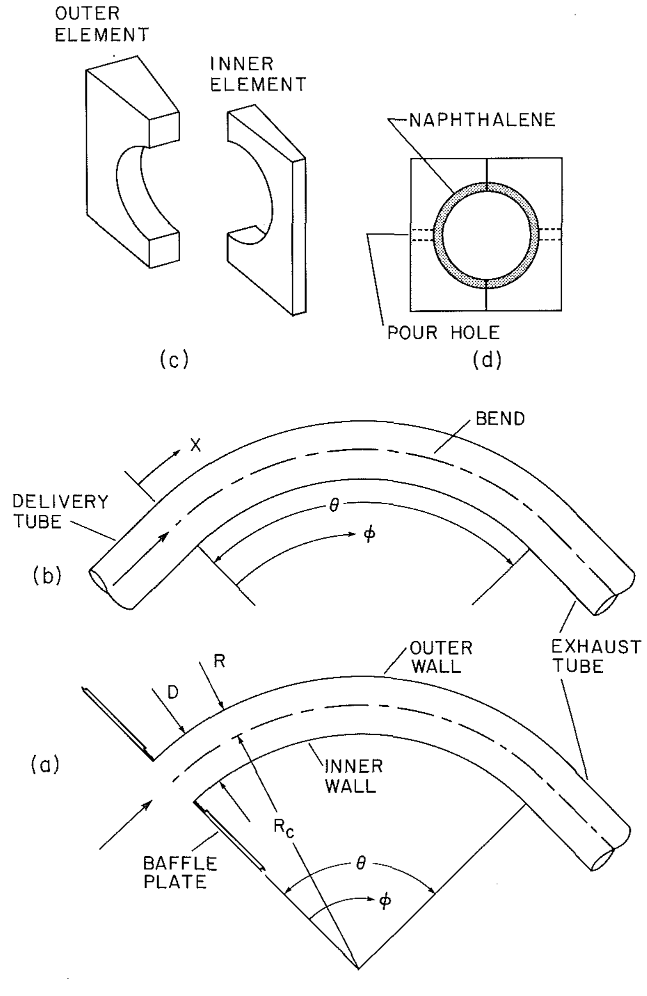

Fig. 1 Apparatus diagrams

Contributed by the Heat Transfer Division for publication in the JOURNAL OF HEAT TRANSFER. Manuscript received by the Heat Transfer Division December 4, 1984.

at the inside and outside of the bend and for the circumferential average. These results are compared with entrance region and fully developed Nusselt numbers for straight tubes and with fully developed Nusselt numbers for curved pipes and helical coils. The visualized fluid flow patterns are presented in photographs.

A survey of the literature revealed the absence of local heat transfer results for bends of circular cross section. Results for fully developed heat transfer for laminar and turbulent flow in helical coils and curved pipes are available in [2-6], but, as will be demonstrated later, a bend is by no means a region of fully developed flow.

The Experiments

With regard to the use of the naphthalene sublimation technique, the well-established analogy between heat and mass transfer provides a one-to-one correspondence between the Sherwood number and the Nusselt number. The boundary condition for the mass transfer (uniform concentration of naphthalene vapor at the bounding wall) corresponds to uniform wall temperature for the analogous heat transfer problem. The advantages of the naphthalene technique are its high accuracy, virtual absence of unaccounted extraneous losses, well-defined boundary conditions, and high resolution. With regard to the latter attribute, note may be taken of the difficulty of obtaining accurate local results in heat transfer experiments in the presence of the uniform wall temperature boundary condition.

The essential features of the experimental apparatus will be described with the aid of Figs. 1(*a-d*), with complete details available in [7]. Figure 1(*a*) displays the setup for the case where air from a large upstream plenum chamber is drawn into the bend through a sharp-edged inlet, while Fig. 1(*b*) shows the setup in which the bend is fed by a hydrodynamic development tube. The bend itself was common to the two configurations. The angle subtended by the bend (i.e., the turning angle) is depicted by θ, while the streamwise coordinate, measured from the bend inlet cross section, is represented by the angle ϕ $(0 \leq \phi \leq \theta)$. As noted earlier, bends characterized by $\theta = 30$, 60, and 90 deg were used during the course of the experiments. The radius of curvature of the bend centerline R_c and the radius of the circular cross section of the bend R yielded the ratio $R_c/R = 9$ which characterized all of the experimental work. The actual diameter D $(=2R)$ of the cross section was 3.175 cm (1.250 in.).

In the setup depicted in Fig. 1(*b*), the hydrodynamic development tube (termed the delivery tube) had a diameter of 3.175 cm, identical to that of the bend. The centerline of the development tube was tangent to that of the bend at their point of intersection (i.e., at the bend inlet). The tube was 30 diameters long – sufficiently long so that a linear pressure distribution existed over an appreciable portion of its length [1].

The special feature of the setup pictured in Fig. 1(*a*) is the baffle plate positioned at the inlet cross section of the bend. Although shown truncated in the figure, the plate was a large circular disk, 50.8 cm (20 in.) in diameter. At the center of the plate there was a sharp-edged aperture whose diameter (3.175 cm) was identical to that of the bend. The thickness of the portion of the plate which bounded the aperture had been reduced to 0.155 cm (0.049 diameters) in order to minimize possible hydrodynamic development of the flow prior to its entry into the bend. In effect, the baffle plate served as the downstream wall of a large plenum chamber (i.e., the laboratory room).

In both setups, the airflow exiting the bend passed into an exhaust tube whose length and diameter were identical to those of the delivery tube.

The system was operated in the open-circuit mode and in suction. Air was drawn from the temperature-controlled, naphthalene-free laboratory room and, upon entering the bend, it received naphthalene vapor due to sublimation at the walls. After passing through the bend, the naphthalene-enriched air discharged into the exhaust tube, from which it was ducted to a flowmeter, a control valve, and to a blower which was vented outside the building.

The bends used in the mass transfer experiments were synthesized by assembling a succession of mass transfer modules, each of which is a miniature bend which turned the flow through 5 deg. Each module was made up of two parts, one of which served as the outer wall of the bend while the other served as the inner wall of the bend. A pictorial view of a module is presented in Fig. 1(*c*). As shown there, the two parts of the module, which are in accurate alignment when assembled in the bend, have been displaced to underscore their separate identities. The modules are seen to be wedge-shaped, as is appropriate for their assemblage to form a bend.

The modules were fabricated from aluminum to very close tolerances. During fabrication, each inner and outer element was equipped with locating pins to ensure proper alignment during subsequent assembly. The assembly process was facilitated by a guideway which cradled the modules and enforced the desired radius of curvature of the bend. The assembled modules were pressed together by self-locking clamps. The 30, 60, and 90 deg bends were respectively synthesized by employing 6, 12, and 18 modules.

Figure 1(*d*) is a front-face view of a module showing an annular layer of naphthalene in place at its bore. Thus, the airflow passing through the bend was bounded by solid naphthalene from which vapor sublimed during the course of a data run. The naphthalene was implanted in the module by a casting process. The centerbody of the mold used in the casting process was curved so as to impart the desired curvature to the naphthalene surface which bounded the flow passage. Pour holes used to introduce molten naphthalene into the mold cavity are shown in the figure. Two of the modules were equipped with thermocouples to measure the

Nomenclature

A = naphthalene surface area
D = diameter of bend cross section
$\mathfrak{D}$ = naphthalene-air diffusion coefficient
K = local mass transfer coefficient, equations (1), (2), and (5)
ΔM = change of mass
$\dot{Q}$ = volumetric flow rate
R = radius of bend cross section
R_c = radius of curvature of bend
Re = Reynolds number = $4\dot{w}/\mu\pi D$
Sh = local Sherwood number = $KD/\mathfrak{D}$
Sh* = fully developed Sh for straight tube
Sh[2] = circumferential-average, fully developed laminar Sh for curved tubes from [2]
Sh[6] = circumferential-average, fully developed turbulent Sh for curved tubes from [6]
$\dot{w}$ = mass flow rate
X = axial distance in straight pipe
θ = turning angle of bend
μ = viscosity
ρ_{nw} = naphthalene vapor density at wall
ρ_{nb} = naphthalene vapor density in bulk flow
τ = duration of data run
ϕ = angular coordinate

Subscripts

i = inner element of module
j = module j
o = outer element of module

surface temperature of the subliming naphthalene. The thermocouples were implanted in the naphthalene during the casting process.

The primary focus of each data run was to determine the change of mass of each of the mass transfer elements due to their exposure to the airflow in the bend. To this end, the mass of each element was measured immediately before and immediately after each run. These measurements were accomplished using a Sartorius electronic analytical balance with a capacity of 166 g. The 0.00001 g resolution of the balance readily accommodated the 0.02–0.06 g change of mass during a data run. The duration of the run was selected to limit the sublimation-related change of diameter of the mass transfer elements ($\sim$0.15 percent change relative to the mean). During the run, the naphthalene surface temperature was read and recorded at regular intervals. Following each data run, supplementary measurements were made to determine the mass transfer which occurred during the assembly and disassembly of the bend, and this information was used as a correction in the data reduction.

Care was also taken to ensure that the mass transfer elements had attained temperature equilibrium at the beginning of a data run. This is a relevant step in the experimental procedure since the concentration of the naphthalene vapor adjacent to the subliming surface is controlled by the surface temperature.

Data Reduction

The mass transfer coefficient K and its dimensionless counterpart, the Sherwood number Sh, were evaluated at each of the mass transfer elements in the bend. In this regard, let j denote a typical module in the array and let j,i and j,o represent the inner wall and outer wall elements at j. Then,

$$K_{j,i} = (\Delta M_{j,i}/\tau A_{j,i})/(\rho_{nw} - \rho_{nb})_j \tag{1}$$

$$K_{j,o} = (\Delta M_{j,o}/\tau A_{j,o})/(\rho_{nw} - \rho_{nb})_j \tag{2}$$

In these equations, $\Delta M_{j,i}$ and $\Delta M_{j,o}$ represent the changes of mass during time τ at the inner and outer elements, and $A_{j,i}$ and $A_{j,o}$ are the corresponding mass transfer surface areas (which were evaluated taking account of sublimation-related surface recession).

The mass transfer is driven by the difference between the naphthalene vapor densities at the wall and in the bulk – analogous to the wall-to-bulk temperature difference for heat transfer. The quantity ρ_{nw}, which is the naphthalene vapor density at the wall, was evaluated from the measured surface temperature by using the vapor pressure/temperature relation for naphthalene [8] in conjunction with the perfect gas law. Note that ρ_{nw} is the same for all elements which comprise the bend.

To determine the bulk density $\rho_{nb,j}$ of the naphthalene vapor at module j, it is first useful to note that the increase in ρ_{nb} between the inlet and outlet of any module m is

$$(\Delta\rho_{nb})_m = [(\Delta M_{m,i} + \Delta M_{m,o})/\tau]/\dot{Q} \tag{3}$$

where $\dot{Q}$ is the volumetric flow rate. With this and noting that $\rho_{nb} = 0$ at the inlet of the bend, it follows that

$$\rho_{nb,j} = \sum_{m=1}^{j-1} (\Delta\rho_{nb})_m + \tfrac{1}{2}(\Delta\rho_{nb})_j \tag{4}$$

The volumetric flow rate was virtually constant along the bend (e.g., 0.2 percent variation for the 90 deg bend at Re = 37,000).

In addition to the mass transfer coefficients $K_{j,i}$ and $K_{j,o}$ for the inner and outer walls, the circumferential-average mass transfer coefficient for each module was evaluated from

$$K_j = [(\Delta M_{j,i} + \Delta M_{j,o})/\tau(A_{j,i} + A_{j,o})]/(\rho_{nw} - \rho_{nb})_j \tag{5}$$

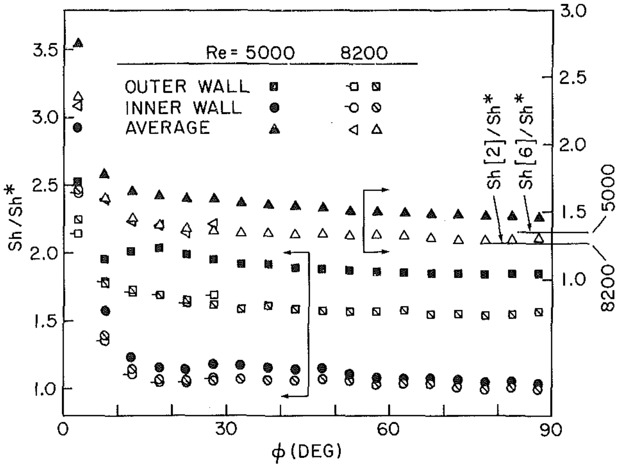

Fig. 2 Sherwood number distributions in tube-fed bends, Re = 5000 and 8200

The various mass transfer coefficients $K_{j,i}$, $K_{j,o}$, and K_j were recast in dimensionless form via the Sherwood number

$$\mathrm{Sh} = KD/\mathfrak{D} \tag{6}$$

The diffusion coefficient $\mathfrak{D}$ was eliminated from the Sherwood number by making use of the Schmidt number $\mathrm{Sc} = \nu/\mathfrak{D}$, where $\mathrm{Sc} = 2.5$ [8] for the naphthalene–air system and ν was evaluated as the kinematic viscosity of air.

The Reynolds number was defined as that for a conventional circular tube of diameter D

$$\mathrm{Re} = 4\dot{w}/\mu\pi D \tag{7}$$

in which $\dot{w}$ is the flow rate through the bend.

Mass (Heat) Transfer Results

Although the presentation of results will be couched in mass transfer terms, the results apply equally well to heat transfer because of the analogy between the two processes. The presentation is subdivided into three parts. The first and second parts respectively convey the streamwise distributions of the Sherwood number for bends fed by a hydrodynamic development tube and for bends which draw fluid through a sharp-edged inlet. These figures also include comparisons with fully developed results for straight tubes and for curved tubes and helical coils. Comparisons with straight-tube entrance region results are made in the third part of the presentation.

The Sherwood numbers reported here are quasi-local in that they are based on measurements at small but finite mass transfer elements. As noted earlier, each element turns the flow through 5 deg. In the graphic presentation of the results, the Sherwood number for a given element is plotted at its angular midpoint, for example, at $\phi = 12.5$ deg for the element situated between $\phi = 10$ and 15 deg.

The Sherwood number distributions for bends fed by a hydrodynamic development tube are presented in Figs. 2–4, while those for bends with sharp-edged inlets are given in Figs. 5–7. Each of these sets of three figures conveys results for seven Reynolds numbers ranging from 5000 to 100,000. To accommodate journal space guidelines, it was necessary to present results for more than one Reynolds number in a given figure and, to this end, the results for certain Reynolds numbers are represented by lines rather than by the actual data. However, sufficient data appear in each figure so that characteristics such as internal consistency and scatter can be assessed. All the data are available in [7]. The expected accuracy of the Sherwood number data is in the 2–3 percent range.

For each Reynolds number, three Sherwood number

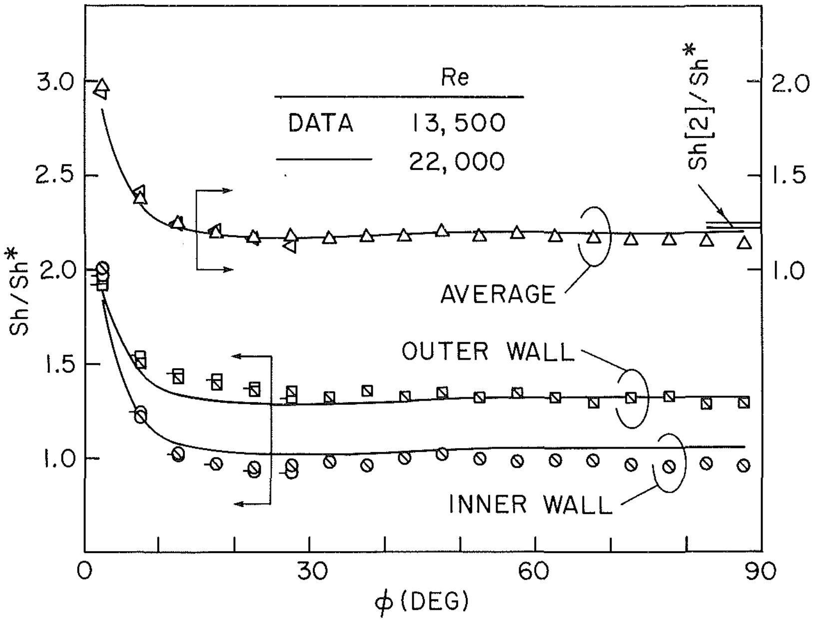

Fig. 3 Sherwood number distributions in tube-fed bends, Re = 13,500 and 22,000

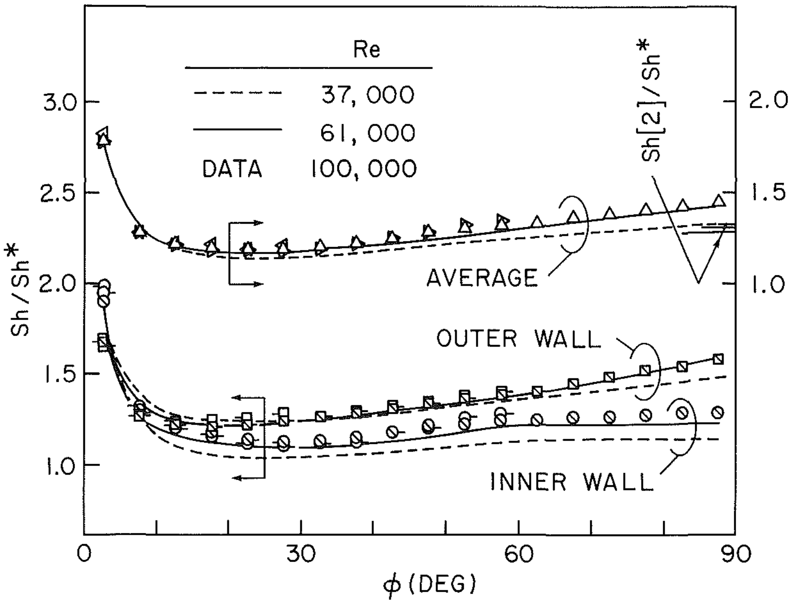

Fig. 4 Sherwood number distributions in tube-fed bends, Re = 37,000, 61,000, and 100,000

distributions are plotted, respectively for the outside of the bend, for the inside of the bend, and for the circumferential average (labeled outer wall, inner wall, and average in the figures). In each figure, the outer wall and inner wall distributions are referred to the left-hand ordinate, while the circumferential-average distributions are referred to the right-hand ordinate (note the upward shift of the right-hand ordinate scale).

The distributions are plotted as a function of the angular coordinate ϕ, with a range of 0 to 90 deg to accommodate the longest of the investigated bends (i.e., $\theta = 90$ deg). Consequently, the data for the 30 and 60 deg bends span only part of the abscissa range. In general, the Sherwood number data in the first 30 deg of a 60 or 90 deg bend agree very well with the data for a 30 deg bend. Similarly, the data in the first 60 deg of a 90 deg bend and the data for a 60 deg bend are virtually the same. Due to the near-congruence of the data for the various bend turning angles, the turning angle was omitted as a parameter in certain of the plotted distributions. This approach facilitated the compact presentation needed to accommodate the aforementioned space guidelines.

The Sherwood number results of Figs. 2-7 are couched in terms of the Sh/Sh* ratio. In this ratio, Sh is the local Sherwood number in the bend, while Sh* is the fully developed Sherwood number in a straight circular tube, where both Sh and Sh* correspond to the same Reynolds number. The motivation for using the Sh/Sh* ratio is to achieve a more compact presentation and also to obtain a direct comparison of the present results with an important benchmark case. Note that since Sh* is a constant at a given Reynolds number, the shape of the Sh/Sh* versus ϕ distribution is identical to the shape of the Sh versus ϕ distribution.

For $\mathrm{Re} \geq 10{,}000$ Sh* was evaluated from the Petukhov-Popov equation

$$\mathrm{Sh} = (f/8)\mathrm{ReSc}/[1.07 + 12.7(\mathrm{Sc}^{2/3} - 1)\sqrt{f/8}] \quad (8)$$

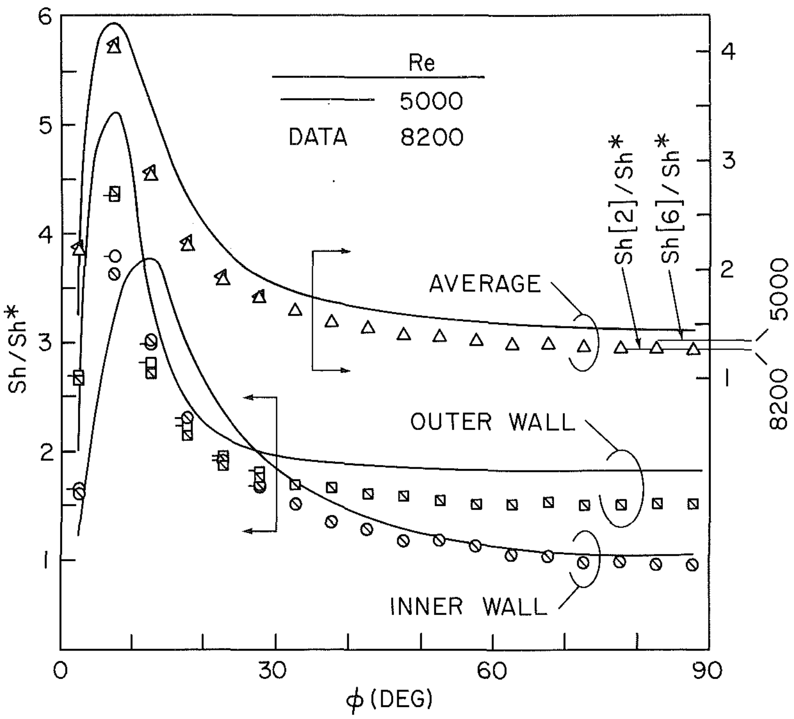

Fig. 5 Sherwood number distributions in bends with a sharp-edged inlet, Re = 5000 and 8200

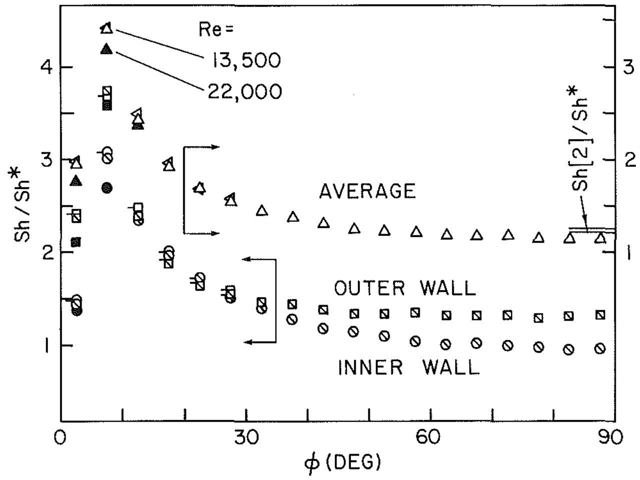

Fig. 6 Sherwood number distributions in bends with a sharp-edged inlet, Re = 13,500 and 22,000

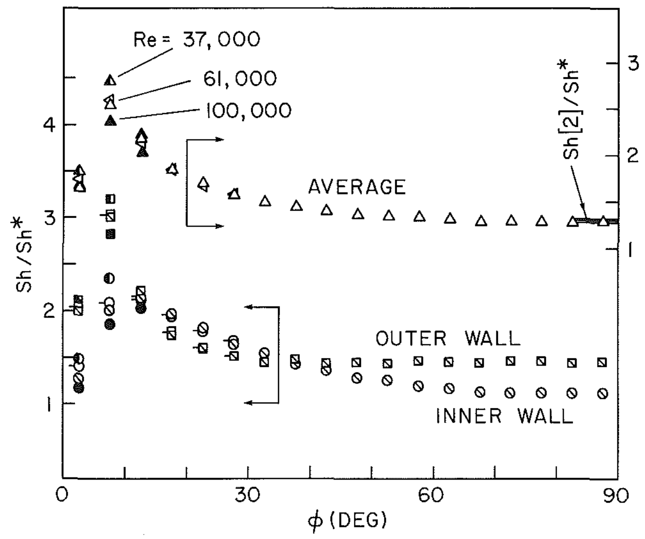

Fig. 7 Sherwood number distributions in bends with a sharp-edged inlet, Re = 37,000, 61,000, and 100,000

$$f = (1.82 \log \mathrm{Re} - 1.64)^{-2} \tag{9}$$

where f is the friction factor. For $\mathrm{Re} < 10{,}000$, the Gnielinski modification of equation (8) was employed for Sh*, whereby Re is replaced by (Re − 1000) and 1.07 is replaced by 1.00.

The figures also convey comparisons of the present results with circumferentially averaged, fully developed Sherwood numbers for curved tubes and helical coils. For the laminar and turbulent regimes, these fully developed Sherwood numbers, taken from [6] and [2] respectively, may be represented by

$$\mathrm{Sh}[6] = 0.836\mathrm{Re}^{0.5}(R/R_c)^{0.25}\mathrm{Sc}^{0.1} \tag{10}$$

$$\mathrm{Sh}[2] = 0.023\mathrm{Re}^{0.85}(R/R_c)^{0.1}\mathrm{Sc}^{0.4} \tag{11}$$

In the presentation format of Figs. 2–7, these fully developed Sherwood numbers are expressed via the ratios Sh[6]/Sh* and Sh[2]/Sh*, which are represented by the horizontal line segments adjacent to the right-hand ordinates of the respective figures. Note that these ratios provide a direct comparison of the fully developed Sherwood numbers for curved tubes and straight tubes.

With the foregoing as general background, attention will now be turned to the specifics of the results.

Bends With Tube-Fed Inlet. The Sherwood number results for the two lowest Reynolds numbers (5000 and 8200) are presented in Fig. 2, those for the intermediate range (13,500 and 22,000) are displayed in Fig. 3, while those for the upper range (37,000, 61,000, and 100,000) are in Fig. 4. An overall examination of these figures reveals that the shape of the Sherwood number distributions evolves with the Reynolds number. In general, the Sherwood number attains a maximum at the tube inlet and then drops off sharply in the first 10 deg of the bend. Thereafter, a more gradual dropoff sets in which, in the case of intermediate and high Reynolds numbers, is arrested and gives way to a streamwise increase.

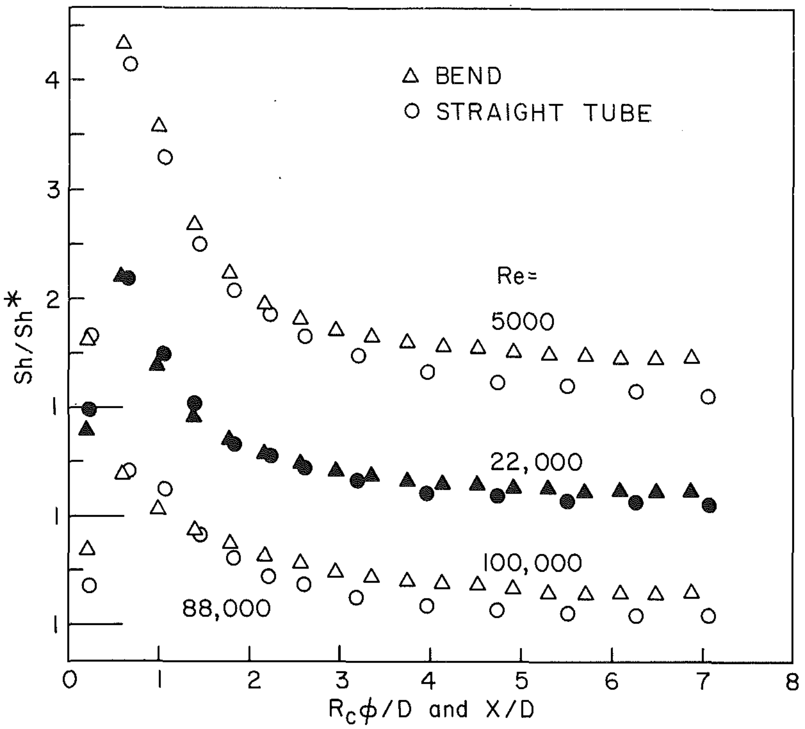

Fig. 8 Comparison of bend and straight-tube Sherwood numbers, sharp-edged inlet, Re = 5000, 22,000 and 88,000/100,000

At the lowest Reynolds number Re = 5000 (Fig. 2), the distributions along the inner and outer walls, respectively, display a local minimum and a local maximum at about $\phi = 20$ deg, whereafter they drop off gradually and appear to be tending toward a constant value. At the next higher Reynolds number, Re = 8200, the decrease is virtually monotonic, although there is a slight residual roll in the inner wall distribution. For both these Reynolds numbers, the circumferential average Sherwood numbers decrease more or less monotonically.

At the next Reynolds number, Re = 13,500 (data points in Fig. 3), the Sherwood numbers are virtually constant for $\phi > 30$ deg. As Re increases to 22,000 (solid lines in Fig. 3), a new pattern begins to emerge wherein a minimum is attained in the $\phi = 20-30$ deg range followed by an increase. In the case of Re = 22,000, the minimum is very shallow and the subsequent slight increase soon gives way to streamwise uniformity. Further development of this pattern occurs at the higher Reynolds numbers (Fig. 4). Downstream of the minimum, the outer wall Sherwood numbers increase steadily and significantly. At the inner wall, there is also an increase which, at $\phi \cong 60$ deg, gives way to a flat distribution. The circumferential average Sherwood numbers also increase steadily, downstream of the minimum.

An appraisal of the results discussed in the preceding paragraphs suggests that for the investigated bend geometries, a 90 deg bend is sufficiently long for the attainment of fully developed mass (heat) transfer when Re ≤ 22,000 but not for higher Reynolds numbers.

Differences in the inner and outer wall Sherwood number distributions have already been noted, and these differences will now be elaborated. At the inlet, the Sherwood numbers at the inner wall exceed those at the outer wall, but this relationship quickly reverses so that for most of the bend, the outer wall Sh values are higher. These variations may be due to convex wall stabilization versus concave wall destabilization. The deviation between the Sherwood numbers at the two walls is substantial at low Reynolds numbers and diminishes as the Reynolds number increases. At Re = 5000, the outer wall and inner wall Sh/Sh* values in the downstream region of the bend are, respectively, about 1.85 and 1.05. The corresponding outer wall/inner wall comparisons at Re = 8200 and 22,000 are 1.55/1.00 and 1.33/1.06. At the higher Reynolds numbers (Fig. 4), even smaller deviations prevail over most of the bend, but they tend to grow at the downstream end as the outer wall distribution ramps up while the inner wall distribution flattens out.

Inspection of Figs. 3 and 4 shows that in each figure, the Sh/Sh* distributions are virtually independent of the Reynolds number. Thus, for the Reynolds numbers of these figures, Sh* is an excellent scaling parameter for the bend Sherwood number distributions. The same cannot be said for the low Reynolds numbers of Fig. 2 where, in particular, the outer wall distributions are deviant. These low Reynolds number deviations may be due to a tendency toward laminarization in the bend, which, however, could not be identified with certainty.

The last issue to be discussed with respect to Figs. 2-4 is comparisons involving the circumferentially averaged, fully developed Sherwood numbers for curved tubes and helical coils. As noted earlier, these results are expressed by the Sh[6]/Sh* and Sh[2]/Sh* ratios portrayed by the line segments situated adjacent to the right-hand ordinates of the figures. Because Sh[2] and Sh[6] correspond to circumferential averages, they will be compared with the present circumferential average Sherwood numbers.

Consider first Figs. 3 and 4 (Re > 10,000), where it is seen that Sh[2]/Sh* is a very weak function of the Reynolds number (obviating the need to label the respective line segments), as are the Sh/Sh* results of the present experiments. The agreement between the Sh/Sh* distributions in the downstream portion of the bend and the Sh[2]/Sh* values is quite satisfactory for Re = 13,500 and 22,000, where the distributions flatten out. However, the ramping up of the distributions for the higher Reynolds numbers precludes a definitive comparison. For the lower Reynolds numbers (Fig. 2), very good agreement prevails between Sh[2]/Sh* and the data at Re = 8200, but there is a moderate deviation between the Sh[6]/Sh* line segment and the data at $Re = 5000$. This may reflect possible inaccuracies of the finite-difference solutions of [6] or of their correlation by equation (10).

The magnitudes of the Sh[2]/Sh* and Sh[6]/Sh* ratios provide a direct comparison of the fully developed mass (heat) transfer results for curved tubes and straight tubes. These ratios fall in the 1.2-1.35 range, reflecting the enhancement associated with the secondary flow in curved tubes.

Bends With Sharp-Edged Inlet. Figures 5-7, which pertain to the sharp-edged inlet, contain Reynolds number groupings similar to those of Figs. 2-4. In Fig. 5, the Sh/Sh* distributions for $Re = 5000$ and 8200 are completely distinct, but this is not the case for the higher Reynolds numbers. Thus, in Fig. 6, the distributions for $Re = 13{,}500$ and 22,000 are virtually identical for $\phi > 10$ deg, with moderate deviations only at the first two measurement stations. The same situation prevails for $Re = 37{,}000$, 61,000, and 100,000 in Fig. 7. It then follows that for $Re > 10{,}000$, Sh* is an effective scaling parameter for the Sh distributions in the bend.

All of the Sh/Sh* distributions of Figs. 5-7 display a common pattern which appears to be well resolved by the naphthalene sublimation measurements. Starting with a moderate value immediately downstream of the inlet, the Sherwood number rises sharply and attains a maximum in the neighborhood of $\phi = 10$ deg, whereafter it drops off – rapidly at first and then slowly. In all cases, the distributions appear to have leveled off in the downstream end of the 90 deg bend.

By contrasting Figs. 5-7 with Figs. 2-4, it is seen that the two types of inlets have a marked effect on the Sherwood number distributions in the bend. For the sharp-edged inlet, the distributions are more regular than those for the tube-fed inlet, attain streamwise uniformity more rapidly, and achieve substantially higher maxima.

The distinctive shape of the distributions in Figs. 5-7 is the result of the separation, reattachment, redevelopment cycle that is associated with the sharp-edged inlet. As observed from the flow visualization to be presented shortly, the reattachment occurs on the outer wall of the bend, at about 8 deg downstream of the inlet. Correspondingly, the highest Sh/Sh* value in each of the investigated bends was encountered in the second outer-wall mass transfer element (plotted at $\phi = 7.5$ deg). These maximum values range from about 5.1 at $Re = 5000$ to 2.8 for $Re = 100{,}000$.

The outer wall Sherwood numbers exceed those for the inner wall in the separated region near the inlet, at reattachment, and in the downstream region $\phi > 30$ deg where the secondary flow has become well organized. In the region between the reattachment and 30 deg, where the flow is shaking off the trauma of reattachment and is reorganizing itself into a helical flow, the Sherwood numbers on the outer and inner walls are approximately the same.

The circumferential average Sh/Sh* values in the downstream portion of the 90 deg bend are in good agreement with the circumferential-average, fully developed, curved-tube Sherwood numbers from the literature, as represented by the Sh[2]/Sh* and Sh[6]/Sh* line segments in Figs. 5–7. This agreement lends credibility to the present experimental technique.

Comparisons With Straight-Tube Entrance Region. The foregoing presentation of results has shown that a bend may be wholly or partly a mass (heat) transfer entrance region, depending on the turning angle. It is, therefore, appropriate to compare the Sherwood number distributions for a bend with those for the entrance region of a straight tube. A search of the literature failed to disclose appropriate straight-tube, entrance region results for the case of the tube-fed inlet. However, results are available for the case of a sharp-edged inlet [9]. In common with those obtained here, the results of [9] were determined using the naphthalene sublimation technique, so that no Schmidt number or Prandtl number scaling is necessary.

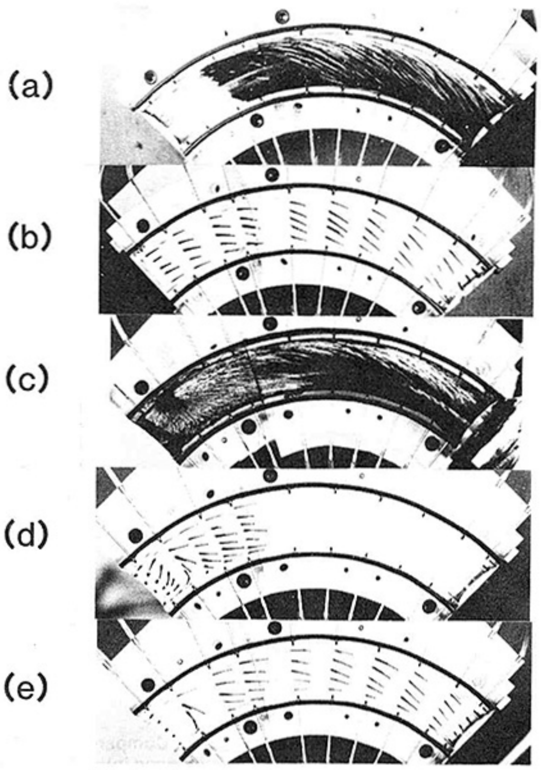

Fig. 9 Flow visualization photographs

For the case of the sharp-edged inlet, comparisons of the circumferential-average Sherwood numbers for the bend with the straight-tube Sherwood numbers of [9] are shown in Fig. 8 for $Re = 5000$, 22,000, and 88,000/100,000. The ordinate variable is Sh/Sh* where, as before, Sh* is the fully developed straight-tube Sherwood number. The abscissa variable is the dimensionless distance from the inlet, either $R_c\phi/D$ for the bend or X/D for the straight tube.

Inspection of the figures indicates generally good agreement between the bend and straight-tube results in the abscissa range between 0 and about 2.4 (ϕ between 0 and 30 deg). In this range of ϕ, the secondary flow in the bend is not yet well organized. With increasing downstream distance, there is a systematic deviation between the two sets of results. The straight-tube Sherwood numbers generally drop off, while those for the bend tend to flatten under the influence of the secondary flow.

Flow Visualization

The oil-lampblack technique was used to visualize the patterns of fluid flow adjacent to the bounding walls of the bend. A plexiglass version of the apparatus, assembled from identical but separate upper and lower walls, was used for the visualization studies. Since the flow patterns adjacent to the upper and lower walls should be identical, the visualization was performed only at one wall (the lower wall). The oil-lampblack mixture was applied in either of two formats – as a continuous coating or as a series of dot-like droplets. Photographs of the flow patterns were taken with the camera looking directly downward into the channel. All the photographs presented in Fig. 9 correspond to a Reynolds number of about 100,000, which is the highest of those employed during the heat transfer and pressure distribution experiments, and to the 90 deg bend. The flow direction in the photographs is from left to right.

The presentation of results will begin with the case in which the flow is delivered to the bend inlet by the hydrodynamic development tube – photographs (*a*) and (*b*). In (*a*), the visualization pattern is characterized by two distinct regions – a clear region extending about 20 deg into the bend from the inlet and a downstream region where there are alternating streaks of black and white. In the initial region, the oil-lampblack mixture was completely blown off by the large wall-adjacent shear forces. This high-shear region is elongated at the inner wall, which suggests that the high velocity core of the flow entering the bend tends to take the shortest path in traversing the initial portion of the bend by moving closer to the inner wall. The streaks in the downstream region are not aligned with the axial direction but cut across the passage from the outer wall to the inner wall. This transverse, wall-adjacent movement of fluid is indicative of a two-lobed secondary flow which is superimposed on the main flow, producing a helical pattern.

The discrete-dot format of photograph (*b*) provides information about the initial portion of the bend and better resolves the angle of the helical flow. It is seen that the secondary flow is already in existence at the first measurement station (3 deg downstream of the inlet), although to a lesser extent than downstream. At the first station, the flow vector makes an angle of about 14 deg with the axial direction, while at stations situated in the downstream portion of the bend, the angle is about 25 deg. Both photographs (*a*) and (*b*) indicate the complete absence of backflow (i.e., flow moving upstream toward the inlet of the bend), which is particularly noteworthy in view of the existence of adverse pressure gradients in the flow.

The visualization results for the case in which the flow enters the bend through a sharp-edged inlet are presented in photographs (*c*)-(*e*). The noteworthy features of (*c*) include: (1) a black spot on the outer wall of the bend centered about 8 deg downstream of the inlet, (2) well-defined streaks emanating in all directions from the black spot, and (3) a black band adjacent to the inlet that cuts across from the outer wall to the inner wall. The flow entering the bend separates from the wall and subsequently reattaches downstream of the inlet at the black spot (1) on the outer wall. The reattached flow fans out along the wall in all directions (2) – downstream, cross-stream, and upstream. The cross-stream component climbs the inner wall and then turns upstream, forming one leg of a recirculation bubble. As the upstreaming fluid nears the inlet, it wells up from the wall, leaving behind the oil-lampblack mixture, which accumulates and forms the black band (3). The absence of reattachment on the inner wall of the bend is noteworthy and may be due to the fact that the inner wall, being convex, recedes from the flow. In the downstream portion of the bend, the visualization pattern in evidence in (*c*) is generally similar to that discussed in connection with (*a*).

In photograph (*d*), the dots in the row immediately adjacent to the inlet do not move during the airflow period, and the dots in the second row were virtually unmoved. The third row of dots indicates upstream flow (i.e., backflow), while the fourth row, which is on the downstream edge of the reattachment spot, indicates either downstream or cross-stream flow. The subsequent rows indicate the development of the helical flow pattern. The downstream flow pattern in (*e*) appears similar to that of (*b*), but the angle between the flow vector and the axial direction is about 18 deg rather than 25 deg.

Concluding Remarks

The experiments performed here have yielded streamwise distributions of the local mass (heat) transfer coefficient for bends of circular cross section having turning angles of 30, 60, and 90 deg. Transfer coefficients were separately determined at the inside of the bend and at the outside of the bend, and these are presented along with the circumferential average. A primary parameter in the experiments was the nature of the flow at the bend inlet. In one case, the flow was delivered to the bend by a hydrodynamic development tube, while in the other, the fluid was drawn into the bend through a sharp-edged inlet. The Reynolds number of the flow was varied over the range from 5000 to 100,000.

The investigated bends were found to be either wholly or partially occupied by a mass (heat) transfer entrance region. In general, the approach toward fully developed conditions was more rapid for a bend with a sharp-edged inlet than for a tube-fed bend. In addition, the shape of the streamwise distribution of the transfer coefficient was also dependent on the initial condition.

For the sharp-edged inlet, the transfer coefficient increased sharply just downstream of the inlet, attained a maximum, and then decreased – rapidly at first, and then more slowly. These characteristics reflect the separation, reattachment, redevelopment cycle that is associated with a sharp-edged inlet. In all the cases investigated here, the aforementioned decrease appeared to have leveled off at the downstream end of the 90 deg bend.

For all the investigated tube-fed bends, the maximum value of the transfer coefficient occurred immediately downstream of the inlet, whereafter the coefficient decreased sharply at first and then more gradually. However, the subsequent shape of the distribution was not universal but depended on the Reynolds number and on whether the distribution corresponded to the inside or the outside of the bend. The maximum transfer coefficient in a tube-fed bend was generally lower than the maximum coefficient for a corresponding bend with a sharp-edged inlet.

For the most part, the transfer coefficients at the outside of the bend were greater than those at the inside of the bend. The deviations between the outside and inside coefficients were greatest at low Reynolds numbers and diminished as the Reynolds number increased.

References

1 Chrysler, G. M., and Sparrow, E. M., "Turbulent Flow and Heat Transfer in Bends of Circular Cross Section: II—Pressure Distribution Experiments," ASME Journal of Heat Transfer, this issue.

2 Seban, R. A., and McLaughlin, E. F., "Heat Transfer in Tube Coils With Laminar and Turbulent Flow," *International Journal of Heat and Mass Transfer*, Vol. 6, 1963, pp. 387-395.

3 Rogers, G. F. C., and Mayhew, Y. R., "Heat Transfer and Pressure Loss in Helically Coiled Tubes With Turbulent Flow," *International Journal of Heat and Mass Transfer*, Vol. 7, 1964, pp. 1207-1216.

4 Mori, Y., and Nakayama, W., "Study on Forced Convective Heat Transfer in Curved Pipes (1st Report, Laminar Region)," *International Journal of Heat and Mass Transfer*, Vol. 8, 1965, pp. 67-82.

5 Mori, Y., and Nakayama, W., "Study on Forced Convective Heat Transfer in Curved Pipes (2nd Report, Turbulent Region)," *International Journal of Heat and Mass Transfer*, Vol. 10, 1967, pp. 37-59.

6 Kalb, C. E., and Seader, T. D., "Fully Developed Viscous-Flow Heat Transfer in Curved Circular Tubes With Uniform Wall Temperature," *AIChE Journal*, Vol. 20, 1974, pp. 340-346.

7 Chrysler, G. M., "Convective Heat Transfer Coefficients for Pipe Flow With Curvature-Induced Secondary Motion," Ph.D. Thesis, Department of Mechanical Engineering, University of Minnesota, Minneapolis, MN, 1984.

8 Sogin, H. H., "Sublimation From Disks to Air Streams Flowing Normal to Their Surfaces," *Trans. ASME*, Vol. 89, 1958, pp. 61-71.

9 Molki, M., "Turbulent Tube-Flow Heat Transfer Coefficients in the Presence of Flow Imbalance in the Tubes of a Parallel Array," Ph.D. Thesis, Department of Mechanical Engineering, University of Minnesota, Minneapolis, MN, 1982.

Use of Melting Point Surface Coatings for Local Convection Heat Transfer Measurements in Rectangular Channel Flows With 90-deg Turns

D. E. Metzger
Fellow ASME

D. E. Larson
Mechanical and Aerospace Engineering
Department,
Arizona State University,
Tempe, AZ 85287

Centrifugal forces tend to produce secondary flows around and within channel turns that can have significant effects on the convection heat transfer distribution over the channel walls. Local Nusselt number distributions are presented for 90-deg turns of radius ratios 2 and 3 in a 3:1 aspect ratio rectangular cross section duct oriented with the principal walls in the direction of centrifugal force. A method employing the melting phase change of a surface coating was used to determine the local heat transfer rates, and a data analysis procedure needed for quantitative application of the method to internal flows is described.

Introduction

Heat transfer in the region within and around bends and turns in flow channels is important to the design and performance of a variety of practical devices. The nature of the secondary flow induced in a turning channel by centrifugal forces has long been of interest [1]. The great majority of studies published since have addressed the phenomenon in terms of its fully developed conditions. Fully developed velocity and temperature fields can be visualized as those established in a continuously and uniformly turning channel well downstream from the start of the bend [2–4]. Physically this condition is reached in helical tube coils, usually after more than a full 360-deg turn.

In contrast, most turns in heat exchange equipment and coolant passages in machine components exist simply for the purpose of changing flow direction, and commonly have turn angles of only 90 or 180 deg. Nevertheless, just as in the more extended turns, centrifugal forces in these abbreviated turns produce secondary flows which tend to both increase average heat transfer and create azimuthal variations in heat transfer. The augmentation in average heat transfer is usually desirable, but the variation in heat transfer around the cross section is often not. Indeed, in some applications such as the cooling of high-temperature turbine components, variations in convection heat transfer rates occurring over small distances can lead to increased thermal stresses and decreased component life [5].

Thus the designer of heat exchanger equipment is interested in the rate of change of both axial and azimuthal heat transfer in and around channel turns. Surprisingly few investigations of developing flow and heat transfer in passage turns of finite angle have been made in the past [6, 7]. Recently, more interest has been shown [8], but with concentration on detailed turbulent flow field measurements rather than heat transfer measurements.

The present study was initiated to provide an assessment of both average heat transfer augmentation and azimuthal variation in heat transfer as they occur through 90-deg turns in rectangular cross section channels typical of cooling passages used in internally cooled gas turbine engine components. The study was also used as a vehicle for further development and evaluation of a relatively new melting point surface coating method for obtaining local heat transfer coefficients.

Before proceeding with a description of this method, it will be useful to briefly review techniques used for measuring local surface heat transfer. Only the most widely used methods will be discussed here; a more complete recent review is available in [9].

The most common method used to determine heat transfer coefficients on localized regions of a convectively cooled surface is to thermally isolate segments of the surface and apply a known amount of electrical power to each segment through attached electric resistance heaters. Usually control is provided for each segment heater so that a desired overall surface thermal boundary condition (commonly isothermal) can be established. By measuring segment surface temperatures and associated fluid temperatures, heat transfer coefficients can be determined [10]. The necessary finite size of the segments and heaters dictates that the measured coefficients are always regional averages, rather than true local values, although quite fine resolution can be obtained with this method [11] if the expense can be justified.

Electric heating of the surface can also be effected by passing current directly through the surface material, without the use of separate heater elements. Commonly this has been accomplished by fabricating the surface from thin strips of metal on an insulated backing. Since the electrical resistivity varies only slightly with temperature, the local heat flux distribution on each strip is nearly uniform; and by use of separate control for each strip, an overall uniform heat flux thermal boundary condition can be established. Thermocouple or infrared measurements are used to determine local strip temperatures and fine resolution of local heat transfer coefficients is possible [12].

A variation on this same method is to overlay the entire surface with a heating element or elements that will generate a uniform heat flux boundary condition. For example, a thin gold layer deposited on plastic film has been used. In turn a thin layer of encapsulated liquid crystals overlays the heater. The liquid crystals allow visual determination of the surface temperatures and contours of constant heat transfer coefficients. Quite accurate and localized determinations of the heat transfer coefficients are possible [13].

In recent years, mass transfer methods, principally the

Contributed by the Heat Transfer Division for publication in the JOURNAL OF HEAT TRANSFER. Manuscript received by the Heat Transfer Division August 20, 1984. Paper No. 84-HT-23.

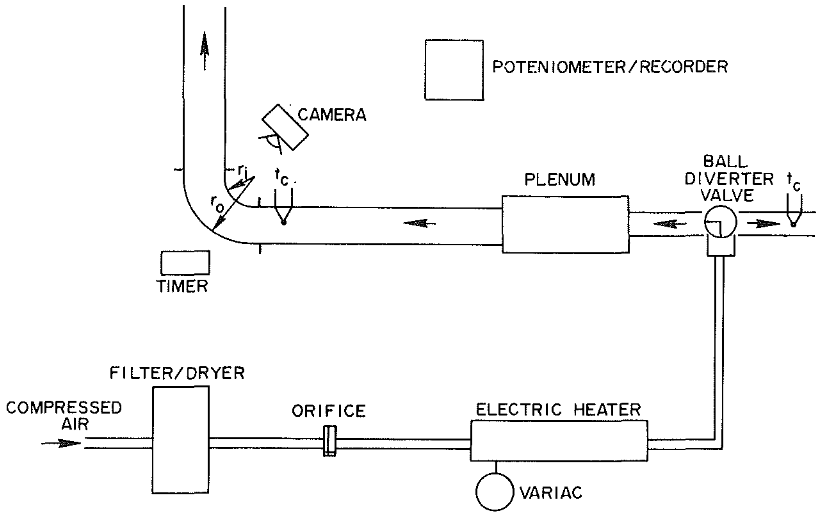

Fig. 1 Apparatus schematic

sublimation of naphthalene, have been used to determine both average [14] and local [15] convective heat transfer coefficients. Average coefficients are determined by weighing the naphthalene surface or surface segment before and after exposure to the air stream. Local coefficients are determined by measuring the local depth of sublimed surface with a profilometer. By using microprocessor control to automate data acquisition, highly detailed and accurate heat transfer coefficient maps over a surface can be obtained [16].

Finally, various types of heat flux gages, for example the commercially available thin foil and Gardon types, have been used for convection heat transfer studies. Although good resolution of local heat transfer coefficients can be achieved, the expense and complexities of multiple gages usually preclude highly detailed mapping of coefficient distributions.

This same issue of expense and complexity exists in many instances with the other methods discussed here as well. In particular, as the surface geometry of interest becomes more complicated, the difficulty and expense of determining local surface heat transfer coefficients through application of electric heaters or profile measurements of a subliming surface increase markedly. In many cases, a particular technique becomes essentially impossible to apply. Even if possible, it may be prohibitively expensive to instrument more than a single fixed test geometry, so that systematic effects of geometry changes (which are often the most important parameters) cannot be studied.

In contrast, the use of melting point surface coatings is inexpensive and appears applicable to even the most irregular surfaces. In this method the surface of interest is sprayed with a thin layer of material having a precise melting point temperature that can be detected visually [17]. A transient test is conducted where the surface is exposed to a heated air flow and melting times at each point on the surface are recorded and related to the heat transfer coefficients at those points. The capability of the method for revealing variations in heat transfer coefficients on complex surfaces has recently been demonstrated [18]. However, the exact nature of the relationship between melting point time and heat transfer coefficient in an actual test situation has not been delineated. Also, the issues of experimental uncertainty and repeatability have not been covered. As part of the objectives of the present study, these items are addressed in order to provide an assessment of the quantitative accuracy obtainable with the method.

Experimental Apparatus and Procedures

Figure 1 shows a schematic of the test apparatus. Laboratory compressed air, filtered and dried, is metered through an ASME standard orifice and supplied to a heating section and following diverter ball valve. In operation the heated flow is diverted away from the test section until a steady-state temperature of approximately 74°C is reached at the exit of the bleed tube. At the same time the test section is shielded from the heated flow and remains uniformly at the laboratory temperature of approximately 23°C.

The test section consists of a 51-cm-long straight section followed by a 90-deg bend and a second 51-cm-long straight

Nomenclature

A = heat transfer surface area
c_p = fluid specific heat
D_h = channel hydraulic diameter
h = convection heat transfer coefficient
k = channel wall thermal conductivity
k_f = fluid thermal conductivity
$\dot{m}$ = mass flow rate
Nu = local Nusselt number = hD_h/k_f
Nu_{av} = average Nusselt number over a single wall at location x
$\overline{\mathrm{Nu}}$ = azimuthal average Nusselt number (average over all four walls at location x)
$\overline{\mathrm{Nu}}_0$ = fully developed $\overline{\mathrm{Nu}}$ in a straight channel
Pr = Prandtl number = $\mu c_p/k$
$\dot{q}$ = surface heat transfer rate
Re = Reynolds number = $\rho V D_h/\mu$
r = radial position
r_i = channel inner radius
r_o = channel outer radius
t = channel wall surface temperature
t_m = fluid mixed mean temperature
U = fundamental solution, see equation (3)
V = channel mean velocity
x = streamwise position
α = channel wall thermal diffusivity
θ = time
μ = fluid dynamic viscosity
ρ = fluid density
τ = time step

Subscripts

1 = denotes quantities evaluated at an upstream station
i = index of mixed mean temperature steps
j = index of streamwise station

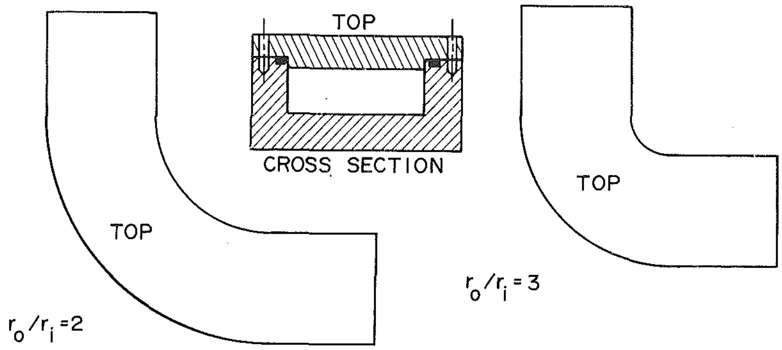

Fig. 2 Turn geometry and channel cross section

section. The entire test section is constructed of transparent acrylic plastic machined to a 3.81 × 1.27 cm rectangular cross section, as shown in Fig. 2. Wall thickness is 0.95 cm for all sides and the top wall is removable to allow coating of the inside surfaces with the phase change material. The assembled duct is sealed with O rings. Two different 90-deg bend sections were employed in the present investigation, $r_o/r_i = 2.0$ and $r_o/r_i = 3.0$, as shown also in Fig. 2.

The coating material used is a commercially available (Tempil Industries, S. Plainfield, NJ) product with a specified melting point of 42.8°C. Calibration tests were performed on the batch purchased prior to its use. The details of these auxiliary tests are presented in [19]. The mean melting temperature for 15 samples was 43.1°C. The lowest and highest melting temperatures observed were 42.8°C and 43.2°C. In both the calibration tests and subsequent use in the test section duct, the melting point is determined visually from the property of the coating to change from opaque white to transparent upon melting. A black background facilitates viewing of the phase change.

In the test facility, a thermal transient is initiated by using the ball valve to suddenly route the heated air flow through the test section. The resulting conduction of heat into the test section walls was numerically simulated on a finite element code using specified heat transfer coefficients of the magnitude and spatial variation expected for the experiments. For these conditions and wall properties of acrylic plastic, the finite element results show that the depth of heating into the wall over the expected test duration is less than the wall thickness; and, in addition, that lateral conduction in the wall has a negligible influence on the local surface temperature response. Also, for the coating thicknesses used in the present study (approximately 0.005 cm) the coating itself has a negligible effect on the wall thermal response. The temperature drop through the coating is estimated to be no more than 0.3°C at the time that melting occurs. At any surface point, the wall temperature can thus be represented by the classical one-dimensional response of a semi-infinite medium to the sudden step application of a convecting fluid at temperature t_m

$$(t-t_i)/(t_m-t_i) = 1-\exp(h^2\alpha\theta/k^2)\operatorname{erfc}(h\sqrt{\alpha\theta}/k) \tag{1}$$

If each surface point of interest were subjected to a true step increase in t_m, then measurement of the required times to reach the known phase change temperature would allow solution of equation (1) for the heat transfer coefficients. This is the essence of the method, with the thin coating of phase change material providing a means of acquiring an array of temperature–time pairs over the surface.

However, in actual internal flow experiments, the wall surfaces will not experience a pure step change in air temperature because of the transient heating of the upstream plenum chamber and duct walls. Nevertheless, equation (1) is a fundamental solution that can be used to represent the response to a superposed set of elemental steps in t_m arranged to represent the actual air temperature rise

$$t-t_i = \sum_{i=1}^{N} U(\theta-\tau_i)\Delta t_m \tag{2}$$

where

$$U(\theta-\tau_i) = 1-\exp\left[\frac{h^2\alpha(\theta-\tau_i)}{k^2}\right]\operatorname{erfc}\left[\frac{h\sqrt{\alpha(\theta-\tau_i)}}{k}\right] \tag{3}$$

In the present experiments, air temperature t_m is determined from thermocouple measurement in the straight entrance section upstream of the 90-deg bend. The t_m variation with time (recorded on strip charts) is approximated by steps, and the resulting superposed solution, equations (2) and (3), is solved for the local surface heat transfer coefficients. In this form the coefficients at all locations are thus based on the mixed mean temperature at the upstream thermocouple (location 1). Denoting this set of coefficients by h_1

$$\dot{q}/A = h_1(t_{m_1}-t) \tag{4}$$

However, for maximum utility, heat transfer coefficients for internal flows should be based instead on local mixed mean temperatures. Here, coefficients based on the local mixed mean temperatures will be denoted by h without subscripts

$$\dot{q}/A = h(t_m-t) \tag{5}$$

Equations (4) and (5) may be used to express h in terms of h_1 and t_m

$$h = h_1(t_{m_1}-t)/(t_m-t) \tag{6}$$

The mixed mean temperature at any streamwise location in the duct can be expressed by an energy balance in the streamwise direction

$$t_m = t_{m_1} - \frac{1}{\dot{m}c_p}\sum_{j=1}^{x-1}\overline{h_{1j}}A_j(t_{m_1}-t) \tag{7}$$

The index j denotes measuring locations in the streamwise (x) direction, and $\overline{h_{1j}}$ denotes azimuthally averaged values. Combining (6) and (7) completes the evaluation of h

$$h = h_1 \Big/ \left[1-\frac{1}{\dot{m}c_p}\sum_{j=1}^{x-1}\overline{h_{1j}}A_j\right] \tag{8}$$

Equation (8) is strictly true only for h and h_1 sets corresponding to a spatially isothermal wall thermal boundary condition. Although this is not precisely the case during the experiments, it is close. At times of interest during the transient for the present experiments, the duct surface temperature differs from uniform by at most ±5 percent of the overall driving potential.

For the present 90-deg bend tests, melting patterns were recorded photographically at 1-s intervals with a motor-driven

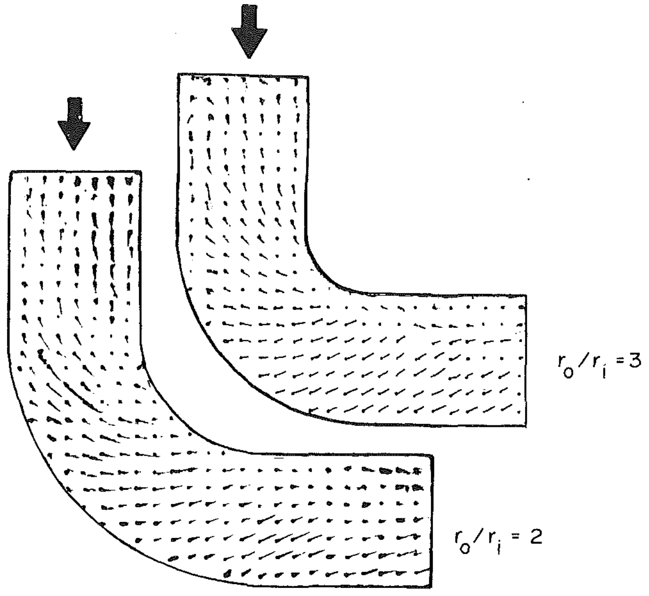

Fig. 3 Flow visualization results

camera during the test transient. The time required for melting at any given location was approximately 15-25 s, as determined from visual comparisons between pairs of adjacent photographs in the sequence. Four separate tests were performed for each geometry in order to record melting patterns on the four sides of the ducts. For $r_o/r_i = 3$, data were reduced at 22 streamwise locations, using 16 azimuthal positions at each location for a total of 352 grid points. For the $r_o/r_i = 2$ case, an identical procedure was followed except 27 streamwise locations were used for a total of 432 grid points. In the curved portion of the duct, the grid is defined with radial lines, resulting in a variation with radius of the elemental grid areas. In instances where azimuthal averages were determined, appropriate weighting factors were used to account for this radial variation in measuring area. For both geometries, the measuring stations extend one hydraulic diameter both upstream and downstream of the bend. Additional details of the test apparatus and procedure may be found in [19].

Results and Discussion

In addition to the heat transfer testing, separate flow visualization experiments were conducted as part of the present study. The visualization method used provides surface streamlines through use of an ink-dot matrix oversprayed with a thin solvent film as described in [20]. The slowly dissolving ink from each dot migrates downstream under the influence of the wall shear forces, creating a gradually thinning tracer line pointing in the direction of the surface flow.

Figure 3 shows this visualization for the two turn sections, both at Re = 1.96×10^4. The mean flow is counterclockwise around the bend, from upper left to lower right. Evidence of strong secondary flow is visible in both cases. The expected radially inward velocity component along the channel long side begins to develop upstream of the start of sidewall curvature and continues well into the straight downstream channel section.

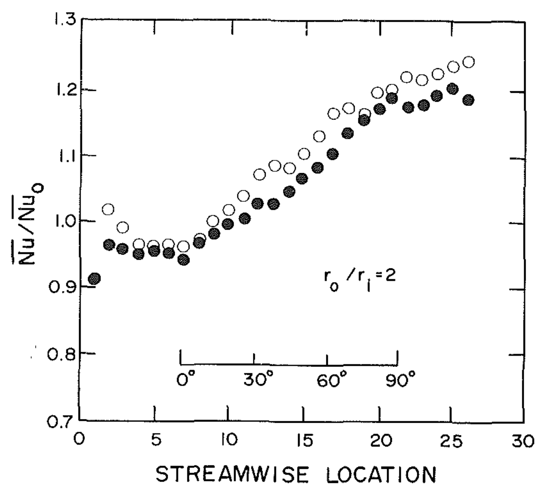

Fig. 4 Cross section mean Nusselt numbers, $r_o/r_i = 2$

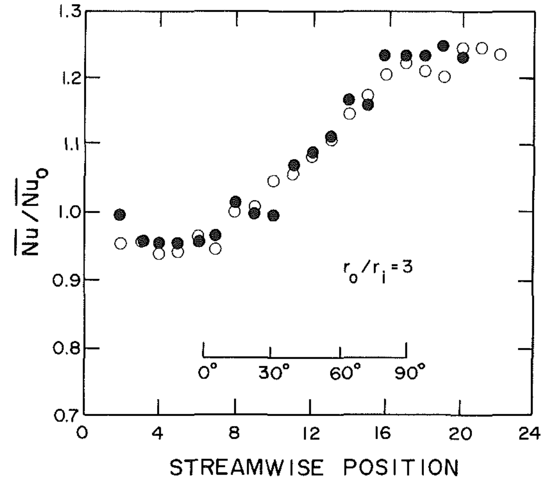

Fig. 5 Cross section mean Nusselt numbers, $r_o/r_i = 3$

The overall effect of this secondary flow is expected to be an enhancement of heat transfer, and this is verified in the results of the present heat transfer tests. Figures 4 and 5 show normalized azimuthal average Nusselt number values for $r_o/r_i = 2$ and 3, respectively. A single Reynolds number of 1.96×10^4 was used for all tests. The entire series of eight test runs (one for each of the four channel walls for both turn geometries) necessary to construct these azimuthal averages was repeated with an entirely new application of the surface coating in order to assess the repeatability of the experimental method. The open and solid symbols in Figs. 4 and 5 denote the original and repeated test runs.

The azimuthal average Nusselt numbers are normalized with fully developed straight channel values: $\overline{\mathrm{Nu}}_0 = 0.021\ \mathrm{Re}^{0.8}\ \mathrm{Pr}^{0.5}$. The generally good agreement of the present results upstream of the bends with these fully developed straight channel values establishes confidence in the experimental method and data reduction.

The enhancement in overall heat transfer by the end of the turn is approximately 20 percent for $r_o/r_i = 2$ and slightly higher for the more sharply turning $r_o/r_i = 3$ bend. These values are in good agreement with the approximately 20 percent enhancement reported in [6] for a 90-deg bend of circular cross section with $r_o/r_i = 1.67$. In [6], the experiments were carried out by electrically heating a thin-wall metal tube, one of the conventional methods listed earlier. The distortion caused by bending the tube to fabricate the turn resulted in an unknown heat flux distribution in the turn itself, so the 20 percent enhancement quoted is taken from measurements in an undistorted straight section just downstream of the turn. This example is an illustration of difficulties that can arise in applying conventional techniques with complex surface geometries.

Figures 6 and 7 present the streamwise distributions of Nusselt numbers averaged across the individual channel walls.

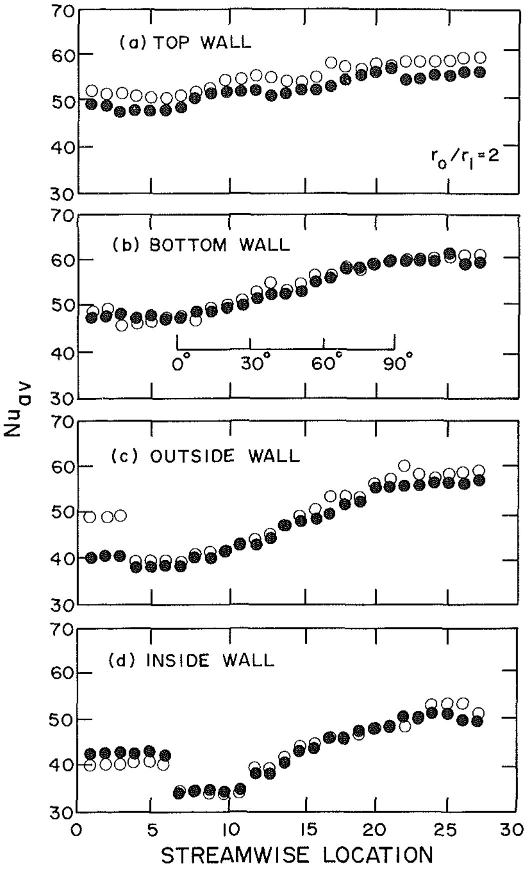

Fig. 6 Single wall Nusselt number averages, $r_o/r_i = 2$

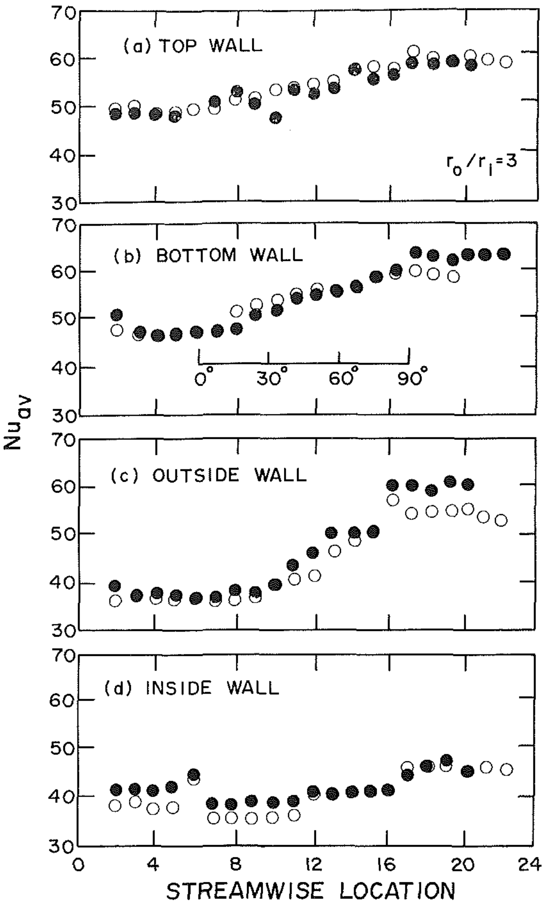

Fig. 7 Single wall Nusselt number averages, $r_o/r_i = 3$

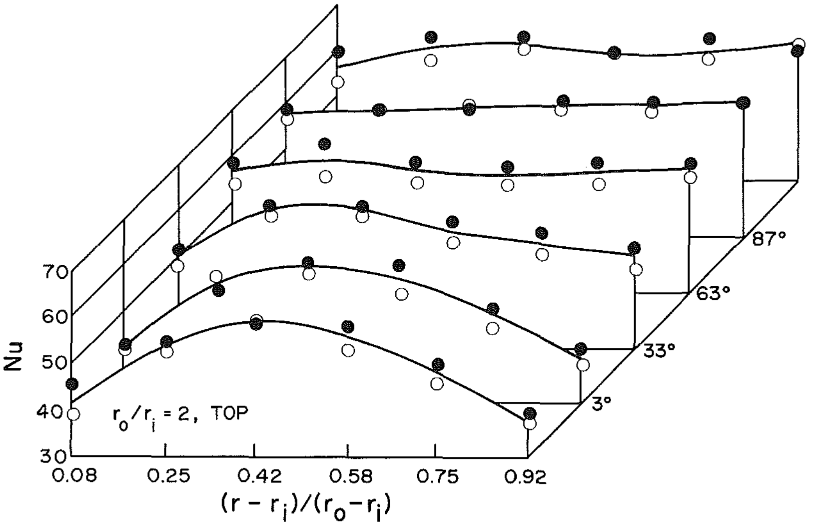

Fig. 8 Radial Nu profiles, top surface, $r_o/r_i = 2$

Again, the solid and open symbols denote two independent test runs at identical conditions. Both turn geometries display similar characteristics.

In both cases, upstream of the turn, the average heat transfer on the bottom wall is slightly lower than that on the top wall. For horizontal flow with cooling of the fluid at the walls, which is the present condition, a slight free convection effect superposed on the forced convection would tend to produce lower heat transfer coefficients on the bottom wall. The Grashof number here is of the order of 10^7, so a slight mixed convection effect at the test $Re = 1.96 \times 10^4$ is possible. The average bottom wall Nusselt number, even though it starts at the beginning of the turn slightly below the top wall value, increases somewhat more rapidly through the turn and ends up slightly above that of the top wall.

Inside and outside wall average Nusselt numbers both start at the beginning of the turn some 20 percent below the average top and bottom wall values. On the outside wall, values increase rapidly through the turn to a level approximately equal to those of the top and bottom walls by the end of the turn. The average inside wall Nusselt numbers display an abrupt drop very close to the beginning of inside wall curvature and then increase through the turn although the increase is quite small for the more sharply turning geometry. The abrupt drop

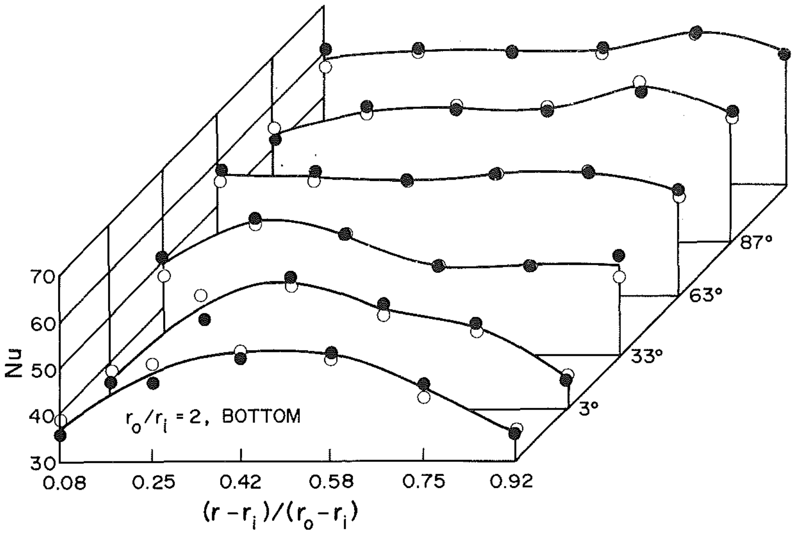

Fig. 9 Radial Nu profiles, bottom surface, $r_o/r_i = 2$

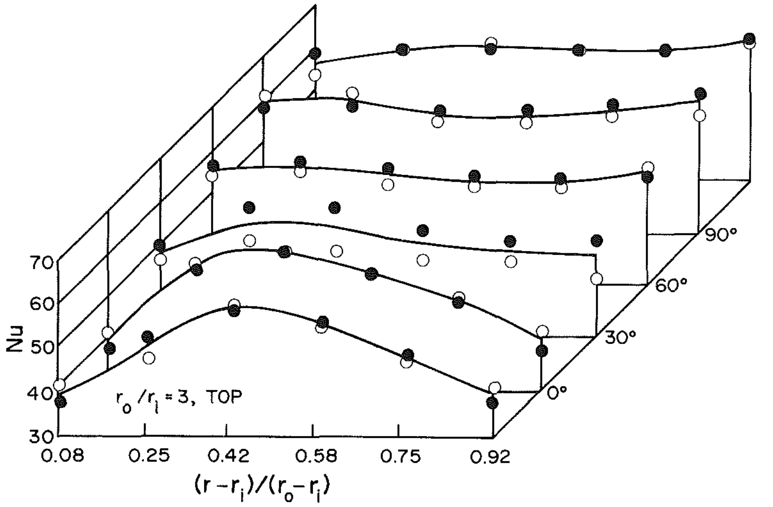

Fig. 10 Radial Nu profiles, top surface, $r_o/r_i = 3$

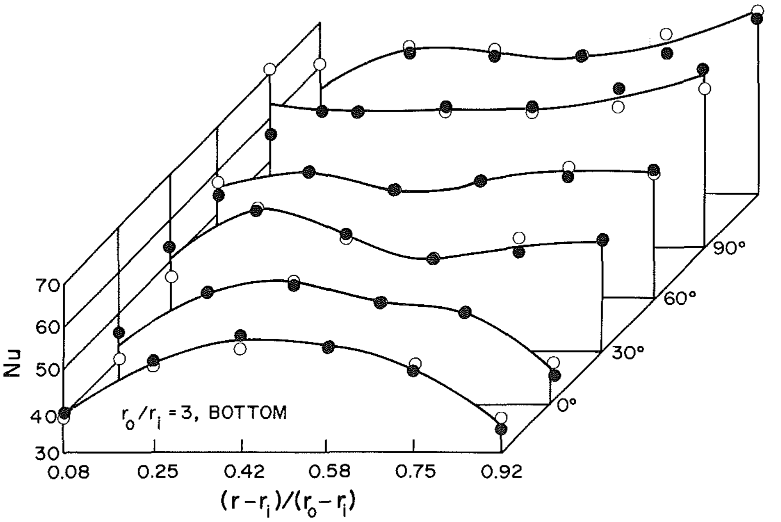

Fig. 11 Radial Nu profiles, bottom surface, $r_o/r_i = 3$

is probably associated with flow separation, with decreases in turbulence production along the convex curved wall [22, 23], or with the collision of the secondary flow boundary layers [24].

No similar explanation is offered for the abrupt drop at the beginning of the outside wall observed in one test run at $r_o/r_i = 2$ (Fig. 6*c*). It appears that the first three open symbols in this figure are abnormally high, since they were not repeated for either this or the $r_o/r_i = 3$ geometry. However, no satisfactory explanation for the error has been found.

The maximum difference in local heat transfer coefficient around the channel cross section at any given streamwise location occurs in the first half of the turn, and this is consistent with the findings presented in [6] for circular cross sections. However, whereas the largest differences reported in [6] were between the top and bottom of the circular cross section, the largest differences in the present case are between the inside wall and top or bottom walls. More importantly, the maximum Nusselt number around a given cross section is never more than about 70 percent higher than the minimum value in the present results. Much larger differences are reported in [6], although the authors state this should be viewed with caution since the measurements were obtained in the bend region where heat flux distribution was distorted to an undetermined extent.

Figures 8-11 display radial distributions of local Nusselt numbers and their streamwise development along the top and bottom walls for both of the turns. The first and last streamwise stations shown in all four figures are located one hydraulic diameter upstream of the turn and one hydraulic diameter downstream of the turn, respectively.

At the upstream stations, a slightly flattened radial profile on the bottom, as compared to the top, is in evidence. This leads to the difference in radially averaged values mentioned above. As the flow proceeds through the turn there is a tendency for the peak in local Nusselt number to move radially inward; and, as this occurs, the peak becomes more pronounced on the bottom wall than it does on the top. For both turns, the radial variation appears to reach a maximum at about 30 deg; the profiles become noticeably more uniform through the balance of the turn.

Overall, the repeatability in local Nusselt number values exhibited in Figs. 8-11 appears to be good, with the exception of a few points. A detailed estimation of the experimental uncertainty is presented in [19], based on the methods of [21]. The uncertainty in local Nusselt number is estimated to be approximately ± 12 percent for a 95 percent confidence level. However, from the observed repeatability and trends that appear to be clearly indicated by the results, this estimate appears conservative.

Summary

The principal conclusions of the present study are summarized as follows:

1 A relatively new experimental method using surface coatings with precise melting points has been successfully used to obtain local convective heat transfer characteristics of flows through 90-deg bends in rectangular cross section channels.

2 A procedure for analyzing the observed local melting times to obtain local heat transfer coefficients has been presented. It accounts for the actual shape of the imposed thermal transient and for the change in fluid mixed mean temperature along an internal flow channel. Without use of adjustable constants, the procedure yields Nusselt numbers that are in good agreement with expected values.

3 Based on the results of repeated tests and estimated experimental uncertainty, melting point coatings, together with the data analysis procedure described, appear very promising for the study of convection heat transfer with complex surface geometries.

4 Local Nusselt numbers, average Nusselt numbers on the four channel walls, and overall azimuthal average Nusselt numbers have been obtained for 90-deg bends with $r_o/r_i = 2$ and 3, both for a channel aspect ratio of 3. In both cases, the azimuthal average heat transfer increases through the turn to approximately 120 percent of its entrance value.

5 The lowest local Nusselt numbers around the channel cross section at a given streamwise location were found on the inside radius wall. Nusselt numbers along the outside radius wall, although higher than those on the inside wall, are generally lower than those on the top and bottom walls, except at the end of the turn where all three are approximately equal. The difference between largest and smallest local Nusselt numbers around the channel cross section occurs in the first half of the bend and never exceeds approximately 70 percent.

References

1 Dean, W. R., "Fluid Motion in a Curved Channel," *Proc. Royal Society of London*, Series A, Vol. 121, 1928, pp. 402-420.

2 Mori, Y., and Nakayama, W., "Study on Forced Convective Heat Transfer in Curved Pipes (1st Report, Laminar Region)," *International Journal of Heat and Mass Transfer*, Vol. 8, 1965, pp. 67-82.

3 Mori, Y., and Nakayama, W., "Study on Forced Convective Heat Transfer in Curved Pipes (2nd Report, Turbulent Region)," *International Journal of Heat and Mass Transfer*, Vol. 10, 1967, pp. 37-59.

4 Mori, Y., Uchida, Y., and Ukon, T., "Forced Convective Heat Transfer in a Curved Channel With a Square Cross Section," *International Journal of Heat and Mass Transfer*, Vol. 14, 1971, pp. 1787-1805.

5 Metzger, D. E., and Mayle, R. E., "Gas Turbine Heat Transfer," *Mechanical Engineering*, Vol. 105, No. 6, June 1983, pp. 44-52.

6 Ede, A. J., "The Effect of a Right Angled Bend on Heat Transfer in a Pipe," *Proceedings, 2nd International Heat Transfer Conference*, 1961, pp. 634-642.

7 Stradden, P. W., and Tailby, S. R., "The Influence of 90° and 180° Pipe Bends on Heat Transfer From an Internally Flowing Gas Stream," *Proceedings, 4th International Heat Transfer Conference*, Vol. 2, FC-4, 1970.

8 Humphrey, J. A. C., Whitelaw, J. H., and Yee, G., "Turbulent Flow in a Square Duct With Strong Curvature," *J. Fluid Mechanics*, Vol. 103, 1981, pp. 443-463.

9 Button, B. L., and Mohamad, T. T., "Experimental Techniques to Determine the Convective Heat Transfer Coefficients for Flat and Curved Surfaces," *High Temperature Technology*, Feb. 1983, pp. 163-170.

10 Metzger, D. E., Berry, R. A., and Bronson, J. P., "Developing Heat Transfer in Rectangular Ducts With Arrays of Short Pin Fins," ASME JOURNAL OF HEAT TRANSFER, Vol. 104, 1982, pp. 700-706.

11 Graziani, R., Blair, M. F., Kopper, F. C., and Mayle, R. E., "An Experimental Study of Endwall and Airfoil Surface Heat Transfer in a Large Scale Turbine Blade Cascade," ASME *Journal of Engineering for Power*, Vol. 102, 1980, pp. 257-267.

12 Mayle, R. E., "A Composite Constant Heat Flux Test Surface," *Heat and Mass Transfer in Rotating Machinery*, Hemisphere, Washington, D.C., 1984, pp. 259-268.

13 Hippensteele, S. A., Russell, L. M., and Stepka, F. S., "Evaluation of a Method for Heat Transfer Measurements and Thermal Visualization Using a Composite of a Heat Element and Liquid Crystals," ASME JOURNAL OF HEAT TRANSFER, Vol. 105, 1983, pp. 184-189.

14 Sogin, H. H., "Sublimation From Discs to Air Streams Flowing Normal to Their Surfaces," *Trans. ASME*, Vol. 80, 1958, pp. 61-71.

15 Sparrow, E. M., and Tao, W. Q., "Enhanced Heat Transfer in a Flat Rectangular Duct With Streamwise-Periodic Disturbances at One Principal Wall," ASME JOURNAL OF HEAT TRANSFER, Vol. 105, 1983, pp. 851-861.

16 Chyu, M. K., "Local Heat/Mass Transfer Distribution for Turbulent Flow Over Roughened Surfaces," Ph.D. Dissertation, University of Minnesota, 1984.

17 Throckmorton, D. A., and Stone, D. R., "Model Wall and Recovery Temperature Effects on Experimental Heat-Transfer Data Analysis," *AIAA Journal*, Vol. 12, 1974, pp. 169-170.

18 Clifford, R. J., Jones, T. V., and Dunne, S. T., "Techniques for Obtaining Detailed Heat Transfer Coefficient Measurements Within Gas Turbine Blade and Vane Cooling Passages," ASME Paper No. 83-GT-58, 1983.

19 Larson, D. E., "Transient Local Heat Transfer Measurements in 90° Bends Using Surface Coatings Having Prescribed Melting Points," MS Thesis, Arizona State University, 1983.

20 Langston, L. S., and Boyle, M. T., "A New Surface-Streamline Flow-Visualization Technique," *Journal of Fluid Mechanics*, Vol. 125, 1982, pp. 53-57.

21 Kline, S. J., and McKlintock, F. A., "Describing Uncertainties in Single Sample Experiments," *Mechanical Engineering*, Vol. 75, Jan. 1953.

22 Mayle, R. E., Blair, M. F., and Kopper, F. C., "Turbulent Boundary Layer Heat Transfer on Curved Surfaces," ASME JOURNAL OF HEAT TRANSFER, Vol. 101, 1979, pp. 521-525.

23 Adams, E. W., and Johnston, J. P., "A Mixing Length Model for the Prediction of Convex Curvature Effects on Turbulent Boundary Layers," Stanford University, Mech. Engr. Dept., Thermosciences Division, Report IL-42, 1981.

24 Talbot, L., and Wong, S. J., "A Note on Boundary Layer Collision in a Curved Pipe," *Journal of Fluid Mechanics*, Vol. 122, 1982, pp. 505-510.

Turbulent Flow Friction and Heat Transfer Characteristics of Single- and Multistart Spirally Enhanced Tubes

R. Sethumadhavan

M. Raja Rao

Department of Chemical Engineering,
Indian Institute of Technology,
Bombay 400076, India

Investigations have been carried out on heat transfer and frictional characteristics of five spirally corrugated tubes of one to four corrugation starts, having the same helix angle, but of varying geometrical aspect ratios, for the turbulent flow of water and 50 percent glycerol. The thermal performance of these tubes was found to be superior compared to a smooth tube. Friction factors and heat transfer coefficients in these rough tubes were analysed on the basis of momentum and heat transfer analogy, and the correlation obtained was tested with the present data and also the published results of previous investigators. Performance evaluation criteria were used for the quantitative demonstration of the benefits offered by these spirally corrugated tubes for heat exchanger applications.

Introduction

In recent years, considerable interest has been focused on techniques for augmenting heat transfer coefficients in different heat transfer equipment. The trend in heat exchanger design continues to be in the direction of obtaining higher heat transfer rate per unit volume. Thus there is an economic incentive to reduce exchanger size in commercial heat exchangers. This is accomplished by introduction of augmentative techniques. There are many augmentative techniques available for getting enhanced heat transfer, e.g., as listed by Bergles [1], each one having its own merits and demerits. The application of these enhancement devices to condensation/convective heat transfer can result in the reduction of pumping power or heat transfer frontal area or increase in the heat transfer rate. Considerable work has been reported on enhanced surfaces like finned tubes [2, 3], sand-grain textures [4], wire-coil inserted tubes [5, 6], and transverse rib roughened tubes [7, 8, 9], and these studies revealed that augmentation observed in the heat transfer coefficient was accompanied by increase in frictional pressure drop.

However, investigative reports [10-13] on the possible application of spirally corrugated tubes for heat transfer suggest that these tubes provide several advantages over other rough surfaces such as: (*i*) easier fabrication, (*ii*) limited fouling, and (*iii*) higher enhancement in the heat transfer rate compared to increase in the friction factor.

Though many studies have been conducted on these tubes, a lack of systematic study on single- as well as multistart spirally corrugated tubes for condensation/convective heat transfer applications hinders the prediction of optimum tube geometry and also the development of unified correlation which can be tested for any type of rough surfaces. The objective of the present investigation, therefore, is to analyze the performance of single- and multistart sprially corrugated tubes for convective heat transfer and to develop suitable expressions, correlating results of the present work as well as those of previous investigations.

Rough Surface Analysis

In spite of many studies conducted on a variety of rough surfaces, a lack of sufficient knowledge on the flow mechanism over rough surfaces denies the prediction of friction factors as well as heat transfer rates by analytical methods. Thus the need for the evaluation of similarity law arises when the smooth channels are replaced by artificially roughened channels.

The similarity law concept was first developed by Nikuradse [14], who applied it with excellent degree of success in correlating the friction results inside sand-grained roughened surfaces. Later, Dipprey and Sabersky [4] and Webb et al. [7] developed friction and heat transfer similarity laws, which are complimentary to Nikuradse's friction similarity law.

Their model is based on a heat-momentum transfer analogy, applied to a two-region flow model. They assumed the existence of two regions, namely, (*a*) inner region, where the law of the wall is applicable, and (*b*) outer region where velocity defect law is effective. In the inner region, the velocity distribution is assumed to depend only on local conditions like y, τ_w, μ, and h and represented by

$$u^+ = \left(\frac{u}{u^*}\right) = \phi_1\left[\frac{yu^*}{\gamma}\right] = \phi_1(y^+) \qquad (1)$$

The outer region is assumed to be insensitive to both roughness of the surface and viscosity of fluid flowing inside the tube. The velocity distribution in this outer region can be represented by

$$\left[\frac{u_{\max} - u}{u^*}\right] = \phi_2(y/h) \qquad (2)$$

Thus the combination of the law of the wall and the velocity defect law gives the velocity distribution equation for the turbulent-dominated part near the wall region, which is given by

$$u^+ = 2.5 \ln(y/h) + R(h^+) \qquad (3)$$

Thus, from the knowledge of velocity distribution inside rough tubes, the friction factor for the turbulent flow of fluid can be obtained by integration of the equation (3) for the entire cross section of the tube. The friction similarity law for rough surfaces can thus be given by

$$R(h^+) = \sqrt{2/f} + 2.5 \ln\left(\frac{2h}{D_i}\right) + 3.75 \qquad (4)$$

Equation (4) suggests that the momentum transfer roughness function $R(h^+)$ is a function of not only the roughness parameters, which describe the tube surface

---

Contributed by the Heat Transfer Division for publication in the JOURNAL OF HEAT TRANSFER. Manuscript received by the Heat Transfer Division July 23, 1983.

geometry, but also fluid properties through the friction factor, as stated below

$$R(h^+) = \phi_3(D_i, h, p, \alpha, h^+, V) \tag{5}$$

and the roughness Reynolds number (h^+) can be given as

$$h^+ = (h/D_i)\mathrm{Re}\sqrt{f/2} \tag{6}$$

For Nikuradse's sand-grain rough surfaces, $R(h^+)$ attained a constant value of 8.48 in the region $h^+ > 70$. This region was termed by him as "fully rough regime." However, studies later performed by Webb et al. [7] and Ganeshan and Raja Rao [15] showed that $R(h^+)$ can have different values for different roughness types and the fully rough region may exist at a still higher value of h^+.

Based on the assumption that wall similarity law applies to both temperature and velocity profiles, Dipprey and Sabersky [4] developed a heat transfer similarity law given by

$$G(h^+, \mathrm{Pr}) = \frac{(f/2\mathrm{St} - 1)}{\sqrt{f/2}} + R(h^+) \tag{7}$$

The heat transfer characteristics of geometrically similar roughness types are accounted for by the friction similarity parameter $R(h^+)$.

Dipprey and Sabersky [4] used equation (7) to correlate turbulent flow heat transfer data ($0.0024 < e/D < 0.044$; $1.2 < \mathrm{Pr} < 5.94$) and obtained the following correlation

$$\frac{(f/2\mathrm{St} - 1)}{\sqrt{f/2}} + 8.48 = 5.19(\mathrm{Pr})^{0.44}(h^+)^{0.20} \tag{8}$$

which is valid for h^+ greater than 70.

Later, Webb et al. [7] used equation (7) to correlate the heat transfer data for rough tubes having a constant (p/e) value of 10, but of varying (e/D) values from 0.01 to 0.04 and Prandtl number in the range of 0.71 to 37.6. An excellent agreement was obtained when both these data were combined. However, for varying (p/e) values of 10 to 40, which represent the nonsimilarity of the tube roughness geometry, the heat transfer data were represented by the equation

$$\frac{(f/2\mathrm{St} - 1)}{\sqrt{f/2}} + R(h^+) = 4.75(\mathrm{Pr})^{0.57}(h^+)^{0.28} \tag{9}$$

for h^+ values greater than 25.

The objective of the present investigation is therefore to develop generalized correlations for friction factors in terms of momentum transfer roughness function $R(h^+)$ and heat transfer coefficients in terms of heat transfer roughness function $G(h^+, \mathrm{Pr})$ and to compare them with previous published data.

Further, performance evaluation criteria suggested by Bergles et al. [16] were used as necessary tools for the selection of the most efficient of the tubes used in the present study.

Experimental Program

Test Tubes. In the present experimental program, five spirally corrugated tubes of varying geometries were used and compared with a standard smooth tube. The smooth tube was used for standardising the experimental setup and also to compare the enhancement obtained in both heat transfer coefficient and friction factor. All the enhanced tubes were fabricated from plain copper tube and were spiralled along their active lengths. The spiral external groove is semicircular in cross section.

A special fabrication technique was used in making of these spiralled tubes, which embosses an internal projection, also known as ridge, in registration with an external groove.

The change in effective pitch of corrugation was obtained in the present work by varying the number of spiral corrugation starts, keeping the helix angle constant at 65 deg. For all the spiralled tubes used in the present study, pitch was defined as the distance between two adjacent grooves. A section of four-start spirally corrugated tube is shown in Fig. 1. The characteristic parameters like pitch of corrugation (p), height of corrugation (h), helix angle (α), the number of spiral starts (N), etc., which define the roughness geometry of the tube, are listed in Table 1.

Test Fluids. Water and 50 percent glycerol flowing in

Nomenclature

A = area (m^2)
C_i = constant in equation (14)
C_p = specific heat (kJ/kg K)
D = tube inside diameter (m)
D_{eq} = equivalent diameter (m), ($D_i - h$)
f = fanning friction factor ($2\tau w g_c/\rho V^2$)
g = acceleration due to gravity (m/s^2)
$G(h^+, \mathrm{Pr})$ = heat transfer roughness function $[(f/2\mathrm{St} - 1)/\sqrt{f}/2 + R(h^+)]$
h = roughness height (m)
h_i = tubeside heat transfer coefficient (W/m^{2}k)
h^+ = roughness Reynolds number $[(h/D_{eq})\mathrm{Re}\sqrt{f}/2]$
K = thermal conductivity (W/mK)
L = length (m)
N = number of starts
p = pitch (m)
P = pumping power (w)
Δp = pressure drop (P_a)
Pr = Prandtl number ($C_p \mu/k$)
Q = heat load (W)
Re = Reynolds number (DVp/μ)
$R(h^+)$ = momentum transfer roughness function $\sqrt{2}/f + 2.5 \ln(2h/D_{eq}) + 3.75$
St = Stanton number ($h_i/G C_p$)
T = temperature (°C)
u = axial point velocity (m/s)
u^* = shear velocity (m/s)
u^+ = dimensionless velocity (u/u^*)
U = overall heat transfer coefficient (W/m^2 K)
V = bulk average velocity (m/s)
y = radial distance from the wall (m)
y^+ = dimensionless radial distance from the wall

Greek Letters

α = helix angle (deg)
μ = dynamic viscosity (Pa.S)
γ = kinematic viscosity (m^2/s)
ρ = fluid density (kg/m^3)
τ_w = shear stress (P_a)

Subscripts

a = augmented tube
b = bulk condition
c = cold liquid
eq = based on equivalent diameter
G = glycerol
i = based on inside diameter
lm = log mean
max = maximum value
o = equivalent smooth tube value
s = smooth tube, steam
w = wall condition, water

turbulent flow inside smooth tube and spirally corrugated tubes were used as test fluids. The Reynolds number range varied from 4000 to 11,000 for 50 percent glycerol and 10,000 to 80,000 for water.

Experimental Work. A schematic diagram of the experimental setup is shown in Fig. 2. The actual test section consisted of 1500-mm-long, double-pipe heat exchanger, the inner tube of which was either a smooth tube or a sprirally corrugated tube. The outer tube of the test rig was a galvanized iron pipe having an i.d. of 75 mm. The test tubes were equipped with twelve chrome-alumel thermocouples, embedded on the tube wall at a distance of 125 mm from each other, and displaced radially by 180 deg. The test section was preceded and followed by smooth tube or spirally corrugated tube calming sections, each of 600 mm length, depending on the tube under study.

At both inlet and outlet, each tube was equipped with three inplane static pressure wall taps, encompassed by a piezometric ring, which in turn was connected to the limbs of a U-tube manometer.

The isothermal pressure drop studies were conducted at 30°C in all the tubes for the turbulent flow of water and 50 percent glycerol. The steady-state pressure drop was measured by means of U-tube manometers having mercury or carbon tetrachloride as manometric fluids depending on the magnitude of flow rate.

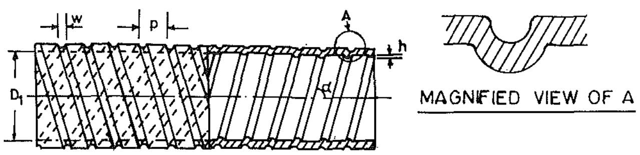

Fig. 1 Characteristic parameters of the roughened tubes used in the present study

Heat transfer studies were conducted for the turbulent flow of water and 50 percent glycerol inside the inner tube of the heat exchanger, using steam condensing at atmospheric pressure as the heating medium. When the steady state was attained, as indicated by the constancy of flow rates and temperatures, flow rates of condensing steam and tubeside test fluid were measured by means of calibrated rotameters. The incoming and outgoing temperatures of the test fluids and also the metal wall temperatures were measured from a precision 0.1°C accurate digital temperature indicator.

The uncertainties in the measured friction factor f and heat transfer coefficient h_i are ±3 percent and ±6 percent, respectively.

Results and Discussion

Friction Factor. The isothermal friction factors and heat transfer coefficients were determined for the turbulent flow of water and 50 percent glycerol inside the smooth tube before carrying out experiments with spirally corrugated tubes. The friction factors for the smooth tube were well correlated by Blasius equation.

$$f = 0.079\,(\mathrm{Re})^{-0.25} \tag{10}$$

over a range of Reynolds number from 5000 to 80,000 with a standard deviation of 2.8 percent and this served the purpose of calibration of experimental setup.

As expected, turbulent flow friction factors in single- and multistart spirally corrugated tubes were significantly higher than in the smooth tube under the same operating conditions as seen from Fig. 3. Tube 4 showed the largest increase of 200 percent in friction factor over the smooth tube, and Tube 2

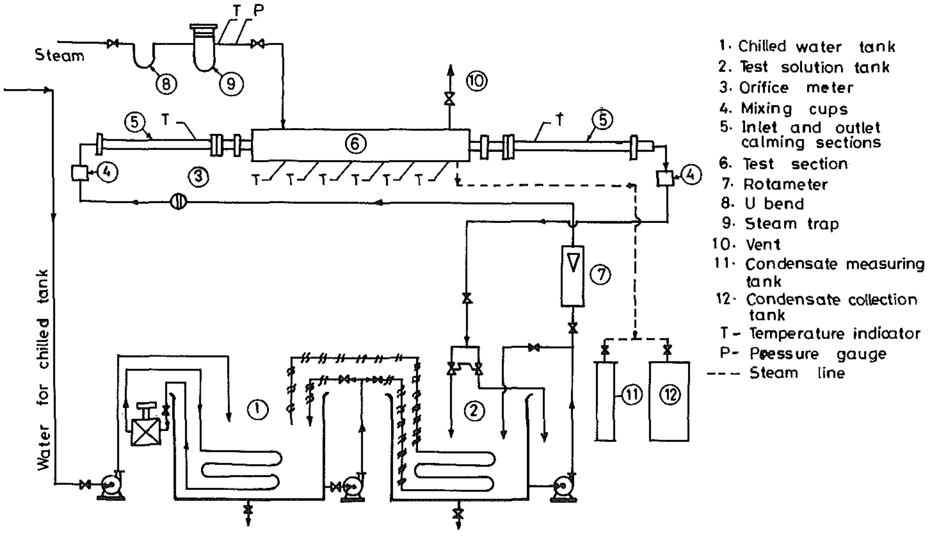

Fig. 2 Schematic diagram of the experimental setup

Table 1 Characteristic dimensions of the spirally corrugated tubes

Sr no.	Tube no.	D_i mm	P mm	h mm	N starts			P/D_i	α deg	L mm
1	0	25.00	–	Smooth	tube	0.893	–	–	–	1500
2	1	25.66	30.0	0.67	1	0.896	0.026	1.170	65	1500
3	2	25.22	15.0	0.35	2	0.894	0.014	0.595	65	1500
4	3	25.45	10.0	0.30	3	0.895	0.012	0.393	65	1500
5	4	25.26	7.5	0.59	4	0.894	0.023	0.297	65	1500
6	5	25.38	30.0	0.77	1	0.894	0.030	1.182	65	1500

showed a minimum increase of 30 percent only. From an examination of the tube characteristics given in Table 1, it is apparent that as the tube pitch decreases, or the number of corrugation starts increases, the friction factor increases. Studies by Mimura and Isozaki [17] showed that closer is the pitch or higher is the groove depth or rib (roughness element) height, the greater will be the friction factor. Figure 3 illustrates the validity of foregoing argument.

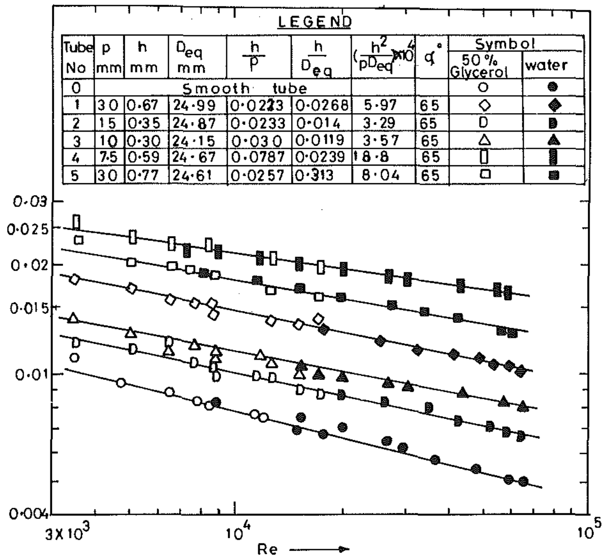

Tube No	p mm	h mm	D_{eq} mm	$\frac{h}{p}$	$\frac{h}{D_{eq}}$	$(\frac{h^2}{pD_{eq}})\times10^4$	α°	Symbol 50% Glycerol	Symbol water
0	Smooth tube							○	●
1	30	0·67	24·99	0·0223	0·0268	5·97	65	◇	◆
2	15	0·35	24·87	0·0233	0·014	3·29	65	D	◗
3	10	0·30	24·15	0·030	0·0119	3·57	65	△	▲
4	7·5	0·59	24·67	0·0787	0·0239	18·8	65	▯	▮
5	30	0·77	24·61	0·0257	0·313	8·04	65	□	■

Fig. 3 Variation of friction factor with Reynolds number for flow of water and 50 percent glycerol in smooth and spirally corrugated tubes

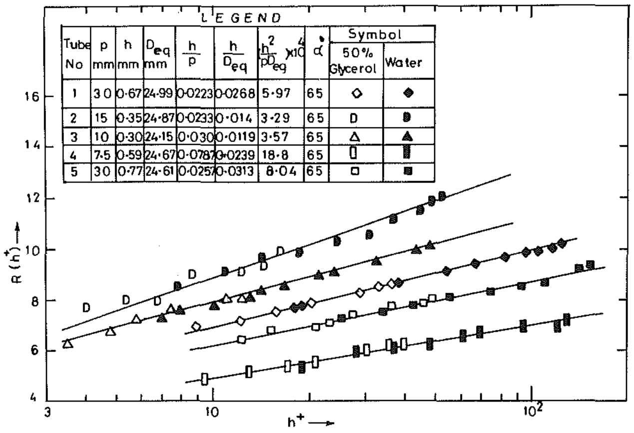

Tube No	p mm	h mm	D_{eq} mm	$\frac{h}{p}$	$\frac{h}{D_{eq}}$	$(\frac{h^2}{pD_{eq}})\times10^4$	α°	Symbol 50% Glycerol	Symbol Water
1	30	0·67	24·99	0·0223	0·0268	5·97	65	◇	◆
2	15	0·35	24·87	0·0233	0·014	3·29	65	D	◗
3	10	0·30	24·15	0·030	0·0119	3·57	65	△	▲
4	7·5	0·59	24·67	0·0787	0·0239	18·8	65	▯	▮
5	30	0·77	24·61	0·0257	0·0313	8·04	65	□	■

Fig. 4 Variation of momentum transfer roughness function ($R(h^+)$) with roughness Reynolds number (h^+) for the flow of water and 50 percent glycerol in spirally corrugated tubes

A characteristic feature of flow in sprirally corrugated tubes is that even at high flow rates, the friction factor continues to decrease with increase in Reynolds number though not as rapidly as for the smooth tube – a behavior earlier observed by Newson and Hodgson [18].

Friction Correlation. The results of friction factor in single- and multistart spirally corrugated tubes were analysed in terms of momentum transfer roughness function $R(h^+)$ and roughness Reynolds number (h^+). Figure 4 shows the variation of $R(h^+)$ with h^+ for the turbulent flow of water and 50 percent glycerol in five spirally corrugated tubes. The spirally corrugated tubes used in the present study were not geometrically similar, because of the different values of (p/h) involved. Owing to this, a vertical spread in $R(h^+)$ values was noted. Earlier Webb et al. [7] also observed a similar spread for the isothermal flow of fluids in the Prandtl number range of 0.7 to 38 inside repeated-rib roughened tubes, having a nonsimilar roughness geometry. For all the tubes, the $R(h^+)$ value increased with increasing (h^+) – a trend also recently reported by Withers [19]. Tube 2 showed the highest value for $R(h^+)$ whereas Tube 4, being the roughest of all the tubes, showed the least value for $R(h^+)$.

Studies by Withers and Habdas [20] revealed the negligible effect of rib width in increasing friction factor. They studied the effect of height and pitch of corrugation separately and observed that the group $(h^2/\rho D_{eq})$ termed as tube severity factor was more useful in correlating friction results. The utility of this group $(h^2/p\ D_{eq})$ in correlating friction factors was later supported by the work of Mehta and Raja Rao [21].

By cross-plotting the present results, $R(h^+)$ was found to vary as $(h^2/p\ D_{eq})^{-0.33}$. The following correlation closely fitted the data points in Fig. 5 within a standard deviation of 6.12 percent

$$R(h^+)(h^2/(p\,D_{eq})^{0.33} = 0.40(h^+)^{0.164} \tag{11}$$

applicable over the range of h^+ from 3 to 200.

Heat Transfer. Heat transfer studies on smooth and spirally enhanced tubes were carried out to obtain the tubeside convective heat transfer coefficients h_i. Since the metal wall temperature was measured directly, h_i was determined from

$$Q = h_i A_i [T_w - T_b]_{\text{lm}} \tag{12}$$

where Q is the mean of Q_s (based on steam condensate measurements) and Q_c (based on coolant test liquid). Only those runs for which heat balance error (HBE), calculated as $[(Q_s - Q_c)/Q_s] \times 100$, is less than ± 5 percent were processed for evaluation of h_i.

With saturated steam condensing at atmospheric pressure on the outside of the tube, the wall temperature was found to vary from 68 to 95°C, depending upon the test liquid and its flow rate. For any run, wall temperature variation along the tube length ranged from 1.5 to 3.5°C, and mean wall tem-

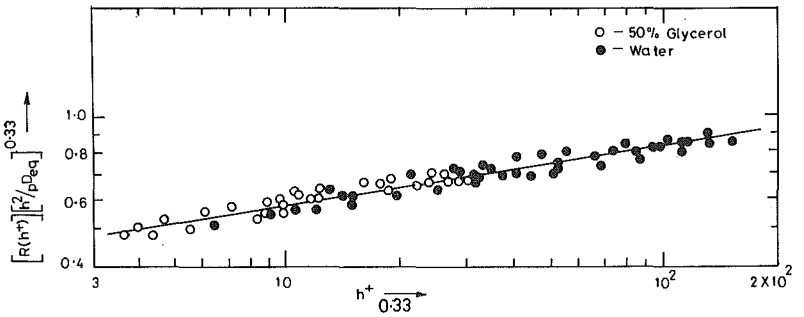

Fig. 5 Variation of $R(h^+)$ $[h^2/pD_{eq}]^{0.33}$ with roughness Reynolds number (h^+) for the flow of water and 50 percent glycerol in spirally corrugated tubes – a final correlation

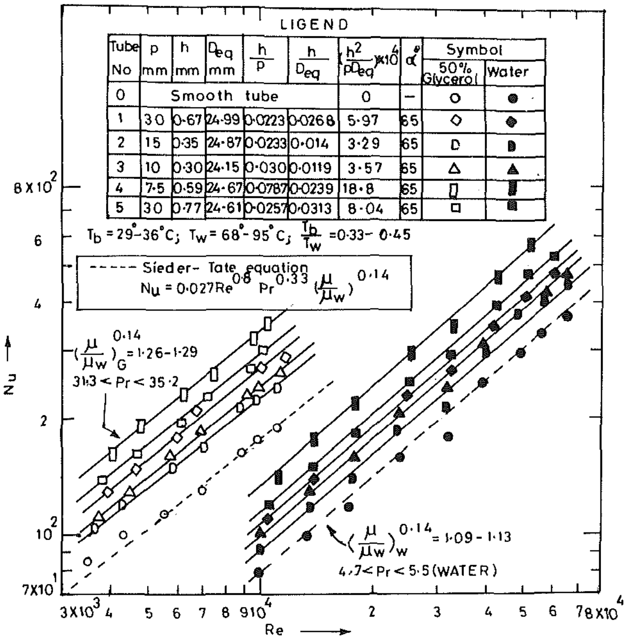

Fig. 6 Variation of Nusselt number with Reynolds number for the turbulent flow of water and 50 percent glycerol in smooth and five spirally corrugated tubes

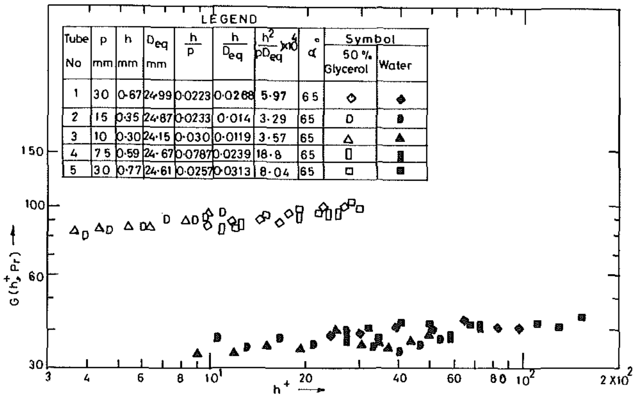

Fig. 7 Variation of heat transfer roughness function $G(h^+, \mathrm{Pr})$ with roughness Reynolds number (h^+) for the heating of water and 50 percent glycerol in spirally corrugated tubes

perature T_w was used in equation (12). The bulk mean temperature T_b, calculated as the arithmetic mean of the test liquid inlet and outlet temperatures, was found to range from 29-36°C, depending on the test fluid and its flow rate. The ratio (T_b/T_w) ranged from 0.33 to 0.45 for the two test liquids used in the present work.

The ratio (μ/μ_w) varied from 5.2 to 6.2 for 50 percent glycerol and 1.90 to 2.30 for water. Thus the viscosity correction factor $(\mu/\mu_w)^{0.14}$ ranged from 1.26 to 1.29 for 50 percent glycerol and 1.09 to 1.13 for water.

The smooth tube heat transfer coefficients were found to agree within ±6 percent with Sieder-Tate equation (13) for turbulent flow heat transfer to water and 50 percent glycerol, except for a few runs in the transition region (3500 < Re < 5600) where the experimental Nusselt numbers were 15 percent greater than the calculated values for 50 percent glycerol.

$$\left[\frac{h_i D_i}{K}\right] = 0.027[\mathrm{Re}]^{0.8}[\mathrm{Pr}]^{0.33}\left[\frac{\mu}{\mu_w}\right]^{0.14} \tag{13}$$

The values of h_i for the turbulent flow of water and 50 percent glycerol inside one smooth tube and five spirally corrugated tubes were analyzed in terms of Nu-Re relationships, and the variation of Nu with Re is shown in Fig. 6. h_o ranged from 9000 to 22,000, and h_i from 2000 to 14,000 for water, and 1400 to 6000 for 50 percent glycerol in the present work in the units W/m^{2}K.

The heat transfer performance of the enhanced tubes was clearly superior to the smooth tube. The Nu augmentation in these tubes varied from 20 to 30 percent for Tube 2 to a maximum of 90 to 95 percent for Tube 4.

The Nusselt number dependence on Reynolds number is more marked in spirally corrugated tubes than in a smooth tube. Kidd [13] observed that the exponents of Re in Nu-Re relationships is greater than 0.8 and is a unique function of surface roughness, especially for rough tubes. Mehta and Raja Rao [21] noticed an increasing trend of Re exponent with increasing tube roughness geometry. The Re exponent value varied from 0.8 for a smooth tube to a maximum of 1.17 for the roughest tube. This fact underlines the importance of computing h_i directly by measuring tube wall temperature without resorting to the Wilson plot technique. Marto et al. [22] and Withers et al. [12], however, used Wilson plot method to compute h_i, for rough tubes, also assuming Sieder-Tate type equation.

$$\left[\frac{h_i D_i}{k}\right] = C_i[\mathrm{Re}]^{0.8}[\mathrm{Pr}]^{0.33}[\mu/\mu_w]^{0.14} \tag{14}$$

and they expected the constant C_i to take care of error involved in using 0.8 as exponent of Re for rough tubes.

Heat Transfer Correlation. The tubeside heat transfer coefficients h_i for the turbulent flow of water and 50 percent glycerol in five spirally corrugated tubes were analyzed in terms of heat transfer roughness function $G(h^+,\mathrm{Pr})$, also known as G-function, and roughness Reynolds number (h^+). The variation of G-function with (h^+) is shown in Fig. 7, and it is found to increase very slowly with an increase in h^+.

It is expected that G-function should be independent of geometrical parameters of corrugation, since $R(h^+)$, which is involved in the computation of G-function, has already taken care of the hydraulic characteristics of the flow and also the roughness parameters. A close inspection of Fig. 7 strongly supports the foregoing argument. Earlier Dalla Donne and Meyer [8] and Webb et al. [7] also observed that G-function is essentially independent of rib geometry for internal rib-roughened tubes. Despite incorporating the term $(p/D_i)^{1/3}$ in the correlation of $G(h^+, \mathrm{Pr})$ with (h^+) Withers [21] observed that even then predicted heat transfer results were found to have a scatter of about 25 percent. In view of the foregoing analysis, the small effect of (p/D_i) was not included in the present heat transfer correlation.

The Prandtl number effect on G-function was evaluated by the treatment of heat transfer results of the test liquids $(5.2 < \mathrm{Pr} < 32)$ used. G-function was found to vary with $\mathrm{Pr}^{0.55}$. This agreed well with the value of 0.57 reported by Webb et al. [7] for repeated rib-roughened tubes in the Prandtl number range of 0.7 to 38. Figure 8 shows the variation of $G(h^+, \mathrm{Pr})(\mathrm{Pr}^{-0.55})$ with (h^+) and the final correlation obtained for both single-start and multistart spirally enhanced tubes was

$$G(h^+,\mathrm{Pr})(\mathrm{Pr}^{-0.55}) = 8.6(h^+)^{0.13} \qquad \text{for } 25 < h^+ < 180 \tag{15}$$

Equation (15) predicted the results of the present work and also the results of Withers [19] for the heating of water in tubes having internal helical ridging as well as those of Gupta and Raja Rao [11] for the heating of fluids for $5 < \mathrm{Pr} < 82$ range, in single-start spirally enhanced tubes with a standard deviation of 7.0 percent. The agreement was found to be good, despite different tube geometries and different test fluids used. This comparison is shown in Fig. 9, and it is clear

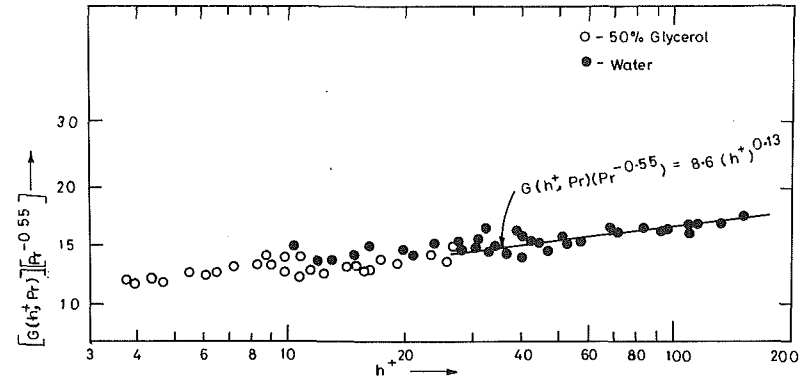

Fig. 8 Variation of $G(h^+, Pr)\ Pr^{-0.55}$ with roughness Reynolds number (h^+) for the flow of water and 50 percent glycerol in spirally corrugated tubes – a final correlation

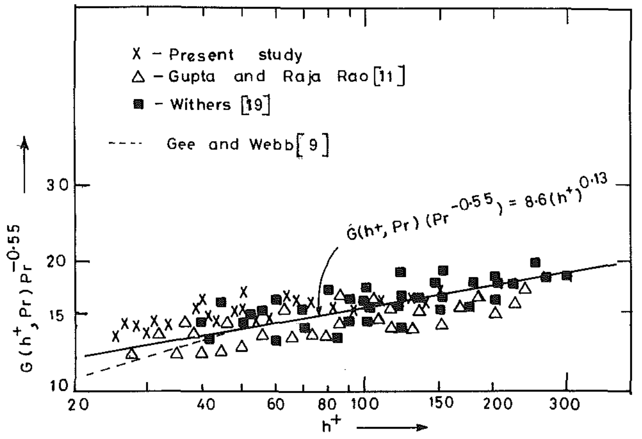

Fig. 9 Comparison of the present correlation with the results of other workers

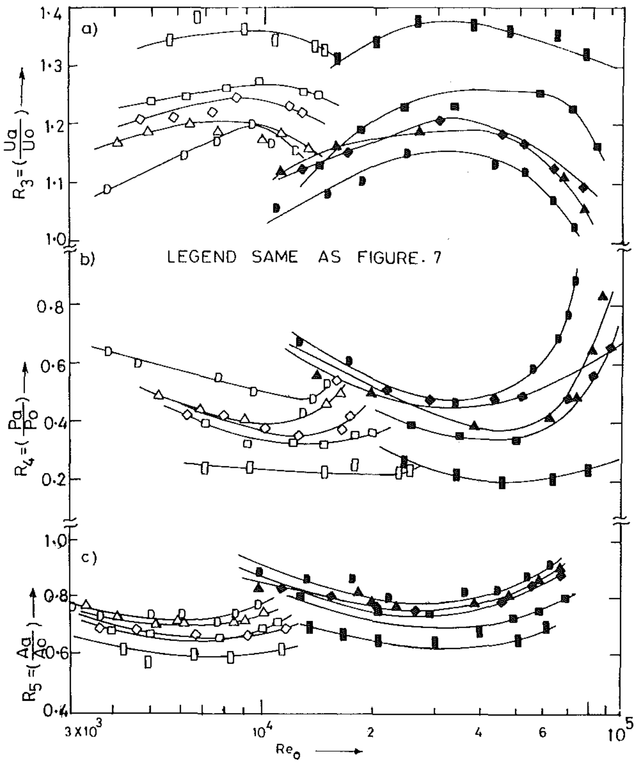

Fig. 10 Variation of performance ratios with equivalent smooth tube Reynolds number

that the proposed correlation (equation (15)) closely represents the present data and published results over a range of h^+ from 25 to 300. The recently published results of Gee and Webb [9] covered limited range h^+ of 5 to 40 and these were seen to be lower than the straight line representing the proposed equation, as seen in Fig. 9.

Performance Evaluation. Bergles et al. [16] outlined several performance criteria for enhanced tubes based on tubeside heat transfer coefficient, keeping various parameters constant for a particular criterion. Thus, in technically evaluating the thermohydraulic performance of five spirally corrugated tubes of the present study, criteria 3, 4, and 5 were used. The design objectives of these three criteria are, respectively,

(*i*) To maximize the heat transfer rate for equal pumping power and heat exchange surface area ($P/Pa = A/Aa = 1$)

(*ii*) To minimize the pumping power for equal heat duty and surface area ($Q/Qa = A/Aa = 1$).

(*iii*) To reduce the tube surface area for equal pumping power and heat duty ($P/Pa = Q/Qa = 1$).

The design advantages, based on these three criteria, offered by spirally corrugated tubes are computed, with normal standard of comparison being a smooth tube of equal inner diameter.

The performance ratios were evaluated as (U_a/U_o) instead of as (hi_a/hi_o) in view of the fact that r, the ratio of combined outside film and metal wall resistance to the inside film resistance, is not zero, but varied from 0.2 to 0.9.

Criterion 3. Figure 10(*a*) shows the variation of performance ratio evaluated as (U_a/U_o) with equivalent smooth tube Reynolds number Re_o. Re_o, which satisfies the constraints of this criterion, is given by

$$\mathrm{Re}_o = \left[\frac{f_a\,\mathrm{Re}_a^3}{0.079}\right]^{0.364} \tag{16}$$

R_3 increased with increase in Re_o up to a critical value, beyond which it decreased with further increase in Re_o for both water and 50 percent glycerol. Tube 4 having a four-start corrugation configuration showed a maximum improvement of 40 percent in R_3 and hence was identified as the most efficient tube. Tube 2 produced a minimum improvement of 15 to 20 percent compared to the smooth tube. The augmentation in other tubes ranged from 20 to 40 percent, and all these five tubes were found to give optimum performance in the Re_o range of 30,000 to 50,000 for water and 6000 to 8000 for 50 percent glycerol.

Criterion 4. The performance ratio R_4 satisfying the constraints of constant heat duty and constant basic geometry of this criterion was derived as

$$R_4 = [f_a \mathrm{Re}_a^3 / 0.079\, \mathrm{Re}_o^{2.75}] \qquad (17)$$

and Re_o was obtained to satisfy the condition $U_o = U_a$. From Fig. 10(*b*), in which performance ratio, evaluated as (P_a/P_o), is plotted against Re_o, it can be seen that R_4 decreased with increasing Re_o, attained a minimum and then started increasing with Re_o. This trend was observed when both water and 50 percent glycerol were used as tubeside fluids.

Based on this criterion, pumping power saving of 30 percent to 40 percent for Tube 2 and 70 to 80 percent for Tube 4 can be achieved. Though the pumping power saving varied from tube to tube, maximum saving occurred in the Re_o region of 10,000 to 15,000 for 50 percent glycerol and 40,000 to 50,000 for water.

Criterion 5. Re_o for criterion 5 was obtained as

$$\mathrm{Re}_o = (0.29 f_a \mathrm{Re}_a{}^3 \mathrm{Pr}^{0.4} / \mathrm{Nu}_a)^{0.512} \qquad (18)$$

The curves representing the results of performance ratio R_5 $[= A_a/A_o = U_o/U_a]$ as a function of Re_o are shown in Fig. 10(*c*). A reduction of 35 to 45 percent in heat exchanger area can be obtained in the event of smooth tube being replaced by Tube 4. Ganeshan et al. [23] also observed a similar reduction in heat exchanger area from his convective heat transfer studies on spirally enhanced tubes. Tube 2 being the least rough tube, produced a minimum saving of 15 to 25 percent in heat exchanger area. Tubes 3, 1, and 5 produced a reduction in the range of 20 to 40 percent. It is further evident from Fig. 10(*c*) that to get optimum thermal performance of the tubes based on this criterion, it would be necessary to use Re_o in the range of 20,000 to 40,000 for water and 6000 to 8000 for 50 percent glycerol.

It should be emphasized that the performance of the tubes evaluated on the basis of these criteria represents the upper limit to heat transfer enhancement, pumping power reduction, and surface area reduction. Further, effect of fouling, cost factor, etc., are not taken into consideration, which might influence the final selection of the tubes for use in heat exchangers.

Conclusion

The results of the present study can be summarized as follows:

1 All spirally corrugated tubes showed an enhancement in tubeside heat transfer coefficient ranging from 15 to 100 percent and friction factor enhancement of 30 to 200 percent when compared to the smooth tube.

2 Tube 4, with larger number of starts ($N=4$) and higher (h/p) ratio of corrugation, was identified as the most efficient tube based on criteria 3, 4, and 5.

3 A correlation for $G(h^+, \mathrm{Pr})$ is proposed based on the results of the present work on single-start and multistart tubes and those of previous investigators on tubes of different roughness geometries.

References

1 Bergles, A. E., "Enhancement of Heat Transfer," *Heat Tranfser 1978*, Hemisphere Publishing, Vol. 6, Washington, D.C., 1978, pp. 89-108.

2 Watkinson, A. P., Miletti, D. L., and Tara-soft, P., "Turbulent Heat Transfer and Pressure Drop in Internally Finned Tubes," *AIChE Symposium Series* No. 131, Vol. 169, 1973, pp. 94-103.

3 Carnavos, T. C., "Heat Transfer Performance of Internally Finned Tubes in Turbulent Flow," *Advances in Enhanced Heat Transfer*, ASME, New York, 1979, pp. 103-114.

4 Dipprey, D. F., and Saberskey, R. H., "Heat and Momentum Transfer in Smooth and Rough Tubes at Various Prandtl Numbers," *International Journal of Heat and Mass Transfer*, Vol. 6, 1963, pp. 329-353.

5 Thomas, D. G., "Enhancement of Film Condensation Heat Transfer Rates on Vertical Tubes by Vertical Wires," *Industrial and Engineering Chemistry Fundamentals*, Vol. 6, 1967, pp. 97-102.

6 Kumar, P., and Judd, R. L., "Heat Transfer with Coiled Wire Turbulence Promoters," *Canadian Journal of Chemical Engineering*, Vol. 48, 1970, pp. 378-383.

7 Webb, R. L., Eckert, E. R. G., and Goldstein, R. J., "Heat Transfer and Friction in Tubes with Repeated-Rib Roughness," *International Journal of Heat and Mass Transfer*, Vol. 14, 1971, pp. 601-617.

8 Dalla Donne, M., and Meyer, E., "Turbulent Convective Heat Transfer from Surfaces with Two Dimensional Rectangular Ribs," *International Journal of Heat and Mass Transfer*, Vol. 20, 1977, pp. 583-620.

9 Gee, D. L., and Webb, R. L., "Forced Convection Heat Transfer in Helically Rib Roughened Tubes," *International Journal of Heat and Mass Transfer*, Vol. 23, 1980, pp. 1127-1136.

10 Smith, J. W., Gowen, R. A., and Charles, M., "Turbulent Heat Transfer and Temperature Profiles in a Rifled Pipe," *Chemical Engineering Science*, Vol. 23, 1968, pp. 751-758.

11 Gupta, R. K., and Raja Rao, M., "Heat Transfer and Friction Characteristics of Newtonian and Power Law Type of Non-Newtonian Fluids in Smooth and Spirally Corrugated Tubes," *Advances in Enhanced Heat Transfer*, ASME, New York, 1979, pp. 103-113.

12 Withers, J. G., Young, E. H., and Lampert, W. B., "Heat Transfer Characteristics of Corrugated Tubes in Steam Condensing Applications," *Chemical Engineering Symposium Series*, No. 174, Vol. 14, 1978, pp. 15-24.

13 Kidd, G. J., Jr., "The Heat Transfer and Pressure Drop Characteristics of Gas Flow Inside Spirally Corrugated Tubes," ASME JOURNAL OF HEAT TRANSFER, Vol. 92, 1970, pp. 513-519.

14 Nikuradse, J., "Gestzmap Igkeit der Turbulenter Steromung in Glatten Rohren," *VDI Forschungsheft*, 1932, pp. 365-360.

15 Ganeshan, S., and Raja Rao, M., "Studies on Thermohydraulics of Single and Multistart Spirally Corrugated Tubes for Water and Time-Independent Power Law Fluids," *International Journal of Heat and Mass Transfer*, Vol. 25, 1982, pp. 1013-1022.

16 Bergles, A. F., Blumenkrantz, A. R., and Taborek, J., "Performance Evaluation Criteria for Enhanced Heat Transfer Surfaces," *Proceedings of Fifth International Heat Transfer Conference*, Vol. 2, 1974, pp. 239-243.

17 Mimura, K., and Isozaki, A., "Heat Transfer and Pressure Drop of Corrugated Tubes," *Desalination*, Vol. 22, 1977, pp. 131-139.

18 Newson, I. H., and Hodgson, T. D., "The Development of Enhanced Heat Transfer Condenser Tubing," *Desalination*, Vol. 14, 1974, pp. 291-297.

19 Withers, J. G., "Tubeside Heat Transfer and Pressure Drop for Tubes Having Helical Internal Ridging with Turbulent/Transitional Flow of Single Phase Fluid," *Heat Transfer Engineering Journal*, Vol. 2, 1980, pp. 46-56.

20 Withers, J. G., and Habdas, E. P., "Heat Transfer Characteristics of Helical Corrugated Tubes for In-Tube Boiling of Refrigerant R-12," *AIChE Symposium Series No. 138*, Vol. 70, 1974, pp. 98-106.

21 Mehta, M. H., and Raja Rao, M., "Investigations on Heat Transfer and Frictional Characteristics of Enhanced Tubes for Condensers," *Advances in Enhanced Heat Transfer*, ASME, New York, 1979, pp. 11-21.

22 Marto, P. J., Reilly, D. J., and Fenner, J. H., "An Experimental Comparison of Enhanced Heat Transfer Condenser Tubing," *Advances in Enhanced Heat Transfer*, ASME, New York, pp. 1-10.

23 Ganeshan, S., Sethumadhavan, R., and Raja Rao, M., "Performance Evaluation of Spirally Corrugated Tubes with Multiple Helical Starts for Turbulent Flow Heat Transfer to High Prandtl Number Power Law Fluids," *Proceedings of 6th National Heat and Mass Transfer Conference*, IIT Madras, HMT 54-81, 1981, D 13-17.

E. M. Sparrow
Fellow ASME

M. A. Ansari

P. C. Stryker

R. Ruiz

Department of Mechanical Engineering,
University of Minnesota,
Minneapolis, MN 55455

Enhanced Heat Transfer From a Horizontal Finned Tube Situated in a Vertical Channel

Experiments were performed to determine the heat transfer characteristics of a horizontal finned tube situated in a vertical channel which is open to the ambient at the top and bottom. The heat transfer from the finned tube is by natural convection and radiation. The response of the finned-tube heat transfer to three geometric parameters was investigated: (1) the vertical position of the tube in the channel, (2) the clearance between the fin tips and the channel walls, and (3) the height of the channel. Experiments were also carried out with the finned tube situated in free space. It was found that in-channel positioning of the finned tube gave rise to substantially higher heat transfer rates than did free-space positioning. With the finned tube situated in the channel, the heat transfer was enhanced by: (1) positioning the tube at the bottom of the channel, (2) small tip-to-wall clearances, and (3) tall channels.

Introduction

Horizontal finned-tube heaters are commonly installed between parallel vertical walls. The channel formed by the walls is open at the top and bottom, and an upflow of air through the channel is induced by buoyancy. The heat transfer from the finned tube is by natural convection and radiation.

In practice, countless variations in the positioning of the finned tube in the channel are encountered. In particular, the finned tube may be found at almost any elevation between the top and bottom of the channel. Large variations also occur in the clearance between the fin tips and the channel walls. Furthermore, the height of the channel may vary significantly from installation to installation.

Each of the three aforementioned geometric parameters—the vertical position of the tube in the channel, the clearance between the fin tips and the walls, and the channel height—should have a significant effect on the heat transfer performance of the finned tube. There are, presumably, rules of thumb and other qualitative guidelines about how the heat transfer responds to changes in these parameters. However, to the best knowledge of the authors, there has not yet been a systematic quantitative study of these issues. The experiments reported here constitute such a study.

Quite apart from the effects of the aforementioned geometric parameters, there is the more fundamental question of how the heat transfer rate for a finned tube situated in an open-ended channel compares with that for a finned tube in free space, away from confining walls. It is not just a matter of which is greater (or less), about which conjectures can be made on the basis of physical reasoning, but how much greater (or less). This issue has, apparently, not been previously addressed in a quantitative manner for finned tubes, and it represents another facet of the present research.

The scope of the work may be elaborated with the aid of Fig. 1. As seen there, a vertical channel is formed by two insulated walls of height H. A finned tube is situated in the space between the walls, with the clearance between the fin tips and the adjacent wall denoted by C. The lateral placement of the finned tube is symmetric with respect to the walls, so that the clearance is identical at the right and the left. The fins are square, with side dimension L.

The investigated vertical positions of the finned tube are illustrated in the figure and are designated there as bottom, quarter-height, and midheight. If X_c denotes the vertical coordinate of the center of the finned tube, these positions correspond to $X_c/H = L/2H$, 1/4, and 1/2. Two channel heights were employed, respectively $H/L = 5$ and 10. The spacing between the fin tips and the adjacent wall was varied from $C/L = 0.078$ to 0.469 in five steps.

For each finned tube/vertical channel configuration, the Rayleigh number was varied by a factor of 20, encompassing the practical range of tube-to-ambient temperature differences. Experiments spanning the same Rayleigh number range were performed for the finned tube in free space.

The main focus of the work is the determination of the combined natural convection/radiation heat transfer characteristics. This focus follows from the fact that it is the combined mode heat transfer that is relevant to practice rather than the separate natural convection and radiation components. The heat transfer results will be reported in a format which highlights the effect of each of the geometric

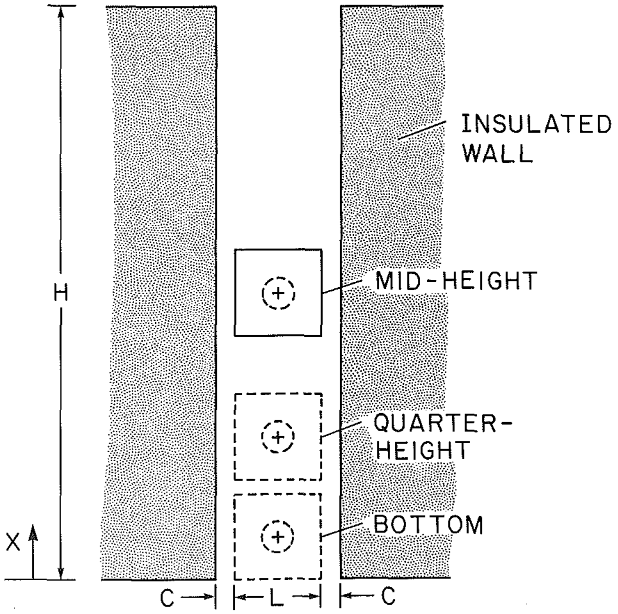

Fig. 1 Horizontal finned tube situated in a vertical channel

Contributed by the Heat Transfer Division for publication in the JOURNAL OF HEAT TRANSFER. Manuscript received by the Heat Transfer Division January 23, 1985.

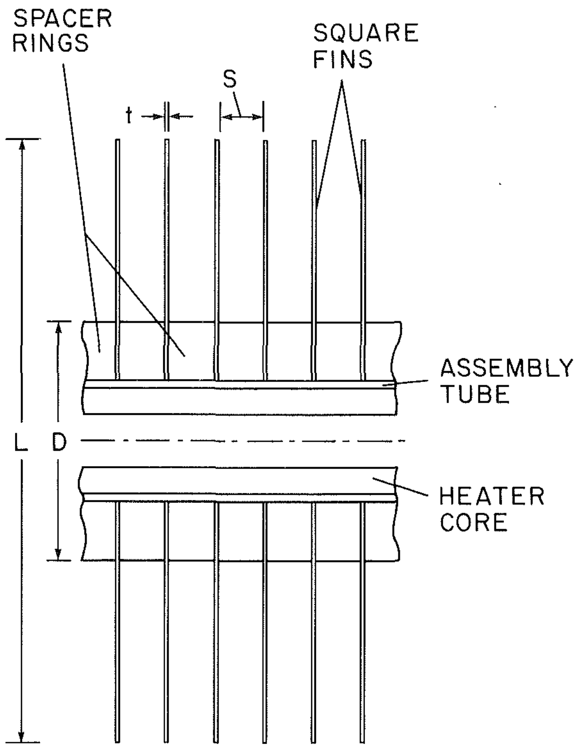

Fig. 2 Details of the finned tube

parameters and which compares the in-channel and free-space positioning of the finned tube. Supplementary data including fin tip temperatures and channel wall temperatures were also collected, and illustrative results based on these data will be presented.

The Experiments

Finned Tube. The heart of the experimental apparatus was the finned tube. It was designed with external dimensions and radiation surface properties which correspond to finned-tube heaters used in practice but had features consistent with the attainment of data of impeccable quality. These features included the absence of contact resistance between the fins and the tube, the absence of extraneous heat losses and end effects, and the attainment of a circumferentially and axially uniform tube wall temperature.

The finned tube, although fabricated from numerous individual components, functioned as a single, continuous unit in which the fins were, in effect, integral with the tube. The design concept is illustrated in a longitudinal sectional view presented in Fig. 2. As indicated there, the finned tube was synthesized by assembling copper spacer rings between square copper fins. The assembly of the apparatus was performed in the vertical orientation, with the successive rings and fins slipped over a precisely machined, mandrellike brass tube (i.e., the assembly tube). The actual assembly operations were performed in a furnace, with solder introduced at all the contacting faces of the rings and fins and with pressure applied to the stack to ensure perfect contact.

Before the assembly operations, all surfaces of the fins and rings to be exposed to the airflow were spray painted with a high-temperature black paint. The emissivity of the painted surfaces was measured with a Gier-Dunkle heated-cavity reflectometer to be 0.87. This emissivity value is typical of paints in general.

The external dimensions of the assembled finned tube, in terms of the notation of Fig. 2 and expressed in cm, are

$$L=8.128,\ D=3.188,\ S=0.584,\ t=0.0508$$

Note that the axial pitch ($S + t$) is 0.635 cm, which corresponds to four fins per inch. This is a pitch commonly encountered in finned-tube heaters. A total of 48 rings and 49 fins were employed, which yielded an overall length of the finned tube of 30.53 cm. The resulting synthesized copper tube had a wall thickness of 0.797 cm (i.e., a thick-walled tube).

A specially fabricated brass heater core, wound to provide both circumferentially and axially uniform heating, was inserted into the bore of the assembly tube, with thermal contact between the core and the tube ensured by the use of copper oxide cement.

The finned tube was equipped with eleven, fine-gage, precalibrated thermocouples (0.0254 cm chromel-constantan) deployed both along the length of the tube and around the circumference. The junctions of the thermocouples were situated 0.0254 cm from the exposed surfaces of the spacer rings, and the leads were led out through the hollow bore of the heater core. Thermocouples of still finer gage (0.00762 cm chromel-constantan) were installed at the tips of representative fins. The junctions were affixed by solder at the centers of the top and bottom edges of the fins, and the leads were laid along the edges to minimize possible conduction-related measurement errors.

The finned tube was suspended from above by 0.06-cm-dia nylon line. This suspension system avoided the extraneous conduction losses which would have occurred with a conventional suspension system.

Further details about the finned tube are available in [1].

Channels. The flow channel was made up of the two principal walls pictured in Fig. 1 plus two end walls (placed perpendicular to the axis of the finned tube). Both principal walls were of identical construction. The basic structural element of each wall was a 1.27-cm-thick plywood sheet to whose rear face angle-iron braces were fastened to ensure flatness. The front face of the plywood was sanded smooth and then covered with a 0.007-cm-thick film of self-adhering, plasticized contact paper in order to present a hydrodynamically smooth surface to the airflow. An insulation pack consisting of 5.08 cm of polystyrene and 8.89

Nomenclature

A = total heat transfer surface area of finned tube
C = clearance between fin tip and channel wall, Fig. 1
D = tube diameter
g = acceleration of gravity
H = height of channel
h = heat transfer coefficient, equation (1)
k = thermal conductivity
L = side length of square fin
Nu = Nusselt number = hS/k
Nu* = Nusselt number for finned tube in free space
Pr = Prandtl number
Q = finned-tube heat transfer rate
Q^* = heat transfer rate for finned tube in free space
Ra = Rayleigh number = $[g\beta(T_w - T_\infty)S^3/\nu^2]$Pr
S = interfin spacing
T_{cw} = channel wall temperature
T_{tip} = fin tip temperature
T_w = tube wall temperature
T_∞ = ambient temperature
t = fin thickness
X = vertical coordinate
X_c = coordinate of center of fin tube
β = coefficient of thermal expansion
ν = kinematic viscosity
ρ = density of air in channel
ρ_∞ = ambient air density

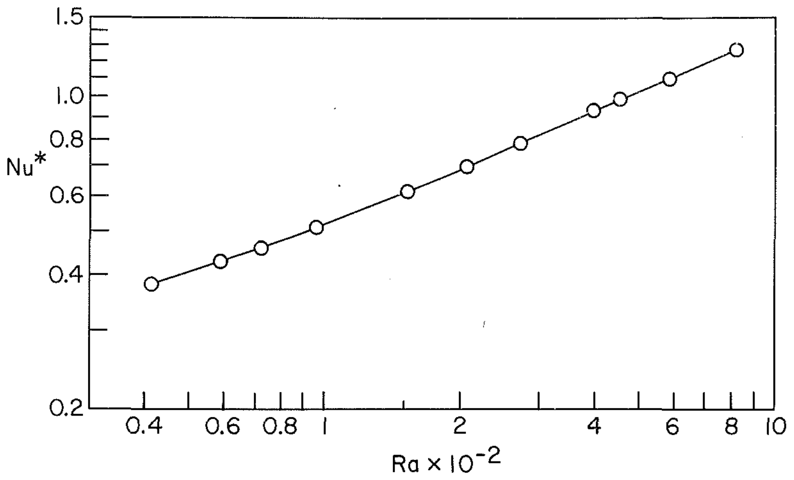

Fig. 3 Heat transfer characteristics of the finned tube in free space

cm of fiberglass was affixed to the rear face of the plywood to block extraneous heat losses.

The measured emissivity of the contact paper was 0.855. This value is typical of the emissivities of the bounding surfaces of the channels used in finned-tube installations.

The temperature distribution along the height of the principal walls was measured by an array of fourteen thermocouples deployed along the spanwise centerline of one of the walls. The thermocouple junctions were installed so as to touch and adhere to the rear face of the contact paper which bounded the airflow.

Two sets of principal walls were employed to respectively form the $H/L = 5$ and 10 channels. In one set, the front face dimensions of the walls were 40.64 × 30.53 cm (height × width), while the corresponding front face dimensions for the other set were 81.28 × 30.53 cm.

Each of the end walls was fabricated from a contact-paper-faced sheet of polystyrene backed by fiberglass, yielding a total thickness of insulation of 11.43 cm. Each end wall was in direct contact with the outboard fin at each end of the array. End walls of 40.64 and 81.28 cm height were used to form the $H/L = 5$ and 10 channels.

Other Aspects. In addition to the surface temperature measurements mentioned earlier, the ambient air temperature was measured at elevations corresponding to the inlet and exit cross sections of the channel. The thermocouples were shielded to eliminate possible radiation-related temperature measurement errors. Power to the heater embedded in the finned tube was provided by a regulated a-c supply constant to within 0.03 percent during a data run.

The experiments were performed in a windowless, interior laboratory situated in a temperature-controlled building. All ventilation to the laboratory was sealed off, and the door was blocked with a 10-cm-thick slab of polystyrene. The instrumentation and power supply were situated in a service corridor adjacent to the laboratory. The laboratory was never entered either during or for a period preceding a data run. At least six hours were allowed for the attainment of steady state.

Results and Discussion

Data Reduction. The results to be presented here are for combined natural convection/radiation heat transfer, because it is these results that are needed in practice. If it were desired to subdivide the combined heat transfer into convective and radiative components, the complexity of the situation would necessitate the use of a highly approximate analysis, yielding results of uncertain accuracy. Furthermore, the component heat transfer results would not be very useful because their synthesis to yield the combined heat transfer would be extremely difficult.

The combined-mode heat transfer coefficient is defined here as

$$h = Q/A(T_w - T_\infty) \qquad (1)$$

Owing to the suppression of extraneous heat losses, the heat transfer rate Q appearing in equation (1) was evaluated directly from the electric power input, and A is the total heat transfer surface area (i.e., the exposed surfaces of the fins and the tube). The tube wall temperature T_w was determined by averaging the readings of the eleven embedded thermocouples. Typically, the deviation of any one thermocouple reading from the average did not exceed 1/4 percent of $(T_w - T_\infty)$. Similarly, the ambient temperature T_∞ was determined by averaging the outputs of the three ambient-air thermocouples (deviations from the average were less than 1/2 percent of $(T_w - T_\infty)$).

The dimensionless representation of the results will be made via Nusselt and Rayleigh numbers defined as

$$\mathrm{Nu} = hS/k, \quad \mathrm{Ra} = [g\beta(T_w - T_\infty)S^3/\nu^2]\mathrm{Pr} \qquad (2)$$

where the interfin spacing S has been used as the characteristic length (see Fig. 2). The thermophysical properties were evaluated at a reference temperature $(T_w + T_\infty)/2$, except that $\beta = 1/T_\infty$ (absolute temperature).

As noted earlier, experiments were performed both with the finned tube situated in free space as well as in a vertical channel. The former will be regarded as a baseline case and will be designated with an asterisk (e.g., Q^*, h^*, and Nu*). The results for the in-channel positioning of the finned tube (Q, H, and Nu) will be compared with those for the free-space positioning via the ratio Nu/Nu*, where both the numerator and denominator correspond to the same value of the Rayleigh number. Since S and k are common to the cases being compared, it follows that

$$\mathrm{Nu}/\mathrm{Nu}^* = Q/Q^* \qquad (3)$$

which gives the enhancement (or degradation) of the finned-tube heat transfer rate due to the in-channel positioning.

Finned Tube in Free Space. The Nusselt number results Nu* for the finned tube in free space are plotted as a function of the Rayleigh number in Fig. 3, where the data have been interconnected by a smooth curve to provide continuity. The increase of Nu* with Ra is not unexpected, but the fact that the slope is substantially in excess of the conventional natural convection 1/4-power is worthy of note. The data lie along a curve of increasing slope, which tends toward a straight line at the higher Rayleigh numbers where $\mathrm{Nu}^* \sim \mathrm{Ra}^{0.43}$. The in-

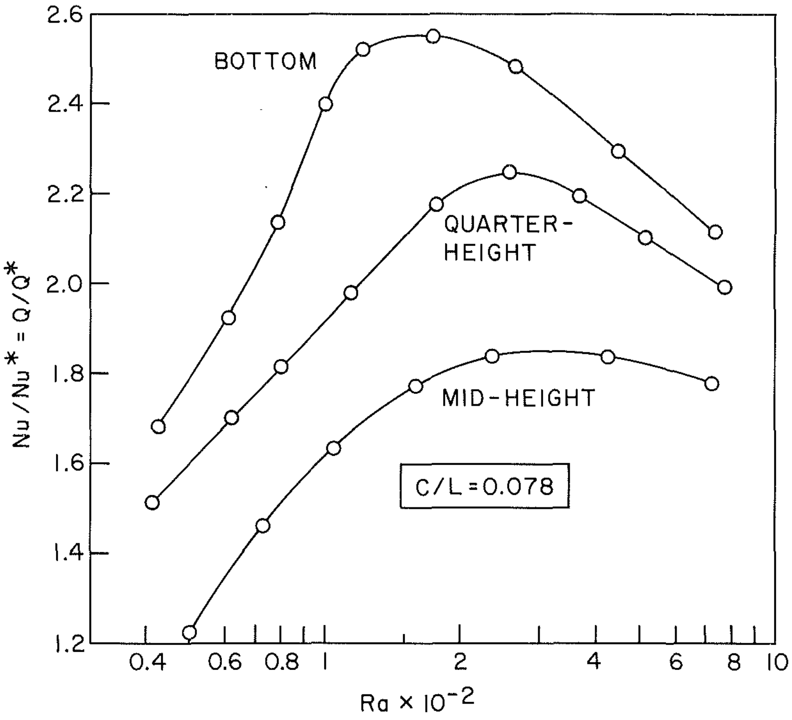

Fig. 4 Response of the finned-tube heat transfer to the vertical position of the tube in the channel; C/L = 0.078 and H/L = 10

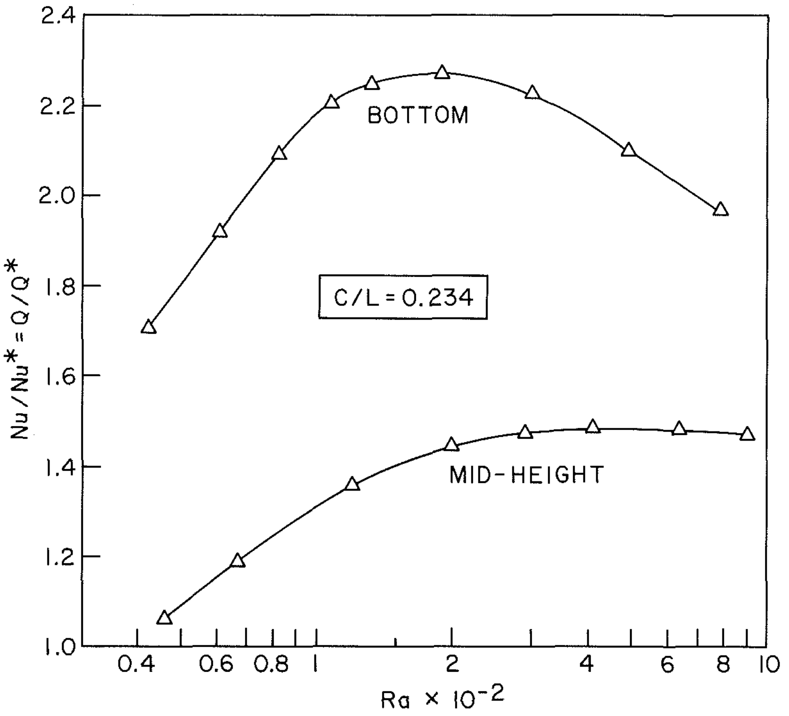

Fig. 5 Response of the finned-tube heat transfer to the vertical position of the tube in the channel; C/L = 0.234 and H/L = 10

crease of the slope is believed to be due to the effect of radiation. At relatively small values of $(T_w - T_\infty)$, i.e., at small Ra, the radiative heat transfer varies nearly linearly with $(T_w - T_\infty)$, while at larger $(T_w - T_\infty)$ there is a stronger dependence.

The seemingly small values of Ra (40 to 800) and the correspondingly small values of Nu* reflect the use of the interfin spacing S as the characteristic length. Had the tube diameter D been used instead of S, the Ra values would have been larger by a factor of about 160 and the Nu* values larger by a factor of about 5.5.

Compared with an unfinned tube of the same length, diameter, and radiative surface properties, the finned tube provides substantial enhancement. At the lowest investigated value of $(T_w - T_\infty)$, the enhancement is nearly a factor of four, while at the largest $(T_w - T_\infty)$, there is an eightfold

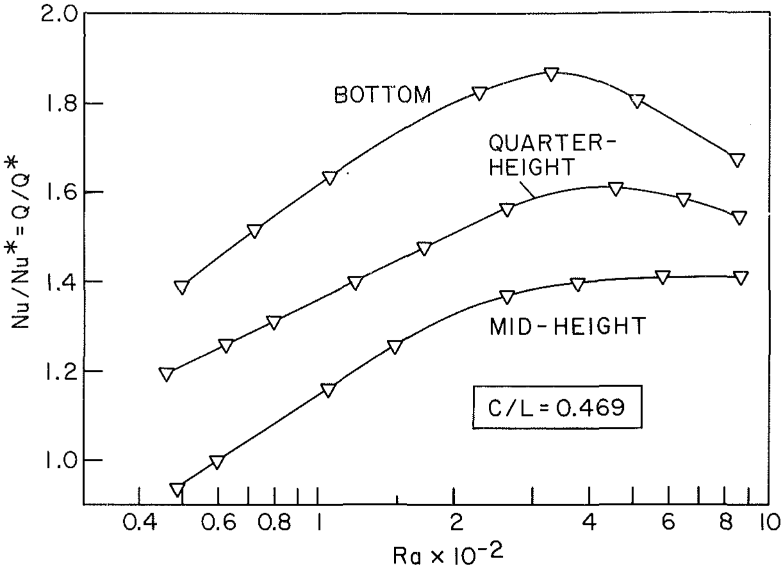

Fig. 6 Response of the finned-tube heat transfer to the vertical position of the tube in the channel; C/L = 0.469 and H/L = 10

enhancement. The ratio of the surface areas of the finned and unfinned tubes is 19.5.

In-Channel Versus Free-Space Positioning. The figures which follow, which convey the Nu/Nu* (= Q/Q^*) ratio, provide an immediate comparison between the finned-tube heat transfer rates for in-channel and free-space positioning. These figures also deal with the influence of various geometric parameters on the in-channel heat transfer. Since, in general, the data show that Nu/Nu* > 1, it follows that in-channel positioning is enhancing. The largest encountered value of Nu/Nu* was 2.55, which reflects a very significant heat transfer enhancement. The extent of the enhancement is favored by tall channels, small tip-to-wall clearances, and placement of the finned tube at the bottom of the channel. Further details of the in-channel-related enhancement will emerge as the individual figures are dealt with.

Effect of Vertical Position. The heat transfer response to the vertical position of the finned tube in the channel will now be explored, and Figs. 4-6 have been prepared for this purpose. In each figure, the Nu/Nu* (= Q/Q^*) ratio is plotted as a function of the Rayleigh number for each of several vertical positions of the finned tube. Each figure corresponds to a fixed clearance C/L, proceeding from a small clearance (Fig. 4) to an intermediate clearance (Fig. 5) to a large clearance (Fig. 6). All the figures are for a channel height of H/L = 10.

The data corresponding to each vertical position have been interconnected by a smooth curve for continuity. The respective positions—bottom, quarter-height, and mid-height—are illustrated in Fig. 2.

The effect of vertical position on the heat transfer can be assessed by comparing the Nu/Nu* values for the respective positions at a given Rayleigh number (i.e., at a given value of $(T_w - T_\infty)$). Since Nu* has a unique value for each Ra, it cancels out when comparisons between positions are being made; for example,

$$(Nu/Nu^*)_{bot}/(Nu/Nu^*)_{mid} = Nu_{bot}/Nu_{mid} = Q_{bot}/Q_{mid} \quad (4)$$

Examination of Figs. 4-6 in light of equation (4) shows that for all Rayleigh numbers and tip-to-wall clearances, the highest heat transfer rates occur when the finned tube is positioned at the bottom of the channel. For instance, at C/L = 0.078 and for Ra values of 100, 300, and 700, Q_{bot}/Q_{mid} = 1.48, 1.32, and 1.19. The corresponding comparison at C/L = 0.234 yields Q_{bot}/Q_{mid} ratios of 1.66, 1.51, and 1.35, while for C/L = 0.469, the corresponding Q ratios are 1.41, 1.35, and 1.22.

The attainment of enhanced heat transfer by a simple vertical repositioning of the finned tube in the channel is of practical relevance. Placement at the bottom of the channel should be incorporated into the installation instructions for all finned tubes.

It is also noteworthy that unlike other heat transfer enhancements, no special devices or basic alterations were necessary to achieve the position-related enhancements. Therefore, there are no economic issues to be considered—that is, the enhancement is cost-free.

To rationalize the superiority of the bottom placement of the finned tube, it is relevant to examine the mechanism which gives rise to fluid flow in the channel. The flow is driven by the imbalance between the bottom-to-top hydrostatic pressure drops outside the channel and inside the channel, that is

$$\rho_\infty gH - \int_0^H \rho g dX \quad (5)$$

The larger the imbalance represented by equation (5), the greater is the rate of mass flow through the channel.

Changes in the vertical position of the finned tube do not affect the first term of equation (5), but the second term is affected via changes in $\rho(X)$. Since the presence of the heated finned tube decreases the density of the air that passes adjacent to it, it follows that the lower the placement of the tube in the channel, the smaller is the value of $\int_0^H \rho g dX$. Consequently, the lower the finned tube, the greater fluid throughflow in the channel and the higher the heat transfer.

Figures 4-6 also allow for further consideration of the issue of in-channel versus free-space positioning of the finned tube. Values of Nu/Nu* (= Q/Q^*) in excess of unity are seen to be the rule, demonstrating the heat transfer enhancement associated with the in-channel positioning. The extent of the in-channel-related enhancement depends on the Rayleigh number. The smallest enhancement occur in the range of the lower Rayleigh numbers which, fortunately, correspond to values of $(T_w - T_\infty)$ that are smaller than those usually encountered in practice. Bottom placement of the finned tube provides the in-channel positioning with its best advantage. For this placement, for Rayleigh numbers relevant to practice, and for small and intermediate tip clearances, it can be concluded that in-channel positioning doubles the heat transfer rate compared with that for free-space positioning

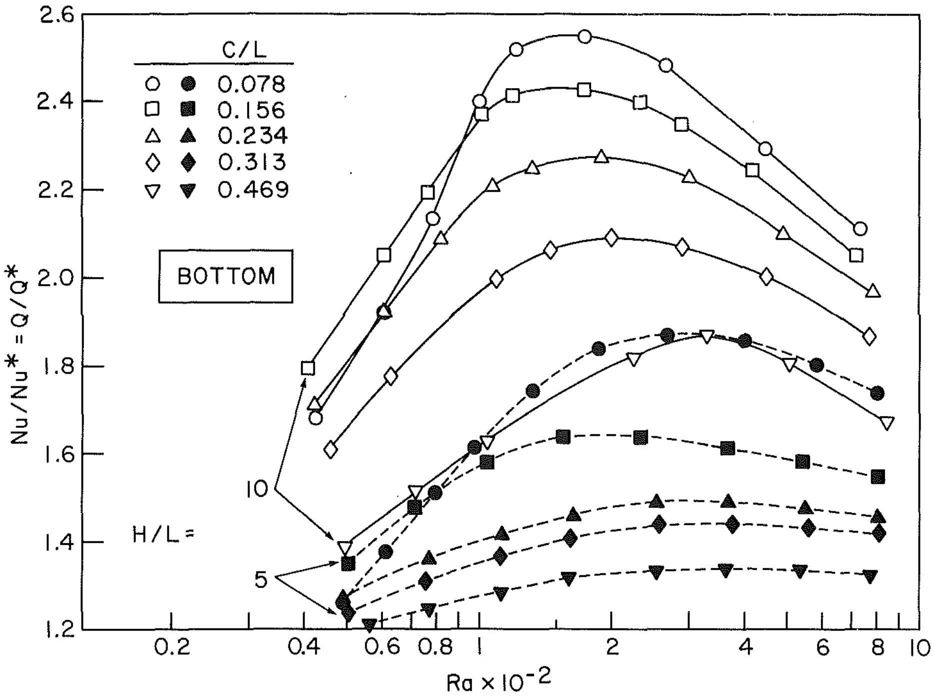

Fig. 7 Response of the finned-tube heat transfer to the tip-to-wall clearance and to the channel height; finned tube at bottom of channel

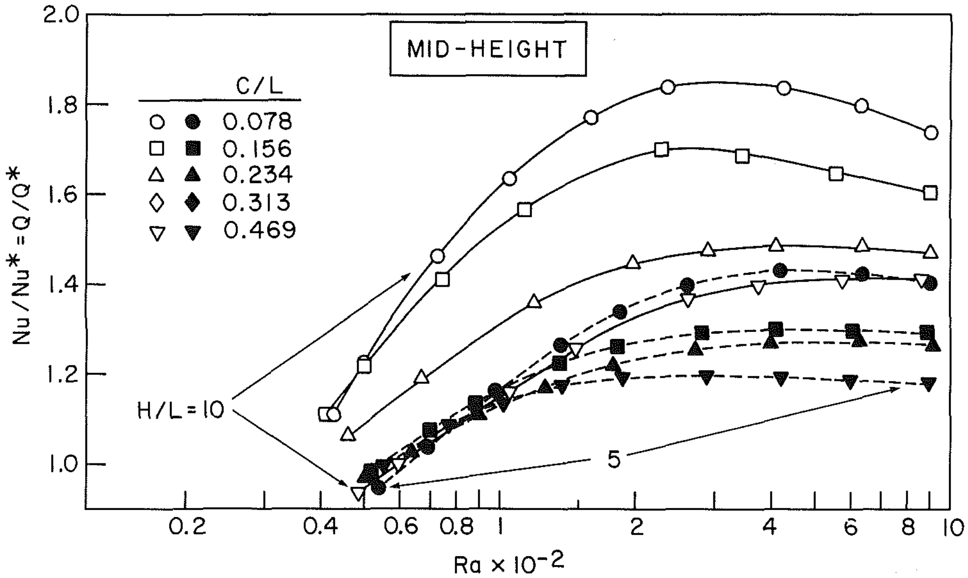

Fig. 8 Response of the finned-tube heat transfer to the tip-to-wall clearance and to the channel height; finned tube at midheight of channel

(note that the doubling corresponds to the $H/L = 10$ channel height).

The curves of Nu/Nu* versus Ra in Figs. 4-6 tend to increase at first, attain a maximum, and then drop off, with the extent of the variation being greater at smaller values of the tip-to-wall clearance C/L. This behavior of Nu/Nu* reflects the fact that Nu and Nu* increase with the Rayleigh number at different degrees of rapidity. In the range of lower Ra, Nu increases more rapidly than does Nu*, whereas at larger Ra, the inverse relationship prevails.

Effect of Tip-to-Wall Clearance. The response of the finned-tube heat transfer to the clearance between the fin tips and the channel walls will now be examined. This information is conveyed in Figs. 7 and 8, respectively, for the bottom and midheight positions of the tube. In each figure, the Nu/Nu* data for each of five tip-to-wall clearances ranging from $C/L = 0.078$ to 0.469 are plotted as a function of the Rayleigh number. The open symbols depict the data for the $H/L = 10$ channel height, while the black symbols are for the $H/L = 5$ channel height. The effect of channel height will be discussed in the next section of the paper.

To assess the effect of the tip-to-wall clearance on the heat transfer when all the other parameters are held fixed, it is appropriate to compare the Nu/Nu* values for the various clearances at fixed Ra, H/L, and vertical position of the finned tube. Since Nu* has a unique value for each Ra, the ratio of the Nu/Nu* values is equal to the ratio of the Nu values.

Both Figs. 7 and 8 indicate that, in general, smaller

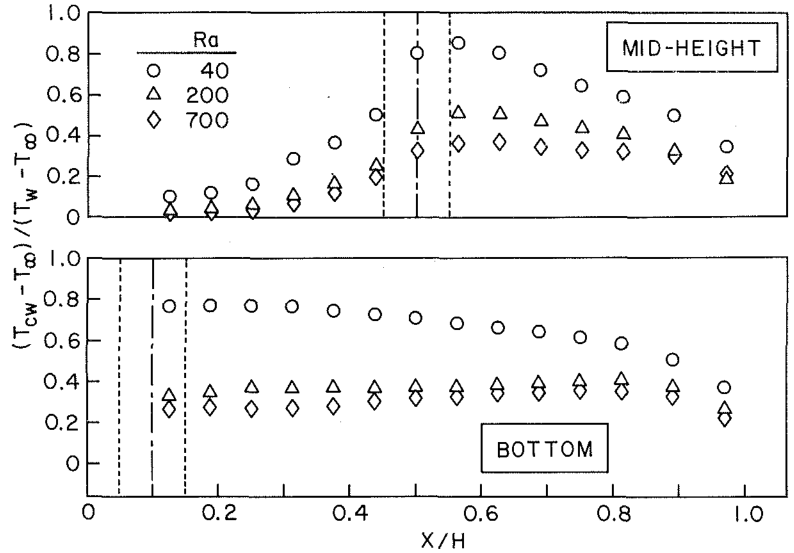

Fig. 9 Illustrative temperature distributions along the height of the channel wall; C/L = 0.078 and H/L = 10

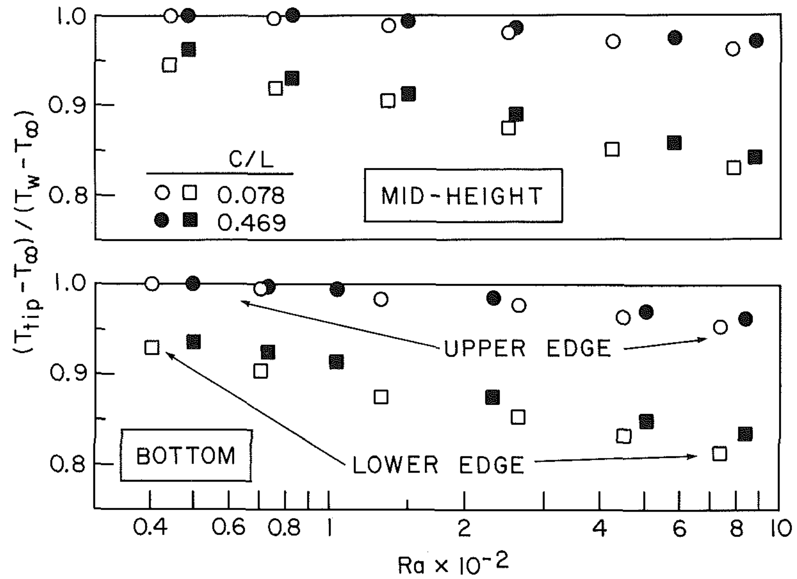

Fig. 10 Illustrative fin tip temperatures; H/L = 10

clearances yield higher rates of heat transfer. In fact, aside from the range of lower Ra (which corresponds to $(T_w - T_\infty)$ values smaller than those of common practice), the heat transfer rate increases monotonically as the clearance decreases. For concreteness, the heat transfer rates corresponding to the smallest and largest investigated clearances, C/L = 0.078 and 0.469, will be compared at Ra = 100, 300, and 700. For bottom positioning and H/L = 10, the $Q_{0.078}/Q_{0.469}$ ratios are 1.48, 1.31, and 1.24, while for H/L = 5 the corresponding ratios are 1.28, 1.40, and 1.32.

Thus, small clearances are clearly enhancing and, in common with the bottom positioning of the finned tube, the enhancement is achieved without cost.

Effect of Channel Height. Figures 7 and 8 also provide information on the heat transfer response to the height of the channel. The channel height effect is readily identified by comparing the open and black symbols, which respectively depict the results for H/L = 10 and 5.

It is evident from both figures that the finned-tube heat transfer rate increases significantly with increasing channel height. For a quantitative assessment, a comparison of the heat transfer rates at H/L = 10 and 5, respectively denoted by Q_{10} and Q_5, will be made for the finned tube at the bottom position and for the smallest tip-to-wall clearance (i.e., at the optimal vertical position and best clearance). For Ra = 100, 300, and 700, the corresponding Q_{10}/Q_5 ratios are 1.48, 1.30, and 1.21.

The enhancement of the finned-tube heat transfer with increased channel height is not achieved without cost, as was the case for the enhancement associated with small tip-to-wall clearance and bottom positioning of the tube. The cost factor is the additional materials needed for the fabrication of the taller channel. Since the wall materials used in conventional installations are generally inexpensive, it is likely that the channel-height-related heat transfer enhancement is cost effective.

Channel Wall and Fin Tip Temperatures. As noted earlier, thermocouples were installed at the fin tips and at the surface of one of the principal walls of the channel. Illustrative results from these temperature measurements will now be presented.

Attention is first turned to the distribution of the channel wall temperature T_{cw} as a function of the vertical coordinate X along the height of the channel. For the presentation of the results, it is convenient to use the dimensionless temperature ratio $(T_{cw} - T_\infty)/(T_w - T_\infty)$. This ratio, which compares the rise of the channel wall temperature above ambient to the rise of the tube wall temperature above ambient, will be plotted as a function of the dimensionless vertical coordinate X/H.

Figure 9 conveys the illustrative wall temperature distributions. The figure is made up of two graphs, respectively, for the cases where the finned tube is positioned at the bottom of the channel and at midheight. In each graph, temperature distributions are plotted for three Rayleigh numbers, namely, Ra = 40, 200, and 700. These distributions correspond to $C/L = 0.078$ and $H/L = 10$.

The vertical coordinate X_c of the center of the finned tube is indicated in each graph by a dot-dashed line, respectively, at $X_c/H = 0.05$ and 0.5. Furthermore, the vertical extent of the finned tube, above and below X_c, is delineated by dashed lines in the graphs.

Examination of Fig. 9 indicates that the shape of the wall temperature distribution is strongly influenced by the position of the finned tube. When the tube is at the bottom of the channel, the temperature is relatively uniform along the wall, only dropping off near the exit of the channel. On the other hand, with the finned tube at midheight, the temperature distribution also tends to peak at midheight. In the latter distribution, note should be taken of the temperature rise at wall locations below the finned tube. This temperature rise is due entirely to radiation. For both positions of the finned tube, higher values of $(T_{cw} - T_\infty)/(T_w - T_\infty)$ are encountered at smaller Rayleigh numbers, reflecting the decreased airflow.

The channel wall temperatures $(T_{cw} - T_\infty)$ in evidence in Fig. 9 are a significant fraction of $(T_w - T_\infty)$. The elevated wall temperatures have a twofold effect on the finned-tube heat transfer, tending to promote greater buoyancy and stronger convection but diminishing the *net* radiation from the tube.

The measured fin tip temperatures T_{tip} are also presented in terms of a dimensionless ratio, namely, $(T_{\text{tip}} - T_\infty)/(T_w - T_\infty)$. If the fins were isothermal, this ratio would be equal to one. Departures of the ratio from unity are, therefore, a measure of the temperature drop in the fins.

Illustrative results for the fin tip temperatures are presented in Fig. 10 in separate graphs for the bottom-positioned and midheight-positioned finned tube. In each graph, $(T_{\text{tip}} - T_\infty)/(T_w - T_\infty)$ is plotted as a function of Ra for two tip positions: (1) the center of the upper edge of the fin (circle data symbols) and (2) the center of the lower edge of the fin (square data symbols). Data are presented for the smallest and largest tip-to-wall clearances, $C/L = 0.078$ and 0.469, respectively, represented by open and black data symbols. All the data are for the $H/L = 10$ channel height.

The figure shows that the tube-to-tip temperature drop is greater at the lower edge of the fin than at the upper edge, which reflects the fact that the air passing over the lower edge is at a lower temperature than that passing over the upper edge. Also, $(T_{\text{tip}} - T_\infty)/(T_w - T_\infty)$ decreases monotonically as the Rayleigh number increases. This decrease is consistent with the increase in the heat transfer coefficient with the Rayleigh number.

In the expected operating range of the finned tube, $(T_{\text{tip}} - T_\infty)/(T_w - T_\infty) \sim 0.97$ at the upper edge and ~ 0.85 at the lower edge. With respect to the circumferential variation of $(T_{\text{tip}} - T_\infty)/(T_w - T_\infty)$, the aforementioned values may be respectively regarded as the maximum and the minimum.

Concluding Remarks

The experiments described here are, seemingly, the first systematic study of the heat transfer characteristics of a horizontal finned tube situated in a vertical channel open at the top and bottom. Four issues were addressed during the course of the experiments: (1) in-channel versus free-space positioning of the finned tube, (2) the vertical position of the finned tube in the channel, (3) the clearance between the fin tips and the channel walls, and (4) the height of the channel.

In-channel positioning yielded substantially higher heat transfer rates than did free-space positioning, with a twofold increase being attainable. For in-channel positioning, the finned-tube heat transfer is enhanced by: (1) placement of the tube at the bottom of the channel, (2) small clearances between the fin tips and the channel walls, and (3) tall channels.

Reference

1 Ansari, M. A., "Natural Convection and Radiation From a Finned Horizontal Tube With Vertical and Horizontal Shrouding Surfaces," Thesis, Department of Mechanical Engineering, University of Minnesota, Minneapolis, MN, 1983.

Enhancement of Combined Heat and Mass Transfer in a Vertical-Tube Heat and Mass Exchanger

R. L. Webb
The Pennsylvania State University,
University Park, PA 16802
Fellow ASME

H. Perez-Blanco
Oak Ridge National Laboratory

This paper studies enhancement of heat and mass transfer between a countercurrent, gravity-drained water film and air flowing in a vertical tube. The enhancement technique employed is spaced, transverse wires placed in the air boundary layer, near the air-water interface. Heat transfer correlations for turbulent, single-phase heat transfer in pipes having wall-attached spaced ribs are used to select the preferred wire diameter, and to predict the gas phase heat and mass transfer coefficients. Tests were run with two different radial placements of the rib roughness: (1) at the free surface of the liquid film, and (2) the base of the roughness displaced 0.51 mm into the air flow. The authors hypothesize that the best heat/mass transfer and friction performance will be obtained with the roughness at the surface of the water film. Experiments conducted with both roughness placements show that the authors' hypothesis is correct. The measured heat/mass transfer enhancement agreed very closely with the predicted values. A unique feature of the enhancement concept is that it does not require surface wetting of the enhancement device to provide enhancement.

Introduction

Several important, basic heat transfer applications involve evaporation from a gravity-drained liquid film to a gas stream or condensation of vapors contained in the gas stream on the liquid film. Depending on the application, the mole fraction of the volatile component in the gas may be very high, e.g., the noncondensible gas problem, or very low, e.g., a cooling tower. The present work attempts to increase the rate of heat and mass transfer by using enhancement techniques. Figure 1 shows the flow geometry considered in this work. Heat is transferred from hot water flowing in the annulus to a gravity-drained water film on the inner tube surface. Heat is transferred from the water film to the air stream by convection and evaporation. At any point in the column, the heat flux from the water film to the air is given by

$$\frac{q}{A_i} = h_a (T_i - T_a) + \lambda M_s K (Y_a - Y_i) \tag{1a}$$

Equation (1*a*) assumes that the surface areas for heat and mass transfer are equal; thus, it assumes complete wetting of the tube wall. Using the heat-mass transfer analogy, equation (1*a*) may be written as

$$\frac{q}{A_i} = h_a \left[(T_i - T_a) + \frac{\lambda M_s}{c_{p,m}} (Y_a - Y_i) \right] \tag{1b}$$

The heat flux across the water film is

$$\frac{q}{A_i} = h_w (T_{w,s} - T_i) \tag{2}$$

For typical problems of the type considered here, $h_a/h_w << 1$. Thus, the dominant resistances to heat and mass transfer are in the gas boundary layer. Enhancement will be beneficial if it is applied to the controlling heat/mass transfer resistance. Since $K \propto h_a$, any technique that increases h_a will also increase K, providing complete wetting of the heat transfer surface is maintained.

Various forms of surface roughness and extended surfaces (fins) have been studied for enhancement of gas and liquid flow in tubes [1]. Hence, techniques such as surface roughness and internal fins may be considered to increase h_a. For purposes of description, the level of heat and mass transfer enhancement will be measured by the "enhancement ratio" E, where

$$E_h = \frac{h_a}{h_{as}} = \frac{\mathrm{Nu}}{\mathrm{Nu}_s} \tag{2a}$$

$$E_m = \frac{K}{K_s} = \frac{\mathrm{Sh}}{\mathrm{Sh}_s} \tag{2b}$$

Although high values for E_h and E_m are desirable, the enhancement should not be obtained at the expense of excessive pressure drop increase. One may measure the efficiency of the enhancement by the "efficiency index" η, where

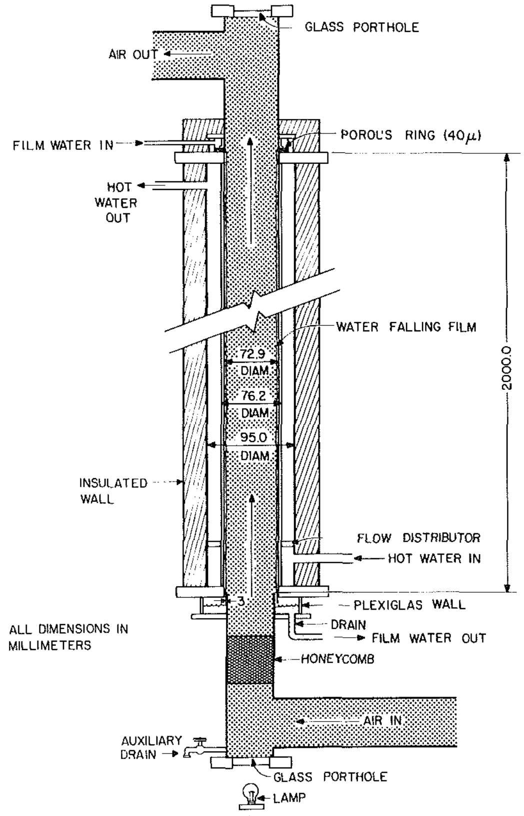

Fig. 1 Schematic of the test section

Contributed by the Heat Transfer Division for publication in the JOURNAL OF HEAT TRANSFER. Manuscript received by the Heat Transfer Division July 3, 1984.

$$\eta_h = \frac{\mathrm{Nu}/\mathrm{Nu}_s}{f/f_s} \tag{3a}$$

$$\eta_m = \frac{\mathrm{Sh}/\mathrm{Sh}_s}{f/f_s} \tag{3b}$$

Internal fins would be effective only if the fin extends into the gas flow, and if the fin surface protruding into the gas is wetted. Such surface wetting may be difficult to achieve. Further, the portion of the fin height contained within the liquid film is of no benefit for enhancement of h_a. The presence of the increased surface area within the liquid film would act to increase the liquid film thickness and to increase the gas pressure drop. Finally, the fin material contained within the liquid film would not be cost effective, since it provides no useful enhancement benefit.

Fujita et al. [2] employed a roughness-type enhancement for the problem illustrated by Fig. 1. They attached a wire mesh-type roughness to the tube wall. Their measurements showed a 50-90 percent enhancement of h_a, accompanied by a 150-180 percent gas pressure drop increase. Consideration of a wall-attached roughness suggests that it offers serious disadvantages. The wire size must be sufficiently large that it causes mixing of the gas boundary layer. However, it will also cause thickening of the liquid film, resulting in increased gas pressure drop and possible liquid entrainment.

Rather than attaching the roughness elements to the inner tube wall, it is more desirable to displace the roughness elements from the tube wall, so that they interact only with the gas boundary layer. Figure 2 shows the proposed enhancement concept, which consists of wires of diameter e spaced at an axial distance p.

A previous study on transverse-rib enhancement with single-phase flow [3] has provided correlations to predict the heat transfer coefficient and friction factor as a function of e/D, p/e, and Re. In this work, the roughness elements were located at the tube wall. Reference [3] also shows that p/e = 10–15 will provide the highest enhancement level for a given wire diameter. Webb and Eckert [4] have proposed guidelines for selecting the preferred roughness height e. The preferred e will yield high heat transfer enhancement without excessive pressure drop increase (high η_h).

The authors propose that the predictive methods presented in [3, 4] may be applied to the enhancement concept illustrated in Fig. 2. Thus, [4] will be used to select the wire diameter e, and the correlations of [3] will be used to predict the air heat transfer coefficient h_a and the friction factor f.

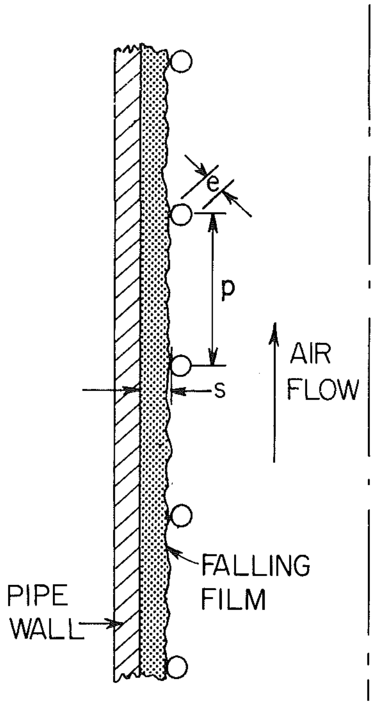

Fig. 2 Repeated-rib roughness concept

Selection of the Enhancement Dimension

The dimensional values that must be specified are:

1 the spacing between the wire and the tube wall s
2 the wire diameter e
3 the wire spacing p

In order to specify the geometric variables s, e, and p, it is necessary to define the flow rate, or Reynolds numbers, of the water film and the gas. The design point for the present study is Re_a = 41,180 and Re_w = 328 with a 73-mm tube internal diameter D.

Calculation of s. The outer diameter of the wire is placed at the water–air interface. Thus, $s = \delta$ (the film thickness). For a vertical gravity-drained laminar film [5]

$$s = \delta = 0.91 \left(\frac{\nu_w{}^2 \mathrm{Re}_w}{g} \right)^{1/3} \tag{4}$$

Using Re_w = 328, the calculated value of s is 0.25 mm.

Nomenclature

A_i = tube-side surface area, m^2
B = friction parameter used in equation (6)
c_p = specific heat, J/(kg•K)
D = pipe diameter, m
e = wire diameter of turbulence promotor, m
e^+ = roughness Reynolds number, equation (5)
E = enhancement ratio, equation (2)
f = fanning friction factor of air
g = acceleration of gravity, m/s^2
h = convective heat transfer coefficient, W/(m^2•K)
k = thermal conductivity, W/(m•K)
K = mass transfer coefficient, kgmol/(m^2•s)
L = pipe length, m
$\dot{m}$ = mass flow rate, kg/s
M_s = molecular weight of steam
Nu = Nusselt number of moist air
p = axial pitch of wires, m
P = pressure, N/m^2
Pr = Prandtl number of air
R = radius
Re = air Reynolds number = $2RV_a/\nu_a$
Re_w = water film Reynolds number = $2\dot{m}_w/\pi R \mu_w$
s = spacing between surface and wire, m
Sc = Schmidt number of air
Sh = Sherwood number of air
T = temperature, K
V = velocity, m/s
W = humidity ratio, kg steam/kg dry air
Y = air mole fraction
δ = falling film thickness, m
η = efficiency index, equation (3)
ρ = density, kg/m^3
λ = latent heat of steam, J/kg
ν = kinematic viscosity, m^2/s
μ = viscosity, kg/s•m

Subscripts

a = air
i = at water–air interface
in = at air inlet
m = mixture
s = smooth surface
v = steam
w = water falling film
∞ = evaluated at air bulk condition

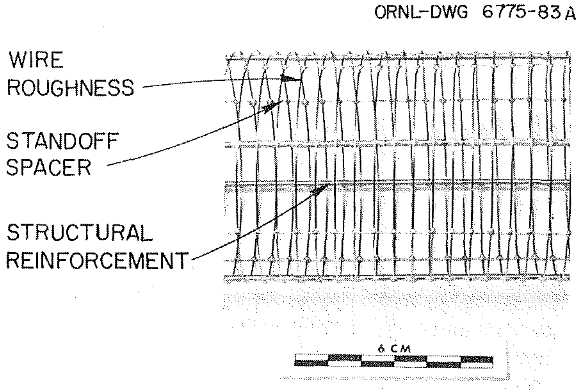

Fig. 3 View of a turbulence promoter

Calculation of e **and** p. As shown by Webb et al. [3], high heat transfer enhancement will be obtained with $p/e = 10$, which will be used here. More detailed consideration is required to select e.

If e is too small, the heat transfer enhancement E_h will be relatively small. As shown in [3], E_h will increase with increasing wire size and approach an asymptotic limit. However, the friction factor will continue to increase as the wire size is increased. The preferred wire size thus depends on a compromise between E_h and η_h. Webb and Eckert [4] recommend that a good design compromise will result if the wire size is selected to satisfy $e^+ = 20$. The term e^+ is the roughness Reynolds number, which may be written as

$$e^+ = \frac{e}{D}\mathrm{Re}_a\sqrt{f/2} \qquad (5)$$

The gas flow friction factor is given by the correlation [3]

$$\sqrt{2/f} = B(e^+) - 2.5\ln\left(\frac{2e}{D}\right) - 3.75 \qquad (6)$$

where $B(e^+)$ is a known function of e^+ for a particular roughness geometry. From [3], at $e^+ = 20$, $B(20) = 4.5$ for the $p/e = 10$ transverse-rib roughness geometry. Using the known values of e^+, $B(e^+)$, D, and Re_a one may simultaneously solve equations (5) and (6) to obtain $e = 0.43$ mm. Hence the wire spacing is $p = 10 \times 0.43 = 4.3$ mm.

Based on commercial availability a 0.51 mm diameter with $p = 5.1$ mm was used for experimental evaluation of the design. The wire was displaced 0.25 mm from the tube wall. This geometry is described as Design I. Figure 3 is a photograph of the completed enhancement device. The wire is wrapped in a helix and soldered to the axial stand-off spacer wires of 0.25-mm diameter. This device was inserted in the test tube.

To test the design hypothesis, a second transverse-rib roughness geomety was fabricated. Design II is identical to Design I, except the stand-off wires are 0.51 mm in diameter. One would expect Design II to yield a small increase of E_h, but a higher air pressure drop, hence a smaller value for η_h.

Theoretical Predictions

Smooth Tube. The Nusselt number for the air flow is predicted using the Dittus-Boelter equation

$$\mathrm{Nu} = 0.023\,\mathrm{Re}^{0.8}\,\mathrm{Pr}^{0.3} \qquad (7)$$

The air flow friction factor is calculated using the Blasius equation

$$f = 0.079\,\mathrm{Re}^{-0.25} \qquad (8)$$

The Sherwood number Sh for water evaporation into the air flow is also calculated using equation (7). For this case, Pr is replaced by Sc and Nu by Sh. In the present study, $\mathrm{Pr} = 0.71$ and $\mathrm{Sc} = 0.58$.

Rough Tube. The friction factor for the $p/e = 10$ transverse-rib roughness with Design I is calculated by equation (6), and the Nusselt number is calculated with equation (9) [3]. The Sherwood number is also calculated with equation (9), replacing Pr by Sc and Nu by Sh

$$\mathrm{Nu} = \frac{\mathrm{Re}\,\mathrm{Pr}\,f/2}{1 + \sqrt{f/2}\left[\bar{g}(e^+)\mathrm{Pr}^{0.57} - B(e^+)\right]} \qquad (9)$$

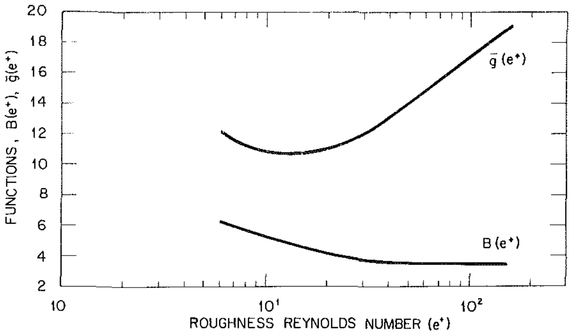

Fig. 4 $\bar{g}(e^+)$ **and** $B(e^+)$ **versus** e^+ **for** $p/e = 10$ **transverse-rib roughness**

Figure 4 shows the curves of $\bar{g}(e^+)$ and $B(e^+)$ developed by Webb et al. [3] for $p/e = 10$ transverse-rib roughness.

For a given e^+, one obtains $B(e^+)$ from Fig. 4 and calculates $\sqrt{2/f}$ from equation (6). The Re_a is then computed using equation (5). Using the known values of $B(e^+)$, $g(e^+)$, and f, Nu and Sh are calculated by equation (9).

The theoretical basis for Design I assumes that the outer diameter of the wire roughness element is at the water-air interface. Hence, equations (6) and (9) are, in a strict sense, applicable only for the $\mathrm{Re}_w = 328$ design point. As the Re_w increases, the water film will partially submerge the wire. Since the liquid film thickness increases as $\mathrm{Re}_w{}^{1/3}$, a moderate flow rate increase is possible, without significant submergence of the wire. For example, a 100 percent increase of Re_w will result in 13 percent submergence of the wire diameter. One would expect Nu and Sh to decrease as Re_w is increased with $\mathrm{Re}_a = 41{,}180$.

Equations (6) and (9) are not applicable to the Design II roughness geometry. This is because the outer diameter of the wire is displaced 0.25 mm from the water film surface into the air stream. An eightfold increase of Re_w (from 328) would be required for the liquid film to contact the outer edge of the wire for Design II. At the $\mathrm{Re}_w = 328$ design point, Design II will act as a "displaced" roughness promoter. Thomas [6] has measured the heat transfer enhancement for such displaced turbulence promoters. He shows a significant increase of Nu, but the friction increase was substantially greater than the Nu increase.

Experimental Program

Test Apparatus. An apparatus was constructed to measure the Nusselt and Sherwood numbers for heat and mass transfer between the water film and gas flowing in the test section illustrated by Fig. 1. The hot water, which serves as a heating source, flows in an annulus having an 11.1-mm clearance. The air flows upward inside the 72.9-mm-dia Monel tube. A falling film of water flows on the inside wall of the tube. This water film is fed via a porous (40 μm) stainless steel sintered ring.

A schematic of the test loop configuration is shown in Fig. 5. The inlet temperatures of the three streams (air, hot water, and falling water film) may be adjusted and automatically controlled at a desired set point. The air humidity was adjusted by means of a steam humidifier and is controlled manually. All flows were set manually to the desired set points. All the temperatures indicated on Fig. 5 were measured by calibrated platinum resistance thermometers

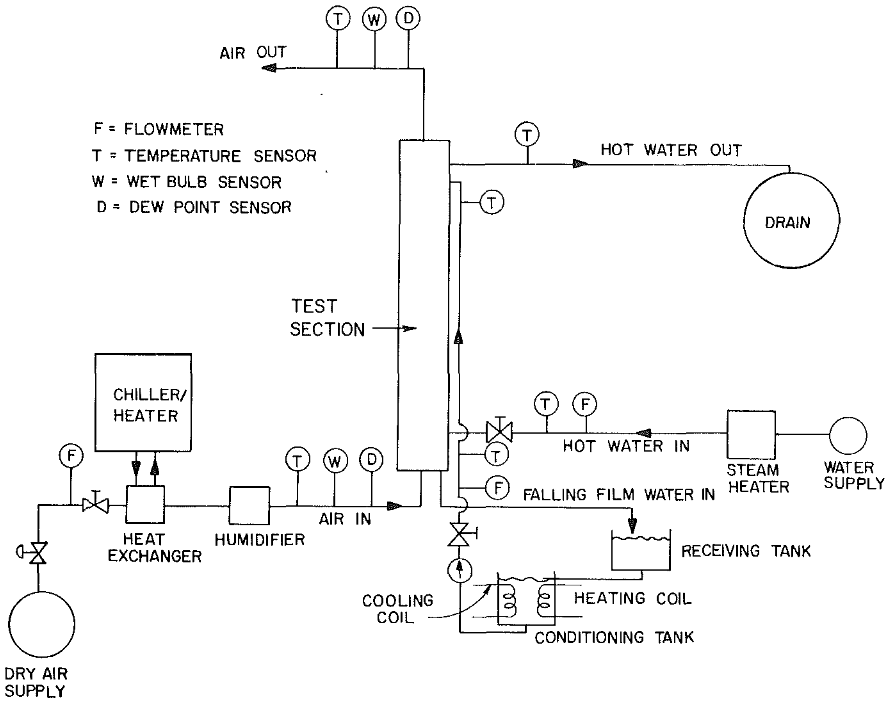

Fig. 5 Flow diagram of test loop

Table 1 Nominal experimental conditions

Air	
Inlet humidity ratio	0.005 kg steam/kg dry air
Inlet temperature	30°C
Mass flow rate	0.027 to 0.045 kg/s
Water film	
Inlet temperature	within 1°C of outlet temperature
Mass flow rate	0.013 to 0.038 kg/s
Hot water (annulus)	
Inlet temperature	43.3°C
Mass flow rate	0.190 kg/s

except the air wet-bulb temperature, for which type T precision-grade thermocouples covered with a wet wick were employed. The air dew point was monitored by means of a condensation hygrometer (General Eastern 1100 DP). The air and hot water flows were measured with turbine flowmeters (Flow Tech FT-56I100-LB and Flow Tech FT-12C20-LJG, respectively). The water falling film flow rate was measured with a paddle flowmeter (Flow Tech FTH-N10-LJS(S)). The outputs of the transducers were measured by a digitizing voltmeter (Hewlett Packard 3456 A) and sent to a desktop HP-85 computer for storage and processing via a parallel interface (HP-IB 8297 A). A programmable scanner (Hewlett Packard 3497 A), controlled by the computer, determined the sequence and frequency of sampling.

Data. Data were taken for the smooth tube and the Design I and Design II roughness elements with the experimental conditions shown in Table 1.

Tests were run over a 15-min period, and each channel was scanned 20 times. Tests in which the standard deviation of any of the measured variables exceeded 0.5 percent of the set value were rejected. Tests in which the heat balance error exceeded 10 percent of the heat lost by the hot water were also rejected. In most tests, the standard deviation of any variable was actually less than 0.1 percent of the value of the variable, and the heat balance error was on the order of 5 percent.

The gas phase heat transfer coefficient was calculated with equation (10), based on analysis given in [7]. Equation (10) accounts for the effect of mass transfer on the gas heat transfer coefficient.

$$h_a = \left[\frac{c_{p,v}}{c_{p,m}} (W_{in} - W_{out}) - \ln \frac{T_w - T_{a,out}}{T_w - T_{a,in}} \right] \frac{m_a}{2\pi RL} \qquad (10)$$

The mass transfer coefficient K is determined by integration of equation (11).

$$m_a \frac{dW}{dz} = 2\pi R M_s K \ln \frac{Y_\infty}{Y_i} \qquad (11)$$

The integration of equation (11), shown in [6], yields

$$\begin{aligned} K = {} & \ln\,[(\ln\,(Y_{\infty,out}/Y_i)/(\ln\,(Y_{\infty,in}/Y_i)] + \\ & \ln Y_{\infty,out}/Y_{\infty,in} + \\ & [(\ln\,(Y_{\infty,in}/Y_i)^2 - (\ln\,(Y_{\infty,out}/Y_i)^2]/(2)(2!) + \\ & [(\ln\,(Y_{\infty,out}/Y_i)^3 - (\ln\,(Y_{\infty,in}/Y_i)^3]/(3)(3!) + \\ & \ldots\ldots + m_a/(2\pi RLM_a Y_i). \, . \end{aligned} \qquad (12)$$

In a strict sense, equation (10) should use T_{wi} (at the water-air interface) rather than the bulk temperature of the water film. An analytical model for the smooth tube design [6] showed that $T_w - T_{wi} = 0.67°C$. The average film temperature was used in equation (10). In all experiments, the exit film temperature was within ± 1°C of the inlet temperature. The Y_i should also be evaluated at the local T_{wi}, rather than T_w, as was done here. Analytical evaluation of the temperature drop across the water film showed that $T_w - T_{wi} \leq 0.67°C$.

The effect of the above uncertainties on h and K was evaluated with an uncertainty analysis. Accounting for the uncertainties involving T_w and all other possible measurement errors, the uncertainties associated with Nu and Sh at the design point are 17 and 10 percent, respectively. The greatest contribution to this uncertainty stems from assuming constant water film temperature. Details of the uncertainty analysis are given in [7].

Experimental Results. Figures 6–8 show the measured values of f, Sh, and Nu versus Re_a for the design water film Reynolds number, 328. Each figure shows experimental results for the smooth tube and the Designs I and II roughness geometries. The solid lines are the predicted values for the smooth tube and Design I. Figure 9 shows the enhancement ratio E_m and the efficiency index η_m for the data of Figs. 6–8.

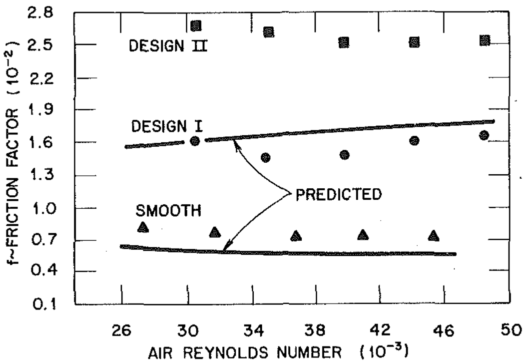

Fig. 6 Friction factor versus Re_a for Re_w = 328

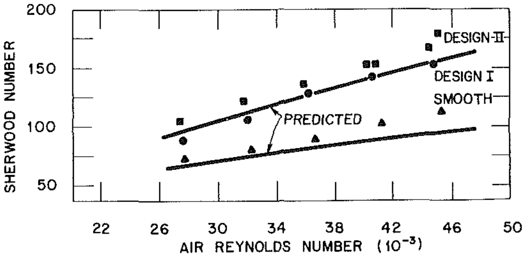

Fig. 7 Sherwood number versus Re_a for Re_w = 328

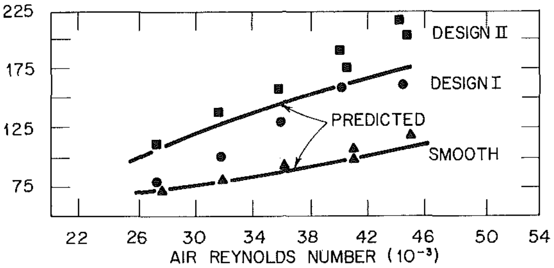

Fig. 8 Nusselt number versus Re_a for Re_w = 328

Figures 10 and 11 show the effect of water film Reynolds number on f and Sh, the smooth tube and Design I geometries.

Discussion

Figure 6 shows that the friction factor of Design I is approximately 100 percent greater than that of the smooth tube. However, the friction factor for Design II is 3.7 times the smooth tube value. The solid lines on Fig. 6 are predicted values using equations (8) and (6) for the smooth and Design I geometries, respectively. The smooth tube f is underpredicted by approximately 20 percent. Underprediction is probable because of waves on the liquid film. Equation (6) predicts f for the Design I geometry within 15 percent.

Figure 7 shows the Sherwood number. The Design I roughness provides a 38 percent enhancement of Sh at the design point (Re_a = 41,180). The Design II geometry provides a 50 percent enhancement. However, the friction factor of Design II is substantially greater than that of Design I. The smooth tube Sh is underpredicted roughly 20 percent—comparable to the friction factor underprediction. One may expect that waves on the liquid film would provide some enhancement of Sh. The Sh predicted by equation (9) for Design I is in excellent agreement with the experimental value.

Figure 8 shows the Nusselt number results. Equation (7) underpredicts the smooth tube Nu from 0 to 15 percent. The predicted Nu for Design I is greater than the experimental values at the lower Re_a conditions. The authors suggest that temperature measurement error may be responsible for the poor agreement between the theoretical and experimental Nu values at the lower values of Re_a. The exit air was saturated for Re < 27,000. It is likely that condensation occurred on the air exit thermometer bulb, which would cause the thermometer to indicate a value below the actual value. Hence, the calculated Nu would be lower than its true value. A 1.0°C error of the exit air temperature at Re = 27,000 would result in a 25 percent error of the Nusselt number. For the evaporative heat exchanger considered here, the heat transfer by evaporation is far greater than the convective heat transfer. Hence, a moderate error in Nu will have a relatively small effect on the heat transfer rate, as calculated by equation (1).

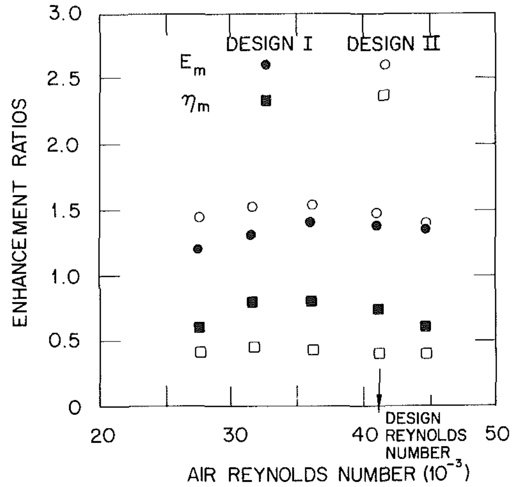

Fig. 9 Enhancement and efficiency ratio for Designs I and II at Re_w = 328

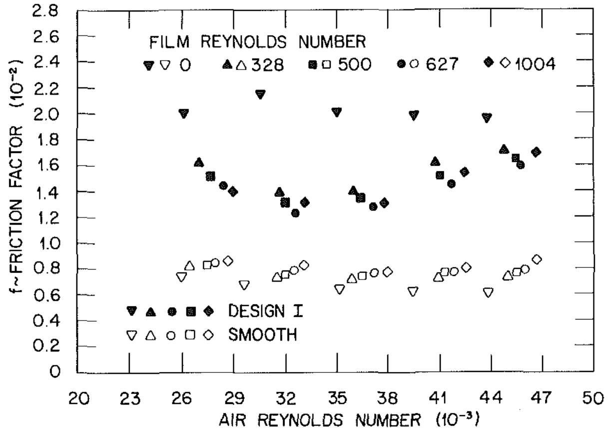

Fig. 10 Friction factor versus Re_a with Re_w as a parameter

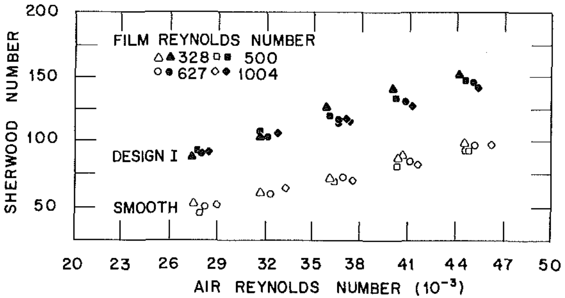

Fig. 11 Sherwood number versus Re_a with Re_w as a parameter

Figure 9 summarizes the magnitude of the mass transfer enhancement and its efficiency index η. The parameters of key practical importance are E_m and η_m. At the design point, E_m = 1.38 and η_m = 0.62. Thus η_m indicates that the enhancement of the mass transfer coefficient is 62 percent as large as the friction increase. As proposed in [4], use of the $e^+ = 20$ design condition promised to provide a good compromise between the maximum E_h and provide a high value for the efficiency index η_m. Examination of Fig. 9 shows that the intended design objectives were realized. Examination of the E_m and η_m at the design point shows that Design II provides only a marginal improvement of E_m, but its η_m is only 0.42 as compared to 0.62 for Design I. The Design I roughness element provides mixing of the gas near the surface of the liquid film, where the dominant heat and mass transfer resistances occur. The Design II roughness elements, which are displaced 0.25 mm from the liquid–air interface, also provide effective boundary layer mixing of the air. However, the element projects so far into the air stream that the increased pressure drag substantially increases the air pressure drop.

Figures 10 and 11 show the effect of increased water-film Reynolds number on f and Sh for the smooth tube and the Design I enhancement. Figure 10 shows that the friction factor of the smooth tube increases as Re_w is increased. However, the friction factor of the Design I enhancement *decreases* with increasing Re_w. The friction factor decreases because as the water flow rate increases, the roughness wire becomes partially submerged in the water film. At $\mathrm{Re}_w = 1000$, only 80 percent of the wire diameter is exposed to the air flow. The friction factor of Design I increases substantially when $\mathrm{Re}_w = 0$ (no water film). This is because of the deeper wire penetration into the air boundary layer.

Figure 11 shows that increasing Re_w has a negligible effect on Sh for the smooth tube. However, the Sh decreases for Design I as Re_w increases. This is because of the partial submergence of the roughness element, which decreases its effective roughness size, causing a reduction of the enhancement. Because the liquid film thickness depends on the 1/3 power of Re_w, moderate increases of Re_w are possible without substantially reducing the level of enhancement.

Conclusions

This study has evaluated a novel enhancement technique for heat and mass transfer between a falling film in contact with a gas flowing in a tube. A distinctive and practical characteristic of the enhancement concept is that it does not require surface wetting to provide mass transfer enhancement. The basic concept employed is mixing of the gas flow near the liquid–air interface. Based on tests of two roughness designs, the preferred geometry places the base of the wire at the liquid–air interface.

The predictive techniques employed in the selection of the roughness size and spacing are based on design correlations for wall attached roughness with single-phase flow. The good agreement between theory and experiment provide validation for the design hypothesis.

A 38 percent enhancement of the mass transfer coefficient was obtained with the preferred enhancement geometry (Design I), with an efficiency index of 62 percent. This efficiency index is comparable to that obtained for enhancement of single-phase flow using transverse-rib roughness.

The analytical design method may be applied to roughness size selection and performance prediction of any application of interest, for a vertical duct of any constant cross-sectional shape.

References

1 Webb, R. L., "Special Surface Geometries for Heat Transfer Augmentation," in: *Developments in Heat Exchanger Technology—I*, D. Chisholm, ed., Applied Science Publishers, England, 1980, Chap. 7, pp. 179–215.

2 Fujita, H., et al., "Effects of Wall Roughness on Heat and Mass Transfer in Countercurrent Flow of Air and Water Film," *Heat Transfer Japanese Research*, Vol. 9, 1980, pp. 42–53.

3 Webb, R. L., Eckert, E. R. G., and Goldstein, J., "Heat Transfer and Friction in Tubes With Repeated-Rib Roughness," *Int. J. of Heat and Mass Transfer*, Vol. 14, 1971, pp. 601–617.

4 Webb, R. L., and Eckert, E. R. G., "Application of Rough Surfaces to Heat Exchanger Design," *Int. J. of Heat and Mass Transfer*, Vol. 15, 1972, pp. 1647–1658.

5 Collier, J. G., *Convective Boiling and Condensation*, 2nd edn., McGraw-Hill, 191, p. 329.

6 Thomas, D. G., "Enhancement of Forced Convection Heat Transfer Coefficient Using Detached Turbulence Promoters," *Ind. and Eng. Chem.—Process Design and Development*, Vol. 6, 1967, pp. 385–390.

7 Perez-Blanco, H., and Bird, W. A., "Study of Heat and Mass Transfer in a Vertical Tube Evaporative Cooler," ASME JOURNAL OF HEAT TRANSFER, Vol. 106, No. 1, Feb. 1984, pp. 210–215.

F. N. Vafaie
Department of Civil and
Mechanical Engineering,
Texas A & I University,
Kingsville, TX 78363
Mem. ASME

J. R. Dunn
Department of Mechanical Engineering,
Texas Tech University,
Lubbock, TX 79409
Mem. ASME

Forced-Convection Heat Transfer for Single and Two-Phase Helical Flow in a Solar Receiver

The heat transfer characteristics of a single-tube, helically coiled receiver for a concentrating solar collector are presented. Heat transfer coefficients were measured for single and two-phase water–steam flow in a helical coil subjected to radiant heating for a range of flow conditions and radiant flux levels. Results are presented for both the local and average heat transfer coefficients in several flow regimes.

Introduction

A problem of major importance to the design of concentrating solar systems is that of the heat transfer characteristics of the solar receiver for these systems. This study investigates the heat transfer characteristics of the solar receiver for a large-scale solar power generation system (Crosbyton Solar Power Project). This high-performance, concentrating solar thermal system is based on the hemispherical dish or Fixed Mirror–Distributed Focus (FMDF) concept (Fig. 1). The receiver in this system consists of tube bundles helically wrapped around a supporting structure (Fig. 2). The system is designed to operate in a water–steam loop and, as such, single-phase liquid, two-phase, and superheated vapor heat transfer conditions are part of the normal operation. Due to the special geometry of the receiver, the tubes are only heated over half of their exterior surface. Additionally, the incident heat flux exhibits a varying degree of nonuniformity, both circumferentially around the receiver and axially along the receiver axis.

Problem Statement

Two factors are of primary importance to the heat transfer characteristics associated with the problem being investigated. The first is the fact that an individual tube receives incident radiation over only half of its exterior surface, as shown in Fig. 2, with the internal heat flux being that which results from two-dimensional conduction around the tube cross section. Axial gradients are assumed small. Coupled with this are the secondary flow patterns associated with the helical flow and radial acceleration (calculated based on total flow; $RA = 2(Gv)/(CD^*g)$ which approached 20,000g). It has been shown [1] that for flow in coils, owing to the centrifugal force and radial acceleration present, liquid droplets entrained in the core of the tube cross section are flung onto the outer wall of the tube, farther from the coil axis. Liquid then spirals back to the inner wall as it moves along the tube and in doing so replenishes the losses due to evaporation and entrainment on the tube wall.

The experimental testing program and data analysis effort were designed to determine the distribution of the internal heat transfer coefficient, both axially in the flow direction and circumferentially around the tube wall. In order to fully simulate the nonuniform heat flux boundary conditions, radiant heating was used in the experimental test program. Detailed explanation of the radiant test facility can be found in [2, 3].

Experimental Apparatus

The test facility was designed to evaluate individual segments of the receiver. It was capable of supplying a two-phase, single-component water–steam mixture to the test section inlet at controlled flow rates and inlet pressures. Both axisymmetric and asymmetric heat flux boundary conditions were tested.

A schematic of the flow loop is shown in Fig. 3. Deionized water was drawn from a storage tank by a positive displacement pump. After regulating the flow rate by the bypass provided, the flow was divided between two fluid circuits, shown by circuits A and B. In circuit A, equipped with a hot oil heat exchanger, superheated vapor with a temperature of up to 300°C was generated. This superheated vapor was then mixed with liquid water from circuit B and delivered to the test section. The effluent of the test section was condensed and subsequently drained.

The flow loop was equipped with pulsation dampeners, pressure relief valves, check valves, and instrumentation for measurement of fluid flow rates, inlet and exit fluid pressures, coil total pressure drop, and fluid temperatures.

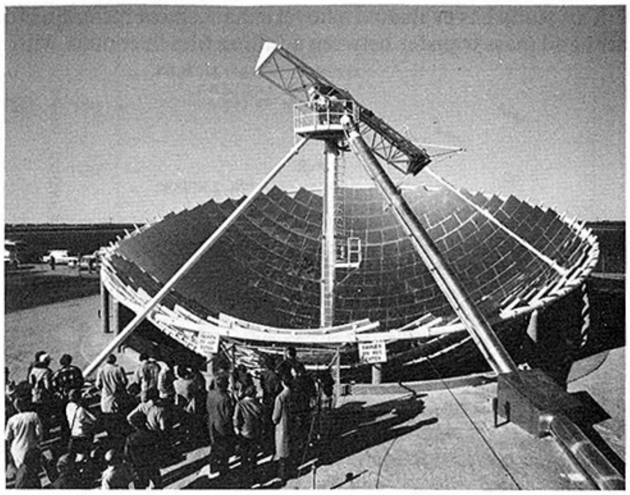

Fig. 1 Fixed mirror distributed focus (FMDF) system

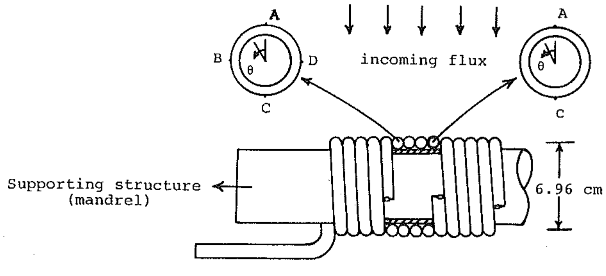

Fig. 2 Coiled tube receiver for FMDF system

Contributed by the Heat Transfer Division for publication in the JOURNAL OF HEAT TRANSFER. Manuscript received by the Heat Transfer Division June 30, 1983. Paper No. 81-WA/HT-13.

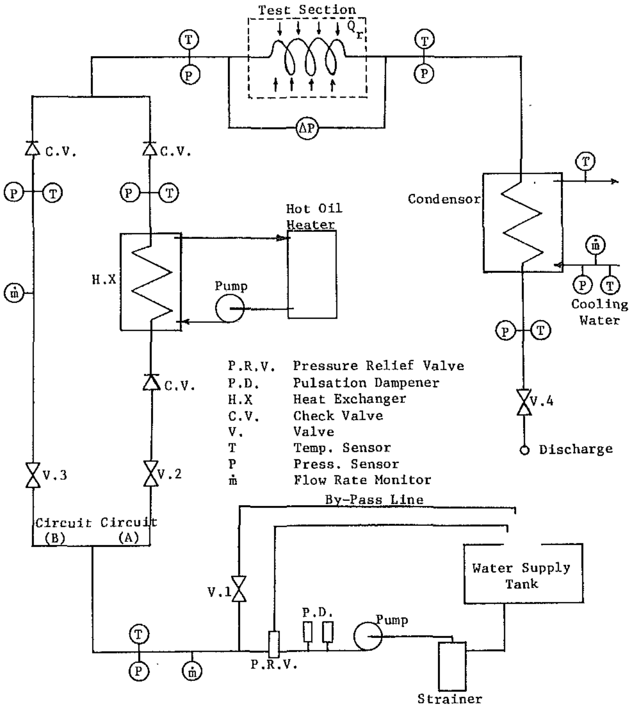

Fig. 3 Test loop schematic

The test section was constructed by wrapping 448 cm (14.7 ft) of type 304 seamless stainless steel tubing with 0.95 cm (3/8 in.) o.d. and 0.124 cm (0.049 in.) wall thickness around a cylindrical mandrel, such that the consecutive turns of the coil were in close contact. The diameter of the coil from tube center to tube center was 6.96 cm (2.74 in.) and the coil had a total of 20 turns.

A total of 42 type K thermocouples were arc welded to the outside surface of the tube at 15 thermocouple stations along the tube axis. Thermocouple stations were 1⅓ turns or 29.9 cm (11.77 in.) apart along the flow direction with the first station located at 11.20 cm (4.414 in.) from test section inlet. There were either two or four thermocouples at each station. The location of thermocouples around the tube cross section for stations with two and four thermocouples is shown in Fig. 2.

The output of all data sensors for fluid pressure, temperature, and flow rate as well as tube wall temperature were monitored by a scanning programmable data logger, with analogue indicators used for continuous visual monitoring and state verification purposes at selected locations.

Experimental Procedure and Data Reduction

A total of 105 experimental runs, including the subcooled liquid, mixed phase, and the superheated vapor conditions, were performed.

To bring the system to a steady-state condition, the tests were usually started with subcooled liquid runs and then the flow was gradually built up to a two-phase mixture allowing ample time between successive increases in the quality at the test section inlet. After the steady-state condition for the preset heat flux and inlet fluid temperature, pressure, and flow was reached, the data were recorded. These data provided measurements of the values of tube wall temperatures at the measurement locations, inlet and exit fluid pressures and temperatures, and the $\theta = 0$ deg surface radiative heat flux.

In order to calculate the internal heat transfer coefficients, temperatures and heat flux values on the interior surface of the tube were needed. In the two-dimensional heat conduction analysis performed (axial heat conduction was assumed negligible), a finite difference model of the tube wall thickness was utilized. Radiative and convective heat losses from tube surface (usually 7-12 percent of total incident radiation), as well as variable tube thermal conductivity were considered in the solution. The boundary conditions required for this analysis were the distribution of temperature and heat flux on the exterior surface of the tube.

Variation of the temperature on the outer tube surface was approximated by a function of the form

$$T(\theta) = a + b\cos\theta \tag{1}$$

where

$$a = (T_A + T_C)/2 \tag{2}$$

$$b = (T_A - T_C)/2 \tag{3}$$

The validity of the above function was tested throughout the experiment by calculating the tube wall temperature at $\theta =$ 90 deg and $\theta =$ 270 deg and comparing with the actual measured values for stations with four thermocouples. Later on as a check on the performance of thermocouples, at several

Nomenclature

A = flow area, m^2
BO = boiling number = $Q/(G \cdot h_{fg})$
CD = coil diameter, tube center to center, m
D = tube inside diameter, m
g = gravitational acceleration, m/s^2
G = mass velocity = $\dot{m}/A$, kg/m^2-s
h = internal heat transfer coefficient, W/m^2-°C
k = fluid thermal conductivity, W/m-°C
$\dot{m}$ = mass flow rate, kg/s
Nu = Nusselt number
o.d. = tube outside diameter, m
P = pressure, kPa
Pr = Prandtl number
q = internal heat flux, W/m^2
Q = incident heat flux, W/m^2
RA = radial acceleration
Re = Reynolds number
T = temperature, °C
ΔT = difference between wall and fluid temperature, °C
v = specific volume, m^3/kg
x = mass quality
X_{tt} = Lockhart-Martinelli parameter =

$$\left(\frac{\mu_f}{\mu_g}\right)^{0.1} \left(\frac{v_f}{v_g}\right)^{0.5} \left(\frac{1-x}{x}\right)^{0.9}$$

θ = angular position around the tube cross section (see Fig. 3), deg
μ = viscosity, kg/m-s
ρ = density, kg/m^3

Subscripts

A = position A ($\theta = 0$ deg) on the tube cross section
b = bulk
C = position C ($\theta = 180$ deg) on the tube cross section
c = critical
f = fluid
g = vapor
W = wall

Superscripts

$\overline{}$ = integrated average values around the circumference of the tube cross section

Table 1 Range of test variables (two-phase runs)

Mass velocity	412–1620 kg/m-s
Inlet pressure	4.14–36.2 bar
Inlet quality	(3.0–65.0) percent
Exit quality	(6.0–72.0) percent
Heat flux	19800–83800 W/m
Reynolds number	15000–117000
Radial acceleration	350–20000g

stations, one more thermocouple was attached to the tube surface at 45 deg angle from location A, and its output was compared with the predictions of the above function. The difference was never more than 10 percent and for the majority of cases it was below 5 percent.

For the distribution of incident heat flux over the exterior surface, two models, a cosine distribution and a uniform distribution of flux over the exposed half of the tube circumference, were examined. For both models the backside of the tube was assumed insulated. In order to decide which model simulates the actual condition more closely, several single-phase test runs were conducted. The actual amount of heat added to the liquid was compared with the theoretical calculations for the two flux distribution models. The uniform distribution model always gave better results (5–12 percent compared to 10–20 percent).

Output from the analysis included the heat flux $q_w(\theta)$ and wall temperature $T_w(\theta)$ at the inside surface of the tube. From these results and the local fluid conditions, as determined by an energy balance on the fluid, the distributions of internal heat transfer coefficients were then determined. In addition, at each thermocouple station, the integrated values of heat transfer coefficient and Nusselt number were calculated from equations of the form

$$\bar{h} = \frac{\bar{q}}{\overline{\Delta T}} \tag{4}$$

$$\overline{\mathrm{Nu}} = \frac{\bar{h}D}{k} \tag{5}$$

where

$$\overline{\Delta T} = (\overline{T}_w - T_b) \tag{6}$$

$$\overline{T}_w = \frac{1}{2\pi}\int_{\theta=0}^{2\pi} T_w(\theta)d\theta \tag{7}$$

$$q = \frac{1}{2\pi}\int_{\theta=0}^{2\pi} q_w(\theta)d\theta \tag{8}$$

In the above equations T_b represents the bulk fluid temperature. Note that for equilibrium two-phase flow, bulk temperature equals the saturation temperature for the local pressure in the tube. In that case the temperature difference used in calculating $\bar{h}$ would be

$$\overline{\Delta T} = (\overline{T}_w - T_{\mathrm{sat}})$$

In addition, other dimensionless groups such as Reynolds number and Prandtl number were also calculated at each thermocouple station. In the mixed-phase region, the necessary properties for the calculation of these quantities were taken as the saturated liquid values calculated at the local pressure at that axial location. Reynolds number was calculated based on total mass flux.

Results and Discussion

This section will present the results corresponding primarily to the circumferentially uniform heat flux on the FMDF receiver which occurs at or near solar noon.

The variables of the experiment (for two-phase runs), along with their operating ranges, are given in Table 1.

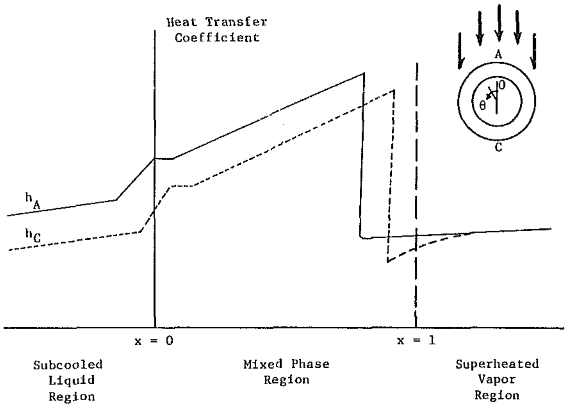

Fig. 4 Model representing the variations in the heat transfer coefficients at θ = 0 deg and θ = 180 deg

It will be helpful at this point to outline briefly the two-phase heat transfer characteristics of straight pipe flow as a basis of comparison with the results obtained in this study for a helical flow.

Collier [4] suggests that for a given heat flux, the forced-convective heat transfer coefficient in a uniformly heated straight pipe flow will experience a slight increase in the single-phase convective heat transfer region and a steeper increase in the subcooled nucleate boiling region, will remain constant in the saturated nucleate boiling region, and will increase linearly with increasing quality in the two-phase forced convective region. In this last region, the flow pattern will change to annular flow, in which the liquid will form a thin layer on the wall with the vapor occupying the core of the tube cross section and the process of nucleation will be replaced by evaporation of the liquid at the liquid–vapor interface.

At the dryout point, when the layer of liquid on the wall has completely evaporated, the heat transfer coefficient will suddenly decrease to a low value corresponding to the heat transfer to dry saturated vapor at the lcoal conditions. From then on as the vapor quality increases, h will also gradually increase to the value corresponding to heat transfer to a single-phase vapor. Flow through a symmetrically heated coiled tube is expected to follow the same pattern, although it has been shown [1] that as a result of the induced secondary flow in a coiled tube, dryout will occur at higher qualities than in a straight pipe flow with the same heat flux level.

For the case of a nonuniformly heated straight tube, heated over half of its exterior surface, one would expect an angular variation of heat transfer coefficient similar to the wall heat flux variation. Thus a location on the tube exposed to the higher heat flux A would be expected to have a higher heat transfer coefficient than the location which only receives energy as a result of circumferential, tube wall conduction C. This is shown characteristically in Fig. 4. As seen from this figure, in the subcooled region and part of the mixed phase region, h_A at any axial location is greater than h_C, until somewhere in the two-phase region at high quality h_A decreases sharply. (In this region, resistance to conduction in the tube wall is primarily larger than the convection resistance at the fluid–wall boundary. As a result the heat flux distribution will be the dominant factor in shaping the distribution of heat transfer coefficient around the inner wall of the tube.) Soon afterward at still higher qualities, h_C will experience this sudden drop. Later on, heat transfer at both locations will gradually recover until it finally levels off in the superheated vapor region. (In this last region, the convective resistance at the fluid–wall boundary is expected to be larger than the conduction resistance in the tube wall. As a result the heat flux at the inner surface of the tube will be approximately uniformly distributed.)

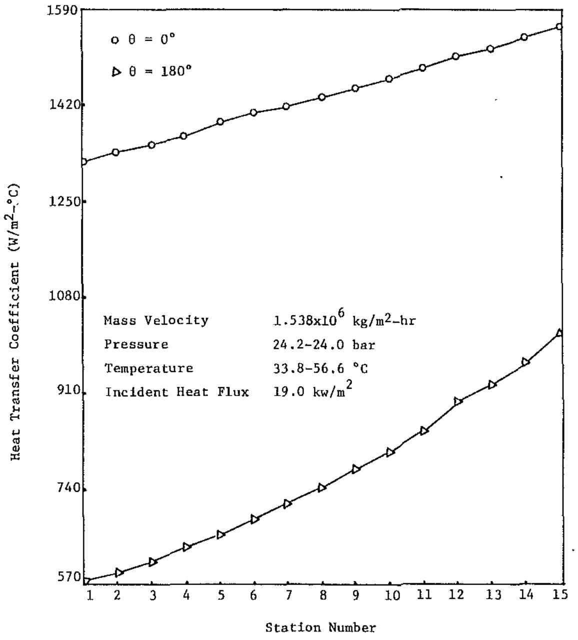

Fig. 5 Axial distribution of heat transfer coefficients at θ = 0 deg and θ = 180 deg, run 93

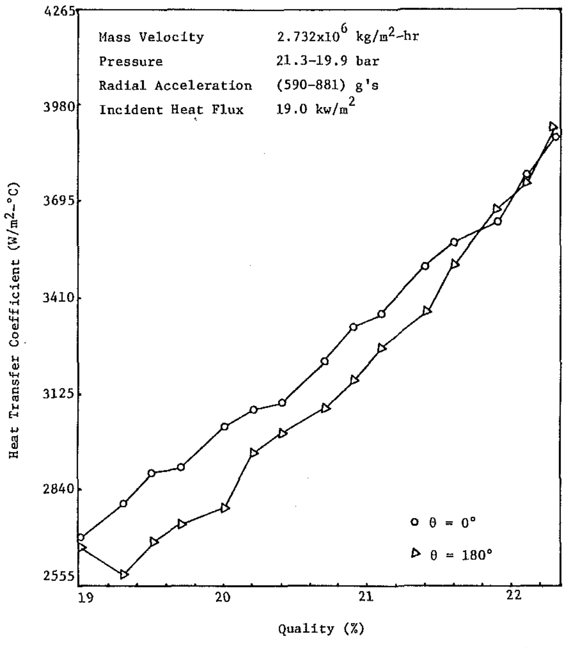

Fig. 6 Axial distribution of heat transfer coefficients at θ = 0 deg and θ = 180 deg, run 105

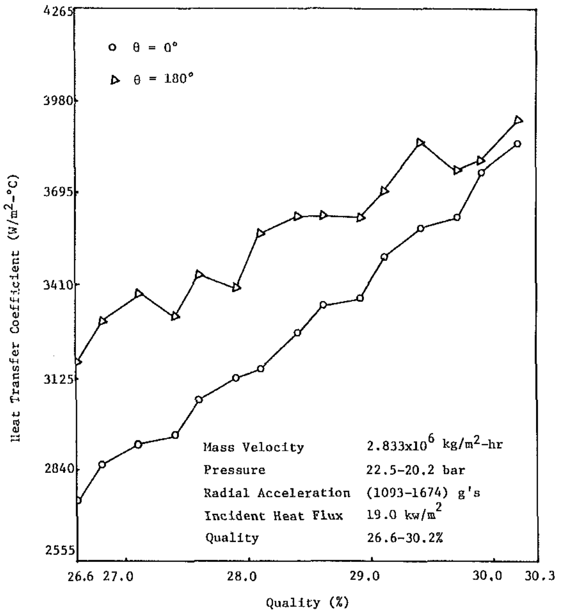

Fig. 7 Axial distribution of heat transfer coefficients at θ = 0 deg and θ = 180 deg, run 104

At this point if the effects of helical geometry (induced radial acceleration, secondary flow, etc.) are included, it is expected that the results of Fig. 4 would shift to the right, such that the transition to dryout at both locations A and C will occur at higher qualities. The magnitude of this shift, though not the same for lines representing h_A and h_C, will depend on the level of asymmetry of heat flux and the strength of the secondary flow in the tube cross section. Also the effect of the radial acceleration and secondary flow on the flow patterns and thermal behavior of the system is such that the orders of magnitude of h_A and h_C with respect to each other will not always follow the same pattern shown in Fig. 5 for flow in an asymmetrically heated straight tube. It is felt that depending on flow parameters such as radial acceleration, level of asymmetry of heat flux, and local pressure (affecting the difference between liquid and vapor densities), h_A may be larger than h_C at one location, while h_C may become larger than h_A at another location along the flow direction.

The results of the analysis predicting the heat transfer characteristics of the system under study are shown in Figs. 5-10. In these figures the variation of the local heat transfer coefficients at locations A and C (θ = 0 deg and θ = 180 deg) on the interior surface of the tube, along the tube axis, are shown.

Figure 5 presents the results for a sample single-phase run. As fluid temperature gradually increases and the fluid properties approach saturated liquid values, the heat transfer at both locations steadily increases, with $h_A > h_C$ throughout the regime.

In Fig. 6 the results for a low-quality run are shown. Close to the test section inlet $h_A > h_C$, continuing the trend from the subcooled liquid region, but as the radial acceleration gradually increases, h_C approaches h_A. Radial acceleration for this run ranges from 590 to 880g, representing a very weak secondary flow in the tube cross section as compared to higher qualities.

Figure 7 corresponds to run No. 104 for which radial acceleration ranges from 1093 to 1674g. As the radial acceleration increases, both the stronger secondary flow and increased gravitational force will remove the vapor bubbles from the outer tube wall (θ = 0 deg) probably as fast as they are formed. As a result of this process, h_A increases such that close to the end of the coil the Nusselt number variation around the circumference of the tube is represented by a straight line. At still higher qualities (outside the quality range of this run), h_A will assume values greater than h_C.

Figure 8 shows the results for run No. 102 for which radial acceleration increases from 2757 to 5119g and the quality ranges from 42.5 to 46.8 percent. Near the test section inlet, h_A is greater than h_C. The flow pattern in this region is probably an annular flow, with liquid forming a thin layer on the wall, possibly much thicker at location C (θ = 180 deg) than at A (θ = 0 deg), such that except for liquid droplets that are carried by the secondary flow from the core section of the tube to location A, heat transfer at this location is mainly to saturated vapor. Because of the higher heat fluxes at this location, the liquid droplets evaporate as soon as they reach this location. The result of this combined process of evaporation of the

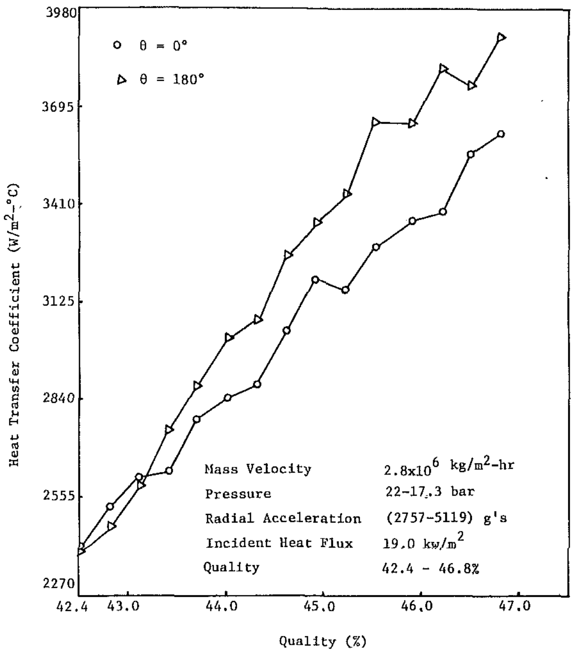

Fig. 8 Axial distribution of heat transfer coefficients at θ = 9 deg and θ = 180 deg, run 102

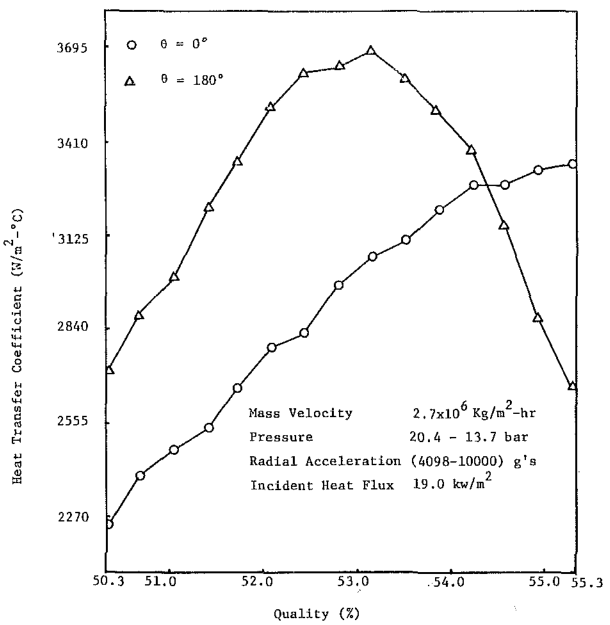

Fig. 10 Axial distribution of heat transfer coefficients at θ = 0 deg and θ = 180 deg, run 100

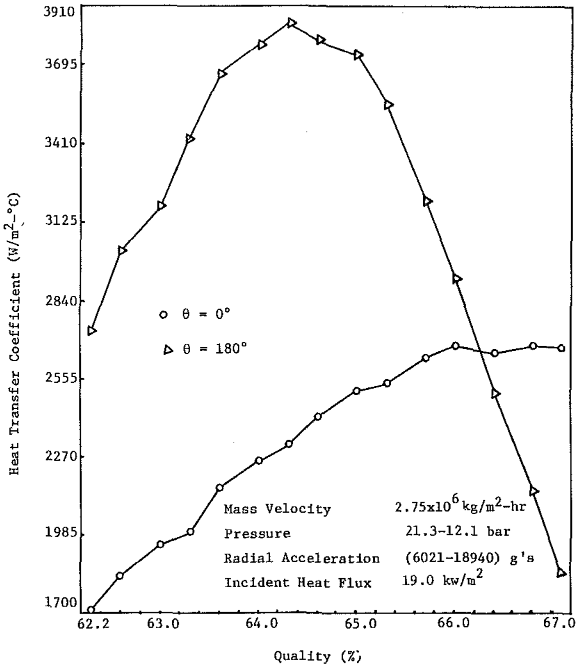

Fig. 9 Axial distribution of heat transfer coefficients at θ = 0 deg and θ = 180 deg, run 98

liquid droplets and heat transfer to saturated vapor is such that h_A is still increasing, but not as fast as h_C, where heat is transferred through evaporation at the liquid vapor interface. Soon after this, as the quality continues to increase, the transition to dryout at location C will take place, after which h_C will rapidly decrease.

Results for run No. 98, for which quality ranged from 62.3 to 67.1 percent, are shown in Fig. 9. Liquid in the flow is now mainly in the form of entrained droplets, and possibly a very thin layer at the θ = 180 deg location. The liquid particles are still carried to the θ = 0 deg location by the secondary flow, where they evaporate as soon as they come into contact with the wall. As a result of this process, h_A is still gradually increasing, with a magnitude possibly corresponding to heat transfer to saturated vapor at local conditions. At θ = 180 deg, h_C reached a maximum value at a quality around 64.5 percent, at which point it experienced a rapid drop, possibly because of the complete evaporation of the liquid film and transition to dryout at this location.

Comparing the results of the experiment with the model of Fig. 4, it is evident that the results generally follow the pattern suggested by this model, except that the order of magnitude of h_A and h_C in the low-quality section of the nucleate boiling region changed such that h_C became larger than h_A. In the midquality range with the aid of secondary flow, h_A assumed a higher value, but later on as the thickness of the liquid layer at A decreased, the heat transfer at this location was mainly to saturated vapor with frequent liquid droplets carried to this location by the secondary flow in the vapor core. Liquid droplets evaporate as soon as they reach this location. The effect of this process was such that the heat transfer coefficient at location A was still increasing, but not as fast as that at location C, where a layer of liquid still existed. As a result h_C gradually became greater than h_A. As mass quality increased, and the layer of liquid at C evaporated, the tube wall at this location experienced a sudden temperature increase (resulting in a sharp decrease in heat transfer coefficient at this location), while at θ = 0 deg incoming entrained liquid droplets in the vapor core kept h_A at moderate values to still higher values of quality. But as the quality increased further and the number of entrained liquid particles decreased, h_A also gradually decreased. As a result of this, the crossover between h_A and h_C, as the model shows, did not take place.

This behavior, as was mentioned earlier, is a function of flow parameters such as the strength of the secondary flow and radial acceleration as well as the pressure in the flow channel, and the same behavior cannot be expected from another system with different geometry or flow conditions.

The results presented here are mainly obtained at a low heat flux, in an effort to allow all of the regions of the flow to develop. As the heat flux increased, the region of rapid decrease in heat transfer coefficient shifted to a lower quality, resulting in an earlier transition to dryout. Very high incident heat fluxes may result in burnout even in the low-quality region of the flow. Under special circumstances of low radial acceleration and high radiation intensities, the flow may not be able to remove the local, low-quality vapor bubbles formed on the outer tube wall. As the heat transfer coefficient at this location decreases, the tube wall temperature will rise, causing a steeper decrease in the heat transfer coefficient. This coupled effect may finally result in burnout.

Increase in pressure and decrease in mass flow rate will have an effect similar to that of increasing the incident flux. This is partly because both increasing the pressure and decreasing the mass flow rate will reduce the radial acceleration. At relatively high pressures as ρ_g approaches ρ_f, the radial acceleration and consequently the secondary flow in the tube cross section will tend to lose their dominant effect on the flow in the coiled tube.

Figure 10 represents the results of the experiment for run 100. The behavior of the heat transfer coefficient at $\theta = 0$ deg and $\theta = 180$ deg is quite similar to run 98 (Fig. 10), except that the sudden drop in h at $\theta = 180$ deg occurs at a lower value of quality. For this run, the mass velocity was lower than that of run 98 while the exit pressure was slightly higher, both contributing to earlier transition to dryout at $\theta = 180$ deg location.

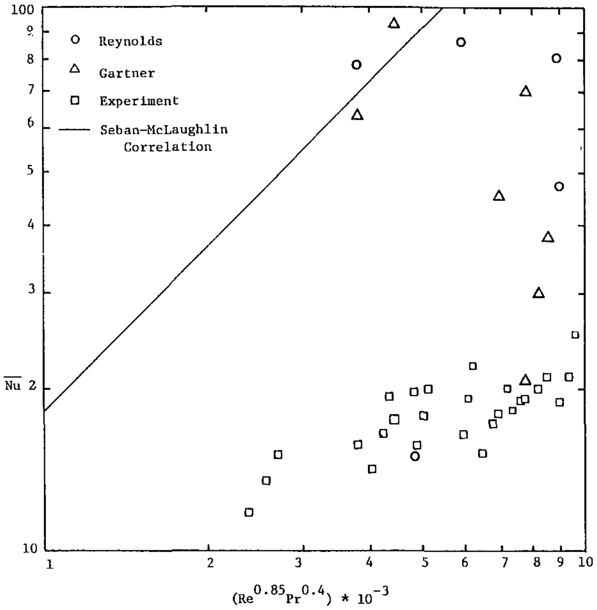

Fig. 11 Comparison between experimental data and Seban-McLaughlin [5], single-phase runs

Comparison of Results

In comparing the heat transfer results of the present analysis to the available analytical results and experimental data in literature, three important facts will become evident: (1) No experimental results for flow in coils with small diameters and tightly wrapped turns are available; (2) the available correlations for flow in coils were mainly derived for single-phase flow of liquids or gases in coils with diameters and coil pitches several times those of the test section used in this study; (3) all of these studies were done on uniformly heated coils.

It was then decided to compare these results to the available data for uniformly heated coils and also to the available analytical results for single-phase flow in asymmetrically heated straight pipes.

In Fig. 11 the experimental results for single-phase runs are plotted as Nu versus ($Re^{0.85}$ $Pr^{0.4}$). Shown in this figure is the line representing the Seban-Mclaughlin correlation [5] for turbulent flow of water in uniformly heated coils, and also the results predicted for single-phase flow of fluids in asymmetrically heated straight pipes [6, 7]. As is noted from this figure, the experimentally determined average Nusselt numbers for the tube cross section fall substantially below those predicted by Seban and Mclaughlin.

Although Reynolds numbers for all but three of the single-phase runs were higher than the critical Reynolds number $\{2*10^4(D/CD)^{0.32}\}$ [8], the experimental results were also compared to the equation given by Seban and McLaughlin [5] for laminar flow of single-phase fluids in coiled tubes. Figure 12 shows that there is an agreement between the measured and predicted results. The solid line shown in this figure was derived by Seban and Mclaughlin as a curve fit to their experimental data for flow of oil (Prandtl number from 100 to 650) in coil-to-tube diameter ratios of 17 and 104.

As for the comparison of the two-phase heat transfer results, data of Crain and Bell [9] and Bell and Owhadi [1] were used as representative of the available data in literature. In Fig. 13 which presents this comparison, the ratio of circumferentially averaged two-phase heat transfer coefficient h_{tp} to that predicted by Seban and Mclaughlin for single-phase flow h_1 is shown as a function of $1/X_{tt}$. The present experimental results have values much lower than those measured for uniformly heated coils, although the trend of the data follows the correlation of Owhadi.

As is noted from the comparison given above, the mean heat transfer coefficients measured in this study are normally below the existing data in the literature. Although the authors, at this point, are not positively certain as to the reason for this

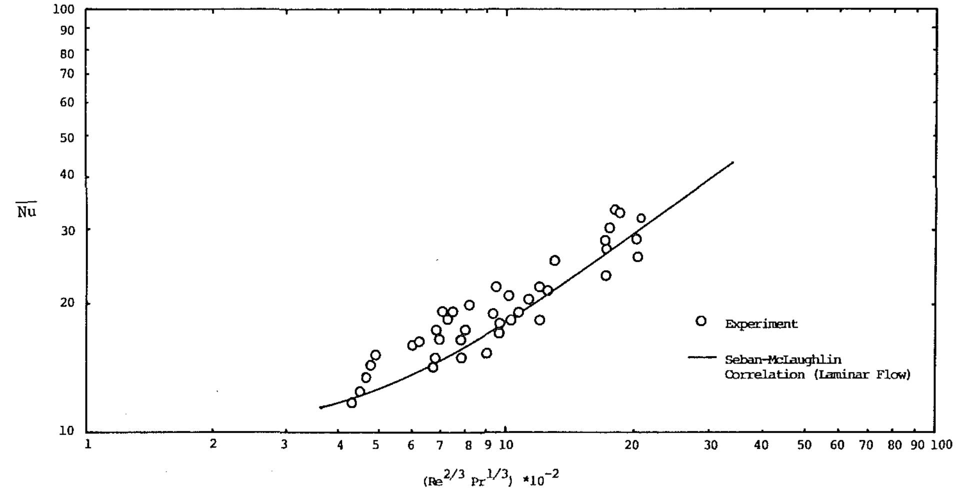

Fig. 12 Comparison between experimental data and Seban-McLaughlin equation for laminar flow

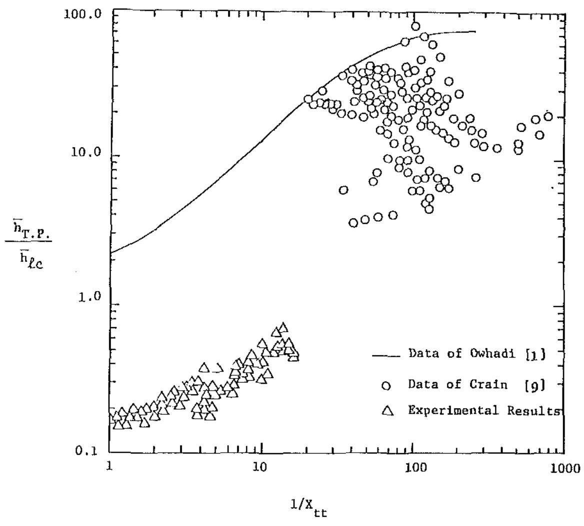

Fig. 13 Comparison of results with data of Owhadi and Crain

phenomenon, the following is offered as a possible explanation. It is hoped that the work in progress by the authors will answer some of these questions.

There are several equations that can be used to predict the transition from laminar to turbulent for flow of single-phase fluids in coils [10]. These equations were derived for coils with coil-to-tube diameter ratios and coil pitches several times larger than the test section used in the present study, and none truly considers the combined effect of coil pitch and diameter on transition Reynolds number. However it is a known fact that as the coil-to-tube diameter ratio and coil pitch decrease, the transition from laminar to turbulent flow in coil is delayed [11]. One could speculate that because of the small diameter and pitch of the coiled tube test section used in this study, for most of the experimental runs the flow was laminar and as a result the heat transfer coefficients correspond to those of laminar flow.

For the experimental results of the two-phase runs, other than what was mentioned above, the asymmetry of heat flux and also low levels of heat flux (as compared to other studies in literature) could be considered as contributing factors to low values of heat transfer coefficients. The effect of these factors can be summarized as follows.

(*a*) **Effect of Asymmetry of Heat Flux.** Figure 14 illustrates the effect of pressure and mass velocity on the flow pattern and the location of dryout in two-phase helical flow [12]. It has been shown that at high pressure (more than 160 atm for flow of water and steam in coiled tube), mass velocity will be the major factor defining the location of dryout and local flow pattern. At low mass velocity, the liquid will be flowing in the bottom of the tube due to the effect of gravity, while at higher mass velocities the liquid will move radially outward attaching to the wall of the tube farthest from the center of curvature.

At lower pressure, the secondary flow takes over. This effect is especially important in the annular flow regime, where the secondary flow in the vapor core causes a circulation in the liquid film. At moderate values of radial acceleration, liquid forms a continuous layer around the tube wall. The secondary flow in the vapor core causes liquid flow from the outer to the inner wall of the tube, constantly replenishing the losses due to evaporation and entrainment. At high qualities, when the continuous liquid film finally breaks, the remaining liquid will be concentrated at the stagnation points of the secondary flow (points closest to and farthest from the coil axis) [1].

The authors believe that as the radial acceleration increases further, the location of dryout on the tube circumference changes. Since the axial velocity of the vapor is much higher than that of the liquid film, it is subjected to a much greater radial accleration, and it tends to move toward the outside of the tube, forcing the liquid to accumulate on the inside surface of the coiled tube (closest to the center of curvature). As the mass quality increases, the thickness of the liquid layer, especially at the point on the tube cross section farthest from the coil axis, decreases, so that finally burnout occurs at that location. This phenomenon is shown in the bottom part of Fig. 14.

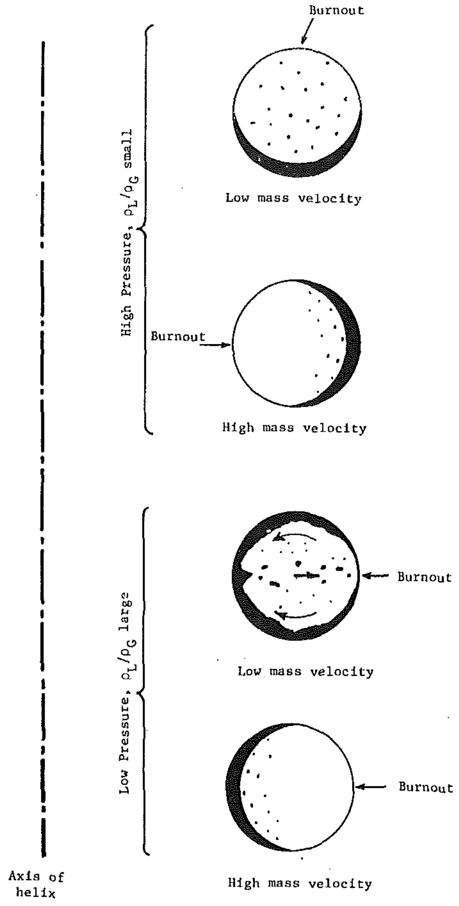

Fig. 14 Location of dryout for flow in helical coil

In this study, because of the very small coil diameter and relatively large mass velocity for most of the experimental runs, the magnitude of radial acceleration is very large compared to the available results in literature. Also for the conditions of this experiment, the location farthest from the coil axis corresponds to the point on the tube surface receiving the maximum heat flux. Although this heat flux for most of the test runs was not high enough to cause immediate burnout, heat transfer at this location is generally to superheated vapor, and low heat transfer coefficients will result. On the side of the tube closest to the coil axis, however, heat transfer is to a layer of liquid, but since the heat flux values at this location are low, heat transfer coefficients will also be small in magnitude. Thus the overall heat transfer coefficients will be lower than other experimental results at comparable Reynold numbers.

(*b*) **Effect of Low Levels of Heat Flux.** Heat flux values for these experiments, especially considering the fact that only half of the tube cross section is heated, are much lower than values used in most of the previous investigations found in literature. The effect of heat flux on boiling heat transfer coefficients has been noted by investigators such as Schrock and Grossman [13], and Crain and Bell [9], who report that there appears to be an effect of heat flux on the heat transfer coefficient, which indicates a decrease in measured heat transfer coefficients as heat flux is decreased.

(c) Effect of Using Bulk Temperature Versus Film Temperature. In calculating heat transfer coefficients in this study, bulk fluid temperature is used. This is the procedure used in most of the previous works on uniformly heated tubes reported in the literature. Under the condition of uniform heating, the assumption that fluid temperature is almost uniform throughout the tube cross section at a given axial location is probably very close to reality.

Reynolds [7] and Gartner [6], in their works on nonuniformly heated straight tubes, calculated and used a wall to fluid temperature difference which was a function of the angular position around the tube cross section.

In this experiment, it was assumed that the secondary flow existing in the tube cross section due to the geometry of the flow channel will result in mixing of the fluid and as such the fluid temperature at any angular position in the vicinity of the tube wall was assumed to be very close to the bulk fluid temperature calculated from the energy balance on the coil. If this assumption is not valid, and fluid temperaure close to the wall at some angular positions is substantially above the bulk fluid temperature, actual heat transfer coefficients will be severalfold larger than those presented here.

Conclusions

Local values of heat transfer coefficient and Nusselt number for single-phase or two-phase flow of water/steam in a coiled tube subjected to asymmetric radiant heating were calculated.

Measured heat transfer coefficients were found to be much lower than the values predicted by using the available correlations in literature (derived for the uniformly heated coils at the same Reynolds number). This apparently contradicts many earlier works which concluded that as the coil-to-tube diameter ratio decreases, heat transfer coefficients must increase. Possible reasons for existence of the apparently low heat transfer coefficients can be summarized as follows:

- flow regimes possibly in the laminar region due to stabilization of flow as a result of special flow geometry
- low heat flux values, considering the effect of asymmetry of heat flux distribution
- effect of large radial acceleration present, on forcing the liquid layer to flow on the inside surface of the coiled tube, where heat flux values are low
- possibility of having a convection-limited heat transfer process
- possible existence of nonisothermal conditions in the fluid at a given cross section

References

1 Bell, K. J., and Owhadi, A., "Local Heat Transfer Measurements During Forced Convection Boiling in a Helically Coiled Tube," *Proc. Instn. Mech. Engrs.*, Vol. 184, Part 3C, 1969-1970.

2 Shinn, K. E., "An Experimental Simulation of Asymmetric Radiant Heating for the FMDF Receiver," M.S. Thesis, Texas Tech University, Lubbock, TX, 1978.

3 Vafaie, F. N., "Forced Convection Heat Transfer to a Single and Two-Phase Steam/Water Mixture in a Helical Coil With Radiant Heating," Ph.D. Thesis, Texas Tech University, Lubbock, TX, 1981.

4 Collier, J. G., *Convective Boiling and Condensation*, McGraw-Hill, New York, 1972.

5 Seban, R. A., and Mclaughlin, E. F., "Heat Transfer in Tube Coils With Laminar and Turbulent Flows," *Int. J. Heat Mass Transfer*, Vol. 6, 1963, pp. 387-395.

6 Gartner, D., Johannsen, K., and Ramm, H., "Turbulent Heat Transfer in a Circular Tube With Circumferentially Varying Thermal Boundary Conditions," *Int. J. Heat Mass Transfer*, Vol. 17, 1974, pp. 1003-1018.

7 Reynolds, W. C., "Turbulent Heat Transfer in a Circular Tube With Variable Circumferential Heat Flux," *Int. J. Heat Mass Transfer*, Vol. 6, 1963, pp. 445-454.

8 Ito, H., "Friction Factor for Turbulent Flow in Curved Pipes," ASME *Journal of Basic Engineering*, Vol. 81, 1959, pp. 123-134.

9 Crain, B., Jr., and Bell, K. J., "Forced Convection Heat Transfer to a Two-Phase Mixture of Water and Steam in a Helical Coil," AIChE Symposium Series, Vol. 69, No. 131, 1973, pp. 30-36.

10 Srinivasan, P. S., Nandapurkar, S. S., and Holland, F. A., "Pressure Drop and Heat Transfer in Coils," *The Chemcial Engineer*, No. 218, 1968, pp. 113-119.

11 Mishra, P., and Gupta, N., "Momentum Transfer in Curved Pipes. 1-Newtonian Fluids," *Ind. Engr. Chem. Process Des. Dev.*, Vol. 18, No. 1, 1979, pp. 130-137.

12 Butterworth, D., and Hewitt, G. F., *Two-Phase Flow and Heat Transfer*, Oxford University Press, 1977.

13 Schrock, V. E., and Grossman, L. M., "Forced Convection Boiling in Tubes," *Nuclear Science and Engineering*, Vol. 12, 1962, pp. 474-491.

14 Mori, Y., and Nakayama, W., "Study on Forced Convection Heat Transfer in Curved Pipes, Second Report, Turbulent Region," *Int. J. Heat Mass Transfer*, Vol. 10, 1967, pp. 35-39.

G. De Jarlais
Mem. ASME

M. Ishii
Mem. ASME

Reactor Analysis and Safety Division,
Argonne National Laboratory,
Argonne, IL 60439

J. Linehan
Department of Mechanical Engineering,
Marquette University,
Milwaukee, WI 53233
Mem. ASME

Hydrodynamic Stability of Inverted Annular Flow in an Adiabatic Simulation

Inverted annular flow was simulated adiabatically with turbulent water jets, issuing downward from large aspect ratio nozzles, enclosed in gas annuli. Velocities, diameters, and gas species were varied, and core jet length, shape, breakup mode, and dispersed core droplet sizes were recorded at approximately 750 data points. Inverted annular flow destabilization led to inverted slug flow at low relative velocities, and to dispersed droplet flow at high relative velocities. For both of these transitions from inverted annular flow, core breakup length correlations were developed by extending work on free liquid jets to include this coaxial, jet disintegration phenomenon. The results show length dependence upon D_J, Re_J, We_J, α, *and* $We_{G,rel}$. *Correlations for core shape, breakup mechanisms, and dispersed core droplet size were also developed, by extending the results of free jet stability, roll wave entrainment, and churn turbulent droplet stability studies.*

I Introduction

Inverted annular flow is important in the areas of LWR accident analysis [1], cryogenic heat transfer [2], and other confined, low-quality film boiling applications. Yet, while many analytical and experimental studies of heat transfer in this regime have been performed, there is very little understanding of the basic hydrodynamics of inverted annular flow [3]. As a result, many film boiling applications are amenable to only limited analysis at present. One example of this can be seen in large-scale LWR safety codes such as TRAC and RELAP, which are essentially constrained by the not-well-understood two-phase thermohydraulics under various accident conditions, including those resulting in inverted annular flow.

Inverted annular flow may be visualized as a liquid jetlike core surrounded by a vapor annulus. The shape of the liquid/vapor interface, the stability of the liquid jet core, and the disintegration/entrainment of this liquid core must be understood, and predictive methods established, in order to clarify the modeling of this regime and the development of interfacial transfer correlations. In typical film boiling experiments, however, control and measurement of the flow parameters necessary for such an understanding is difficult, if not impossible, to achieve. As a result, our present knowledge of inverted annular flow hydrodynamics is limited to flow regime observations [4], void fraction measurements [5], and dispersed droplet size measurements [6]. Therefore, the principle objective of this study was to systematically investigate the effect of various flow parameters on jet core hydrodynamics, by means of an adiabatic simulation. Such a simulation, unlike actual film boiling experiments, allowed ready establishment of velocities, geometries, and fluid properties.

II Review of Jet Stability Literature

Adiabatic simulation of inverted annular flow hydrodynamics was achieved by establishing coaxial liquid core, gas annulus, jet flow conditions. In analyzing the results of this simulation, there are only a few previous studies of coaxial jet stability upon which to build. There are, however, many studies of free liquid jet stability, most of them concerning jets issuing into stagnant, low-density gas media. It is

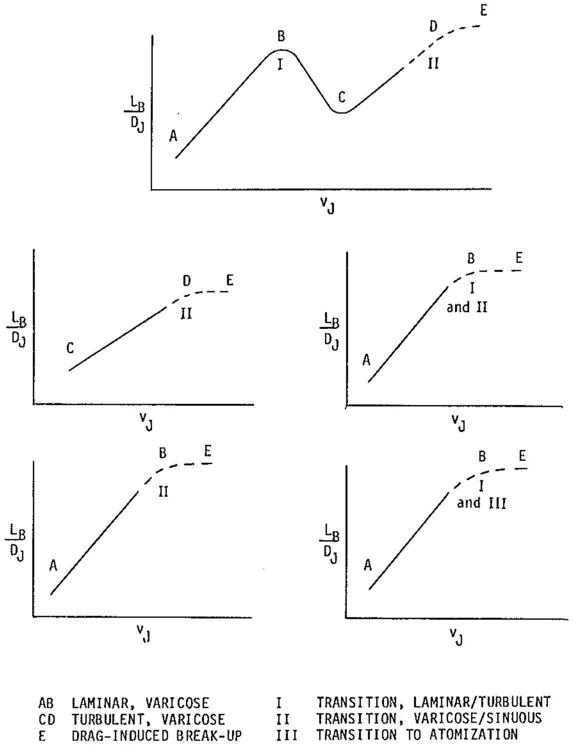

Fig. 1 Possible breakup behavior, free jets

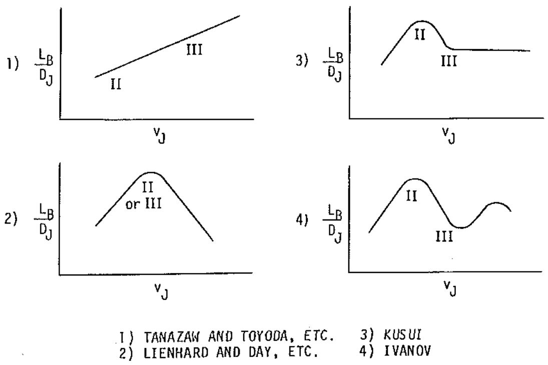

Fig. 2 Drag-induced breakup behavior, free jets

Contributed by the Heat Transfer Division and presented at the 21st National Heat Transfer Conference, Seattle, Washington, 1983. Manuscript received by the Heat Transfer Division November 7, 1983.

obvious that there are significant differences between free liquid jets and the coaxial liquid/gas jets of inverted annular flow. For coaxial jets, pressure and shear forces exerted by the gas annular jet, and the presence of solid boundary, may strongly influence the stability of the liquid core jet. Nevertheless, the existing studies on free jet breakup may give significant insight to inverted annular flow hydrodynamics.

Free Jet Stability. For free jets, jet character and breakup have often been represented on curves of jet length divided by jet diameter versus jet velocity (L_B/D_J versus v_J) as in Fig. 1 and Fig. 2. Three different breakup mechanisms have been identified, with distinctions also made between laminar and turbulent jets. In Fig. 1, the regions labeled *AB* and *CD* represent the varicose breakup of laminar and turbulent jets, respectively. This breakup is characterized by symmetric waves, resulting in alternating points of jet contraction and expansion. For laminar flow, both analytical and experimental studies have produced expressions for varicose breakup length [7, 8, 9], initial surface disturbances [7, 9], and maximum growth rate wavelength [7, 10, 11]. The transition from laminar to turbulent nozzle outflow (point I of Fig. 1) has been studied in detail [9, 12, 13, 14]. For turbulent, varicose breakup, experimental studies have produced expressions for breakup length [9, 14-18], initial surface disturbances [14, 17, 18], and maximum growth rate wavelength [16, 17]. For both laminar and turbulent varicose breakup, it was found that breakup behavior was independent of ambient density [19].

Ambient properties do, however, become important in the region labeled *E* in Figs. 1 and 2, where jet breakup is due to interfacial drag. Point II in these figures represents the transition from varicose to drag-induced breakup, which has been studied both analytically and experimentally [7, 15, 19, 20], and appears to occur at lower relative velocities for turbulent jets than for laminar jets. At low relative velocities, drag-induced breakup is characterized by asymmetric waves, resulting in sinuous jet deformation, while at high relative velocities atomization occurs. Confusion between the laminar/turbulent transition for varicose breakup and the varicose/drag-induced breakup transition is quite possible, since both may result in decreasing breakup lengths and asymmetric jet deformation (growth of macroscale eddies in the case of turbulent, varicose breakup), and since the onset of turbulence may lead to drag-induced breakup. The transition from sinuous breakup to atomization (point III in Figs. 1 and 2) has also been studied in some detail [16, 20, 21]. Region *E* has been drawn as a dotted line in Fig. 1, since even general trends in breakup length for drag-induced breakup are disputed. The calculations of Levich [22] and the experiments of Tanazawa and Toyoda (as cited in [23]) indicate L_B monotonically increases with increasing v_J values, while several experiments have shown L_B to decrease monotonically with increasing v_J [19, 21, 24]. Finally, Kusui [25] found that L_B first decreases, then reaches a constant value with increasing v_J, while Ivanov [26] suggested that L_B may first decrease, then increase, and finally decrease once again as v_J is increased. These widely divergent results, depicted in Fig. 2, may be due to different jet length definitions, since atomization creates a complicated flow pattern, or due to different breakup length measurement techniques (visual/photographic observation versus conductance probe measurements). Dimensional, empirical expressions have been formulated for dispersed droplet sizes resulting from jet atomization [21, 27].

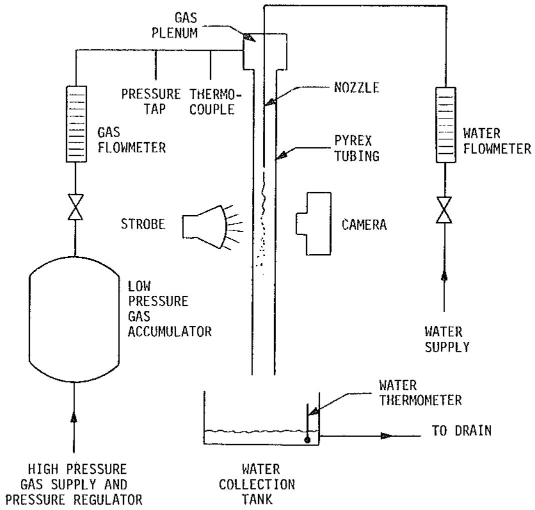

Fig. 3 Schematic diagram of test apparatus

Nomenclature

d = droplet diameter

$d_{\max}$ = average maximum droplet diameter

D_J = free jet, or core jet, diameter

D_o = outer diameter of gas annulus

g = gravitational acceleration

j_G = gas volumetric flux (superficial velocity)

j_J = liquid jet volumetric flux (superficial velocity)

K = constants, used in equations (4), (5), (8), (10)

L_B = jet breakup length

m = constants, used in equations (4), (5), (6), (7), (8), (10)

$N_{\mu F}$ = liquid viscosity number, defined by equation (19)

$N_{\mu G}$ = gas viscosity number, defined by equation (30)

$N_{\mu J}$ = liquid jet viscosity number = $\mathrm{We}_J/\mathrm{Re}_J$

$\mathrm{Re}_{G,\mathrm{rel}}$ = gas Reynolds number = $\rho_G v_{\mathrm{rel}} D_H/\mu_G$

Re_J = liquid jet Reynolds number = $\rho_J v_J D_J/\mu_J$

v_J = liquid jet velocity

v_{rel} = relative velocity $= |v_G - v_J|$

We_d = droplet Weber number defined by equation (25)

We_G = gas Weber number, free jet = $\rho_G v_J^2 D_J/\sigma$

$\mathrm{We}_{G,\mathrm{rel}}$ = gas Weber number = $\rho_G v_{\mathrm{rel}}^2 D_J/\sigma$

We_J = liquid jet Weber number $= \rho_J v_J^2 D_J/\sigma$

$\mathrm{We}_{J,\mathrm{rel}}$ = liquid jet Weber number $= \rho_J v_{\mathrm{rel}}^2 D_J/\sigma$

X = parameters defined by equations (6), (7)

α = void fraction

δ = initial disturbance

$\Delta\rho$ = density difference = $\rho_J - \rho_G$ or $\rho_F - \rho_G$

λ = wavelength of maximum growth rate

μ_F = liquid viscosity

μ_G = gas viscosity

μ_J = liquid jet viscosity

ρ_F = liquid density

ρ_G = gas density

ρ_J = liquid jet density

σ = surface tension

Subscripts

I = transition from laminar to turbulent flow

II = transition from varicose to sinuous, drag-induced breakup

III = transition to atomization or roll wave entrainment breakup

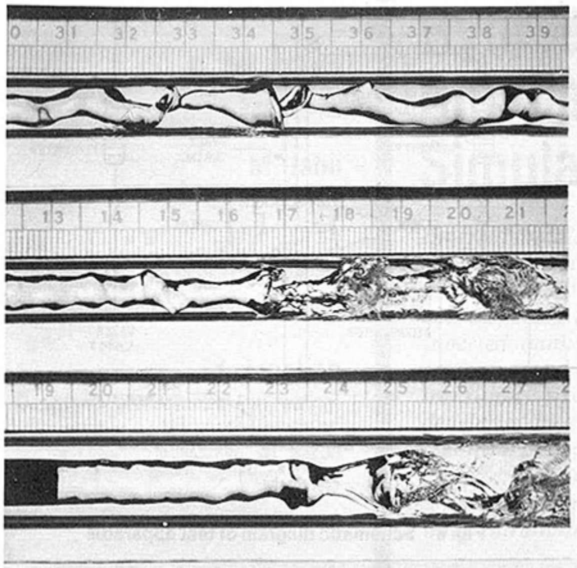

TOP : SINUOUS, DRAG-INDUCED BREAK-UP
MIDDLE: ROLL WAVES FORMING ON SINUOUS WAVE CRESTS
BOTTOM: ROLL WAVE ENTRAINMENT BREAK-UP, FORMATION OF ROUGH-WAVY ANNULAR FLOW OBSCURES VIEW

Fig. 4 Typical photographs

Coaxial Jet Stability. Unlike free, liquid jets, very little is known about confined, coaxial liquid and gas jets. Using numerical methods, Jensen [28] generated curves of wavelength and jet length for a confined water/steam system. However, his analysis was limited to plane, rather than cylindrical, jets, in laminar, varicose breakup only. His results for wavelength show a range of approximately

$$D_J < \lambda < 15 D_J \tag{1}$$

with λ decreasing with increasing values of $\mathrm{We}_{J,\mathrm{rel}}$, and increasing with increasing void fraction. His results for jet length are extended out to v_{rel} values of up to 12 m/s, which, in light of free jet literature and the experiments reported on later in this paper, would indicate actual conditions far removed from varicose breakup, especially at the larger gas densities of his calculations. However, the general trends from Jensen's curves are interesting, showing the effect of Kelvin-Helmholtz instability on accelerating varicose breakup of jets when in confined geometries. In rough approximation, these curves show that

$$L_B/D_J \sim (\rho_G/\rho_J)^{-1.3}(\alpha)^{1.3}(v_J)(\mathrm{We}_{J,\mathrm{rel}})^{-1.4} \tag{2}$$

Working with liquid jet gas pumps, in which a high-velocity jet entrains a flow of gas, Cunningham and Dopkin [29] found that maximum efficiency was obtained when mixing throat length equaled the breakup length of the atomized jet. Their empirical expression for jet length

$$L_B/D_J = 7.86 \times 10^6 \left(\frac{\alpha}{1-\alpha}\right)\left(\frac{v_G}{v_J}\right)\mathrm{Re}_J^{-1} \tag{3}$$

and their observation that increasing gas density decreases jet length are useful. However, for a liquid jet gas pump, v_G is not an independent variable. Rather, v_G is a function of geometry and jet breakup characteristics. This prevents equation (3) from being applied directly to other coaxial jet situations, such as inverted annular flow film boiling.

III Inverted Annular Flow Experiment

This experiment was designed to simulate the hydrodynamic behavior of inverted annular flow in an adiabatic test section, using turbulent water jets enclosed in coaxial gas annular jets. See Fig. 3 for a schematic diagram of the test system. The water jets issued from large aspect ratio nozzles made of thin-walled stainless steel tubing. To simulate inverted annular flow conditions, these nozzles were coaxially centered within Pyrex tubing, and gas was introduced through the gap between the stainless steel and the Pyrex. Parameters varied in the experiment included jet velocity, jet diameter, gas velocity, gas annulus outer diameter, and gas species. The series of tests performed are summarized in the following table (D_J and α are at nozzle exit):

Test series	D_J (cm)	Nozzle length (cm)	D_o (cm)	α	Gas species
*A*7	0.425	41.	1.66	0.934	N_2
*B*2	0.763	46.	1.36	0.685	N_2, He, R-12
*B*3	0.902	67.	1.36	0.560	N_2, He, R-12
*C*1	0.604	37.	0.90	0.549	N_2
*C*2	0.763	46.	0.90	0.281	N_2

All tests were performed near atmospheric pressure, with flow directed downward. Upward flow was attempted, but the use of low-velocity jets, coupled with easy wetting of the outer wall (which would not occur in true film boiling inverted annular flow) made this impossible. Even with downward-directed flow, wall wetting by entrained droplets at high gas velocities made data acquisition difficult. A detailed description of the test apparatus and procedures may be found in [30].

Jet core breakup lengths were observed visually, with the aid of a strobe light with a 3 μs, 0.5 w-s light pulse. Breakup length was observed to be quite variable, so that a minimum of 100-200 length observations was made to determine an average breakup length at each set of flow conditions. This variability in breakup length is similar to that observed for free jets [11, 15, 17]. For example, Chen and Davis [17] found that 150 separate length measurements were required to establish L_B with a 5 percent probability level and a tolerance of $3D_J$. For high gas velocities, a small number of photographs was sometimes used to verify the lengths determined visually, as jet surface roll waves, small droplets, and wall wetting made viewing more difficult. Jet length under these conditions was defined as the point at which the disintegrating jet was continuously wetting the wall, or, when observed, as the point at which the entire core had been deformed into giant, sheetlike segments developing from large-amplitude roll waves. This latter type of breakup developed very suddenly, over a very short distance compared to the entire jet core length. Breakup mechanisms could, for some flow conditions, also be determined visually. However, for transitional regions, where competing breakup mechanisms were present, visual determination of such mechanisms was difficult.

Photographic observations were accomplished using a Graphlex 4×5 camera, ASA 3000 film, and the 3 μs strobe flash for lighting. Aside from verifying breakup lengths, photographs were taken to establish the dominant breakup mechanisms for flow conditions where this could not be done visually. For all other flow conditions, one or more photographs were taken at every second or third gas velocity value, as v_G was monotonically increased or decreased at a given v_J value. From these photographs, the maximum growth rate wavelength, and maximum dispersed droplet size (for roll wave entrainment) were measured whenever possible. For the short (3 μs) exposure times of these photographs, resolution of small, high-velocity droplets was possible. Typical photographs are shown in Fig. 4.

For the large diameter, large aspect ratio nozzles of this

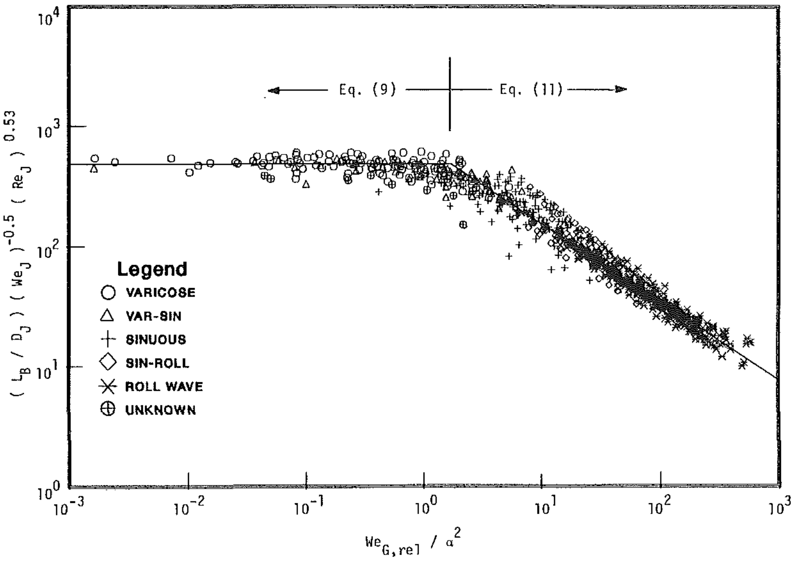

Fig. 5 Breakup length correlation

experiment, velocities low enough to establish laminar nozzle outflow would have resulted in severe jet acceleration and thinning due to gravity, with an attendant sharp increase in the gas flow area at the liquid nozzle exit. Even at the higher liquid velocities used, gravity acceleration became significant downstream, for some of the longer varicose and sinuous jets. To account for gravity acceleration effects, velocities and geometries were sometimes calculated for points downstream of the nozzle exit. Such velocity and geometry corrections are noted in the following section on data analysis.

Velocity and geometry corrections for acceleration due to interfacial shear were not included in the data analysis. For varicose and sinuous breakup, relative velocities were moderate, and the interface was relatively smooth (for turbulent jets, rapid dissipation resulted in only a few, large macroscale eddies downstream of the nozzle exit), so that acceleration due to shear was estimated to be at least an order of magnitude less than gravitational acceleration. At higher velocities, breakup lengths (and times) decreased drastically as roll waves appeared, so that even shear stresses comparable to those of rough-wavy annular flow [31], while causing acceleration of the same order of magnitude as gravity, would not have time to accelerate the jet core significantly. In addition, jet core diameter and surface smoothness under these high-velocity flows were observed to remain relatively constant until very near the breakup point, when large-amplitude deformations occurred rapidly.

IV Analysis of Results

In this section, the results of the experimental investigation are analyzed. Previous results from studies on jet stability, annular flow roll wave entrainment, and churn turbulent flow droplet stability were incorporated in the development of correlations of the experimental data. The analysis includes jet core breakup length, core breakup mechanisms, interfacial surface characteristics, and dispersed core droplet size data. A complete listing of all the data may be found in [30].

Jet Core Breakup Length. To correlate jet breakup length, the data were divided into two regions, one in which gas flow conditions had no influence, and a second in which gas flow did have an influence. In this first region, the ability of the various correlations for turbulent free jets in varicose breakup [9, 14–18] to correctly correlate the experimental jet length data was tested, using linear regression techniques. These free jet breakup correlations can be generalized into two basic forms

$$L_B/D_J = K_1 \cdot [\mathrm{We}_J]^{m_1} \tag{4}$$

and

$$L_B/D_J = K_2[\mathrm{Re}_J]^{m_2}\sqrt{\mathrm{We}_J} \tag{5}$$

For this linear regression analysis, jet diameter and Weber number were adjusted to represent values at 1/2 the breakup time, assuming only gravitational acceleration, to represent average values during time of flight. This adjustment was not large for most of the data, especially for shorter breakup lengths, and was made even less important by the form of equations (4) and (5) in which the term

$$D_J \cdot [v_J^2 D_J]^m = X_1 \tag{6}$$

appears. If gravitational acceleration adjustments were also made for the value of Re_J, the term from equation (5)

$$D_J \cdot [v_J D_J]^{m_2} [v_J^2 D_J]^{1/2} = X_2 \tag{7}$$

would also be of interest. Viewing equations (6) and (7) in light of the continuity equation, it becomes apparent that the value of X_1, relevant if D_J and We_J are adjusted for jet acceleration effects, is only a weak function of such adjustments, especially at m values approaching 1/3. In addition, if D_J, We_J, and Re_J values are adjusted for acceleration effects, it is apparent that the value of X_2 is also only a weak function of such adjustments, especially at m_2 values near $-1/2$.

However, the jet Reynolds number was not adjusted to account for acceleration of the jet after leaving the nozzle, since free jet correlations for L_B [16] and initial surface disturbance [14, 18, 19] would indicate that

$$\ln\,(D_J/2\delta) = K_2[\mathrm{Re}_J]^{m_2} \tag{8}$$

and δ, the initial jet surface disturbance, should be a function of conditions at the nozzle exit, rather than at some downstream point.

For this region, displaying no breakup length dependence upon void fraction, gas velocity or gas density, 85 data points were available for analysis. Using linear regression techniques, and the correlation forms given by equations (5) and (6), a best fit of the data was obtained with the following correlation

$$L_B/D_J = 480[\mathrm{Re}_J]^{-0.53}\sqrt{\mathrm{We}_J} \tag{9}$$

For this correlation, the correlation coefficient was 0.89 and the standard deviation (of log-log values) was 0.066. Equation (9) is in general agreement with Miesse's result [16], although for a substantially different nozzle design (long tubes versus industrial orifices).

For the region in which gas flow conditions affected L_B, initial analysis determined that L_B was strongly dependent upon the value of $(\rho_G v_{\rm rel}^2/\alpha^2)$. This is easily understood, since interfacial drag and pressure reduction over wave crests (Bernoulli effect) should be functions of $\rho_G\, v_{\rm rel}^2$. Furthermore, for confined geometries, gas acceleration over wave crests is at least roughly proportional to $1/\alpha$ (for small α and moderate wave amplitude). The appearance of We_G in free jet correlations [15, 16, 19] and the results of Jensen's [28] calculations, equation (2), represent similar relationships.

For this second jet core breakup length region, where dependence upon void fraction, gas velocity, and gas density was well established, 533 data points were available for analysis. In light of the discussion in the previous paragraph, a correlation of the data for this region was formulated by modifying equation (9)

$$L_B/D_J = K_2 \cdot [\mathrm{Re}_J]^{-0.53}\sqrt{\mathrm{We}_J}[\mathrm{We}_{G,\rm rel}/\alpha^2]^{m_3} \quad (10)$$

Using linear regression techniques, the 533 data points, and the correlation form given by equation (10), the following correlation was developed

$$L_B/D_J = 685 \cdot [\mathrm{Re}_J]^{-0.53}\sqrt{\mathrm{We}_J} \cdot [\mathrm{We}_{G,\rm rel}/\alpha^2]^{-0.645} \quad (11)$$

For this correlation, the correlation coefficient was 0.967 and the standard deviation (of log-log values) was 0.094. As in the previous breakup length correlation, all flow parameters except Re_J were adjusted to represent those at 1/2 the breakup time, assuming only gravity acceleration of the jet core.

The two curves defined by equations (9) and (11) intersect at a value of

$$[\mathrm{We}_{G,\rm rel}/\alpha^2] = 1.73 \quad (12)$$

and this can be used as the criterion for determining regions of applicability for the two equations.

Jet breakup length data are presented in Fig. 5, plotted against the correlations given by equations (9) and (11). A total of 741 jet breakup length observations were made, with 113 data points in the transitional region near $[\mathrm{We}_{G,\rm rel}/\alpha^2] = 1.73$. Some of the data scatter shown by this figure may be due to the difficulties previously mentioned in defining jet length consistently in light of wall wetting and widely different void fractions.

It should be noted that equation (11), applied to free jets, would indicate L_B/D_J is proportional to $v_J^{-0.82}$, a result very similar to that presented by Lienhard and Day [24]. Also, equation (11) shows trends similar to those calculated by Jensen [28], especially the dependence upon void fraction.

From the free jet literature, it may be conjectured that, for laminar, confined, coaxial jets, equations (9) and (11) might be replaced by

$$L_B/D_J = 12[1 + 3N_{\mu J}]\sqrt{\mathrm{We}_J} \quad (13)$$

for the region with no dependence upon gas flow parameters [7] and by

$$L_B/D_J = 35[1 + 3N_{\mu J}]\sqrt{\mathrm{We}_J} \cdot [\mathrm{We}_{G,\rm rel}/\alpha^2]^{-0.645} \quad (14)$$

for the region of drag-induced breakup [19], with a transition at

$$[\mathrm{We}_{G,\rm rel}/\alpha^2]_{\rm II} = 5.3 \quad (15)$$

assuming that the L_B dependence upon $[\mathrm{We}_{G,\rm rel}/\alpha^2]$ is the same for both laminar and turbulent jets.

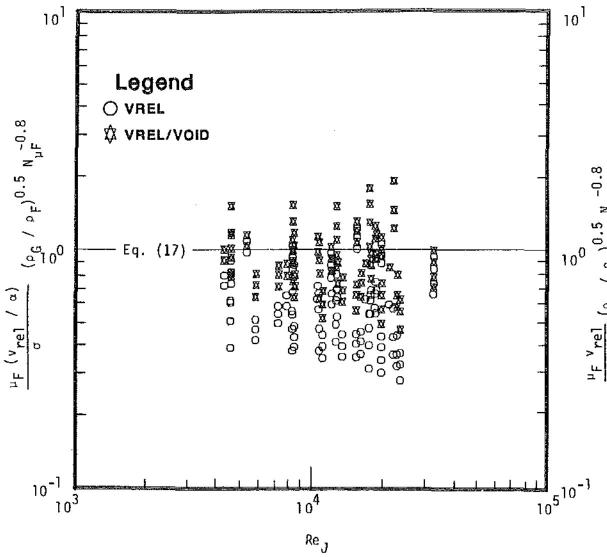

Fig. 6 Roll-wave entrainment inception correlation

Jet Core Breakup Mechanisms. As in free jets, three regimes, or breakup mechanisms, were observed for these confined coaxial jets. The first two mechanisms, varicose and sinuous breakup, proved to be similar to those noted for free jets. The transition from varicose to sinuous behavior was, however, difficult to define from observations of jet shape, due to distortions of the jet core imposed by the growth of macroscale turbulent eddies. This resulted in many data points being classified as varicose-sinuous or regime-unknown. To help resolve this difficulty, the transition point was defined as the region on the jet length curve (Fig. 5) where interfacial drag first becomes important, in effect using the same criterion as Fenn and Middleman [19]. From the two jet length correlations developed, equations (9) and (11), the transition criterion is then defined as

$$[\mathrm{We}_{G,\rm rel}/\alpha^2]_{\rm II} = 1.73 \quad (16)$$

for these turbulent, coaxial jets. This is comparable to Iciek's [15] value of $\mathrm{We}_{G,\rm II} = 1.2$ for turbulent jets, and substantially lower than Fenn and Middleman's value of $\mathrm{We}_{G,\rm II} = 5.3$ for laminar jets. To appreciate the magnitude of the relative velocities at this varicose/sinuous transition, equation (16) would indicate that $v_{\rm rel,II} \doteq 2.4$ m/s for typical $C1$ test series conditions.

The third mechanism of jet breakup observed in these experiment is that of roll wave entrainment. Roll waves first appeared on the crests of sinuous waves, while at higher relative velocities roll waves caused jet breakup before the core exhibited any sinuous behavior. A single roll wave often developed over a substantial portion of the jet circumference, deforming into a thin, skirtlike sheet. Ligaments or individual droplets could be seen being sheared from the roll-wave crests (see Fig. 4). Except at the highest of void fractions, it was not possible to view the entire dispersal of the liquid jet core, due to wall wetting.

To analyze the data on the inception of roll-wave entrainment for this experiment, use was made of roll-wave entrainment studies in annular flow. Assuming that entrainment begins when the drag force due to high shear gas flow acting on wave crests exceeds the retaining force due to surface tension, Ishii and Grolmes [32] developed entrainment inception criteria for various regimes within annular flow. For rough turbulent flow, in which the liquid friction factor is assumed to be independent of liquid Reynolds number, their entrainment inception criteria are

$$\frac{\mu_F j_G}{\sigma}\sqrt{\frac{\rho_G}{\rho_F}} \geqq N_{\mu F}^{0.8}, \text{ for } N_{\mu F} < 1/15 \quad (17)$$

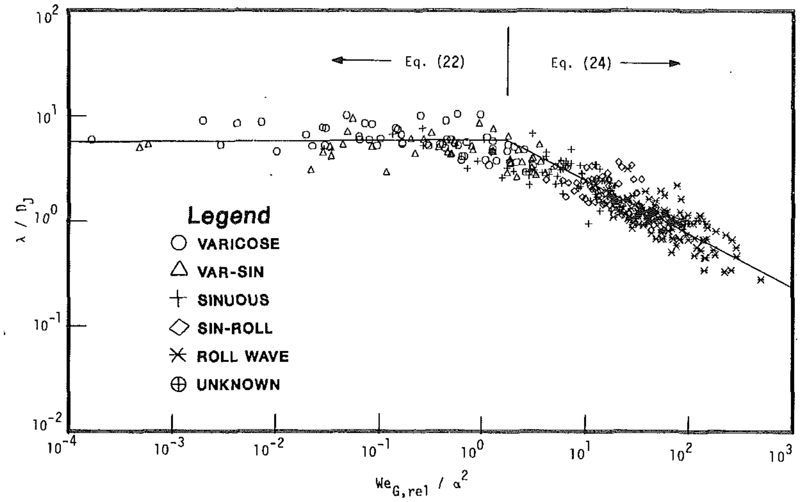

Fig. 7 Jet core surface wavelength correlation

$$\frac{\mu_F j_G}{\sigma}\sqrt{\frac{\rho_G}{\rho_F}} \geqq 0.1146, \text{ for } N_{\mu F}>1/15 \tag{18}$$

where the viscosity number $N_{\mu F}$ is based upon the Taylor instability wavelength, and is defined as

$$N_{\mu F}=\frac{\mu_F}{(\rho_F \sigma \sqrt{\sigma/g\Delta\rho})^{1/2}} \tag{19}$$

To compare the present data with these criteria, the term j_G was replaced with v_{rel}, or with v_{rel}/α (see Fig. 6). Experimental scatter is significant, since for each test run there was a range of gas velocities over which sinuous and roll-wave breakup were competing, making it impossible to define a single point as the start of roll-wave jet breakup. From the discussion of jet breakup length correlations, one might assume that v_{rel}/α would be the correct term to use in place of j_G. Values of α and v_{rel} were corrected to represent those at 1/2 the breakup time (assuming only gravitational acceleration) while the initial Re_J values were used for Fig. 6.

Figure 6 shows the comparison of equation (17) to the experimental data of the onset of entrainment. There are two different symbols in the figure, i.e., one based on the relative velocity v_{rel}, used in the place of j_g in equation (7), and other based on v_r/α in place of j_g. Although the general physical trend can be explained in terms of the order of magnitude by either correlation, the use of v_{rel}/α appears to work better. This is expected, because for the breakup length correlation the correct velocity scale in Weber number was found to be v_{rel}/α for the inverted annular flow, see equation (10). From these comparisons, it can be concluded that the entrainment mechanism should be based on the roll-wave entrainment and that the onset of entrainment can be predicted from a standard correlation for usual film flow with small modification for the reference relative velocity.

For comparison with free jet literature, where atomization has not been established as being due to roll-wave entrainment, one can insert "typical" fluid property values into equations (17) and (18). For a turbulent water jet issuing into air

$$v_{J,\mathrm{III}} \doteq 16 \text{ m/s} \tag{20}$$

Using this $v_{J,\mathrm{III}}$ value to calculate a typical $\mathrm{We}_{G,\mathrm{III}}$ value, for a 0.2-cm-dia jet such as Miesse [16] used for much of his data, would result in an atomization criterion of

$$\mathrm{We}_{G,\mathrm{III}}=7.7 \tag{21}$$

which is comparable to Miesse's value of 6.35.

Jet Core Surface Characteristics. Surface conditions were observed for varicose, sinuous, and roll wave breakup conditions, with wavelength/jet diameter plotted against $\mathrm{We}_{G,\mathrm{rel}}/\alpha^2$ in Fig. 7. All values were corrected to represent conditions at the point of observation, assuming only gravitational acceleration, since local flow parameters should be more appropriate in correlating locally observed wavelength values.

The various symbols in the figure indicate that the flow regime transition has occurred in the order of the varicose, sinuous, and roll-wave instabilities as the $\mathrm{We}_{G,\mathrm{rel}}/\alpha^2$ has increased. By taking into account the uncertainties associated with the visual identifications, it can be seen that the first transition between the varicose and sinuous is well predicted by equation (12). Furthermore, Fig. 7 shows that the average breakup length may be correlated by two correlations as discussed below. This also implies that in terms of the breakup mechanisms the sinuous and roll-wave instabilities are closely related.

For varicose breakup there is considerable variation in the data. The 85 data points in the varicose breakup region have an average wavelength of

$$\lambda=5.8 D_J \tag{22}$$

with a standard deviation of 1.8 D_J. This maximum growth rate wavelength is comparable to Rayleigh's expression [10]

$$\lambda=4.51 D_J \tag{23}$$

along with those of other researchers [7, 11, 16, 17].

In the drag-induced breakup region, wavelength steadily decreases to less than one jet diameter, with increasing values of $[\mathrm{We}_{G,\mathrm{rel}}/\alpha^2]$. Using a least-squares method, assuming λ/D_J is a function solely of $[\mathrm{We}_{G,\mathrm{rel}}/\alpha^2]$, and forcing the λ expression to have a value of 5.8 D_J at $[\mathrm{We}_{G,\mathrm{rel}}/\alpha^2]=1.73$, the following expression was obtained for the maximum growth rate wavelength, in the drag-induced breakup region.

$$\lambda=7.6[\mathrm{We}_{G,\mathrm{rel}}/\alpha^2]^{-0.5} \cdot D_J \tag{24}$$

This correlation was developed using the 252 data points with $[\mathrm{We}_{G,\mathrm{rel}}/\alpha^2]$ values greater than 3.0, to avoid λ values near the varicose/sinuous breakup transition point. The log-log standard deviation for the data, using equation (24), is 0.128.

The following generalizations can be made regarding the shapes of the surface waves observed. For low void fractions, roll waves were limited in amplitude by the proximity of the Pyrex wall. At higher void fractions, however, roll waves were able to grow to large dimensions, sometimes deforming the jet into sheets and ligaments with no discernible cylindrical core. This large deformation normally occurred within the last few jet diameters of jet length. Near the inception of

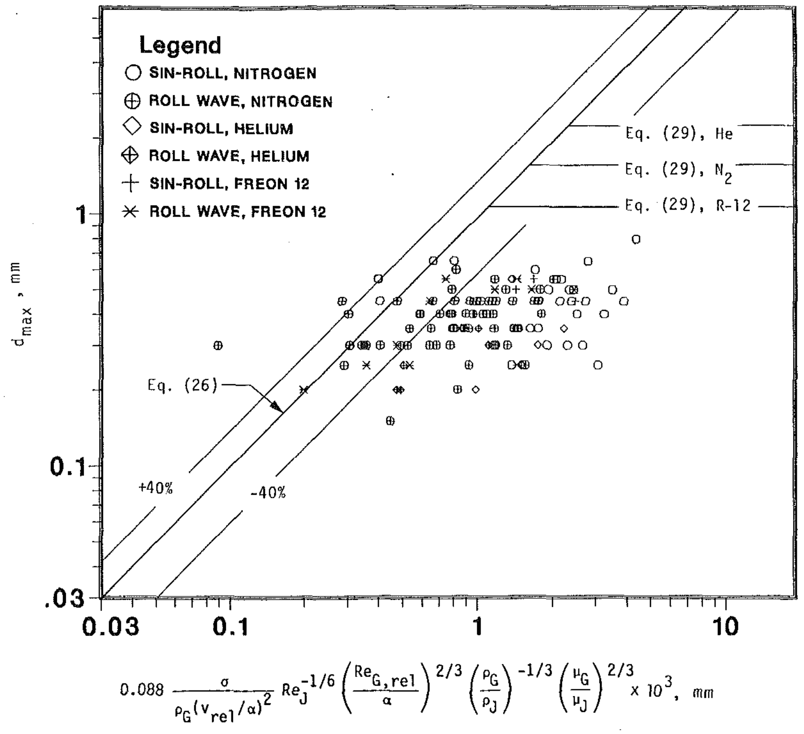

Fig. 8 Dispersed droplet size correlation, roll-wave entrainment breakup

roll waves, jets under sinuous breakup no longer had a smooth sinusoidal shape. Wave crests became pointed, and downstream surfaces of each wave were at much steeper slopes than upstream surfaces (see Fig. 4). Such surface distortions were predicted by Filyand [33] using nonlinear analysis.

Dispersed Core Droplet Size. For varicose and sinuous jet breakup, the core is initially dispersed into large liquid slugs. As first suggested by Tyler [34], these slugs should have the same volume as a cylinder of jet diameter and of length equal to the maximum growth rate wavelength. Equations (22) and (24) can be used to give wavelength values for varicose and sinuous jets, respectively. The subsequent disintegration of these large slugs was not observed in the experiments, due to wall wetting and limited observation length beyond the point of jet breakup. It is assumed that these slugs would disintegrate according to standard droplet breakup mechanisms based on the Weber number criterion, such as [35]

$$\mathrm{We}_d = \frac{\rho_G v_G^2 d_{\max}}{\sigma} = 8 \sim 17 \tag{25}$$

However, at low void fractions, the slugs, becoming more spherical beyond the jet breakup point, may expand radially, accelerating the gas flow and perhaps inducing roll-wave entrainment.

For roll-wave entrainment jet breakup, wall wetting resulted in only a limited number of photographs being obtained in which droplets were observed immediately after being sheared from roll-wave crests. From these photographs, maximum droplet diameters were measured, within an accuracy of ~0.05 mm. Most droplet diameters observed were within the range of 0.25–0.55 mm for flows ranging from early roll-wave inception to well-established roll-wave entrainment breakup of the jet core.

To analyze these limited data, use was again made of roll-wave entrainment studies in annular flow. Kataoka et al. [35] related the force balance on a ligament about to be torn from a roll-wave crest to the interfacial shear stress in annular two phase flow. Modifying their droplet size expression to account for geometric differences between annular flow and the present experimental study ($v_{\rm rel}/\alpha$ in place of j_G, gas annulus hydraulic diameter in place of annular flow gas core hydraulic diameter), the average maximum droplet diameter is predicted by

$$d_{\max} = 0.088 \frac{\sigma}{\rho_G (v_{\rm rel}/\alpha)^2} \mathrm{Re}_J^{-1/6} \left(\frac{\mathrm{Re}_{G,\rm rel}}{\alpha} \right)^{2/3} \cdot (\rho_G/\rho_J)^{-1/3} (\mu_G/\mu_J)^{2/3} \tag{26}$$

with a volume mean diameter equal to $d_{\max}/3.13$, according to their droplet size distribution correlation.

This expression was used to predict droplet diameters at the flow conditions of the test trials in which roll-wave entrained droplets were actually observed. Conditions were adjusted to represent those at the point of observation, assuming only gravitational acceleration. For short breakup lengths, such acceleration adjustments were minimal. The observed maximum droplet diameters were then plotted against the $d_{\max}$ values predicted by equation (26) in Fig. 8. Although the number of data points is limited, and the concept of average maximum diameter becomes vague when only a few droplets are observed at each data point, the results show general agreement in the high relative velocity region (small predicted diameters).

The velocity dependence of $v_{\rm rel}^{-3/2}$ indicated by equation (26) is similar to the $v_{\rm rel}^{-1}$ dependence indicated for free jets [21, 27]. However, those free jet studies showed liquid viscosity and density dependence opposite to that of equation (26).

Figure 8 shows that equation (26) starts to overpredict the droplet size at low relative velocities. These discrepancies can be very significant. There are two reasons for this shortcoming. Firstly, equation (26) has been derived from a force balance on the roll-wave crest, and the data base for equation (26) is from the standard annular flow experiments where the relative velocity is high. Therefore, the validity of equation

(26) at low relative velocities has not been confirmed previously. Secondly, there should be a physical limit on the stable droplet size in highly turbulent situations such as considered in the present case. Then, even if large droplets are entrained, they should disintegrate due to the droplet instability. This limit should be included in analyzing the droplet size observed in the experiment. The criterion for the maximum stable spherical drop is obtained below. For churn turbulent two-phase flow, the relative velocity between phases is nearly independent of dispersed particle size, and is given by Ishii [36] as

$$v_{\mathrm{rel}} = \sqrt{2}\left(\frac{\sigma g \Delta\rho}{\rho_G^2}\right)^{1/4} \tag{27}$$

It can be postulated that a droplet in a turbulent two-phase flow regime will be stable only if it maintains an undistorted, spherical shape. Then, when the flow regime for droplets is in the distorted particle, rather than wake flow regime, the droplet will be unstable [37]. For wake flow regime, Ishii [36] gives the following expression for relative velocity

$$v_{\mathrm{rel}} = \frac{d}{4}\left[\frac{(g\Delta\rho)^2}{\mu_G \rho_G}\right]^{1/3} \tag{28}$$

Combining equations (27) and (28), a maximum stable spherical droplet diameter can be found

$$d_{\max} = 4\left(\frac{2\sigma}{g\Delta\rho}\right)^{1/2} N_{\mu G}^{1/3} \tag{29}$$

where $N_{\mu G}$ is the gas viscosity number, based on the Taylor instability wavelength, and is defined as

$$N_{\mu G} = \frac{\mu_G}{(\rho_G \sigma \sqrt{\sigma / g\Delta\rho})^{1/2}} \tag{30}$$

For the typical densities and viscosities encountered in the experiment, equation (29) would predict maximum droplet diameters of 1.1 mm, 1.6 mm, and 2.3 mm for Freon-12, nitrogen, and helium test series runs, respectively. These values are much closer to the largest droplet diameters observed (0.8 mm) compared to the larger sizes predicted by equation (26), and are indicated in Fig. 8. Equation (29) may therefore be used to predict the upper bound of applicability for equation (26).

In an attempt to observe dispersed core droplet size beyond the point of wall wetting and the inception of rough wavy annular film flow, a limited number of trials was run using a shortened *B*2 test section, fitted with a Lucite exit fitting to divert the liquid annular flow away from the test section exit. Photographs were taken at the exit, with the distance between the jet breakup point and section exit varied. Results were obtained at several water/nitrogen flow conditions within the roll-wave entrainment regime. For locations near the jet breakup point, large slugs and ligaments from the distorted jet core, created when roll waves expanded to the Pyrex wall, were observed, while at nozzle/test section exit distances roughly twice as large as the jet breakup length, only dispersed droplets appeared. Most of these droplets had diameters in the range of 0.25 – 0.55 mm. Larger droplets, with diameters of 1-3 mm, were also observed. The sizes of these large droplets are in closer agreement with equation (29) (predicts 1.6 mm) than equation (25) (predicts 4-12 mm).

To compare dispersed droplet size data obtained in this experiment with actual inverted annular flow is difficult, since most low-quality film boiling experiments do not produce such data. An exception is the PWR FLECHT SEASET series of experiments. In a report by Lee et al. [6], dispersed droplet sizes and velocities are examined at various distances above the quench front. Most of the droplets are in the range of 0.5 to 1.5 mm, with velocities from 1 m/s up to 12 m/s. Smaller droplets, however, may have been overlooked in these experiments, due to relatively long exposure times for their photography (motion picture cameras at speeds up to 2500 frames per second). In the analysis of extensive FLECHT SEASET data by Kocamustafaogullari and Ishii [37], it was found that equation (26) was useful in predicting droplet diameters at high vapor flow rates. At low vapor flow rates, however, they found that equation (26) greatly overpredicted droplet sizes, and that equation (29), instead, became applicable. These are the same conclusions as were reached in the analysis of droplet size data of the present study.

V Conclusions

The results of this experiment in which inverted annular flow was simulated in an adiabatic test section have been correlated in terms of jet core breakup length (equations (9) and (11)), jet core surface wavelength (equations (22) and (24)) and dispersed core droplet size (equations (26) and (29)). Jet core breakup mechanisms have been identified, criteria for the transitions from one mechanism to another have been established (equations (16), (17), and (18)), and descriptions of core deformation under these breakup mechanisms have been given. These results should aid in the understanding of inverted annular flow hydrodynamics. They should also be of interest for applications, such as liquid jet gas pumps, in which adiabatic, coaxial liquid/gas jets are used. In addition, these experimental results can be extended to encompass free jet breakup conditions, where $\alpha = 1$ and $v_{\mathrm{rel}} = v_J$. Such an extension may help to clarify the conflicting results of previous studies in the area of drag-induced jet breakup behavior.

It must be noted that this adiabatic simulation of inverted annular flow, while producing a great deal of useful information, does have certain limitations. The absence of film boiling conditions (no wall wetting, an inward-directed radial force at the core surface due to vapor generation) may limit the applicability of these results. Physical constraints of test section construction limited this study to void fractions no lower than 0.28. Finally, events beyond the jet core breakup point could not be observed in great detail, due to wall wetting.

Acknowledgments

This work was performed at Argonne National Laboratory, under the auspices of the U.S. Nuclear Regulatory Commission. We would like to thank Drs. N. Zuber and M. Young of the NRC for their guidance and assistance in this research, and to thank G. Lambert, E. Sowa, and A. Tokuhiro of ANL for help in constructing the experimental apparatus.

References

1 Groeneveld, D. C., "Post-dryout Heat Transfer at Reactor Operating Conditions," *Proceedings of The National Topical Meeting on Water Reactor Safety*, American Nuclear Society, Salt Lake City, Utah, Mar. 26-28, 1973, pp. 321-350.

2 Chi, J. W. H., "Slug Flow and Film Boiling of Hydrogen," *J. Spacecraft*, Vol. 4, 1967, pp. 1329-1332.

3 Chen, J. C., Sundaram, R. K., and Ozkaynak, F. T., "A Phenomenological Correlation for Post-CHF Heat Transfer," NUREG-0237, 1977.

4 Laverty, W. F., and Rohsenow, W. M., "Film Boiling of Saturated Nitrogen Flowing in a Vertical Tube," ASME JOURNAL OF HEAT TRANSFER, Vol. 89, 1967, pp. 90-98.

5 Ottosen, P., "An Experimental and Theoretical Investigation of Inverse Annular Film Flow and Dispersed Droplet Flow, Important Under LOCA Conditions," Riso National Laboratory, Denmark, Report No. R-424, 1980.

6 Lee, N., Wong, S., Yeh, H. C., and Hochreiter, L. E., "PWR FLECHT SEASET Unblocked Bundle, Forced and Gravity Reflood Task Data Evaluation and Analysis Report, NRC/EPRI/Westinghouse Report No. 10," NUREG/CR-2256, EPRI NP-2013, WCAP-9891, 1981.

7 Weber, C., "Zum Zerfall eines Flussigkeitsstrahles," *Z. Angew. Math. Mech.*, Vol. 11, 1931, pp. 136-154.

8 Tyler, E., and Watkin, F., "Experiments With Capillary Jets," *Phil. Mag.*, Vol. 14, 1932, pp. 849-881.

9 Grant, R. P., and Middleman, S., "Newtonian Jet Stability," *AIChE J.*, Vol. 12, 1966, pp. 669-678.

10 Lord Rayleigh, "On the Instability of Jets," *Proc. Lond. Math. Soc.*, Vol. 10, 1878, pp. 4-13.

11 Christiansen, R. M., and Hixson, A. N., "Breakup of a Liquid Jet in a Denser Liquid," *Ind. Eng. Chem.*, Vol. 49, 1957, pp. 1017-1024.

12 Smith, S. W. J., and Moss, H., "Experiments With Mercury Jets," *Proc. Roy. Soc.*, Vol. A-93, 1917, pp. 373-393.

13 Iciek, J., "The Hydrodynamics of a Free, Liquid Jet and Their Influence on Direct Contact Heat Transfer—II," *Int. J. Multiphase Flow*, Vol. 8, 1982, pp. 251-260.

14 Phinney, R. E., "Breakup of a Turbulent Liquid Jet in a Low Pressure Atmosphere," *AIChE J.*, Vol. 21, 1975, pp. 996-999.

15 Iciek, J., "The Hydrodynamics of a Free Liquid Jet and Their Influence on Direct Contact Heat Transfer—I," *Int. J. Multiphase Flow*, Vol. 8, 1982, pp. 239-249.

16 Miesse, C. C., "Correlation of Experimental Data on the Disintegration of Liquid Jets," *Ind. Eng. Chem.*, Vol. 47, 1955, pp. 1690-1701.

17 Chen, T.-F., and Davis, J. R., "Disintegration of a Turbulent Water Jet," *Proc. ASCE, Hyd. Div.*, Vol. 90, 1964, pp. 175-206.

18 Van de Sande, E., and Smith, J. M., "Jet Break-up and Air Entrainment by Low Velocity Turbulent Water Jets," *Chem. Eng. Sci.*, Vol. 31, 1976, pp. 219-224.

19 Fenn, R. W., and Middleman, S., "Newtonian Jet Stability: The Role of Air Resistance," *AIChE J.*, Vol. 15, 1969, pp. 379-383.

20 Ohnesorge, W., "Die Bildung von Tropfen an Dusen und die Anflosung flussiger Strahlen," *Z. Angew. Math. Mech.*, Vol. 16, 1936, pp. 355-359.

21 Merrington, A. C. and Richardson, E. G., "The Break-up of Liquid Jets," *Proc. Phys. Soc.*, Vol. 59, 1947, pp. 1-13.

22 Levich, V. G., "Physicochemical Hydrodynamics," Prentice-Hall, New York, 1962.

23 McCarthy, M. J., and Molloy, N. A., "Review of Stability of Liquid Jets and the Influence of Nozzle Design," *Chem. Eng. J.*, Vol. 7, 1974, pp. 1-20.

24 Lienhard, J. H., and Day, J. B., "The Breakup of Superheated Liquid Jets," ASME *J. Basic Eng.*, Vol. 92, 1970, pp. 515-522.

25 Kusui, T., "Liquid Jet Flow Into Still Gas," *JSME Bulletin 5*, Vol. 11, 1968, pp. 1084-1090.

26 Ivanov, V. A., "Disintegration of a Liquid Jet," *J. Appl. Mech. Tech. Phys. USSR*, Vol. 7, 1966, pp. 19-23.

27 Nukiyama, S., and Tanasawa, Y., "Experiment on Atomization of Liquid," *Trans. JSME*, Vol. 5, 1939, pp. 63-68.

28 Jensen, R. T., "Inception of Liquid Entrainment During Emergency Cooling of Pressurized Water Reactors," Ph.D. Thesis, Utah State University, 1972.

29 Cunningham, R. G., and Doplin, R. J., "Jet Breakup and Mixing Throat Lengths for the Liquid Jet Gas Pump," ASME *J. Fluids Eng.*, Vol. 96, 1974, pp. 216-226.

30 De Jarlais, G., "An Experimental Study of Inverted Annular Flow Hydrodynamics Utilizing an Adiabatic Simulation," M.S. Thesis, Marquette University, Milwaukee, WI 1983.

31 Wallis, G. G., *One Dimensional Two-Phase Flow*, McGraw-Hill, New York, 1969.

32 Ishii, M., and Grolmes, M. A., "Inception Criteria for Droplet Entrainment in Two-Phase Cocurrent Film Flow," *AIChE J.*, Vol. 21, 1975, pp. 308-318.

33 Filyand, L. V., "Instability and Breakup of Capillary Liquid Jets in a Parallel Airstream," *Fluid Dynamics*, Vol. 16, 1981, pp. 424-428.

34 Tyler, E., "Instability of Liquid Jets," *Phil. Mag.*, Vol. 16, 1933, pp. 504-518.

35 Kataoka, I., Ishii, M., and Mishima, K., "Generation and Size Distribution of Droplets in Annular Two-Phase Flow," ASME *J. Fluid Eng.*, Vol. 105, 1983, pp. 230-238.

36 Ishii, M., "One-Dimensional Drift-Flux Model and Constitutive Equations for Relative Motion Between Phases in Various Two-Phase Flow Regimes," ANL-77-47, 1977.

37 Kocamustafaogullari, G., De Jarlais, G., and Ishii, M., "Droplet Generation During Core Reflood," *Trans. Am. Nucl. Soc.*, Vol. 44, 1983, pp. 804-805.

M. K. Jensen
Assistant Professor.
Mem. ASME

H. P. Bensler
Graduate Student.

Department of Mechanical Engineering,
University of Wisconsin—Milwaukee,
Milwaukee, WI 53201

Saturated Forced-Convective Boiling Heat Transfer With Twisted-Tape Inserts

Introduction

Twisted-tape swirl generators have been studied analytically and experimentally by many investigators. Various fluids and flow conditions have been used in single-phase, two-phase, and two-component flows to determine the effect of twisted-tape inserts on the heat transfer processes. Reviews of twisted-tape investigations have been included in comprehensive general surveys of augmentation [1, 2] as well as in specialized surveys [3, 4]. It is evident from these reviews and from a bibliography of the literature [5] that the effect of twisted-tape swirl generators on saturated, forced-convective boiling heat transfer coefficients has not been established. The available data in this regime are quite limited and are contradictory.

Allen [6] performed one of the earliest studies with saturated R-114 in natural circulation boiling with twisted-tape inserts. Heat transfer, at a given temperature difference, was higher for the flow with tape-generated swirl than for the flow without swirl. Foure et al. [7], working with annular water flow, also obtained improved heat transfer, as well as improved flow stability. Heat transfer was improved by 25 to 40 percent for the same pumping power. However, neither of these studies presented much data nor was any design guidance given. Two studies on liquid metals [8, 9] (as cited by Poppendiek and Gambill [4]) suggested that the swirl flow heat transfer in the quality region for both mercury and sodium was greater than that of axial flow over the whole quality range. Increases in the heat transfer coefficients in the order of 100 percent were realized in the low vapor quality regions.

On the contrary, Herbert and Sterns [10] found that the heat transfer coefficients for low-pressure steam were unaffected by swirl. The axial and swirl flow data followed similar trends with little difference being discernible between the two flows. Very little data of a quantitative or usable nature were presented. In addition, the vapor quality level was not indicated.

Blatt and Adt [11] presented data on heat transfer and pressure drops for saturated R-11 and water. Correlations were presented which described their data. These indicate improved heat transfer only at low heat fluxes, low qualities, and small radial accelerations, and increased pressure drop for all cases. However, Lopina and Bergles [12] suggested that errors were made in the data reduction in this paper and that the results have to be considered questionable.

The qualitative effects of twisted-tape inserts also have been discussed in several papers. Cumo et al. [13] found much improved heat transfer for a once-through vapor (R-12) generator in counterflow with twisted-tape inserts. However, no detailed measurements were made and only general information and trends were presented. Overall power transferred to the fluid with twisted tapes was much higher than that without twisted tapes because of improved CHF characteristics. No detailed or usable information for design purposes on the saturated boiling regimes was presented. Sephton [14] used a loosely fitting twisted tape and obtained 30 to 90 percent increases in the overall heat transfer coefficient in an evaporative desalination process. No information was obtained for the twisted-tape side alone. Hunsbedt and Roberts [15] used twisted tapes in a sodium-heated annulus. The water side bulk boiling coefficients were not explicitly investigated as the overall convective coefficient was of prime importance in this study. They suggested, though, that the steam-side heat transfer coefficients may be higher than those predicted by Chen's correlation [16] for axial flow. Pai and Pasint [17] obtained improved performance in a once-through vapor generator using twisted tapes. Much of the improvement appears to be attributable to the suppression of the CHF condition. Only qualitative figures are presented on the trends observed; no data were presented.

Because of the limited data available and because of the contradictory results, an experimental investigation was performed to determine the effect of twisted-tape swirl generators on saturated, forced-convective boiling heat transfer. R-113 was used as the working fluid because of its desirable physical properties in modeling forced convection boiling in laboratory situations and because its behavior is similar to that experienced with other fluorocarbon refrigerants. A vertical test section was chosen to eliminate stratification problems which commonly occur in horizontal tubes so that data could be obtained from similar flow regimes in both the smooth tube and twisted-tape geometries.

Only heat transfer data are presented and discussed in this paper. The pressure drop data and a pressure drop prediction method have been presented in [18].

Experimental Apparatus

Local heat transfer coefficients were obtained with upward-flowing R-113 in a vertical, uniformly heated stainless steel test section which was inserted into a closed flow loop (Fig. 1). The fluid flowrate to and the pressure in the test section were controlled by bypassing fluid around the test section and by adjusting valves downstream of the test section. Inlet fluid conditions were set by adjusting the power to variable-power electric preheaters or the flow to a steam-to-R-113 heat exchanger. Valves just upstream of the test section were used to keep a high pressure (1.5 MPa) in the preheaters so that when a large pressure drop was taken across those valves the liquid would flash into a liquid/vapor mixture (if required). This large pressure drop also prevented thermal-hydraulic instabilities in the test section. A four-thermocouple thermopile was located just upstream of these flashing valves to measure the liquid temperature prior to flashing. After passing through the test section, the two-phase mixture flowed through pressure control valves and a water-cooled condenser; the liquid R-113 then flowed through one of three calibrated rotameters.

Contributed by the Heat Transfer Division for publication in the Journal of Heat Transfer. Manuscript received by the Heat Transfer Division June 5, 1984.

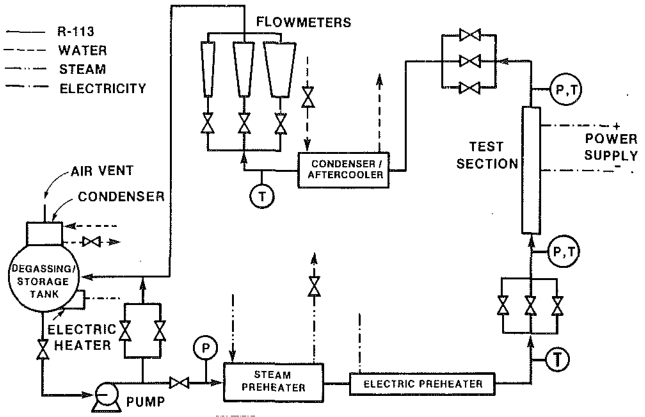

Fig. 1 Schematic of test loop

A high-accuracy (±0.69 kPa) pressure gage was used to measure the test-section inlet pressure. A thermocouple located near the pressure tap was used to measure the fluid temperature at that point and served as a check on the saturation temperature obtained from the pressure measurement. Pressure drops were measured with a manometer. Direct-current power was supplied to the test section by a low ripple (< 1 percent) power supply. Test-section current was obtained from a calibrated shunt. Test-section voltage drop, shunt voltage, and all thermocouple voltages were measured using a high-accuracy (± 1 μV) digital voltmeter, which was part of a Hewlett-Packard data acquisition system.

The test section was constructed from 8.10/9.53-mm-dia 304 stainless steel tubing with a heated length of 1200 mm, an unheated entrance length of 527 mm, and an unheated exit length of 76 mm. Electric power was conducted to the tube through bus bars soldered to the tube. The tube was electrically insulated from the rest of the flow loop. Twenty thermocouples, whose beads were electrically insulated from the tube, were spaced along the outside of and fastened securely to the tube.

Three twisted tapes were tested. The tape-twist ratios (length for 180 deg twist/inside tube diameter) were $y = 3.94$, 8.94, and 13.92. The tapes were made from 0.254-mm-thick 304 stainless steel. Their lengths were approximately 1835 mm so that the tape went from the beginning of the unheated entrance length to the end of the unheated exit length. The average tape width was 7.85 mm. The tape was held firmly in place at its upper end so that it could not move during a test. It would have been desirable to use either a nonconducting tape or an insulated tape. However, no material could be found which would not react with the fluid at the elevated fluid temperatures. Corrections for power dissipation in the tape are discussed in the Experimental Procedures section.

A guard heater was used to eliminate heat losses from the test section. Fiberglass insulation about 25 mm thick was held tightly in place around the test section with a 50 mm i.d. copper pipe. Insulated Nichrome wire was attached to the inside of the copper pipe as were three thermocouples. Another 25-mm layer of fiberglass insulation was then used to completely enclose the copper pipe. This guard heater covered the heated portion of the test section. The guard heater power was adjusted until its temperature was approximately that of the test section. A second guard heater with an attached thermocouple was used to eliminate heat losses from the piping between the flashing valves and the inlet bus bar. The power to this guard heater was adjusted so its temperature was approximately the same as the inlet fluid temperature. These two guard heaters had separate power supplies so that the temperature of each could be independently set. The test section and flow loop were heavily insulated.

Experimental Procedure

The R-113 was thoroughly degassed prior to any testing by boiling the R-113 in the storage/degassing tank, condensing the R-113 vapor in a water-cooled condenser, and venting the liberated gases to the atmosphere. The condensed R-113 was returned to the tank. The loop was then sealed to prevent any air from going back into solution. At this point the experiment was ready to begin.

The flow rate to and pressure in the test section were set to predetermined levels by adjusting the appropriate valves. The guard heater was turned on. The preheated pressure was set at 1.5 MPa and power and/or steam to the preheaters turned on. The temperature at the outlet of the electric preheaters was set such that a specified test-section inlet quality would be obtained when the pressure of the liquid R-113 was reduced to the test-section pressure. An enthalpy balance across the flashing valves was used to determine the test-section inlet quality. Test-section quality at any location was calculated from an energy balance between the enthalpy gain of the fluid and the electrical power dissipation in the test section. Specified wall heat fluxes were set by adjusting the voltage drop across the test section.

Before any data were taken once the flow conditions were set, the flow loop was allowed to come to steady state. The heat flux was then set at the highest desired value, the test section allowed to come to thermal equilibrium, and all data

Nomenclature

C = constant
c_p = specific heat, J/kgK
D = tube diameter, m
F = two-phase Reynolds number factor
G = mass velocity, kg/m^{2}s
h = heat transfer coefficient, W/m^{2}K
h_{fg} = enthalpy of vaporization, J/kg
k = thermal conductivity, W/mK
N = number of data points
P = pressure, Pa
Pr = Prandtl number = $\mu c_p/k$
ΔP = pressure difference related to ΔT, Pa

q'' = heat flux, W/m^2
Re = Reynolds number = GD/μ
S = suppression factor
T = temperature, K
ΔT = $T_w - T_{\text{sat}}$, K
x = quality
X_0 = bubble growth parameter, equation (8), m
y = tape twist ratio (length for 180 deg twist/inside diameter)
(dp/dz) = pressure gradient, Pa/m
α = $(1/2 \cdot y)(4y^2 + \pi^2)^{0.5}$
β = volumetric coefficient of thermal expansion, 1/K

μ = dynamic viscosity, kg/ms
ρ = density, kg/m^3
σ = surface tension, N/m
χ = Martinelli factor = $((1-x)/x)^{0.9} (\rho_g/\rho_l)^{0.5} \cdot (\mu_l/\rho_g)^{0.1}$

Subscripts

g = vapor
h = hydraulic
l = liquid
NB = nucleate boiling
sat = saturation
TP = two-phase
tt = twisted tape
w = wall

then were taken; the heat flux then was lowered to the next value and the procedure was repeated.

Inside wall temperatures were calculated using the measured outside wall temperature and the measured power dissipation in the one-dimensional steady-state heat conduction equation for thin-wall tubes. Fluid temperatures were obtained from the R-113 saturation curve using pressure measurements along the tube. Local heat transfer coefficients were calculated from $h = q''/(T_w - T_{sat})$.

The heat flux for the axial flow data was calculated from the total power dissipated in the test section and the tube inside surface area; for the tests with the twisted-tape inserts, the power dissipated in the tape was first subtracted from the total power dissipated across the test section. (This adjustment also was made when calculating the inside wall temperature.) The power correction was accomplished by comparing the resistance of the bare tube to the resistance of the tube-twisted-tape combination. The resulting twisted-tape heat transfer coefficient was in very good agreement (within 2 percent) with an analysis by Lopina and Bergles [19] which accounted for both the power dissipation in the tape and heat conduction to the tape from the wall assuming zero contact resistance between tape and tube. Because of the good agreement, a reproducible electrical resistance situation was assumed to have been established. From the present data, the heat conduction appeared to be negligible compared to the power dissipation. The heat fluxes reported on the figures represent the actual wall heat flux.

Tests were run with an empty tube and with the three twisted-tape inserts. The nominal ranges of the two-phase experimental conditions covered in this study were as follows:

Heat flux	0 to 50,000 W/m^2
Inlet quality	0 to 61 percent
Outlet quality	0 to 78 percent
Inlet pressure	276, 551, and 827 kPa
Mass velocity	120 to 1600 kg/m^{2}s
Tape-twist ratio	3.94, 8.94, and 13.92

In addition, several single-phase heat transfer tests were run. In all, 81 tests were run with axial flow and 232 tests were run with the twisted tapes. Uncertainties in the experimental data, as estimated through a propagation-of-error analysis, are suggested to be: P, ± 1.5 kPa; G, ± 2 percent; x, ± 3 percent; q'', ± 1 percent; h, ± 5 percent. Typical data are shown in the following figures. Complete details of the experimental apparatus and procedures and data tables can be found in [20].

Results and Discussion

Experimental Results. Single-phase (nonboiling) and two-phase boiling heat transfer data were obtained over wide ranges of pressure, quality, heat flux, mass velocity, and tape-twist ratios. The single-phase axial and swirl flow data were consistent with data obtained in other investigations as were the axial flow boiling heat transfer data. The swirl flow boiling heat transfer data generally indicated significant improvements in the heat transfer coefficients compared to axial flow at the same conditions.

The single-phase axial and swirl flow data were taken over a Reynolds number range from about 3200 to 49,000. At the lower Reynolds numbers some thermal entrance effects were present but this effect diminished as the flow increased. Entrance effects also were present with the swirl flows but were much smaller in magnitude and length. The entrance region data were eliminated from the evaluation of the data because the fully developed heat transfer behavior was of primary concern. There was fair agreement between the axial flow data and predictions by the Dittus-Boelter correlation [21] (equation (2)). However, a better overall prediction was obtained by changing the leading coefficient in equation (2) from 0.023 to 0.020; this resulted in an average h_{pred}/h_{exp} of 0.973 and an average absolute deviation between the predicted and experimental data of 0.033. For the single-phase swirl flow data, the correlation by Lopina and Bergles [22] (equation (9)) was used. Since this relation was a modification of the Dittus-Boelter equation, the leading coefficient also was changed to 0.020 to be consistent with the axial flow

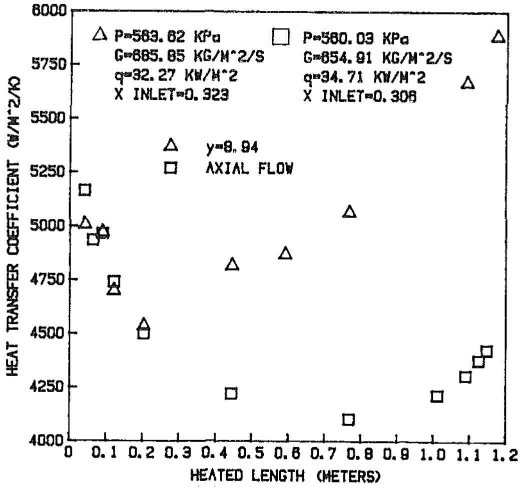

Fig. 2 Entrance effects in boiling heat transfer data

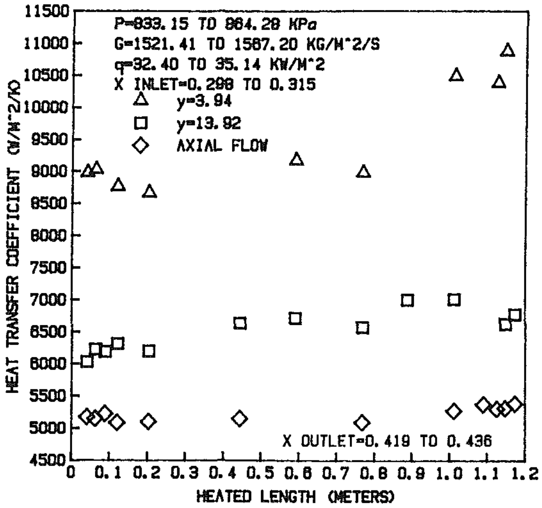

Fig. 3(*a*) Effect of tape-twist ratio on heat transfer coefficients

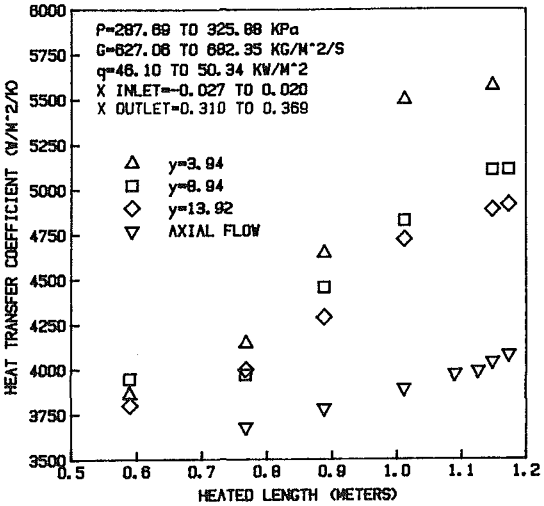

Fig. 3(*b*) Effect of tape-twist ratio on heat transfer coefficients

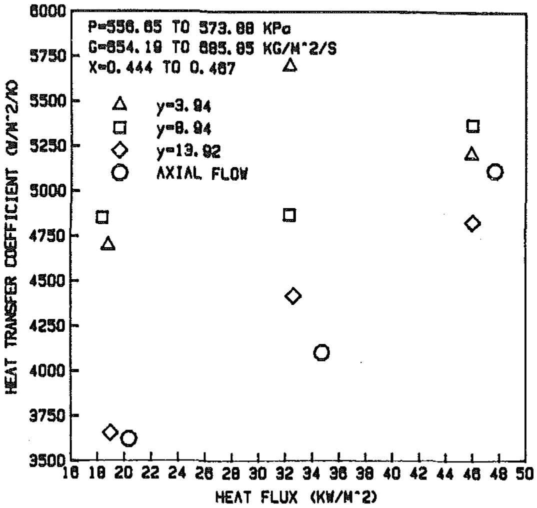

Fig. 4 Effect of heat flux on heat transfer coefficients

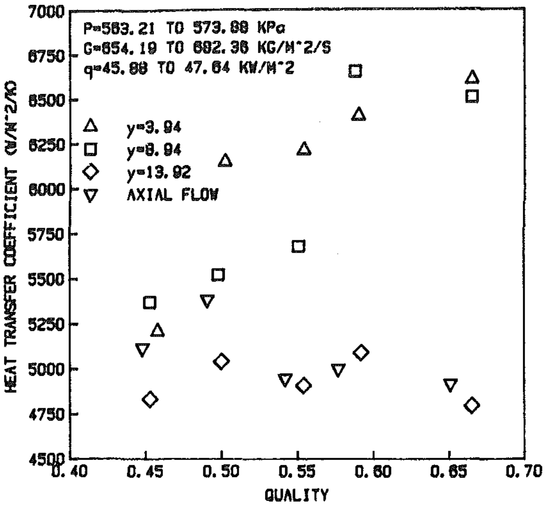

Fig. 5 Effect of quality on heat transfer coefficients

correlation. Generally, there was good agreement between the swirl flow data and the predictions from equation (9). For all the single-phase swirl flow data, an average $h_{\text{pred}}/h_{\text{exp}}$ of 1.041 was obtained with an average absolute deviation of 0.089.

The axial and swirl flow boiling heat transfer data also had thermal entrance effects. As shown in Fig. 2, the magnitude and length of the entrance effects were smaller with the twisted tapes than with the axial flow. The magnitude of the entrance effects decreased with increasing quality, heat flux, and mass velocity and with decreasing pressure. For some conditions no entrance effects were present. Entrance effects have been discussed in more detail in [20]. Only data not in the entrance region (after the minimum point in the heat transfer coefficient versus length curve) were analyzed since the fully developed boiling heat transfer region was the regime of interest.

The twisted-tape swirl generators generally increased the forced-convection boiling heat transfer coefficients. As shown in Figs. 3(*a*) and 3(*b*), there can be significant increases in the swirl flow heat transfer coefficient compared to the axial flow depending on the flow conditions. The increase was much higher at higher qualities and mass velocities and with smaller tape-twist ratios. At some conditions (low qualities and mass flows) there was not much difference between the axial and swirl flow heat transfer coefficients; apparently, nucleate boiling effects dominated convective effects so that the twisted tapes did not greatly affect the heat transfer behavior. The increase in the swirl flow heat transfer coefficients was in the range of about 0 to 90 percent.

As the heat flux increased the tape-twist ratio had less effect on the heat transfer coefficients (Fig. 4). At lower heat fluxes at fixed flow conditions the variation between the axial and swirl flow heat transfer coefficients was substantial but the differences decreased as the heat flux increased. Perhaps at the lower heat fluxes, convective effects with the swirl flows are much stronger than those in the axial flow and nucleation in the film flow on the wall are comparable in the two geometries. This would result in higher swirl flow heat transfer coefficients. However, as the heat flux increases, the convective effects would not be affected but the nucleation would be much larger. Since the nucleation characteristics are probably comparable in the swirl and axial flows, then the nucleation effects would tend to start dominating the convective effects. This would tend to lessen the spread among the heat transfer coefficients from the various twist-tape ratios and the axial flow, as shown. At high qualities, nucleation is generally considered to be suppressed. However, there is disagreement in the literature on this point. In particular, Mesler [23, 24] argues that nucleation can still occur at high qualities. The data presented here seem to support that view. However, much more work needs to be performed to clarify this point.

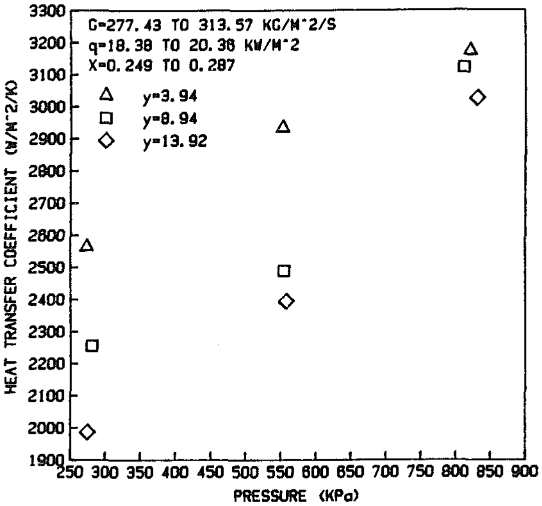

Fig. 6 Effect of pressure on heat transfer coefficients in swirl flow

With increasing quality with fixed other conditions (Fig. 5), the convective effects would be stronger as the tape-twist ratio decreased. This is consistent with single-phase swirl flow experience. As the quality increases, the effective two-phase velocity also increases which will lead to higher heat transfer coefficients.

As the pressure increases the differences among the heat transfer coefficients caused by the three twisted tapes decrease (Fig. 6). For the same quality at increasing pressures, the two-phase velocity decreases. Thus, convective effects should begin to decrease so that the effect of the twisted tapes should begin to diminish.

The data presented in these figures are typical of all the data taken in this investigation. As is evident, there is some scatter in the data but the trends are as described. However, for these data to be most useful, a correlation which predicts these trends is required. Therefore, a correlation was developed which satisfactorily predicted all the swirl flow data.

Correlation of Data. The procedure followed to correlate the twisted-tape heat transfer data was: (1) Obtain a reasonable prediction of the present axial flow heat transfer coefficients using well-established correlations from the literature; (2) modify the axial flow correlation to predict the swirl flow data. With good prediction of the swirl flow data

Table 1 Accuracy of Predicted Data With Various Combinations of Correlating Equations

Correlating equations used	$\frac{\Sigma(h_{\text{pred}}/h_{\text{exp}})}{N}$		$\frac{\Sigma\lvert(h_{\text{pred}}/h_{\text{exp}})-1\rvert}{N}$	
	Axial[1]	Swirl[2]	Axial[1]	Swirl[2]
1, 2 or 8[3], 3, 5, 6	1.024	1.085	0.197	0.241
1, 2 or 8[3], 4, 5, 6	0.981	1.075	0.231	0.263
1, 2 or 8[3], 3, 5, 7	1.073	1.042	0.203	0.222
1, 2 or 8[3], 4, 5, 7	1.042	1.031	0.227	0.244

[1] N = 981
[2] N = 2682
[3] Only the first term in equation (8) was used in predicting the swirl flow data.

using the modified axial flow correlation, then the effect of the twisted tapes should be described well.

The Chen correlation [16] was used to predict the axial flow heat transfer data. This relation

$$h_{TP} = h_l F + h_{NB} S \tag{1}$$

was evaluated at the experimentally measured wall superheats (to avoid biasing the data as discussed by Dhar and Jain [25]) using several expressions for the two-phase Reynolds number factor F, the suppression factor S, and the nucleate pool boiling heat transfer coefficient h_{NB}.

The liquid-only single-phase heat transfer coefficient h_l was evaluated from the Dittus-Boelter [21] equation

$$h_l = C\,\text{Re}_l^{0.8}\text{Pr}_l^{0.4}k_l/D \tag{2}$$

where the liquid-only Reynolds number was $\text{Re}_l = G(1-x)D/\mu_l$. The leading coefficient in equation (2) was modified to reflect the actual single-phase heat transfer data taken with the present test section. As previously mentioned, the modified value was $C = 0.020$.

Two two-phase Reynolds number factors F were used. One was a curve fit of Chen's data which was presented in [26]. This expression is:

$$\begin{aligned} F &= 1 && \text{for } 1/\chi < 0.1 \\ F &= 2.35(1/\chi + 0.213)^{0.736} && \text{for } 1/\chi \geq 0.1 \end{aligned} \tag{3}$$

The second expression was that given by Chen [16]

$$F = (\,(dp/dz)_{TP}/(dp/dz)_l\,)^{0.444} \tag{4}$$

The two-phase pressure gradient (with and without twisted tapes) used was that presented in [18].

The nucleate pool boiling heat transfer coefficient was evaluated with the Forster-Zuber [27] correlation

$$h_{NB} = 0.00122\,\frac{k_l^{0.79}c_{P,l}^{0.45}\rho_l^{0.49}}{\sigma^{0.5}\mu_l^{0.29}h_{fg}^{0.24}\rho_g^{0.24}}\,\Delta T^{0.24}\Delta P^{0.75}S \tag{5}$$

For the suppression factor, a curve fit of Chen's data, as was presented in [26], was used

$$S = 1/(1. + 2.53\times10^{-6}\text{Re}_{TP}^{1.17}) \tag{6}$$

where $\text{Re}_{TP} = F^{1.25}\,\text{Re}_l$. In addition, the expression developed by Bennett et al. [28] was also used

$$S = (k_l/h_l F X_0)(1 - \exp(-h_l F X_0/k_l)\,) \tag{8}$$

where $X_0 = 0.041(g_c\sigma/g(\rho_l - \rho_v))^{0.5}$.

Various combinations of the above expressions were used in equation (1) to predict the axial flow heat transfer data. As shown in Table 1, the four combinations of the two F and two S factors when used in equation (1) and using the Forster-Zuber correlation (equation (5)) all gave comparable results in predicting the axial flow data. (Individual F and S factors are paired based on how they were derived or obtained. Thus, equations (3) and (6) and equations (4) and (7) are paired. However, using the other combinations demonstrates that there is little difference in using one factor versus another.) There generally was good agreement between the predicted and the experimental data. The magnitude of the average deviation between the predicted and experimental data was attributable to the fact that the correlations tended to overpredict the data at low qualities and mass velocities and to underpredict the data as the quality increased. Nevertheless, the overall prediction of the 981 axial flow data points was good, and it was decided that these correlations were adequate to use as references with which to evaluate and correlate the effect of the twisted tapes.

Twisted-tape swirl generators do not disrupt the flow in a tube as do other enhancement devices such as transverse ribs or roughened surfaces. Rather, the flow is across a smooth surface with the surface geometry guiding the flow. Because of this, the heat transfer behavior for axial and swirl flows should be similar. Therefore, to predict the twisted-tape boiling heat transfer coefficients, the axial tube correlation initially was modified in two ways: (1) A single-phase heat transfer coefficient developed for tape-generated swirl flow was used in place of the single-phase axial flow correlation; (2) the hydraulic diameter was used instead of the tube diameter.

The single-phase swirl flow correlation used was developed by Lopina and Bergles [22]. The first term in equation (8) accounts for increased fluid velocity at the tube wall caused by the twisted tape and the second term accounts for a centrifugal convection due to buoyancy. In this correlation

$$h_{tt} = \frac{k_l}{D_h}\,C(\alpha\text{Re}_h)^{0.8}\text{Pr}^{0.4} + 0.193(\text{Re}_h/y)^2(D_h/D)\,\beta\Delta T\text{Pr}^{1/2} \tag{8}$$

the leading coefficient again was changed to 0.20 to reflect the single-phase data from this experiment and the liquid-only Reynolds number was evaluated as it was in equation (2). The hydraulic diameter was used except where noted.

Using the four combinations of F and S factors, the Lopina and Bergles swirl flow equation, and the hydraulic diameter, the swirl flow data were consistently overpredicted by an average of 60 percent. Thus, it was necessary to correlate the data slightly differently. The Lopina and Bergles swirl flow equation was developed for single-phase flows with large differences (up to about 75°C) between the wall and fluid temperatures. In single-phase flows, because of large density differences between the fluid at the wall and in the cooler core, centrifugal body forces tend to cause the cooler fluid to be centrifuged to the wall and the hotter fluid to flow into the core thus enhancing the convective heat transfer process. In two-phase flows the centrifugal body forces would tend to separate the phases, depositing the liquid at the wall and segregating the vapor in the core. There is no significant temperature variation between the liquid and vapor phases so that enhanced convection due to cooler fluid sweeping the surface would not occur as is the case in single-phase flows. Likewise, at moderate to high qualities, the liquid would be mainly on the walls and forced convection vaporization would occur at the liquid-vapor interface; thus, there would be no "natural convection" effects in this two-phase flow which would be analogous to the natural convection effects in single-phase flows. Therefore, only the first term in equation (8) was then used in the Chen relation to predict the swirl flow data.

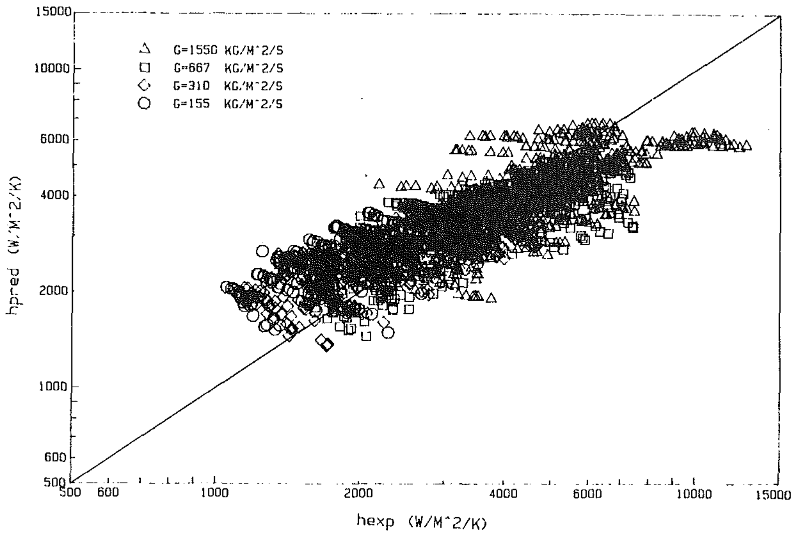

Fig. 7 Comparison between predicted and experimental data

Table 1 indicates the predictions of the data using the various combinations of the F and S factors, the hydraulic diameter, and the first term in equation (8). The first set of columns represents how well the prediction generally goes through the complete data set. The second set of columns shows the average absolute deviations between the experimental data and the predictions. Generally, there was a good overall prediction of the 2682 data points for all the geometries. The scatter between the predicted and experimental data is shown in Fig. 7. As was the case for the axial flow, there tended to be an overprediction in the data at lower qualities and mass velocities and an underprediction as the quality and mass velocity increased. This behavior was consistent with the axial flow predictions. Hence, with better prediction of the axial flow behavior the swirl flow data would have been predicted better also. It should be noted that the swirl flow data were slightly underpredicted at the smaller tape-twist ratios and slightly overpredicted at the larger tape-twist ratios.

The Bennett et al. [28] suppression factor (equation(7)) when used with either F factor (equation (3) or (4)) gave better predictions than those by the curve fit of Chen's original data (equation (6)). This probably is due to the Bennett et al. suppression factor taking into account the effect of geometry and flow (through the single-phase heat transfer coefficient) on the suppression factor. The use of either F factor correlation with the Bennett et al. suppression factor seems reasonable; the predicted results are comparable with a slight tradeoff between improved accuracy in the average $(h_{\text{pred}}/h_{\text{exp}})$ or in the average absolute deviation $|(h_{\text{pred}}/h_{\text{exp}})-1|$.

For the majority of the data shown in the figures and in data not shown, the greatest difference in heat transfer coefficients was between the axial and swirl flows, as expected; generally, there was a 20 to 40 percent difference at the same flow conditions. The variation among the three tape-twist ratios was usually in the order of 10 percent. Note that by using only the first term in the single-phase swirl flow heat transfer correlation (equation (8)) the majority of the difference between the axial and swirl flow convective heat transfer coefficients used in the Chen relation (equation (1)) is attributable to the use of the hydraulic diameter; α varies from 1.077 at $y = 3.94$ to 1.006 at $y = 13.92$ and, hence, has only a small effect compared to the hydraulic diameter. Therefore, the major effect of the twisted tape on the convective heat transfer coefficient can be attributed to the reduction in the hydraulic diameter with a further effect in the range of 10 percent attributable to changes in the twist ratio itself. Thus, it appears that if in the Chen correlation, S and F factors can be found which accurately predict the axial flow heat transfer, then that correlation can be modified to predict swirl flow data only by using the hydraulic diameter and by accounting for the increased fluid velocity at the tube wall.

Conclusions

An experimental investigation has been conducted to study the effect of twisted-tape swirl generators on saturated, forced-convective boiling heat transfer. Axial and swirl flow heat transfer coefficients were obtained in a straight, vertical tube over a range of pressures, qualities, heat fluxes, and tape-twist ratios. The following conclusions can be drawn from this investigation:

1 Twisted tapes increase the heat transfer coefficients in saturated forced-convective boiling heat transfer compared to axial flow at the same flow conditions.

2 The swirl flow heat transfer coefficient increases (compared to axial flow at the same flow conditions) with decreasing tape-twist ratio and with increasing quality, pressure, and heat flux. The effect of decreasing tape-twist ratios decreases with increasing pressure.

3 The Chen correlation used to predict axial flow boiling heat transfer coefficients can predict swirl flow boiling heat transfer coefficients if account is taken of the increased fluid velocity at the tube wall and the hydraulic diameter is used instead of the tube diameter. The effect of the twisted-tape geometry on the suppression factor can be incorporated by using the Bennett et al. [28] suppression factor (equation (8)). Either expression for the F factor can be used.

Acknowledgments

This research is based on work supported by the National Science Foundation under Grant No. MEA-8117226.

References

1 Bergles, A. E., "Survey and Evaluation of Techniques to Augment Convective Heat and Mass Transfer," *Progress in Heat and Mass Transfer*, Vol. 1, 1969, pp. 331-424.

2 Bergles, A. E., "Enhancement of Heat Transfer," *Sixth International Heat Transfer Conference—Toronto*, Vol. 1, 1978, pp. 89-108.

3 Gambill, W. R., and Bundy, R. D., "An Evaluation of the Present Status of Swirl-Flow Heat Transfer," ASME Paper No. 62-HT-42.

4 Poppendiek, H. F., and Gambill, W. R., "Helical Forced-Flow Heat Transfer and Fluid Dynamics in Single and Two-Phase Systems," *Proceedings of the International Conference on the Peaceful Uses of Atomic Energy*, New York, United Nations, 1965, Vol. 8, pp. 274-283.

5 Bergles, A. E., Webb, R. L., Junkhan, G. H., and Jensen, M. K.,

"Bibliography on Augmentation of Convective Heat and Mass Transfer," Heat Transfer Laboratory Report HTL-19, ISU-ERI-AMES-79206, Iowa State University, Ames, IA, May 1979.

6 Allen, C. F., AEC R&D Report K-1487, Oct. 1961.

7 Foure, C., Moussez, C., and Eidelman, D., "Technique for Vortex Type Two-Phase Flow in Water Reactors," *Proceedings of the International Conference on the Peaceful Uses of Atomic Energy*, New York, United Nations, 1965, Vol. 8, pp. 255–261.

8 Longo, J., General Electric Co., Quarterly Progress Reports 2, 3, and 4, Contract NAS 3-2528, Apr. and July 1963.

9 Poppendiek, H. F., Greene, N. D., MacDonald, F. R., Sabin, C. M., Livett, R. K., and Thompson, A. S., AEC Contract AT(04-3)-409, GLR-15, Sept. 1962–Aug. 1963.

10 Herbert, L. S., and Sterns, U. J., "An Experimental Investigation of Heat Transfer to Water in Film Flow. Part II—Boiling Runs With and Without Induced Swirl," *Canadian Journal of Chemical Engineering*, Vol. 46, 1968, pp. 408–412.

11 Blatt, T. A., and Adt, R. R., Jr., "The Effects of Twisted-Tape Swirl Generators on the Heat Transfer Rate and Pressure Drop of Boiling Freon 11 and Water," ASME Paper No. 65-WA-42, 1963.

12 Lopina, R. F., and Bergles, A. E., "Subcooled Boiling of Water in Tape-Generated Swirl Flow," ASME JOURNAL OF HEAT TRANSFER, Vol. 95, 1973, pp. 281–283.

13 Cumo, M., Farello, G. E., Ferrari, G., and Palazzi, G., "The Influence of Twisted Tapes in Subcritical, Once-Through Vapor Generators in Counterflow," ASME JOURNAL OF HEAT TRANSFER, Vol. 96, 1974, pp. 365–370.

14 Sephton, H. H., "Interface Enhancement for Vertical Tube Evaporators: A Novel Way of Substantially Augmenting Heat and Mass Transfer," ASME Paper No. 71-HT-38.

15 Hunsbedt, A., and Roberts, J. M., "Thermal-Hydraulic Performance of a 2MWt Sodium-Heated, Forced Recirculation Steam Generator Model," ASME JOURNAL OF HEAT TRANSFER, Vol. 96, 1974, pp. 66–76.

16 Chen, J. C., "Correlation for Boiling Heat Transfer to Saturated Fluids in Convective Flow," *I&EC Process Design and Development*, Vol. 5, No. 3, 1966, pp. 322–329.

17 Pai, R. H., and Pasint, D., "Research at Foster Wheeler Advances Once-Through Boiler Design," *Electric Light and Power*, Jan. 1965, pp. 66–70.

18 Jensen, M. K., Pourdashti, M., and Bensler, H. P., "Two-Phase Pressure Drop With Twisted-Tape Swirl Generators," *International Journal of Multiphase Flow*, Vol. 11, 1985, pp. 201–211.

19 Lopina, R. F., and Bergles, A. E., "Heat Transfer and Pressure Drop in Tape Generated Swirl Flow," M.I.T. Engineering Projects Report No. DSR 70281-47, June 1967.

20 Bensler, H. P., "Saturated, Forced-Convective Boiling Heat Transfer With Twisted-Tape Inserts," M.S. thesis, University of Wisconsin—Milwaukee, 1984.

21 Dittus, F. W., and Boelter, L. M. K., *Publ. Eng.*, Vol. 2, 1930, p. 443.

22 Lopina, R. F., and Bergles, A. E., "Heat Transfer and Pressure Drop in Tape-Generated Swirl Flow of Single-Phase Water," ASME JOURNAL OF HEAT TRANSFER, Vol. 91, 1969, pp. 434–442.

23 Mesler, R. B., "A Mechanism Supported by Extensive Experimental Evidence to Explain High Heat Fluxes Observed During Nucleate Boiling," *AIChE Journal*, Vol. 22, 1976, pp. 246–252.

24 Mesler, R. B., "An Alternate to the Dengler and Addoms Convection Concept of Forced Convection Boiling Heat Transfer," *AIChE Journal*, Vol. 23, 1977, pp. 448–453.

25 Dhar, P. L., and Jain, V. K., "On Evaluation of Correlations for Prediction of Heat Transfer Coefficient in Nucleate Flow Boiling," *International Journal of Heat and Mass Transfer*, Vol. 25, 1982, pp. 1250–1251.

26 Bergles, A. E., Collier, J. G., Delhaye, J. M., Hewitt, G. F., and Mayinger, F., *Two-Phase Flow and Heat Transfer in the Power and Process Industries*, Hemisphere, Washington, D.C., 1981, p. 250.

27 Forster, H. K., and Zuber, N., "Dynamics of Vapor Bubbles and Boiling Heat Transfer," *AIChE Journal*, Vol. 1, 1955, pp. 531–535.

28 Bennett, D. L., Davis, M. W., and Hertzler, B. L., "The Suppression of Saturated Nucleate Boiling by Forced Convective Flow," *AIChE Symposium Series No. 199*, Vol. 76, 1980, pp. 91–103.

R. C. Dykhuizen

R. P. Roy
Mem. ASME

Department of Mechanical and
Aerospace Engineering,
Arizona State University,
Tempe, AZ 85287

S. P. Kalra
Nuclear Power Division,
Electric Power Research Institute,
Palo Alto, CA 94304

A Linear Time-Domain Two-Fluid Model Analysis of Dynamic Instability in Boiling Flow Systems

A linear analysis of dynamic instability in boiling flow systems has been carried out in the time domain. An unequal velocity, unequal temperature two-fluid model description of boiling flow is used. Instability threshold results of the density-wave oscillation type obtained have been compared with experimental data from Refrigerant-113 and water systems with satisfactory agreement.

Introduction

Boiling flow systems are susceptible to dynamic instabilities of various types such as flow excursions and flow oscillations [1-3]. Formidable problems in maintaining system performance, control, and integrity can arise during such instabilities. Among the dynamic instabilities, the most common is a low frequency (0.1-2 Hz, typically) oscillatory flow instability of the limit cycle type termed "density-wave oscillations" (DWO) [4-6]. Boiling water nuclear reactor (BWR) cores and steam generators of the once-through type (OTSG) may be affected by DWO during unusually high "power-to-flow" ratio operations [7, 8].

A considerable amount of effort has been devoted to the development of analytical models of boiling flow system dynamic instabilities in general and of DWO in particular. Most of these have been analyzed in the frequency domain [6, 9-15]. A few investigators have developed dynamic instability models in the time domain [16-20]. Descriptions of vapor-liquid flow in these studies range from homogeneous, equilibrium to drift-flux, nonequilibrium formulation.

In the work presented here, a time-domain two-fluid (unequal velocity, unequal temperature, equal bulk pressure) representation of boiling flow has been adopted. A linear dynamic stability model is developed keeping in mind that the systems being studied are multi-input, multi-output (MIMO) systems. The objective is to construct a linear state space model of the system in the form of a vector differential equation:

$$\dot{\mathbf{x}} = [A]\mathbf{x} + [B]\mathbf{u} \tag{1}$$

where $\mathbf{x}$ is the state vector and $\mathbf{u}$ the input vector.

Once such a model is constructed, inherent linear stability information for the system can be readily obtained by calculating the eigenvalues of the matrix $[A]$. Questions associated with controllability and observability of system models which arise in the frequency-domain approach are of no concern in this approach [21]. Furthermore, once the matrices $[A]$ and $[B]$ in equation (1) have been constructed, it is a simple matter to study the system frequency response [22, 23]. The work reported here is also a proper first step toward the development of a nonlinear time-domain model of dynamic instability (e.g., DWO limit cycles) in boiling flow systems, which is our eventual goal.

In conjunction with the two-fluid description of boiling flow, well-accepted constitutive relations have been used in this work whenever possible.[1] Comparison of predicted dynamic instability threshold conditions with experimental data from two sources are reported. Both of these feature electrically heated test sections, with one using Refrigerant-113 as the working fluid [13], and the other using water [25].

Problem Formulation

The thermohydrodynamic model developed is general enough to permit dynamic stability investigation of a channel in a parallel, multichannel configuration; a complete boiling flow loop; or a portion of a boiling flow loop. BWR primary coolant system and once-through steam generators are examples of such configurations.

Before applying the model to analyses of complex systems, it was deemed necessary to compare its predictions to dynamic instability data collected in well-controlled laboratory experiments. Figure 1 depicts, schematically, a typical laboratory setup [13, 25] consisting of a heated boiling channel with a large unheated bypass line. In our model representation, the components located upstream of the heated channel inlet (e.g., pipes of various diameters and lengths, preheaters, filters, flowmeters, etc.) with the exception of the inlet throttle valve (when present) are lumped into an equivalent inlet pipe of appropriate inertia, friction, and gravitational head. The inlet throttle valve is included separately as an orifice of coefficient K_i. The flow in the inlet

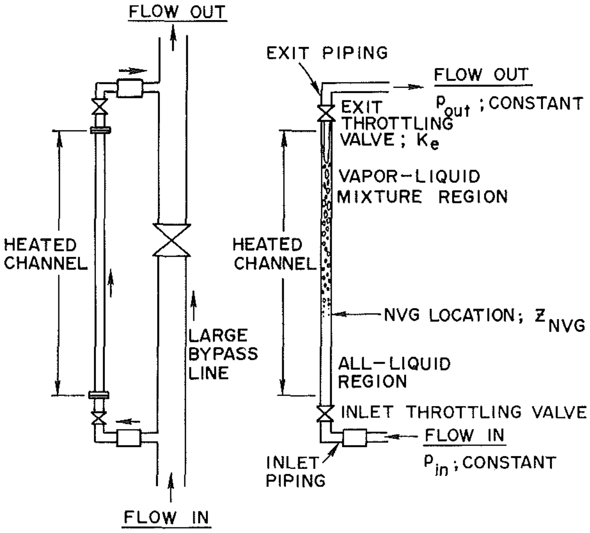

(a) PHYSICAL SYSTEM (b) MODEL

Fig. 1 A heated boiling channel with a large bypass line

---

[1] The majority of these are briefly presented here. Further details can be obtained from [24].

Contributed by the Heat Transfer Division and presented at the 22nd National Heat Transfer Conference, Niagara Falls, NY, August 1984. Manuscript received by the Heat Transfer Division June 25, 1985.

piping is assumed incompressible. Components downstream of the channel exit are modeled as two-phase compressible flow similar to the heated channel. The large unheated bypass line is modeled so as to impose a constant pressure drop boundary condition across the heated channel.[2] The fluid typically enters the heated channel as subcooled liquid and exits as either vapor-liquid mixture or superheated vapor depending upon the operating condition.

The Model

I Phase Conservation Equations. The equations are formulated by considering each phase (k; $k = G$ for vapor, $k = L$ for liquid) separately and then time- and cross-sectional area averaging the local, instantaneous conservation equations [27, 28]. The quasi-one-dimensional, macroscopic equations (written per unit mixture volume) are

Mass

$$\frac{\partial}{\partial t}[\langle \alpha_k \rangle_2 \bar{\bar{\rho}}_k] + \frac{\partial}{\partial z}[\langle \alpha_k \rangle_2 \bar{\bar{\rho}}_k \langle \bar{\bar{u}}_{kz} \rangle_2] = \langle \Gamma_k \rangle_2 \tag{2}$$

z *Momentum*

$$\begin{aligned}
&\frac{\partial}{\partial t}[\langle \alpha_k \rangle_2 \bar{\bar{\rho}}_k \langle \bar{\bar{u}}_{kz} \rangle_2] + \frac{\partial}{\partial z}[C_k \langle \alpha_k \rangle_2 \bar{\bar{\rho}}_k \langle \bar{\bar{u}}_{kz} \rangle_2{}^2] \\
&= -\langle \alpha_k \rangle_2 \frac{\partial \bar{\bar{p}}}{\partial z} + \underbrace{\frac{P_w}{A_{x-s}} \alpha_{kw} \tau_{w,z}}_{\text{(wall friction)}} + g_z \rho_k \langle \alpha_k \rangle_2 + \langle \Gamma_k u_{kI,z} \rangle_2 + \underbrace{F^k{}_{ID,z}}_{\text{(interfacial drag)}} \\
&\underbrace{\pm \bar{\mu} \langle \alpha_d \rangle_2 \langle \alpha_c \rangle_2 \bar{\bar{\rho}}_c \left[\frac{\partial}{\partial t}(\langle \bar{\bar{u}}_{dz} \rangle_2 - \langle \bar{\bar{u}}_{cz} \rangle_2) + \langle \bar{\bar{u}}_{dz} \rangle_2 \bullet \frac{\partial}{\partial z}(\langle \bar{\bar{u}}_{dz} \rangle_2 - \langle \bar{\bar{u}}_{cz} \rangle_2)\right]}_{\text{(added mass effect)}}
\end{aligned} \tag{3}$$

The added mass effect term originates from the interfacial pressure distribution around the discrete phase [29]. The coefficient $\bar{\mu}$ is postulated to have values in the range (0, 1) with 0.5 being a typical value for spherical shape of the discrete phase (e.g., bubble, droplet).

Internal Energy

$$\begin{aligned}
&\frac{\partial}{\partial t}[\langle \alpha_k \rangle_2 \bar{\bar{\rho}}_k \bar{\bar{h}}_k] + \frac{\partial}{\partial z}[\langle \alpha_k \rangle_2 \bar{\bar{\rho}}_k \bar{\bar{h}}_k \langle \bar{\bar{u}}_{kz} \rangle_2] = \frac{\bar{\bar{q}}''_{wk} P_h}{A_{x-s}} + \langle \alpha_k \rangle_2 \frac{\partial \bar{\bar{p}}}{\partial t} \\
&\quad + \langle \bar{\bar{\alpha}}_k \rangle_2 \langle u_{kz} \rangle_2 \frac{\bar{\bar{\partial}} p}{\partial z} + \langle \Gamma_k \bar{\bar{h}}_{kI} \rangle_2 + \underbrace{\left\langle \frac{\bar{\bar{q}}''_{kI}}{L_s} \right\rangle_2}_{\text{(interfacial, } G\text{–}L\text{, heat transfer rate)}}
\end{aligned} \tag{4}$$

In the preceding equations, the following definitions have been introduced

$$\langle \bar{\bar{u}}_{kz} \rangle_2(z, t) \triangleq \frac{\langle \alpha_k(\mathbf{r}, t) \bar{\bar{u}}_{kz}(\mathbf{r}, t) \rangle_2}{\langle \alpha_k \rangle_2(z, t)} \tag{5.1}$$

$$C_k(z, t) \triangleq \frac{\langle \alpha_k \bar{\bar{u}}_{kz}{}^2 \rangle_2}{\langle \alpha_k \rangle_2 \langle \bar{\bar{u}}_{kz} \rangle_2{}^2} \tag{5.2}$$

The two distribution parameters C_G and C_L embody the effects of the transverse distributions of phase fractions and axial velocities. In a sense, these are similar to the distribution parameter C_0 of drift-flux models [30]. For uniform transverse distributions, both are equal to unity. All calculational results presented in this paper correspond to the value of unity for these two parameters.

Since parts of a boiling flow system may be occupied by single-phase liquid or single-phase vapor, consistent macroscopic conservation equations for them will be required. These are obtained by assigning the value of unity to the appropriate phase fraction (α_G or α_L). Furthermore, no G–L interfacial terms will be present.

Nomenclature

a = thermal diffusivity, m^2/s
A_{x-s} = cross-sectional area of flow channel, m^2
A_w = cross-sectional area of heated wall, m^2
B = mass transfer number, equation (28)
C_k = distribution parameter, equation (5.2)
C_p = specific heat at constant pressure, J/kg•K
D = hydraulic diameter of channel, m
D_b = bubble diameter, m
D_d = droplet diameter, m
D_w = equivalent diameter of channel based on wetted perimeter
$\bar{\bar{f}}_k$ = k-phase time average of variable f_k
$\langle f \rangle_2$ = cross-sectional area-averaged value of variable

$$f(\mathbf{r}, t) \triangleq \frac{1}{A_{x-s}} \int_{A_{x-s}} f(\mathbf{r}, t)\, dA$$

g_z = gravitational acceleration in z direction, m/s^2
G = mass flux, kg/m^2•s
h_{f0} = single-phase liquid forced convection heat transfer coefficient, W/m^2•K
h_k = enthalpy per unit mass of phase k, J/kg
h_{ncb} = nucleate boiling heat transfer coefficient, W/m^2•K
k = thermal conductivity
K = orifice coefficient $\triangleq \dfrac{\Delta p}{\rho u^2}$
j_G = vapor volumetric flux, m/s
L_H = heated length of channel, m
$\dfrac{1}{L_s}$ = interfacial (G–L) area concentration, m^{-1}
$N_{\text{sub,in}}$ = subcooling number

$$\triangleq \frac{(h_{\text{sat}} - h_{\text{in}})}{h_{fg}(p_{\text{in}})} \bullet \left[\frac{\rho_L - \rho_G}{\rho_G}\right]_{\text{sat at } p_{\text{in}}}$$

$N_{pch,\text{eq}}$ = equilibrium phase change number

$$\triangleq \frac{q''_w \bullet P_h}{A_{x-s} \bullet h_{fg}(p_{\text{in}})} \bullet \left[\frac{\rho_L - \rho_G}{\rho_L \rho_G}\right]_{\text{sat at } p_{\text{in}}} \bullet \frac{L_H}{u_{Lz_{\text{in}}}}$$

---

[2] This representation is quite appropriate so long as the ratio of the bypass flowrate to the heated channel flowrate remains large (e.g., larger than 20 [26]). However, if the flowrates become comparable, it will be necessary to include the dynamics of the bypass line in the model. This is straightforward.

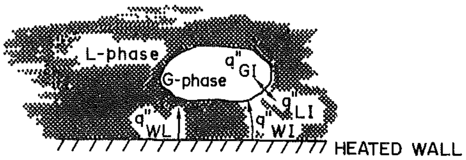

Fig. 2 Wall and interfacial heat fluxes

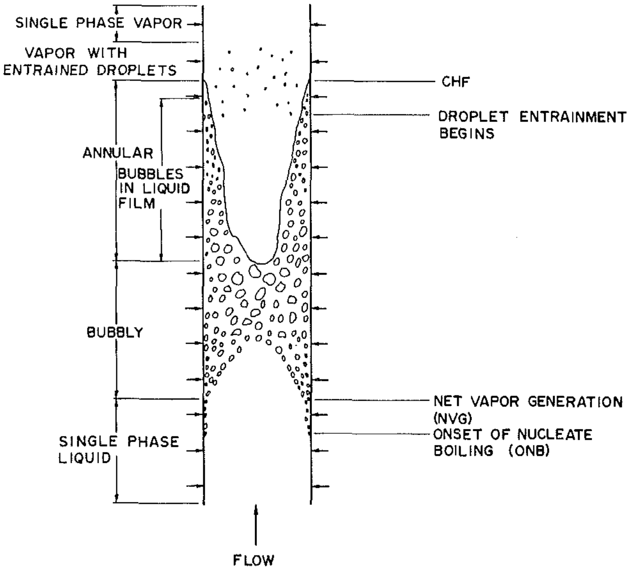

Fig. 3 The flow regimes considered

For the sake of clarity, we will henceforth dispense with the symbols of time averaging and cross-sectional area averaging.

II Heated Channel Wall Energy Equation. The channel wall (typically thin and a good heat conductor) temperature is assumed to be radially uniform, and the wall material properties are assumed to be constant. Per unit length of channel

$$A_w P_w C_w \cdot \frac{\partial T_w(z,t)}{\partial t} = A_w q'''_w(z) - P_h q''_w(z,t) \qquad (6)$$

Note that equation (6) is written such that there is a certain lumped representation in the axial direction also. This lumping is across each finite difference cell only (see Fig. 4).

Equations (2) through (6) comprise the nonlinear governing equations for the system.

III Interfacial (G–L) *Transfer Equations.* The equations are reduced to

Mass

$$\sum_{k=G,L} \Gamma_k = 0 \qquad (7)$$

z Momentum

$$u_{kI,z} = u_{I,z} \qquad (8)$$

where $u_{I,z}$ is the "intrinsic axial velocity" of mass generation [31].

Internal Energy

The equation is (Fig. 2)

$$\sum_{k=G,L} \Gamma_k h_{kI} = -\sum_{k=G,L} \frac{q''_{kI}}{L_s} + \frac{q''_{wI}}{L_s} \qquad (9)$$

Postulating that the *G-L* interface(s) will always be at saturation condition

$$h_{kI} = h_{\mathrm{sat}}(z) \qquad (10)$$

Thus, equation (9) permits calculation of Γ_k if the interfacial heat fluxes and area concentrations are known.

IV The Flow Regime Map and Associated Criteria. Figure 3 shows the simplified flow regime description included in our model. The associated criteria are as follows:

- For onset of nucleate boiling, the wall superheat criterion proposed by Sato and Matsumura is adopted [32]

$$(T_w - T_{\mathrm{sat}}) = \left[\frac{8\sigma T_{\mathrm{sat}} v_{fg} q''_w}{k_L h_{fg}}\right]^{0.5} \qquad (11)$$

Nomenclature (cont.)

p = pressure, Pa
Pe = Peclet number
P_w = wetted perimeter, m
P_h = heated perimeter, m
q''_{kI} = interfacial heat flux, W/m^2
q''_w = wall heat flux, W/m^2
q'''_w = volumetric heat generation rate in wall, W/m^3
q''_{wk} = heat flux from wall to phase k, W/m^2
q''_{wI} = heat flux from wall to G-L interface, W/m^2
Re = Reynolds number
t = time, s
$\mathbf{u}$ = input vector
u_{kz} = k-phase velocity, z component, m/s
v = specific volume, m^3/kg
x_{eq} = thermodynamic equilibrium quality
$\mathbf{x}$ = state vector
z = axial coordinate, m
ΔT_{sub} = subcooling, K
α_k = k-phase fraction
Γ_k = mass generation rate, per unit mixture volume, of phase k, kg/m^{3}s
δ_G = vapor core diameter in annular regime, m
δ_L = two times the liquid film thickness in annular regime, m
μ = dynamic viscosity, N•s/m^2
$\bar{\mu}$ = added mass coefficient
ν = kinematic viscosity, m^2/s
ρ_k = k-phase density, kg/m^3
σ = surface tension, N/m
$\tau_{w,zk}$ = wall friction force on phase k in z direction

Subscripts

b = bubble
c = continuous phase, or critical value
d = discrete phase, or droplet
fg = saturated liquid to saturated vapor transition
i = cell number
I = interface
k = phase
m = mixture
0 = steady-state value
sat = saturation
w = wall

- To mark the beginning of the two-phase flow region, the net vapor generation (NVG) criterion for liquid bulk subcooling is used [13, 33]

$$(\Delta T_{\text{sub}})_{\text{NVG}} = \frac{q''_w}{\left\{\left(\frac{455k_f}{D_h}\right)X + (0.0065GC_p)\,Y\right\}} \tag{12}$$

where

$$X = 1 - \exp\left(-\frac{0.48\times 10^5}{\text{Pe}}\right)$$

$$Y = 1 - \exp(-0.98\times 10^{-5}\,\text{Pe})$$

- Bubbly flow is postulated to exist between the NVG location and $\alpha_G = \alpha_{\text{annular}}$. No slug flow regime is included. Between $\alpha_G = \alpha_{\text{annular}}$ and an α_G so large that nucleate boiling can no longer be sustained at the wall because of the thinness of the liquid film (forced convection evaporation begins here), a vapor core exists along with an annular liquid film at the wall interspersed with vapor bubbles. The value of α_{annular} where the vapor core is begun has been treated as a parameter adjustable between 0.40 and 0.55 in our model. All calculation results presented in this paper correspond to $\alpha_{\text{annular}} = 0.55$.
- Entrainment of liquid droplets into the vapor core is postulated to be dictated by the vapor velocity. A critical velocity suggested by Steen and Wallis [34] is adopted

$$\frac{j_G \mu_G}{\sigma}\left(\frac{\rho_G}{\rho_L}\right)^{1/2} = 2.5\times 10^{-4} \tag{13}$$

- Wall dryout is considered to occur at an equilibrium quality calculated from the critical heat flux correlation for low mass flux proposed by Macbeth [35]

$$(x_{\text{eq}})_{\text{CHF}} = 1.0 - \frac{q''_w}{0.15\,h_{fg}\,(D_w)^{-0.1}(G)^{0.51}} \tag{14}$$

V Other Constitutive Equations

(*i*) *Wall Friction.* For single-phase flow, the Fanning friction coefficient (a function of flow velocity and wall roughness) is used.

For Refrigerant-113 vapor-liquid mixture flow, the Lockhart-Martinelli two-phase flow multiplier [36] is used. For steam-water mixture flow, the Martinelli-Nelson correlation as modified by Mendler [37] is used.[3]

(*ii*) *Interfacial* (G-L) *Drag.* For the bubbly region, the following expression suggested by Rivard and Torrey [38] is used for the interfacial drag on the vapor phase

$$F^G_{ID,z} = -\frac{3}{8}\rho_m\left[C_b\,|u_{Gz} - u_{Lz}| + \frac{24\nu_m}{D_b}\right]A\,(u_{Gz} - u_{Lz}) \tag{15}$$

where A is a function of the interfacial area per unit volume

$$A = \frac{2\alpha_G}{D_b} \tag{16}$$

The coefficient C_b is [39, 40]

$$\begin{aligned} C_b &= 240 && \text{for} \quad \text{Re}_b \le 0.1 \\ &24/\text{Re}_b && \text{for} \quad 0.1 < \text{Re}_b < 1.9 \\ &18.5/\text{Re}_b^{0.6} && \text{for} \quad 1.9 \le \text{Re}_b < 500 \\ &0.44 && \text{for} \quad \text{Re}_b \ge 500 \end{aligned} \tag{17}$$

For the vapor core–annular liquid film interface, a relation proposed by Solbrig et al. [31] is adopted with the exception that their postulated interfacial roughness effect is not included[4]:

$$F^G_{ID,z} = -\frac{0.01\rho_G\,|u_{Gz} - u_{Lz}|\,(u_{Gz} - u_{Lz})}{\delta_G} \tag{18}$$

In both the above cases, $F^L_{ID,z}$, the interfacial drag on the liquid phase, is considered to be equal and opposite to $F^G_{ID,z}$.

For entrained liquid droplets, an expression similar to equation (15) is used

$$F^L_{ID,z} = \frac{3}{8}\rho_m\left[C_d\,|u_{Gz} - u_{Lz}| + \frac{24\nu_m}{D_d}\right]A'\,(u_{Gz} - u_{Lz}) \tag{19}$$

where $A' = 2\alpha_L/D_d$ and the coefficient C_d is calculated from equation (17) except that Re_b is replaced by Re_d. Again, $F^G_{ID,z}$ is considered to be equal and opposite to $F^L_{ID,z}$.

(*iii*) *Wall Heat Transfer.* The heat flux from the channel wall to the fluid in the region upstream of wall dryout is represented by

$$q''_w = h_{f0}(T_w - T_L) + h_{ncb}(T_w - T_{\text{sat}}) \tag{20}$$

The first term on the right-hand side of equation (20) represents forced convection heat transfer to the liquid phase (q''_{wL} in Fig. 2). The second term represents the nucleate boiling contribution which we consider to be transported directly to the G-L interfaces (q''_{wI} in Fig. 2). The superposition scheme is similar to that used by Rohsenow in subcooled partial nucleate boiling regions and by Chen for saturated boiling heat transfer [36]. The nucleate boiling contribution is zero upstream of onset of nucleate boiling. Also, since the flow is considered to be single-phase liquid in the region between the ONB and NVG locations, the nucleate boiling heat transfer contribution is directed back to the liquid. For saturated boiling, the single-phase heat transfer contribution becomes negligible.

The Dittus-Boelter correlation is used for h_{f0}, the single phase liquid heat transfer coefficient. For h_{ncb}, the nucleate boiling heat transfer coefficient, the Chen correlation [41] is used for Refrigerant-113 and the Thom correlation [42] for water.

Downstream of wall dryout, a correlation for heat transfer to vapor with entrained water droplets proposed by Heineman and recommended by Tong [43] is adopted

$$q''_w = h_{\text{mist}}(T_w - T_{\text{sat}}) \tag{21}$$

where

$$h_{\text{mist}} = 0.0157\,\frac{k_f}{D_h}\left(\frac{G_G D_h}{\mu_G}\right)^{0.84}_{\text{film}}\left(\frac{c_{pG}\mu_G}{k_G}\right)^{0.33}_{\text{film}}\left(\frac{L}{D_h}\right)^{-0.04} \tag{22}$$

This heat is directed to the vapor phase via the q''_{wG} term. The subscript "film" in equation (22) denotes that the vapor properties are evaluated at the average of the wall and the bulk vapor temperatures.

Finally, for heat transfer from the wall to vapor only, the Dittus-Boelter correlation is used.

(*iv*) *Interfacial Heat Transfer.* The interfacial heat fluxes are given by (Fig. 2)

$$q''_{GI} = h_{GI}(T_{\text{sat}} - T_G) \tag{23}$$

$$q''_{LI} = h_{LI}(T_{\text{sat}} - T_L) \tag{24}$$

where h_{GI} and h_{LI} are the heat transfer coefficients on the vapor side and the liquid side of the interface, respectively.

At vapor bubble surface, the following expressions are used for the heat transfer coefficients [31, 28]

$$h_{GI} = \frac{16.134k_G}{D_b} \tag{25}$$

---

[3] The reason for including the Mendler modification is the excellent agreement between calculated and measured pressure drops in steam-water flow obtained by Takitani et al. [25] in their experiments.

[4] Sufficient interfacial drag was achieved from the remaining bubbles in the annular liquid film.

$$h_{LI}=k_L\left[\frac{2.0}{D_b}+\left\{\frac{|u_{Gz}-u_{Lz}|}{\mathrm{Pr}_L^{0.33}\pi a_L D_b}\right\}^{0.5}\right] \tag{26}$$

For annular flow, the Dittus–Boelter correlation based on the diameter of the vapor core (δ_G) is used to calculate h_{GI}. For h_{LI}, the larger of the following two values is adopted

$$\frac{4k_L}{\delta_L} \text{ (conduction through liquid film) or} \tag{27}$$

$$\frac{0.023\,\mathrm{Re}_L^{0.8}\mathrm{Pr}_L^{0.4}k_L}{\delta_L} \text{ (turbulent liquid film flow)}$$

where δ_L is taken to be equal to twice the liquid film thickness. The liquid film Reynolds number Re_L is defined as $\rho_L|u_{Gz}-u_{Lz}|\delta_L/\mu_L$.

At liquid droplet surface, the relations used are

$$h_{GI}=\frac{k_G}{(1+B)}\left[\frac{2.0}{D_d}+\left\{\frac{|u_{Gz}-u_{Lz}|}{\mathrm{Pr}_G^{0.33}\pi a_G D_d}\right\}^{0.5}\right] \tag{28}$$

$$h_{LI}=\frac{16.134k_L}{D_d} \tag{29}$$

In equation (28), the mass transfer number B [44] defined as $(h_G-h_L)/h_{fg}$, has been introduced. Otherwise, it is the dual of the bubble interface heat transfer coefficient correlation.

(v) *Interfacial Area Concentration.* For bubbly flow, the relation adopted is

$$\frac{1}{L_s}=\frac{6\alpha_G}{D_b} \tag{30}$$

where D_b, the bubble diameter, is postulated to follow the behavior

$$D_b=(\text{a constant})\bullet\alpha_G{}^{0.5} \tag{31}$$

The exponent of 0.5 in equation (31) is introduced by us in lieu of the commonly used value of 0.33 to account for some coalescence. That an exponent larger in value than 0.33 implies bubble coalescence can be seen from calculation of bubble number density in the fluid as a function of α_G. Either half the channel transverse dimension or the liquid film thickness (in case of annular flow), whichever is applicable, is prescribed as the upper limit on the calculated value of bubble diameter. The constant coefficient in equation (31) is adjusted in value *once* at the outset for each fluid (water, Refrigerant-113, etc.) so that the steady-state vapor fraction axial profile predicted by the model matches *one* experimental data run well. It is then maintained invariant from then on. We note that this coefficient in equation (31) is the only other adjustable parameter (in addition to α_{annular}) contained in the model.[5]

For annular flow, we use

$$\frac{1}{L_s}=\frac{4\delta_G}{D^2} \tag{32}$$

For vapor with entrained droplets, the expression used is

$$\frac{1}{L_s}=\frac{6\alpha_L}{D_d} \tag{33}$$

where D_d, the droplet diameter, is calculated from a relation proposed by Cumo and recommended by Chen [45]

$$D_d=123.1\left(1-\frac{p}{p_c}\right)^{0.31}\frac{\mu_L}{Gx_{\text{eq}}} \tag{34}$$

(vi) *Thermodynamic and Transport Properties.* Relations from TRAC reports (e.g., [46]) as well as some developed on the basis of Keenan et al. [47] are used for steam and water. For Refrigerant-113, data from DuPont bulletins [48] are used.

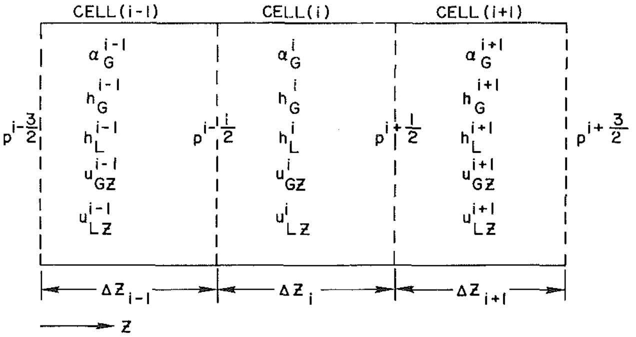

Fig. 4 Discrete cells and state variables

Solution Strategy

The analysis proceeds as follows:

Step 1 Obtaining the State Equation Set. The system of partial differential equations, equations (2)–(4), (6), is converted into a system of ordinary differential equations with time (t) as the only independent variable, by finite differencing in the space (z) coordinate. The flow channel is subdivided into discrete cells (i; $i=1,\ldots,N$) as shown in Fig. 4. Finite differencing is performed in accordance with the second upwind (donor cell) scheme which is both conservative and transportive [49]. As an example, the *k-phase internal energy equation*, equation (4), becomes, for a typical cell i

$$\frac{d}{dt}(\alpha_{ki}\rho_{ki}h_{ki})-\alpha_{ki}\frac{dp_i}{dt}=$$

$$\frac{\alpha_{k_{i+1/2}}\rho_{k_{i+1/2}}h_{k_{i+1/2}}u_{kz_{i+1/2}}-\alpha_{k_{i-1/2}}\rho_{k_{i-1/2}}h_{k_{i-1/2}}u_{kz_{i-1/2}}}{\Delta z_i}$$

$$+\frac{q''_{wki}\bullet P_{hi}}{Ax-s_i}+\alpha_{ki}u_{ki}\bullet\frac{(p_{i+1/2}-p_{i-1/2})}{\Delta z_i}$$

$$+\Gamma_{ki}h_{k_{\text{sat}i}}+\left(\frac{q''_{kI}}{L_s}\right)_i \tag{35}$$

Note that the subscripts ($i+1/2$) and ($i-1/2$) denote cell junction values. These values, with the exception of pressure p, are assigned via donor celling. The pressure is defined at the junctions.

Now using the following relation

$$\frac{\partial\rho_k}{\partial t}=\frac{1}{u_{k1}}\bullet\frac{\partial p}{\partial t}+\frac{1}{u_{k2}}\bullet\frac{\partial h_k}{\partial t} \tag{36}$$

where

$$\frac{1}{u_{k1}}=\left(\frac{\partial\rho_k}{\partial p}\right)_{h_k}$$

$$\frac{1}{u_{k2}}=\left(\frac{\partial\rho_k}{\partial h_k}\right)_p$$

Equation (35) can be rewritten as:

$$\rho_{ki}\alpha_{ki}+\frac{\alpha_{ki}h_{ki}}{u_{k_{2i}}}\bullet\frac{dh_{ki}}{dt}+\rho_{ki}h_{ki}\frac{d\alpha_{ki}}{dt}+\frac{\alpha_{ki}h_{ki}}{u_{k_{1i}}}$$

$$-\alpha_{ki}\bullet\frac{dp_i}{dt}=(\text{the right-hand side}) \tag{37}$$

Both the NVG and the dryout (or CHF) locations along the channel can be expected to move during transients. In an-

---

[5] It may be possible to model this coefficient in terms of the reduced pressure of the system, the latent heat of vaporization of the liquid, and the surface tension.

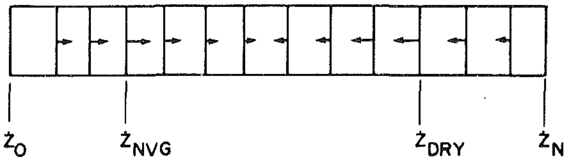

Fig. 5 Moving cell boundaries

ticipation of large-amplitude movements (oscillations) that could be encountered during nonlinear DWO simulations to be carried out in the future, a moving cell boundary formulation was devised. This scheme can be thought of as describing the movements of three accordians in series. The upstream boundary of the first heated cell (z_0) and the downstream boundary of the last heated cell (z_N) are kept fixed. The calculated movements of the NVG point (z_{NVG}) and the wall dryout point (z_{dry}) are then considered as inputs to the determination of the movement of all the other cell boundaries. A typical scenario is shown in Fig. 5. Additional terms arise in the finite-differenced equations in accounting for the moving cell boundaries. These can be obtained via a procedure, suggested by Bein and Yahlom [50], which is based on the use of Leibnitz's rule for differentiating an integral and involves the time derivative of the NVG and dryout locations ($\dot{z}_{\text{NVG}}$, $\dot{z}_{\text{dry}}$). Note that z_{NVG} and z_{dry} become additional state variables.

The nonlinear state equation set has now been obtained

$$[M]\dot{\mathbf{x}} = \mathbf{f}(\mathbf{x}, \mathbf{u}) \tag{38}$$

where **x** is the state vector

$$[\ldots; T_{w_i}, p_i, h_{Gi}, h_{Li}, \alpha_{Gi}, u_{Gz_i}, u_{Lz_i}; \ldots]^T \tag{39}$$

and **u** is the input vector. The input vector will consist of input variables that we may wish to study the system response to (e.g., heat input rate to the channel, pressure, etc.).

Step 2 Calculation of the Steady-State Operating Point. For specific inputs ($\mathbf{u} = \mathbf{u}_0$) and boundary conditions (e.g., constant pressure drop across the heated channel), the system steady-state operating point $\mathbf{x}_0$ is solved for

$$0 = \mathbf{f}(\mathbf{x}_0, \mathbf{u}_0) \tag{40}$$

Our solution proceeds cell by cell, in a march from the system inlet to the outlet. A simple and efficient numerical method for the solution of the simultaneous nonlinear equation set in many variables, equation (40), was devised and has been reported elsewhere [51].

Step 3 Linear Stability Analysis. Equation set (38) is linearized, by small perturbation method, around the steady-state operating point to yield

$$[M_0]\frac{d(\delta\mathbf{x})}{dt} = [N_0](\delta\mathbf{x}) + [Q_0](\delta\mathbf{u}) \tag{41}$$

The perturbation state vector $\delta\mathbf{x}$ in equation (41) is comprised of the set of state variables

$$\delta\mathbf{x} = [\ldots; \delta T_{wi}, \delta p_i, \delta h_{Gi}, \delta h_{Li}, \delta\alpha_{Gi}, \delta u_{Gzi}, \delta u_{Lzi}; \ldots]^T \tag{42}$$

The elements of the matrix $[M_0]$ are easily calculated by analytical means. The elements of the matrix $[N_0]$ are evaluated numerically by computer. The vector differential equation (41) can be rewritten as

$$\frac{d(\delta\mathbf{x})}{dt} = ([M_0]^{-1}[N_0])(\delta\mathbf{x}) + ([M_0]^{-1}[Q_0])(\delta\mathbf{u}) \tag{43}$$

The eigenvalues of the matrix $([M_0]^{-1}[N_0])$ determine the inherent linear stability of the system. Eigenvalue(s) with positive real part indicate instability. For oscillatory instabilities such as DWO, this means that two complex conjugate eigenvalues having slightly positive real part appear. While the positive real part indicates instability, the imaginary part yields the oscillation frequency. It is interesting to note that it will be possible to locate dynamic instabilities over the entire frequency range (from low to high frequencies) as well as static instability of the Ledinegg type (zero frequency) via inspection of the eigenvalues.

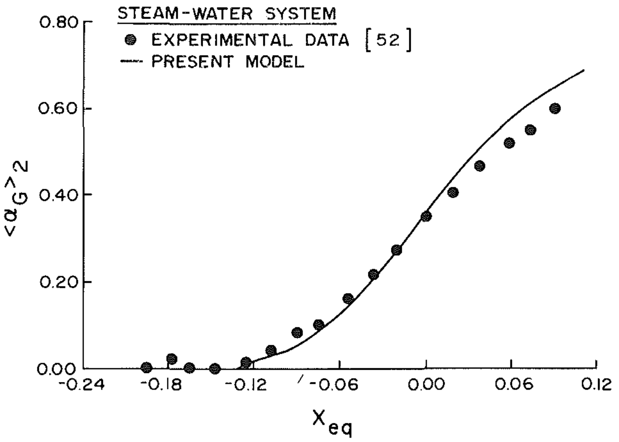

Fig. 6 Steady-state vapor fraction profiles along a heated channel

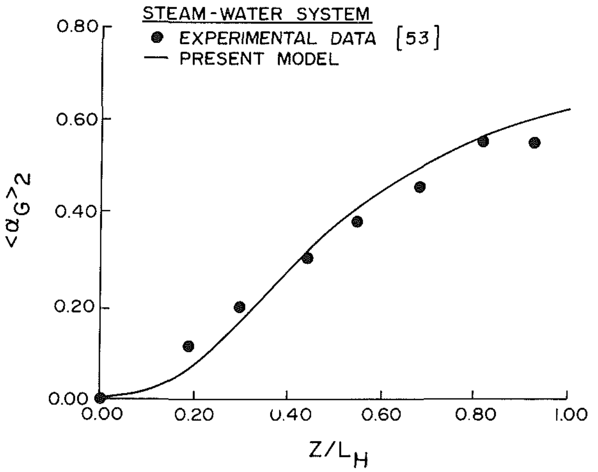

Fig. 7 Steady-state vapor fraction profile along a rod bundle

Results

Steady-State Analysis. Calculations were carried out for several water and Refrigerant-113 systems. Results obtained were compared with experimental data whenever available. The comparisons were generally quite satisfactory. Two examples are presented in the following.

Figure 6 shows the predicted and experimentally obtained vapor fraction profile along a heated channel for the following situation [52]:

test fluid:	water
heated channel:	tube, 12 mm i.d.
inlet mass flux:	961 kg/m^2•s
inlet pressure:	6.84 MPa
inlet temperature:	466 K
wall heat flux:	1.13×10^6 W/m^2

Figure 7 shows the predicted and experimentally obtained vapor fraction profile along a heated rod bundle for experiment No. 313 009 [53]:

heated channel:	36-rod bundle
inlet mass flux:	1107 kg/m^2•s
exit pressure:	5.00 MPa
inlet subcooling:	4.4 K
heat input rate:	2980 kW

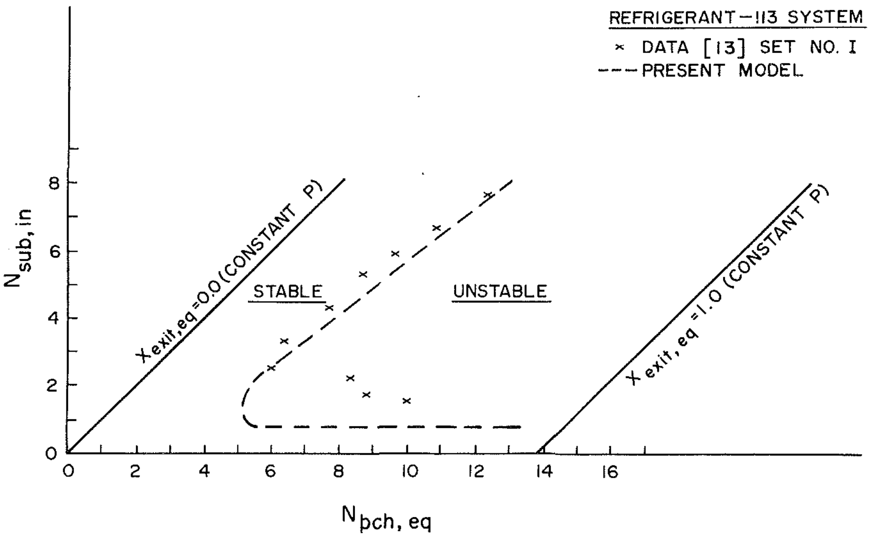

Fig. 8 Comparison of experimental data on DWO threshold with model predictions

Table 1 Comparison with steam-water system DWO threshold data [25]

Experiment No.	p (Pa)	G (kg/m^2·s)	$T_{L_{in}}$ (K)	K_{inlet}	Experiment Q_{in} (kW)	Experiment τ_{osc} (s)	Model Q_{in} (kW)	Model τ_{osc} (s)
128-07	4.255×10^6	318.	425.1	250	92.5	6.0	88.5	6.5
1008-06	4.255×10^6	298.	417.1	250	86.1	6.5	86.1	7.1
1125-33	4.083×10^6	220.	419.1	250	63.6	9.0	62.3	9.2
121-04	4.296×10^6	335.	431.1	260	96.7	6.0	93.6	6.0
122-05	4.053×10^6	220.	422.1	260	61.9	9.0	62.3	9.0

Data from the FRIGG experiments [53] have been matched well previously by detailed three-dimensional boiling flow models such as [54].

Linear Stability Analysis. Analyses have been carried out for both Refrigerant-113 [13] and water [25] systems. The results to be presented here pertain to a 25-cell representation of the heated channel for the Refrigerant-113 system and a 28-cell representation for the water system. In both cases, the results obtained were invariant for larger number of cells. In our calculations, the instability threshold was obtained for a particular system by beginning with a nominal operating condition which was stable and then increasing the heat input rate in small steps until the system became slightly unstable.

Figure 8 shows a comparison of the predicted DWO thresholds with experimental data for the Refrigerant-113 system [13]. The subcooling number ($N_{\text{sub,in}}$) versus equilibrium phase change number ($N_{pch,\text{eq}}$) plane introduced by Ishii and Zuber [11] is used. The agreement is quite good.

Table 1 shows a comparison of DWO threshold data for the water system [25] with our predictions. Again, the agreement is satisfactory.

It should be noted here that the frequency of the limit cycle that a nonlinear system settles into may not be exactly the same as the oscillation frequency exhibited at the instability threshold. Experimental data such as in Table 1 reflect the limit cycle frequency. A linear analysis such as the present work yields the oscillation frequency at the instability threshold.

Parameter Sensitivity Study. It is important to carry out detailed parametric study of a model such as the one presented here for it is only in this that the characteristic features of the system as a whole emerge. The following were investigated for their effects on the predicted instability threshold results:

(*i*) *Inlet throttling,* K_i. It was found that increasing inlet throttling is stabilizing; this is in agreement with experimental and analytical findings of earlier investigators.

(*ii*) *Outlet throttling,* K_e. Increasing this is destabilizing; however, sensitivity of a flow system to this parameter is not as strong as it is to K_i.

(*iii*) *System pressure,* p. Increasing the system pressure is generally stabilizing.[6]

(*iv*) *Frictional pressure drop.* Increasing this component of the overall pressure drop in the two-phase region of the heated channel is generally destabilizing, whereas increasing it in the all-liquid region upstream is generally stabilizing.

(*v*) *Interfacial drag.* Increasing or decreasing this decreases or increases the relative velocity between the two phases; its effect on the predicted instability threshold does not exhibit any definite trend (either stabilizing or destabilizing).

(*vi*) *Added mass coefficient,* $\bar{\mu}$. Variations in the value of this parameter within the allowed range (0 to 1) did not affect the predicted values of the instability threshold significantly.

(*vii*) *The distribution parameters,* C_G *and* C_L. Calculations based on postulated transverse distributions of phase fractions and axial velocities indicate that both parameters can range in value from slightly less than 1 to approximately 1.4 depending on the flow regime [28]; in general, dynamic threshold predictions were found to be insensitive to changes in these two parameters.

(*viii*) Our calculations indicate that flow channels with large inlet throttling coefficient (K_i), such as the experimental system of [25], typically require relatively large increases in

---

[6] It should be noted that the stability of systems such as BWRs may be affected differently by changes in system pressure due to neutronic feedback.

heat input rate (compared to channels with small inlet throttling, e.g., [13]) to go from a barely stable operating condition to a slightly unstable one. This renders accurate modeling of systems such as [25] all the more important.

Discussion

Some noteworthy features of the model presented here are summarized in the following:

1 The NVG location is allowed to move with time in accordance with the dictates of the governing conservation equations and criterion; for example, it can oscillate in response to flow oscillation; the formulation here is of the "movable cell boundary" type.

2 The wall CHF (or dryout) location is modeled similarly.

3 Although the flow regime map incorporated in the model is a simple one, it is thought to represent the systems studied adequately; a more complicated map can be included without much difficulty.

4 Two parameters were treated as adjustable in this model. One is α_{annular}, the α_G value where a vapor core region is postulated to begin in the channel. The range of variation allowed for α_{annular} is taken to be from 0.40 to 0.55. Calculations indicate that values equal to or slightly less than 0.50 yield somewhat better agreement of predicted vapor fraction profiles with experimental data when compared to the presently adopted value of 0.55. However, the corresponding dynamic instability threshold results would be slightly worse (by anywhere between two and four percent).

5 A two-fluid model description of transient boiling flow is only as good as the constitutive relations adopted; we have tried to use well-accepted relations and criteria whenever possible. Clearly however, much remains to be done in this area.

6 It is a simple matter to investigate the frequency response of a boiling flow system to various input perturbations once the linear time-domain model has been constructed.

7 The time-domain linear model presented here predicts the dynamic instability threshold for two different systems and fluids well. This work is the first step toward developing a nonlinear model of such instabilities.

Acknowledgments

This work was supported by Electric Power Research Institute, Nuclear Power Division, under research project RP 495-2.

References

1 Bergles, A. E., "Instabilities in Two-Phase Flow Systems," *Two-Phase Flows and Heat Transfer in the Power and Process Industries*, Hemisphere, Washington, 1981.

2 Stenning, A. H., and Veziroglu, T. N., "Flow Oscillation Modes in Forced Convection Boiling," *Proc. 1965 Heat Transfer and Fluid Mechanics Institute*, Stanford University Press, 1965, pp. 301-316.

3 Lahey, R. T., Jr., and Drew, D. A., "An Assessment of the Literature Related to LWR Instability Modes," NUREG/CR-1414, 1980.

4 Neal, L. G., Zivi, S. M., and Wright, R. W., "The Mechanism of Hydrodynamic Instabilities in Boiling Flow Systems," *Proc. Symposium on Two-Phase Flow Dynamics*, Eindhoven, 1967.

5 Zuber, N., "Flow Excursions and Oscillation in Boiling Two-Phase Flow Systems With Heat Addition," *Proc. Symposium on Two-Phase Flow Dynamics*, Eindhoven, 1967.

6 Yadigaroglu, G., and Bergles, A. E., "An Experimental and Theoretical Study of Density-Wave Oscillations in Two-Phase Flow," MIT Report DSR 74 629-3, 1969; Yadigaroglu, G., and Bergles, A. E., "Fundamental and Higher-Mode Density-Wave Oscillations in Two-Phase Flow," ASME JOURNAL OF HEAT TRANSFER, Vol. 94, 1972, pp. 189-195.

7 Waaranpera, Y., and Anderson, S., "BWR Stability Testing: Reaching the Limit Cycle Threshold at Natural Circulation," *Trans. American Nuclear Society*, Vol. 39, 1981, p. 868.

8 France, D. M., Roy, R. P., Carlson, R. D., and Chiang, T., "Dynamic Stability Experiments in Sodium-Heated Steam Generators," *Liquid Metal Engineering and Technology*, British Nuclear Energy Society, 1984, Vol. 2, pp. 195-201.

9 Jones, A. B., "Hydrodynamic Stability of a Boiling Channel," KAPL-2170, 1961.

10 Efferding, L., "DYNAM—A Digital Computer Program for Study of the Dynamic Stability of Once-Through Boiling Flow With Steam Superheat," GAMD-8656, 1968.

11 Ishii, M., and Zuber, N., "Thermally Induced Flow Instabilities in Two-Phase Mixtures," *Proc. Fourth International Heat Transfer Conference*, Paris, 1970, Vol. V, Paper B 5.11.

12 Lahey, R. T., and Yadigaroglu, G., "A Lagrangian Analysis of Two-Phase Hydrodynamics and Nuclear-Coupled Density-Wave Oscillations," *Proc. Fifth International Heat Transfer Conference*, Tokyo, 1974, Vol. IV, Paper B 5.9.

13 Saha, P., "Thermally Induced Two-Phase Flow Instabilities Including the Effect of Thermal Non-Equilibrium Between the Phases," Ph.D. thesis, Georgia Institute of Technology, 1974; Saha, P., Ishii, M., and Zuber, N., "An Experimental Investigation of Thermally-Induced Flow Oscillations in Two-Phase Systems," ASME JOURNAL OF HEAT TRANSFER, Vol. 98, 1976, pp. 616-622.

14 Chan, K. C., "Thermal-Hydraulic Stability Analysis of Steam Generators," Ph.D. thesis, University of California, Berkeley, 1979; Chan, K. C., and Yadigaroglu, G., "STMFREQ—An Advanced Code for Stability Analysis of Steam Generators," *Transactions ANS*, Vol. 33, 1979, pp. 980-982.

15 Park, G. C., Podowski, M., Becker, M., and Lahey, R. T., Jr., "The Development of NUFREQ-N, an Analytical Model for the Stability Analysis of Nuclear-Coupled Density-Wave Oscillations in Boiling Water Nuclear Reactor," NUREG/CR-3375, July 1983.

16 Takahashi, R., and Futami, T., "Theoretical Study of Flow Instability of a Sodium-Heated Steam Generator," *Nuclear Engineering and Design*, Vol. 41, 1977, pp. 193-204.

17 Takitani, K., and Sakano, K., "Density-Wave Instability in Once-Through Boiling Flow Systems (III)—Distributed Parameter Model," *J. Nuclear Science and Technology*, Vol. 16, No. 1, 1979, pp. 16-29.

18 Reisch, F., and Vayssier, G., "A Nonlinear Digital Computer Model Requiring Short Computation Time for Studies Concerning the Hydrodynamics of Boiling Water Reactors," *Nuclear Engineering and Design*, Vol. 9, 1969, pp. 196-210.

19 Brimley, W., Nicoll, W. B., and Strong, A. B., "Flow Oscillations in Fixed Pressure-Drop Flow-Boiling Systems With Random Excitation," *International Journal of Heat and Mass Transfer*, Vol. 19, 1976, pp. 1379-1386.

20 Kornfilt, J., and Lee, J. C., "Stability Analysis of Boiling Water Systems and Steam Generators," *Proc. Nuclear Reactor Thermal-Hydraulics*, Santa Barbara, 1983, Vol. II, pp. 1012-1019.

21 Schultz, D. G., and Melsa, J. L., *State Functions and Linear Control Systems*, McGraw-Hill, New York, 1967.

22 Takahashi, Y., Rabins, M. J., and Auslander, D. M., *Control and Dynamic Systems*, Addison-Wesley, 1970.

23 Su, M.-G., Roy, R. P., Dykhuizen, R. C., and Kalra, S. P., "Frequency Response of Boiling Flow Systems Based on a Two-Fluid Model," 1985 (to be published).

24 Dykhuizen, R. C., "A Two-Fluid Model of Dynamic Instability for Boiling Flow Systems," Ph.D. thesis, Department of Mechanical and Aerospace Engineering, Arizona State University, 1985.

25 Takitani, K., and Takemura, T., "Density-Wave Instability in Once-Through Boiling Flow Systems (I)—Experiment," *Journal of Nuclear Science and Technology*, Vol. 15, No. 5, 1978, pp. 355-364.

26 Carver, M. B., "Effect of Bypass Characteristics on Parallel-Channel Flow Instabilities," *Proc. Instn. Mech. Engineers*, Vol. 184, No. 3G, Paper 11, 1969-70.

27 Ishii, M., *Thermo-Fluid Dynamic Theory of Two-Phase Flow*, Eyrolles, Paris, 1975.

28 Roy, R. P., and Ho, S., "An Unequal Velocity, Unequal Temperature Two-Fluid Description of Transient Vapor-Liquid Flow in Channels," *Nuclear Science and Engineering*, Vol. 81, 1982, pp. 459-467.

29 Stuhmiller, J. H., "The Influence of Interfacial Pressure Forces on the Character of Two-Phase Flow Model Equations," *International Journal of Multiphase Flow*, Vol. 3, 1977, pp. 551-560.

30 Zuber, N., and Findlay, J. A., "Average Volumetric Concentration in Two-Phase Flow Systems," ASME JOURNAL OF HEAT TRANSFER, Vol. 87, 1965, pp. 453-468.

31 Solbrig, C. W., McFadden, J. H., Lyczkowski, R. W., and Hughes, E. D., "Heat Transfer and Friction Correlations Required to Describe Steam-Water Behaviour in Nuclear Safety Studies," Fifteenth National Heat Transfer Conference, San Francisco, 1975.

32 Sato, T., and Matsumura, H., "On the Condition of Incipient Subcooled Boiling With Forced Convection," *Bulletin Japan Society of Mechanical Engineers*, Vol. 7-26, 1964, pp. 392-398.

33 Jain, P. K., Nourmohammadi, K., and Roy, R. P., "A Study of Forced Convection Subcooled Boiling in Heated Annular Channels," *Nuclear Engineering and Design*, Vol. 60, 1980, pp. 401-411.

34 Wallis, G. B., *One-Dimensional Two-Phase Flow*, McGraw-Hill, New York, 1969.

35 Tong, L. S., "Boiling Crisis and Critical Heat Flux," AEC Critical Review Series, 1972.

36 Collier, J. G., *Convective Boiling and Condensation*, McGraw-Hill, New York, 1981.

37 Tong, L. S., *Boiling Heat Transfer and Two-Phase Flow*, Wiley, New York, 1965.

38 Rivard, W. C., and Torrey, M. C., "Numerical Calculation of Flashing From Long Pipes Using a Two-Fluid Model," LA-6104-MS, 1975.

39 Bird, R. B., Stewart, W. E., and Lightfoot, E. N., *Transport Phenomena*, Wiley, New York, 1960.

40 Rohatgi, U. S., Jo, S., and Neymotin, L., "Constitutive Relations in TRAC-PD2," NUREG/CR-3073, 1982.

41 Chen, J. C., "Correlation for Boiling Heat Transfer to Saturated Fluids in Convective Flow," *I and EC Process Design and Development*, Vol. 5, 1966, p. 332.

42 Thom, J. R. S., et al., "Boiling in Subcooled Water During Flow up Heated Tubes or Annuli," *Proc. Inst. Mech. Eng.*, Vol. 180, 1965, p. 226.

43 Tong, L. S., "Heat Transfer Mechanisms in Nucleate and Film Boiling," *Nuclear Engineering and Design*, Vol. 21, 1972, pp. 1-25.

44 Yuen, M. C., and Chen, L. W., "Heat Transfer Measurements of Evaporating Water Droplets," *International Journal of Heat and Mass Transfer*, Vol. 21, 1978, pp. 537-542.

45 Chen, J. C., Ozkaynak, F. T., and Sundaram, R. K., "Vapor Heat Transfer in Post-CHF Region Including the Effect of Thermodynamic Non-Equilibrium" *Nuclear Engineering and Design*, Vol. 51, 1979, pp. 143-155.

46 "TRAC-P1A, An Advanced Best-Estimate Computer Program for PWR LOCA Analysis," NUREG/CR-0065, LA-7777-MS, 1979.

47 Keenan, J. H., Keyes, F. G., Hill, P. G., and Moore, J. G., *Steam Table (SI Units)*, Wiley, New York, 1978.

48 E. I. DuPont De Nemours and Co., Bulletins FST-11, -1, E-113, 1976-1979.

49 Roache, P. J., *Computational Fluid Dynamics*, Hermosa, 1976.

50 Bein, M., and Yahlom, R., "Dynamic Simulation of an LMFBR Steam Generator," *Proc. Second Power Plant Dynamics, Control and Testing Symposium*, Knoxville, TN, 1975.

51 Dykhuizen, R. C., Roy, R. P., and Kalra, S. P., "Numerical Method for Solution of Simultaneous Nonlinear Equations and Application to Two-Fluid Model Equations of Boiling Flow," *Numerical Heat Transfer*, Vol. 7, 1984, pp. 225-234.

52 Bartolomei, G. G., et al., "An Experimental Investigation of True Volumetric Vapor Content With Saturated Boiling in Tubes," *Thermal Engineering*, Vol. 29, No. 3, 1982, pp. 132-135.

53 Nylund, O., et al., "FRIGG Loop Project," FRIGG-2, ASEA-ATOM, 1968.

54 Singhal, A. K., et al., "ATHOS—A Computer Program for Thermal-Hydraulic Analysis of Steam Generators," Vol. 1-3, EPRI NP-2698-CCM, 1982.

The Effect of Turbulence-Suspended Light Particles on Dryout for Pool Boiling From a Horizontal Surface

V. P. Carey
Assoc. Mem. ASME

E. Markovitz[1]

Y. K. Chuah[2]

Department of Mechanical Engineering,
University of California,
Berkeley, CA 94720

Experimental measurements are reported which indicate the relationship between particle loading and dryout heat flux for pool boiling from a horizontal surface covered with a mixture of water and light particles. This study specifically examines the dryout conditions for particles which have low settling velocities and are easily suspended by the bubble-generated turbulence in the liquid pool above the surface. Dryout data are presented for pool boiling of mixtures of saturated water and glass beads with diameters ranging from 0.105 mm to 0.475 mm. Data are also presented for methanol and glass beads. At high particle loadings, a portion of the load is suspended, while the remainder forms a layer on the surface. The dryout mechanism apparently is similar to the Helmholtz instability mechanism previously identified as the cause of dryout in shallow beds of heavy particles. However, the suspension of particles in the liquid pool produces very unusual trends in the dryout data. In particular, conditions have been observed in which a decrease *in the heat flux can cause dryout to occur. An approximate theoretical model of the particle suspension mechanism is proposed and used to predict the dryout conditions for very light particles. This model explains the trends in the data and predicts dryout conditions which compare favorably with the experimental results for very light particles.*

Introduction

In a number of technological applications, circumstances may arise which cause particulate contaminants to be introduced into a liquid system in which boiling occurs. These particles may settle to form a layer on horizontal surfaces, or, if they are very light, they may be suspended by turbulence in the liquid.

Residue from manufacturing processes, corrosion products, and precipitation of dissolved contaminants are possible sources of particulates in evaporators in power or refrigeration systems. In time, a layer of accumulated particles may cover portions of the heated surface, locally altering the vaporization process. In chemical and food processing it is often necessary to boil solid-liquid slurries in which particles tend to settle into a layer on horizontal surfaces. Boiling in an unconfined layer of debris covering a heated surface can also occur after a hypothetical accident in a liquid-cooled nuclear reactor.

Of particular importance in the applications described above is the effect which a layer of unconfined particles has on the dryout or critical heat flux. Knowledge of the effect of a particle layer on dryout is of special importance for analysis of post-accident reactor heat transfer, since dryout near heat dissipating surfaces may cause overheating and loss of structural integrity. As a result, there have been several studies of the dryout behavior in particle beds typical of post-accident situations. Gabor et al. [1] conducted experiments to determine the dryout heat flux in beds of unconfined UO_2 particles. The particles were a mixture of diameters between 100 μm and 1000 μm. The variation of dryout heat flux with bed loading was determined experimentally for volumetrically heated and bottom-heated beds saturated with either water or sodium.

In the water tests, Gabor et al. [1] observed the formation of channels which facilitated the escape of vapor. In shallow beds, these channels extend through the full depth of the bed, while for deep beds, they exist only in the top portion of the bed. The reported "spontaneous leveling" of the beds suggests that they were at least partially fluidized.

Dhir and Catton [2] presented additional dryout heat flux data for inductively heated beds of unconfined steel and lead particles distributed in size between 295 μm and 787 μm. Water, methanol, and acetone were used as coolants. A semitheoretical model was presented for dryout for a bottom-heated shallow layer which postulated vapor choking above the layer as the mechanism for dryout. Correlations for deep-bed dryout were also presented. As bed depth is increased, the data of Gabor et al. [1] for bottom-heated beds suggest that the dryout mechanism undergoes a transition from the vapor choking at shallow beds to a mechanism similar to that for rigid porous media in deep beds.

Additional dryout heat flux data were recently obtained by Jones [3] for bottom-heated beds of lead, copper, glass, and steel beads with sizes between 390 μm and 1100 μm. Water and organic fluids were used as coolants.

Most of the dryout data obtained in the studies described above have been for layers of particles with high terminal velocities. This is largely a consequence of the expectation that debris from an accident in a nuclear reactor will consist mostly of large heavy metal particles. However, the particulates which result from corrosion or solute precipitation in boiling systems are expected to be small and light with correspondingly low terminal velocities. In addition, chemical and food processing often requires boiling of slurries which contain fine, low-density particles with low settling velocities.

When rigorous boiling occurs on a horizontal heated surface in a liquid containing heavy particles, the particles are usually confined by gravity to a layer on the surface. If this layer is thin it will tend to be fluidized by the upward vapor and liquid motion through it. If a similar system contains very light particles, however, the distribution of particles will

---

[1] Present address: Lockheed Missiles and Space Company, Sunnyvale, CA 94086.

[2] Present address: Solar Energy Research Institute, Golden, CO 80401.

Contributed by the Heat Transfer Division for publication in the JOURNAL OF HEAT TRANSFER. Manuscript received by the Heat Transfer Division September 14, 1984.

differ in one important respect. For particles with very low terminal velocities, the bubble-generated turbulence in the liquid above the surface will suspend some of the particles.

The capacity of the turbulence in the liquid pool to suspend particles above the layer on the heated surface adds a new element to the dryout behavior of the system. The objective of the present study was to determine the effect which this added mechanism has on dryout. Dryout conditions were experimentally determined for bottom-heated mixtures of glass beads in water or methanol. Our experimental results indicate that suspension of particulates by turbulence in the liquid can produce unusual dryout behavior. In particular, our results indicate that conditions can arise in which decreasing the heat flux can cause dryout. In addition to experimental measurements, a semitheoretical model of the dryout conditions is proposed which incorporates the effect of suspended particles. This model predicts dryout conditions which agree well with our data for very light particles.

Experimental Results

The apparatus used in the experiments is shown in Fig. 1. The copper cylinder was heated from below by an electric resistance heater. The heat flux to the top surface of the cylinder was determined from thermocouple measurements of the temperature gradient in the cylinder. The mean surface temperature was also determined by extrapolating the measured subsurface temperature profile. Two different systems of this type were used to determine whether the size of the test section affected the results. One system had a heated surface 3.8 cm in diameter while the diameter for the other was 5.1 cm.

The water in the annular region between the test section and the outer glass cylinder was maintained at saturation by heating with two auxiliary heaters, thus preventing heat leakage from the test section. The boiling process in and above the porous layer was visually observed through the glass walls of the test section.

Experimental results are reported here for boiling of water and methanol at atmospheric pressure with spherical glass beads as the particles. The particle sizes used in the present experiments are given in Table 1. All glass beads were supplied by Brau Melsungen. These beads were graded into the size ranges indicated in Table 1. The density of the beads for each size was determined by measuring the volume of water displaced by a given mass of beads. For all sizes, the density was found to be 2.75 ± 0.05 g/cm^3. The terminal velocities listed in Table 1 are measured values obtained by timing the fall of individual particles in a column of liquid at the saturation temperature. The terminal velocities of the particles in the liquids tested here range between 2.4 and 12.5 cm/s. The corresponding terminal Reynolds numbers are in the transition range between Stokes flow and fully turbulent flow.

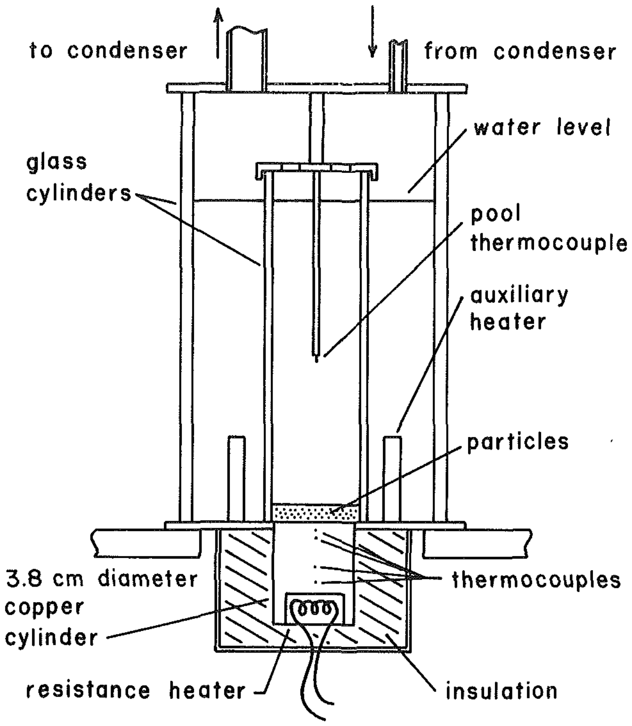

Fig. 1 Experimental apparatus

Prior to each experiment with water, the entire apparatus was taken apart and cleaned with acetone and distilled water to eliminate any contamination from previous experiments. Once reassembled, the apparatus was filled with distilled water to a predetermined height and heated to saturation at atmospheric pressure. The water was allowed to boil vigorously for several minutes to remove any dissolved air. A pool boiling curve was determined for the system at the beginning of each experiment. The agreement of this curve with previous ones assured that the nucleation behavior of the surface was essentially the same, and that the thermocouples were reading properly.

After the pool boiling curve was determined, the power was set to the desired heat flux and a pool boiling point was measured. With the heat flux held constant, particles were added into the test section through the top, in amounts

Nomenclature

C_0 = constant in equation (19)
d_p = mean diameter of beads
D = diameter of test section
g = gravitational acceleration
h_{fg} = latent heat of vaporization
H_p = liquid pool height
H_L = height of particle layer on bottom of test section
l = mixing length
m''_D = dryout particle load per unit area, g/cm^2
m''_L = particle load per unit area in layer, g/cm^2
m''_s = suspended load per unit area, g/cm^2
$m''_{\mathrm{MAX}} = 0.6\,\rho_P (1-\alpha) H_P$
n = exponent in equation (5)

q'' = heat flux
q''_d = dryout heat flux
$q''_z = 0.131\,\rho_g^{1/2} h_{fg} [g(\rho_f - \rho_g)\sigma]^{1/4}$
$q''_R = \rho_g h_{fg} [\sigma g(\rho_f - \rho_g)/\rho_f^2]^{1/4}$
$\mathrm{Re} = v_T d_p / \nu_f$
u'_c = characteristic turbulent fluctuating velocity
v_s = settling velocity of particles
v_T = single particle terminal velocity in stagnant liquid
z = vertical coordinate measured upward from bottom of test section
α = mean vapor void fraction

$\Gamma = m''_s/[\rho_P(H_P - H_L)(1-\alpha)]$
ϵ = effective turbulent diffusivity of particles
$\eta = (z - H_L) v_T/\epsilon$
$\eta_H = (H_p - H_L) v_T/\epsilon$
ν_f = kinematic viscosity of liquid
ν_g = kinematic viscosity of vapor
ρ_f = liquid density
ρ_g = vapor density
ρ_P = particle density
σ = surface tension
ϕ = bed porosity = $1 - \Omega$
Ω = volume fraction of particles

Table 1 Glass beads sizes and corresponding symbols used in figures. Experiments in water are indicated by the solid symbols for the 3.8-cm test section and open symbols for the 5.1-cm test section. The half-filled symbol represents tests in methanol with the 5.1-cm test section.

Mean grain diameter (mm)	Diameter range (mm)	Symbols used in Figures	Re Water	Re Methanol
0.105	0.10 - 0.11	●, ○, ◑	11	6.2
0.175	0.17 - 0.18	■, □	28	
0.275	0.25 - 0.30	▲	72	
0.475	0.45 - 0.50	◆	203	

ranging from 20 to 80 g, until the particle load was close to the expected dryout load. Then the particles were added 20 g at a time. The particles were added slowly, with occasional checks for instability. It took about 3 min to add the entire 20 g. If dryout occurred before all 20 g was added, the remainder was weighed to determine the exact dryout load. Saturated water was added to the test section as required during the test to keep the water level at the predetermined height. For the tests with methanol, similar procedures were followed.

After addition of the particles, if dryout did not occur, the system was permitted to stabilize for 5 min, and the thermocouple readings were recorded to verify that the heat flux was constant. When addition of particles caused the surface temperature to rise above 200°C, it was assumed that dryout had occurred, and the power was shut off to prevent damage to the heating surface.

Water dryout data for the four particle sizes in Table 1 are plotted in Fig. 2. Based on analysis of the heat leakage from the copper cylinder, the uncertainty in the heat flux measurements is estimated to be within ± 4 percent for all reported data. The heat flux is estimated to be uniform to within ± 1.5 percent across the surface at the bottom of the test section. Considering the precision of the scale used to weigh the particles and the control of the particle addition process at dryout, the uncertainty in the measured values of the particle load at dryout is estimated to be within ± 5 percent for all our data.

Also shown in Fig. 2 is the corresponding shallow-bed dryout correlation of Dhir and Catton [2]

$$q_d'' = q_z''[1 - 0.092\, m_L''/(\rho_p \sqrt{\sigma/g(\rho_f - \rho_g)})] \tag{1}$$

As the particle load increases, measured dryout data for heavy particles [1, 3] typically decrease along the Dhir and Catton [2] curve and level off at the dryout heat flux for a rigid particle bed. The dryout condition for a rigid bed of each of the particle sizes is also shown in Fig. 2. The predictions for particles with $d_p < 0.36$ mm were obtained using the dryout criteria of Udell [4] with the Kozeny-Carman formula for the permeability of the bed. For $d_p > 0.36$ mm, where interfacial shear and inertia effects on the two-phase flow in the bed are stronger, the dryout correlation of Ostensen and Lipinski [5] for beds of larger particles was used. These correlations are listed below

$$q_d'' = \frac{0.00168\phi^3 d_p^2 h_{fg}(\rho_f - \rho_g) g}{\nu_g (1-\phi)^2} \quad (d_p < 0.36 \text{ mm}) \tag{2}$$

$$q_d'' = \frac{0.245\, h_{fg}[\rho_f \rho_g g d_p \phi^3/(1-\phi)]^{1/2}}{[1 + (\rho_g/\rho_f)^{1/4}]^2} \quad (d_p \geq 0.36 \text{ mm}) \tag{3}$$

Note that the particle size range indicated for each correlation applies only for water at atmospheric pressure [5]. A bed porosity of 0.4 was assumed to estimate the deep bed dryout limits shown in Fig. 2.

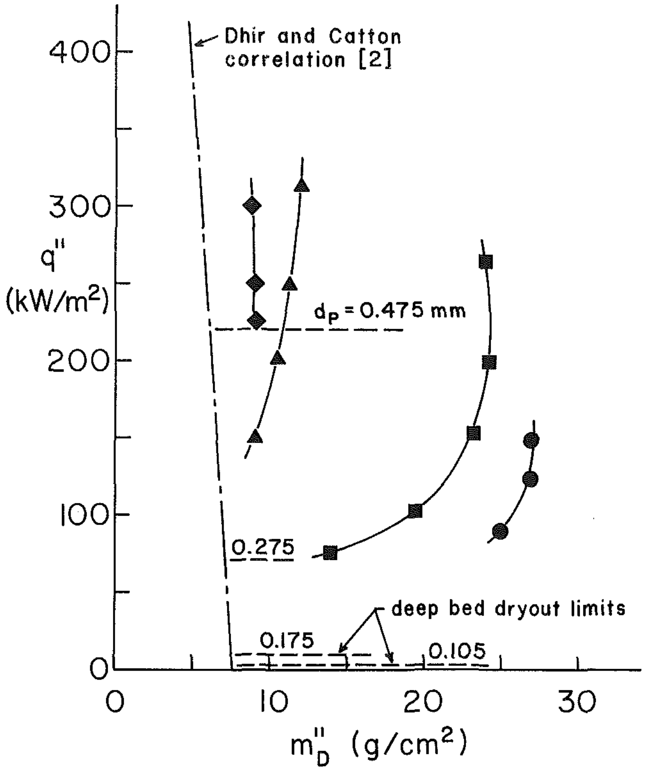

Fig. 2 Experimentally determined dryout conditions for glass beads in water with a pool height of 20 cm in the 3.8-cm test section: The data shown are for mean particle diameters of 0.105 (●), 0.175 (■), 0.275 (▲) and 0.475 (◆) mm

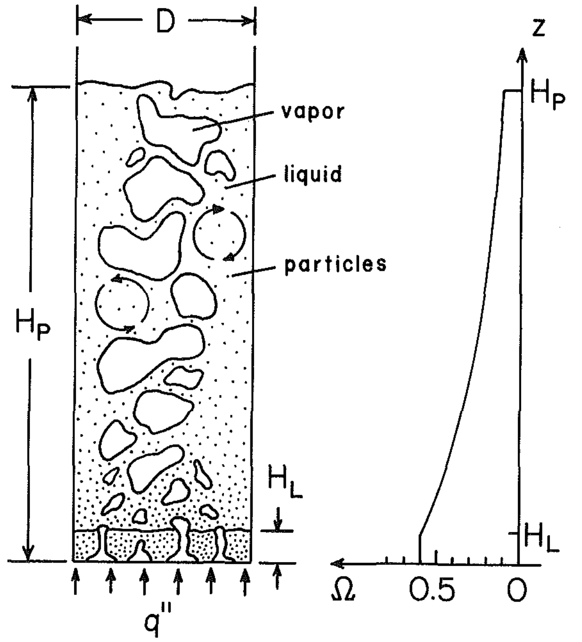

Fig. 3 Schematic diagram of boiling process and postulated particle concentration distribution

During the experiments, it was visually observed that as particles were added to the system at constant heat flux, all particles are suspended by the turbulence in the pool until the maximum possible suspended load is reached. This upper limit is dependent on the kinetic energy of the turbulence, which, in general, increases with heat flux. Beyond this limit, additional particles settle to the bottom, forming a layer which increases in height as more particles are added.

It was visually observed that, near dryout, part of the

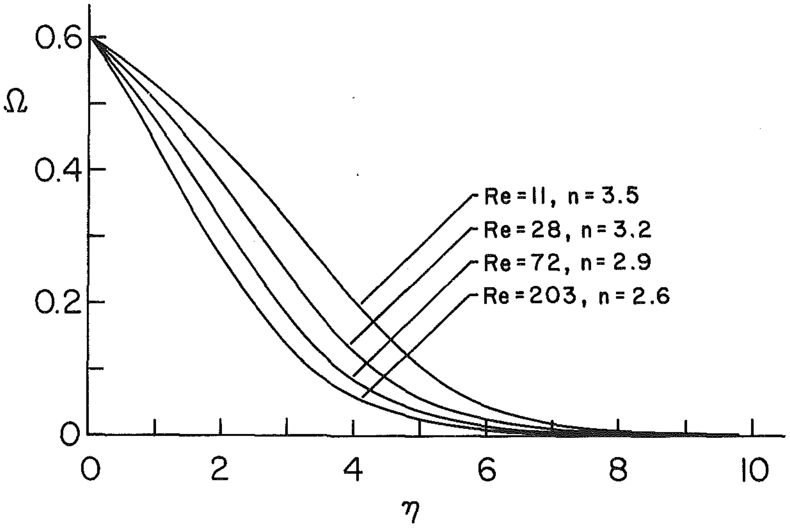

Fig. 4 Calculated concentration profiles in the pool

particle load lay in a fluidized layer on the bottom, while the remainder was suspended in the pool above the layer. We distinguish between these two regions based on the apparent mechanisms of particle mobility. In the layer, the particles are nearly in contact, but the layer visually appeared fluid as vapor passed through it. Hence we refer to the layer as fluidized. Above the layer, particles are swept into the pool by turbulence in the liquid. We have chosen to refer to this as suspended material, since it is supported by turbulence and not by a through-flow of liquid, as in fluidized beds.

The presence of part of the particle load as a layer on the bottom suggests that the dryout mechanism may be similar to that proposed by Dhir and Catton [2] for shallow beds of heavy particles heated from below. When the height of the layer reaches the limit indicated by the Dhir and Catton [2] correlation, dryout occurs. This postulated mechanism forms the basis of the dryout model discussed in the next section.

Several interesting trends can be observed in the dryout data in Fig. 2. As the mean particle diameter gets smaller, the deviation of the data from the Dhir and Catton correlation increases. It can also be seen in Fig. 2 that for a given particle size, as the heat flux increases, the deviation from the Dhir and Catton correlation also tends to increase. This is related to the kinetic energy of the turbulence in the pool, which increases with increasing heat flux. This increases the capacity of the pool to suspend particles, which means a greater load is needed to "saturate" the pool and form a layer of sufficient height to cause dryout.

Of special note are the locations where the dryout curves have a positive slope. One example is the curve for $d_p = 0.175$ mm for heat flux values between 100 and 200 kW/m^2. If a system is operating at $q'' = 150$ kW/m^2 with a particle load of 20 g/cm^2, the data indicate that a decrease in heat flux to 75 kW/m^2 will produce dryout.

For any condition slightly above the dryout curve where it has a positive slope, a decrease in heat flux may cause dryout. This unusual characteristic may be explained in terms of the postulated mechanisms already discussed. A decrease in heat flux reduces the kinetic energy of turbulence in the liquid pool, which reduces its capacity to suspend particles. The decrease in heat flux causes some of the load that was suspended to settle into the layer on the surface. If the increase in layer height is great enough, dryout may occur. Hence, for this system, decreasing the heat flux does not prevent dryout, but actually causes it to occur.

Additional experiments also indicate that the addition of subcooled water to the test section can also cause dryout. Subcooling the liquid pool causes the vapor bubbles to condense as they rise, which reduces their production of turbulence in the pool. This, in turn, reduces the capacity of the pool to suspend particles, causing particles to settle into the layer at the bottom. The resulting increase in layer height at the bottom can cause dryout to occur. Hence, the addition of subcooled liquid to the system can cause rather than prevent dryout for these conditions.

It should be noted that all experiments reported here correspond to increasing the particle load at constant heat flux. Additional experiments were also tried with increasing q'' for a constant particle load. For small particles and large particle loadings, two system states are sometimes possible. If the particles were undisturbed as the heat was applied, the system would dry out near the deep bed limit. However, if the bed was stirred mechanically or enough natural agitation existed, the system sometimes reached a stable operating point with part of the load suspended and the remainder in a layer on the bottom. The results obtained for experiments run in this manner were found to depend strongly on the nature of the start-up transient, and hence are very system specific.

Analysis

In the dryout model proposed here, it is assumed that the mechanism which causes dryout is essentially the same as that proposed by Dhir and Catton [2] for shallow layers heated from below. Dryout is assumed to result from vapor choking due to Helmholtz instability in the pool above the layer on the bottom. Implicit in this model is the assumption that the presence of suspended particles in the pool does not strongly affect the Helmholtz instability mechanism. This is clearly expected to be true as the particle concentration Ω approaches zero.

At high particle concentrations, the presence of particles in the liquid will increase its density above that of the pure liquid. It may therefore seem appropriate to replace the liquid density in the Dhir and Catton [2] correlation by the mean density of the liquid–particle mixture. However, doing so produces only a very small change in the dryout conditions predicted by the present analysis for our experimental conditions. To simplify the analysis, we have therefore assumed that the variation of the mean pool density with particle concentration has a negligible effect on the Helmholtz instability mechanism. Based on this assumption, the dryout condition predicted by the Dhir and Catton correlation is taken to be correct, independent of the particle concentration in the pool above the layer.

The observed configuration of the system near dryout is shown schematically in Fig. 3. The concentration of particles

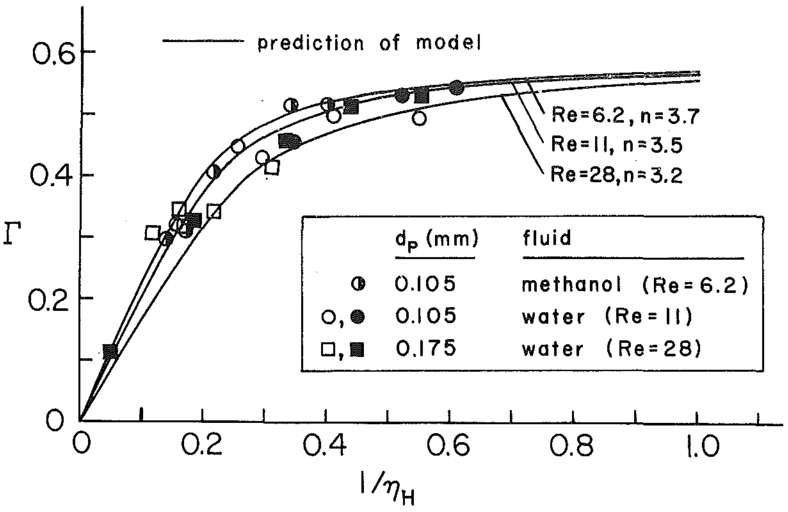

Fig. 5 Comparison of the calculated Γ variations with experimental data: The solid and open symbols correspond to the 3.8-cm and 5.1-cm test sections, respectively; the methanol data were taken in the 5.1-cm test section

in the fluidized layer at the bottom is assumed to be 0.6, the approximate value for incipient fluidization [6]. In the pool above the layer, a concentration gradient is postulated to exist, with Ω decreasing with height from the value of 0.6 at the top of the layer. The existence of the concentration gradient could be visually observed in the test section during the experiments as a decrease in the cloudiness of the pool with height.

At equilibrium, since there is no net vertical flow of liquid, the downward settling of particles must be balanced by the upward diffusion of particles due to the bubble-induced turbulence in the pool. This balance is written mathematically as

$$-\rho_p \Omega v_s - \rho_p \epsilon \frac{d\Omega}{dz} = 0 \qquad (4)$$

The first term on the left side of equation (4) is the downward flux of particles at the settling velocity v_s. The second term represents the upward diffusion of particles due to the turbulence in the system. The form of this term assumes that the upward diffusion of particles can be approximated by an effective turbulent diffusivity multiplied by the concentration gradient, in the manner often used for turbulent mass transfer. This is reasonable for very small, light particles which closely follow the liquid flow. However, it is expected to be less accurate as the particle size and terminal velocity increase, and the interaction of the particle motion with the fluid becomes more complex. It is interesting to note that an equation similar to equation (4) was proposed by Soo [7] as a simple model of suspension of particles in turbulent flow in pipes.

Based on experimental data Richardson and Zaki [8] have proposed the following empirical relation for the dependence of settling velocity on particle concentration

$$v_s = v_T(1-\Omega)^{n-1} \qquad (5)$$

Here v_T is the terminal velocity of a single particle in stagnant liquid which can be calculated from currently available correlations for spheres [9]. For spherical particles, the exponent n depends on the terminal Reynolds number for a single particle as given below [8]

$$n = 4.45\,\mathrm{Re}^{-0.10} \quad (1 < \mathrm{Re} < 500) \qquad (6)$$

Equation (5) implies that the settling velocity is not strongly affected by the level of turbulence in the system. The successful use of this relation to predict the motion of particles in sedimentation processes and fluidized beds [6] for a wide range of flow conditions would seem to confirm its validity. Equation (5) would therefore appear to be a suitable prediction of the settling velocity for the turbulent system considered here. It is worth noting that equation (5) with n = 3 was also used by Soo [7] to predict the suspension of particles in turbulent pipe flows.

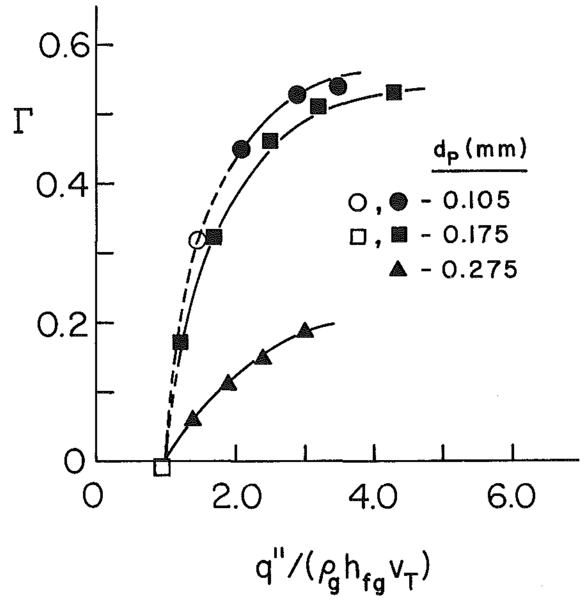

Fig. 6 Variation of experimentally determined Γ values with $q''/(\rho_g h_{fg} v_T)$; all data shown are for water; the solid and open symbols correspond to data for the 3.8-cm and 5.1-cm test sections, respectively

Substituting equation (5) into equation (4) yields

$$\frac{d\Omega}{dz} + \frac{v_T}{\epsilon}\Omega(1-\Omega)^{n-1} = 0 \qquad (7)$$

The boundary condition for this equation is taken to be that the particle concentration equals 0.6 at the top of the layer on the bottom. This results in a continuous concentration profile in the system.

$$\Omega = 0.6 \quad \text{at} \quad z = H_L \qquad (8)$$

For convenience, we define

$$\eta = (z - H_L)v_T/\epsilon \qquad (9)$$

whereupon equation (7) and equation (8) can be stated as

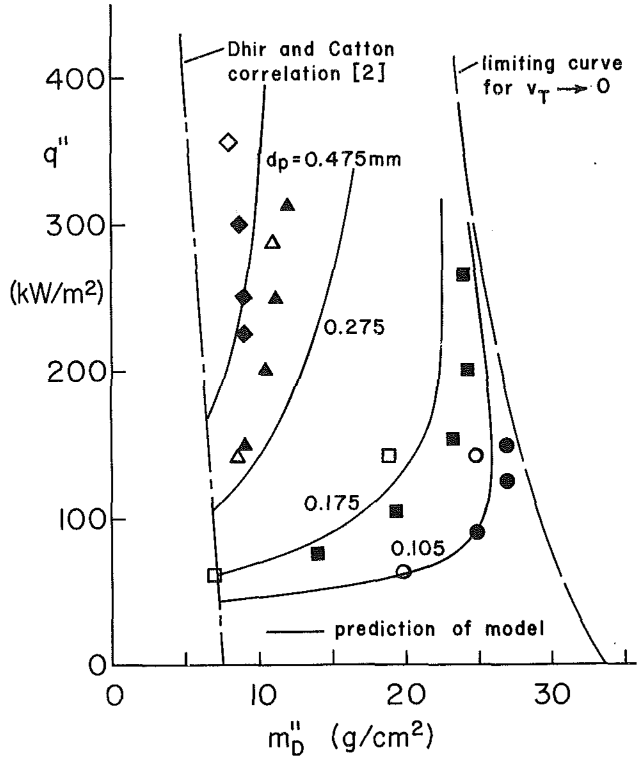

Fig. 7 Comparison of the experimentally determined dryout conditions with the model predictions; all results are for glass beads in water with a pool height of 20 cm; the data shown are for mean particle diameters of 0.105 (○,●), 0.175 (□,■), 0.275 (△, ▲) and 0.475 (◇,◆) mm; the solid and open symbols correspond to data for the 3.8-cm and 5.1-cm test sections, respectively

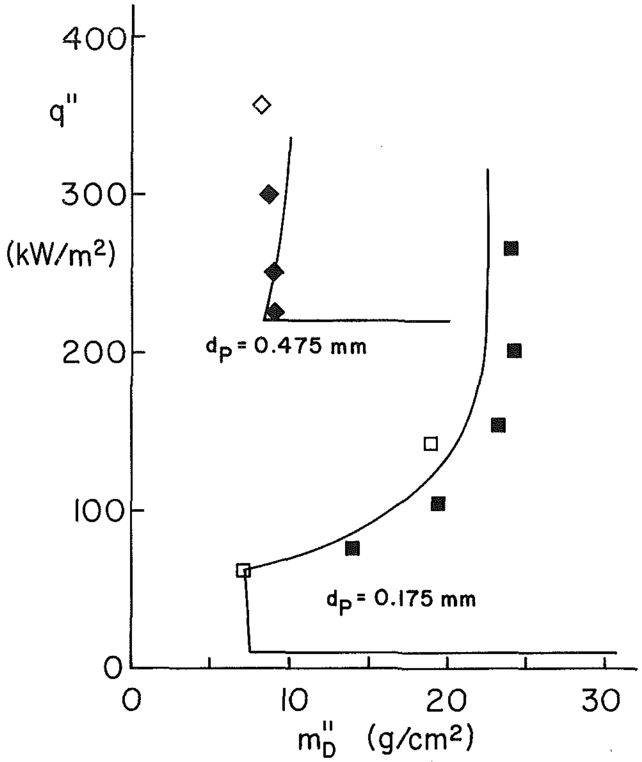

Fig. 8 Full dryout curves for glass beads in water with a pool height of 20 cm; the curves shown are for d_p = 0.175 mm (□,■) and d_p = 0.475 mm (◇,◆); the solid and open symbols correspond to data for the 3.8-cm and 5.1-cm test sections, respectively

$$\frac{d\Omega}{d\eta}+\Omega(1-\Omega)^{n-1}=0 \tag{10a}$$

$$\Omega=0.6 \quad \text{at} \quad \eta=0 \tag{10b}$$

The total quantity of particles suspended above the settled layer, per unit of surface area, is given by

$$m_s''=\rho_p(1-\alpha)\int_{H_L}^{H_p}\Omega\, dz \tag{11}$$

This is rewritten in nondimensional form as

$$\Gamma=\frac{1}{\eta_H}\int_0^{\eta_H}\Omega\, d\eta \tag{12}$$

where

$$\eta_H=(H_P-H_L)\,v_T/\epsilon \quad \text{and} \quad \Gamma=m_s''/[\rho_p(H_p-H_L)(1-\alpha)] \tag{13}$$

Equation (10*a*) with boundary condition (10*b*) was solved numerically using a fourth-order predictor-corrector numerical scheme. The numerical scheme also computed values of Γ as a function of η_H from the concentration profiles. The calculated variations of Ω with η for various values of η are shown in Fig. 4. The volume fraction of particles in the pool Γ is computed using equation (12). The variations of Γ with $1/\eta_H$ for three values of n are shown in Fig. 5. The n values shown in Figs. 4 and 5 are those determined from equation (6) for each of the particle sizes listed in Table 1.

To determine the physical amount of suspended particles from Γ curves like those shown in Fig. 5, the value of ϵ must be known to evaluate η_H. This, of course, requires knowledge of the characteristics of the turbulence in the pool. Here, the turbulence is assumed to be isotropic throughout the pool, and a simple mixing-length model is adopted. It is therefore assumed that

$$\epsilon \propto u_c' l \tag{14}$$

where u_c' is a characteristic velocity associated with the turbulent velocity fluctuations and l is a characteristic mixing length. We further postulate that

$$u_c' \propto q''/(\rho_g h_{fg}\alpha) \tag{15}$$

Note that $q''/(\rho_g h_{fg}\alpha)$ is the mean velocity at which the vapor rises through the pool. Since the vapor motion is the source of the turbulence, it is reasonable to assume that u_c' is comparable to $q''/(\rho_g h_{fg}\alpha)$.

The flow of vapor in the pool above the layer in our apparatus was observed to be in the churn-turbulent flow regime, with the vapor flowing upward in large distorted bubbles, as shown schematically in Fig. 3. Since the turbulence is generated by the rising bubbles, it is assumed here that the characteristic mixing length of the turbulence can be approximated by the mean bubble diameter. We therefore assume that

$$l \propto \left[\frac{\sigma}{g(\rho_f-\rho_g)}\right]^{1/2} \tag{16}$$

where the right side of equation (16) is the characteristic length scale of the bubbles, which is dictated by a balance between buoyancy and surface tension forces.

Combining equations (13)-(16) yields

$$\frac{1}{\eta_H}=\frac{\epsilon}{v_T(H_P-H_L)}\propto\frac{1}{(H_P-H_L)}\left[\frac{\sigma}{g(\rho_f-\rho_g)}\right]^{1/2} \times\left[\frac{q''}{\rho_g h_{fg} v_T \alpha}\right] \tag{17}$$

Assuming that the mass loading in the layer at dryout is given by the Dhir and Catton correlation (1), the mass of particles suspended in the pool can be calculated from the total particle load as follows

$$m_s''=m_D''-10.9\,\rho_p\sqrt{\sigma/g(\rho_f-\rho_g)}\,[1-q''/q_z''] \tag{18}$$

Values of Γ were computed using equations (13) and (18) for the measured dryout conditions in water for three of the particle sizes, and the results are shown in Fig. 6. Note that the curves in Fig. 6 indicate that $\Gamma \rightarrow 0$ as $1/\eta_H \rightarrow 0$, which, from equation (17), implies $\Gamma \rightarrow 0$ as $q'' \rightarrow 0$. However, as shown in Fig. 6, our experimental data suggest instead that $\Gamma \rightarrow 0$ as $q''/(\rho_g h_{fg} v_T) \rightarrow 1$. A more physical way of veiwing this is that the superficial vapor velocity $q''/\rho_g h_{fg}$ must exceed the terminal velocity of a single particle before significant suspension of particles occurs. Alternatively, it may be stated that the kinetic energy of the turbulence must reach a threshold value, which depends on the terminal velocity of the particles, before particles are suspended.

The condition for incipient suspension of particles noted above provides an approximate means for estimating when particle suspension will be important. In particular, this condition implies that if metal particles were added to this system in the size and heat flux ranges considered here, there would be little or no suspension of particles.

Based on the observations discussed above, the relation for $1/\eta_H$ is modified to the following form

$$\frac{1}{\eta_H}=\frac{\epsilon}{v_T(H_P-H_L)}=\frac{C_0}{\alpha(H_P-H_L)}\left[\frac{\sigma}{g(\rho_f-\rho_g)}\right]^{1/2}\times\left[\frac{q''}{\rho_g h_{fg} v_T}-1\right] \tag{19}$$

Here C_0 is an undetermined constant of proportionality.

In general, the vapor void fraction is dependent on the rate of vapor flow through the system, which depends on the heat flux. Pool boiling experiments were run over a range of heat flux conditions to determine the dependence of α on q''. The mean void fraction was determined by measuring the height of the liquid level in the system at each heat flux, shutting off the heat input, and measuring the liquid level again after boiling had stopped. These data have been curve-fit to obtain the following relation

$$\alpha=\frac{q''/q_R''}{1.9(q''/q_R'')+2.63} \tag{20a}$$

$$q_R''=\rho_g h_{fg}[\sigma g(\rho_f-\rho_g)/\rho_f^2]^{1/4} \tag{20b}$$

The form of equation (20) is suggested by correlations presented in Wallis [6], for churn-turbulent flow, with the constants optimized to match the data for our system. The values of α predicted by equation (20) for pure liquid were compared with several measured values of α with particles in the system at the same heat flux. It was found that for the conditions considered here, the void fraction for the system with particles differed only slightly from the prediction of equation (20). Hence, equation (20) was used to evaluate α even with particles in the system.

Assuming that the porosity is 0.4 in the fluidized layer, and its height is given by the Dhir and Catton [2] correlation at dryout, the suspension model can be combined with equation (1) to yield the following prediction of dryout conditions when particles are suspended

$$m_L''=10.9\,\rho_p\sqrt{\sigma/g(\rho_f-\rho_g)}\,[1-q''/q_z''] \tag{21}$$

$$H_L=m_L''/(0.6\rho_p) \tag{22}$$

$$1/\eta_H=\frac{2.15}{\alpha(H_P-H_L)}\left[\frac{\sigma}{g(\rho_f-\rho_g)}\right]^{1/2}\left[\frac{q''}{\rho_g h_{fg} v_T}-1\right] \tag{23}$$

$$m_D''=m_L''+\rho_p[H_P-H_L][1-\alpha]\Gamma(1/\eta_H) \tag{24}$$

The value of $C_0 = 2.15$ in equation (23) was chosen to provide an optimum fit to all our experimental data. Values of Γ for each value of $1/\eta_H$ must be obtained from numerical calculations using equations (10) and (12). For $1/\eta_H < 0$, Γ is taken to be zero. Comparisons of the experimental data with the predicted dryout conditions using equations (20)–(24) are shown in Figs. 5 and 7. Agreement with the smaller particles is quite good. The deviation for the 0.275-mm particle is larger, while agreement with the data for 0.475 mm is fairly good. As they get larger, the particles are expected to interact with the turbulence in a more complex manner, and act less like a passive contaminant. Hence, agreement of the data with our simple effective-diffusivity model is expected to be somewhat worse for the larger particles.

However, in Fig. 7, agreement does not get systematically worse with increasing particle size. The data for $d_p = 0.275$ mm deviate the most. For $d_p = 0.275$ mm, the terminal velocity of a single particle in stagnant water is just about in the middle of the transition range (see Table 1). The free-stream turbulence in the liquid pool may alter the settling behavior of the particles in the transition range so that equation (5) is no longer accurate. Particles near the Stokes flow range, or those already having fully turbulent drag characteristics, may be much less affected. This would seem to be a likely cause for the singular deviation of the data for $d_p = 0.275$ mm.

A reduction in particle drag due to a premature transition to fully turbulent behavior would increase the terminal velocity of the particles and shift the data to the left in Fig. 7. The data for $d_p = 0.275$ are to the left of the model prediction in Fig. 7, suggesting that this mechanism may be at least partly responsible for the deviation.

It can be seen in Figs. 5 and 7 that the data obtained with the two different test sections are in fairly close agreement. Although the difference in the size of the two test sections is not large, this does suggest that the size of the test section does not strongly affect the dryout conditions. The model predictions are also seen to compare favorably with data for both water and methanol, which have values of surface tension which differ by a factor of three. This supports our choice of the bubble length scale in equation (16) as the characteristic integral scale of the turbulence.

Overall, the trends predicted by the model compare favorably with the experimental data, even at large particle sizes. In the limit of $v_T \rightarrow 0$, all particles would be suspended. Then, no layer would form until enough particles were added to raise the particle concentration, in the region not occupied by vapor, to a level above that for incipient fluidization ($\Omega = 0.6$) throughout the pool. Dryout would then occur, provided the heat flux is above the deep bed limit. The limiting particle load at which this would occur is given by

$$m_{\mathrm{MAX}}''=0.6\,\rho_p(1-\alpha)H_P \tag{25}$$

This limiting condition is also plotted in Fig. 7. Both the data and the theoretical curves approach this limit as the particle size gets smaller and the heat flux gets larger. This behavior is expected since increaisng q'' and decreasing d_p both increase the capacity of the system to suspend particles.

Figure 7 shows only the distortion of the Dhir and Catton relation due to particle suspension. In general, for a system with particle suspension, one can determine the full dryout curve by combining the model results with the Dhir and Catton correlation and the deep bed dryout limit. Full dryout curves, obtained in this manner, are shown for two of the particle sizes considered here in Fig. 8. If the heat flux is below the deep bed limit, no dryout occurs, regardless of the particle load. Above this limit, dryout is defined by the Dhir and Catton correlation or the prediction of the model.

Conclusions

The experimental data presented here indicate that suspension of particles causes the dryout conditions to deviate strongly from the Dhir and Catton [2] correlation for shallow beds of heavy particles heated from below.

The experimentally determined dryout curves indicate that for some combinations of particle loading and heat flux, a decrease in heat flux may actually cause dryout to occur. This occurs because decreasing the heat flux diminishes the capacity of the pool to suspend particles, causing some of the particles that were suspended to settle to the bottom. If the resulting increase in the height of the layer on the bottom is large enough, dryout may occur.

Dryout may also result from the addition of subcooled liquid to the pool for essentially the same reason. Condensation of the vapor bubbles as they rise through the subcooled pool reduces their capacity to produce turbulent kinetic energy, and thereby reduces the pool's capacity to suspend particles. Our experimental results also suggest that a threshold level of heat flux, given by $q'' = \rho_g h_{fg} v_T$, is required before significant suspension of particles will occur. Although the model of the particle suspension mechanism presented here treats the transport in a very approximate manner, its predictions compare favorably with our experimental data.

In general, our results suggest that in boiling systems which contain significant quantities of light particulates, a reduction in heat flux or addition of subcooled water may not be appropriate actions to avoid dryout.

Acknowledgments

The authors wish to acknowledge support for this research by the National Science Foundation under research grant MEA-8307212. The efforts of Ms. L. Donahue in preparation of the manuscript are also appreciated.

References

1 Gabor, J. D., Sowa, E. S., Baker, L., Jr., and Cassulo, J. C., "Studies and Experiments on Heat Removal From Fuel Debris in Sodium," ANS. Fast Reactor Safety Meeting, Los Angeles, CA, Apr. 1974.

2 Dhir, V., and Catton, I., "Dryout Heat Fluxes for Inductively Heated Particulate Beds," ASME JOURNAL OF HEAT TRANSFER, Vol. 99, 1977, pp. 250-256.

3 Jones, S. W., "Study of Dryout Heat Fluxes," Ph.D. dissertation, Northwestern University, Evanston, IL, 1982.

4 Udell, K. S., "Heat Transfer in Porous Media Considering Phase Change and Capillarity—The Heat Pipe Effect," *International Journal of Heat and Mass Transfer*, in press, 1985.

5 Ostensen, R. W., and Lipinski, R. J., "A Particle Bed Dryout Model Based on Flooding," *Nuclear Science and Engineering*, Vol. 79, 1981, pp. 110-140.

6 Wallis, G. B., *One-Dimensional Two-Phase Flow*, McGraw-Hill, New York, 1969.

7 Soo, S. L., *Fluid Dynamics of Multiphase Systems*, Blaisdell Publishing Company, Waltham, MA, 1967.

8 Richardson, J. F., and Zaki, W. N., "Sedimentation and Fluidisation: Part I." *Transactions of the Institute of Chemical Engineers*, Vol. 32, 1954, pp. 35-53.

9 Clift, R., Grace, J. R., and Weber, M. E., *Bubbles, Drops, and Particles*, Academic Press, New York, 1978, p. 114.

S. Fukusako
Associate Professor.

T. Komoriya
Graduate Student.

N. Seki
Professor.

Department of Mechanical Engineering,
Hokkaido University,
Sapporo 060, Japan

An Experimental Study of Transition and Film Boiling Heat Transfer in Liquid-Saturated Porous Bed

Experimental investigations of transition and film boiling in a liquid-saturated porous bed are reported. The porous bed contained in a vertical circular cylinder is made up of packed spherical beads whose diameters range from 1.0 to 16.5 mm, while the depth of the bed overlying the heating surface varies from 10 to 300 mm. Water and fluorocarbon refrigerants R-11 and R-113 are adopted as testing liquids. Special attention is focused on the effect of the diameter of spherical beads on boiling heat transfer in the transition boiling region. It is found that for the small bead diameters the steady boiling heat transfer rises monotonically with temperature from nucleate boiling through the film boiling region, without going through a local maximum.

Introduction

Boiling heat transfer in a liquid-saturated porous bed is a subject of growing interest. Applications include high-flux heat transfer porous surfaces, heat-transport characteristics in heat pipes, and heat recovery from liquid-dominated geothermal reservoirs.

In this paper some experimental observations of boiling heat transfer in liquid-saturated porous beds are reported for transition and film boiling regions. Most of the previous studies [1-14, 20] of boiling heat transfer in liquid-saturated porous layers have been for the purpose of finding the methods to augment nucleate pool boiling.

Castello and Redeker [20] investigated boiling heat transfer to ethanol from a stainless steel heater by a capillary wicking material to determine the ability of the wicking to convey coolant to a heater. They found that the full capabilities of capillary wicking to supply a heater could not be realized without proper venting of vapor produced by boiling.

Takeyama et al. [1, 2] examined an augmentation of nucleate boiling heat transfer by a variety of porous layers, consisting of particles such as steel balls, sandy iron, bronze balls, and glass beads. Ferrell and Alleavitch [3] studied the mechanism of boiling heat transfer from a wick-covered, heated surface, and concluded that the mechanism of the boiling heat transfer from wick-covered surface was one of conduction across a thin, liquid-saturated film being in contact with the heated surface.

The effect of the particle property of porous beds on pool boiling heat transfer was investigated by using fluorocarbon refrigerants by Shibayama et al. [4], who proposed a correlation equation based on their experiments. A visual observation of boiling in porous media was made by Cornwell et al. [15], who used a polyurethane form layer 6 mm thick. They claimed that vapor and liquid areas coexisted at the heating surface over a wide range of heat flux and the extent of these areas might be correlated with the heat flux.

Boiling heat transfer characteristics in a water-saturated porous bed were studied by Sugawara et al. [6, 7], who determined the effects of particle size and particle properties on boiling heat transfer. Sommerton et al. [8] conducted an experimental investigation of dryout in an inductively heated bed of steel spheres with a wide variation of the overlying coolant depth, and found that the ratio of dryout heat flux to critical heat flux was in good agreement with other experimental results. The pool boiling from a commercial porous metallic matrix surface was studied by Bergles and Chyu [9], who pointed out that the excellent steady boiling characteristics were confirmed and that the resultant boiling curve hysteresis did not appear to have been previously reported. Nakayama et al. [10] investigated the effects of pore diameters and system pressure on nucleate boiling heat transfer from a porous surface specially manufactured. They observed that intense bubble formation did not necessarily yield a high heat transfer performance and that liquid suction and evaporation inside the cavities were a probable mechanism of boiling with small temperature difference.

Recently, Bau and Torrance [11, 12] studied the boiling in a vertical circular cylinder which was filled with low-permeability, water-saturated porous materials. They observed that an almost isothermal, two-phase (wet steam) zone was formed near the bottom with the onset of boiling and that this zone was overlaid by a liquid layer with an essentially linear vertical temperature gradient and its temperature was oscillatory whenever the height of the two-phase zone exceeded a critical value. Itoh and Nishikawa [13] pointed out that an optimum coating thickness existed for a porous surface manufactured with particles of constant diameter. Furthermore, they found that for copper surfaces and copper particles this optimum thickness could be represented as four times the diameter of the sintered particle used in the coating.

From the preceding literature survey, it is apparent that very little is known about the boiling heat transfer characteristics of a liquid-saturated porous bed in the transition boiling and film boiling regions.

The objective of the research reported here is to make an experimental study of the boiling heat transfer characteristics of a liquid-saturated porous bed and to correlate the experimental results. In particular, special attention is focused on the effect of diameter of the beads on boiling behavior in the transition boiling and film boiling regions.

Experimental Apparatus and Procedure

The experimental apparatus is shown schematically in Fig. 1. The apparatus consists of an inner Pyrex tube 60 mm in diameter and 450 mm in height and an outer Pyrex tube 178 mm in diameter and 620 mm in height. The inner tube was filled with a liquid-saturated porous bed, while the other annulus was used as an insulating thermal guard. To maintain

---

Contributed by the Heat Transfer Division for publication in the JOURNAL OF HEAT TRANSFER. Manuscript received by the Heat Transfer Division February 1, 1984.

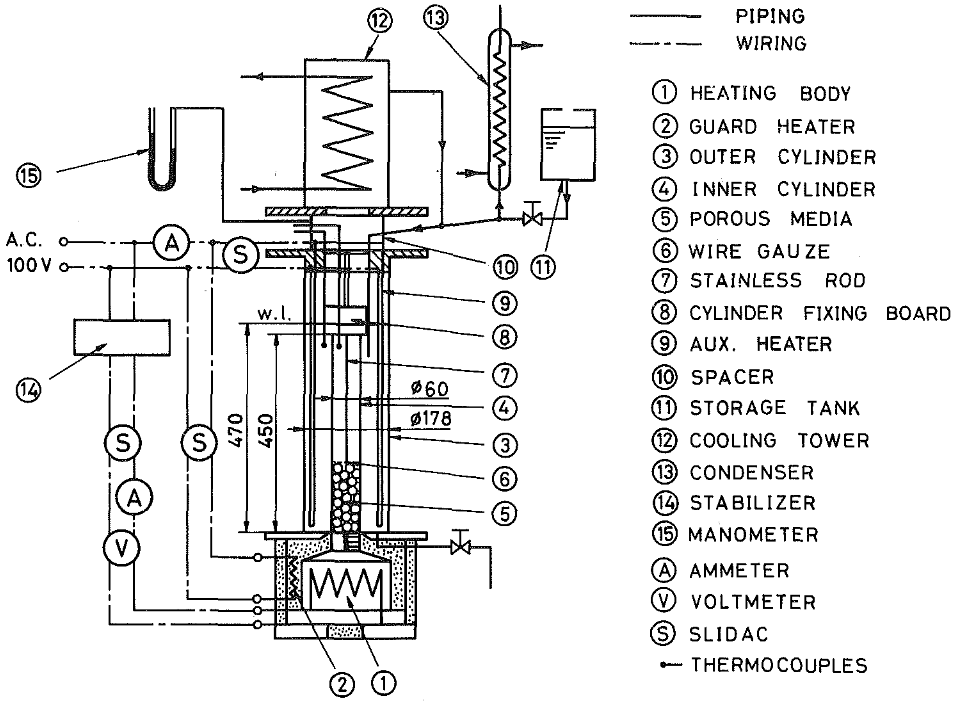

Fig. 1(*a*) **Schematic diagram of experimental setup**

the saturation temperature within the inner tube, two guard heaters were inserted in the annulus.

The inner tube and the outer annulus were filled to the same height with testing liquid and a constant liquid level was held above the heating surface. To prevent fluidization of the porous bed, a screen plate (26 mesh) on the bed was pressed downward with a mechanical screwjack. All of the data reported here were taken at atmospheric pressure. As is shown in Fig. 1(*a*), a reservoir tank for maintaining system pressure and liquid level, a liquid make up tank, and condensate collection equipment were utilized.

The heater assembly and its sectional dimension are presented in Fig. 1(*b*). This assembly includes a cylindrical copper block 80 mm in diameter and 172 mm in length on top, and the main mica heaters, inserted into the copper fins below. Nine copper-constantan thermocouples positioned radially at three levels in the upper heater block were arranged axially, as shown in Fig. 1(*b*). The surface temperature was estimated by extrapolating the temperature distributions obtained by the thermocouples.

The heat flux was evaluated by measuring the temperature gradient along the central axis, and it was also determined by

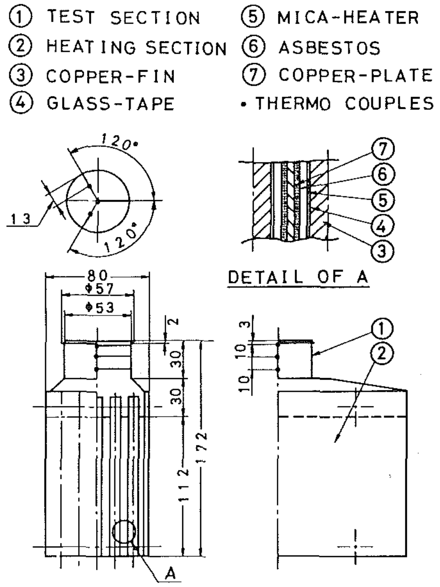

Fig. 1(*b*) **Detail of heater assembly**

Nomenclature

C = specific heat
d_p = diameter of beads
g = gravitational acceleration
Gr = modified Grashof number = $d_p{}^3 g(\rho_l - \rho_v)\rho_v/\mu_v{}^2$
H_p = height of liquid-saturated porous bed
L = heat of vaporization
Nu_l,Nu_v = Nusselt numbers, $qd_p/(\Delta T_s \lambda_{ml})$, and $qd_p/(\Delta T_s \lambda_{mv})$, respectively
Pr = Prandtl number
q = heat flux
$q_{\min}$ = minimum heat flux
Re = modified Reynolds number = $qd_p/(\epsilon\mu_v L)$
T_s = temperature of saturation liquid
T_w = temperature of heating surface
T_x = local temperature in porous bed
ΔT_s = temperature difference between heating surface and saturation liquid = $T_w - T_s$
ΔT_x = temperature difference between porous bed and saturation liquid = $T_x - T_s$
We = Weber number = $q_{\min}{}^2 d_p/(\rho_v \sigma L^2)$
ϵ = void ratio
λ = thermal conductivity
μ = viscosity
ρ = density
σ = surface tension

Subscripts

l = liquid
m = equivalent
p = bead particle
v = vapor

Table 1 Dimensions of beads

Material	d_p (mm)	H_p (mm)	ε (-)
Glass	1.1	30 ∿ 300	0.39
	2.0		0.40
	5.3		0.41 ∿ 0.45
	16.3		0.49 ∿ 0.50
Steel	2.0	10 ∿ 80	0.40
	4.0	10 ∿ 300	0.41 ∿ 0.42
	11.0	30 ∿ 300	0.44 ∿ 0.45
Worked Iron	1.0	10 ∿ 80	0.41
Aluminum	16.5	80	0.50

subtracting the heat loss from the total electric power delivered to the test section. The maximum limit of the difference between both evaluations was ascertained to be less than ±3 percent. Two copper-constantan thermocouples 0.1 mm in diameter were embedded in the porous bed to determine the temperature within the bed. In addition, a long slender shielded probe with a thermocouple was traversed axially along the axis of the inner tube to measure the temperature distribution in the bed.

Commercially available spherical materials were used for the porous bed. They include four kinds of spherical beads (steel, worked iron, aluminum, and glass) with diameters ranging from 1.0 to 16.5 mm, as listed in Table 1. The porosity ϵ was measured by displacing water as a bed was packed, and the permeability k was obtained from the Kozeny-Carman formula [14] as $k = (d_p^2/180)(\epsilon^3/(1-\epsilon)^2)$. Prior to the experiments, the spherical beads and the tubes were thoroughly washed with acetone and water.

The depth of the porous bed overlying the heating surface was changed over the range of 10 to 300 mm. Experiments were carried out by starting from a quiescent initial state where the temperature of the porous bed was that in the saturation condition. It took about 1 to 3 hr to reach an initial saturation state. The heat flux at the heating surface was increased in a sequence of small steps up to film boiling region. Before each run, the surface was carefully polished with a soft cloth dampened with acetone and water.

Results and Discussion

Measurements were made as the temperature differences between the heating surface and the saturated liquid varied from 3 to 220 K. As a supplement to the main body of experiments, auxiliary pool boiling experiments were made without the porous bed. The repeatability of the data was good, generally within ±10 percent of the average. The experimentally determined heat fluxes were compared with the previous data [15, 16] for an upward facing heater. The comparison showed that the present data were in good agreement with the previous results [15, 16]. A more complete documentation of the data is included in [17].

Effect of Bead Diameter on Boiling Heat Transfer. The experimental data for fluorocarbon R-11 are presented Figs. 2 and 3, respectively, using glass beads and metal beads of various size. In each figure, the ordinate is the heat flux q at the heating surface, while the abscissa is the temperature difference ΔT_s between the heating surface and the saturated liquid.

In the nucleate boiling region, the heat fluxes for the porous bed at a prescribed ΔT_s increase in comparison with those for pool boiling without a porous bed. It is also observed in the figures that for the comparatively large bead diameters the heat flux increases with an increase in ΔT_s, and then approaches a peak heat flux which tends to decrease with decreasing of bead diameter. Moreover, Figs. 2 and 3 show that for small bead diameters (1.0, 1.1, and 2.0 mm) the heat flux increases continuously and monotonically from the nucleate boiling to the film boiling without going through a peak heat flux. Of great interest is the fact that the data for the small bead diameters in the so-called transition boiling region between the nucleate boiling and film boiling regions were obtained at steady-state conditions. Figure 4 shows the

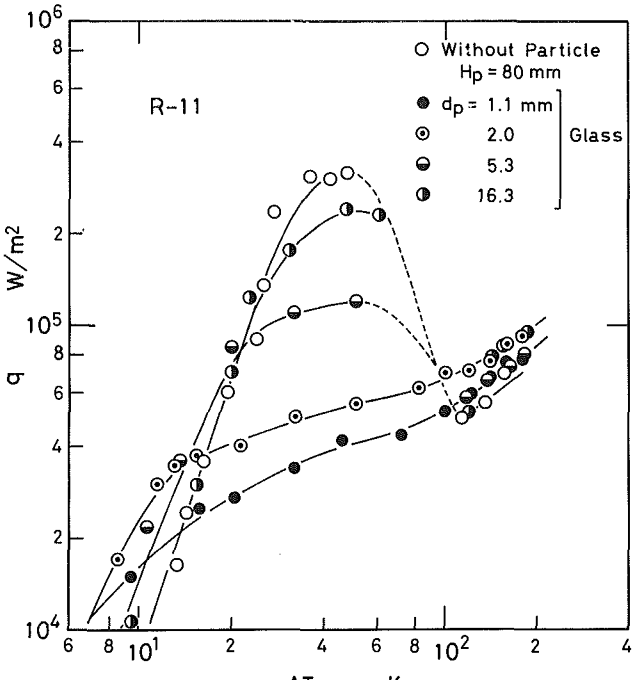

Fig. 2 Effect of bead diameter on boiling heat transfer

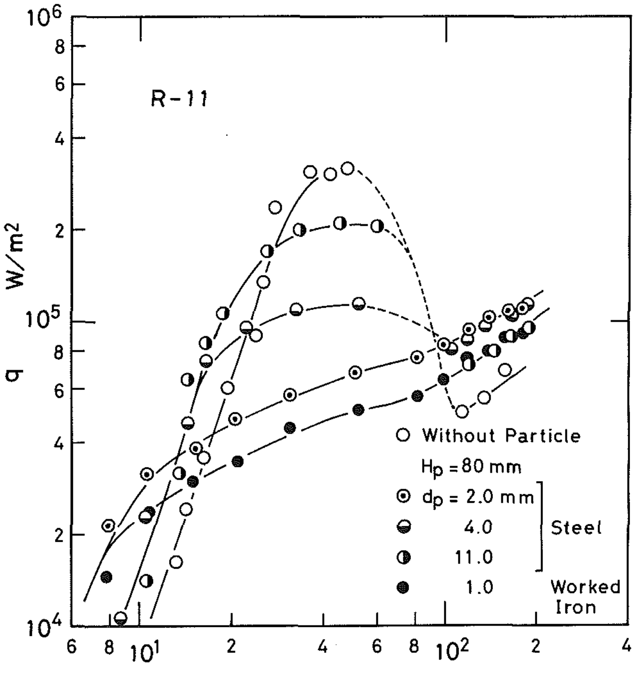

Fig. 3 Effect of bead diameter on boiling heat transfer

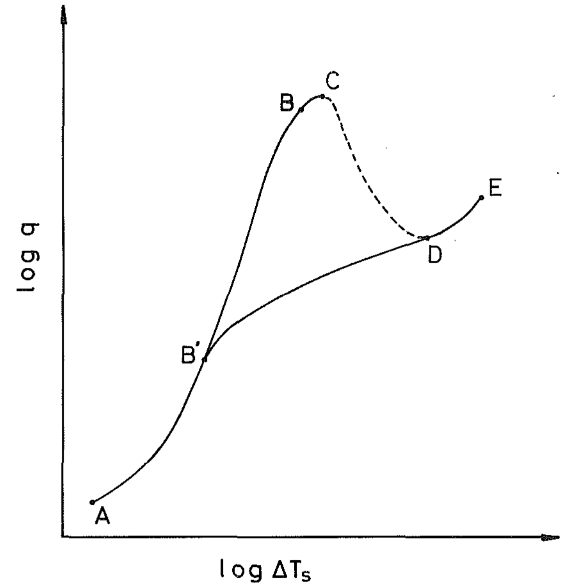

Fig. 4 Definition of boiling character

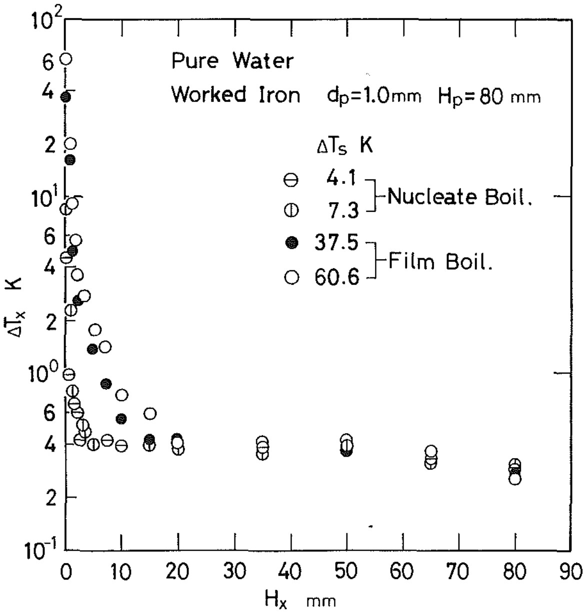

Fig. 5 Temperature distributions within porous bed

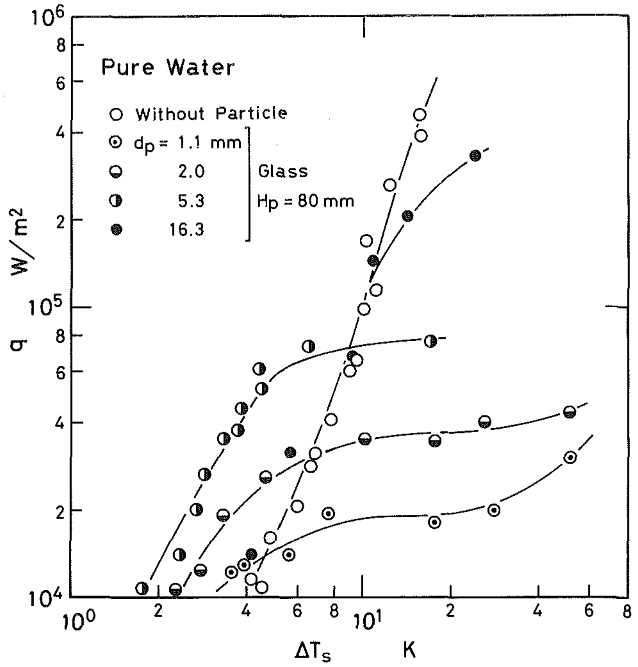

Fig. 6 Effect of bead diameter on boiling heat transfer

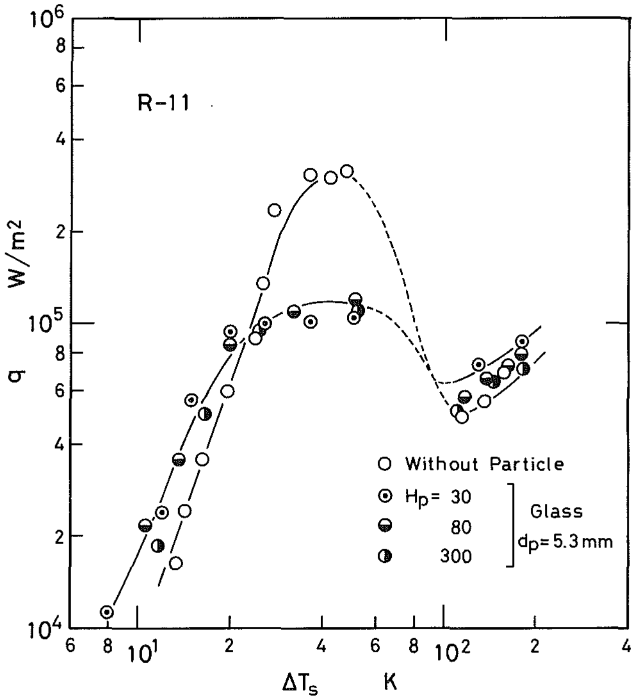

Fig. 7 Effect of porous-bed depth on boiling heat transfer

form of typical curves observed in the experiments for the beds composed of large, and comparatively small, diameter beads. For the larger beads the range A-B may be defined as the nucleate boiling region, the heat flux at point C as the peak heat flux, the heat flux at point D as the minimum heat flux, and the range D-E as the film boiling region. On the other hand, for comparatively smaller diameter beads, the range A-B′ may be defined as the nucleate boiling region, the range B′-D temporarily as the "transition boiling" region, and the range D-E as the film boiling region.

The higher heat fluxes that occur at lower ΔT_s are probably the result of the finlike effect of beads in contact with the heating surface. It might also be that there are more nucleation sites based on the cavities composed of beads in contact with the heating surface.

As the ΔT_s level is increased, it is expected that the number of spots on which bubbles start becomes larger, and that the heating surface is densely populated with bubbles. Thus, for small bead diameters, the supply of liquid to the heating surface through small passages among the beads appears to become choked. Furthermore, to remove the vapor bubble from the heating surface, vapor pressure must overcome the frictional resistance of flow through the small passages of the porous structure. Therefore, for beds composed of small beads the difficulty in the removal of vapor bubbles appears to be caused by a sequence of the facts mentioned above.

Cornwell et al. [5] studied boiling in a water-saturated porous medium composed of polyurethane 6 mm in thickness. They found that the vapor and liquid regions in the porous medium coexisted simultaneously and continuously at the heating surface over a wide range of heat fluxes. In Fig. 5, the temperature distributions measured are plotted as ΔT_x versus H_x with ΔT_s as the parameter, where ΔT_x is $T_x - T_s$ and H_x is

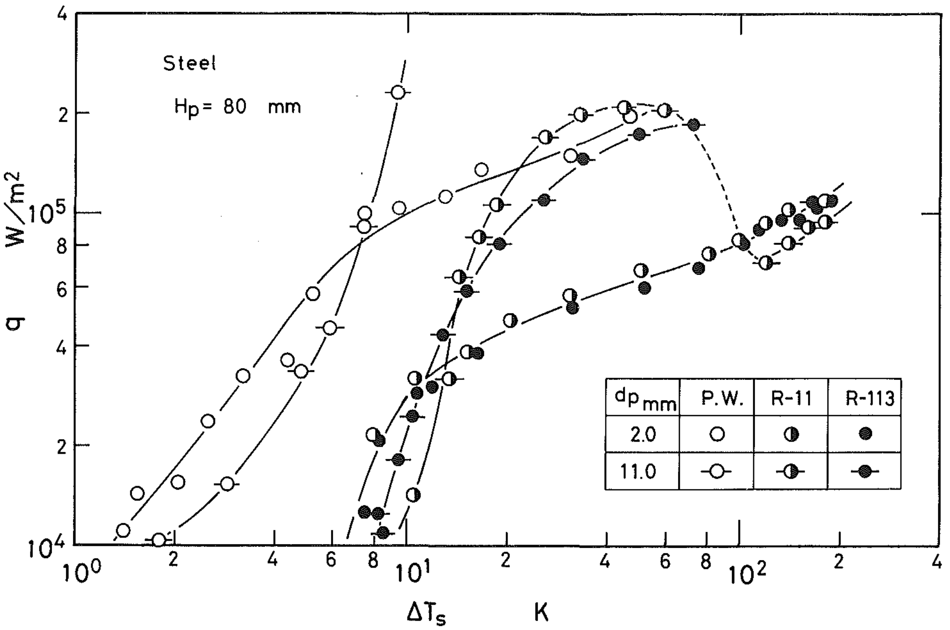

Fig. 8 Effect of working liquid property on boiling heat transfer

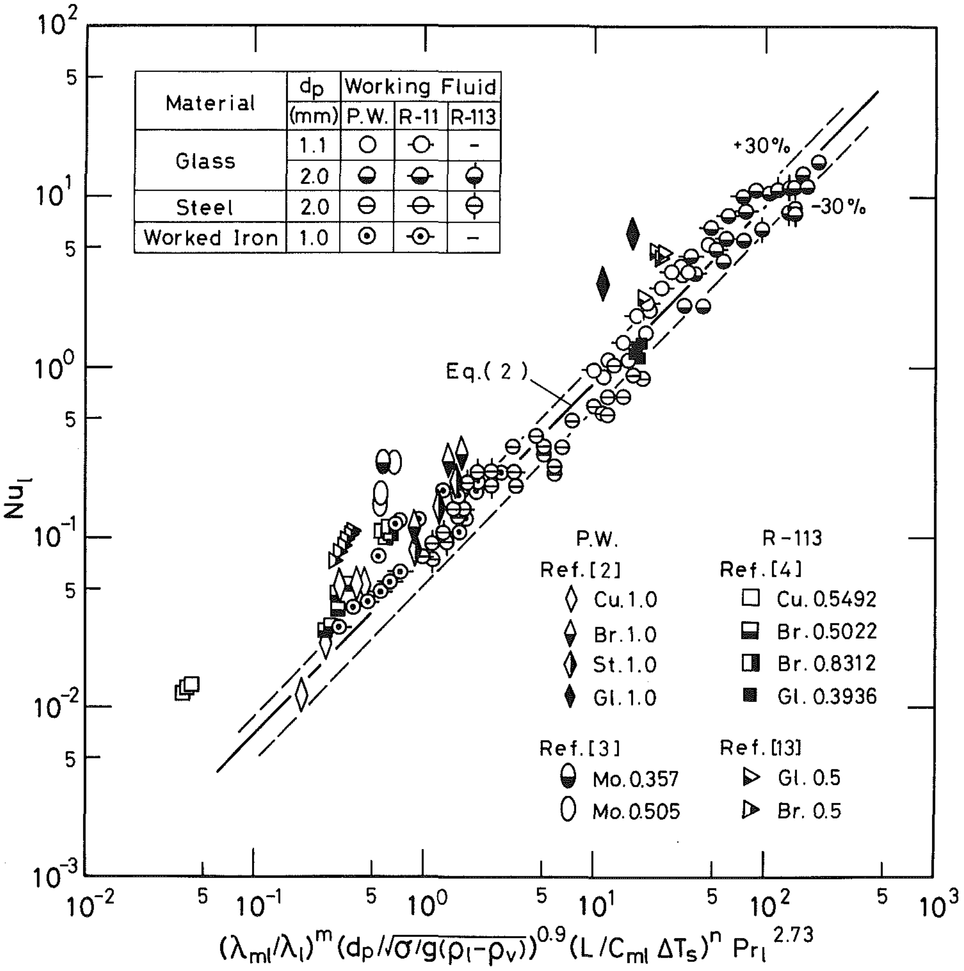

Fig. 9 Correlation of transient boiling heat transfer

the distance within the porous bed from the heating surface. These curves are the results of the time-averaged data. It is seen in the figure that for the nucleate boiling region there is a thermal boundary layer of about 2 to 3 mm thickness, while for the transition boiling region it grows to about 10 to 15 mm in thickness. This phenomenon appears to suggest that the vapor and liquid areas coexist at the heating surface in the transition boiling region.

Figure 6 shows the boiling heat transfer results for glass beads when the working fluid was distilled water. It appears that the characteristics of the boiling curves in this case may be quite similar to those of Figs. 2 and 3.

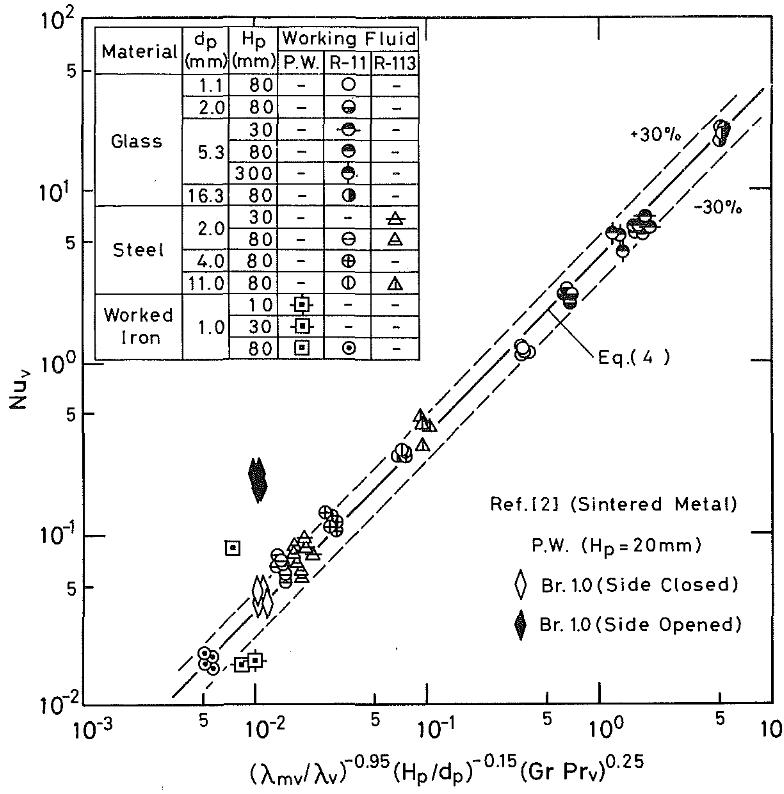

Fig. 10 Correlation of film boiling heat transfer

Effect of Porous-Bed Depth on Boiling Heat Transfer. The q results are presented as a function of ΔT_s in Fig. 7. In the figure, there are three groupings of data which respectively correspond to depths of $H_p = 30$, $H_p = 80$, and $H_p = 300$ mm, in addition to the pool boiling data. These data reveal no distinguishable influence of depth. This suggests that the essential mechanism of boiling heat transfer is determined in the comparatively thin layer of beads near the heating surface.

Effect of Thermophysical Properties of Beads and Working Liquids on Boiling Heat Transfer. Figure 8 shows the effect of the thermophysical properties of the working liquid on boiling heat transfer. Distilled water and Refrigerants R-11 and R-113 were utilized as the testing liquids. The differences between the thermophysical properties of R-11 and R-113 are very small except for the Prandtl number and saturation temperature. Thus, it seems reasonable that the characteristics of boiling curves for the fluorocarbon R-11 are both qualitatively and quantitatively in good agreement with those for the fluorocarbon R-113 all over the boiling regions.

On the other hand, the heat fluxes in distilled water increased markedly compared with those for both R-11 and R-113. This might be because the boiling temperature, latent heat, surface tension, and thermal conductivity of water are much greater than those of R-11 and R-113. However, it is of interest that the boiling behavior for the distilled water is quantitatively different from that of the fluorocarbon refrigerants at a prescribed ΔT_s, but qualitatively similar to them.

The effects of the properties of the beads on boiling curve characteristics are shown in Figs. 2 and 3, which respectively correspond to glass beads and metal beads as the bed material for a bed depth of 80 mm. The thermal conductivity of glass beads is 0.74 W/mK, while that of metal beads (worked iron) is 59.3 W/mK. The figures show that the boiling heat flux for the metal beads at a prescribed ΔT_s is greater than for the glass beads in the range of nucleate boiling. These higher heat fluxes are probably caused by the finlike effect of the beads in contact with the heating surface.

Correlation Equations

A number of experiments for a variety of working liquids, physical characteristics of beads, bead diameters, and bed depths were carried out to investigate the boiling performance in liquid-saturated porous beds. Attention will now be turned to the correlation of the resulting heat flux data.

We found that for the transition boiling range, the heat transfer coefficient defined in terms of the difference between the heating surface and saturation temperatures might be expressed by the following functional relation among dimensional groups

$$\mathrm{Nu}_l = f(d_p/\sqrt{\sigma/g(\rho_l-\rho_v)},\ L/(C_{ml}\Delta T_s),\ \mathrm{Pr}_l,\ \lambda_{ml}/\lambda_l,\ d_p/H_p) \qquad (1)$$

which contains the diameter of the beads making up the bed d_p, the Prandtl number of the liquid Pr_l, and several groups containing such fluid properties as heat of vaporization L, liquid specific heat C_l, saturation temperature T_s, surface tension σ, liquid density ρ_l, vapor density ρ_v, and liquid thermal conductivity λ_l. The C_{ml} and λ_{ml} are the equivalent specific heat and equivalent thermal conductivity, defined as $C_{ml} = \epsilon C_l + (1-\epsilon)C_p$ and $\lambda_{ml} = \epsilon\lambda_l + (1-\epsilon)\lambda_p$ where ϵ is the void ratio of the porous bed.

The transition data are plotted in terms of these dimensionless groups in Fig. 9. A best fit through these points yields the final correlation equation in the form

$$\mathrm{Nu}_l = 7.50\times10^{-2}(d_p/\sqrt{\sigma/g(\rho_l-\rho_v)})^{0.9}(L/C_{ml}\Delta T_s)^m \mathrm{Pr}^{2.37}(\lambda_{ml}/\lambda_l)^n \qquad (2)$$

where

$$m = 1.30(d_p/\sqrt{\sigma/g(\rho_l-\rho_v)})^{0.6}\mathrm{Pr}_l^{-0.8}$$

and

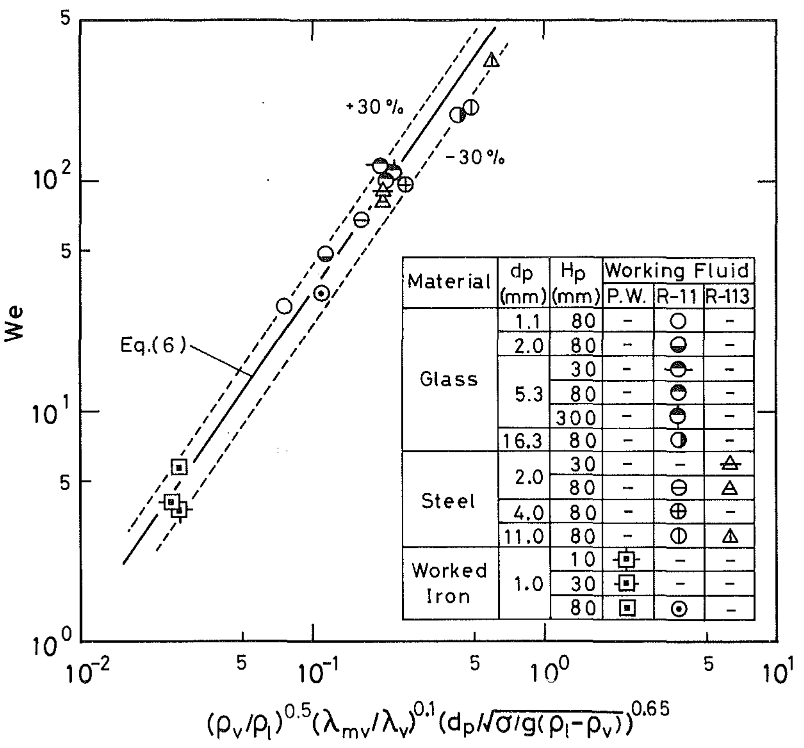

Material	dp (mm)	Hp (mm)	Working Fluid P.W.	R-11	R-113
Glass	1.1	80	-	○	-
	2.0	80	-	◒	-
	5.3	30	-	-◓-	-
		80	-	◓	-
		300	-	◓	-
	16.3	80	-	◑	-
Steel	2.0	30	-	-	-△-
		80	-	⊖	△
	4.0	80	-	⊕	-
	11.0	80	-	⦶	△
Worked Iron	1.0	10	-⊡-	-	-
		30	-⊡-	-	-
		80	⊡	⊙	-

Fig. 11 Correlation of minimum heat flux

$$n = -0.59\mathrm{Pr}_l^{0.3}$$

The experimental results of previous investigators [2-4, 13] are also shown for comparison. It is clear that equation (2) correlates most of the other data within ±40 percent. The data for very small diameter beads [3, 13] are an exception.

Bromley [18] derived a theoretical equation for film boiling heat transfer assuming conduction through a laminar vapor film. The resulting equation was of the same form as Nusselt's for film condensation. Using a model similar to Bromley's [18], we obtained the following relation

$$\mathrm{Nu}_v = f(\mathrm{Gr},\ \mathrm{Pr}_v,\ L/(C_{mv}\Delta T_s),\ \lambda_{mv}/\lambda_v,\ d_p/H_p) \qquad (3)$$

where Gr is the modified Grashof number defined as $d_p{}^3 g(\rho_l-\rho_v)\rho_v/\mu v^2$, Pr_v the Prandtl number of the vapor, C_{mv} the equivalent specific heat defined as $\epsilon C_v + (1-\epsilon)C_p$, and λ_{mv} the equivalent thermal conductivity defined as $\epsilon\lambda_v + (1-\epsilon)\lambda_p$. The physical property values of the liquid were evaluated at the saturated liquid temperature, and those of the vapor at $(T_w + T_s)/2$.

All of the present film boiling data are correlated in Fig. 10 in accordance with equation (3). It is observed that the Nusselt number has a weak dependence on d_p/H_p. In the figure, the experimental results of [2] are also shown for comparison. A best fit through these points yields the following correlation

$$\mathrm{Nu}_v = 4.10(\mathrm{GrPr}_v)^{0.25}(L/C_{mv}\Delta T_s)^{0.04} (\lambda_{mv}/\lambda_v)^{-0.95}(d_p/H_p)^{0.15} \qquad (4)$$

It should be noted that the data used for correlating equation (4) were obtained within the H_p values ranging from 10 to 300 mm.

We turn next to the minimum heat flux. Berenson [19] correlated Zuber's minimum heat flux prediction and showed that the lead constant had to be specified experimentally. We can recast Berenson's prediction into the following dimensionless functional equation for the minimum heat flux

$$\mathrm{We} = f(d_p/\sqrt{\sigma/g(\rho_l-\rho_v)},\ \rho_v/\rho_l,\ \lambda_{mv}/\lambda_v) \qquad (5)$$

where We is a Weber number defined as $q_{\min}{}^2 d_p/(\rho_v \sigma L^2)$.

The experimental data obtained for the comparatively larger diameter beads are plotted in terms of equation (5) in Fig. 11. A best fit through these points yields the final correlation equation

$$\mathrm{We} = 9.21\times 10^3(d_p/\sqrt{\sigma/g(\rho_l-\rho_v)})^{0.65} (\rho_v/\rho_l)^{0.5}(\lambda_{mv}/\lambda_v)^{0.1} \qquad (6)$$

Conclusions

An experimental investigation of transition and film boiling heat transfer in a liquid-saturated porous bed has been described. Water and fluorocarbon refrigerants R-11 and R-113 were used as the working liquids. Varying the diameter of the beads, the bed depth, and the heat flux, we have found that:

1 For small bead diameters q rises continuously and monotonically with ΔT_s from nucleate boiling to film boiling without going through a peak heat flux.

2 The heat transfer coefficients in the transition boiling and film boiling regions can be reasonably correlated by equations (2) and (4), respectively, while the minimum heat flux is given by equation (6).

Acknowledgments

The authors are indebted to Mr. N. Hotta for his help in the experiments.

References

1 Tsuchiya, M., Shimizu, S., and Takeyama, T., "Pool Boiling in Water With Steel Ball," *6th National Heat Transfer Symposium of Japan*, 1969, pp. 25-28.

2 Satoh, H., Ohuchi, M., and Takeyama, T., "Boiling Heat Transfer From Porous Surfaces," *11th National Heat Transfer Symposium of Japan*, 1974, pp. 97-100.

3 Ferrell, J. K., and Alleavitch, J., "Vaporization Heat Transfer in Capillary Wick Structures," *Chem. Engng. Symp. Ser.*, Vol. 66, 1970, pp. 82-91.

4 Shibayama, S., Shioka, S., and Kitagawa, R., "Heat-Transfer Characteristics (Modeling of Evaporation in Heat Pipe)," *Preprints of 861st Conference* of JSME, 1975, pp. 65-68.

5 Cornwell, K., Nair, B. G., and Patten, T. D., "Observation of Boiling in Porous Media," *Int. J. Heat Mass Transfer*, Vol. 19, 1976, pp. 236-238.

6 Sugawara, A., Takahashi, I., Ohba, S., and Sugawara, S., "Pool Boiling From Surface With Particulated Bed," *15th National Heat Transfer Symposium of Japan*, 1978, pp. 169–171.

7 Sugawara, A., and Takahashi, I., "Boiling Heat Transfer in Porous Media," *18th National Heat Transfer Symposium of Japan*, 1981, pp. 352–354.

8 Somerton, C., Catton, I., and Thompson, L., "An Experimental Investigation Into Dryout in Deep Debris Bed," ASME Paper No. 81-WA/HT-17, 1981.

9 Bergles, A. E., and Chyu, M. C., "Characteristics of Nucleate Pool Boiling From Porous Metallic Coatings," ASME JOURNAL OF HEAT TRANSFER, Vol. 104, 1982, pp. 279–285.

10 Nakayama, W., Daikoku, T., Kuwahara, H., and Nakajima, T., "Dynamic Model of Enhanced Boiling Heat Transfer on Porous Surfaces. Part I: Experimental Investigation," ASME JOURNAL OF HEAT TRANSFER, Vol. 102, 1980, pp. 445–450.

11 Bau, H. H., and Torrance, K. E., "Thermal Convection and Boiling in a Porous Medium," ASME Paper No. 81-WA/HT-18, 1981.

12 Bau, H. H., and Torrance, K. E., "Boiling in Low-Permeability Porous Materials," *Int. J. Heat Mass Transfer*, Vol. 25, 1982, pp. 45–55.

13 Itoh, T., Nishikawa, K., and Tanaka, K., "Enhanced Heat Transfer by Nucleate Boiling at Sintered Metal Layer; Discussion on Sintered Layer and Experiments by Piled Layer and Form Layer," *Refrigeration*, Vol. 57, 1982, pp. 77–81.

14 Bird, R. B., Stewart, W. E., and Lightfoot, E. N., *Transport Phenomena*, Wiley, 1960, p. 199.

15 Torikoshi, K., "Experimental Study of Boiling Heat Transfer for Fluorocarbon Refrigerant R-11," M.E. Thesis, Department of Mechanical Engineering, Hokkaido University, 1974.

16 Seki, N., Fukusako, S., and Torikoshi, K., "Experimental Study on the Effect of Orientation of Heating Circular Plate on Film Boiling Heat Transfer for Fluorocarbon Refrigerant R-11," ASME JOURNAL OF HEAT TRANSFER, Vol. 100, 1978, pp. 624–628.

17 Komoriya, T., "Experimental Study of Boiling Heat Transfer in a Liquid-Saturated Porous Bed," M.E. Thesis, Department of Mechanical Engineering, Hokkaido University, 1982.

18 Bromley, L. A., "Heat Transfer in Film Boiling," *Chemical Engineering Progress*, Vol. 46, 1950, pp. 221–227.

19 Berenson, P. J., "Film Boiling Heat Transfer From a Horizontal Surface," ASME JOURNAL OF HEAT TRANSFER, Vol. 83, 1961, pp. 351–357.

20 Costello, C. P., and Redeker, E. R., "Boiling Heat Transfer and Maximum Heat Flux for a Surface With Coolant Supplied by Capillary Wicking," *Chem. Eng. Progr. Symposium Ser.*, No. 41, Vol. 59, 1963, pp. 104–113.

A. W. Reed
Fluid Mechanics and Heat Transfer
Division 1512,
Sandia National Laboratories,
Albuquerque, NM 87185
Assoc. Mem. ASME

A Mechanistic Explanation of Channels in Debris Beds

A mechanistic explanation of channeling during boiling in unconsolidated particulate debris beds is formulated by combining a free-body force diagram and the capillary pressure-saturation curve for porous media. The model is consistent with the principles of two-phase flow in porous media and provides boundary conditions for the flow equations in the unchanneled region. Experimental evidence for spherical particles presented here implies that the solid matrix in the channeled region cannot maintain a shear force and therefore behaves like a fluid without being fluidized in the classical sense.

1 Introduction

The cooling of a heated particulate bed immersed in a fluid has been a topic of interest in the field of liquid metal fast breeder reactor safety for about thirteen years [1]. There is general agreement about the fundamental cooling mechanism. Liquid from the overlying pool flows downward into the bed where it is heated into vapor. The vapor then travels upward, reaches the top of the bed, and exits into the overlying pool. Dryout occurs when the liquid can no longer reach a portion of the bed, and the particles proceed to heat up past the saturation temperature of the liquid.

The bottom section of a heated particulate bed is typically modeled as a porous material in which there is two-phase counterflow [2]. The top of the bed, in which channels have been observed, has been a source of controversy. Dhir and Catton [3] have argued that this section is fluidized. More recently, the approach has been to treat the liquid in the channeled zone hydrostatically. With the aid of correlations predicting the depth of this zone, the one-dimensional saturation equation describing the unchanneled region can be solved and dryout predicted [2, 4, 5].

These two views can be reconciled by an analysis of the statics of the particle bed at the channel wall. This analysis is combined with the capillary pressure-saturation curve to produce a correlation for the channel depth, which is dependent on the state of stress of the solid matrix. The Mohr-Coulomb law for failure of unconsolidated porous materials provides only an order-of-magnitude bound on this stress state. Experiments in which channel depths are measured are used to infer a spherical state of stress in the solid matrix, which in turn provides closure for the channel depth analysis.

2 Statics of Channels

In shallow particle beds, the experimentally measured dryout powers are in excess of those predicted by two-phase porous flow models. The difference has been attributed to the effect of channels. It is shown here that the porous flow equations suggest the existence of a channel-like effect when the boundary condition at the top of the bed is examined.

Experiments [6] indicate that the vapor exits a particle bed in the form of bubbles which are on the order of 1 cm in diameter. A large bubble radius means that the liquid and vapor pressures are about equal. Applying continuity of pressure across the interface between the top of the bed and the pool, one concludes that the liquid and vapor pressures at the top of the bed must also be nearly equal. This small pressure difference can be located on the Leverett curve (Fig. 1), which relates the capillary pressure to the saturation in uncemented particulate porous media. Because the debris bed is initially filled with liquid before the vapor is generated, the drainage curve is appropriate. Negligible capillary pressure corresponds to a saturation of unity. This value of saturation at the top of the bed presents an unacceptable physical consequence. It implies that the flow area for the vapor at the top of the bed is zero and that the vapor velocity must approach infinity as it exits the bed. However, one would expect solid particles in the path of the vapor to be elutriated when the vapor reached their terminal velocity. Thus there must be some mechanism like channels which provides for reasonable vapor exit velocities.

The paradox is extended by a more careful examination of the Leverett curve. A finite pressure difference must exist before the saturation in the particulate bed can differ from unity. This corresponds to the pressure differential necessary for the vapor to penetrate the largest voids in the porous matrix. Higher pressure differences correspond to the penetration of smaller voids. This drop from a finite pressure difference in the section describable by two-phase porous flow to the negligible pressure difference found at the top of the bed can be explained by the existence of channels.

A model for channeling must provide two pieces of information: the depth of the channeled region and the capillary pressure at the bottom of this region. The latter can be

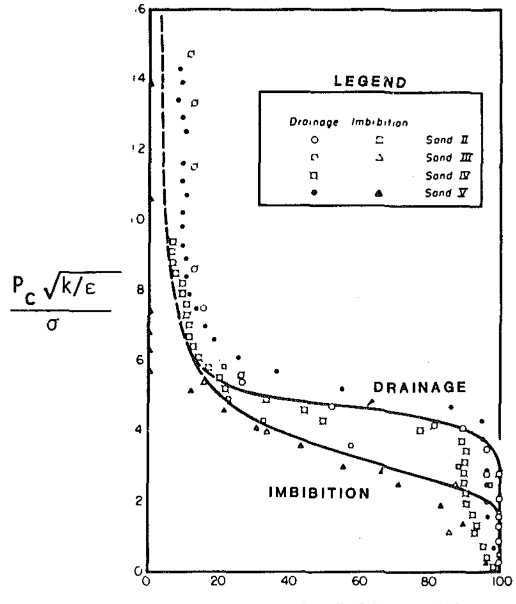

Fig. 1 Correlation of data from height-saturation experiments on clean unconsolidated sands [7]

Contributed by the Heat Transfer Division for publication in the JOURNAL OF HEAT TRANSFER. Manuscript received by the Heat Transfer Division May 9, 1983.

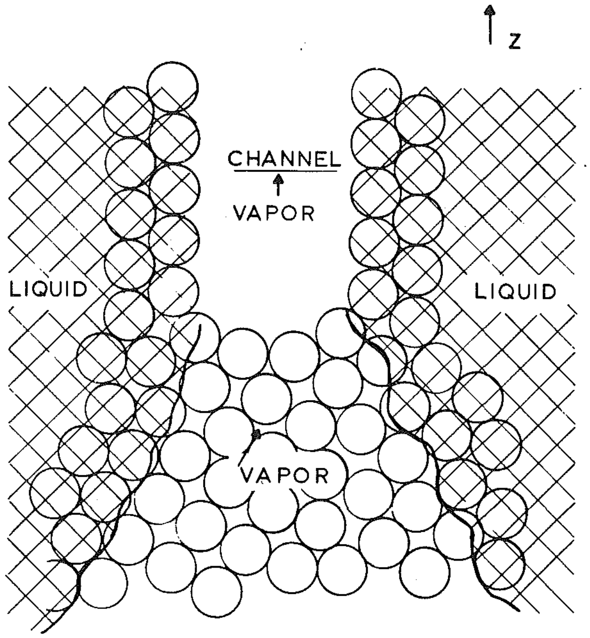

Fig. 2 Schematic of vapor feeding into a channel

estimated using the observation [5] that particles which occasionally fall into a channel are swept out. Figure 2 depicts a possible liquid–vapor geometry at the base of a channel. As the vapor rises, the saturation increases, the flow area for the vapor decreases, and the interstitial vapor velocity increases. When the vapor velocity is sufficiently large, particles can be entrained by the vapor and a channel is possible.

The average interstitial velocity in the z direction immediately below the channel is

$$V_{v,i}=\frac{q_v}{(1-S_m)\epsilon} \tag{1}$$

where q_v is the superficial velocity of the vapor based on the entire bed area and S_m is the saturation immediately below the channel. If the vapor feeds into the bottom of the channel only, then the average vapor velocity in the channel is

$$V_{v,c}=\epsilon V_{v,i} \tag{2}$$

In a volume-heated bed, this is

$$V_{v,c}=\frac{1}{1-S_m}\int_0^{L-h}\frac{\ddot{Q}(1-\epsilon)}{\rho_v h_{fg}}dz \tag{3}$$

If the vapor velocity in the channel is set to the terminal velocity of a solid particle, then equation (3) may be solved for S_m. The capillary pressure at the base of the channel can then be obtained from the Leverett curve using S_m.

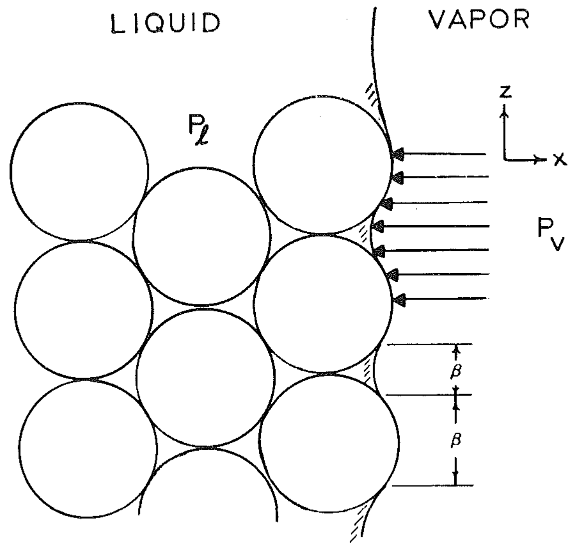

Fig. 3 Microscopic view of channel interface

Consider the case of 356-μm steel particles ($\rho=7859$ kg/m^3) immersed in water. The total dryout flux as reported by Keowin is about 762 kW/m^2 [8]. The terminal velocity of a particle in steam at one atmosphere is about 8.4 m/s. The terminal velocity argument yields a value for S_m of 0.933.

The argument here is incomplete. The change in velocity that occurs when the vapor leaves the interstice and enters the channel requires a corresponding pressure increase which is not included in the calculations. This pressure rise can be reduced to zero if the vapor is assumed to penetrate the sides of the base of the channel as well as the bottom so that the interstitial vapor velocity is equal to the channel vapor velocity. It is difficult to visualize the geometry in this portion of the channel, and the two-dimensional nature of the vapor flow probably contributes to its definition. Additionally, the velocity in the channel could be lower or higher than the particle terminal velocity in free space. However, the quantity of primary importance is the capillary pressure at the bottom of the channeled region. This turns out to be fairly insensitive to the value of saturation for saturations greater than 0.7 (Fig. 1). Therefore, in the absence of a clear physical argument, and due to the insensitivity of the final result, the saturation at the bottom of the channeled region is approximated by the value 0.99.

A bound on the channel depth can be obtained by examining the geometry of a channel, drawing a free-body diagram of the solid constituent, and applying the principles of soil mechanics. Figure 3 is a schematic of a vertical channel wall. Vapor in the channel contacts both liquid and solid

Nomenclature

d = average particle diameter
g = gravitational constant
h = channel depth
h_{fg} = enthalpy of evaporation
J = Leverett J function
$=P_c\sqrt{\frac{k}{\epsilon}}\,\sigma\cos\theta$
k = laminar permeability
k_v = vapor laminar relative permeability
K = stress ratio in solid matrix
P = pressure
P_c = capillary pressure

q = superficial velocity
$\ddot{Q}$ = volumetric heat generation in solid
S = saturation
$=\frac{\text{(liquid volume)}}{\text{(nonsolid volume)}}$
z = vertical distance
ϵ = void fraction
θ = liquid/solid contact angle
κ = turbulent permeability
κ_v = turbulent relative permeability of vapor
μ = absolute viscosity

ρ = density
σ = surface tension
τ_{zz} = vertical stress
τ_{xx} = horizontal stress
ϕ = friction angle

Subscripts

a = active
c = channel
i = interstitial
l = liquid
p = passive
s = solid
v = vapor

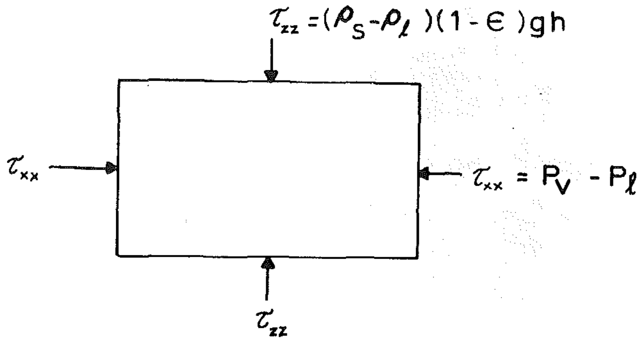

Fig. 4 Free-body diagram of element of solid porous material

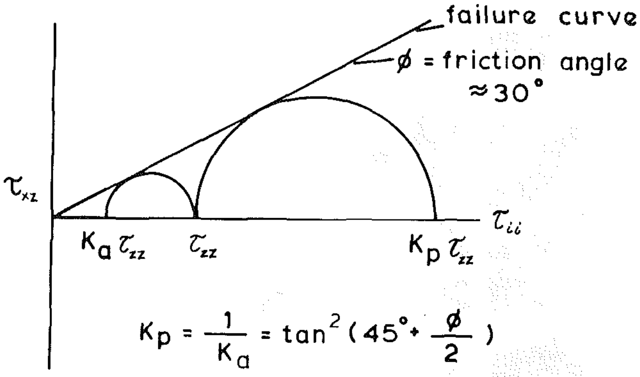

Fig. 5 Mohr-Coulomb failure law

surfaces. The liquid exists at a lower pressure than the vapor, but is kept from receding by the surface tension.

The horizontal normal stress on the solid matrix (τ_{xx}) can be divided into two parts. Let β be the fraction of the projected particle surface area exposed to the vapor (Fig. 3). Integrating the pressure around the particle and averaging over the total projected area, one finds that the first part of the horizontal stress is

$$\tau_{xx1} = \beta(P_v - P_l) \tag{4}$$

The second part is due to the so-called "membrane force" of the liquid-vapor interface acting upon the solid. The magnitude of this force is equal to the product of the liquid-vapor pressure difference and the projected liquid-vapor interfacial area. Averaging this force over the total projected area

$$\tau_{xx2} = (1 - \beta)(P_v - P_l) \tag{5}$$

The total horizontal normal stress is the sum of these two components, and is independent of β.

$$\tau_{xx} = P_v - P_l = P_c \tag{6}$$

Gravity acting upon the solid immersed within the liquid produces a vertical stress on the solid matrix (Fig. 4). The shear stress on the channel wall is assumed to be small compared to the normal stresses. Therefore

$$\tau_{zz} = (\rho_s - \rho_l)(1 - \epsilon)g(L - z) \tag{7}$$

$$\tau_{xz} \approx 0 \tag{8}$$

The porous matrix adjacent to a channel can change in two ways. If the vapor pressure is too low, the particles will slide inward and the channel will collapse. Alternatively, if the vapor pressure is too large, the particles will be forced outward and the channel will expand. For unconsolidated particulate beds, these failure limits are described by the Mohr-Coulomb failure law [9]. The failure curve on the Mohr diagram (Fig. 5) is approximately linear for small loads. The angle of the failure curve is known as the friction angle. This angle can vary from about 25 to 50 deg, depending upon the particle size, porosity, saturation, and solid properties.

A state of stress described by a Mohr's circle which lies below the failure curve is stable. A Mohr's circle which crosses the failure curve describes a state which will fail. A state of impending failure is described by a Mohr's circle which is tangent to the failure curve. For the given value of vertical stress, there are two possible modes of failure. The Rankine active state occurs when

$$\frac{\tau_{xx}}{\tau_{zz}} = K_a = \left[\tan^2\left(45\text{ deg} + \frac{\phi}{2}\right)\right]^{-1} \tag{9}$$

This is the state of impending channel collapse. The Rankine passive state occurs when

$$\frac{\tau_{xx}}{\tau_{zz}} = K_p = \tan^2\left(45\text{ deg} + \frac{\phi}{2}\right) \tag{10}$$

This is the state of impending channel expansion. Combining equations (9) and (10)

$$K_a \tau_{zz} \leq \tau_{xx} \leq K_p \tau_{zz} \tag{11}$$

Substituting equations (6) and (7) into equation (11)

$$K_a(\rho_s - \rho_l)(1 - \epsilon)g(L - z) \leq P_c \leq K_p(\rho_s - \rho_l)(1 - \epsilon)g(L - z) \tag{12}$$

At the bottom of the channel

$$L - z = h$$

and the capillary pressure is

$$P_c \approx P_c(S = 0.99) \tag{13}$$

Substituting equation (13) into equation (12)

$$K_a(\rho_s - \rho_l)(1 - \epsilon)gh \leq P_c(S = 0.99) \leq K_p(\rho_s - \rho_l)(1 - \epsilon)gh \tag{14}$$

The unknown in the above equation is the channel depth h. Rearranging,

$$\frac{h_0}{K_p} \leq h \leq \frac{h_0}{K_a} \tag{15}$$

where

$$h_0 = \frac{P_c(S = 0.99)}{(\rho_s - \rho_l)(1 - \epsilon)g}$$

The value of the capillary pressure at a saturation of 0.99 is calculated from a fit for the Leverett drainage curve.

$$P_c = 0.3771\sigma \cos\theta \sqrt{\frac{\epsilon}{k}} S^{-0.2430} \tag{16}$$

$$P_c(S = 0.99) = 0.3771\sigma \cos\theta \sqrt{\frac{\epsilon}{k}}$$

This analysis yields bounds on the channel depth, which is linearly dependent on the stress ratio in the solid. For a friction angle of 30 deg

$$K_a(\phi = 30\text{ deg}) = 0.33 \tag{17}$$

and

$$K_p(\phi = 30\text{ deg}) = 3.00$$

The bounds for the channel depth predicted by equation (15) are too far apart. In order to accurately predict the channel depth, the stress ratio in the solid matrix must be known.

3 Experiment

Since the present theoretical analysis could only bound the channel depth, it was decided to try to measure the depth directly. A thin transparent test section (Fig. 6) was built with a gas plenum at its base. At the bottom of the test section was a layer of 16 mesh nylon screening material. A mixture of sieved solid shot and liquid was poured into the test section and allowed to settle. Liquid was added to increase the depth

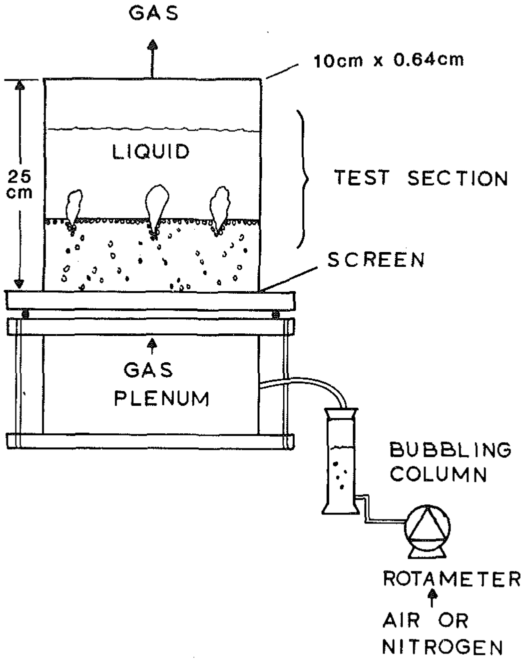

Fig. 6 Thin test section

of the overlying pool. The section was then lightly tapped several times to help the shot settle further. The particles, although smaller than the openings in the screen, did not pass through because of the surface tension of the liquid.

During the experiment, gas (air or nitrogen) was piped into the plenum after being saturated with the liquid vapor in the bubbling column. From the plenum, the gas penetrated the mesh, percolated through the particulate bed, bubbled into the overlying liquid pool, and escaped through the top of the test section to the atmosphere.

Initially, spherical glass shot were used in the hope that the translucent nature of the glass-liquid matrix would make the identification of channels easier. While individual channels could be traced, they were normally thinner than the test section thickness and appeared only as faint lines (Fig. 7). The most prominent feature of the experiment was the jump in the saturation which occurred at the bottom of the channeled region. The channeled zone was completely saturated with liquid. The saturation of the lower zone decreased with increasing gas flow rate. With one exception, the depth of the top zone did not change with gas flow rate.

To evaluate the significance of these two zones, consider the differential equation for saturation in the unchanneled zone as it applies to this experiment [5].

$$\frac{dS}{dz}=\left\{\frac{1}{\dfrac{\partial J}{\partial S}\sqrt{\dfrac{\epsilon}{k}}}\right\}\left\{\frac{1}{\sigma\cos\theta}\left[(\rho_l-\rho_v)g-\frac{\mu}{kk_v}q_v-\frac{\rho_v}{kk_v}|q_v|q_v\right]\right\} \tag{18}$$

In the vicinity of the bottom of the channels, the saturation is large. This forces the vapor relative permeability k_v to be small and thereby causes the saturation gradient to be large. Below the channels, the saturation gradient drops in magnitude and becomes more dependent on the gas flow rate. It can therefore be concluded that the interface between the two zones corresponds to the bottom of the channels.

Further tests were conducted with iron shot instead of glass. Again, with few exceptions, individual channels were difficult to see. Fortunately, the same jump in saturation seen in the experiments with glass shot could be discerned (Fig. 8).

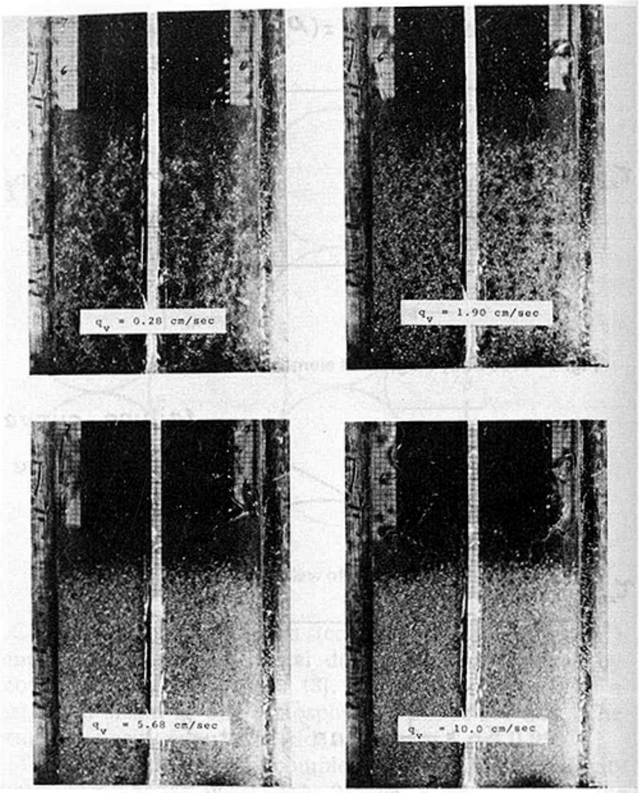

Fig. 7 Gas flow in unconsolidated alcohol-glass matrix ($d = 651$ μm)

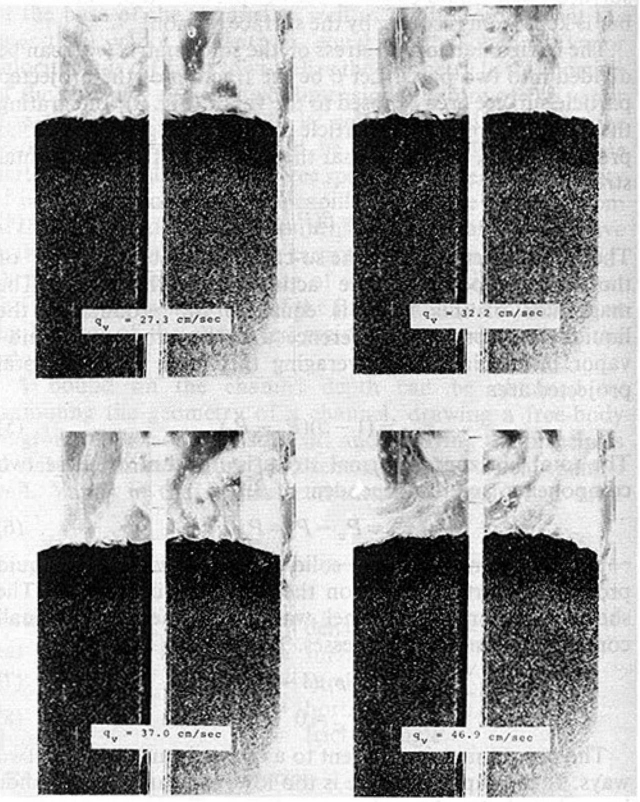

Fig. 8 Gas flow in unconsolidated water-iron matrix ($d = 651\mu$m)

Plots of channel depth as a function of particle diameter are shown in Figs. 9 and 10. The solid curves are the analytical predictions of channel depth assuming a stress ratio of unity. For this case

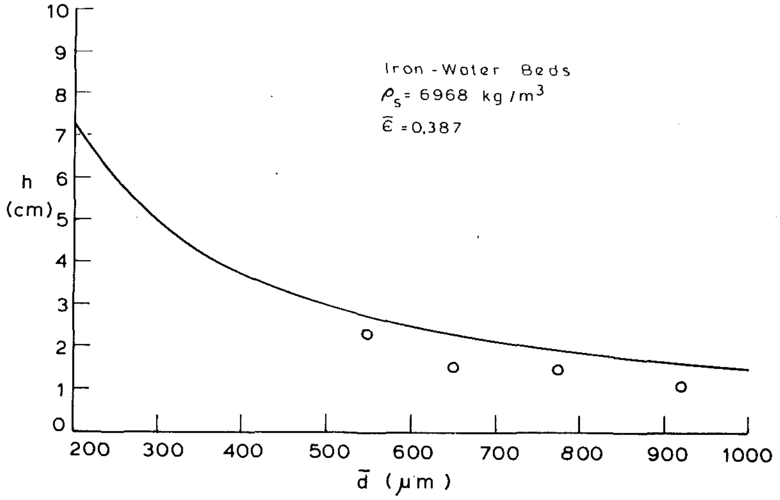

Fig. 9 Channel depth versus particle diameter

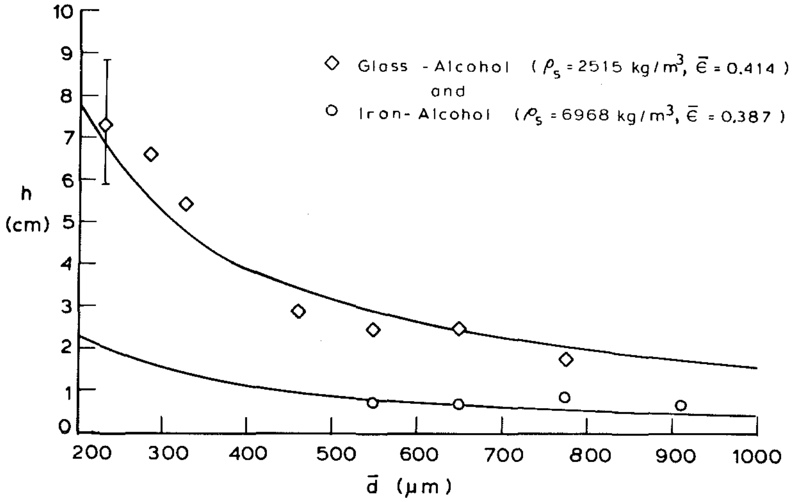

Fig. 10 Channel depth versus particle diameter

$$h = h_0 = \frac{P_c(S=0.99)}{(\rho_s - \rho_l)(1-\epsilon)g} \tag{19}$$

Using equation (16) for P_c and the Ergun equation for the laminar relative permeability k, the channel depth reduces to

$$h = \frac{0.3771\sqrt{150}\sigma \cos\theta}{(\rho_s - \rho_l)gd\epsilon}. \tag{20}$$

The predictions shown in Figs. 9 and 10 are based on a zero contact angle. The iron-water data would be better fitted if a 45 deg contact angle were assumed.

Since a stress ratio of unity seems to fit the data reasonably well, the implications of this ratio should be explored. The Mohr's circle for this state reduces to a point. No shear forces exist in any coordinate frame.

The absence of shear forces can be explained mechanistically. The growth and departure of bubbles and the effect of secondary liquid flows which impact the growing bubbles cause pressure fluctuations in the gas which are transmitted as oscillations in the horizontal stress exerted on the channel wall. These oscillations appear to cause vigorous vibrations of the channel wall and a corresponding particle motion. Frictional forces cannot be transmitted between particles because of the lack of sustained contact. Without these frictional forces, the solid matrix cannot maintain a shear force.

This model explains a number of observations. In previous test sections [5], a channel sometimes formed against the transparent wall. Frequently, a particle at the channel wall was spinning. The drag force from the vapor in the channel produced a torque on the particle. In the absence of any frictional forces from neighboring particles, the observed particle was free to spin.

Secondly, the analysis is based on a vertical channel. However, channels exist at all angles, including the horizontal. The analysis remains unchanged for inclined channels in the absence of solid shear forces.

Finally, the model addresses the problem of fluidization in the channeled region. The region is not fluidized in the classical sense. However, the solid matrix cannot maintain a shear force statically, and therefore takes on the appearance of a fluid.

The obvious omissions from Figs. 8 and 9 are data from a glass shot-water test. This combination yielded unstable channels. For the particle diameter range of 400 to 1000 μm, the predicted channel depths are between 56 and 140 mm. The bed depth was 200 mm. At a gas superficial velocity of less than about 0.2 m/s, the channel depth seemed to be consistent with a stress ratio of unity, although the saturation discontinuity was difficult to discern at this gas velocity. When the gas flow was increased, one channel would propagate downward surrounded by a fully saturated zone. When the channel reached the bottom of the bed, the plenum pressure dropped rapidly and the channel collapsed. The plenum

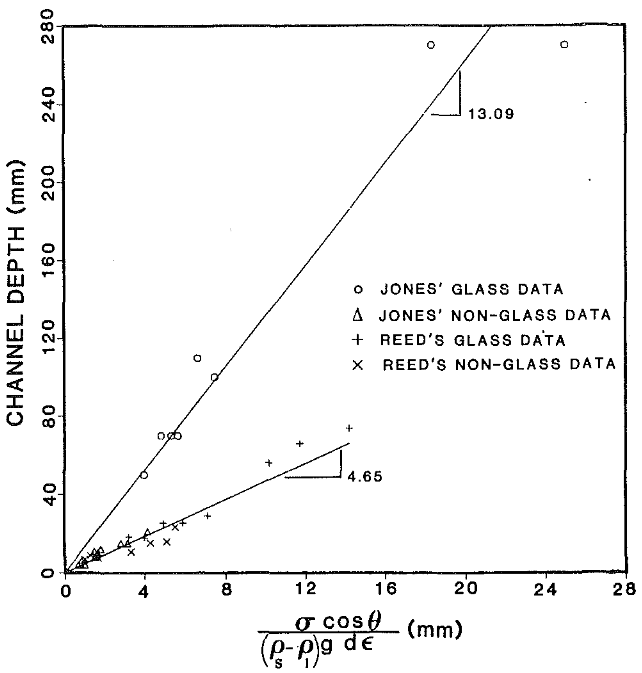

Fig. 11 Channel depth versus depth parameter

pressure would then increase until the channel opened, and the pressure once again dropped. This "burping" is characteristic of a channel which has penetrated a gas pocket.

The cause of the instability is unknown. Two parameters were changed when water was substituted for alcohol in the glass shot bed. The glass-liquid density difference decreased by 12 percent and the surface tension increased by a factor of three. However, when iron shot was used with water, the increased solid-liquid density difference suppressed the instability. Liquid sodium has a surface tension which is two to four times greater than that of water. Whether this results in unstable channels in sodium-fuel debris beds is unknown.

4 Comparison With Other Models

In addition to this formulation, two other correlations have been independently proposed for channel length. Schwalm and Nijsing [10] suggest the form

$$h_c = J(S_m)\,\sigma\sqrt{\frac{\epsilon}{k}}\,\rho_s(1-\epsilon)g \qquad (21)$$

The buoyancy effect of the liquid on the solid is missing here. Additionally, the value of S_m is selected from an extrapolation of the saturation profile predicted by the unchanneled porous flow equations.

Jones et al. [11] suggest the correlation

$$h_c = \frac{6\sigma}{(\rho_s-\rho_l)g\epsilon d}H \qquad (22)$$

This is identical to equation (20), except for the coefficient. The "6" in (22) is based upon a hydraulic radius argument for capillary rise. The value of 4.62 presented in this paper is based upon a curve fit [5] of Leverett's original data [7] and an assumed value for S_m of 0.99.

While the value of the currently proposed coefficient is more physically justified than that of [11], it has no intrinsic accuracy. Leverett's measurements of the P_c-S curve were conducted on unconsolidated sand samples ranging in diameter from 45 μm to 180 μm. The use of Leverett's correlation in these calculations is an extrapolation outside the range of his data. The problem is compounded by the fact that the P_c-S curve should have some dependence upon particle shape, but the nature of that dependence is unknown. Therefore, the value of P_c at $S=0.99$ has an unquantified error band.

Another source of uncertainty in the coefficient is in the determination of S_m. A theoretically appropriate value cannot be proposed without some idea of the interfacial geometry at the base of the channel. The value of 0.99 was chosen in this paper because of the simple geometry that it suggests and the relative insensitivity of the final result to the assumption. An alternative to this approach was proposed by Lipinski [2], who suggested that there is continuity in the vapor pressure gradient at the base of the channel. Implicit in this requirement is the assumption that the solid matrix immediately below the channels is also in a spherical stress state. The validity of this assumption is currently impossible to assess, but the final result should be fairly insensitive to the requirement.

In order to determine the appropriate value of the coefficient, data presented in this paper were combined with those of Jones in a plot (Fig. 11) of channel depth as a function of the quantity

$$\frac{\sigma\cos\theta}{(\rho_s-\rho_l)gd\epsilon}$$

The data appear to divide naturally into two groups. The first group consists of all but Jones' glass data. A linear least-squares fit of this group yields a slope of 4.65. This appears to be the appropriate coefficient for channeling associated with spherical stresses, and agrees well with the coefficient of 4.62 derived for equation (20).

The appearance of a second group, consisting of Jones' glass data and having a slope of 13.09, is somewhat of a surprise. The linearity of these data suggests that these channels are not merely unstable, as suggested by Jones, but in fact have a predictable depth which is consistent with a nonspherical stress state. If one assumes that the Rankine-active state is appropriate for this data group, then, by equation (9), the friction angle inferred from the data is 28 deg. This is a reasonable value for unconsolidated particles.

There is an interesting difference in the glass data reported herein and those of Jones. In this study, stable channels associated with spherical stresses were observed in mixtures of glass and methyl alcohol. Jones used the same mixture and observed channels associated with the Rankine active state. It is suggested that the critical factor causing this difference is the thickness of the test section. Jones used a cylindrical section which allowed channels to move in three directions. The test section for these experiments was thin, and the channels were two-dimensional. Therefore, any future effort to analyze the instability which triggers the shift from the spherical to the active state must take into account the full dimensionality of the problem.

5 Conclusion

Channels in unconsolidated debris beds are the result of capillary effects which allow a net force to be transmitted from the fluids to the solid matrix. The stress normal to the channel wall transferred to the matrix is limited by the maximum pressure difference that the porous structure can maintain. Beyond this pressure difference point, the vapor penetrates the interstices and the two-phase porous flow equations become applicable. The dependence of capillary pressure upon saturation in porous media is described by the Leverett curve.

The response range of the solid matrix is described by the Mohr-Coulomb failure conditions. Measurements of channel depth imply that the matrix is in a hydrostatic state of stress caused by the absence of frictional forces between particles. The inability of the matrix to sustain shear forces gives it the appearance of a fluid without being fluidized. Based upon this stress state, a formula for channel depth (equation (20)) is derived. A comparison with other channel data indicates that in some glass-liquid mixtures, the solid matrix is described by the Rankine active state, which produces deeper channels than the hydrostatic state.

Acknowledgments

The author wishes to thank Professors W. Rohsenow and P. Griffith for their invaluable advice and assistance.

References

1 Sowa, E. S., Hesson, J. C., et al., "Heat Transfer Experiments Through Beds of UO in Boiling Sodium," *Trans. Amer. Nucl. Soc.*, Vol. 14, No. 2, Nov. 1971, p. 725.

2 Lipinski, R. J., "A Model for Boiling and Dryout in Particle Beds," NUREG/CR-2646, SAND82-0765, Sandia National Laboratories, June 1982.

3 Dhir, V., and Catton, I., "Dryout Heat Fluxes for Inductively Heated Particulate Beds," ASME JOURNAL OF HEAT TRANSFER, Vol. 99, May 1977, pp. 250-256.

4 Lipinski, R. J., "A One-Dimensional Particle Bed Dryout Model," *A.N.S. Transactions*, Vol. 38, 1981, pp. 386-387.

5 Reed, A. W., "The Effect of Channeling on the Dryout of Heated Particulate Beds Immersed in a Liquid Pool," Ph.D. Thesis, MIT, Cambridge, MA, Feb. 1982.

6 Gabor, J. D. et al., "Studies and Experiments on Heat Removal From Fuel Debris in Sodium," *Proc. Fast Reactor Safety Conf.*, CONF-740701, U.S. Atomic Energy Commission, 1974, p. 283.

7 Leverett, M. C., "Capillary Behavior in Porous Solids," *Transactions of AIME*, Vol. 142, 1941, pp. 152-169.

8 Mitchell, G. W., Lipinski, R. J., and Schwarz, M. L., "Heat Removal From a Stratified UO2-Sodium Particle Bed," NUREG/CR-2412, 1982.

9 Lambe, T. W., and Whitman, R. V., *An Introduction to Soil Mechanics*, Wiley, New York, 1966.

10 Schwalm, D., and Nijsing, R., "The Influence of Subcooling on Dryout Inception in Sodium-Saturated Fuel Particle Beds With Top Cooling and Adiabatic Bottom," *Nuclear Engineering and Design*, Vol. 70, 1982, pp. 201-208.

11 Jones, S. W., et al., "A Theory for Prediction of Channel Depth in Boiling Particulate Beds," *Transactions of the ASME*, Vol. 104, 1982, pp. 806-808.

K. Vafai
Department of Mechanical Engineering,
Ohio State University,
Columbus, OH 43210
Mem. ASME

S. Whitaker
Department of Chemical Engineering,
University of California,
Davis, CA 95616

Simultaneous Heat and Mass Transfer Accompanied by Phase Change in Porous Insulation

This paper analyzes the accumulation and migration of moisture in an insulation material. The problem is modeled as a two-dimensional, transient, multiphase flow in a porous slab. The local volume-averaging technique is used to arrive at a rigorous and fundamental formulation of the heat and mass transfer process in an insulation system. The controlling parameters and assumptions are presented in detail. The equations are solved by devising a two-phase numerical scheme to obtain the condensation regions and the factors which affect the temperature distribution. The phase change process and its effects on the temperature, vapor density, moisture content, liquid content, and the vapor pressure distributions are discussed in detail. The significant transport mechanisms are identified and a simplified formulation of heat and mass transfer, accompanied by phase change, in an insulation system is presented.

1 Introduction

Transport processes in porous media have been the subject of extensive investigations due to the applicability of such studies in a variety of problems, such as geothermal operations, soil hydrology, nuclear waste disposal, drying technology, and energy conservation. A very important area in the field of energy conservation is the effect of condensation on the performance of high-porosity insulation materials.

A typical insulation material consists of a solid matrix, a gas phase which itself consists of air and water vapor, and a very small amount of adsorbed liquid water. When the insulation matrix is exposed to environments of different temperature and humidity, diffusion and bulk convection of the air, vapor, and liquid occur. In addition, air infiltration due to small differences in total pressure across the insulation matrix augments this transport process. Condensation occurs at any point in the insulation where the water vapor concentration becomes greater than the saturation concentration corresponding to the temperature at that point. As the condensation takes place the latent heat of vaporization is released which acts as a heat source for the heat transfer process. The condensation also creates a liquid phase which may be pendular or mobile due to the capillary action and gravity. In summary, the complete problem is a combined mass, momentum, and energy transfer in a porous medium containing a multiphase mixture of air, vapor, and water in the void space. The general aspects of combined transport in porous media [1-7] are used in formulating and understanding the physics of condensation processes in the porous insulation.

It is crucial to gain a fundamental understanding of the conditions which promote condensation, as condensation will significantly affect energy transfer across the insulation matrix. This in turn greatly influences the R value of the insulation. Furthermore, condensation directly affects the physical integrity of the insulation and its deterioration. A more thorough knowledge of the condensation process in an insulation material will allow better predictions of the condensation rates and the qualitative effects of the controlling parameters. In addition, an understanding of the condensation process will ultimately help in establishing the design locations for the vapor barriers.

The analysis in this paper quantifies the process of moisture accumulation and presents a rigorous and fundamental formulation of heat and mass transfer, accompanied by phase change, in an insulation system. The pertinent variables in an insulation system are presented and the significant transport mechanisms are identified. The variations among the pertinent variables are thoroughly investigated for two types of basic step changes in the temperature and moisture content boundary and initial conditions. Finally, a simplified formulation of heat transfer, accompanied by phase change, in an insulation system is presented. This is done through a systematic investigation of the rigorous formulation to determine which mechanisms have a negligible effect on the pertinent variables.

2 Analysis

The formulation of the problem is based on using the local volume-averaging technique for mass, momentum, and energy equations for each phase to derive the governing equations for the condensation process in an insulation material. This is done by associating with every point in the porous medium a small volume V bounded by a closed surface A. In general, the volume V is composed of three phases. These are: the solid phase V_σ, the liquid phase $V_\beta(t)$, and the gas phase $V_\gamma(t)$. An intrinsic phase average for a quantity ϕ in phase α is defined as

$$<\Phi_\alpha>^\alpha = \frac{1}{V_\alpha(t)} \int_{V_\alpha(t)} \Phi_\alpha dV \tag{1}$$

where Φ_α is a quantity associated with the α phase. Another quantity of interest is the spatial average for the quantity Φ which is defined as

$$<\Phi> = \frac{1}{V} \int_V \Phi \, dV \tag{2}$$

Several simplifying assumptions are made in order to obtain the governing equations for condensation in insulation materials:

I The total gas phase pressure in the insulation matrix is constant. This pressure is denoted by p_{total}.

II The insulation material is homogeneous and isotropic.

III The solid-liquid-gas system is in local thermal equilibrium.

IV The liquid and the gas mass flux vectors are in the

Contributed by the Heat Transfer Division for publication in the JOURNAL OF HEAT TRANSFER. Manuscript received by the Heat Transfer Division May 9, 1984.

same direction. However, there are no restrictions on the magnitudes of the liquid and the gas mass flux vectors.

V The inert gas component in the insulation matrix, which is air, is stagnant. However, the vapor is mobile.

Assumptions I, II, and III are usually justified for an insulation material and assumption IV is physically appealing and justifiable. The simplifying assumption V places the emphasis on the condensation process. Assumption V allows both vapor and liquid phases to be mobile. The nondimensional governing equations, obtained after considerable algebraic manipulation of previous work [1-3] on drying, are given in dimensionless form as

Energy equation:

$$<\rho>C_p\frac{\partial<T>}{\partial t}-\Lambda\,\psi_s(\nabla S\cdot\nabla<T>)$$
$$-\psi_T\Lambda(\nabla<T>\cdot\nabla<T>)$$
$$+\Lambda\,\psi_g(\mathbf{g}\cdot\nabla<T>)+<\dot{m}>=\nabla\cdot(k_{\mathrm{eff}}\nabla<T>) \tag{3}$$

Moisture transport equation:

$$\frac{\partial S}{\partial t}=\nabla\cdot(\psi_s\nabla S)+\nabla\cdot(\psi_T\nabla<T>)-\nabla\cdot(\psi_g\mathbf{g}) \tag{4}$$

Gas phase equation:

$$\frac{\partial(\epsilon_\gamma<\rho_v>^\gamma)}{\partial t}-\frac{<\dot{m}>}{P_4}=\psi_D\nabla^2<\rho_v>^\gamma \tag{5}$$

Volumetric constraint:

$$\epsilon_\sigma+\epsilon_\beta+\epsilon_\gamma=1 \tag{6}$$

Thermodynamic relations:

$$<p_a>^\gamma=p_{\mathrm{total}}-<p_v>^\gamma \tag{7}$$

$$<p_a>^\gamma=P_{11}<\rho_a>^\gamma<T> \tag{8}$$

$$<p_v>^\gamma=P_8<\rho_v>^\gamma<T> \tag{9}$$

$$<p_v>^\gamma=\exp\left[-\frac{2P_9}{<T>}-P_{10}\left(\frac{1}{<T>}-\frac{1}{T_0}\right)\right] \tag{10}$$

where

$$\rho=\frac{\bar{\rho}}{\bar{\rho}_0},\ C_p=\frac{\bar{C}_p}{\bar{c}_0},\ T=\frac{\bar{T}}{\Delta\bar{T}},\ \rho_i=\frac{\bar{\rho}_i}{\bar{\rho}_0},\ k_i=\frac{\bar{k}_i}{\bar{k}_{0,\mathrm{eff}}} \tag{11}$$

$$p_i=\frac{\bar{p}_i}{\bar{p}_{v,0}},\ x_i=\frac{\bar{x}_i}{\bar{L}},\ c_i=\frac{\bar{c}_i}{\bar{c}_0} \tag{12}$$

$$k_{\mathrm{eff}}=\frac{\bar{k}_{\mathrm{eff}}}{\bar{k}_{0,\mathrm{eff}}},\ t=\frac{\bar{t}}{\bar{L}^2/\bar{\alpha}_{0,\mathrm{eff}}},\ \mathbf{g}=\frac{\bar{\mathbf{g}}}{\bar{g}_0},$$

$$\dot{m}=\frac{\dot{\bar{m}}}{\bar{\rho}_0\bar{c}_0\Delta\bar{T}\ \bar{\alpha}_{0,\mathrm{eff}}/\bar{L}^2\Delta\bar{h}_{\mathrm{vap}}} \tag{13}$$

$$\psi_s=\frac{\bar{D}}{\bar{\alpha}_{0,\mathrm{eff}}},\ \psi_D=\bar{D}_{v,\mathrm{eff}}/\bar{\alpha}_{0,\mathrm{eff}},\ \alpha_{0,\mathrm{eff}}=\frac{\bar{k}_{0,\mathrm{eff}}}{\bar{\rho}_0\bar{c}_0} \tag{14}$$

Nomenclature

C_p = dimensionless mass fraction averaged heat capacity = $\bar{C}_p/\bar{c}_0$

$\bar{c}_i$ = dimensional heat capacity at constant pressure for phase i, Ws/kgK

$\bar{c}_0$ = dimensional reference heat capacity at constant pressure, Ws/kgK

$\bar{D}$ = moisture transport coefficient, m^2/s

$\bar{D}_{v,\mathrm{eff}}$ = vapor effective diffusivity coefficient, m^2/s

$\mathbf{g}$ = dimensionless gravity vector

$\Delta\bar{h}_{\mathrm{vap}}$ = enthalpy of vaporization per unit mass, J/kg

$\bar{k}_i$ = dimensional thermal conductivity for phase i, W/mK

$\bar{k}_T$ = a parameter which is related to the gradient of the capillary pressure with respect to temperature, kg/ms^{2}K

k_{eff} = dimensionless effective thermal conductivity = $\bar{k}_{\mathrm{eff}}/\bar{k}_{0,\mathrm{eff}}$

$\bar{K}_\beta$ = liquid phase permeability, m^2

$\bar{L}$ = characteristic length of the insulation, m

Le = Lewis number = $\alpha_{0,\mathrm{eff}}/\bar{D}$

$\dot{m}$ = dimensionless condensation rate = $\dot{\bar{m}}/[\bar{\rho}_0\bar{c}_0(\bar{T}_H-\bar{T}_C)\,\bar{\alpha}_{0,\mathrm{eff}}/\bar{L}^2\Delta\bar{h}_{\mathrm{vap}}]$

p_{total} = dimensionless total pressure in the enclosure = $\bar{p}_{\mathrm{total}}/\bar{p}_{v,0}$

$\bar{R}_a$ = air gas constant, Nm/kgK

$\bar{R}_v$ = vapor gas constant, Nm/kgK

S = the moisture content, defined in equation (17)

t = dimensionless time = $\bar{t}/(\bar{L}^2/\bar{\alpha}_{0,\mathrm{eff}})$

T = dimensionless temperature = $\bar{T}/(\bar{T}_H-\bar{T}_C)$

$\bar{T}_H$ = reference temperature for the hot side of the insulation, K

$\bar{T}_C$ = reference temperature for the cold side of the insulation, K

$\bar{\alpha}_{0,\mathrm{eff}}$ = reference effective thermal diffusivity = $\bar{k}_{0,\mathrm{eff}}/\bar{\rho}_0\bar{c}_0$, m^2/s

ϵ = volume fraction

ζ = the ratio of the magnitudes of the gas phase to the total mass flux, defined in equation (18)

$\bar{\mu}_\beta$ = liquid dynamic viscosity, kg/ms

ρ = dimensionless total density = $\bar{\rho}/\rho_0$

ρ_v = dimensionless vapor density = $\bar{\rho}_v/\bar{\rho}_0$

$\bar{\rho}_i$ = dimensional density for phase i, kg/m^3

$\bar{\sigma}_{\beta\gamma}$ = surface tension at the vapor and gas interface, N/m

ψ_i = denotes different thermophysical properties of the insulation system, defined in equations (14)-(16)

Subscripts, Superscripts, and Symbols

a = air phase

D = reference to the parameter ψ_D, defined in equation (14)

eff = effective properties

g = reference to the parameter ψ_g, defined in equation (16)

i = ith phase

0 = reference quantities

s = reference to the parameter ψ_s, defined in equation (14)

T = reference to the parameter ψ_T, defined in equation (15)

v = vapor phase

vap = vaporization

α = α phase

β = liquid phase

γ = gas phase

σ = solid phase

$\bar{\ }$ = dimensional quantities

$<\ >$ = "local volume average" of a quantity

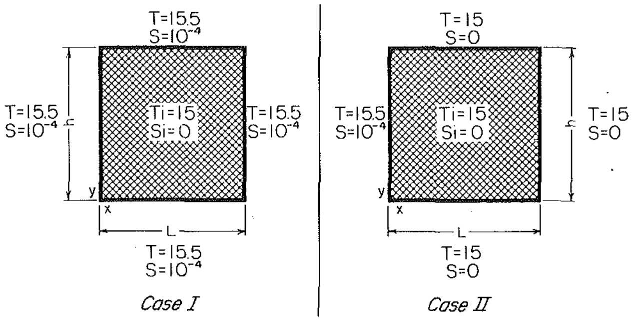

Case I

Case II

Fig. 1 **Transient condensation in an insulation slab for two different cases**

$$\psi_T = \frac{\epsilon_\beta \bar{K}_\beta \nabla \bar{T} \bar{k}_T}{\bar{\alpha}_{0,\mathrm{eff}} (\epsilon_\beta + \epsilon_\gamma) \bar{\mu}_\beta} \tag{15}$$

$$\psi_g = \frac{\epsilon_\beta (\bar{\rho}_\beta - \bar{\rho}_\gamma) \bar{K}_\beta \bar{L} \, \bar{g}_0}{\bar{\alpha}_{0,\mathrm{eff}} \bar{\mu}_\beta (\epsilon_\beta + \epsilon_\gamma)} \tag{16}$$

$$S = (\epsilon_\beta P_1 + \epsilon_\gamma < \rho_v >^\gamma) / P_1 (\epsilon_\beta + \epsilon_\gamma) \tag{17}$$

$$\zeta = \frac{(\psi_D) \,|\, \nabla < \rho_v >^\gamma |}{P_1 (\epsilon_\beta + \epsilon_\gamma) \,|\, \psi_s \nabla S + \psi_T \nabla < T > - \psi_g \bar{g} \,|} \tag{18}$$

$$\Lambda = P_1 [P_2 (1 - \zeta) + P_3 \zeta] (\epsilon_\beta + \epsilon_\gamma) \tag{19}$$

$$\Delta \bar{T} = \bar{T}_H - \bar{T}_C$$

$$< \rho > = \epsilon_\sigma \rho_\sigma + \epsilon_\beta \rho_\beta + \epsilon_\gamma (< \rho_v >^\gamma + < \rho_a >^\gamma) \tag{20}$$

$$C_p = \frac{\epsilon_\sigma \rho_\sigma c_\sigma + \epsilon_\beta \rho_\beta c_\beta + \epsilon_\gamma (c_v < \rho_v >^\gamma + c_a < \rho_a >^\gamma)}{< \rho >} \tag{21}$$

$$k_{\mathrm{eff}} \cong \epsilon_\sigma k_\sigma + \epsilon_\beta k_\beta + \epsilon_\gamma \frac{(k_v < \rho_v >^\gamma + k_a < \rho_a >^\gamma)}{< \rho_v >^\gamma + < \rho_a >^\gamma} \tag{22}$$

and

$$P_1 = \frac{\bar{\rho}_\beta}{\bar{\rho}_0}, \; P_2 = \frac{\bar{c}_\beta}{\bar{c}_0}, \; P_3 = \frac{\bar{c}_\gamma}{\bar{c}_0}, \; P_4 = \frac{\Delta \bar{h}_{\mathrm{vap}}}{\bar{c}_0 \Delta \bar{T}} \tag{23}$$

$$P_8 = \frac{\Delta \bar{T} \, \bar{R}_v \bar{\rho}_0}{\bar{P}_{v,0}}, \; P_9 = \frac{\bar{\sigma}_{\beta\gamma}}{\bar{r}_0 \bar{\rho}_\beta \bar{R}_v \Delta \bar{T}} \tag{24}$$

$$P_{10} = \frac{\Delta \bar{h}_{\mathrm{vap}}}{\bar{R}_v \Delta \bar{T}}, \; P_{11} = \frac{\Delta \bar{T} \, \bar{R}_a \bar{\rho}_0}{\bar{P}_{v,0}} \tag{25}$$

Based on the above equations the primary variables for porous insulation are: T, the temperature; S, the moisture *content;* ρ_v*, the vapor density;* p_v*, the vapor pressure;* ϵ_β*, the* liquid volume fraction; and ϵ_γ, the gaseous volume fraction. The quantities with a subscript "0" refer to the reference quantities, and the variables with a bar on top refer to dimensional quantities.

The boundary conditions for these equations are considered in detail in the next section. In developing the governing equations it is assumed that the moisture transport coefficient D is a constant. However, without any available experimental data, the moisture transport coefficient is not a known quantity. Therefore, experimental investigations are needed in this area. The value of D which was used in this analysis was 4 × 10^{-5} m^2/s. This value is based on the fact that the moisture transport coefficient is dominated by the gas phase diffusion for very small values of the liquid content.

In analyzing the heat and mass transfer process in porous insulation the following physical data were used in the numerical computations: $\bar{L} = 0.12$ m, $\epsilon_\sigma = 0.03$, $\bar{T}_H = 313$ K, $\bar{T}_c = 293$ K, $\bar{\rho}_0 = 32$ kg/m^3, $\bar{c}_0 = 842$ Ws/kgK, $\bar{\sigma}_{\beta\gamma} = 0.073$ kg/s^2, and $\bar{K}_\beta = 10^{-10}$ m^2. These data correspond to a typical fibrous insulation material.

3 Transient Condensation in an Insulation Slab

To analyze the significance of the condensation problem in an insulation material, two different cases are considered. These cases are shown in Fig. 1. In Case I the entire periphery of the slab is suddenly subjected to a different temperature and moisture content and in Case II only one surface of the slab is subjected to a different temperature and moisture content.

In both cases the transient behavior for all of the pertinent variables is analyzed and a sample of the results is presented. The specific boundary and initial conditions which were used for Cases I and II were:

Case I

$$\begin{gathered} T(x=0,\ L;\ y;\ t) = 15.5 \\ T(x;\ y=0,\ h;\ t) = 15.5 \\ S(x=0,\ L;\ y;\ t) = 10^{-4} \\ S(x;\ y=0,\ h;\ t) = 10^{-4} \\ \text{Initial conditions:} \\ T(x;\ y;\ t=0) = 15 \\ S(x;\ y;\ t=0) = 0 \end{gathered} \tag{26}$$

Case II

$$\begin{gathered} T(x=0;\ y;\ t) = 15.5 \\ T(x=L;\ y;\ t) = 15 \\ T(x;\ y=0,\ h;\ t) = 15 \\ S(x=0;\ y;\ t) = 10^{-4} \\ S(x=L;\ y;\ t) = 0 \\ S(x;\ y=0,\ h;\ t) = 0 \\ \text{Initial conditions:} \\ T(x;\ y;\ t=0) = 15 \\ S(x;\ y;\ t=0) = 0 \end{gathered} \tag{27}$$

The dimensionless temperature at the boundary is chosen to correspond to a hot and humid environment on the outside and a colder environment inside of the insulation slab.

One of the objectives of this investigation is to show how the pertinent variables vary with respect to each other for the two types of basic step changes in moisture content and temperature boundary conditions given in equations (26) and (27). These two cases provide two kinds of fundamental step changes in the temperature and humidity of the environment surrounding an insulation slab.

To analyze the above two cases, equations (3) to (10) were solved subject to boundary conditions (26) and (27). The nine unknowns in these equations are: $< T >$, S, $< \dot{m} >$, $< \rho_v >^\gamma$, $< p_v >^\gamma$, $< \rho_a >^\gamma$, $< p_a >^\gamma$, ϵ_β, and ϵ_γ. The nine equations which will uniquely define these unknowns are equations (3) to (10) plus equation (17). These equations were solved using an upwind differencing scheme for the convective terms. The upward differencing was possible since the analysis provided an explicit expression for the direction of the liquid and vapor velocities.

4 Two-Phase Format Numerical Scheme

Initially the insulation slab was assumed to be composed of a solid matrix, water vapor, and air. That is

$$\epsilon_\beta = 0 \qquad \text{at } t = 0 \tag{28}$$

Although this condition could be relaxed very easily, this

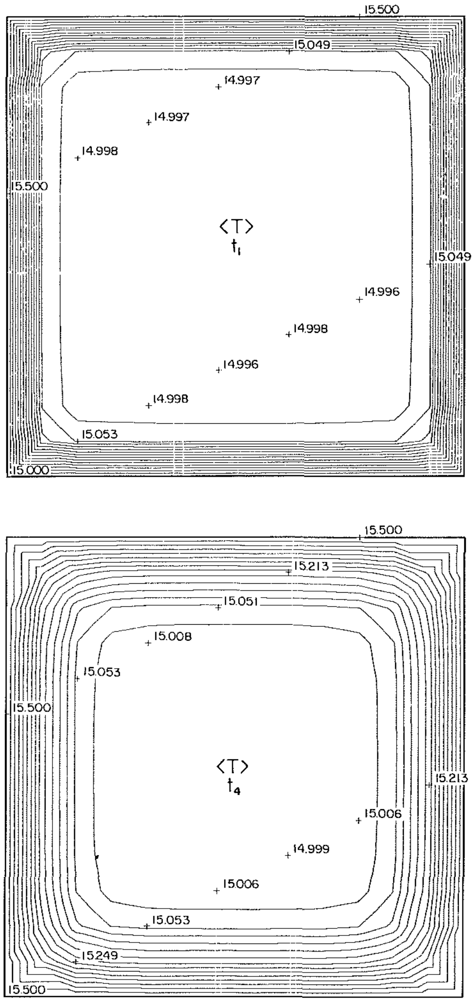

Fig. 2 Spatial variation of temperature inside the insulation slab at two different times (Case I): $t_1 = 2.3 \times 10^{-3}$, $t_4 = 1.4 \times 10^{-2}$

choice was considered to correspond to a more fundamental situation. With no liquid present in the insulation matrix the value of ζ, which is the ratio of the gas phase to the total mass flux, becomes:

$$\zeta = 1 \qquad \text{at } t = 0 \tag{29}$$

In addition, due to the large value of the liquid density compared to the vapor density, the moisture content inside of the slab becomes approximately zero, i.e.

$$S = 0 \qquad \text{at } t = 0 \tag{30}$$

It should be noted that the boundary conditions on the moisture content and the temperature are given by equations (26) and (27). These were discussed in the previous section. At the beginning of the condensation process an appropriate condition for the condensation rate is:

$$<\dot{m}> = 0 \qquad \text{at } t = 0 \tag{31}$$

Based on the experimental results of Langlais et al. [8] values of $\epsilon_\beta < 10^{-6}$ were considered to be part of the adsorbed water. Therefore, at any time and location in the slab for which ϵ_β was less than 10^{-6}, the condensation rate was set equal to zero. For $\epsilon_\beta > 10^{-6}$, again based on Langlais' data [8], condensation was assumed to have actually occurred. Equation (10) was used and the condensation rate $<\dot{m}>$ was found from the governing equations. Starting with the initial values of the temperature and moisture content, equations (3) to (10) were solved by two different formats depending on the value of ϵ_β. These were:

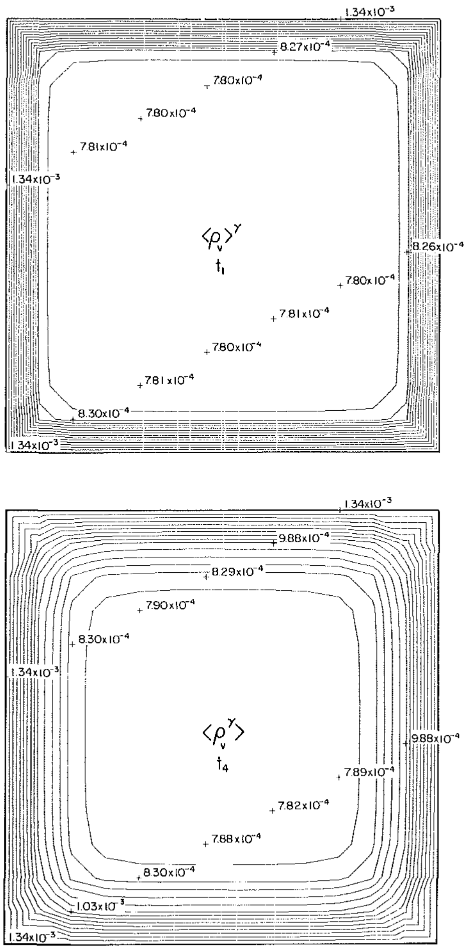

Fig. 3 Vapor density contours at two different times corresponding to Fig. 2 (Case I)

Format I. This format was followed for any time and location in space for which $\epsilon_\beta < 10^{-6}$.

1 Initial values of $<\rho_v>^\gamma$, $<p_v>^\gamma$, $<p_a>^\gamma$, and $<\rho_a>^\gamma$ were obtained from equations (17), (9), (7), and (8). (Step 1 was applied only at the initial time step $t = 0$.)

2 $<\dot{m}>$ was set equal to zero as discussed above.

3 $<\rho_v>^\gamma$ was obtained from the gas phase equation (5).

4 S and $<T>$ were obtained from equations (3) and (4).

5 ϵ_β and ϵ_γ were obtained from equation (17) and the volumetric constraint.

6 The ζ distribution was obtained from equation (18).

7 $<p_v>^\gamma$, $<p_a>^\gamma$, and $<\rho_a>^\gamma$ were obtained from the thermodynamic relations.

8 $<p_v>^\gamma$ and $<\rho_v>^\gamma$ were solved for from equations (10) and (9), respectively.

9 If, at any location, the $<\rho_v>^\gamma$ obtained in step 3 was greater than or equal to the one obtained in step 8, then Format II was adopted for the next time step at that location.

Format II. This format was followed for any time and location in space for which $\epsilon_\beta > 10^{-6}$.

1 $<p_v>^\gamma$, $<\rho_v>^\gamma$, $<p_a>^\gamma$, $<\rho_a>^\gamma$, and ϵ_γ were obtained from the thermodynamic relations and the volumetric constraint. (Step 1 was applied only at the initial time step $t = 0$.)

2 The moisture content distribution was obtained from equation (4).

3 The temperature distribution was obtained from equation (3).

4 The new moisture content and temperature distributions

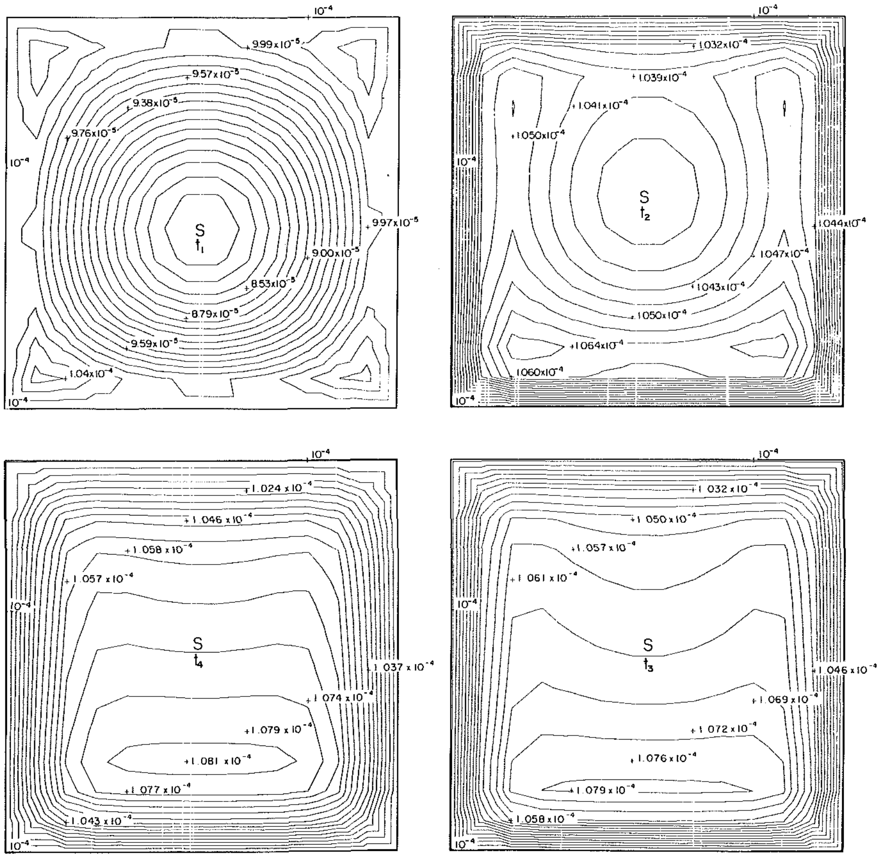

Fig. 4 Spatial variation of the moisture content inside the insulation slab at four different times corresponding to Fig. 2 (Case I)

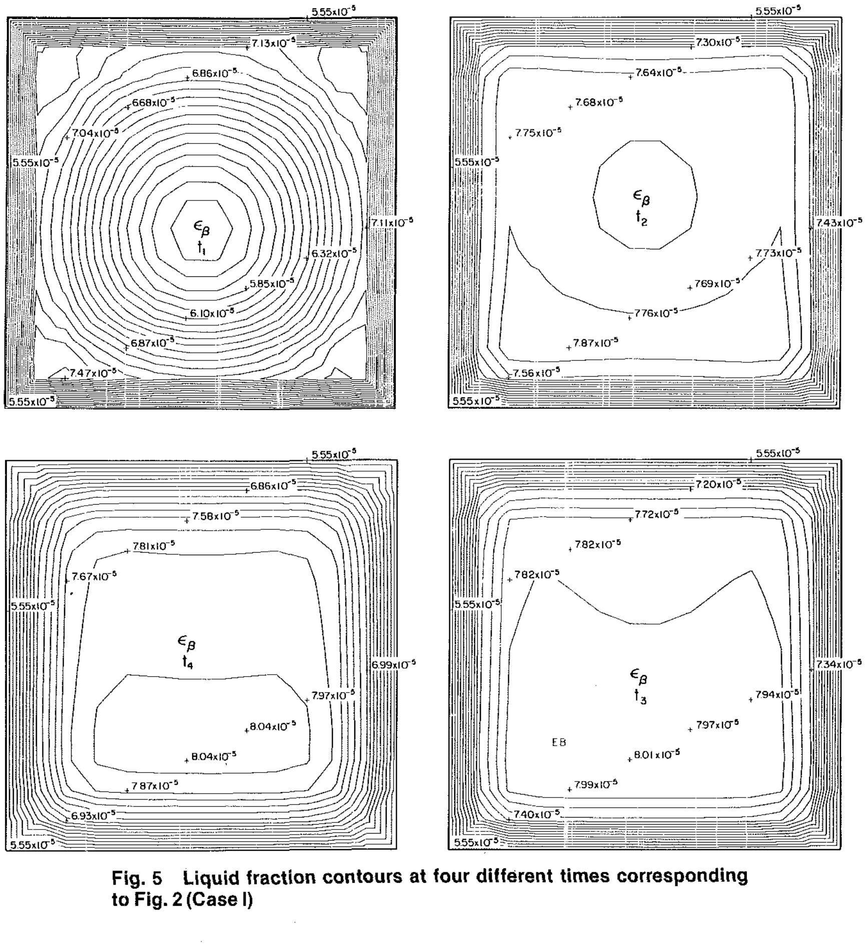

Fig. 5 Liquid fraction contours at four different times corresponding to Fig. 2 (Case I)

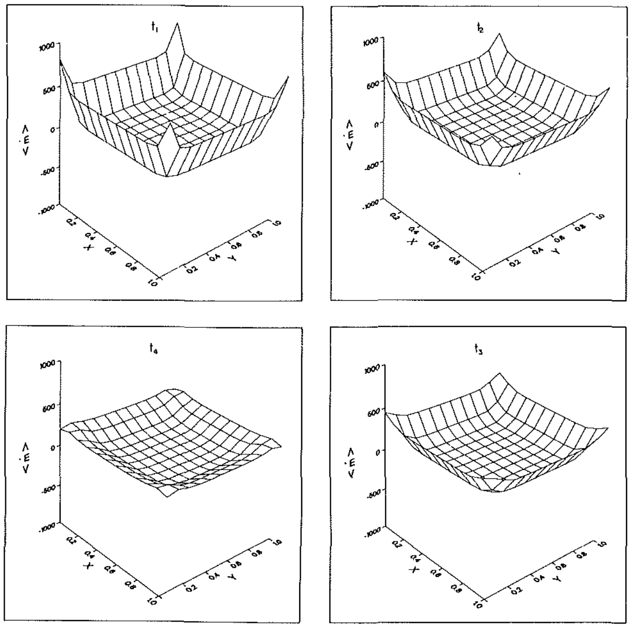

Fig. 6 Three-dimensional condensation and evaporation rate plots at four different times corresponding to Fig. 2 (Case I)

were used to find the distributions for $<p_v>^\gamma$, $<\rho_v>^\gamma$, $<p_a>^\gamma$, $<\rho_a>^\gamma$, ϵ_γ, and ϵ_β from the thermodynamic relations, the volumetric constraint, and equation (17).

5 The ζ distribution was obtained from equation (18).

6 The condensation rate was obtained from equation (5).

To the authors' knowledge this two-dimensional computational analysis, which accounts for the phase change process, is presented for the first time.

5 Discussion of Results and Conclusions

Results are presented for a square fibrous insulation slab. The pertinent variables for both cases are the temperature, moisture content, liquid fraction, vapor density, and the condensation rate. Figures 2–6 present the spatial variations of these quantities for Case I at several different times. Crosses are marked at every $m + 2$ (where m is the number of grid points in the x direction) node in the numerical mesh system. Corresponding values are printed to the right of each cross. Figures 4, 5, and 6 demonstrate some significant changes which occur in the growth characteristics of S, ϵ_β, and $<\dot{m}>$. The times t_1, t_2, t_3, and t_4 were chosen to reflect these significant changes. However, there are no significant changes in the growth characteristics of $<T>$ and $<\rho_v>^\gamma$ at times t_2 and t_3. These variables are therefore presented only at times t_1 and t_4.

As expected, the interior temperature of the slab increases with time when the boundary temperature is suddenly increased, as can be seen in Fig. 2. This rise in temperature is the result of simultaneous diffusion and convection of heat from the boundary as well as moisture condensation. Condensation acts as a source of local heat generation and evaporation acts as an energy sink. The increase in temperature starts at regions close to the exterior boundary and gradually moves inward. This wavelike propagation is also observed for S, ϵ_β, $<\rho_v>^\gamma$, and $<\dot{m}>$. In the three-dimensional plot (Fig. 6) the condensation regions have a positive value of $<\dot{m}>$ and the evaporation regions have a negative value of $<\dot{m}>$.

In the beginning, as condensation occurs, the liquid and moisture contents increase in the regions close to the external boundary where the temperature is close to the initial interior temperature. As the temperature close to the external boundary increases with time the liquid and moisture content should decrease in that region. However, in the regions away from the immediate external boundary, where the temperature has not increased or has increased only slightly, the liquid and moisture contents should increase. These trends can be seen in Figs. 2–6. Also seen in Figs. 2–6 are regions of mild evaporation. The evaporation leads to a drop in temperature in those regions.

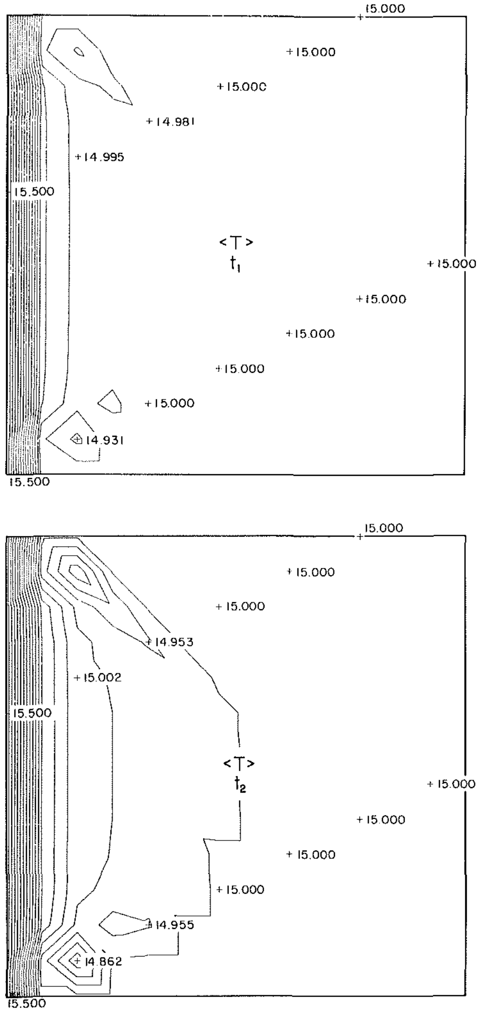

Fig. 7 Spatial variation of temperature inside the insulation slab at two different times (Case II): $t_1 = 2.3 \times 10^{-3}$, $t_2 = 4.6 \times 10^{-3}$

One of the important parameters which affects this relative movement of the temperature wavefront compared to the liquid and the moisture wavefronts is the ratio of the effective thermal diffusivity to the moisture transport coefficient. This ratio, which is known as the Lewis number Le, also affects the liquid content inside the insulation slab. Increasing the Lewis number decreases ϵ_β at a given time and position, and decreasing Le increases ϵ_β at a given time and position.

In the regions where condensation occurs, the temperature inside the slab increases continuously causing the vapor pressure to increase. This is expected from equation (10), since $p_{10} \gg p_9$. Consequently the vapor density increases with time. This is because $<\rho_v>^\gamma = <p_v>^\gamma / P_8 <T>$ and although $1/<T>$ decreases as $<T>$ increases, the increase in $<p_v>^\gamma$ with an increase in $<T>$ not only offsets the decrease in $1/<T>$ but it results in a net increase in $<\rho_v>^\gamma$ with temperature. This behavior can be observed in Fig. 3. In the above calculations it is assumed that the liquid content has not deteriorated the structural integrity of the porous matrix. This is a reasonable assumption to make for small amounts of liquid content, as is the case here. It should also be noted that

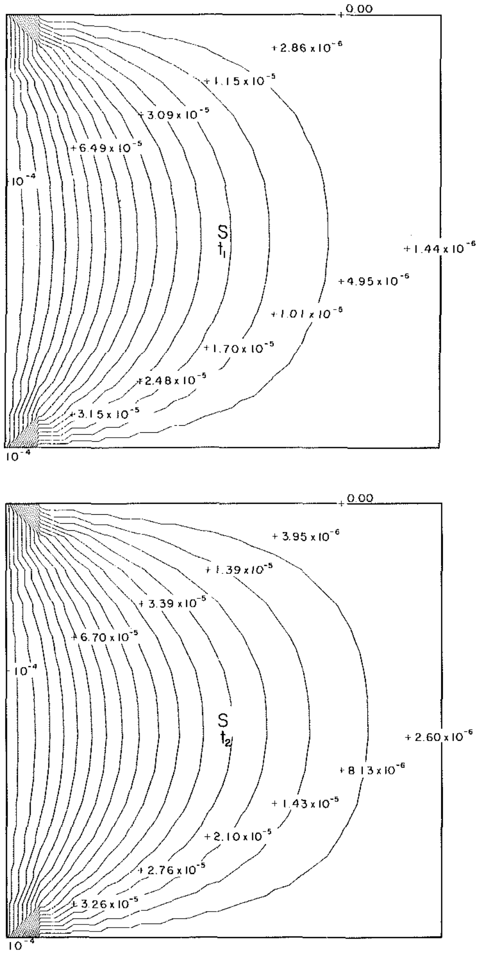

Fig. 8 Spatial variation of the moisture content inside the insulation slab at two different times corresponding to Fig. 7 (Case II)

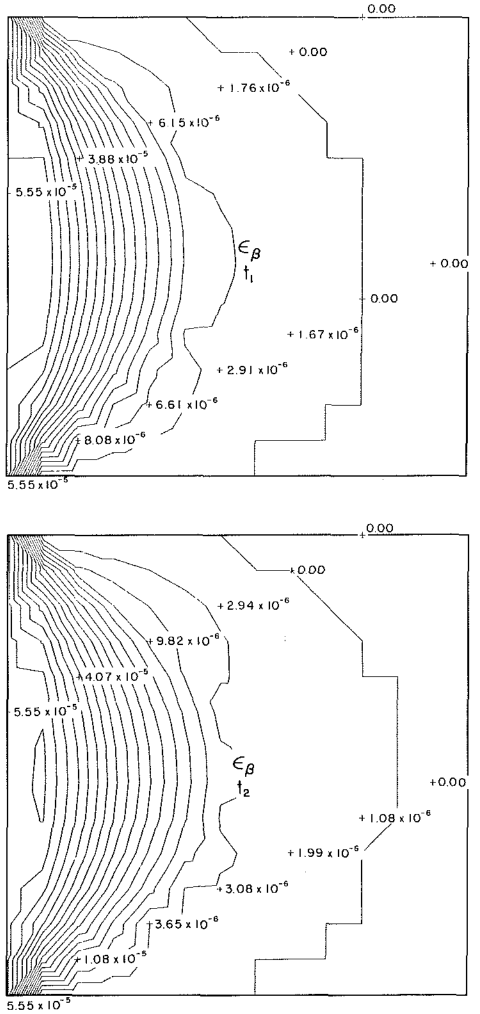

Fig. 9 Liquid fraction contours at two different times corresponding to Fig. 7 (Case II)

a larger liquid fraction is created at the bottom of the insulation slab, due to the gravity forces, as seen in Figs. 4 and 5.

Figures 7-10 present the results of Case II for $<T>$, S, ϵ_β, and $<\rho_v>^\gamma$ at two different times. It can be seen that the discussion used to describe the behavior of temperature, liquid fraction, and condensation rate for Case I also prevails here. The wavelike propagation of information from the left-hand boundary is clearly displayed in these figures. The propagation of the condensation front from the left side of the insulation slab as well as the regions where condensation and evaporation occur are displayed in three dimensions in Fig. 11 at four different times. Again a drop in temperature is observed in the evaporation regions. Condensation distorts the temperature distribution significantly. The temperature distribution changes very little from the initial condition when there is no condensation for the two times shown in Fig. 7. This is due to the very low conductivities of fibrous insulation and vapor and the absence of any phase change.

The physics and the accuracy of the numerical solution were tested in four different ways. First, it was observed that for the case of zero gravity, all of the variables should be symmetric with respect to the center of the insulation slab. This was indeed the situation for all of the cases which were tested. Figure 12 presents the moisture and liquid content contour plots for Case I when the gravitational forces are neglected.

Second, it is expected that for longer times the variables $<T>$, ϵ_β, ϵ_γ, $<p_v>^\gamma$, $<\rho_v>^\gamma$, and S, inside of the slab, become uniform and approach the values at the periphery of the slab. Furthermore the condensation rate should approach zero due to the uniform temperature inside of the slab. This was tested and confirmed for a number of different situations. Figure 13 presents the temperature and the vapor pressure contours at two later times for Case I. Figure 14 presents the three-dimensional condensation rate plots corresponding to Fig. 13. It is clear from Fig. 14 that the condensation rate does approach zero as it should.

Third, the accuracy of the numerical scheme was checked by increasing the number of grid points and the number of time steps. An increase in the number of grid points requires an increase in the number of time steps and a large increase in the time required to run the program. This is due to the large number of variables which have to be processed simultaneously. It was observed that although an increase in the number of grid points increased the quality of the contour lines (making them much smoother), it did not significantly alter the qualitative features of the contour plots. Therefore, to conserve the computer time and expense, a grid size of 15 × 15 was used.

Fourth, for no condensation and no convection, the numerical results are expected to reduce to a conduction case. This was observed by the numerical results.

From numerous numerical computations it is found that in general:

1 The direct coupling between the moisture content S and the temperature $<T>$ in the energy equation is weak. Therefore the term representing this coupling,

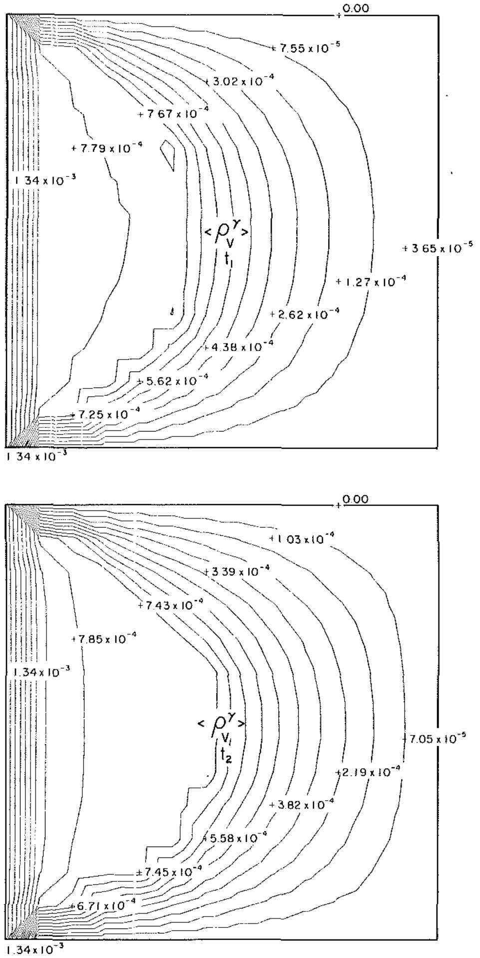

Fig. 10 Vapor density contours at two different times corresponding to Fig. 7 (Case II)

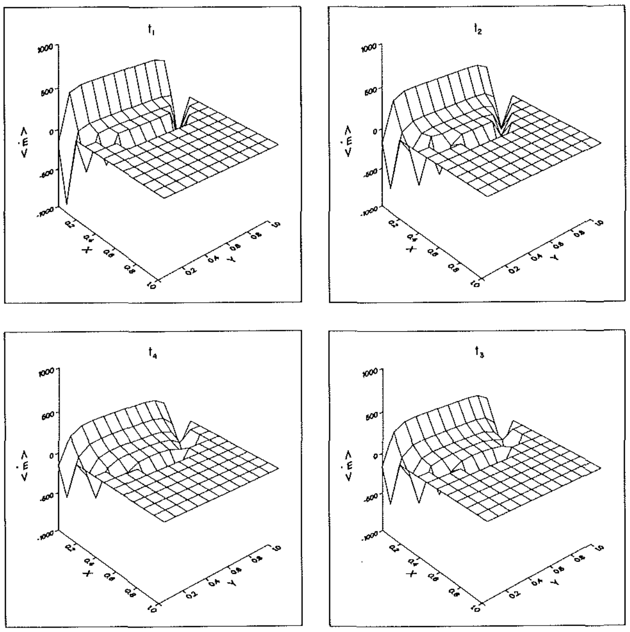

Fig. 11 Three-dimensional condensation and evaporation rate plots at four different times (Case II): $t_1 = 2.3 \times 10^{-3}$, $t_2 = 4.6 \times 10^{-3}$, $t_3 = 6.9 \times 10^{-3}$, $t_4 = 9.3 \times 10^{-3}$

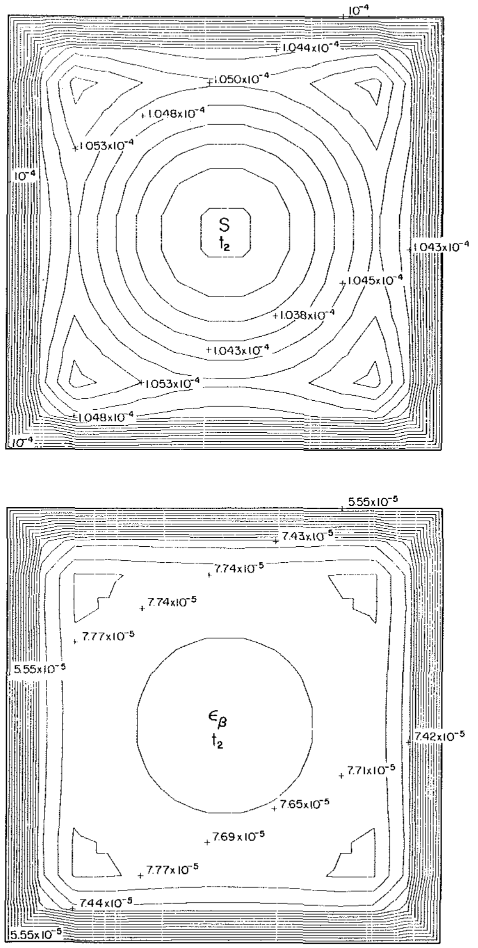

Fig. 12 Moisture and liquid fraction at $t_2 = 4.6 \times 10^{-3}$ when the gravitational effects are neglected

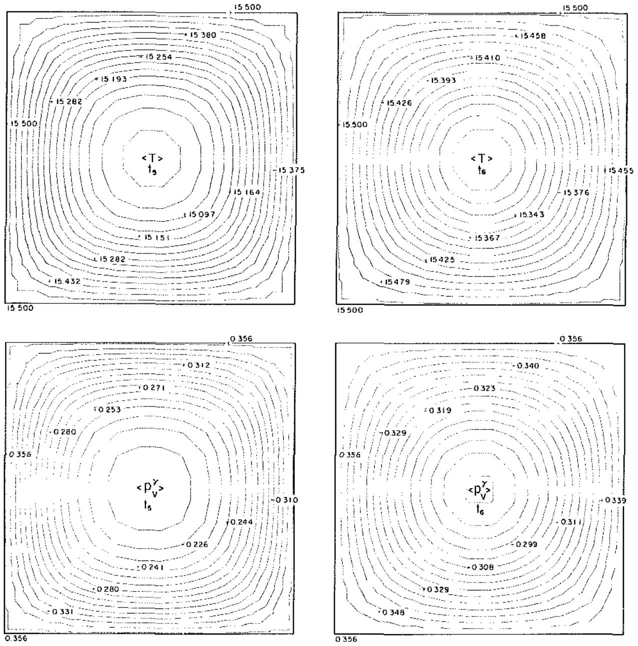

Fig. 13 Temperature and vapor pressure distributions approach toward steady state; presented at two different times: $t_5 = 6.9 \times 10^{-2}$, $t_6 = 0.21$

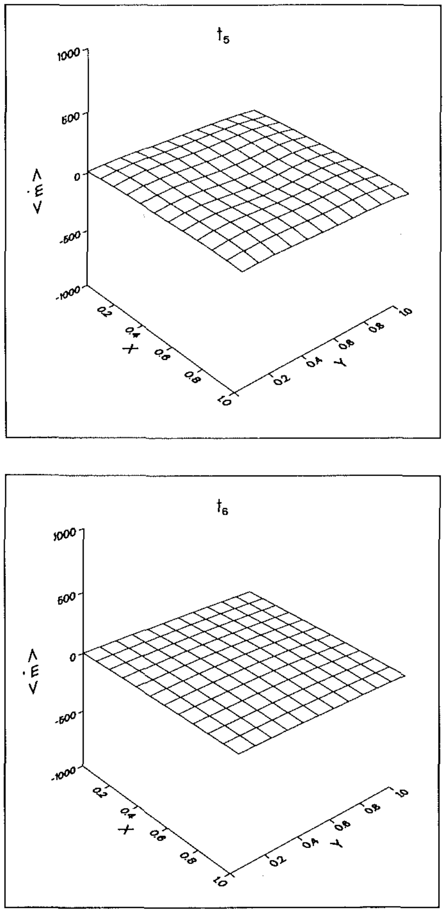

Fig. 14 Three-dimensional condensation rate distribution approach toward steady state corresponding to Fig. 13

$\Lambda\psi_s(\nabla S \cdot \nabla <T>)$, might be neglected for some practical problems.

II The term in the energy equation which accounts for the capillary pressure dependence on the temperature has a small effect on all of the pertinent variables. Therefore the term $\psi_T\Lambda(\nabla <T> \cdot \nabla <T>)$ in equation (3) can be neglected for some cases.

III The term related to the gravitational effects in the energy equation, $\Lambda\psi_g(\mathbf{g} \cdot \nabla <T>)$, can be neglected for most cases.

IV The term $\nabla \cdot (\psi_T \nabla <T>)$ (in the moisture transport equation) which accounts for the capillary pressure dependence on the temperature has a significant effect on all pertinent variables except the temperature field, where it has a small effect.

V The term $\nabla \cdot (\psi_s \nabla S)$, which represents the moisture flux, has a very important influence on all of the pertinent variables.

VI The term $\nabla \cdot (\psi_g \mathbf{g})$ in the moisture transport equation has a significant effect on all of the pertinent variables except the temperature field, where it has a small effect.

VII The variations in the total density ρ and the mass fraction-averaged heat capacity C_p do not alter the results significantly.

VIII Increasing the Lewis number decreases the liquid content and decreasing the Lewis number increases the liquid content at a given time and position.

IX The highest condensation regions seem to be located at the corners of the insulation slab.

Based on these results the following simplified version of equation (3) is recommended for analyzing the temperature distribution in a porous insulation material

$$\rho C_p \frac{\partial <T>}{\partial t} + <\dot{m}> = \nabla \cdot (k_{\text{eff}} \nabla <T>) \qquad (32)$$

It should be noted that the results presented in this section were computed without making any simplifications. Further investigations on heat and mass transfer in porous insulation are recommended.

References

1 Whitaker, S., "Simultaneous Heat, Mass and Momentum Transfer in Porous Media: A Theory of Drying," *Advances in Heat Transfer*, Vol. 13, Academic Press, New York, 1977.

2 Whitaker, S., "Advances in Theory of Fluid Motion in Porous Media," *Ind. Eng. Chem.*, Vol. 61, 1969, pp. 14–28.

3 Whitaker, S., "Toward a Diffusion Theory of Drying," *Ind. Eng. Chem. Fundam.*, Vol. 16, 1977, pp. 408–414.

4 Luikov, A. V., *Heat and Mass Transfer in Capillary-Porous Bodies*, Pergamon, Oxford, 1966.

5 Ceaglske, N. M., and Hougen, O. A., "Drying Granular Solids," *Ind. Eng. Chem.*, Vol. 29, 1937, pp. 805–813.

6 Eckert, E. R. G., and Faghri, M., "Moisture Migration in an Unsaturated Porous Medium," *IJHMT*, Vol. 23, 1980, pp. 1613–1623.

7 Burns, P. J., Chow, L. C., and Tien, C. L., "Convection in a Vertical Slot Filled With Porous Insulation," *IJHMT*, Vol. 20, 1977, pp. 919–926.

8 Langlais, C., Hyrien, M., and Karlsfeld, S., "Moisture Migration in Fibrous Insulating Material Under the Influence of a Thermal Gradient," in: *Moisture Migration in Buildings*, ASTM STP 779, 1982, pp. 191–206.

Effectiveness of Series Assemblies of Divided-Flow Heat Exchangers

A. Pignotti
TECHINT S.A.,
Buenos Aires, Argentina

Formulas are derived for the effectiveness of a series assembly of two divided-flow exchangers, as a function of the heat capacity rate ratio, and the partial effectivenesses of the components. Six possible connections are discussed: overall parallel flow and counterflow, with either mixing of the intermediate divided streams, or direct or crossed coupling of the same. It is shown that when both exchangers are alike, and direct coupling is used, the simplifying mixing assumption leads to a systematic overestimate of the effectiveness of the assembly. The size of this effect is discussed and illustrated with explicit solutions for TEMA J exchangers with one and two tube passes.

1 Introduction

In the approximation neglecting phase-change and temperature dependence of the heat transfer coefficients and specific heats (henceforth called linear approximation), it is easy to obtain simple formulas for the overall effectiveness of pairs of coupled heat exchangers as a function of the heat capacity rate ratio and the effectivenesses of the components [1]. Two possible series connections are shown in Figs. 1(*a*) and 1(*b*), both with perfect mixing of each of the fluids between the exchangers. In the following, they are denoted parallel flow and counterflow series connection with mixing, respectively. The corresponding expressions for the global effectiveness are

$$P'_M = P_A + P_B - P_A P_B (1+R) \qquad (1a)$$

for the parallel flow case and

$$P''_M = [P_A + P_B - P_A P_B (1+R)]/(1 - R P_A P_B) \qquad (1b)$$

for the counterflow case.

In this article, we deal with divided-flow exchangers, in which one of the fluids has either two inlet or two outlet nozzles. When two such exchangers are used in a series-connected assembly, if the streams are mixed between the exchangers, such as indicated in Fig. 2, equations (1*a*) and (1*b*) are still valid. Indeed, if we expand the boundaries of the exchangers *A* and *B* in Fig. 2 to include the mixing and dividing of the intermediate streams, respectively, we are left with a configuration exactly equivalent to that of Fig. 1. It is usual, however, to connect the exchangers as shown in Fig. 3 (direct connection), and it is also conceivable to couple them as indicated in Fig. 4 (crossed connection). In either case, formulas (1*a*) and (1*b*) are no longer valid.

In practice, the counterflow direct connection of Fig. 3(*b*) is almost exclusively used: Counterflow is selected because it yields a higher effectiveness, and direct coupling is chosen because it simplifies the piping connections. For simplicity, and in the absence of a proper solution, equation (1*b*) is commonly used to calculate the overall effectiveness. The question is: How much error is committed by this simplification and is it on the safe side or the unsafe side?

In the following, we answer this question by deriving general expressions for the effectiveness of an assembly of two series-connected divided-flow exchangers, which include the additional degrees of freedom required for the description of these configurations, and compare the results with equations (1*a*) and (1*b*). We illustrate our conclusions with the examples of the 1-1 and 1-2 TEMA J exchangers, which are solved analytically and evaluated numerically over the region of practical interest.

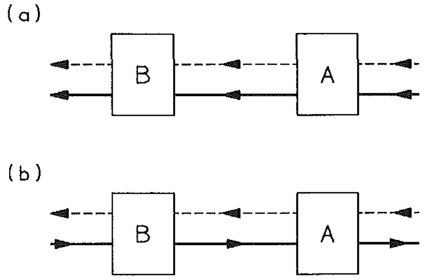

Fig. 1 Series connection of two exchangers: (*a*) parallel flow; (*b*) counterflow

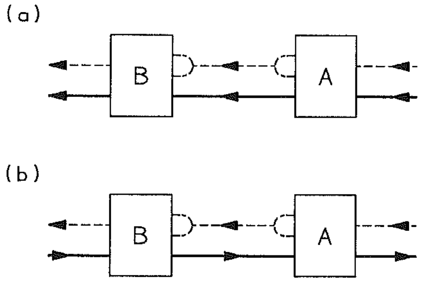

Fig. 2 Series connection of two divided-flow exchangers with intermediate mixing: (*a*) parallel flow; (*b*) counterflow

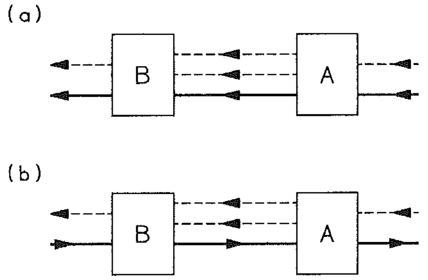

Fig. 3 Unmixed direct series connection of divided-flow exchangers: (*a*) parallel flow; (*b*) counterflow

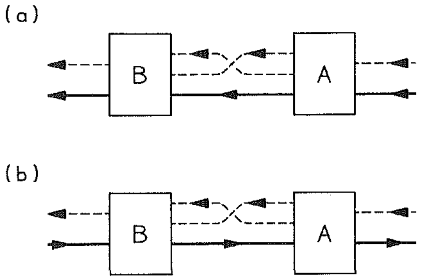

Fig. 4 Unmixed crossed series connection of divided-flow exchangers: (*a*) parallel flow; (*b*) counterflow

---

Contributed by the Heat Transfer Division for publication in the JOURNAL OF HEAT TRANSFER. Manuscript received by the Heat Transfer Division October 11, 1984.

In the TEMA J examples, the "divided fluid" is, of course, the shell fluid. It is theoretically possible, however, to have other heat exchanger configurations, in which the tube fluid is divided into two separate streams, which are not mixed in the outlet. Because the formulas derived in this article would apply equally well to such arrangements, we characterize the fluids as "divided fluid" and "undivided fluid." We only use the "shell fluid" and "tube fluid" notation when dealing with specific examples. Furthermore, we avoid the "hot fluid" and "cold fluid" notation because our formulas hold regardless of which fluid is warmer.

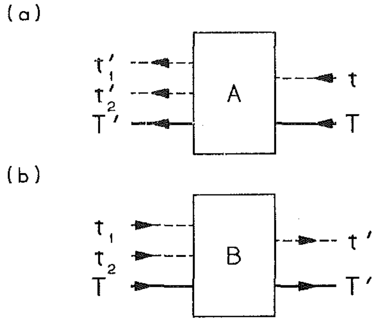

Fig. 5(*a*) Block diagram representing a divided-flow exchanger with two inlet and three outlet nozzles; (*b*) similar diagram with three inlet and two outlet nozzles

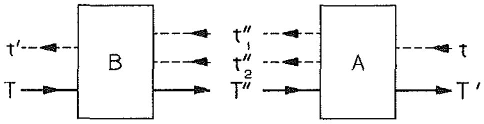

Fig. 6 Diagram showing temperature variables used in the case of counterflow series connection

2 Parallel Flow Connection

In the linear approximation, the effect of the divided-flow heat exchanger of Fig. 5(*a*) can be described by a 3×2 matrix M_A which relates the outlet to the inlet temperatures in the following fashion [2]

$$\begin{vmatrix} t'_{A_1} \\ t'_{A_2} \\ T'_A \end{vmatrix} = \begin{vmatrix} 1-P_{A_1} & P_{A_1} \\ 1-P_{A_2} & P_{A_2} \\ RP_A & 1-RP_A \end{vmatrix} \begin{vmatrix} t_A \\ T_A \end{vmatrix} = M_A \begin{vmatrix} t_A \\ T_A \end{vmatrix} \qquad (2)$$

where P_{A_1} and P_{A_2} are the partial effectivenesses of the divided fluid, defined as

$$P_{A_1} = (t'_{A_1} - t_A)/(T_A - t_A) \qquad (3)$$
$$P_{A_2} = (t'_{A_2} - t_A)/(T_A - t_A)$$

and P_A is the total effectiveness

$$P_A = \delta_{A_1} P_{A_1} + \delta_{A_2} P_{A_2} \qquad (4)$$

Here δ_{A_1} and δ_{A_2} are the flowrate fractions of streams 1 and 2, respectively.

In a similar way, the divided-flow exchanger of Fig. 5(*b*), with three inlet and two outlet nozzles, is represented in the linear approximation by a 2×3 matrix $\hat{M}_B$ such that [2]

Nomenclature

A = heat transfer surface area, m^2
a, b = auxiliary expressions defined in equations (43) and (44)
c, C = specific heat of shell and tube fluids, J/kg°C
D = auxiliary expression defined in equation (38)
F = logarithmic mean temperature difference correction factor
H = matrix relating the set of temperatures chosen as dependent variables to the set of independent temperatures
$\hat{H}$ = same as H, for the process in which the directions of flow have been reversed
$H_{11}, H_{12}, H_{21}, H_{22}$ = elements of matrix H
M = matrix relating the outlet to the inlet temperatures
$\hat{M}$ = same as M, for the process in which the directions of flow have been reversed
N_{tu} = number of transfer units referred to the shell fluid, for a single J-shell exchanger = UA/cw
P = divided fluid total thermal effectiveness of heat exchanger
P' = divided fluid thermal effectiveness of parallel flow series assembly of heat exchangers
P'' = divided fluid thermal effectiveness of a counterflow series assembly of heat exchangers
P_1, P_2 = partial effectiveness of streams 1 and 2 of a divided-flow heat exchanger
R = heat capacity rate ratio = cw/CW
S = matrix defined by equation (14)
t, T = inlet temperatures of divided and undivided fluids, °C
t', T' = outlet temperetures of divided and undivided fluids, °C
t_1, t_2 = inlet temperatures of streams 1 and 2 of the divided fluid, °C
t'_1, t'_2 = outlet temperatures of streams 1 and 2 of the divided fluid, °C
t''_1, t''_2, T'' = intermediate temperatures in a pair of connected divided-flow exchangers, °C
U = overall coefficient of heat transfer, W/m^2 °C
w, W = mass flow rates of shell and tube fluids, kg/s
α, β, γ = auxiliary quantities defined in equations (35)-(37)
δ_1, δ_2 = flowrate fractions of streams 1 and 2
Δ = parameter defined in equation (11)

Subscripts

A, B = belonging to the exchanger labeled A or B
C = unmixed crossed connection, such as shown in Fig. 4
D = unmixed direct connection, such as shown in Fig. 3
M = perfect mixing of the intermediate streams, such as shown in Figs. 1 and 2

$$\left|\begin{array}{c} t'_B \\ T'_B \end{array}\right| = \left|\begin{array}{ccc} \delta_{B_1}(1-P_{B_1}) & \delta_{B_2}(1-P_{B_2}) & P_B \\ \delta_{B_1}RP_{B_1} & \delta_{B_2}RP_{B_2} & 1-RP_B \end{array}\right| \left|\begin{array}{c} t_{B_1} \\ t_{B_2} \\ T_B \end{array}\right| = \hat{M}_B \left|\begin{array}{c} t_{B_1} \\ t_{B_2} \\ T_B \end{array}\right| \qquad (5)$$

with

$$P_B = \delta_{B_1} P_{B_1} + \delta_{B_2} P_{B_2} \qquad (6)$$

If exchanger B happens just to coincide with exchanger A, except for the inversion of the direction of flow of both fluids, we have [3]

$$\begin{aligned} P_{A_1} &= P_{B_1} \\ P_{A_2} &= P_{B_2} \\ \delta_{A_1} &= \delta_{B_1} \\ \delta_{A_2} &= \delta_{B_2} \end{aligned} \qquad (7)$$

and, consequently, $P_A = P_B$.

Consider now the coflow direct connection of Fig. 3(a). In this assembly the outlet streams of the A exchanger are input to the B exchanger, and the coupling is such that it requires $\delta_{B_1} = \delta_{A_1}$, $\delta_{B_2} = \delta_{A_2}$, $t_{B_1} = t'_{A_1}$, $t_{B_2} = t'_{A_2}$, $T_B = T'_A$. Therefore, the combination is described by a 2×2 matrix M_D such that

$$\left|\begin{array}{c} t'_B \\ T'_B \end{array}\right| = M_D \left|\begin{array}{c} t_A \\ T_A \end{array}\right| = \left|\begin{array}{cc} 1-P'_D & P'_D \\ RP'_D & 1-RP'_D \end{array}\right| \left|\begin{array}{c} t_A \\ T_A \end{array}\right| \qquad (8)$$

where

$$M_D = \hat{M}_B M_A \qquad (9)$$

In equation (8), the standard expression for the matrix M_D in terms of R and the effectiveness P'_D of the parallel flow direct connection has been exhibited [1].

From equations (2), (5), (8), and (9) we obtain

$$P'_D = P_A + P_B - (1+R)P_A P_B - \Delta \qquad (10)$$

where

$$\Delta = \delta_1 \delta_2 (P_{A_1} - P_{A_2})(P_{B_1} - P_{B_2}) \qquad (11)$$

with

$$\delta_1 \delta_2 = \delta_{A_1} \delta_{A_2} = \delta_{B_1} \delta_{B_2}$$

The expression thus obtained for P'_D differs from the mixed case expression of equation (1a) by the term $-\Delta$. Observe that when exchangers A and B have the same physical characteristics, i.e., when equations (7) hold, from equations (7) and (11), it follows that Δ is positive definite. Therefore, it is not a conservative approximation to use the simplified expression (1a) for the direct parallel flow connection.

In a similar way, an expression can be derived for the parallel flow crossed connection of Fig. 4(a). The only difference is that this connection requires

$$\delta_{B_1} = \delta_{A_2},\ \delta_{B_2} = \delta_{A_1},\ t_{B_1} = t'_{A_2},\ t_{B_2} = t'_{A_1},\ \text{and}\ T_B = T'_A \qquad (12)$$

This can be expressed in matrix notation in the form

$$\left|\begin{array}{c} t_{B_1} \\ t_{B_2} \\ T_B \end{array}\right| = S \left|\begin{array}{c} t'_{A_1} \\ t'_{A_2} \\ T_A{}' \end{array}\right| \qquad (13)$$

with

$$S = \left|\begin{array}{ccc} 0 & 1 & 0 \\ 1 & 0 & 0 \\ 0 & 0 & 1 \end{array}\right| \qquad (14)$$

From equations (2), (5), and (13), we conclude that the parallel flow crossed assembly is described by a matrix M_C such that

$$M_C = \hat{M}_B S M_A = \left|\begin{array}{cc} 1-P'_C & P'_C \\ RP'_C & 1-RP'_C \end{array}\right| \qquad (15)$$

whence, using equations (2), (5) and (15), we obtain

$$P'_c = P_A + P_B - (1+R)P_A P_B + \Delta \qquad (16)$$

Here Δ is again given by equation (11).

The crossed connection is possible, for the case $A = B$, only if streams 1 and 2 have equal flowrates. This is an immediate consequence of equations (7) and (12) and the relation $\delta_{A_1} + \delta_{A_2} = 1$. Within this restriction, it is still true that Δ is positive definite and, therefore, we can write

$$P'_D < P'_M < P'_C \qquad (17)$$

3 Counterflow Connection

An analysis similar to that of the previous section can be performed for the counterflow connection of Figs. 3(b) and 4(b). In this case, a convenient way of labeling the temperatures of the streams involved is shown in Fig. 6. With this notation, expressions analogous to equations (2) and (5) can be written in the form

$$\left|\begin{array}{c} t''_1 \\ t''_2 \\ T' \end{array}\right| = M_A \left|\begin{array}{c} t \\ T'' \end{array}\right| \qquad (18)$$

and

$$\left|\begin{array}{c} t' \\ T'' \end{array}\right| = \hat{M}_B \left|\begin{array}{c} t''_1 \\ t''_2 \\ T \end{array}\right| \qquad (19)$$

with the same expressions used before for the matrices M_A and $\hat{M}_B$. After partial inversion [2] is performed on the above expressions, we can write

$$\left|\begin{array}{c} t''_1 \\ t''_2 \\ T'' \end{array}\right| = H_A \left|\begin{array}{c} t \\ T' \end{array}\right| \qquad (20)$$

and

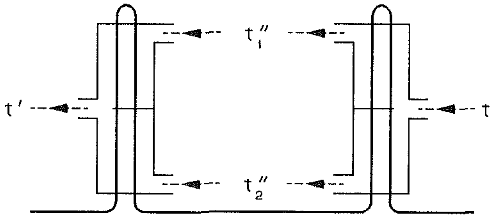

Fig. 7 Pair of 1-2 TEMA J exchangers; two directions of tube flow and three different shell fluid connections are considered in the text

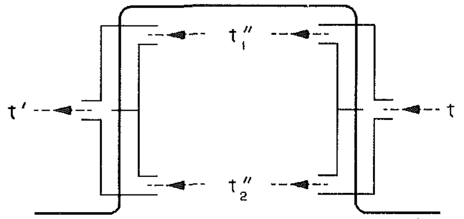

Fig. 8 Pair of 1-1 TEMA J exchangers; two directions of tube flow and three different shell fluid connections are considered in the text

$$\begin{vmatrix} t' \\ T \end{vmatrix} = \hat{H}_B \begin{vmatrix} t_1'' \\ t_2'' \\ T'' \end{vmatrix} \tag{21}$$

where

$$H_A = \frac{1}{1-RP_A} \begin{vmatrix} 1-RP_A-P_{A_1} & P_{A_1} \\ 1-RP_A-P_{A_2} & P_{A_2} \\ -RP_A & 1 \end{vmatrix} \tag{22}$$

and

$$\hat{H}_B = \frac{1}{1-RP_B} \begin{vmatrix} \delta_{B_1}(1-P_{B_1}-RP_B) & \delta_{B_2}(1-P_{B_2}-RP_B) & P_B \\ -\delta_{B_1}RP_{B_1} & -\delta_{B_2}RP_{B_2} & 1 \end{vmatrix} \tag{23}$$

We therefore have

$$\begin{vmatrix} t' \\ T \end{vmatrix} = H_D \begin{vmatrix} t \\ T' \end{vmatrix} = \hat{H}_B H_A \begin{vmatrix} t \\ T' \end{vmatrix} \tag{24}$$

which, after a new partial inversion, can be written as

$$\begin{vmatrix} t'' \\ T' \end{vmatrix} = \frac{1}{H_{D_{22}}} \begin{vmatrix} H_{D_{11}}H_{D_{22}} - H_{D_{12}}H_{D_{21}} & H_{D_{12}} \\ -H_{D_{21}} & 1 \end{vmatrix} \begin{vmatrix} t \\ T \end{vmatrix} \tag{25}$$

Comparing this expression with the standard one in terms of the effectiveness of the counterflow direct connection P''_D and the heat capacity rate ratio R [1]

$$\begin{vmatrix} t' \\ T' \end{vmatrix} = \begin{vmatrix} 1-P_D'' & P_D'' \\ RP_D'' & 1-RP_D'' \end{vmatrix} \begin{vmatrix} t \\ T \end{vmatrix} \tag{26}$$

we obtain

$$1/H_{D_{22}} = 1 - RP_D'' \tag{27}$$

or

$$P_D'' = \frac{1}{R}\left[1 - \frac{1}{H_{D_{22}}}\right] \tag{28}$$

From equations (22), (23), (24), and (28) we finally obtain

$$P_D'' = \frac{1}{R}\left[1 - \frac{(1-RP_A)(1-RP_B)}{1-RP_AP_B-R\Delta}\right] \tag{29}$$

As in the parallel flow case, the crossed connection of Fig. 4(b) requires the insertion of the matrix S, this time in the matrix product of equation (24), such that

$$H_C = \hat{H}_B S H_A \tag{30}$$

whence

$$P_c'' = \frac{1}{R}\left[1 - \frac{1}{H_{C_{22}}}\right] = \frac{1}{R}\left[1 - \frac{(1-RP_A)(1-RP_B)}{1-RP_AP_B+R\Delta}\right] \tag{31}$$

Again we observe that equations (29) and (31) differ from equation (1b) only by the term containing Δ. The above form of the expressions for P_D'' and P_C'' has chosen to exhibit the fact that, for $A=B$, a correlation similar to that of equation (17) holds, namely

$$P_D'' < P_M'' < P_C'' \tag{32}$$

4 TEMA J Exchanger

As a first example we discuss the series connection of two equal 1-2 TEMA J shell-and-tube exchangers shown in Fig. 7, in which the shell fluid is divided into two streams of equal flowrates ($\delta_1 = \delta_2 = 1/2$), and each stream is mixed at any cross section of the J shell. The actual interconnection of the shell streams of the two exchangers and the direction of flow of the tubeside fluid are not indicated in Fig. 7, in order to allow for the six alternatives shown in Figs. 2-4. Observe that we do not need to consider cross connecting the tubeside fluid between the two exchangers. This would consist in admitting at the top of the second exchanger the tubeside fluid from the bottom of the first one, but it can be readily seen that this crossing operation leads to a configuration that is entirely equivalent to that obtained by crossing the shellside streams.

From [2] or [4], the following expressions for the partial effectiveness are obtained (because $A = B$, we drop the corresponding subscripts)

$$P_1 = 2\alpha/D \tag{33}$$

$$P_2 = 2\alpha(2\alpha+2\beta-1)/D \tag{34}$$

where

$$\alpha = \exp(-N_{tu}/2)\sinh(\gamma N_{tu}/2)/\gamma \tag{35}$$

$$\beta = \exp(-N_{tu}/2)\cosh(\gamma N_{tu}/2) \tag{36}$$

$$\gamma = \sqrt{1+R^2/4} \tag{37}$$

$$D = [\beta + \alpha(1+R/2)]^2 + 2\alpha(\alpha+\beta-1) \tag{38}$$

Here N_{tu} is the number of transfer units of a single J shell exchanger, referred to the shell fluid. Hence

$$P = (P_1+P_2)/2 = 2\alpha(\alpha+\beta)/D \tag{39}$$

and

$$\Delta = (P_1-P_2)^2/4 = [2\alpha(\alpha+\beta-1)/D]^2 \tag{40}$$

With the above expressions and equations (1a), (1b), (10), (16), (29), and (31), the effectiveness of the six possible coupling of Figs. 2-4 is obtained, and a computer search for the highest percentage deviation between the direct (Fig. 3) and crossed (Fig. 4) connection is performed. The region of interest is limited to values of LMTD correction factor F for the whole assembly larger than 0.5. With this restriction, the largest deviations do not exceed 0.5 percent. The results obtained are

$$\mathrm{Max}[100(P_c' - P_D')/\mathrm{P_D}'] = 0.50 \text{ percent}$$

and

$$\mathrm{Max}[100(P_C'' - P_D'')/P_D''] = 0.35 \text{ percent}$$

A similar exhanger, with only one tube pass, shown in Fig. 8, is our next example. This exchanger is just one half of a 2-2 TEMA G exchanger, and the 3 × 2 matrix that describes it can be found in [3], again for $\delta_1 = \delta_2 = 1/2$. For $R \neq 2$ we have

$$P_1 = (1-a)/(1-aR/2) \tag{41}$$

$$P_2 = (1-b)(1-R/2)/(1-aR/2)(1+R/2) \tag{42}$$

with

$$a = \exp[-(1-R/2)N_{tu}] \tag{43}$$

and

$$b = \exp[-(1+R/2)N_{tu}] \tag{44}$$

The corresponding expressions for $R=2$ are

$$P_1 = N_{tu}/(1+N_{tu}) \tag{45}$$

$$P_2 = (1-b)/2(1+N_{tu}) \tag{46}$$

The search for maximum deviation subject to the constraint $F > 0.5$ now gives for parallel flow connection

$R = 7.12$; $N_{tu} = 0.32$; $P_D' = 0.120$; $P_M' = 0.123$; $P_C' = 0.127$

and for counterflow connection

$R = 0.844$; $N_{tu} = 3.60$; $P_D'' = 0.795$; $P_M'' = 0.829$; $P_C'' = 0.856$

The corresponding percentage spreads, defined as in the

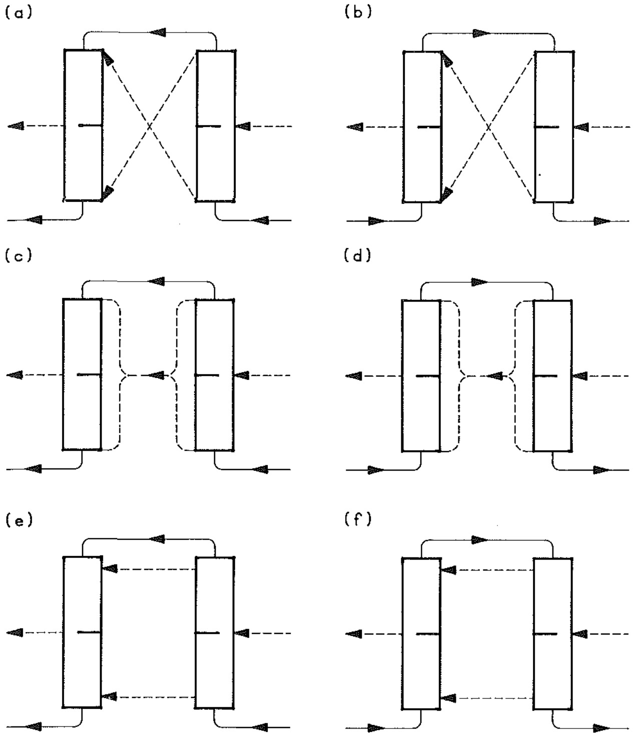

Fig. 9 Schematic diagrams representing the six couplings considered for a 1·1 TEMA J exchanger: (*a*) parallel flow crossed, (*b*) counterflow crossed, (*c*) parallel flow mixed, (*d*) counterflow mixed, (*e*) parallel flow direct, (*f*) counterflow direct

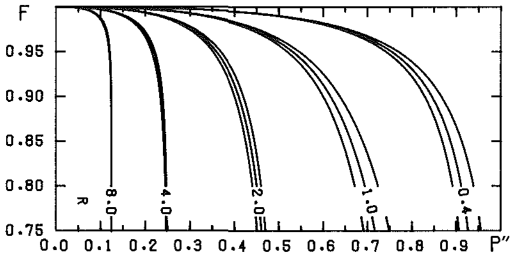

Fig. 10 LMTD correction factor *F* for a counterflow assembly of two 1-1 TEMA J exchangers; for each value of *R*, upper, middle and lower curves correspond to the couplings of Figs. 9(*b*), 9(*d*), and 9(*f*), respectively

previous example, are 5.8 and 7.7 percent, respectively. These values are considerably larger than those found in the case of two tube passes.

5 Discussion

The inequalities (17) and (32) show that, in the case of equal exchangers ($A = B$), the direct connection of Fig. 3 is always less effective than the crossed one of Fig. 4. In other words, the effectiveness is lower when the last stream encountered by the undivided fluid in one exchanger is the first one met in the following one, and higher otherwise. This is quite analogous to correlations observed in the comparison of alternative connections of unmixed streams in multipass crossflow exchange [5], but the present result is more general, because it is independent of the details of the exchange mechanism in the block diagrams of Figs. 2-4. It is only restricted to the domain of the linear approximation stated in the introduction, and by the requirement that the pair of coupled exchangers is such that either one can be accurately described as the "flow-reversed" version of the other one, i.e., as having the same geometry but opposite direction of flow for both fluids [3].

Because the counterflow direct connection of Fig. 3(*b*) is almost exclusively used, for the reasons given in the introduction, and having established that in that case the error committed by the practice of using equation (1*b*) is always on the unsafe side, it is of interest to examine how sizable is this error. The error is shown to depend on a single parameter Δ, which is quadratic in the difference between the partial effectivenesses of the two streams. Therefore, if this difference is 10 percent we have

$$\Delta < (0.1)^2 \delta_1 \delta_2 \leq 0.0025 \tag{47}$$

which is likely to give rise to a negligible effect.

The first example considered is quite balanced between streams 1 and 2. Indeed, in the J shell exchangers with two tube passes, each of the shell streams undergoes counterflow exchange with one of the tube passes, and parallel flow exchange with the other one. Therefore, both streams tend to emerge from the shell with similar temperatures, and this explains the smallness of the effect found. This effect may only be expected to be larger in oversized exchangers, which have been excluded from our numerical search because of low values of the LMTD correction factor *F*. In contrast to this, when there is only one tube pass, one stream is subject to counterflow exchange and the other one to parallel flow exchange. This sharp asymmetry gives rise to the sizable effect quoted at the end of the previous section.

6 Summary and Conclusions

We summarize the results obtained by focusing on the example of two equal 1-1 TEMA J exchangers with $\delta_1 = \delta_2 = 1/2$. Figure 9 shows the six possible connections labeled (*a*) to (*f*). The corresponding formulas for the combined effectiveness, obtained from equations (1*a*), (1*b*), (10), (16), (29), and (31) with $P_A = P_B = P$, are the following:

$$P'_C = 2P - (1+R)P^2 + \Delta \tag{48a}$$

$$P''_C = P'_C / (1 - RP^2 + \Delta) \tag{48b}$$

$$P'_M = 2P - (1+R)P^2 \tag{48c}$$

$$P''_M = P'_M / (1 - RP^2) \tag{48d}$$

$$P'_D = 2P - (1+R)P^2 - \Delta \tag{48e}$$

$$P''_D = P'_D / (1 - RP^2 - \Delta) \tag{48f}$$

The letter in the above equation labels coincides with the corresponding label in Fig. 9, e.g., equation (48*d*) is valid for Fig. 9(*d*). In equations (48) we have

$$P = (P_1 + P_2)/2 \tag{49}$$

$$\Delta = (P_1 - P_2)^2/4 \tag{50}$$

with P_1 and P_2 given by equations (41) and (42) for the 1-1 TEMA J exchanger considered. (If two tube passes are present, the same equations apply with P_1 and P_2 given by equations (33) and (34).) With these expressions, the LMTD correction factor *F* is calculated and plotted in Fig. 10 for the counterflow arrangements of Figs. 9(*b*), (*d*), and (*f*). For each value of *R*, the upper curve corresponds to the crossed coupling of Fig. 9(*b*), the middle one to the mixed coupling of Fig. 9(*d*), and the lower one to the most common direct coupling of Fig. 9(*f*). The latter is equivalent, and gives the same results, as a 2-2 TEMA G exchanger. It is apparent that the usual practice of replacing the lower curve by the middle one is inadequate and unsafe.

Our conclusions can be summarized as follows:

- When coupling two equal divided-flow exchangers, whether in overall counterflow or parallel flow connection, the effectiveness of the assembly is always highest for the crossed coupling (Fig. 4), lowest for the direct coupling (Fig. 3), and intermediate for mixed coupling (Fig. 2).
- Therefore, the practice of using the simpler formulas of the

mixed case for the most common direct coupling implies an approximation that is always on the unsafe side.

- The error committed by the above approximation is often small, but in cases in which there is a strong asymmetry, such as the 1-1 TEMA J exchanger, it is not negligible.
- Therefore, when sizable asymmetries are present, the full expressions derived in this article should be used for the effectiveness of the assembly.

7 Acknowledgments

The author is indebted to Dr. Jerry Taborek of HTRI for suggesting this problem.

References

1 Domingos, J. D., "Analysis of Complex Assemblies of Heat Exchangers," *Int. J. Heat Transfer*, Vol. 12, 1969, pp. 537-548.

2 Pignotti, A., "Matrix Formalism for Coupled Heat Exchangers," ASME JOURNAL OF HEAT TRANSFER, Vol. 106, 1984, pp. 352-360.

3 Pignotti, A., "Flow Reversibility of Heat Exchangers," ASME JOURNAL OF HEAT TRANSFER, Vol. 106, 1984, pp. 361-368.

4 Jaw, L., "Temperature Relations in Shell-and-Tube Exchangers Having One Pass Split-Flow Shells," ASME JOURNAL OF HEAT TRANSFER, Vol. 86, 1964, pp. 408-416.

5 Pignotti, A., and Cordero, G., "Mean Temperature Difference in Multipass Crossflow," ASME JOURNAL OF HEAT TRANSFER, Vol. 105, 1983, pp. 584-591.

R. Sheikholeslami

A. P. Watkinson

Department of Chemical Engineering,
The University of British Columbia,
Vancouver, B.C. V6T 1W5

Scaling of Plain and Externally Finned Heat Exchanger Tubes

The performance of copper and mild steel plain heat exchanger tubes and an externally finned mild steel tube was studied under calcium carbonate scaling conditions. Under a constant heat flux for 70-h periods the fouling resistance generally increased linearly with time. The effect of velocity on the rate of scale formation is presented for the three tubes and results compared with the model of Hasson.

Introduction

During heat transfer operations with many liquids an undesirable fouling film builds up on the heat transfer surface. The rate of growth of this fouling layer depends on the nature of the fluid, the velocity, the surface material, the temperature, and the nature of the fouled layer. In cooling water systems, calcium carbonate is a major component of fouling deposits. In the absence of a removal or release process, the fouling rate

$$dR_f/d\theta = w/\rho_f k_f \tag{1}$$

is constant with time and depends on the deposition rate w, which is a function of the fluid mechanics and the water chemistry. Hasson et al. [1] developed the most successful model for predicting calcium carbonate scaling rates, in which scaling is based on diffusion of calcium and carbonate ions from the bulk of the fluid followed by crystallization of $CaCO_3$ on the hot wall.

The deposition rate is given by

$$w = K_R[(\mathrm{Ca}^{++})_i(\mathrm{CO}_3^{=})_i - K_{sp}] \tag{2}$$

The concentrations of calcium and carbonate at the interface are eliminated using the mass transfer expressions

$$\begin{aligned} w = K_D[(\mathrm{Ca}^{++}) - (\mathrm{Ca}^{++})_i] = K_D[(\mathrm{CO}_2) \\ - (\mathrm{CO}_2)_i] = 0.5K_D[(\mathrm{HCO}_3^-) - (\mathrm{HCO}_3^-)_i] \end{aligned} \tag{3}$$

and the deposition rate at "low" pH or approximately pH < 8.5 is found by solution of equation (4)

$$\begin{aligned} K_1(w/K_R + K_{sp})(w/K_D + y) \\ = 4K_2x^2(1 - w/K_D x)(z/2 - w/K_D)^2 \end{aligned} \tag{4}$$

where $x = [\mathrm{Ca}^{++}]$, $y = [\mathrm{CO}_2]$, and $z = [\mathrm{HCO}_3^-]$.

If $[\mathrm{Ca}^{++}] >> [\mathrm{CO}_3^{=}]$ this equation reduces to

$$w = 0.5\ K_D x b\ ((1 + 4ac/b^2)^{1/2} - 1)/a \tag{5}$$

with

$$\left.\begin{aligned} a &= 1 - 4K_2K_Rx/K_1K_D \\ b &= y/x + 4K_2K_Rz/K_1K_D + K_{sp}K_R/K_Dx \\ c &= K_2K_Rz^2/K_1K_Dx - K_{sp}K_Ry/K_Dx^2 \end{aligned}\right\} \tag{6}$$

Earlier work [2] had shown that this model predicted scaling rates well on copper tubes where concentrations of scaling species were such that the scaling rates were below 4×10^{-6} m^{2}K/kJ. The purposes of this work were to investigate (*i*) the effect of tube material on $CaCO_3$ scaling, (*ii*) the applicability of Hasson's equation to predict the scaling rates on different metals, and (*iii*) the prediction of scaling on externally finned tubes from plain tube data.

Experimental Work

Artificially hardened water was prepared by adding $Ca(NO_3)_2 \cdot 4H_2O$ and $NaHCO_3$ solutions to water. This hard water at 25°C was recirculated through the shell side of the double pipe heat exchanger (Fig. 1) which consisted of a 37 mm i.d. × 1.15 m long glass tube containing the metal tube in which steam was condensed. Copper and mild steel plain tubes of 19.1 mm o.d. with 15.3 mm and 13.3 mm i.d. respectively were used. The annulus therefore had an equivalent diameter of 17.9 mm. The externally finned tube, supplied by Bas-Tex Ltd., had 12 longitudinal fins 6 mm high × 0.5 mm thick × 1.2 m long mounted on a prime surface of 19.1 mm o.d. This tube had a wetted perimeter of 204 mm, and the annulus an equivalent diameter of 8.69 mm. The heated hard water leaving the test section was cooled in a heat exchanger and re-entered the feed tank through an AMF Cuno Mikro-Klean 50 micron cartridge filter. To avoid corrosion during testing of mild steel tubes nitrogen was first bubbled through the water to remove oxygen, and the feed tank was blanketed in nitrogen. Total alkalinity, pH, and water hardness were determined by standard methods. Water samples filtered through a 1-micron filter paper showed negligible (< 1 ppm) suspended solids. As the scale deposited during operation, the steam pressure was raised from its initial value of 115.2 kPa to yield a constant heat flow with time. Thus the temperature at the scale/water interface should remain constant with time. Make-up chemicals were added intermittently to the tank to keep the water quality as constant as possible. The overall heat transfer coefficient based on the outside prime surface area of the metal tube was calculated as

$$U_o = m\ C_p \Delta T/\mathrm{LMTD}\ A_o \tag{7}$$

and the fouling resistance evaluated as

$$R_f = 1/U_o - 1/U_o\ (\theta = 0) \tag{8}$$

Results and Discussion

Typical output data are shown in Fig. 2. At 0.3 m/s annular velocity, as the tube fouled, the overall heat transfer coefficient of the plain mild steel tube decreased by 13.8 percent from 1.45 kW/m^{2}K to 1.25 kW/m^{2}K over 70 h. A rapid decrease of 15–20 percent in the total alkalinity and hardness occurred during the first 4 h at a rate of 20 mg $CaCO_3$/L-h followed by a slower decrease of 4.5 mg $CaCO_3$/L-h during the rest of the run.

The copper tube and both mild steel tubes were tested over the annular velocity range of 0.3 to 0.8 m/s, which corresponded to Reynolds numbers based on equivalent hydraulic diameters of 12,000 to 29,000 for the plain tubes and 7000 to 16,000 for the finned tube. Table 1 summarizes the results. As expected the clean overall coefficients increase with velocity and are higher for the copper tube and the externally finned tube than for the mild steel plain tube. At identical operating conditions the coefficients after fouling for the finned tube and for the copper tube are also higher than for the plain mild steel tube (Fig. 3). The ratio of clean

---

Contributed by the Heat Transfer Division for publication in the JOURNAL OF HEAT TRANSFER. Manuscript received by the Heat Transfer Division October 2, 1984.

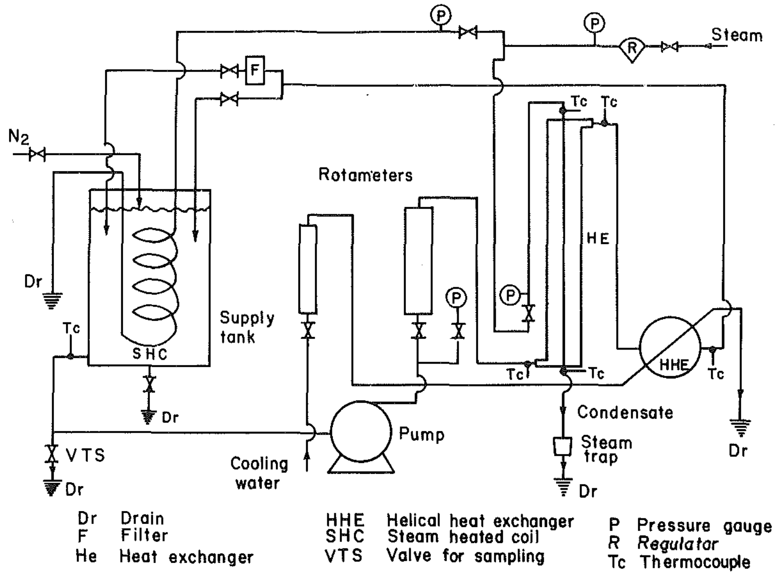

Fig. 1 Flow diagram of apparatus

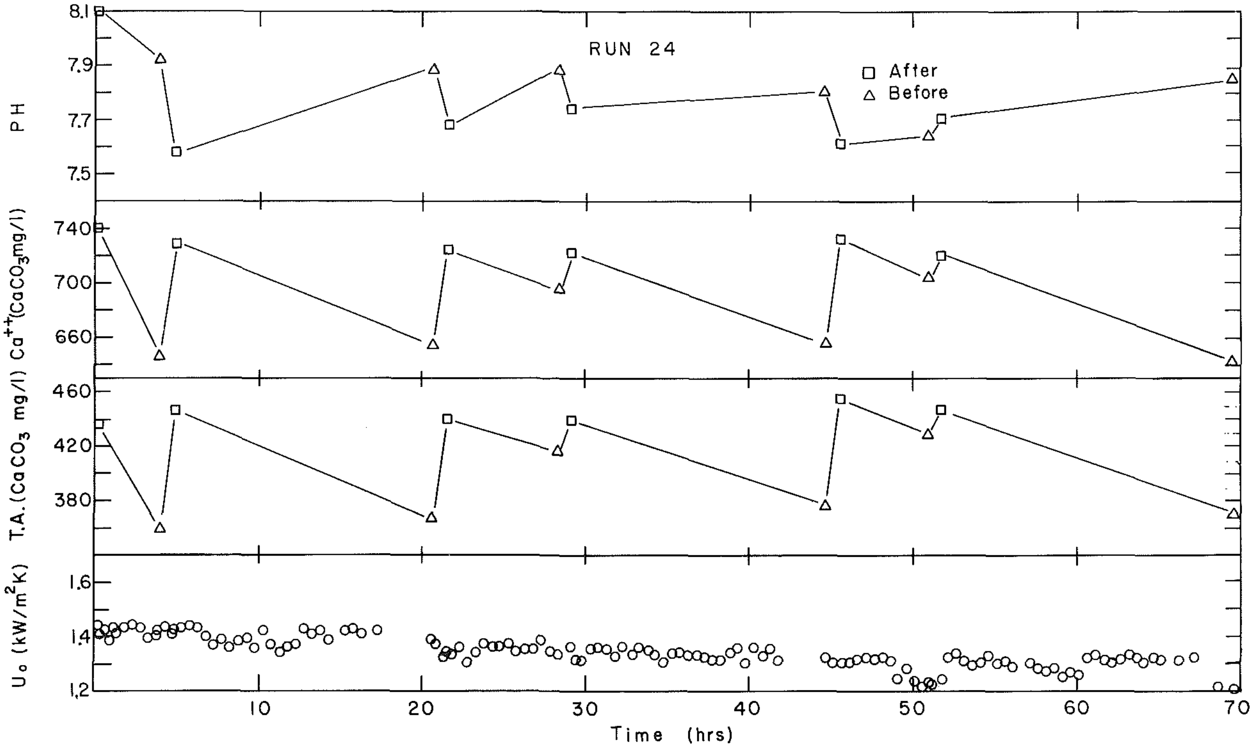

Fig. 2 Typical plot of water chemistry parameters and overall heat transfer coefficient versus time ($V = 0.3$ m/s, plain steel tube)

Nomenclature

A_o = outside area of prime surface, m^2

C_p = heat capacity of water, kJ/kg-K

k_f = thermal conductivity of deposit, W/mK

K_D = mass transfer coefficient for ion, m/s

K_R = rate constant for crystallization, m^4/s-mol

K_{sp} = solubility product of CaCO$_3$, (mol/m^3)^2

K_w = ion product of water, (mol/m^3)^2

K_1 = molar dissociation constant of carbonic acid, mol/m^3

K_2 = second molar dissociation constant of carbonic acid, mol/m^3

LMTD = log mean temperature difference steam/water, K

m = mass flowrate of water, kg/s

R_f = fouling resistance, m^{2}K/kW

U_o = overall coefficient based on outside area, W/m^{2}K

V = velocity of water in annulus, m/s

w = deposition rate of scale, kg/m^2-s

x = calcium ion concentration in bulk liquid, mol/m^3

y = carbon dioxide concentration in bulk liquid, mol/m^3

z = bicarbonate ion concentration in bulk liquid, mol/m^3

ρ_f = density of deposit, kg/m^3

θ = time, s

Table 1 Summary of results

Vol. Flow** Rate x 10^5 (m^3/s)	Finned Mild Steel								Plain Mild Steel								Copper							
	Run	q	T.A.*	Ca^{++}*	pH	U_o (kW/m^2K)			Run	q	T.A.*	Ca^{++}*	pH	U_o (kW/m^2K)			Run	q	T.A.*	Ca^{++}*	pH	U_o(kW/m^2K)		
		(kW)	ave	ave	ave	Start	End	%Drop		(kW)	ave	ave	ave	Start	End	%Drop		(kW)	ave	ave	ave	Start	End	%Drop
23.67	27	9.8	371	661	7.64	1.61	1.54	4.3	24	8.4	415	697	7.78	1.45	1.25	13.8	38	9.9	361	659	7.69	1.70	1.48	12.9
	30	10.1	365	650	7.54	1.69	1.45	14.2																
32.00	28	11.3	347	633	7.60	2.00	1.78	11.0	29	9.1	351	639	778	1.58	1.32	16.5								
39.83	26	12.7	361	648	7.58	2.24	2.02	9.8	23	11.2	358	644	7.68	1.84	1.43	22.3	37	12.5	346	642	7.81	2.28	1.80	21.1
									33	9.4	353	640	7.93	1.63	1.48	9.2								
47.50	31	13.85	340	626	7.64	2.32	2.10	9.5	25	10.9	356	651	7.45	1.90	1.63	14.2								
55.00	32	15.45	318	603	7.68	2.70	2.15	19.6	20[1]	11.9	351	700	7.74	2.02	1.80	10.9	36	13.4	320	619	7.79	2.4	1.80	25.0
									21[2]	13.5	360	641	7.72	2.50	2.15	14.0								
									22	12.0	348	639	7.63	2.18	1.85	15.1								

T.A. = total alkalinity
Ca^{++} = hardness
* Units in mg $CaCO_3/\ell$
U values based on nominal (bare-tube) outside area
Plain annular cross sectional area = 79.128 x $10^{-5} m^2$
Finned annular cross sectional area = 69.528 x $10^{-5} m^2$

1. Initial Steam Pressure 129 kPa
2. Initial Steam Pressure 129 kPa, Initial Feedwater Temperature 30°C

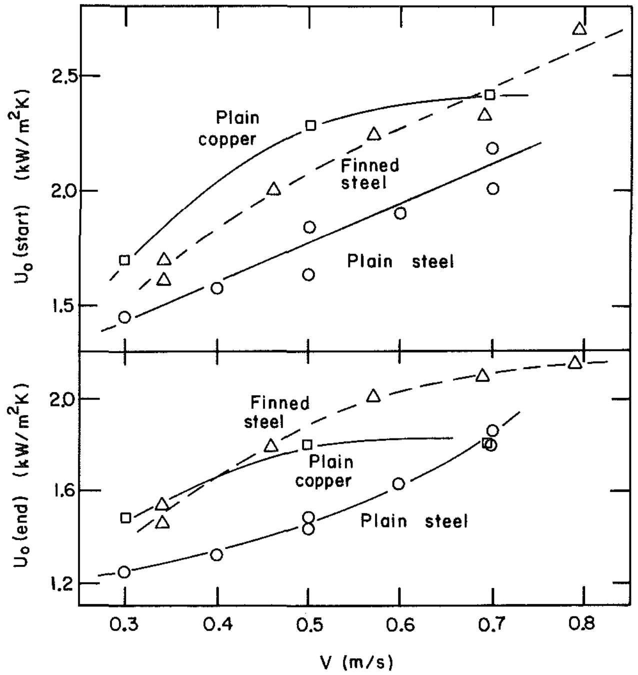

Fig. 3 Overall heat transfer coefficients at beginning and end of 70-h run versus velocity in annulus

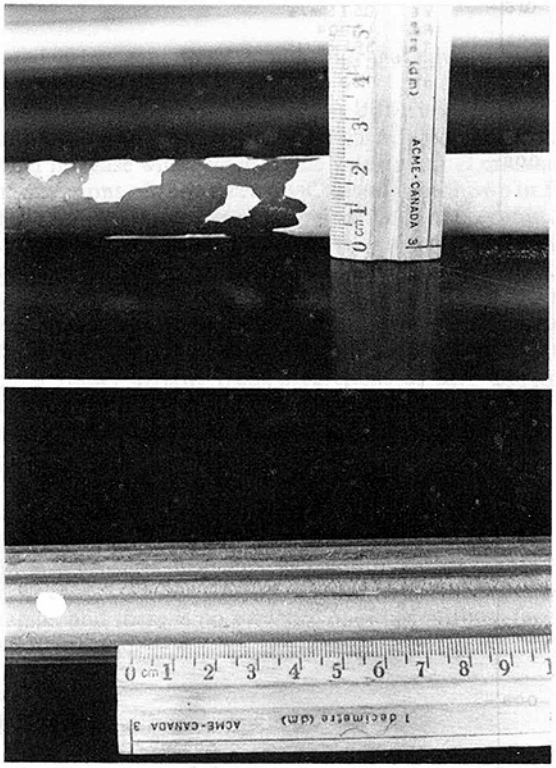

Fig. 4 Scale deposits on (*a*) plain steel tube, (*b*) Bas-Tex finned tube

coefficients of the finned tube to the plain tube is about 1.25 which is roughly as expected given the relative wall thicknesses, and the calculated total surface efficiency of 53 percent. This ratio increased slightly to 1.3 upon fouling.

The thickness of the deposits increased with distance from the water inlet. In the case of the finned tube, the deposits were mostly formed on the prime surface. On the fins, the thickness of the scale decreased with distance from the base to the tip. Deposits on the copper and on the plain mild steel tube were hard and brittle, and could be cracked off easily. However, the deposits on the finned mild steel tube had to be scraped off with a spatula, which produced light grayish powder (Fig. 4).

Since the scaling solution was not highly concentrated, the scaling rate was expected to be slow and given the adherent nature of the $CaCO_3$ scale, the scaling rate was expected to be constant with time. Figure 5 shows typical plots of R_f versus time for the three tubes tested. The linear increase in R_f values is seen in Fig. 5(*a*). Much of the scatter arose from uneven values of the heat flow caused by fluctuations in cooling water flowrate. Near the beginning of some runs R_f became negative. This is attributed to increases in the heat transfer coefficient caused by the rough fouling layer. Linear plots of R_f versus time were found for most runs. Asymptotic behavior was noted only in a few instances (Fig. 5*b*), such as when the mild steel tube was used for the first time (Run 23) or with the noncorroding copper tube at the lowest velocity (Run 38). Clearly there is some surface condition which influences the scale formation. For both these cases, the initial rate was very much higher than usual, and in the former case the ultimate scaling resistance was also abnormally high. In a

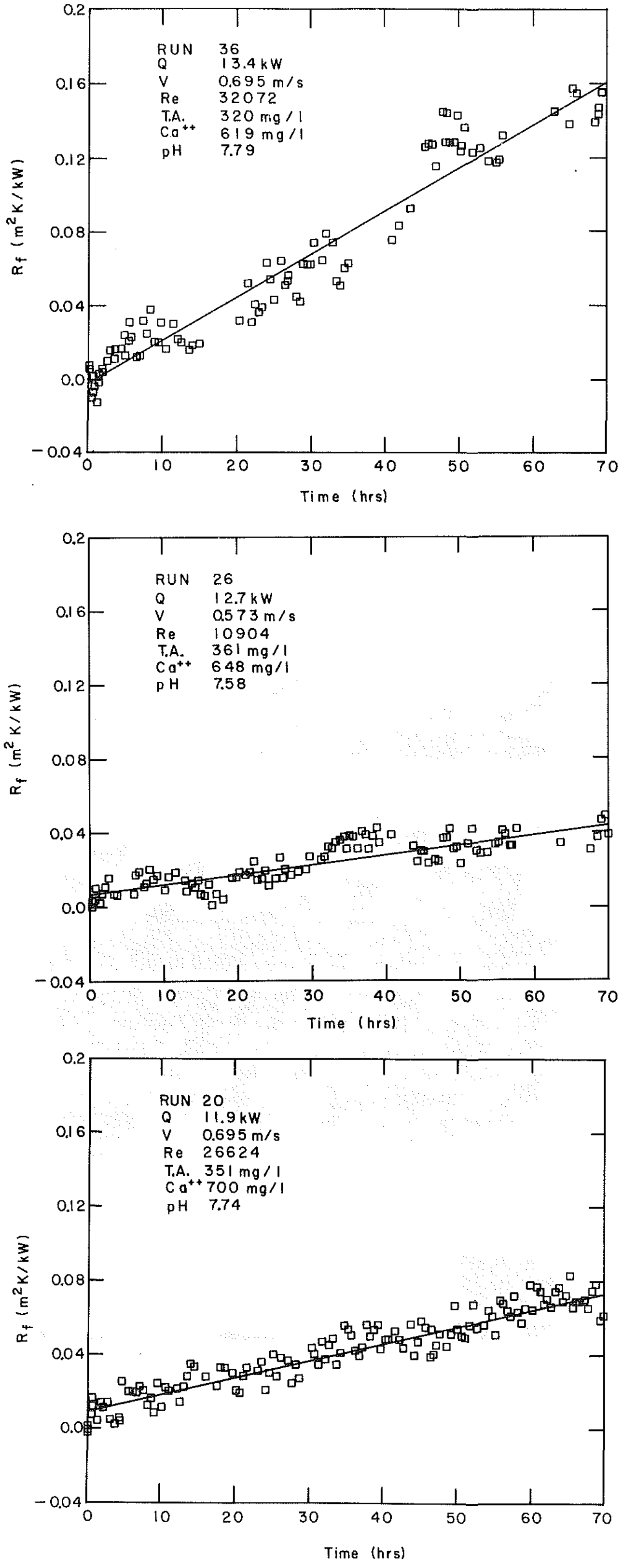

Fig. 5(a) Typical plots of fouling resistance versus time

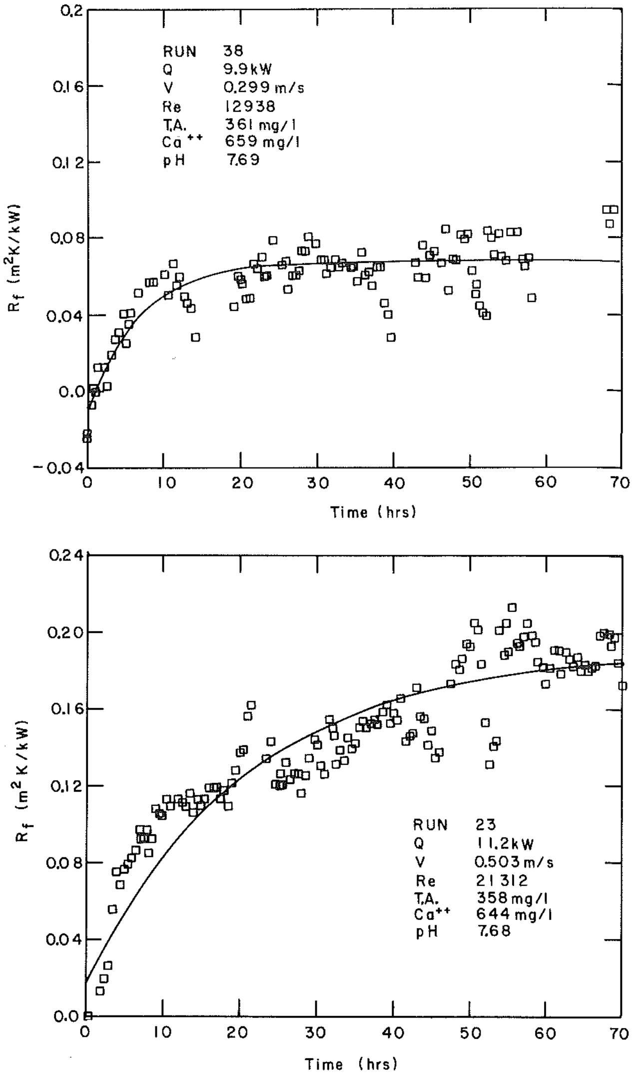

Fig. 5(b) Typical plots of fouling resistance versus time

repeated run on the mild steel tube (Table 1) scaling was linear, and less extensive.

Figure 6 shows the fouling resistance at the end of the run and the scaling rate versus the annular velocity. Because scaling was generally linear with time the curves are similar in each plot. For both the steel tubes the rate generally decreases with increasing velocity at $V > 0.3$ m/s. The rate is clearly higher on the plain tube at equal velocity. When plotted versus the film Reynolds number based on the equivalent diameter, the same trends are noted, although the finned tube data correspond to lower Reynolds numbers. There was some scatter particularly with the plain mild steel tube where a higher temperature run at 0.5 m/s yielded a much higher scaling resistance than anticipated while in another case fouling resistance was low for an inexplicable reason. Since the fouling resistance for the finned tube is based on the prime area, *for the same fouling resistance the weight* of deposit/total area and hence the scale thickness is smaller by about 15 percent on the finned tube than the plain tube. The main effect of tube material in fouling is reportedly to add corrosion products to the deposit [3]. The copper tube, which has a different surface chemistry and would be less susceptible to corrosion than the mild steel tube, behaved quite differently, showing a steady increase in amount of scale and scaling rate with velocity. At a low velocity of 0.3 m/s the copper tube showed asymptotic scaling with a very rapid rise in R_f to 0.05 m^{2}K/kW over the initial 10 h followed by a very slow increase to about 0.08 m^{2}K/kW. This rate is not shown in Fig. 6. The rapid initial growth under these conditions may have been due to the formation of a porous, less

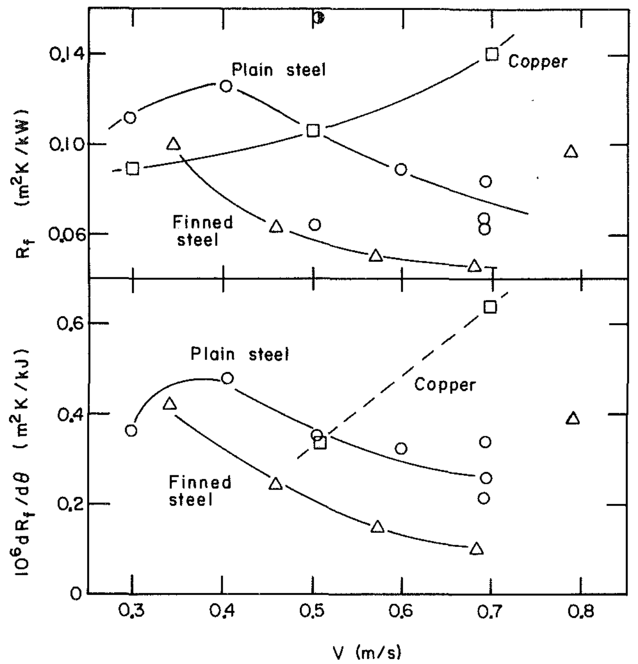

Fig. 6 Fouling resistance after 70 h and scaling rate versus velocity in annulus

tenacious scale, which subsequently failed to grow further due to removal processes. Prior work [2] has shown scaling rates of copper tubes to increase with velocity.

Previous work on fouling of tubes with longitudinal external fins is rare. Knudsen and McCluer [4] found that for calcium sulfate scaling on tubes with transverse external fins the fouling factors were less than for plain tubes. Data reported by Katz et al. [5] and by Webber [6] also indicated less pronounced fouling on finned tubes than on plain tubes. The mathematical models of Epstein and Sandhu [7], in which a uniform deposit thickness over finned and prime surface is assumed, show that an increase in thermal resistance caused by the fouling deposit is less pronounced on an extended surface than on a plain surface given the same deposit thickness. Thus the present results generally confirm what is in the prior literature. For enhanced surfaces which increase the heat transfer rate by an increase in heat transfer coefficient rather than by extension of the surface, fouling resistance is approximately the same as for plain surfaces. Thus Knudsen and Roy [8] reported the same fouling factor based on outside projected area for plain and spirally grooved tubes and Watkinson [9] found the same fouling resistance inside spirally indented and plain tubes.

Comparison With Model

Predictions of scaling rate via Hasson's model were made as follows. The average film temperature was calculated from inlet and outlet conditions and taking the inside wall temperature to be that of the steam. From the measured average pH, total alkalinity, and calcium ion concentrations, the values of carbonate, bicarbonate, and dissolved carbon dioxide were determined using established equations for the temperature dependence of K_1, K_2, K_{sp}, and K_w [10]. The mass transfer coefficient was determined using the Colburn analogy, using the equivalent diameter for the plain and finned-tube annuli, and calculated diffusivities for ionic species. Roughness effects on K_D were not accounted for. The value of K_R was given by Gazit and Hasson [11]. Once equation (4) was solved to obtain w, then the scaling rate was evaluated using equation (1) with average values for ρ_f of 2650 kg/m^3 and k_f of 2.2 W/mK [2].

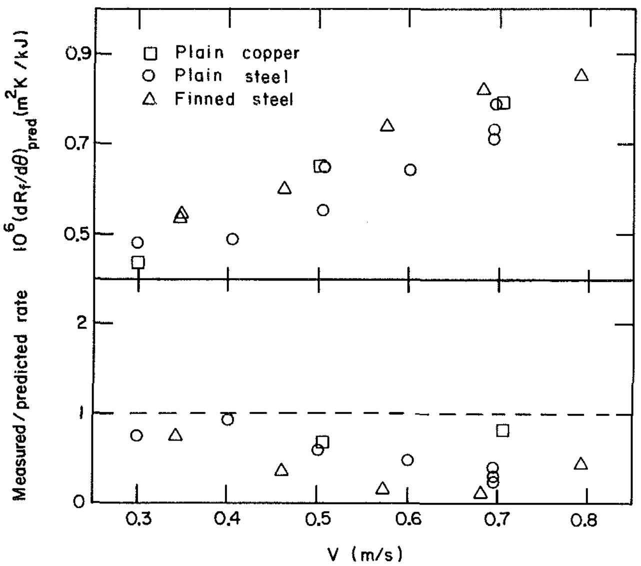

Fig. 7 Scaling rates predicted via equation (4) and ratio of measured to predicted rates versus velocity in annulus

Because the Hasson model assumes diffusion followed by crystallization is the mechanism for scaling, it predicts scaling rates that increase with velocity. The expected rates calculated for the situations of the current experiments are shown in Fig. 7. Differences in water chemistry and temperature account for the scatter in the plot of predicted rate versus velocity. Comparison with Fig. 6 shows that the observed velocity effects are essentially opposite to the predicted values. Figure 7 shows that in magnitude the measured rates are generally similar to those predicted by the equations of Hasson, but the measured values diverge from predictions as the velocity is increased. The average ratio of measured to predicted rate is about 0.4, which is probably not too bad for an a priori prediction method for the rate of scale formation. An underestimation of the scale thermal conductivity could perhaps be the reason that the average predicted values are high. More disturbing however is the difference in trend with velocity. Falling scaling rates with increasing velocity are commonly found where particulate fouling dominates or where deposits are fragile, and there is no evidence of either of these factors in the present case.

Conclusion

These studies of hard water scaling have shown that compared to a plain tube, an externally finned mild steel tube has a lower fouling resistance. Scale appears to concentrate on the prime surface, resulting in a fouling resistance after 70 h of 50-60 percent of that on a plain tube. Thus after scaling, the ratio of heat transfer coefficients of finned to plain tube increases. As velocity was increased in the Reynolds number range 10,000-25,000 the scaling rate on the mild steel tubes decreased slightly, contrary to predictions of the model of Hasson. The measured scaling rates were about 40 percent of those predicted by the model. On a plain copper tube, the fouling resistance after 70 h was close to that of the mild steel tube at a Reynolds number of about 22,000 and increased with velocity.

Acknowledgments

This work was supported by an NSERC operating grant to

A. P. Watkinson. Bas-Tex Ltd. kindly supplied the finned tube.

References

1 Hasson, D., Sherman, H., and Biton, M., "Prediction of Calcium Carbonate Scaling Rates," *Proceedings 6th International Symposium on Fresh Water From the Sea*, Vol. 2, 1978, pp. 193-199.

2 Watkinson, A. P., "Water Quality Effects on Fouling From Hard Waters," in: *Heat Exchangers—Theory and Practice*, J. Taborek, G. F. Hewitt, and N. Afgan, eds., Hemisphere, 1983, pp. 853-861.

3 Suitor, J. W., Marner, W. J., and Ritter, R. B., "The History and Status of Research in Fouling of Heat Exchangers in Cooling Water Service," *Canadian Journal of Chemical Engineering*, Vol. 55, 1977, pp. 374-380.

4 Knudsen, J. G., and McCluer, H. K., "Hard Water Scaling of Finned Tubes at Moderate Temperatures," *Chemical Engineering Progress Symposium Series*, Vol. 55, No. 9, 1959, pp. 1-4.

5 Katz, D. L., Knudsen, J. G., Balekjian, G., and Grover, S. S., "Fouling of Heat Exchangers," *Petroleum Refiner*, Vol. 33, No. 4, 1954, pp. 123-125.

6 Webber, W. O., "Under Fouling Conditions Finned Tubes Can Save Money," *Chemical Engineering*, Vol. 67, No. 6, 1960, pp. 149-152.

7 Epstein, N., and Sandhu, K., "Effect of Uniform Fouling Deposit on Total Efficiency of Extended Heat Transfer Surfaces," *Sixth International Heat Transfer Conference*, Toronto, Vol. 4, 1978, pp. 397-402.

8 Knudsen, J. G., and Roy, B. V., "Studies on Scaling of Cooling Tower Water," in: *Fouling of Heat Exchanger Surfaces*, R. W. Bryers, ed., Engineering Foundation, 1983, pp. 517-530.

9 Watkinson, A. P., "Scaling of Spirally Indented Heat Exchanger Tubes," ASME JOURNAL OF HEAT TRANSFER, Vol. 97, 1975, pp. 490-492.

10 Wiechers, H. N. S., Sturrock, P., and Marais, G. V. R., "Calcium Carbonate Crystallization Kinetics," *Water Research*, Vol. 9, 1975, pp. 835-845.

11 Gazit, E., and Hasson, D., "Scale Deposition From an Evaporating Falling Film," *Desalination*, Vol. 17, 1975, pp. 339-351.

Selecting Optimum Plate Heat Exchanger Surface Patterns

W. W. Focke
Research Associate.
Chemical Engineering Research Group,
Council for Scientific and
Industrial Research,
Pretoria, Republic of South Africa

With appropriate simplifications, plate heat exchanger dimensions and performance can be described by suitable combinations of the base dimensionless groups: Colburn j factor, friction factor, and Reynolds number. Such combinations are used to construct graphic methods for finding optimum geometries (patterns that minimize the surface area required for heat transfer) subject to various constraints. It was found that the number of potentially optimum geometries increased with increasing number of constraints. In plate heat exchangers, the heat transfer performance is related to the pumping power expended. Therefore, in modular plate heat exchangers, the fixed plate lengths limit design flexibility in that heat transfer and pressure drop cannot be varied independently. This limitation can be partly overcome by using interchangeable chevron-type plates of different corrugation inclination angles in the same plate pack.

Introduction

Comprehensive heat exchanger optimization is a formidable task, complicated by many qualitative considerations affecting the selection of a surface pattern [1]. Even at the present level of computing power available, it requires an expenditure that in most cases cannot be justified in terms of the likely gain [2]. Experience and engineering judgment, therefore, will continue to be vital.

It is usual to introduce simplifying assumptions to make the optimization problem more manageable. Unfortunately, this often detracts from the validity of inferred conclusions. In the past, inadequate recognition of such limitations has led to contradictory results [2]: Extrapolating the results of a generalized surface optimization to a complete heat exchanger for a particular application is not generally permissible. However, the modular nature of the commercial plate heat exchanger (PHE) necessitates an *a priori* surface pattern selection. As only a few plate sizes are usually available, design flexibility is limited and is determined by the surface pattern(s) chosen. Therefore, the selection of optimum surface geometries is crucial for compact heat exchangers such as the PHE and must necessarily be based on general principles.

A *surface pattern* or *geometry* is defined as the geometric proportions of the surface modifications which are assumed to be of small scale relative to the plate size. A *configuration* is defined as a surface of fixed dimensions [3]. In this paper, the identification of optimum surface patterns using dimensionless performance plots is emphasized, rather than a comparison of configurations for which a dimensional basis is more appropriate [2].

The present analysis is applicable primarily to plate-type heat exchangers with the controlling heat transfer resistance on one side, but it is extended to include some pressure drop limited designs. The objective is to minimize heat exchanger surface area, subject to various constraints.

Plate Heat Exchangers

A plate heat exchanger is usually comprised of a stack of corrugated metal sheets, in mutual contact, which are held together in a frame by a pressing arrangement. Each plate has four apertures serving as inlet and outlet ports. The heat transfer passages are formed by adjacent plates. Sealing is provided by peripheral gaskets arranged so that the two streams exchanging heat pass through alternate channels.

For the present purpose, it is convenient to define the equivalent diameter as twice the average plate spacing and to base calculations on the projected plate area rather than on the developed surface area. These conventions can be justified partly by noting that PHE flow channels are basically derivatives of low aspect ratio rectangular ducts. More important is the fact that the equivalent diameter assumes physical significance in terms of overall plate heat exchanger dimensions. For other types of heat exchanger, the concept of an equivalent diameter always involves a measure of arbitrariness [2].

Thermal-Hydraulic Characteristics of Surface Patterns

Shah [1] indicated that the j and f versus Re curves are sufficient to describe the thermal-hydraulic performance of a given surface pattern. In PHEs, transition to turbulence may occur at Reynolds numbers as low as 100. Empirical correlations [4–7], in the turbulent regime, usually take the form

$$j = a\mathrm{Re}^{b} \tag{1}$$

$$f = c\mathrm{Re}^{d} \tag{2}$$

Reported values for the correlation constants [4–7] typically fall within the following ranges

$$0.009 < a < 0.95; \quad -0.4 < b < -0.15;$$
$$1.2 < c < 120; \quad -0.6 < d < -0.09 \tag{3}$$

The corrugated pattern on the heat exchanger plates has a significant influence on the heat transfer and pressure drop characteristics. Many proprietary patterns have been

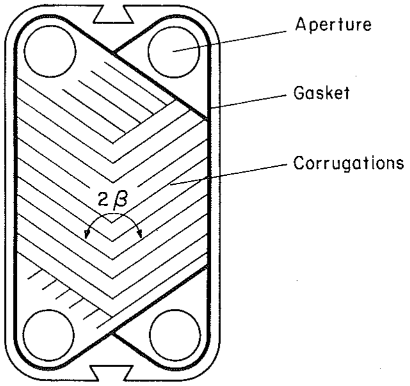

Fig. 1 Typical chevron or herringbone plate

Contributed by the Heat Transfer Division for publication in the JOURNAL OF HEAT TRANSFER. Manuscript received by the Heat Transfer Division October 12, 1983.

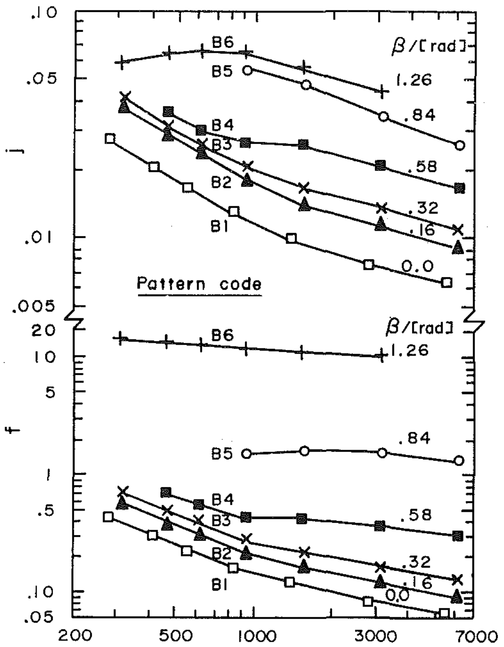

Fig. 2 Thermal-hydraulic performance curves for chevron patterns of different corrugation inclination angles (data from [5])

developed but chevron or herringbone patterns are widely used (Fig. 1). These consist of troughed plates with corrugations inclined at an angle to the flow direction. The plates are assembled with the patterns on consecutive plates pointing in opposite directions, thereby producing a three-dimensional flow passage of almost constant overall cross-sectional flow area.

The available data indicate that the angle β between the plate corrugation and the main flow direction is the major parameter influencing the thermal-hydraulic performance of chevron patterns [4, 5]. The data of Savostin and Tikhonov [5] illustrate the effect of this parameter on the j and f curves. Their data[1] were recalculated using the present definitions for equivalent diameter and heat transfer surface area, and are presented in Fig. 2. Since chevron-type patterns are those most likely to be used in industry, this data set will be used most of the time to illustrate the methods developed in the text for comparing plate heat exchanger surface patterns. These methods are, however, fairly general and can be applied to any surface pattern for which the curves of j and f versus Re are available.

In addition, it has been shown [3, 8] that (turbulent convective) heat transfer per unit surface area correlates remarkably well with energy dissipation per unit volume according to a single parameter, which depends on geometric factors only. For finned tubes, this parameter was identified by LaHaye et al. [3] as the characteristic length between successive boundary layer disruptions.

For a given plate heat exchanger pattern, the relationship between heat transfer performance (represented by a modified Nusselt number) and the power requirement per unit volume is obtained by combining equations (1) and (2)

$$j\mathrm{Re} = m(f\mathrm{Re}^3)^n \qquad (4)$$

A plot of the exponent n versus the logarithm of m will be termed a modified LaHaye performance plot. Figure 5 shows such a plot for all published plate heat exchanger data [5–7]; it includes geometries other than those of chevron or herringbone type. It is evident from Fig. 5 that the two parameters ae correlated [8]; the exponent n tends to decrease with increases in the coefficient m.

Idealizations

The following simplifying idealizations are made; the validity of points *(i)* to *(vi)* is discussed in more detail by McKillop and Dunckley [9]:

---

[1] Patterns B1 to B6 (corresponding to corrugation inclination angles varying from 0 to 1.26 rad) were made from very thin metal sheets. The corrugations approximated to sine curves with wavelengths, amplitudes, and internal radii of curvature of 2.57, 3.8, and 0.6 mm, respectively, for B1 to B6 and 2.56, 7.0, and 0.12 mm, respectively, for pattern B17 [5].

Nomenclature

A = heat exchanger surface area, m^2
A_c = cross-sectional free flow area = $Wd_e/2$, m^2
A_p = projected plate area, m^2
a, b = correlation constants; Colburn j factor equation (1)
C = heat capacity rate, W/°C
c_p = fluid heat capacity, J/(kg°C)
c, d = correlation constants; friction factor equation (2)
d_e = equivalent diameter, twice the spacing between plates, m
f = Darcy friction factor = $(2\Delta P d_e)/(\rho u^2 L)$
h = convective heat transfer coefficient, W/(m^2°C)
I = intercept of operating line on modified LaHaye plot (Fig. 5); equation (10)
j = Colburn j factor = $(h\mathrm{Pr}^{2/3})/(\rho u c_p)$
k = fluid thermal conductivity, W/(m°C)
L = channel length, m
m, n = correlation constants; equation (4)
n_c = number of channels per fluid
N_{tu} = number of transfer units = $(UA)/C_{\min}$
ntu = stream number of transfer units = $(hA)/C$
P = pumping power, W
ΔP = pressure drop, Pa
Pr = Prandtl number = $\mu/(c_p k)$
q = heat duty, W
Re = Reynolds number = $(\rho u d_e)/\mu$
R_c = capacity ratio = $C_{\min}/C_{\max}$
S = slope of operating line on modified LaHaye plot (Fig. 5); equation (10)
T_i = hot stream inlet temperature, °C
t_i = cold stream inlet temperature, °C
U = overall heat transfer coefficient, W/(m^2°C)
u = fluid mean flow velocity = $\omega/(\rho A_c)$, m/s
V = exchanger volume occupied by limiting stream (one stream), m^3
W_p, W = plate width, width of idealized PHE channel, m
X = pressure drop ratio
α = $1/(j\mathrm{Re})$
β = angle between plate corrugation and main flow direction, see Fig. 1, rad
ϵ = thermal effectiveness = $q/\{C_{\min}(T_i - t_i)\}$
λ = constraint parameter; equation (9), $f\mathrm{Re}^2/j$
μ = fluid dynamic viscosity, Pas
ρ = fluid density, kg/m^3
ω = mass flow rate, kg/s

Subscripts

i, 1, 2 = index subscripts
max = maximum
min = minimum
r = required

(*i*) *The heat transfer coefficient is constant along the length of a channel.* This implies constant fluid physical properties and the absence of entrance effects, i.e., turbulent flow.

(*ii*) *Heat transfer resistances caused by fouling and channel wall thermal conductivity are negligible.* This is usually the case owing to the high levels of turbulence prevailing in the PHEs and the thin-gage metal plates used, respectively.

(*iii*) *No heat loss to the surroundings.* The dead air spaces between the end and cover plates in conventional PHEs closely resemble adiabatic walls, making this a reasonable idealization.

(*iv*) *No conduction of heat in the direction of fluid flow* by either channel walls or fluid streams.

(*v*) *Equal flow distribution to channels in the same pass.* This idealization is an approximation for any number of plates but significant deviations from this ideal can occur with highly viscous and non-Newtonian fluids or with large exchangers at high flow rates.

(*vi*) *True countercurrent flow.* In practice, large plate packs operate very close to true countercurrent flow. The maximum deviation occurs with three thermal plates [10], but even in this case the log-mean temperature difference correction factor F is as high as 0.94. The F factor is simply the ratio of the number of transfer units for a true countercurrent flow exchanger to the number of transfer units achieved in the actual exchanger, at equal thermal effectiveness and the same initial temperature difference between the two fluids.

(*vii*) *Equal number of flow channels in each loop.* As the number of channels in the two loops differs by one at most [11], this idealization is a good approximation for heat exchangers with many plates.

(*viii*) *Single-pass operation.* Multipass operation has a detrimental effect on the thermal effectiveness of the plate heat exchanger and is usually avoided in practice. The effect is, however, less severe when both sides have the same number of passes.

The main point of these idealizations is to simplify the analysis. Small deviations from this "ideal" PHE do not necessarily invalidate the conclusions drawn later since they will affect all patterns in a similar way. In fact, it is conceivable that deviations from the assumed ideal may favor the optimum pattern. For instance, an optimum pattern requiring few plates could have more homogeneous flow distribution than a less-than-optimum pattern requiring more plates to achieve the given task.

With the above idealizations, a loop of n_c channels for one fluid stream is equivalent, in terms of performance, to a single channel with the same equivalent diameter and length but with plate width equal to n_c times the original plate width. The dimensions of this model channel are shown in Fig. 3. Note that in the model channel, heat transfer takes place through both side walls. The heat transfer area is given by [11]

$$A = 2n_c A_p \tag{5}$$

and the exchanger volume on one fluid side is given by

$$V = n_c A_p d_e/2 = A d_e/4 \tag{6}$$

The heat transfer coefficient depends on the superficial fluid velocity which, in turn, is determined by the cross-sectional free flow area ($A_c = n_c W_p d_e/2 = W d_e/2$). It follows that the stream number of heat transfer units ($ntu = hA/C$) depends on the equivalent diameter, total heat transfer area and plate length, but is independent of the number of channels per se. From idealization (*vi*), it follows that the number of heat transfer units can be expressed explicitly as a function of the heat transfer duty

$$N_{tu} = \ln\,[(1 - R_c\epsilon)/(1-\epsilon)]/(1 - R_c) \tag{7}$$

where

$$\epsilon = q/[C_{\min}(T_i - t_i)]$$

Therefore, a constraint in the heat transfer duty is equivalent to a constraint in N_{tu}. The exchanger number of heat transfer units and the stream number of transfer units are related by

$$1/(C_{\min} N_{tu}) = 1/(C_1 ntu_1) + 1/(C_2 ntu_2) \tag{8}$$

Thus three independent dimensions of the plate heat exchanger suffice to determine the geometric influences on performance. For the present purpose, it is convenient to choose the equivalent diameter,[2] plate length, and total surface area. From these, the cross-sectional free flow area for each stream follows directly: $A_c = A d_e/4L$.

As three dimensionless numbers containing length dimensions also exist, it is possible to construct dimensionless groups containing only one of the heat exchanger dimensions. Table 1 provides a summary of such dimensionless expressions which focus on specific dimensions and/or performance parameters of the plate heat exchanger design. As will be illustrated later, these groups are very useful when comparing one surface pattern with another.

Optimization of Plate Patterns

At present, it is still not possible to predict, from basic principles, the performance parameters for a particular plate pattern. The optimization procedure therefore necessitates the selection of one (or perhaps a few) pattern(s) from the set for which the thermal and hydraulic performance curves are known.

The thermal engineer sizing a plate heat exchanger for a given duty will always take both fluid streams into account. This presents no problems since only a few plate sizes are generally available. The design engineer who determines the pattern to be embossed on the plates has greater freedom of choice. However, it is not possible for him to foresee all possible applications nor is it reasonable to expect that a limited set of plates could be optimum in all cases. The design engineer is therefore justified in making simplifying assumptions that would guide him in the selection of a small set of patterns which will provide performance close to the optimum in most cases. For this reason, the additional (simplifying) idealization, that the heat transfer rate is controlled by the fluid stream with the lower heat capacity rate ($C_{\min}$), is made.

This means that the heat transfer coefficient on the other side is considered to be very high (approaching infinity).[3] This idealization is relaxed in the Appendix to include pressure drop limited designs. Since wall and fouling resistances are idealized negligible, $N_{tu} = UA/C_{\min} + hA/C_{\min} = ntu$ from equation (8).

Unconstrained Optimization

For most applications, the optimum heat exchanger is the one capable of transferring a specified quantity of heat at the lowest total cost. The total cost is made up of capital costs which are related to heat exchanger size and complexity, and operating costs which are related to the thermodynamic efficiency of the exchanger. In the absence of any constraints and once a given surface has been selected, the optimum heat exchanger dimensions can be found by a procedure illustrated by Kröger [12]. This method requires cost factors for materials, manufacture and energy, all of which are dependent on location and time.

In the absence of universal cost factors, it is still instructive

---

[2] Note that the equivalent diameter represents a link between surface geometry and surface configuration/heat exchanger size.

[3] Alternatively we may assume that the two fluid streams have the same flow rate and identical physical properties, in which case $N_{tu} = ntu/2$ by equation (8).

Table 1 Physical significance of some dimensionless groups in plate heat exchanger context

Base dimensionless groups	$\mathrm{Re} = 4\omega L/(\mu A)$ $j = d_e \mathrm{ntu} \mathrm{Pr}^{2/3}/(4L)$ $f = 8\rho \Delta P A_c^3/(\omega^2 A)$	
Heat exchanger dimensions in terms of performance for constant ntu, ΔP, ω and fluid physical properties. (Applicable to exchangers for which plate length is continuously variable.)	$(f/j)^{1/2} = A_c[8\rho\Delta P/(\omega^2 \mathrm{ntu} \mathrm{Pr}^{2/3})]^{1/2}$	Cross-sectional free flow area
	$(f/j^3)^{1/2} = A[8\rho\Delta P/(\omega^2 \mathrm{ntu}^3 \mathrm{Pr}^2)]^{1/2}$	Surface area
	$(f\mathrm{Re}^2/j)^{1/2} = d_e[8\rho\Delta P/(\mu^2 \mathrm{ntu} \mathrm{Pr}^{2/3})]^{1/2}$	Equivalent diameter
	$(f\mathrm{Re}^2/j^3)^{1/2} = L[128\rho\Delta P/(\mu^2 \mathrm{ntu}^3 \mathrm{Pr}^2)]^{1/2}$	Channel length
Performance groups at constant equivalent diameter, channel length, mass flow rate and fluid flow properties. (Applicable to modular plate heat exchangers)	$1/\mathrm{Re} = \mu A_c/(\omega d_e)$	Cross-sectional free flow area
	$= \mu A/(4\omega L)$	Surface area
	$j = \mathrm{ntu}\, d_e \mathrm{Pr}^{2/3}/(4L)$	Heat transfer
	$f\mathrm{Re}^2 = 2\rho\Delta P d_e^3/(\mu^2 L)$	Pressure drop
Volume specific groups [Transfer analogy equation (4)]	$j\mathrm{Re} = \omega d_e^2 \mathrm{ntu} \mathrm{Pr}^{2/3}/(4\mu V)$	Number of transfer units per unit volume
	$f\mathrm{Re}^3 = 2d_e^4\rho^2 P/(\mu^3 V)$	Energy dissipation per unit volume ($V = Ad_e/4$)

to consider the limiting cases. It is assumed that the capital cost is proportional to the total heat exchanger surface area and that operating costs are proportional to the pumping power. Since there are no constraints, no absolute "best" surface can be found; the relative merit of surfaces can only be compared on some common basis, e.g. comparison at constant cross-sectional free flow area and equivalent diameter. Although this is related to the frame size[4] required for plate heat exchangers, it is a more important consideration for other compact heat exchangers such as radiators.

To find the lowest surface area and minimum pumping power for constant A_c, surface patterns $1/(j\mathrm{Re})$ and $f\,\mathrm{Re}^3$ respectively should be plotted against $1/\mathrm{Re}$ (see Table 1). The data of Savostin and Tikhonov [5] have been plotted in this way in Fig. 4, which shows that the two best surfaces are extremes in the spectrum of available patterns. Only one "minimum surface area pattern" (B6 with $\beta = 1.26$) is indicated over the whole operating range, but it also requires more pumping power than any other geometry. An "optimum" compromise between the extremes can be found only through a proper cost analysis.

Pressure Drop Constraint

Pressure drop restrictions are often imposed. Consider the case where only the pressure drop of the heat transfer limiting stream is constrained. It is also assumed that plate length can be varied continuously and the results are therefore applicable only to plate-type heat exchangers for which this is possible. The effect of a fixed plate length (as for modular plate heat exchangers) is investigated at a later stage. A generalization to other pressure drop limited designs is explored in the Appendix.

Kern [2] shows that for a given surface pattern:

- N_{tu} $(= hA/C_{\min})$ increases with decreasing Re
- ΔP strictly decreases with decreasing Re, and therefore
- N_{tu} increases with decreasing ΔP.

These trends are also evident from the expressions for ΔP ($\Delta P = [\mu^2 L/\{2\rho d_e^3\}]f\mathrm{Re}^2$), and $N_{tu} = [4L/\{d_e \mathrm{Pr}^{2/3}\}]j$), in Table 1, and from the values that the correlation constants in equations (1) and (2) can assume [equation (3)]. Since the surface area required to achieve a given task also decreases with increasing pressure drop, it follows that the optimum pattern can be found from the condition that ΔP and N_{tu} should match exactly with the imposed constraints.

---

[4] Width and length of the plate pack.

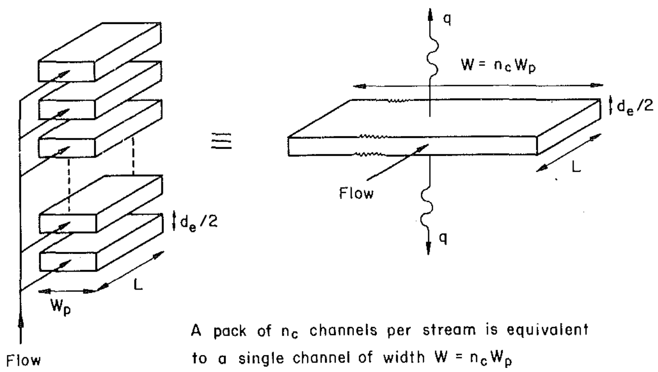

Fig. 3 Simplified model of a plate heat exchanger

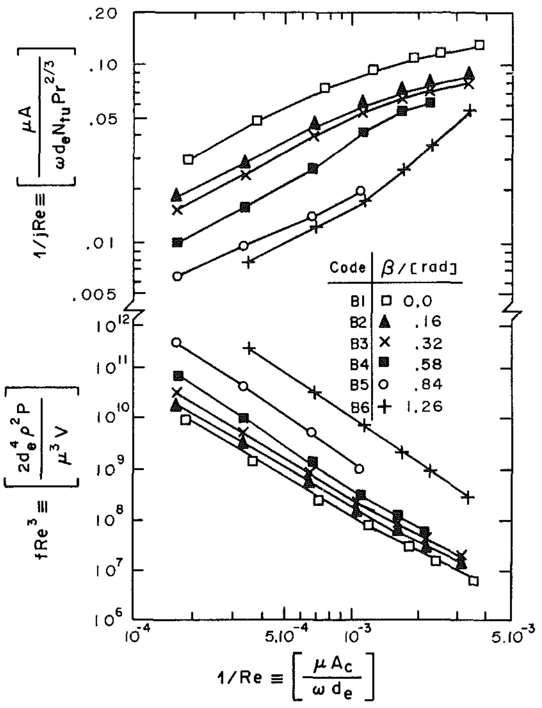

Fig. 4 Comparison of chevron patterns on the basis of an equal cross-sectional free flow area (data from [5])

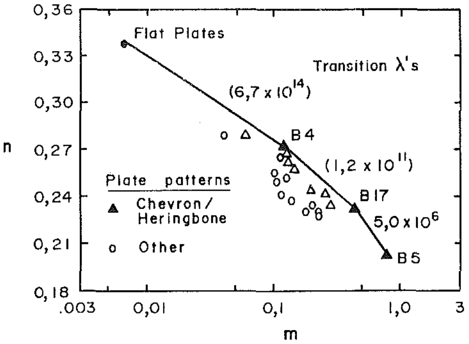

Fig. 5 Modified LaHaye performance plot [8]. Patterns B4, B5 and B17 [5] are all of chevron type. The range over which each of these geometries is optimum is given by the transition values of the dimensionless constraint parameter λ.

Table 2 Optimum surface patterns under a pressure drop restriction (data for patterns of [5])

Pattern code	Performance plot coordinates		Transition	$\alpha \times 10^3$	
	n	m	λ	$\lambda = 10^5$	$\lambda = 10^9$
B5	0.202	0.76	5×10^6	76.6	7.45
B17	0.231	0.427	1.2×10^{11}	94.7	5.92
B4	0.272	0.118		254	8.06
Maximum performance ratio $\alpha_{max}/\alpha_{min}$				3.3	1.36

Based on this condition, an expression for the surface area requirement of optimum patterns can be derived by eliminating the plate length from equations (1) and (2)

$$\alpha = [m\lambda^n]^{1/(n-1)} \tag{9}$$

where

$$\alpha \equiv 1/(j\text{Re}) = \mu A/(\omega d e N_{tu} \text{Pr}^{2/3})$$

is the (minimum) surface area required to achieve the required duty, in dimensionless form, and

$$\lambda \equiv f\text{Re}^2/j = 8\rho\Delta P d_e^2/(\mu^2 N_{tu} \text{Pr}^{2/3})$$

is a dimensionless expression of the pressure drop and heat transfer duty constraints; in the practical range, $\lambda \le 10^{10}$; at $\lambda \le 10^5$, the flow ceases to be turbulent.

LaHaye et al. [3] have suggested that a dimensionless performance plot could be used to guide the designer in the vicinity of the optimum pattern but do not provide details. If equation (9) is rewritten as

$$n = \ln(\alpha)/\ln(\alpha/\lambda) + \ln(m)/\ln(\alpha/\lambda) \tag{10}$$

it follows that at constant λ (the given dimensionless constraint), patterns requiring equal α (i.e., equal surface areas) fall on a straight line with slope $S = 1/\ln(\alpha/\lambda)$ and intercept $I = \ln(\alpha)/\ln(\alpha/\lambda)$ on the modified LaHaye performance plot, Fig. 5. In practice, one finds $\alpha < 1$ and $\lambda >> 1$; the slope of the line is therefore negative.

Taking the partial derivatives of ln (α) with respect to ln (m) and n, one finds:

$$\partial \ln(\alpha)/\partial \ln(m) = 1/(n-1) < 0$$

and

$$\partial \ln(\alpha)/\partial \ln(n) = -n \ln(m\lambda)/(n-1)^2 < 0 \text{ (since } m\lambda > 1 \text{ in practice).}$$

This shows that ln (α) (and therefore α, the required surface area) decreases with increasing n and m.

According to equation (10), any straight line (the operating line) on the modified LaHaye plot (Fig. 5) corresponds to a unique dimensionless (pressure drop and heat transfer) constraint and dimensionless surface area. The latter is given by [see equation (10)]

$$\alpha = \exp(I/S) \tag{11}$$

Since the slope is negative, the argument in the exponential is negative and lower surface areas are indicated by higher intercepts. However, the operating line must also comply with the performance of the pattern under investigation and must therefore pass through the coordinates of that pattern on the LaHaye plot.

Consider a straight line on the modified LaHaye plot which passes through the coordinates of one particular pattern only, while the coordinates of all other available patterns lie to the left and below. At the operating conditions corresponding to the slope and intercept of this line, this particular pattern is optimum, i.e., it requires the smallest heat transfer surface area.

Therefore, the best patterns can be found by connecting those points, on the LaHaye dimensionless performance plot, which form the right-hand boundary for all points (see solid-line segments in Fig. 5). The slope and intercept of these line segments also define the operating ranges (performance parameter λ) over which a pattern is optimum. In terms of the

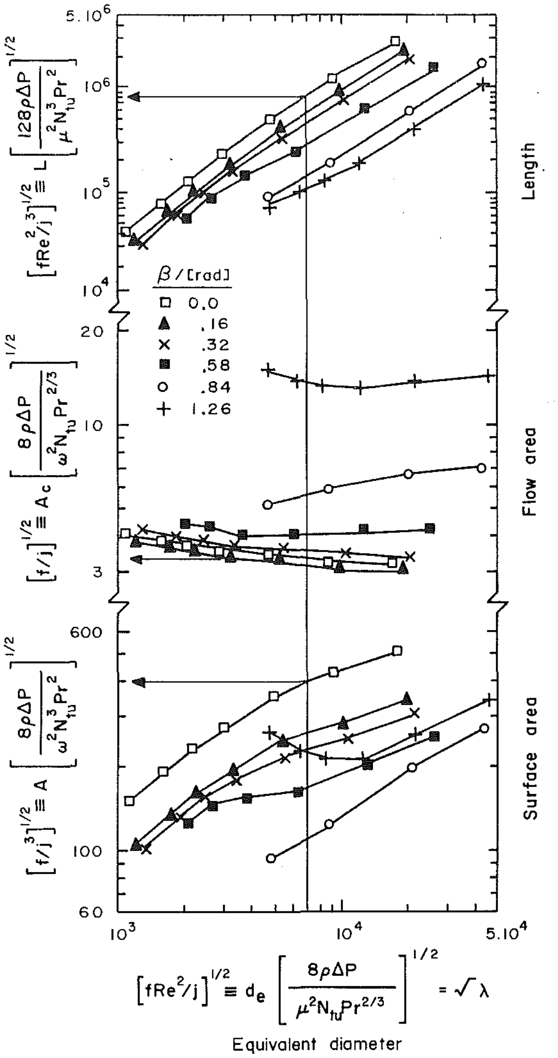

Fig. 6 Modified Bergwerk plot [13] for chevron patterns [5]

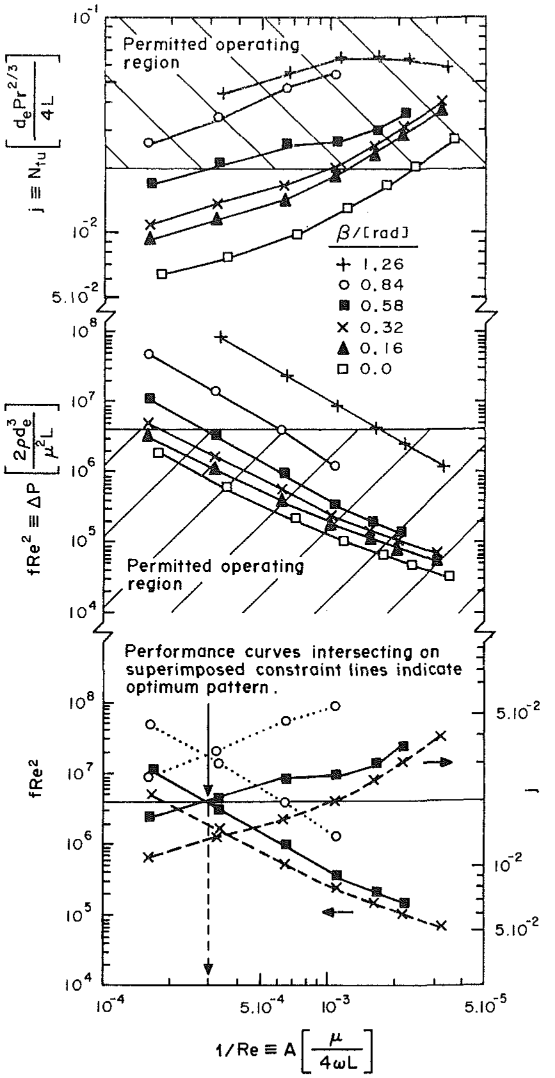

Fig. 7 Finding the optimum chevron pattern for given pressure drop and channel length constraints (data from [5])

coordinates of two such patterns, the λ value from equation (9) will be

$$\lambda = [m_1^{n_2-1}/(m_2^{n_1-1})]^{1/(n_1-n_2)} \tag{12}$$

Optimum patterns thus arrived at have been identified in Fig. 5 (B4, B5, B17, and flat plates). This plot contains the coordinates of published performance data for commercial PHEs and other plate patterns [4–7]. Any patterns lying to the left are worse than the set of boundary points (indicated by solid symbols in Fig. 5).

Through the introduction of a pressure drop constraint, the number of potentially optimum (minimum surface area) geometries has been increased from one to four. Of these, only the bottom two patterns need to be considered, as the λ values at which the others become optimum far exceed experimental (and practical) operating ranges. The area requirements of three optimum patterns are compared in Table 2 for two values of the operating range parameter λ. The lower limit $\lambda = 10^5$ of this parameter corresponds approximately to a value at which the flow ceases to be turbulent, while the upper limit corresponds to that of the experimental data. The most important conclusion to be drawn from Table 2 is that there is a significant reduction in the performance ratio with increasing λ, i.e., changing from a factor of 3.3 at $\lambda = 10^5$ to only 1.36 at $\lambda = 10^9$.

From equation (9), it also follows that in the turbulent regime the total surface area is proportional to a positive power of the equivalent diameter

$$A \propto d_e^{(1-3n)/(1-n)} \tag{13}$$

Since $1/5 < n < 1/3$, this power ranges from approximately zero for flat plate channels to about 1/2 for a chevron pattern with $\beta = 0.84$ rad. Therefore, performance can be improved by simply reducing the equivalent diameter. It is interesting that the improvement is most pronounced for the optimum pattern $\beta = 0.84$ rad.

Once a set of optimum patterns has been identified on the synoptic LaHaye dimensionless performance plot, the patterns can be compared in more detail on a modified Bergwerk plot [13]. The ordinates of these plots are proportional to the channel length, free flow area, and surface area, respectively. The abscissa is the square root of the dimensionless performance parameter [$\sqrt{\lambda}$, see equation (9)] and is proportional to the equivalent diameter. The exchanger dimensions are those of the exchanger with a minimum surface area for a given surface pattern. Figure 6 is termed a modified Bergwerk plot [13] because the group $(fRe^2/j^3)^{1/2}$ is used instead of Bergwerk's group $(1/j)$, which is less acceptable as it contains the equivalent diameter as well as being proportional to the flow length. Thus, the effect of varying the equivalent diameter on the overall heat exchanger dimensions can be more conveniently investigated using the present set of ordinates because only the abscissa is proportional to the equivalent diameter.

The data for chevron patterns [5] have been plotted in this way in Fig. 6, in which pattern B5 with $\beta = 0.84$ rad provides the lowest surface area designs in accordance with its identification as an optimum pattern in Fig. 5. However, to achieve this, it requires the second largest free flow area whereas the plate length is only the second lowest. An interesting feature of Fig. 6 is the relative insensitivity of the free flow area (A_c) to the performance parameter λ. It indicates that the plate width (of the model channel) is roughly proportional to the inverse of the equivalent diameter ($W \propto 1/d_e$). Figure 6 also shows the importance of plate length; for a given geometry, the cross-sectional area is approximately constant and plate length becomes the variable that has to be adjusted to accommodate the given performance constraints (ΔP and N_{tu}). The existence of an optimum equivalent diameter is also indicated for pattern B6 ($\beta = 1.26$) on the $(f/j^3)^{1/2}$ plot.

Plate Length Constraint

In practice, only a limited number of plate sizes are available owing to the high cost of pressing tools. Therefore, the additional constraint of a fixed plate length must be considered. Now pressure drop and N_{tu} constraints are conveniently expressed in terms of the dimensionless groups $f\mathrm{Re}^2$ and j, respectively. Similarly, the required surface area can be expressed as $1/\mathrm{Re}$ (see Table 1).

For the family of corrugated patterns investigated by Savostin and Tikhonov [5], both ΔP and N_{tu} strictly increase with corrugation inclination angle β at constant Re. A graphic method for determining the optimum corrugation inclination angle, therefore, can be constructed as follows (see Fig. 7):

Plot the ΔP and N_{tu} constraints on the $f\mathrm{Re}^2$ and j versus $1/\mathrm{Re}$ graphs, respectively. Then superimpose the $f\,\mathrm{Re}^2$ plot (on transparent graph paper) on the j versus $1/\mathrm{Re}$ plot so that the constraint lines coincide. The performance curves of the optimum corrugated pattern will cross exactly on the superimposed constraint lines (pattern B4 with $\beta = 0.58$ rad in the example). Performance curves intersecting above or below the constraint lines correspond to patterns requiring additional surface area (i.e., more plates) to satisfy ΔP and N_{tu} restrictions, respectively.

If the pattern is not available for which the performance curves intersect on the constraint lines, the next best available pattern will be one of the two available for which the intersection occurs just above and below the superimposed constraint lines (in this example either $\beta = 0.32$ rad or $\beta = 0.84$ rad). The optimum one is found by comparing the intersection of the $f\,\mathrm{Re}^2$ curve (for the upper pattern) and the j curve (for the lower pattern) with the superimposed constraint lines. The pattern for which this intersection lies to the left of that for the other pattern requires the least surface area and corresponds to the optimum corrugation inclination angle (in the example $\beta = 0.84$ rad).

The graphic procedure is illustrated in Fig. 7. Pattern B4 with $\beta = 0.58$ rad is the optimum geometry, subject to the (arbitrarily chosen) pressure drop and heat transfer duty constraints of $f\,\mathrm{Re}^2 = 4 \times 10^6$ and $j = 2 \times 10^{-2}$, respectively. However, every intersection of the two performance curves defines a potentially optimum design for that geometry, subject to constraints corresponding to the position of the intersection. For example, pattern B3 with $\beta = 0.32$ rad will require the least surface area for constraints of $f\,\mathrm{Re}^2 = 1.5 \times 10^6$ and $j = 1.3 \times 10^{-2}$. This shows that there are operating conditions at which any given pattern of the family will require less surface area than any of the other patterns. In particular, the number of potentially optimum geometries has increased considerably by consideration of the additional constraint of fixed plate length. Note, however, that ability to vary the corrugation inclination angle β compensates only partly for the loss of freedom to vary plate length.

This, then, is the dilemma of the manufacturer of modular plate heat exchangers. Practice dictates a design flexibility that could be achieved only if plate length and/or corrugation inclination angle were continuously variable. Fortunately, it appears feasible [11, 14] to mix plates of different corrugation angles in the same plate pack and in this way achieve a performance equivalent to a plate of an intermediate angle: A channel formed by two adjacent plates of $\beta = 0.52$ rad and $\beta = 1.05$ rad gave friction and Colburn j factors similar to a $\beta = 0.79$ rad channel [14]. By choosing only a few suitable and interchangeable patterns, a significant degree of design flexibility can be attained.

Therefore, the final objective should be to find such a set of optimum and interchangeable patterns. All patterns identified on the LaHaye performance plot (Fig. 5) as potentially optimum were of the chevron type, suggesting that this is the optimum pattern. The number of different plate patterns (i.e., of different corrugation inclination angles) that should be available for optimum design depends on the range of plate lengths to be manufactured.

Conclusions

By basing heat transfer surface area on projected plate area, defining the equivalent diameter as twice the average plate spacing and using reasonable simplifying idealizations, appropriate combinations of the base dimensionless groups j, f, and Re assume physical significance in terms of exchanger performance and dimensions. These combinations of the base groups can be used to construct graphic methods of determining optimum (i.e., requiring the minimum total heat transfer surface area) surface patterns (geometries) subject to a minimum heat transfer duty and various other constraints. This analysis revealed a trend toward an increasing number of potentially optimum patterns with an increasing number of constraints:

- *No constraint.* The pattern providing the highest overall heat transfer coefficient is best but also requires the highest pressure drop.
- *Pressure drop constraint.* This applies to plate-type exchangers for which the plate length is continuously variable. The optimum pattern makes full use of the available pressure drop. Several potentially optimum patterns, all of which are chevron type, have been identified on a LaHaye performance plot (Fig. 5). Further examination of such patterns on a modified Bergwerk plot (Fig. 6) revealed the existence of optimum equivalent diameters for at least one geometry ($\beta = 1.26$ rad).
- *Pressure drop and length constraints.* This case applies to the commercial modular plate heat exchanger of fixed plate length/size. A novel graphic procedure reveals that design flexibility requires a continuously variable corrugation inclination angle. This can be achieved partly by using interchangeable chevron patterns of different corrugation inclination angles in the same plate pack.

The above conclusions were based on the assumption that the overall heat transfer coefficient is determined by one fluid stream. However, they are believed to be more generally valid and it can be shown that the results apply directly to some pressure drop limited designs, provided the N_{tu} used in the text is multiplied by an appropriate correction factor.

References

1 Shah, R. K., "Compact Heat Exchanger Selection Methods," *Heat Transfer*, Vol. 4, 1978, pp. 185-191.

2 Kern, J., "Zur Bewertung von Kompakt-Waermeaustauschern," *Waerme und Stoffuebertragung*, Vol. 13, 1980, pp. 205-215.

3 LaHaye, P. G., Neugebauer, F. J., and Sakhuja, R. K., "A Generalized Prediction of Heat Transfer Surfaces," ASME Journal of Heat Transfer, Vol. 96, 1974, pp. 511-517.

4 Focke, W. W., "Plate Heat Exchangers," CSIR Report CENG 445, Feb. 1983, CERG-CSIR, P.O. Box 395, Pretoria 0001, RSA.

5 Savostin, A. F., and Tikhonov, A. M., "Investigation of the Characteristics of Plate Type Heating Surfaces," *Teploenergetika*, Vol. 17, No. 9, 1970, pp. 75-78.

6 Buonopane, R. A., and Troupe, R. A., "A Study of the Effects of Internal Rib and Channel Geometry in Rectangular Ducts, Part II: Heat Transfer," *AIChE J.*, Vol. 15, 1969, pp. 592-596.

7 Emerson, W. H., "The Thermal and Hydrodynamic Performance of a Plate Heat Exchanger, I. Flat Plates; II. An APV Exchanger; III. A De Laval Exchanger; IV. A Rosenblad Exchanger," NEL Reports 283-286, Apr. 1967, National Engineering Laboratory, Glasgow, U.K.

8 Focke, W. W., "Turbulent Convective Transfer in Plate Heat Exchangers," *International Communications in Heat and Mass Transfer*, Vol. 10, No. 3, 1983, pp. 201-210.

9 McKillop, A. A., and Dunckley, W. L., "(Plate Heat Exchangers) Heat Transfer," *Industrial and Engineering Chemistry*, Vol. 52, No. 9, Sept. 1960, pp. 740-745.

10 Buonopane, R. A., Troupe, R. A., and Morgan, J. C., "Heat Transfer Design Method for Plate Heat Exchangers," *Chemical Engineering Progress*, Vol. 59, No. 7, July 1963, pp. 57-61.

11 Marriott, J., "Performance of an Alfaflex Plate Heat Exchanger," *Chemical Engineering Progress*, Vol. 73, No. 2, Feb. 1977, pp. 73-78.

12 Kröger, D. G., "Design Optimization of an Air-Oil Heat Exchanger," *Chemical Engineering Science*, Vol. 38, No. 2, 1983, pp. 329-333.

13 Bergwerk, W., "The Utilization of Research Data in Heat Exchanger Design," Thermodynamics and Fluid Mechanics Convention, Institution of Mechanical Engineers, Paper No. 16, Apr. 1964, pp. 55-64.

14 Focke, W. W., and Lombard, M., "Thermohydraulic Performance of Plate Heat Exchanger Configurations Consisting of Mixed Plates," CSIR Report CENG 533, Aug. 1984, CERG-CSIR, P.O. Box 395, Pretoria 0001, RSA.

APPENDIX

The pressure drop limiting stream satisfies the following condition: The ΔP constraint of the other stream will automatically be satisfied, provided that the ΔP constraint of the pressure drop limiting stream is satisfied. The analysis is based on the assumption that the heat exchanger operates in the turbulent regime where the empirical correlations, equations (1) and (2), are valid. In practice, the most common design conditions are:

$$q \geq q_r \tag{14}$$

$$\Delta P_i \leq (\Delta P_i)_{\max} \tag{15}$$

The constraint on the heat transfer duty is equivalent to a constraint in N_{tu} using equation (7).

The pressure drop limiting stream can be found as follows: Label the two streams in such a way that

$$X_r = (\Delta P_1)_{\max}/(\Delta P_2)_{\max} \leq 1 \tag{16}$$

The actual pressure drop ratio for the two streams can be derived from the definition of the friction factor because the free flow area is the same for both fluid streams

$$X = [(\rho_2 \omega_1^2)/(\rho_1 \omega_2^2)][(\omega_1 \mu_2)/(\omega_2 \mu_1)]^d \tag{17}$$

Calculate the minimum and maximum of this quantity for the range of patterns available [see equation (3) for the range of variations in the exponent d] and compare X with X_r. If

$$X \leq X_r \forall d \tag{18}$$

i.e., if the actual pressure drop ratio is less than the ratio of maximum pressure drops for all patterns, then stream 2 is pressure drop limiting. Otherwise, if

$$X \geq X_r \forall d \tag{19}$$

stream 1 is pressure drop limiting. If neither of these two conditions is satisfied, a pattern can be found that would make optimum use of both pressure drops. The actual pressure drop ratio [equation (17)] depends on the mass flow rates, the physical properties ρ and μ, and on plate geometry, as expressed in the exponent d. Obviously, the plate geometry will have no effect (and hence a limiting stream will always exist) when

$$\omega_1/\omega_2 = \mu_1/\mu_2 \tag{20}$$

so that equation (17) is independent of the plate geometry (or the exponent d).

Relabel the streams so that stream 1 is pressure drop limiting. As fouling and wall resistances are negligible, the overall heat transfer coefficient is given by

$$1/U = 1/h_1 + 1/h_2 \tag{21}$$

By defining $ntu_i \equiv h_i A/C_i$

$$N_{tu}/ntu_1 = (C_1/C_{\min})[1 + (C_1 ntu_1)/(C_2 ntu_2)]^{-1} \tag{22}$$

is obtained, which by expansion of the ratio ntu_1/ntu_2 becomes

$$N_{tu}/ntu_1 =$$

$$(C_1/C_{\min})[1 + (C_1/C_2)\{(\omega_1 \mu_2)/(\omega_2 \mu_1)\}^b (\mathrm{Pr}_2/\mathrm{Pr}_1)^{2/3}]^{-1} \tag{23}$$

Two limiting conditions where geometry of the plate has no influence on this correction factor are apparent:

- $(C_1 ntu_1)/(C_2 ntu_2) << 1$. This condition is equivalent to the case of the pressure drop limiting stream limiting the overall heat transfer rate. The appropriate correction factor to the N_{tu} value used in the main text reduces to

$$N_{tu}/ntu_1 = C_1/C_{\min} \tag{24}$$

- $\omega_1/\omega_2 = \mu_1/\mu_2$. This condition also guarantees a pressure drop limited design. However, as the range of variation and the actual values of the exponents b and d are small, this condition remains valid provided the ratio $(\omega_1 \mu_2)/(\omega_2 \mu_1)$ is sufficiently close to one. The appropriate correction factor for this case is

$$N_{tu}/ntu_1 = (C_1/C_{\min})[1 + (C_1/C_2)(\mathrm{Pr}_2/\mathrm{Pr}_1)^{2/3}] \tag{25}$$

R. E. Taylor

B. H. Kelsic[1]
Mem. ASME

Thermophysical Properties Research Laboratory,
School of Mechanical Engineering,
Purdue University,
West Lafayette, IN 47906

Parameters Governing Thermal Diffusivity Measurements of Unidirectional Fiber-Reinforced Composites

Limitations in applying the concept of thermal diffusivity to coarse-weave fiber-reinforced composites are examined. Using the flash technique for measuring the apparent diffusivity, the effects of fiber fraction, fiber/matrix thermal conductivity ratio fiber orientation, and specimen length are studied. The conductivity ratio was the major factor governing the thermal behavior of the composite. The fiber fraction was the next most controlling parameter. Specimen length and fiber orientation can be used to modify the behavior of composites.

Introduction

Fiber-reinforced composites offer improved mechanical and thermal properties over many conventional materials. These high-performance materials possess higher strength-to-weight ratios, better corrosion and wear resistance and longer fatigue life than standard lightweight/high-strength metals.

The greatest percentages of fiber-reinforced materials are used in the aircraft/aerospace industry. In particular, graphite fibers are the most commonly used. Lightweight carbon/epoxy combinations are useful in applications such as aircraft tail sections, fuselage panels, and wing skins. Carbon/carbon materials are frequently used in high-temperature applications, including brake linings for the DC-10 and rocket nozzles.

Fiber-reinforced composites have also gained the attention of the automotive, tooling, and sporting goods industries. Car bodies and brake linings, hammers and dies, tennis racquets, bicycle pedals, and fishing rods have all been successfully manufactured from fiber-matrix combinations.

While much study has been devoted to studying the mechanical behavior of the materials, a comparable understanding of the thermal behavior is lacking. In the past ten years, only aerospace applications of carbon/carbon have provided the impetus for thermal studies.

One of the most relevant, and yet most difficult, investigations being conducted in the thermal industry regards the thermal diffusivity of oriented fiber composites. Taylor [1] and Luc and Balageas [2] have found that fiber spacing and sample length are significant factors in determining the apparent diffusivity of carbon/carbon composites. Some analysts apply the Rule of Mixtures, deriving an "effective thermal diffusivity" from the thermal properties and volume fractions of the constituents. Others have developed empirical formulas for predicting the conductivities in the transverse and longitudinal directions of orientation [3, 4]. Taylor has suggested that off-axis testing may result in a more accurate overall thermal diffusivity than the effective diffusivity predicted by the Rule of Mixtures [5]. In general, however, very little testing has been done to correlate experimental findings with theory.

The objectives of this research were to study the effects of thermal conductivity ratio, fiber fraction, fiber orientation, and specimen length upon the thermal diffusivity of coarse-weave unidirectional fiber-reinforced composites. The laser flash technique was used to measure thermal diffusivity. Finite element modeling characterized heat flow through test specimens. Limitations upon the governing parameters are offered.

Mathematical Model

Thermal diffusivity is a transport property which describes how quickly heat propagates through a material during a transient state. If there are no internal heat sources or sinks, and if the thermal conductivity is independent of temperature and position, the one-dimensional heat diffusion equation for transient conditions may be written

$$\frac{\partial^2 T}{\partial \chi^2} = \frac{1}{\alpha}\frac{\partial T}{\partial t} \tag{1}$$

Equation (1) is the energy equation used to describe the heat transport through homogeneous materials. For heterogeneous materials, however, each constituent has particular thermophysical properties and the thermal conductivity k cannot be removed outside the del operator. In principal, then, thermal diffusivity has no physical meaning for heterogeneous materials. In practice, however, diffusivity techniques have been successfully extended to many composites. Given an adequate sample thickness or similar constituent diffusivities, "effective" properties of a material can be measured.

The flash method for determining thermal diffusivity was first described by Parker et al. in 1961 [6]. In this method, a high-intensity short-duration light pulse is absorbed in the front face of the test specimen. The radiation source may be a laser or a flash lamp, having an irradiation time of about 0.001 s or less. The resulting temperature rise of the rear face of the test sample is measured and recorded. The thermal diffusivity is determined from the temperature rise versus time curve of the rear surface. For the case where the heat pulse is represented by a Delta function, there are no heat losses, heat flow is one-dimensional, and thermal diffusivity does not vary with temperature, the dimensionless temperature can be expressed as

$$V = \frac{T(L,t)}{T_{\max}(L)} = 1 + 2\sum_{n=1}^{\infty}(-1)^n \exp(-n^2\pi^2\alpha t/L^2) \tag{2}$$

where α is the thermal diffusivity and $x = L$ at the rear surface.

The thermal diffusivity can be determined from equation (2). When the rear face temperature has achieved half its maximum value ($V = 0.5$), at time $t_{1/2}$, then

---

[1] Presently at Ball Aerospace Systems Division, P.O. Box 1062, Boulder, CO 80306

Contributed by the Heat Transfer Division for publication in the JOURNAL OF HEAT TRANSFER. Manuscript received by the Heat Transfer Division August 20, 1984.

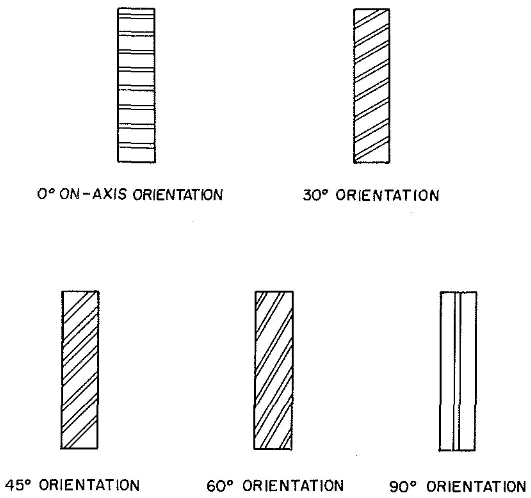

Fig. 1 Fiber orientations

$$\pi^2 \alpha t_{1/2}/L^2 = 1.38 \qquad (3)$$

In this expression $t_{1/2}$ is called the "half-time," referring to the time required for the rear face to achieve ½ its maximum temperature rise.

The advantages of the flash method over other thermal diffusivity measurement techniques are the small sample size and the short experiment duration. Test specimens typically have a diameter of a small coin and a thickness of 0.1–0.4 cm. The experimental duration is less than 1 s for most materials, but may be as high as 20 s for poor conductors.

Mathematical corrections can be applied to cases where finite pulse time, heat losses, and nonuniform heating exist. In this study, heat loss corrections were applied [7].

The importance of the thermal conductivity ratio was one of the parameters studied in this research. The ratio can easily vary between 1 and 1000 using common matrix and fiber materials. This ratio can be quite large compared to the heat capacitance ratio. Indeed, for many composites, the heat capacitance ratio is close to one, so its contribution is small compared to that of the thermal conductivity ratio.

Experimental Apparatus and Procedures

A Korad K-1 neodymium laser rod provided the energy pulse for the flash experiments. The test specimen was centered in a sample holder inside a long horizontal furnace. A bell jar cover ensured minimal convection heat losses from the furnace and sample holder. Samples were tested at 100°C in an air atmosphere.

The sample rear face temperature was measured with an indium antimonide infrared detector. The detector was focused on the rear face of the sample. The vernier was adjusted to render a viewing spot size of about 0.6-cm diameter. This spot size permits temperature integration over at least one fiber matrix unit cell. For homogeneous samples, a smaller spot size is acceptable since the rear face temperature is uniform across the entire area.

Unidirectional fiber-reinforced composites were fabricated for testing. Three fiber/matrix combinations were used: copper/epoxy, stainless steel/epoxy, and stainless steel/Cerrocast.[2] Copper and steel wire were used as the fibers. The wire diameters were 0.0775 cm and 0.0813 cm for the copper and steel, respectively. The fiber spacing was varied to provide fiber fractions of 1.3, 5.8, and 23 percent. Bulk composites were cast and then test samples were machined from the blocks. All samples were nominally 0.2 cm thick. Thorough descriptions of the samples and the test apparatus are given in Kelsic [8]. The importance of a good fiber-matrix bond cannot be overestimated. Two precautions were taken in this study to ensure that only well-bonded samples were used. First, it was observed that if debonding was likely, it would occur during machining. Broken bonds could be observed visually. Second, diffusivity tests were run using debonded samples. The samples were tested before and after deliberate debonding. The debonding resulted in erratic spikes and strong deviations from the curve observed for the bonded samples.

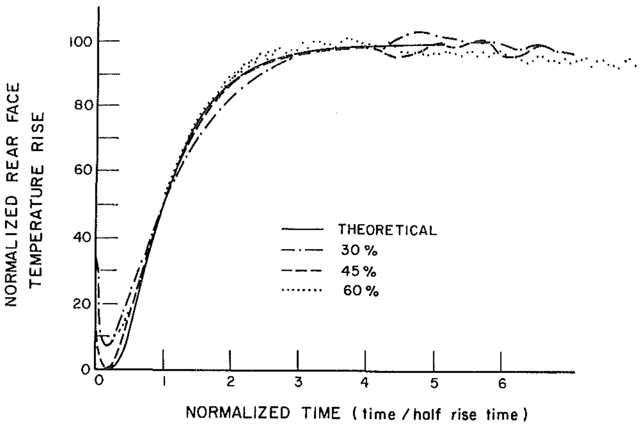

Fig. 2 Thermal rise curves for 23 vol. percent SS/epoxy

The fiber-matrix thermal conductivity ratios studied were 1000, 25, and 0.5. Fiber fractions of 1.3, 5.8, and 23 percent were examined. The fiber diameter and the specimen length were relatively constant.

On-axis and off-axis samples were machined. "On-axis" indicates a fiber alignment parallel, or on-axis, to the laser pulse. The fibers are perpendicular to the faces of the sample. "Off-axis" orientations describe the angles between the fiber direction and the laser pulse direction. Thus a 30 deg off-axis alignment means the fibers are oriented at an angle 30 deg to the laser pulse direction. Off-axis samples of 30, 45, 60, and 90 deg were studied. Figure 1 exhibits the fiber alignment configurations.

The specimen faces were prepared to ensure equal fiber and matrix emissivities. The epoxy specimen faces were painted black; the Cerrocast faces were roughened using Silicon Carbide Powder. All samples were examined visually for uniform and complete surface roughness. A few were examined microscopically.

Measurement Results and Discussion

The behavior of the thermal rise curve illustrates the degree of agreement or deviation from the theoretical rise curve for a homogeneous material. If there are no heat losses or heterogeneous uncoupled phenomena in which heat flows through the two phases are more or less independent of each other, the experimental curve follows the theoretical curve closely. Deviations attributable to noise, amplification, or laser flashby can frequently be eliminated or smoothed, with the net effect of a curve close to the theoretical model. To provide direct comparison between samples of different materials, temperatures, thicknesses, absorptivities, etc., results are normalized by the maximum temperature attained and the time required to reach ½ of the maximum rise.

SS/Epoxy

The on-axis SS/epxoy and the samples cut at an angle of 45 deg to the fiber followed the theoretical curve for a

---

[2] *Cerrocast is a low-temperature melting alloy comprised of bismuth and tin. It is available from the Cerro Corporation.*

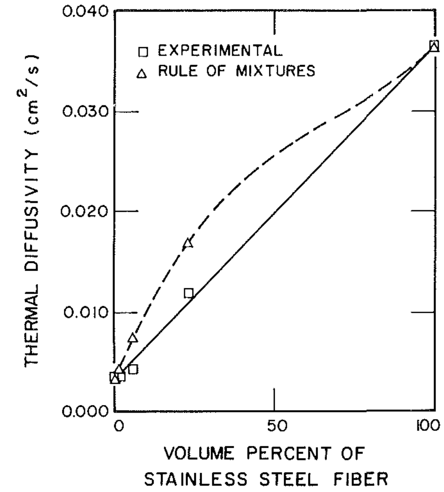

Fig. 3 Experimental and mixtures diffusivities of SS/epoxy

homogeneous material well. A modest spike, with a subsequent lead less than 5 percent of the normalized magnitude, occurred for the 23 percent V_f sample. Samples cut at 30, 60, and 90 deg exhibited spikes and early time leads for all fiber fractions. Figure 2 exhibits thermal rise curves for the 23 percent V_f samples.

A comparison between the on-axis experimental diffusivity and values calculated from the Rule of Mixtures is useful. The Rule of Mixtures computes thermal diffusivity for a composite according to the relation [3]

$$\alpha_c = \frac{V_f k_f + V_m k_m}{V_f(\rho c)_f + V_m(\rho c)_m} \tag{4}$$

Figure 3 presents mixtures diffusivities versus experimental diffusivities. Deviations between theoretical diffusivity and the experimental values are significant. A 30 percent difference exists between the mixtures and experimental (extrapolated) diffusivities at a 50 percent fiber fraction. This suggests that while the Rule of Mixtures affords a good order-of-magnitude approximation for composite diffusivity, it is not reliable if more exact values are required.

For each fiber orientation, thermal diffusivity increased with increasing fiber fraction. The slope of the increase was greatest for the 0 deg (on-axis) orientation and least for the 90 deg orientation. The 90 deg diffusivities remain relatively flat, indicating behavior dominated by the matrix. The presence of fibers perpendicular to the laser pulse does not significantly augment heat transfer through the material. Figure 4 presents the diffusivity values for each fiber orientation as a function of fiber fraction.

Thermal diffusivity decreases as the fiber angle relative to the laser pulse increases. This trend is illustrated in Fig. 5. As the orientation angle approaches 90 deg, the diffusivity approaches the matrix diffusivity. For the low-fiber fraction of 1.3 percent, the decreasing slope is gentle; fiber orientation does not greatly affect diffusivity at this fiber fraction. For the higher fiber fraction of 23 percent, however, diffusivity is dramatically affected by fiber orientation.

Off-axis data can be used to verify the results of on-axis testing. From [9], the heat flux equation can be expressed in the form

$$\begin{Bmatrix} -Q_i \\ -Q_j \\ -Q_k \end{Bmatrix} = \begin{bmatrix} k_{ii} & k_{ij} & k_{ik} \\ k_{ji} & k_{jj} & k_{jk} \\ k_{ki} & k_{kj} & k_{kk} \end{bmatrix} \begin{Bmatrix} dT/di \\ dT/dj \\ dT/dk \end{Bmatrix} \tag{5}$$

For orthotropic materials, where i, j, and k are the principal axes, equation (5) reduces to

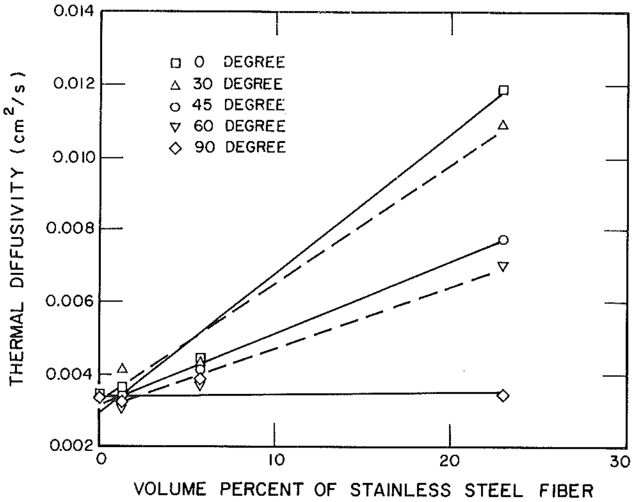

Fig. 4 Thermal diffusivity as a function of fiber fraction and fiber orientation for SS/epoxy

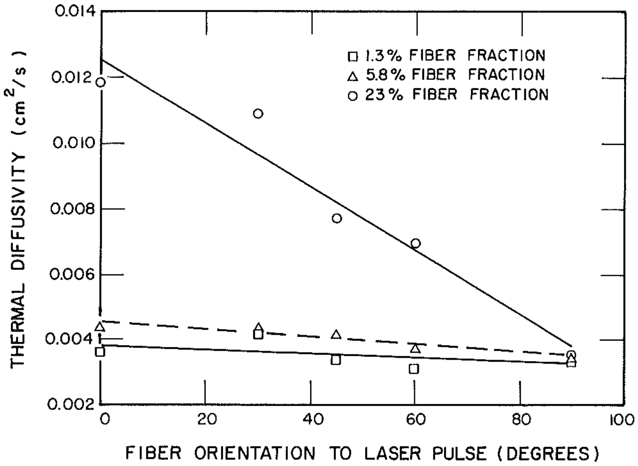

Fig. 5 Thermal diffusivity as a function of fiber orientation for SS/epoxy

$$\begin{Bmatrix} -Q_i \\ -Q_j \\ -Q_k \end{Bmatrix} = \begin{bmatrix} k_{ii} & 0 & 0 \\ 0 & k_{jj} & 0 \\ 0 & 0 & k_{kk} \end{bmatrix} \begin{Bmatrix} dT/di \\ dT/dj \\ dT/dk \end{Bmatrix} \tag{6}$$

From on-axis testing, the principal conductivities k_{ii}, k_{jj}, and k_{kk} can be derived from their respective diffusivity values using the definition of thermal diffusivity

$$\alpha_{nn} = \frac{k_{nn}}{c\rho} \tag{7}$$

Off-axis conductivity values can be obtained from the on-axis values using the directional cosines. In the off-axis direction n, the conductivity is

$$k_{nn} = 1_{ni}{}^2 k_i + 1_{nj}{}^2 k_j + 1_{nk}{}^2 k_k \tag{8}$$

where 1_{ni} is the cosine of the angle between between the n and i vectors, etc.

For the two-dimensional case, where n is in the plane normal to the k axis, equation (8) can be written

$$k_{nn} = \cos^2 \theta_{ni} k_i + \cos^2 \theta_{nj} k_j \tag{9}$$

or

$$k_{nn} = \cos^2 \theta_{ni}(k_i - k_j) + k_j \tag{10}$$

Figure 6 presents the geometrical and experimental diffusivity values versus fiber fraction. The geometrical conductivities increase at approximately the same rate as the

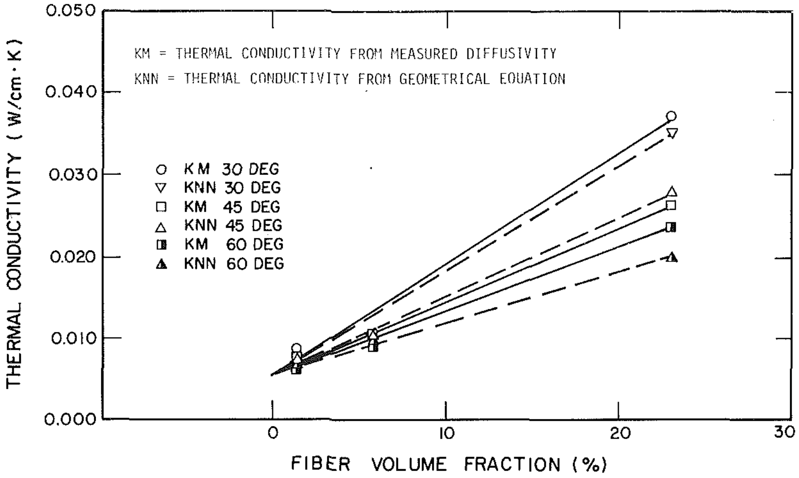

Fig. 6 Measured versus geometric conductivity as a function of fiber fraction for SS/epoxy

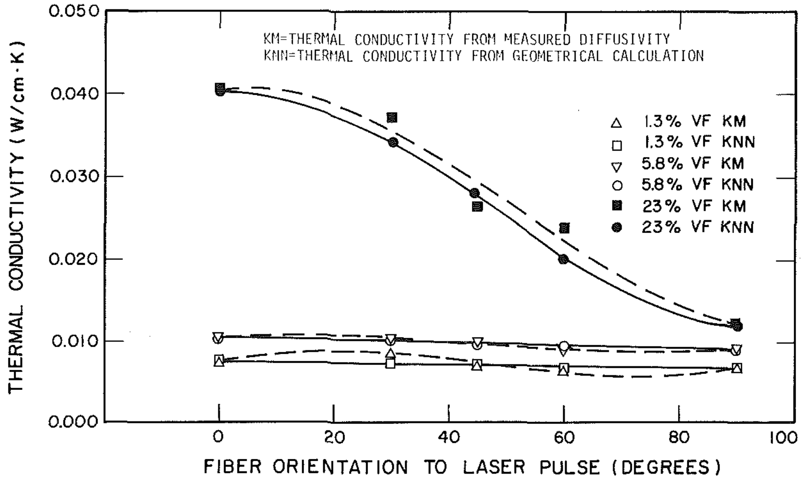

Fig. 7 Measured versus geometric conductivity as a function of fiber orientation for SS/epoxy

experimental values, with increasing fiber fraction. The 45 deg fiber orientation represents the closest agreement between experimental and theoretical conductivities. The 60 deg orientation represents the worst agreement, possibly attributable to the increased dominance of the matrix and the correspondingly low diffusivity values.

The conductivities are clearly a function of fiber orientation for high fiber fractions. Figure 7 shows that as the angle increases, the thermal conductivity decreases. The linear trend is sharp for the 23 percent V_f samples and relatively flat for the 1.3 percent V_f samples. There is good agreement between the experimental and the geometrical conductivities.

The SS/Cerrocast samples, having a fiber-matrix conductivity ratio of 0.5, behaved in a near-homogeneous fashion, as expected. Some samples exhibited early time uncoupled behavior, probably due to interface microvoids or debonding. Of the three off-axis orientations (30, 45, 60 deg), the samples cut at 45 deg to the fiber exhibited the least deviation from the theoretical curve.

The diffusivities decreased linearly for increasing fiber fraction. As shown in Fig. 8, fiber orientation has little influence upon the diffusivity of this composite. The controlling factor appears to be the fiber fraction.

Copper/epoxy samples, having a fiber/matrix conductivity ratio of 1000, were tested using the flash technique. The thermal rise curves exhibited a sharp spike and early rise followed by a smooth curve. This behavior suggests severe uncoupling between the copper fiber and the matrix. An attempt was made to separate the two curves but for this sample length, the heat transfer through the copper fiber was too fast for the data acquisition system to collect the necessary number of data points. This occurrence is not unusual for thin samples, particularly for very conductive materials. A much thicker sample cannot be used because very thick samples, e.g., 1-6 in. in length, have heat losses from their radial surfaces exceeding the limits of correction methods applicable to the laser flash method.

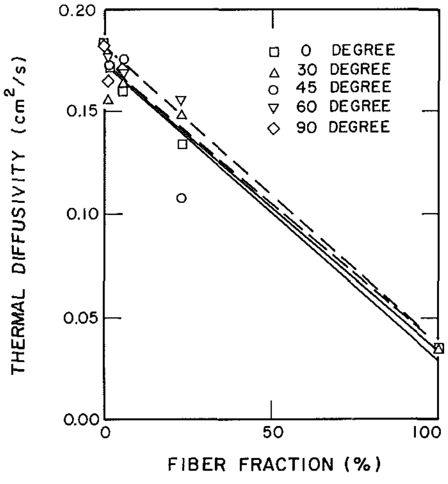

Fig. 8 Thermal diffusivity of SS/Cerrocast as a function of fiber fraction

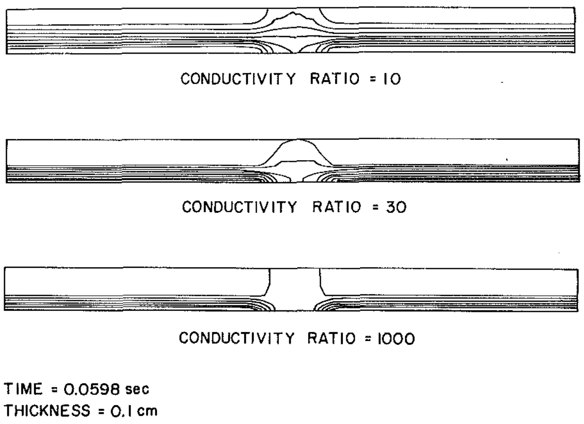

Fig. 9 Isotherms illustrating heat flow in a sample containing a single fiber at the center

Since the thermal rise curves for copper/epoxy displayed severe uncoupling, the associated thermal diffusivity values are meaningless. Therefore the conductivity ratio of 1000 far exceeds the measurable limits of thermal diffusivity for coarse fiber composites of this sample length.

A two-dimensional finite element program was used to model heat flow through heterogeneous composites. Although a three-dimensional analysis would more accurately describe the thermal response of axisymmetric fibers in a rectangular grid, this program is sufficient for showing the influence of specimen length and of conductivity ratio upon thermal diffusivity.

An axisymmetric cell having a centered fiber was used. The fibers were taken to be arranged in a rectangular array, similar to the experimental specimens. Adiabatic boundary conditions were assumed.

Isotherms illustrate the interface gradient and the contrast between outer and inner nodes. Figure 9 presents the heat wave patterns for three conductivity ratios in a sample containing a single fiber at its center. The gradient for the conductivity ratio of 10 is mild compared to the sample having a conductivity ratio of 30. The degree of fiber-matrix homogenization is related to the slope of the gradient. The steeper the gradient, the greater the degree of uncoupling.

For thin samples, heat rapidly propagates through the fiber, causing a steep temperature gradient at the interface. For longer samples, the gradients are less steep, indicating greater heat transfer across the interface. In a sense, the thicker sample can be considered more homogeneous than the thin sample. Indeed, Jortner [10] suggested that for parts much thicker than the high gradient surface layer, the material may be considered homogeneous. However, the heterogeneity of the thermal skin must be considered for high rates of heat transfer in thin samples or across the thermal skin.

Conclusions

The behavior of the thermal rise curves and the computed diffusivity values were useful indicators of the degree of homogeneity assumed by each test specimen. Specimens in which the constituents appeared to act independently were described as uncoupled. Specimens that exhibited behavior approaching the theoretical model were judged near-homogeneous.

The fiber/matrix conductivity ratio is the major factor governing the thermal behavior of the composite. Ratios above about 100 will result in uncoupled phenomena. For ratios below 100, it may be possible to obtain only modest deviations from ideal behavior by controlling sample size and fiber orientation. Modest deviations do not prohibit application of the concept of apparent diffusivity. As the conductivity ratio approaches one, the behavior approaches that of a homogeneous material.

The fiber fraction percentage is the second most controlling parameter of thermal behavior. Thermal diffusivity is a linear function of fiber fraction. It approaches the fiber diffusivity as the fiber fraction increases. For low fiber fractions, it approaches the matrix diffusivity.

Specimen length is a factor which can modify the behavior of any composite, given a fixed conductivity ratio and constant fiber fraction. As the length increases, the specimen approaches homogeneity. As the length decreases, uncoupling may result. For high conductivity ratios, however, the length required to assume homogeneous behavior is generally impractical.

The experimental approach of off-axis testing has been shown to correlate well with geometrical calculations using on-axis diffusivities. Of the conductivity ratios studied, the correlation was most useful for the ratio of 25. For the low conductivity ratio of 0.5, orientation does not significantly affect thermal diffusivity calculations. Off-axis samples oriented at 45 deg exhibited the least uncoupling. The 30 and 60 deg orientations offered no advantage over the on-axis analysis.

Although this research was limited to unidirectionally reinforced materials, the results can be extended to two-dimensional and three-dimensional-reinforced composites. It was shown that fibers oriented 90 deg to the flux direction do not greatly influence the thermal behavior. For on-axis testing of two-dimensional and three-dimensional-reinforced composites, therefore, only the fibers in the flux direction will have a noticeable affect. Fibers perpendicular to the flux will be homogenized with the matrix and uncoupling will not be a dominating factor.

For off-axis testing of two-dimensional and three-dimensional-reinforced composites, a 45 deg orientation of two of the axes to the laser pulse is expected to give the best results. This orientation was the most beneficial for the unidirectional case, so it is likely that the symmetry afforded by the 45 deg cut will aid homogenization within two-dimensional and three-dimensional-reinforced composites.

Acknowledgments

This work was performed under Grant No. MEA-8204070 for the National Science Foundation. The support of NSF and of Dr. Win Aung, in particular, are gratefully acknowledged.

References

1 Taylor, R. E., "Thermal Diffusivity of Composites," VIII Europ. Conf. on Thermophysical Properties, Baden-Baden (RFA), Sept. 1982.

2 Luc, A. M., and Balageas, D. L., "Thermal Behavior of Directional Reinforced Composites Subjected to Pulse Heat Fluxes," VIII Europ. Conf. on Thermophysical Properties, Baden-Baden (RFA), Sept. 1982.

3 Agarwal, B. D., and Broutman, L. J., *Analysis and Performance of Fiber Composites*, Wiley, New York, 1980.

4 Powers, A. E., "Conductivity in Aggregates," Report No. KAPL-2145, G.E. Company, Knolls Atomic Power Lab., 1961.

5 Taylor, R. E., Jortner, J., and Groot, H., "Thermal Diffusion in Carbon/Carbon Composites," AFOSR-TR-82-0959 (ADA121491), June 1982.

6 Parker, W. J., Jenkins, R. J., Butler, C. P., and Abbott, G. L., "Flash Method of Determining Thermal Diffusivity, Heat Capacity and Thermal Conductivity," *Journal of Applied Physics*, Vol. 32, No. 9, 1961, pp. 1679–1684.

7 Clark, L. M., and Taylor, R. E., *Journal of Applied Physics*, Vol. 46, No. 2, 1975, pp. 714–719.

8 Kelsic, B. H., "A Study of Heat Transfer in Unidirectional Fiber-reinforced Composites," M.S. Thesis, Purdue University, Aug. 1984.

9 Carslaw, H. S, and Jaeger, J. C., *Conduction of Heat in Solids*, 2nd ed., Oxford University Press, 1959.

10 Jortner, J., and Taylor, R. E., "Off Axis Thermal Diffusivity Testing of 3D Carbon-Carbon Composites," presented at 4th Carbon-Carbon Nozzle Technology Meeting, Monterey CA, Oct. 1982.

11 Desphande, M. S., "On the Interpretation of Off-Axis Thermal Diffusivity Data for Coarse-Weave Composites," *Thermal Conductivity 18*, T. Ashworth and D. R. Smith, eds., Plenum Press, New York, 1985, pp. 625–637.

The Melting Process of Ice Inside a Horizontal Cylinder: Effects of Density Anomaly

H. Rieger[1]

H. Beer

Institut für Technische Thermodynamik,
Technische Hochschule,
6100 Darmstadt,
Federal Republic of Germany

In the present investigation heat transfer during melting of ice confined within a heated, horizontal cylinder is studied experimentally and by analysis. Because of the well-known density inversion effect of water in the proximity of the melting point of ice the first-order influence of convection flow for phase change processes becomes obvious. Depending on the inner diameter of the cylinder and on the specific temperature value $T_w > 0°$ *of the cylinder wall, quite different shapes of the melting ice body, the flow pattern, and the temperature field were predicted by numerical analysis. Also provided are local and overall heat transfer coefficients, revealing a reasonable agreement between experiments and predicted data. Computations were performed for wall temperatures in the range* $4°C \leq T_W \leq 15°C$ *and two inner diameters of the cylinder.*

Introduction

In the past, heat transfer during liquid–solid or solid–liquid phase change processes of materials with nearly constant thermophysical properties in its fluid phases has been studied theoretically and by experiments for various geometric configurations, physical parameters, and boundary conditions. The work recently done in this field was originally motivated by the need for design aids and prediction tools for thermal control systems in satellites and spacecraft structures utilizing the advantages of latent heat-of-fusion energy conversion. Nevertheless there are many other technical areas, such as casting technology, nuclear power safety analysis, the fast-widening discipline of crystal growth as well as the economic design of latent heat-of-fusion energy storage systems, where the understanding of the hydro- and thermodynamic phenomena during solid–liquid phase change is of considerable importance.

Mathematically the given problem can be identified as a moving boundary problem, because the size and shape of the fluid region (melt) alters as the melting or solidification process advances with time. Immediately after a short initial period the prevailing influence of natural convection flow on heat transport becomes obvious, leading to a further increase of complexity in the mathematical treatment. So it appears impossible to find closed-form analytical solutions to such problems for relevant physical parameters and boundary conditions. Because semi-analytical approaches like series solutions, based on perturbation methods, are strongly limited to situations in which heat conduction is the dominant mode [1], direct numerical methods have to be applied to obtain reliable predictions of complex phase change processes.

Finite-difference solutions to the melting problem around a vertical tube, including the effect of natural convection, were first presented by Sparrow et al. [2], who neglected some terms in the governing set of equations. In contrast numerical solutions to the solidification problem around a horizontal cylinder, based on the full equation set, were obtained by Saitoh and Hirose [3]. Like Sparrow et al. [2], they used a functional transformation technique (Landau transformation) for immobilization of the moving solid–liquid interface. Therefore all computations can be done in a computational domain fixed in time and space. Singularity problems, however, may be encountered as the melt front traverses the origin of the chosen coordinate system.

To circumvent problems associated with the moving interface, Rieger et al. [4] introduced numerically generated coordinate systems fitted to the shape of the boundaries in order to study the melting process around a horizontal cylinder. Although more laborious, the resulting scheme seems to be the more flexible approach. Recently the results gained in [4] were excellently confirmed by computations of Prusa and Yao [5], who applied a simple radial transformation based on a polar-coordinate system to obtain a body-fitted coordinate system.

For the melting problem of a phase change material enclosed in a horizontal cylinder, several numerical studies are available [6, 7]. Most of the works cited deal with phase change materials for which the assumption of constant thermophysical properties may be justified as conceptual simplification in the framework of numerical analysis.

The present study will focus attention on the striking influence of natural convection flow on heat transfer and resulting interface shapes with the ice–water system. The observed phenomena are mainly due to the nonlinear relationship between density and temperature in the vicinity of the melting point of ice, known as density anomaly. These peculiarities in the physical behavior of water in conjunction with the specific aspects concerning heat transfer in the past have motivated many studies of thermally driven flows in water at temperatures near the maximum density point. Up to now, only Saitoh and Hirose [3] have tackled the problem of solidification of ice around a horizontal cylinder, taking into account the moving interface. The reverse problem of ice melting inside a cylinder for a particular case was mentioned by the same authors in [7]. In light of these results it seems appropriate to investigate the melting process of ice enclosed in a horizontal cylinder in more detail.

The schematic diagram of the problem under study is depicted in Fig. 1. It shows the heated horizontal cylinder with inner radius R_0 whose wall is kept at constant temperature. The shape of the partially melted ice body will be a function of angular position φ and time t and described by the relation $r = r(\varphi, t)$. As an essential condition for problem definition it is assumed that the melting solid remains stationary during the phase change process. In fact such a configuration, where the frozen PCM is fixed by inner tubes, has been proposed for possible application as a solar energy storage system [8]. The physical situation considered will also occur in double-tube heat exchangers designed as latent heat storage systems, when the inner tube is out of operation. In the experiment an un-

---

[1] Present address: Dornier GmbH, BF 30, 7990 Friedrichshafen 1, FRG

Contributed by the Heat Transfer Division and presented at the ASME 22nd National Heat Transfer Conference, Niagara Falls, New York, August 1984. Manuscript received by the Heat Transfer Division October 29, 1984. Paper No. 84-HT-10.

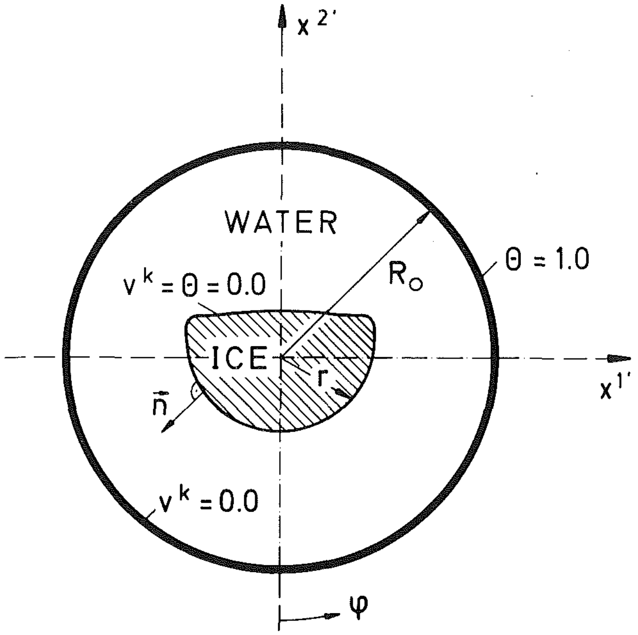

Fig. 1 Schematic representation of the physical model with boundary conditions (solid material fixed at the center)

controlled movement due to gravitational forces is prevented by fixing the ice body near its center. A detailed description of the experimental setup and the specific procedures necessary with the ice–water system may be found in [9].

Analysis

Because generality was the objective of the code developed, the grid generation technique, proposed by Thompson et al. [10], was applied to analyze the moving boundary problem. In this technique body-fitted curvilinear coordinate systems are obtained as solutions of coupled quasilinear elliptic, partial differential equations. An excellent survey of the methods available was quite recently given by Thompson [11].

Nevertheless the conservation equations for mass, momentum, and energy, govering the problem under study, have to be formulated necessarily for a general Euclidean reference frame. Because tensor analysis will allow for the discussion of coordinate invariant quantities the description will be expressed concisely in tensor notation, as used in, e.g., [12].

To simplify analysis some principal assumptions concerning the mathematical model should be introduced: For studies of natural convection flow, it is convenient to consider water as an incompressible Newtonian fluid with constant thermophysical properties except the density, for which the validity of the Boussinesq approximation is adopted. Restricting the mathematical model to laminar and planar flow the governing set of equations may be reduced further by substituting the primitive variables (velocity and pressure) by stream function ψ and vorticity ω as new dependent variables.

The general differential form for conservation laws, valid in an unsteady coordinate system $x^i = x^i(x^{j'}, t)$ may be written as [13]

$$\frac{1}{\sqrt{g}} \frac{\partial}{\partial t} (\sqrt{g} A) + \nabla \cdot [A(\mathbf{v} + \mathbf{w}) + B] = C \tag{1}$$

Here A represents the quantity to be preserved, C a source term, B the corresponding diffusive flux and $\sqrt{g}$ the Jacobian of transformation. By specifying appropriate expressions for the quantities A, B, and C the nondimensional form of the governing equations in vorticity-stream function formulation can be derived, as shown in more detail in [9].

Nondimensional Governing Equations. By defining the following dimensionless variables and groups, the number of parameters will be reduced

$$\begin{aligned} &(x^{i'})^* = (x^{i'})/R_0 \qquad (i' = 1, 2) \\ &\psi^* = \psi/a, \ \omega^* = (\omega R_0^2)/a \\ &\theta = (T - T_i)/(T_w - T_i), \ \mathrm{Fo} = at/R_0^2 \\ &\mathrm{Ste} = \frac{c_p(T_c - T_i)}{h_f}, \ \tau = \mathrm{Fo} \cdot \mathrm{Ste} \\ &\mathrm{Pr} = \nu/a \end{aligned} \tag{2}$$

Asterisks denote dimensionless quantities, which have been omitted in the nondimensional form of the governing equations given below.

Nomenclature

a = thermal diffusivity = $k/c\rho_0$
$b_i, \tilde{b}_i$ = coefficients, equations (7), (8)
c = specific heat
A, B, C = dummy variables
e_{ijk} = permutation symbol = 1 if ijk cyclic; = -1 if ijk anticyclic; = 0 otherwise
Fo = Fourier number = $at/R_0{}^2$
g^{ij}, g_{ij} = contra- and covariant components of metric tensor
g = determinant of metric tensor = $(g_{11}g_{22} - g_{12}g_{21})$ 2-dim.
$\tilde{g}$ = acceleration of gravity
$g^{1/2}$ = Jacobian of transformation
h_f = heat of fusion
m = mass
$\mathbf{n}$ = normal unit vector
Nu = Nusselt number
Pr = Prandtl number = ν/a
$\tilde{\mathrm{Ra}}$ = expression defined as $\tilde{g}R_0{}^3(T_w - T_i)/(\nu a)$
r = distance from center of cylinder to solid–liquid interface
p^i = source function, equation (12)
R_0 = inner radius of cylinder
$\tilde{s}$ = function, equation (8)
Ste = Stefan number = $c(T_w - T_i)/h_f$
t = time
T = temperature
$\mathbf{v}$ = fluid velocity vector
$\mathbf{w}$ = grid velocity vector
$x^{i'}$ = Cartesian reference frame, $(x^{1'}, x^{2'}) \equiv (x, y)$
x^i = curvilinear coordinate system, $(x^1, x^2) \equiv (\xi, \eta)$
$\beta_j^{i'}$ = hybrid tensors = $\partial x^{i'}/\partial x^j$
Γ_{ij}^k = Christoffel symbol of second kind = $\beta_{m'}^k \cdot (\beta_i^{m'})_{,j}$
θ = dimensionless temperature = $(T - T_i)/(T_w - T_i)$
λ = thermal conductivity
ρ = density
ν = kinematic viscosity
ξ, η = coordinate directions
τ = dimensionless time, Fo•Ste
φ = angle of perimeter
$\tilde{\phi}$ = scalar field
ψ, ψ = velocity potential, stream function
ω, ω = vorticity vector, vorticity
∇ = nabla operator = $(\mathbf{g}^i, \partial_i)$
∇^2 = Laplace operator = $\nabla \cdot \nabla$

Subscripts and Superscripts

c = cylinder
f = fusion
i = ice
l = liquid
r_0 = reference state
s = solid
w = wall
* = dimensionless quantity
$\bar{}$ = mean value

$$\mathrm{Ste}\ \omega_{,\tau} + w^i \omega_{,i} + \frac{e^{ij3}}{\sqrt{g}} (\psi_{,j}\omega)_{,i} - \Pr(g^{ij}\omega_{,ji} - \omega_{,k} g^{ij}\Gamma^k_{ij})$$

$$- \tilde{\mathrm{R}}\mathrm{a}\ \Pr \frac{e^{ij3}}{\sqrt{g}} \tilde{s}_{,i} \tilde{\phi}_{,k'} \beta_j^{k'} = 0 \quad (3)$$

$$\omega + (g^{ij}\psi_{,ji} - \psi_{,k} g^{ij}\Gamma^k_{ij}) = 0 \quad (4)$$

$$\mathrm{Ste}\ \theta_{,\tau} + w^i \theta_{,i} + \frac{e^{ij3}}{\sqrt{g}} (\psi_{,j}\theta)_{,i} - (g^{ij}\theta_{,ji} - \theta_{,k} g^{ij}\Gamma^k_{ij}) = 0 \quad (5)$$

with

$$w^i + \mathrm{Ste}\, x^{k'}_{,\tau} \beta^i_{k'} = 0 \quad (6)$$

It should be noted that in (3) $\tilde{s}$ is given by (8) and $\tilde{\phi}$ has the particular derivatives $(\tilde{\phi}_{,1'}, \tilde{\phi}_{,2'}) \equiv (0, 1)$.

Density–Temperature Relationship of Water. To describe the nonlinear function between density and temperature for water in the range $0 \leq T \leq 20°\mathrm{C}$, the well-known relation given by Fujii [14] is used

$$\frac{\rho - \rho_r}{\rho} = - \sum_{i=1}^{4} b_i T^i \quad (7)$$

Introducing the dimensionless temperature $\theta = (T - T_i)/(T_w - T_i) = (T - T_i)/\Delta T$, where T_i stands for the fusion temperature of ice ($T_i = T_0$) and T_w for the wall temperature of the cylinder, one gets

$$\frac{\rho - \rho_0}{\rho} = - \Delta T \sum_{i=1}^{4} \tilde{b}_i \theta^i = - \Delta T\, \tilde{s}(\theta) \quad (8)$$

Appropriate expressions for the coefficients $\tilde{b}_i$ may be found, e.g., in [15]. It should be noted that Fujii's values for the constants b_i and the derived forms $\tilde{b}_i$ provide one of the most accurate representations of density as function of temperature in the range mentioned. The density values computed from (7) agree with the tabulated data of Landolt–Börnstein [16] to within five digits.

Boundary and Initial Conditions. Under the assumption that phase change will definitely take place at the fusion temperature $T = T_f = T_i$, and therefore solid and fluid phase are separated by an isothermal interface, an energy balance at the solid–liquid interface leads to

$$\frac{\lambda_s}{\lambda_l} (g^{(ii)} \theta_{,j})_{\mathrm{solid}} - (g^{(jj)} \theta_{,j})_{\mathrm{liquid}} = \left(\frac{\rho_s}{\rho_l}\right) \beta^j_{i'} x^{i'}_{,\tau} \quad (9)$$

$$(\text{for } x^j = \text{const})$$

where the fact of an isothermal interface has been used for simplification. In (9) it is assumed that a coordinate line x^j = const constitutes the bounding interface.

Besides this interface condition, the boundary conditions at the cylinder wall, at the melt front as well as at the symmetric line, have to be specified. Almost all computations were performed with the assumption of a symmetric melting process due to the vertical axis, which saves, to a great extent, computer time and costs.

For $\tau > 0$:

$\theta = 1;\ \psi = 0;\ \omega = -g^{(ii)} \psi_{,ii}$ at the cylinder wall $(x^i = \text{const})$ (10a)

$\theta = 0;\ \psi = 0;\ \omega = -g^{(ii)} \psi_{,ii}$ at the interface $(x^i = \text{const})$ (10b)

$g^{jk} \theta_{,k} = 0;\ \psi = 0;\ \omega = 0$ at the symmetric line $(x^j = \text{const}, j \neq i)$ (10c)

The kinematic no-slip condition (10b) at the solid–liquid interface is required on the assumption of constant density during phase change. So in effect $\rho_l/\rho_s = 1$ was used in the interface condition (9). As mentioned above, the equation set (3–5) has a singularity at $\tau = 0$, which can be overcome by introducing a similarity transformation as proposed by Prusa and Yao [5]. Another way to circumvent this problem is to start the computations with data taken from an approximate integral solution of the corresponding conduction problem, which is given by, e.g., [17]

$$\tau = \frac{1}{4} (1 + \mathrm{Ste}/2)[1 - r_i^2 (1 - 2 \ln r_i)] \quad (11)$$

Although based on quasi-steady assumptions, equation (11) will be accurate to within 2 percent, when compared to the corresponding solution, presented in [5]. One has to remember, however, that this error will fade away and appears only in the very first moments of the computations, where convection is not present. The above stated error margin should be related to an initial annular gap of 6 percent width (based on R_0) and the parameter range under study.

Generation of Coordinate System. Applying the finite-difference method for problems with a complex shape of the solution domain, it must be ensured that the underlying coordinate system has sufficient smoothness properties, so that possible mesh spacing ratios and the corresponding rates of change will not cause strong false-diffusion effects. Elliptic differential operators exhibit the expected property to smooth out those discontinuities rapidly. This is one of the reasons why curvilinear coordinate systems, numerically generated as solutions of an elliptic boundary-value problem, fit so closely together when coupled to schemes based on the finite-difference method.

As proposed by Thompson [9], the generating equation set in the fixed computational plane is given by

$$g^{jk} (\beta_j^{l'})_{,k} + \beta_i^{l'} p^i = 0 \quad (12)$$

With the Cartesian coordinates as dependent variables equation (12) constitutes a set of coupled quasi-linear elliptic partial differential equations, which may be solved by providing the Dirichlet data $x^{l'} = x^{l'}(x^k)$ on the boundaries.

The possibility to influence the properties of the grid in a desired manner is given by supplying appropriate source functions p^i to the generating set (12). The approach proposed by Middlecoff and Thomas [18] was found to give a workable method.

Numerical Procedure. As pointed out, the governing set of equations for the moving boundary problem under study consists of the equations (3–5) and (12), which yield in two dimensions five coupled, nonlinear partial differential equations. By applying the finite-difference method, all terms involved, including the convection terms, are discretized by second-order central finite difference operators in space and second-order backward difference approximations in time. This results in a totally implicit procedure.

It should be noted that a more involved analysis, subject to moving boundary problems and a detailed description of the numerical procedures considered, may be found in [15]. There also effective schemes, driven by multigrid procedures [19] and based on the primitive variables, are developed for use in general curvilinear coordinate systems.

Results and Discussion

Numerical solutions to the melting problem of ice inside a horizontal cylinder have been obtained for wall temperatures T_w = 4, 6, 8, 10, 15°C and two cylinder radii R_0 = 16 and 32 mm. Experiments, performed for verification of the theoretical predictions, are characterized by the parameters T_w = 6, 8.5, 10, 15°C and an inner tube radius R_0 = 30 mm. Due to the limited extent of this paper the presentation of the results has to be restricted to the reproduction of solutions for

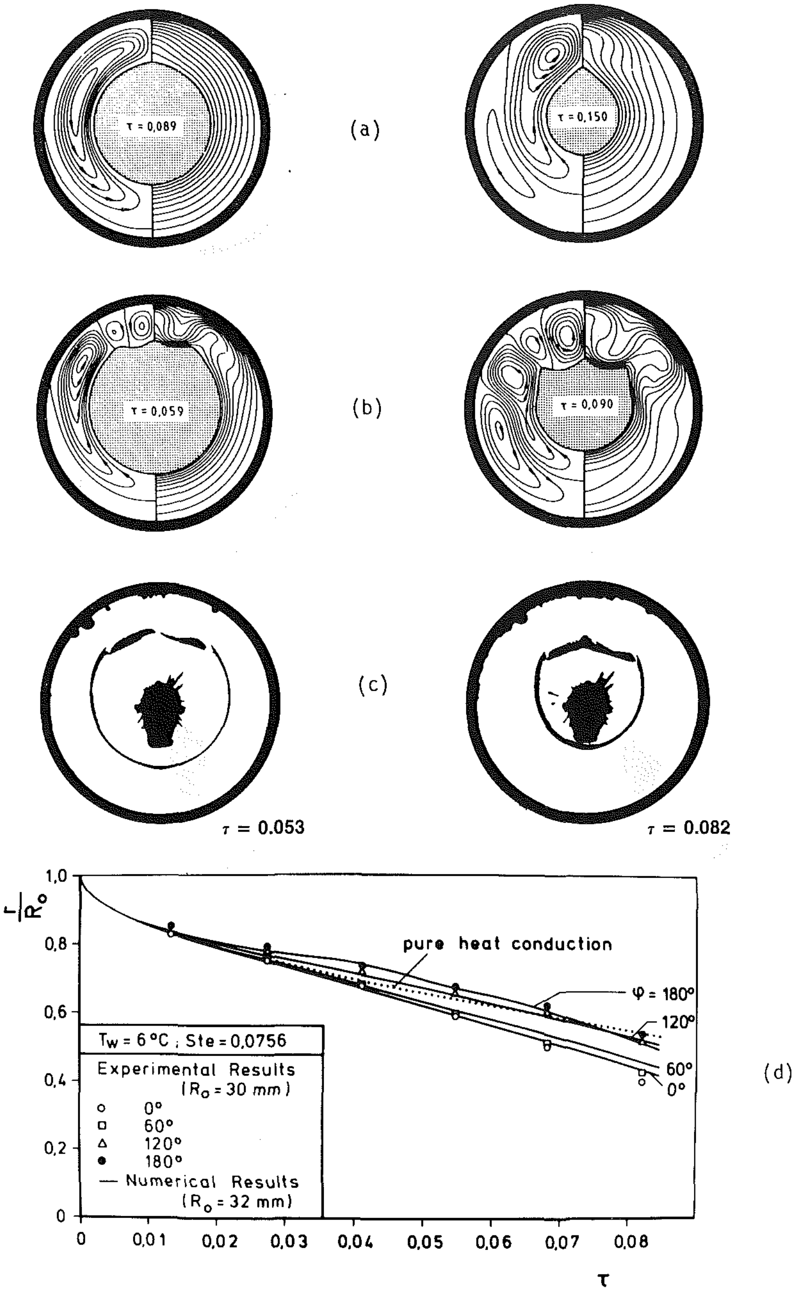

Fig. 2 Numerical and experimental melt front contours, isotherms (right) and stream function (left) for a wall temperature T_w = 6°C at different dimensionless times τ: (*a*) R_0 = 16 mm, (*b*) R_0 = 32 mm, (*c*) experimental melt front contours (T_w = 6°C, R_0 = 30 mm), (*d*) local interface positions for different angles of perimeter φ as a function of dimensionless time τ

only two distinct time stages for each parameter set. More details may be found in [15].

In Fig. 2 the numerical predictions as well as photographs from the experiment for two time stages and $T_w = 6°\mathrm{C}$ are presented. Also provided are the interface positions as function of the dimensionless time τ for various angles of perimeter φ. Due to the specific temperature dependence of density in the range $0°\mathrm{C} \leqq T \leqq 4°\mathrm{C}$ the developing flow will be different from that in "normal" fluids. For $T_w = 6°\mathrm{C}$ the density will be higher at the wall leading to a downward-directed flow and vice versa at the interface. Quite similar to the case $T_w = 4°\mathrm{C}$, which is not depicted here, the phase change process for $T_w = 6°\mathrm{C}$ and $R_0 = 32$ mm is characterized by the onset of a thermal instability in the top region of the gap, so that in the final stages of the process four roll cells govern the heat transport to the melting ice body. An impression of the evolution process may be gained from the experiment (Fig. 2*c*). In an early stage the cylindrical ice body will level off at the top and a wavy surface in the axial direction will be observed during the test run, indicating a three-dimensional flow in that region. In the photographs this fact is elucidated by the broadened interface contours, which are caused by multireflections of light at the elevations of the ice body. So an integrated state is shown, which is in close agreement with the computed solutions. Quite similar findings were reported about the melting process of an ice cylinder inside a large tank [20], where boundary effects surely could be neglected.

A direct comparison between prediction and experiment is depicted in Fig. 2(*d*), which supports the visual impressions

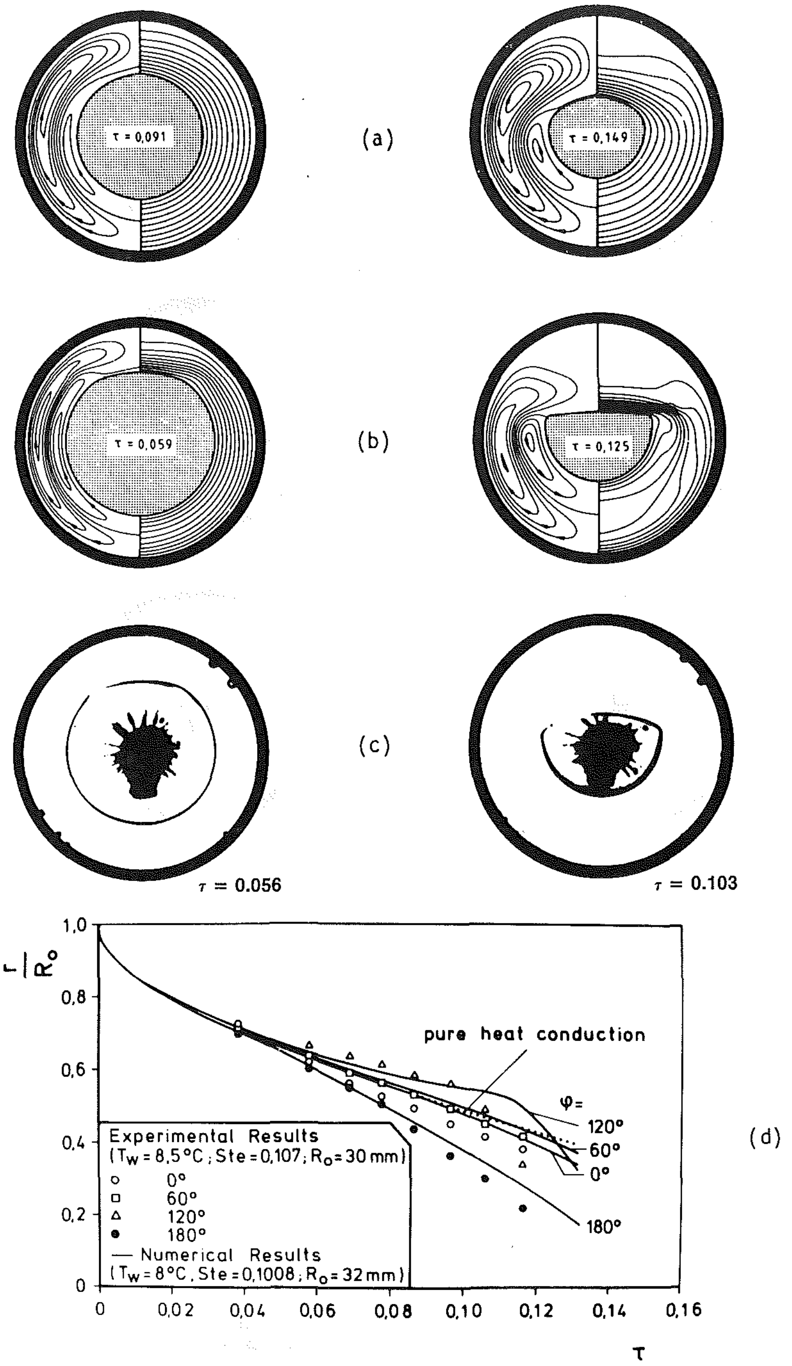

Fig. 3 Numerical and experimental melt front contours, isotherms (right) and stream function (left) for a wall temperature T_W = 8°C at different dimensionless times τ: (*a*) R_0 = 16 mm, (*b*) R_0 = 32 mm, (*c*) experimental melt front contours (T_W = 8.5°C, R_0 = 30 mm), (*d*) local interface positions for different angles of perimeter φ as a function of dimensionless time τ

obtained. For angles $\varphi \leq 60$ deg the experiment reveals somewhat larger interface velocities. This can be explained by the assumptions made in the mathematical model. No density changes during phase change have there been taken into account, slowing down the interface velocities in the numerical simulation. A quantitative estimate of this effect, however, is aggravated by the fact that the inner radii of the cylinder in experiment and computation are slightly different.

Nevertheless only small deviations between experimental and theoretical findings can be stated. A particular behavior must be expected for T_w = 8°C, because the density of water at the melting front and at the cylinder wall is approximately the same. Regarding Fig. 3, no additional roll cells above the ice body can be detected, indicating that for both radii no thermal instabilities will occur. This is probably due to the inner of the two primary eddies, which will damp out all perturbations growing up. The strength of this flow cell, however, is weakened throughout the process by the changing arc length proportions of the corresponding boundaries. So mainly the roll cell located at the wall side will determine the heat transfer to the melting ice body. For R_0 = 32 mm (Fig. 3*b*) a semicircular interface contour is predicted in the final stages of the process, which was confirmed by the corresponding experiment (Fig. 3*c*).

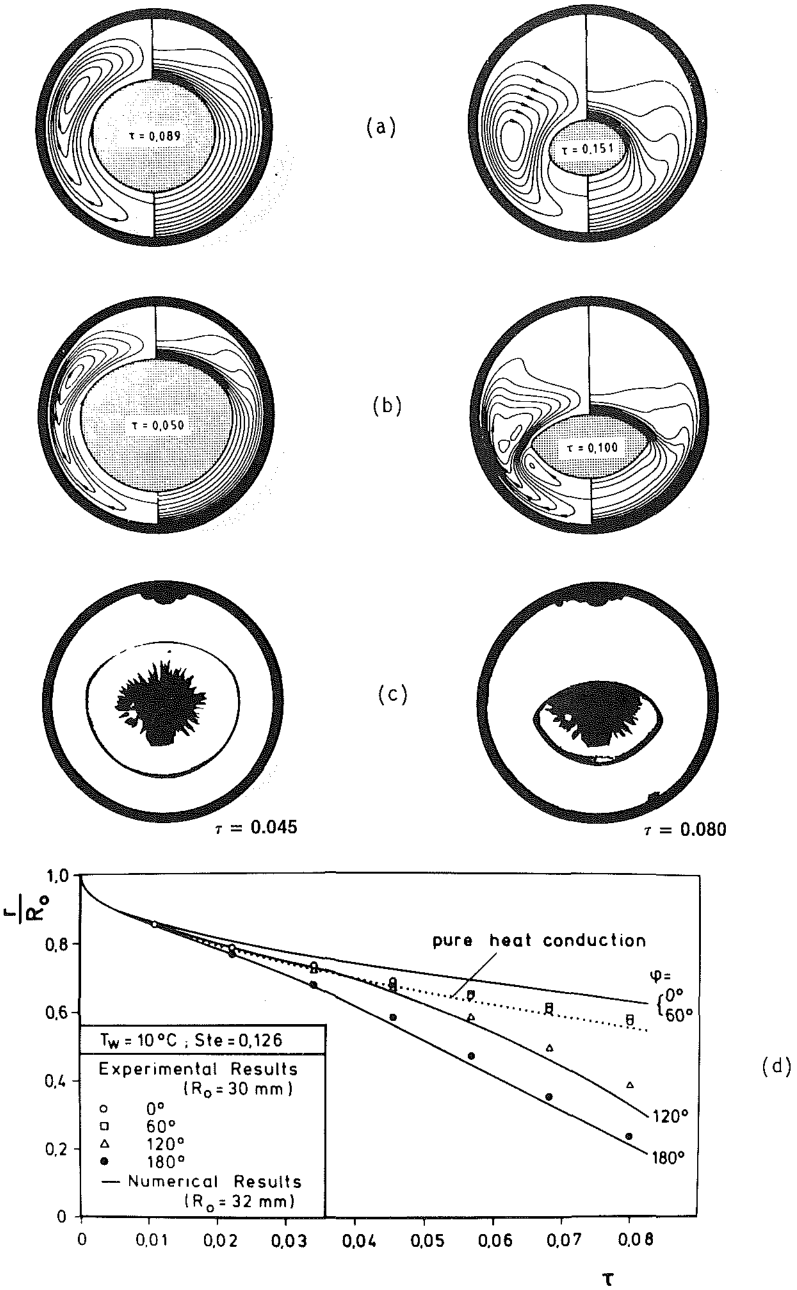

Fig. 4 **Numerical and experimental melt front contours, isotherms (right) and stream function (left) for a wall temperature T_W = 10°C at different dimensionless times τ: (*a*) R_0 = 16 mm, (*b*) R_0 = 32 mm, (*c*) experimental melt front contours (T_W = 10°C, R_0 = 30 mm), (*d*) local interface positions for different angles of perimeter φ as a function of dimensionless time τ**

For a direct comparison Fig. 3(*d*) displays the data of the local interface positions as a function of time. As for the case T_w = 6°C, the experimental results show a faster propagation speed of the melt front, which was explained earlier. The timewise behavior of numerical findings and experimental results, however, are basically the same.

From the density-temperature relationship of water it must be expected that the roll cell situated near the cylinder wall will increasingly influence heat transfer with rising wall temperatures. This trend can be recognized for the case T_w = 10°C in Fig. 4. Because of the growing strength of the roll cell, heat transport is improved considerably at the upper stagnation point of the ice body, which results in a more downward-directed movement of the solid. This fact can be derived from the temperature field (Fig. 4*b*), which shows strongly condensed isotherms at the upper interface. At the end of the melting process the ice body becomes extremely lens shaped for R_0 = 32 mm. A reasonable agreement with the experiments (Fig. 4*c*) can be stated.

Finally the case T_w = 15°C remains to be discussed (Fig. 5). It becomes obvious that the influence of density anomaly weakens considerably, but nevertheless still is present. A "streamlined" design of the melting solid was observed for "normal" fluids at smaller values of Ste and Ra. In contrast to this an almost circular shape of the ice body is produced at the end of the simulation for both radii at T_w = 15°C. The melting process for R_0 = 32 mm (Fig. 5*b*) shows a particular behavior. A thermal instability suddenly develops, leading to a secondary roll cell in the bottom region of the melting gap. Comparing the experimental observation (Fig. 5*c*) with the

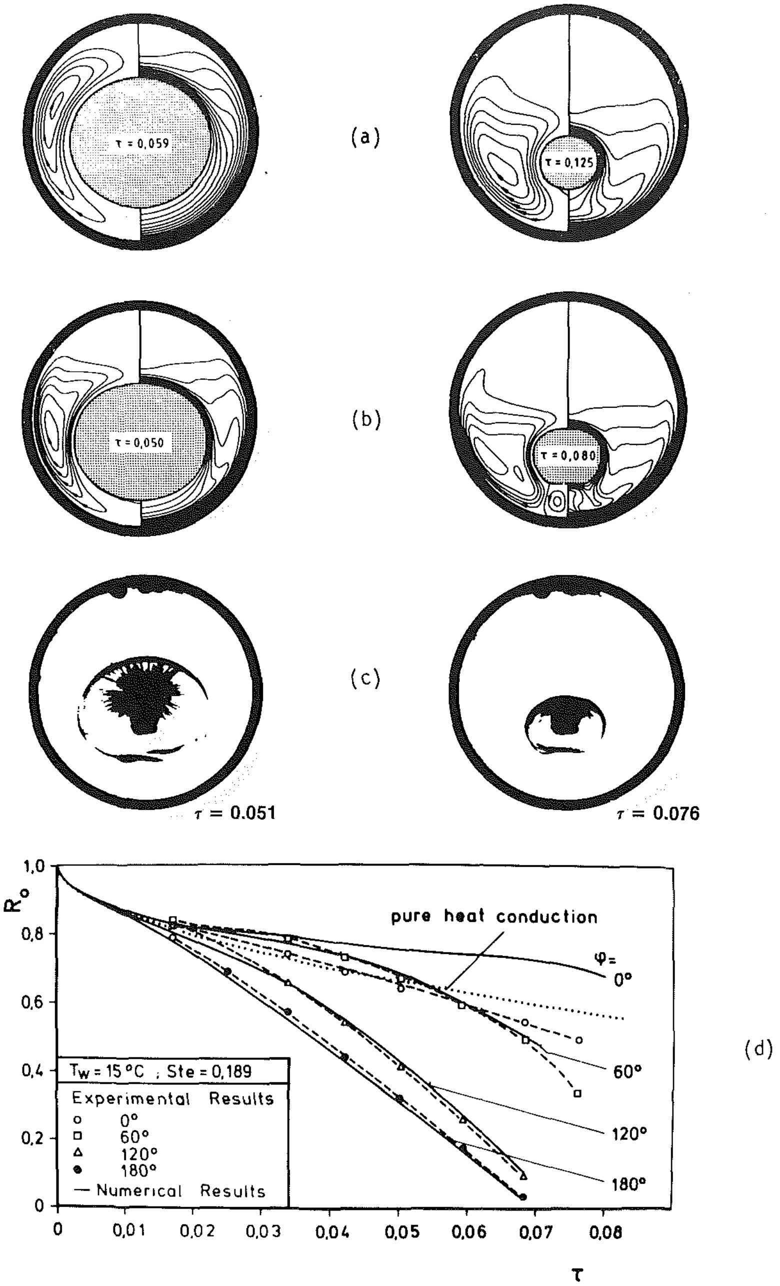

Fig. 5 Numerical and experimental melt front contours, isotherms (right) and stream function (left) for a wall temperature T_W = 15°C at different dimensionless times τ: (*a*) R_0 = 16 mm, (*b*) R_0 = 32 mm, (*c*) experimental melt front contours (T_W = 15°C, R_0 = 30 mm), (*d*) local interface positions for different angles of perimeter φ as a function of dimensionless time τ

predictions (Fig. 5*b*) some discrepancies appear at early stages of the melting process. In the experiment a three-dimensional fluid flow was observed, improving heat transfer in the lower part of the gap. This change of the flow characteristics cannot be realized correctly by the mathematical model. Looking at the local interface positions (Fig. 5*d*), however, a close agreement can be found for 60 deg $< \varphi <$ 180 deg.

The molten mass fraction m/m_0 as a function of the dimensionless time τ is depicted in Fig. 6 for all cases considered. For both radii the smallest melting rate is observed in the case T_w = 8°C, while the highest melting rate is obtained for T_w = 15°C. Different trends concerning heat exchange, however, can be found for the remaining two wall temperatures. So a quite similar graph results for T_w = 4°C and 10°C with the smaller tube radius R_0 = 16 mm. Considering R_0 = 32 mm, almost the same timewise behavior can be confirmed for T_w = 6°C and T_w = 10°C.

Figure 7 shows the overall heat transfer coefficient at the cylinder wall $\overline{\mathrm{Nu}}_c$ as a function of the dimensionless time τ. The overall heat transfer coefficient is defined as

$$\overline{\mathrm{Nu}}_c = -\frac{1}{\pi}\int_0^{\pi} (\mathbf{n}\cdot\nabla\theta)\, d\varphi \qquad (13)$$

In accordance with the results of Fig. 6, for R_0 = 16 mm and 4°C $\leqq T_w \leqq$ 15°C all curves show only minor deviations from heat transport governed by heat conduction. The occurrence of maxima at $\tau \simeq 0.055$ for R_0 = 32 mm and t_w = 4°*C*, respectively, 6°*C* can be explained by the development of secondary vortices in the upper melt region. At later times

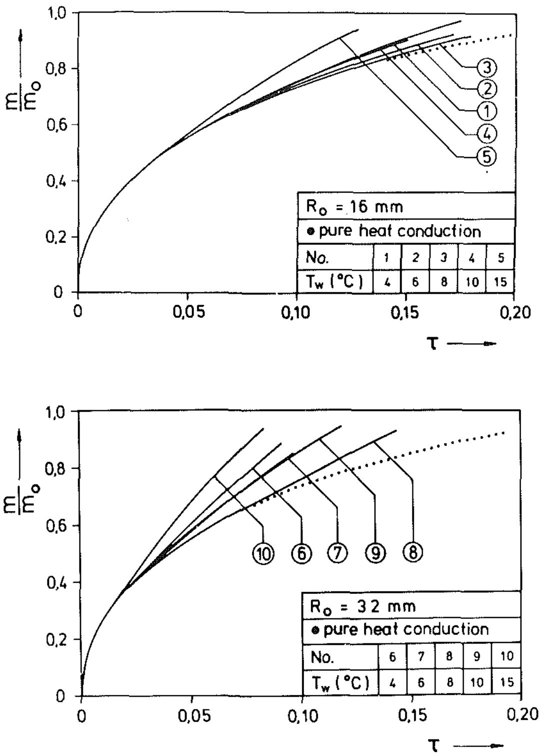

Fig. 6 Predicted molten mass fraction m/m_0, as a function of dimensionless time τ for different wall temperatures T_w: (a) R_0 = 16 mm, (b) R_0 = 32 mm

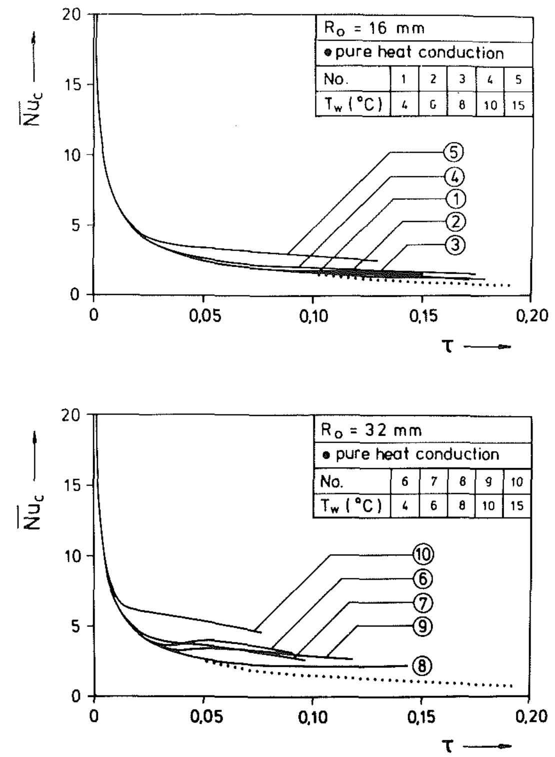

Fig. 7 Overall heat transfer coefficient at the tube wall $\overline{Nu_c}$ versus dimensionless time τ for different wall temperatures T_w: (a) R_0 = 16 mm, (b) R_0 = 32 mm

heat transfer is decreasing monotonically with time for all wall temperatures considered.

Conclusions

It can be stated that the mechanisms governing heat transport during the melting process of ice inside a horizontal cylinder are determined by complex flow configurations in the range of parameters studied. For both cylinder radii heat transfer will become minimum in the proximity of $T_w \simeq 8°C$. The experiments as well as the computations show that heat transfer is enhanced at the lower part of the ice body for $T_w < 8°C$ due to the density effect, resulting in an upward directed movement of the solid body. Similar to melting processes in "normal" fluids, the ice body shifts downward for $T_w > 8°C$. Due to the close agreement obtained between experimental and predicted data, confidence in the solutions of the nontrivial computations is further increased. The theoretical results gained so far contribute essentially toward a better understanding of the phenomena observed in phase change processes taking place in the ice-water system.

References

1 Yao, L. S., and Chen, F. F., "Effects of Natural Convection in the Melted Region Around a Heated Horizontal Cylinder," ASME JOURNAL OF HEAT TRANSFER, Vol. 102, 1980, pp. 667-672.

2 Sparrow, E. M., Patankar, S. V., and Ramadhyani, S., "Analysis of Melting in the Presence of Natural Convection in the Melt Region," ASME JOURNAL OF HEAT TRANSFER, Vol. 99, 1977, pp. 520-526.

3 Saitoh, T., and Hirose, K., "Numerical Method for the Two-Dimensional Freezing Problem Around a Horizontal Cylinder Encompassing a Density Inversion Point," *Bulletin of the JSME*, Vol. 24, 1981, pp. 147-152.

4 Rieger, H., Projahn, U., and Beer, H., "Analysis of Heat Transport Mechanisms During Melting Around a Horizontal Circular Cylinder," *International Journal of Heat and Mass Transfer*, Vol. 25, 1982, pp. 137-147.

5 Prusa, J., and Yao, L. S., "Melting Around a Horizontal Heated Cylinder: Part II—Numerical Solution for Isothermal Boundary Condition," ASME JOURNAL OF HEAT TRANSFER, Vol. 106, 1984, pp. 469-472.

6 Rieger, H., Projahn, U., Bareiss, M., and Beer, H., "Heat Transfer During Melting Inside a Horizontal Tube," ASME JOURNAL OF HEAT TRANSFER, Vol. 105, 1983, pp. 226-234.

7 Saitoh, T., and Hirose, K., "High Rayleigh Number Solutions to Problems of Latent Heat Thermal Energy Storage in a Horizontal Cylinder Capsule,"ASME JOURNAL OF HEAT TRANSFER, Vol. 104, 1982, pp. 545-553.

8 Katayama, K., et al., "Heat Transfer Characteristics of the Latent Heat Thermal Energy Storage Capsule," *Solar Energy*, Vol. 27, 1981, pp. 91-97.

9 Rieger, H., and Beer, H., "The Influence of Density Anomaly of Water on the Melting Process of Ice Inside a Horizontal Cylinder," ASME Paper No. 84-HT-10.

10 Thompson, J. F., Thames, F. C., and Mastin, C. W., "Automatic Numerical Generation of Body-Fitted Curvilinear Coordinate System for Field Containing Any Number of Arbitrary Two-Dimensional Bodies," *Journal of Computational Physics*, Vol. 15, 1974, pp. 299-319.

11 Thompson, J. F., Warsi, Z. U. A., and Mastin, C. W., "Boundary-Fitted Coordinate Systems for Numerical Solution of Partial Differential Equations—A Review," *Journal of Computational Physics*, Vol. 47, 1982, pp. 1-108.

12 Flügge, W., *Tensor Analysis and Continuum Mechanics*, Springer-Verlag, Berlin/Heidelberg/New York, 1972.

13 Warsi, Z. U. A., "Conservation Form of the Navier-Stokes Equations in General Nonsteady Coordinates," *AIAA Journal*, Vol. 19, 1981, pp. 240-242.

14 Fujii, T., "Fundamentals of Free Convection Heat Transfer," *Prog. Heat Transfer Engng.*, Vol. 3, 1974, pp. 66-67.

15 Rieger, H., "Numerische Berechnung von Wärmetransportvorgängen bei laminaren, freien Konvektionsströmungen in beliebigen, festen sowie zeitabhängigen, ebenen Geometrien," Doctoral Dissertation, Techn. Hochschule Darmstadt, 1983.

16 Landolt-Börnstein, *Zahlenwerte und Funktionen*, Vol. II, Springer, Berlin, 1971, pp. 36-37.

17 Bareiss, M., "Der Wärmetransport an schmelzende Medien unter Berücksichtigung der Vorgänge in Latentwärmespeichern," Doctoral Dissertation, Technische Hochschule Darmstadt, 1982.

18 Thomas, P. D., and Middlecoff, J. F., "Direct Control of the Grid Point Distribution in Meshes Generated by Elliptic Equations," *AIAA Journal*, Vol. 18, 1980, pp. 652-656.

19 Rieger, H., Projahn, U., and Beer, H., "Fast Iterative Solution of Poisson Equation With Neumann Boundary Conditions in Nonorthogonal Curvilinear Coordinate Systems by a Multiple Grid Method," *Numerical Heat Transfer*, Vol. 6, 1983, pp. 1-16.

20 Saitoh, T., and Hirose, K., "Thermal Instability of Natural Convection Flow Over a Horizontal Ice Cylinder Encompassing a Maximum Density Point," ASME JOURNAL OF HEAT TRANSFER, Vol. 102, 1980, pp. 261-267.

C. Gau

R. Viskanta
Fellow ASME

Heat Transfer Laboratory,
Scool of Mechanical Engineering,
Purdue University,
West Lafayette, IN 47907

Melting and Solidification of a Pure Metal on a Vertical Wall

This paper reports on the role of natural convection on solid–liquid interface motion and heat transfer during melting and solidification of a pure metal (gallium) on a vertical wall. The measurements of the position of the phase-change boundary as well as of temperature distributions and temperature fluctuations were used as a qualitative indication of the natural convection flow regimes and structure in the melt during phase transformation taking place in a rectangular test cell heated or cooled from one of the vertical walls. For melting, the measured melt volume and heat transfer coefficients are correlated in terms of relevant dimensionless parameters. For solidification, the measured volume of metal solidified on the wall is compared with predictions based on a one-dimensional model.

Introduction

Heat transfer in the processing of materials involving solid–liquid phase transformations (melting and solidification) is commonplace in such fields as metallurgy, crystal growth from melts and solutions, purification of materials, and solidification of metals. The associated density gradients in a gravitational field can induce natural convection flows. Convection in the liquid phase influences the process in two different ways, one of which is beneficial and the other of which can be detrimental. During melting convection increases the overall transport rate and, hence, the growth rate of the new phase, which is desirable. On the other hand, during solidification convection decreases the growth of the new phase and also seems to affect the morphology of the solid–liquid interface adversely [1, 2]. The nature of the solid is largely determined by what occurs in the vicinity of the solid–liquid interface. The heat release (absorption), density change, and other processes that take place in the vicinity of the transformation front result in nonuniformities along the front that cause its shape to change. The resulting density gradients in the liquid generate buoyancy-driven convection that can affect the transport of heat, constituent chemicals, and the growth rate.

Melting and solidification heat transfer from a vertical side (wall) has been receiving research attention, and a recent review is available [3]. However, most of the studies have been with materials other than metals. The authors have been able to identify only relatively few studies which were concerned with the effects of buoyancy-induced natural convection in the liquid metal during solidification [4–7]. The effect of natural convection on solidification of metals has been recognized for some time and a review is available [4]; however, much of the information is qualitative in nature and very little effort has been made to give a quantitative interpretation of solidification and of melting in the presence of natural convection. Szekeley and Chhabra [5] appear to have been the first to demonstrate experimentally and analytically the importance of natural convection on the interface shape in a rectangular tank with the heat source and sink on the two opposite, vertical sidewalls. Solidification experiments from above with lead [6] and with a Lipowitz metal [7] have shown that convection in the melt decreases the rate of solidification. The composition stratification of a eutectic before the initiation of melting from below was found to suppress natural convection and to decrease the melting rate [7]. The heat transfer literature has failed to reveal any melting and solidification studies with pure metals in which the interface shape and motion, the phase-change rate, and convective heat transfer have been measured and reported for the situation where the material was heated or cooled from a vertical wall. No comparisons between analytical predictions and experimental data have been found in the heat transfer or the metallurgy literature. Yet, such information is of considerable practical importance to solidification of castings and other materials processing problems [1, 8].

The purpose of this paper is to report on an experimental study of buoyancy-induced flow in the melt and its effect on the solid–liquid interface motion and heat transfer during melting and solidification of a pure metal (gallium) from a vertical wall. Melting and solidification experiments have been performed in a rectangular test cell with the heat source and the heat sink at the two opposite sidewalls of the test cell. The importance of natural convection in the melt on the shape of the phase-change boundary and its motion as well as on heat transfer is demonstrated from the measurements of temperature distributions. The natural convection flow patterns are deduced indirectly from the measured solid–liquid interface positions and temperatures.

Experiments

Apparatus and Instrumentation. Solidification and melting experiments were performed in a rectangular test cell (Fig. 1) that had inside dimensions of 8.89 cm in height, 6.35 cm in width, and 3.81 cm in depth. The two end walls, which served as the heat source/sink, were made of multipass heat exchanger machined from a copper plate. The copper surfaces were plated with a layer of 0.0127-mm-thick chromium for protection against corrosion. The top, bottom, and sidewalls were made of Plexiglass. The two vertical sidewalls were 1.27-cm-thick plates to support the cell, and, for better insulation, the front and back sidewalls had a 0.318-cm air gap between the plates. One of the plates is 0.318 cm thick and the other is 0.635 cm thick. A feed line connected to a hole in the bottom of the heated plate was used to fill or drain the melt. A long, thin cable electric heater was inserted in the tube to maintain the inside metal in liquid phase.

The horizontal temperature distributions in the central region along the top wall, the center line, and the bottom wall of the test cell were measured with copper constantan (type K) thermocouples having wire diameter of 0.127 mm. A total of 26 equally spaced thermocouples were installed on the top and the bottom walls. The precise location of thermocouples along the top and the bottom walls was insured by placing them in small holes which were drilled in the walls. The thermocouples were then inserted close to the surface of the walls and were then sealed. A total of 17 other thermocouples, used to measure the temperature distribution along the center line, were made into a thermocouple rack. Each pair of

---

Contributed by the Heat Transfer Division for publication in the JOURNAL OF HEAT TRANSFER. Manuscript received by the Heat Transfer Division February 10, 1984.

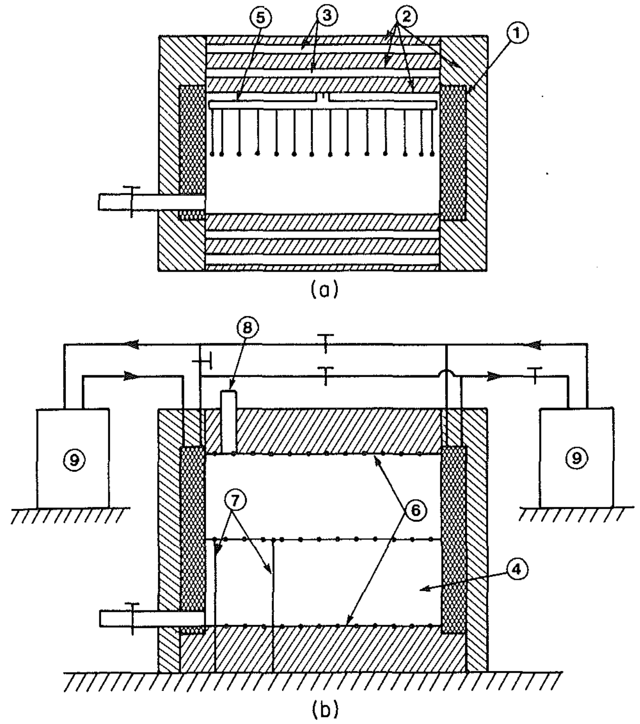

Fig. 1 Schematic diagram of the test cell, top view (*a*) and front view (*b*): (1) heat source and/or sink, (2) Plexiglass wall, (3) air gap, (4) phase-change material, (5) thermocouple rack, (6) thermocouples along the walls, (7) small-diameter thermocouples, (8) hole for filling material, and (9) constant temperature baths

thermocouple wires was sheathed in a 0.584-mm-dia stainless steel tube and was then attached perpendicularly to a 2.38-mm-dia stainless steel tube. The sheathed thermocouples were arranged in a horizontal plane and in a direction perpendicular to the front and the back walls where the temperature gradient in the liquid was the smallest. The arrangement minimized heat conduction along the small stainless steel tubes and therefore reduced the measurement error.

Two additional thermocouples were inserted through small holes drilled in the bottom wall to measure the temperature fluctuations. One was located in the central region away from the heated vertical wall; the other was located 24 mm away from the wall. The thermocouple junctions were coated with a thin layer of high-thermal-conductivity epoxy for protection. The d-c part of the signal of the temperature fluctuations was suppressed and the small a-c component could be amplified and recorded.

The test cell was placed in a transparent box made of Lexan in which the temperature could be regulated and kept constant by a temperature controller. The purpose of the controlled environment was to reduce the temperature difference between the test cell and environment, thus minimizing the heat loss/gain from the test cell to the ambient surroundings. A heat storage material was also placed in the box to minimize the frequent on-and-off switching of the heater and to keep the inside temperature close to a constant value.

Experimental Procedure and Data Reduction. The metal used in the experiments was gallium. It had a purity of 99.6 percent and a fusion temperature of 29.78°C. There were several reasons for selecting gallium. First, the thermophysical properties are reasonably well established [9]. Second, it has a fusion temperature close to the ambient, which is conducive to experimentation. Third, the metal is important technologically as it is usually combined with other pure elements to form electronic and industrial materials such as semiconductors, laser diodes, solar cells, and magnetic bubble devices. The main disadvantages are that it is very expensive (about one dollar per gram, depending on purity) and is anisotropic. Pure solid gallium appears in polycrystalline form and the crystals have an orthorhombic structure. The thermal conductivity of the solid crystal is highly anisotropic and is 40.82 W/mK along the *a* axis of the crystal, 88.47 W/mK along the *b* axis, and 15.99 W/mK along the *c* axis [9]. The thermal conductivity of the liquid is still anisotropic but not much different along each of the crystal axes.

Before each experiment the metal was melted and poured into the preheated test cell through the sprue on the left side (Fig. 1). Provision was made to avoid air bubble entrapment in the test cell. This was accomplished during the filling procedure by slightly lifting one of the sidewalls where a small hole had been drilled near the top plate. This hole was sealed after the test cell was filled.

The initial temperature inside the test cell was kept uniform and only a single phase was allowed to exist. This was done by circulating a constant temperature fluid in both heat exchangers at a temperature slightly above or below the fusion point for a sufficient period of time. Melting or solidification was initiated by switching one of the heat exchangers to another constant temperature bath preset at a different temperature. A uniform solid temperature was reached, usually from 1°C to 2°C below the fusion temperature of the material, before melting was initiated. This was done in an attempt to minimize the subcooling as a parameter of the problem.

The pour-out method and the probing method were adopted to examine and/or measure the shape of the solid-liquid interface [7]. At predetermined times the phase-change process was terminated, and the liquid (melt) was rapidly poured out. In the process of draining the liquid, some forced

Nomenclature

A = aspect ratio = H/L
A_w = heat transfer area
c = specific heat
Fo = Fourier number = $\alpha t/L^2$
H = height of the cavity
Δh_f = latent heat of fusion
L = length of cavity
$\tilde{\mathrm{Nu}}$ = Nusselt number = $\bar{h}H/k_l$
k = thermal conductivity
Ra = Rayleigh number = $g\beta(T_w - T_f)H^3/\alpha\nu$
Ste = Stefan number = $c_l(T_{wb} - T_f)/\Delta h_f$ for melting and $c_s(T_f - T_{wl}/\Delta h_f$ for solidification
s = solid–liquid interface position
T = temperature
t = time
V = volume
V_0 = volume of test cell
W = cavity width
x = coordinate along the horizontal length of the test cell
α = thermal diffusivity
β = thermal expansion coefficient
δ = dimensionless interface position = s/H
ν = kinematic viscosity
τ = dimensionless time; τ_l = $\mathrm{Fo}_l\mathrm{Ste}_l$ for melting and τ_s = $\mathrm{Fo}_s\mathrm{Ste}_s$ for solidification

Subscripts

c = characteristic length or cooled
h = heated wall
f = fusion point of material
l = liquid phase
s = solid phase
w = wall

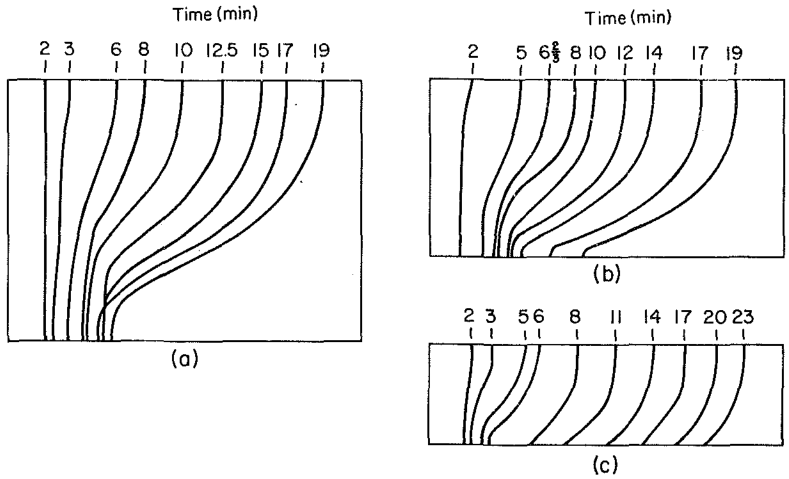

Fig. 2 Interface shape traced at preselected times during melting from a side using pour-out method: (*a*) T_{wh} = 38.0°C, A = 0.714, (*b*) T_{wh} = 38.3°C, A = 0.5, and (*c*) T_{wh} = 38.7°C, A = 0.286

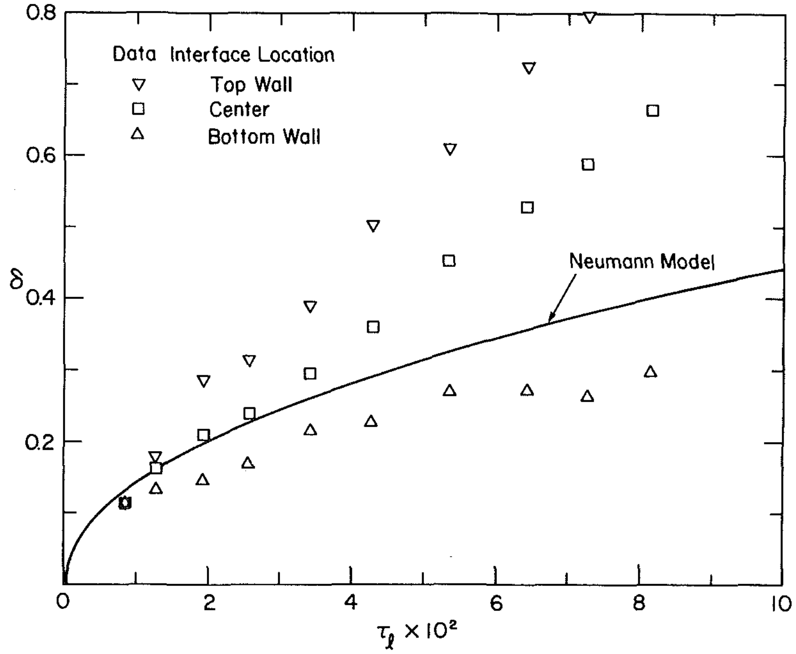

Fig. 3 Comparison of the local melting rate with the Neumann solution for Ste_s = 0.0408, A = 0.714

convection effect was introduced, but since the interface was bared very rapidly the effect on the interface is considered to be minimal. The solid-liquid interface position was traced and/or photographed.

Melting From a Vertical Wall

Interface Shape. The interface shape observed during the melting of gallium from the side was smooth and flat in the direction perpendicular to the front and back walls of the test cell. This suggests that fluid motion and heat transfer in that direction was small, and the effect of natural convection recirculation on the interface motion can justifiably be neglected. The interface shape traced at preselected times is shown in Fig. 2. At very early times, before the buoyancy-driven flow was initiated or when fluid motion was still very weak, the interface shape was flat and parallel to the heated wall of the test cell. Heat transfer was dominated by conduction.

As the heating progressed the buoyancy-driven convection in the melt started to develop and continued to intensify. This is evidenced by the appearance of a nonuniform melt layer (Fig. 2*a*, $t = 3$ min) receding from the top to the bottom of the test cell. This is particularly evident in Fig. 2(*a*) for the larger aspect ratio test cell (A = 0.714). A flow structure typical of natural convection-driven phase-change systems is observed. Fluid is heated as it rises along the hot wall. The flow is deflected and descends along the solid-liquid interface with higher melting occurring at the top where the fluid is at higher temperatures. Fluid motion associated with phase change at the interface was negligible since there is very little difference in the density of the solid and liquid phases. Melting at the bottom is nearly terminated at later times (for times from 12.5 to 17 min), and the interface shape becomes almost flat. This is in part due to the very high thermal conductivity of liquid gallium, which has been cooled to nearly fusion temperature in the vicinity of the interface in the lower part of the test cell. Experiments performed with higher sidewall temperatures yielded similar results.

Significant differences in the local melting rate that alter the

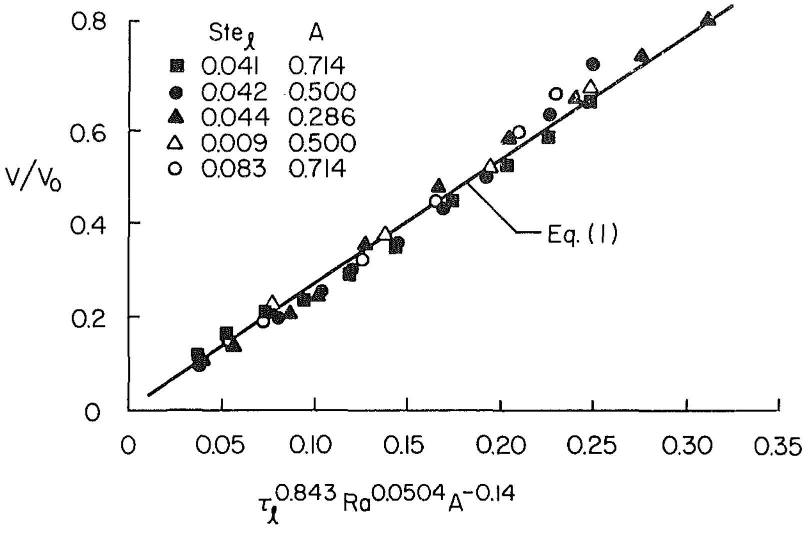

Fig. 4 Correlation of the melted volume data

shape of the interface are evident from the interface contours shown in Fig. 2. Physically, heat transfer near the bottom of the melt-filled cavity is lower because of the recirculation pattern established in the liquid. For a higher aspect ratio cavity the recirculation is stronger and produces a lower melting rate in this region (compare Figs. 2*a* and 2*c* at $t = 17$ min). A comparison of the measured interface positions near the bottom wall with the predictions based on the Neumann model [10] showed that the interface moved more slowly (Fig. 3). The results suggest that the recirculation which was established in the liquid became more intense as time progressed and decreased the melting rate near the bottom of the cell where the cooled liquid flowed from the interface toward the heated wall.

Comparison of the results given in Fig. 2 with those reported in the literature for melting of *n*-octadecane [11, 12] shows that there is much more melting near the bottom of the test cell with gallium. The shapes of the interface contours are also significantly different. This is attributed, in part, to large differences in the thermophysical properties between the paraffin and the metal and due to the difference in the flow structure in the two phase-change materials.

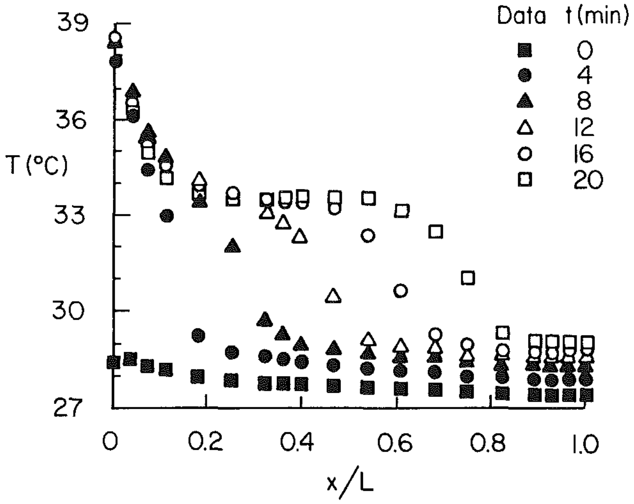

Fig. 5 Temperature distribution along the centerline during melting from a side: T_{wh} = 38.3°C, A = 0.5

Melting Rate. The melted volume fractions at each time for different aspect ratio cavities and Rayleigh numbers (or Stefan numbers) were measured and are presented in Fig. 4. Attempts were made to correlate V/V_0 with the group $\tau_l \mathrm{Ra}^{1/4}/A$ as a parameter which is similar to the one suggested in the literature [12], except that A was included here to take into account the different length scales defined in τ_l and Ra; however, the data could not be collapsed onto a single line. Therefore, each of the variables in the group $\tau \mathrm{Ra} A$ was treated as a separate parameter in the regression analysis. A least-squares fit of the data was found to yield the following equation

$$\frac{V}{V_0} = 2.708 \tau_l^{0.843} \mathrm{Ra}^{0.0504} A^{-0.14} \qquad (1)$$

When heat transfer in the melt is by conduction (only during about the first 2 min of the experiments, see Fig. 2), the melted volume V/V_0 is proportional to $\tau_l^{0.5}$. In the presence of natural convection, the melted volume V/V_0 is proportional to $\tau_l^{0.843}$. Since the empirical correlation was obtained by a least-squares fit of the experimental data the short times (about 2 min time period compared to the total melting time of about 20 min) when heat transfer is by conduction only are not reflected in the correlation, because there should be no dependence on the Rayleigh number during this period. The effect of the aspect ratio on the melting rate could not be conclusively deduced from equation (1), because the cell height which is used in the Rayleigh number may not be meaningful for the problem considered. For natural convection without phase change in a cavity heated from a side the heat transfer rate increases with the aspect ratio [15]. Therefore, an increase in the melting rate with aspect ratio should have been expected.

In a correlation where the Stefan number instead of the Rayleigh number was chosen as a correlation parameter, a similar correlation equation to the one found earlier [14] in a different system could be obtained. The melted volume fraction was found to be

$$V/V_0 = 6.278\, \tau_l^{0.842}\, \mathrm{Ste}_l^{0.0393}\, A^{0.0137} \qquad (2)$$

This correlation also indicates a very weak dependence of the melted volume fraction on the aspect ratio. The melting rate measured has been compared with the Neumann solution [10]. Near the end of the process, the melted volume is about 1.75 times that which would be expected in the absence of natural convection in the melt.

Temperature Distribution. During the early melting stages the horizontal temperature distributions along the top wall,

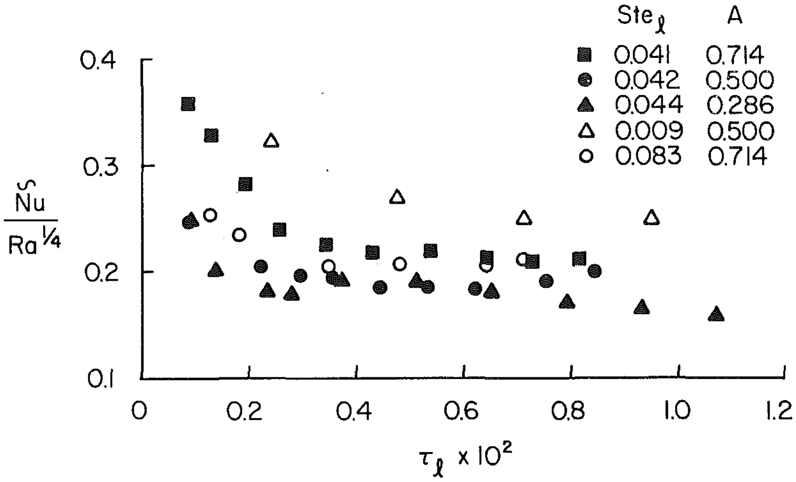

Fig. 6 Timewise variation of the heat transfer parameter

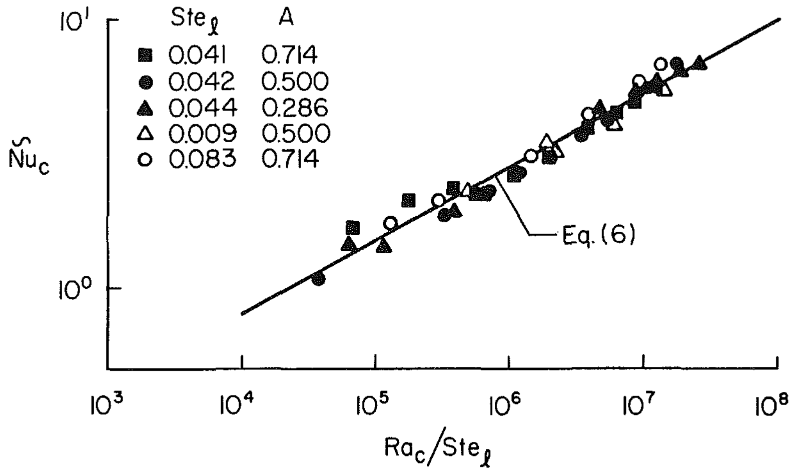

Fig. 7 Correlation of the average Nusselt number in terms of the characteristic Rayleigh number Ra_c

center, and the bottom wall were linear and were nearly the same. Conduction was the dominant mode of heat transfer. At later times, the fluid motion produced by buoyancy resulted in nonlinear temperature distributions which were different at each height [13]. Due to the expected clockwise circulation of the melt driven by buoyancy, steep horizontal temperature gradients were observed at the two boundaries of the liquid-filled cavity (Fig. 5). Along the vertical heated wall the largest temperature gradient occurred near the bottom region and the smallest near the upper region. Along the interface the trends were opposite. The horizontal temperature gradients at each height near the heated wall and the interface changed little after natural convection was initiated and established.

The temperature gradients at the three different heights in the region away from the heated wall and interface gradually decreased as the melting proceeded. The reduction of the temperature gradient is attributed to the growth of the main circulation flow and of the melt layer. The temperature gradient along the center line (Fig. 5) decreased the most and approached zero at later stages of the melting process (t = 16 min). No reversal of temperature gradient was ever observed. The gradual change of temperatures suggests that no significant change of flow structure can be expected. The flow was laminar and remained so for the entire duration of the melting process.

Temperature fluctuations were measured near (4.74 mm) and farther away (24 mm) from the heated wall. The traces of the thermocouple output indicated a sharp increase and small fluctuations shortly after the interface passed over the sensor [13]. However, the frequency and the mean temperature showed gradual increases and became steady at later times as the fluid circulated in a much more stable manner.

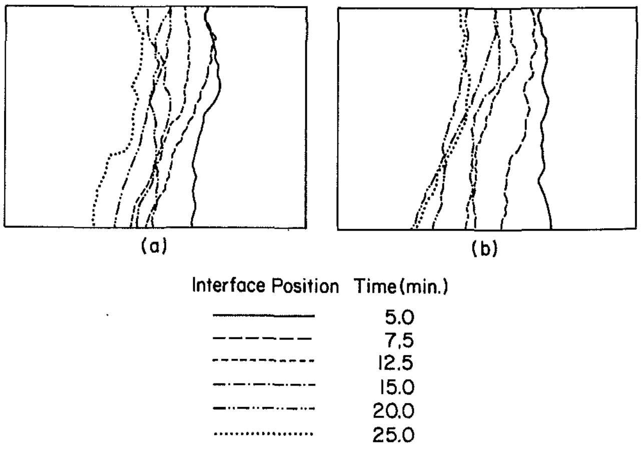

Fig. 8 Traces of interface shape along (*a*) the front wall and (*b*) the back wall of the test cell during solidification from a side: T_{wc} = 10.2°C, T_{wh} = 33.2°C, A = 0.714

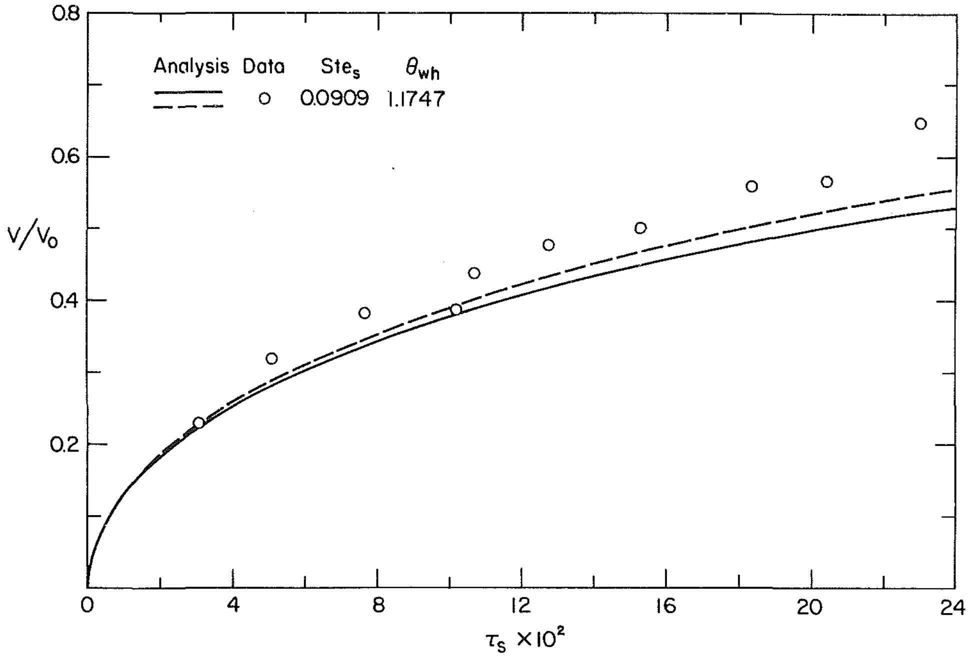

Fig. 9 Comparison between experimental data and predictions for the melted volume fraction

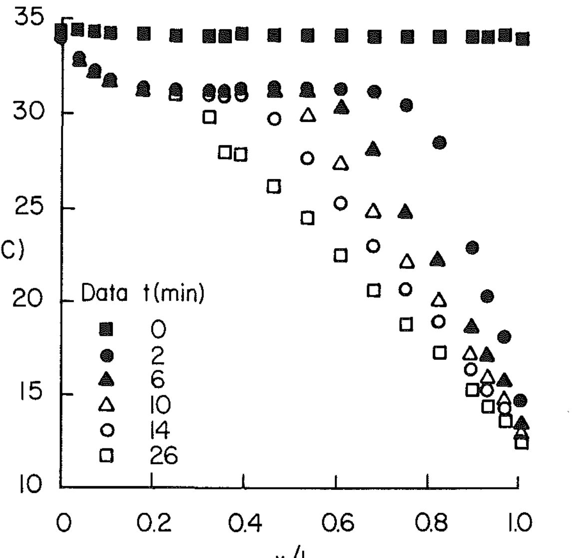

Fig. 10 Temperature distribution along the center line during solidification from a side: T_{wc} = 12.5°C, T_{wh} = 34.0°C, and A = 0.5

Average Heat Transfer Coefficient. With the knowledge of the melted volume at a specific time the total heat transferred to the phase change material can be estimated and the time-average (spatial) heat transfer coefficient can be calculated [14]. The time-average heat transfer coefficient was defined by

$$\tilde{h} = \frac{Q_t}{A_w(T_w - T_f)t} = \frac{\int_0^t \left[\int_{A_w} q\,dA \right] dt}{A_w(T_w - T_f)t} \tag{3}$$

where the total heat input Q_t or heat stored in the phase-change material is given by

$$Q_t = \int_{V_s(t)} \rho_s c_s (T_f - T_0(p))\, dV_s(p) + \rho_l V_l \Delta h_f + \int_{V_l(t)} \rho_l c_l (T_l(p) - T_f)\, dV_l \tag{4}$$

The time-averaged heat transfer coefficient can be written in dimensionless form as

$$\tilde{\mathrm{Nu}} = \frac{\tilde{h}H}{k_l} = (V/V_0)(1 + \mathrm{Ste}/2)/A\tau_l \tag{5}$$

The heat transfer coefficients were correlated in terms of standard heat transfer parameter $\tilde{\mathrm{Nu}}/\mathrm{Ra}^{1/4}$, where the height H of the test cell was used as characteristic length. The timewise variation of the Nusselt number is presented in Fig. 6. At early times, the parameter $\tilde{\mathrm{Nu}}/\mathrm{Ra}^{1/4}$ is large, because the melt layer is relatively thin and heat transfer is dominated by conduction. Growth of the melt layer increases the thermal resistance and decreases the heat transfer coefficient. The decrease in the parameter $\tilde{\mathrm{Nu}}/\mathrm{Ra}^{1/4}$ levels off after natural convection is initiated. At later times in the process, the heat transfer parameter $\tilde{\mathrm{Nu}}/\mathrm{Ra}^{1/4}$ indicates that convection-dominated quasi-steady melting has been reached for the largest but not for the smallest aspect ratio test cells.

As shown in Fig. 6, the parameter $\tilde{\mathrm{Nu}}/\mathrm{Ra}^{1/4}$ is a function of the Stefan number and the aspect ratio. For smaller Stefan numbers the dimensionless heat transfer parameter shifts up and to the right. This was also found in a different melting system [14] and was attributed to the use of improper characteristic length for defining the Rayleigh number. The most probable reason for the heat transfer parameter being inversely proportional to the Stefan number may be that the parameter itself could not completely characterize the natural convection flow and heat transfer process in the liquid during melting when the size and shape of the liquid-filled cavity changes with time. For quasi-steady melting the average Nusselt number was well correlated with the Rayleigh number [11, 16]. However, since convection-dominated quasi-steady melting does not appear to have been fully reached in the present experiments no attempt was made to correlate the data in a form of a standard natural convection correlation.

Even though the entire melting process is transient in nature, and one of the boundaries of the heat sink (solid-liquid interface) is not planar, an average melt layer thickness has sometimes been used as a characteristic length l_c in correlating the heat transfer data. A simple relation between $\tilde{\mathrm{Nu}}_c$ and Ra_c as well as Ste_l has been obtained for a different system [14]. The least-squares fit of the data was found to yield the following empirical equation

$$\tilde{\mathrm{Nu}}_c = \frac{\tilde{h} l_c}{k_l} = 0.0631 \left(\frac{\mathrm{Ra}_c}{\mathrm{Ste}_l} \right)^{0.274} \tag{6}$$

A comparison of the data with the equation is presented in Fig. 7. All the data points collapse nicely onto a single line. The correlation is valid in the conduction, transition, and natural convection regimes.

Solidification on a Vertical Wall

Interface Shape. The exposed interface shape at different times was examined and traced along the front and back walls by pouring out the liquid at specific times during each run (Fig. 8). The interface shape was very irregular. The anisotropy in the thermal conductivity and the crystallographic effects [17, 18] played a dominant role in controlling the interface shape, not only during the early time when conduction in the solid predominated over convection in the melt but also at later time when natural convection played an important role in controlling the interface motion.

The irregular interface shape has prohibited inferring the flow structure in the melt filled cavity. However, because of the arrangement of the heat source and the cavity geometry, a clockwise circulation of liquid which rose near the isothermal side (left) and fell near the cool interface could be expected. The local flow structure and heat transfer near the interface would be influenced by the irregular interface morphology and shape and vice versa. Therefore, especially at later times the interaction of natural convection in the melt with anisotropic conduction in the solid and the crystallographic effects made the analysis of the growth morphology and of the flow structure along the interface more complicated. Experiments were repeated, but the interface shape and the flow structure in its vicinity were not reproducible. The interface and the fluid motion near the bottom of the test cell sensed the upstream effects, i.e., the irregular interface shape and its interaction with the flow.

Solidification Rate. At early times, the local solidification rate along the interface is controlled primarily by conduction in the solid and crystallographic effects at the interface. The effect of natural convection heat transfer on the interface shape and motion is relatively small. At later times when natural convection plays an important role in controlling the interface motion, higher solidification rates in the bottom region can be observed (Fig. 8).

The total frozen volume fractions at different times were measured and are compared in Fig. 9 with the predictions based on planar interface motion [7]. The heat transfer coefficient at the interface was obtained from the literature [15] for steady-state natural convection in a cavity heating from the side. The coefficient has been multiplied by a factor of 0.45 as suggested because the ratio W/H is close to unity. The dashed line in Fig. 9 shows the predictions based on the heat transfer coefficient being reduced by 20 percent. The predicted solidification rates are lower than the measured ones. The higher rate measured at later times is attributed to the anisotropy in the thermal conductivity of gallium crystal and possibly to the increase in the surface area afforded by the irregular crystalline structure relative to a plane surface. In addition, the assumption of a planar interface shape and the use of steady-state heat transfer coefficient (in the absence of phase change) in the model may contribute to the discrepancy. Initially, the solidification rate is relatively high due to the sharp temperature gradient in the solid but gradually decreases due to the increase in the thermal resistance of the solid layer. During the final stages, the rate is primarily retarded by natural convection in the melt.

Temperature Distribution. Despite the irregular interface shape and the flow field in its vicinity, which were not reproducible for each experiment, the temperature distributions exhibited trends which were somewhat similar to those during the melting when natural convection was well established. The highest temperature gradient along the heated vertical plate was found near the bottom region and the smallest was found near the top. An opposite trend for the temperature gradient was observed along the solid-liquid interface. Along the center line, the core was nearly isothermal. An increase in temperature from the bottom to the top region was observed [13]. Therefore, a clockwise circulation of flow can be inferred. The temperatures along the center and the top wall in the melt remained nearly the same shortly after the solidification process was initiated and remained so until just before the solid-liquid interface approached the thermocouple junctions, whereas the temperature along the bottom wall decreased slowly. This suggests that the flow in the upper region of the melt is more readily established than near the bottom region.

The temperature distributions along the center, the top, and the bottom walls in the solid are linear and nearly the same [11]. The slightly higher temperature along the top and the bottom walls may be due to the smaller heat conduction along or across the Plexiglass wall from either the melt or the environment. The temperature gradient in the solid is large initially as compared to the temperature gradient near the interface in the melt. Natural convection begins to play an important role in controlling the solidification process during the later stages when the temperature gradient in the solid decreases with the increase of the solid thickness.

Conclusions

In spite of the large thermal conductivity, the experimental results have clearly established the important role played by natural convection during melting of a pure metal from a vertical sidewall. The phase-change boundary, the melting rate, and heat transfer were greatly affected by buoyancy-driven natural convection. Qualitative flow structure was deduced indirectly from the interface shape and motion and reaffirmed by temperature measurements. Laminar flow persisted throughout the melting process, and nearly quasi-steady melting was attained at later stages. The melted volume fraction and heat transfer were well correlated in terms of relevant dimensionless parameters.

During solidification of gallium from a sidewall, the interface shape was controlled not only by the natural convection circulation in the melt but also by the combined crystallographic effects and anisotropy of the gallium crystal. The interface morphology was irregular, and the shape was not reproducible. The buoyancy-induced flow and its structure inferred from the observations of phase-change boundary shape and motion and the temperature distribution in the melt were found to be similar to those during melting. The solidification rate was higher near the bottom than near the top. The fraction of the total solidified volume measured at different times agreed reasonably well with the predictions based on a one-dimensional model.

Acknowledgments

The work described in this paper was supported by the National Science Foundation Heat Transfer Program under grant No. MEA-8313573.

References

1 Flemings, M., *Solidification Processing*, McGraw-Hill, New York, 1974.

2 Carruthers, J. R., "Thermal Convection Instabilities Relevant to Crystal Growth From Liquids," in: *Preparation and Properties of Solid State Materials*, W. R. Wilcox, ed., Marcel Dekker, New York, 1973, Vol. 3, pp. 1-121.

3 Viskanta, R., "Phase-Change Heat Transfer," in: *Solar Heat Storage: Latent Heat Materials*, G. A. Lane, ed., CRC Press, Boca Raton, FL, 1983, Chap. 5.

4 Cole, G. S., "Transport Processes and Fluid Flow," in: *Solidification*, T. J. Hughel and G. F. Bolling, eds. *Proceedings of Seminar of American Institute of Metallurgical Engineers*, Metal Park, OH, 1969, pp. 201-274.

5 Szekeley, J., and Chhabra, P. S., "The Effect of Natural Convection on the Shape and Movement of the Melt-Solid Interface in the Controlled Solidification," *Metallurgical Transactions B*, Vol. 1, 1970, pp. 1195-1203.

6 Chiesa, F. M., and Guthie, R. I. L., "Natural Convection Heat Transfer Rate During the Solidification and Melting of Metals and Alloy Systems," ASME JOURNAL OF HEAT TRANSFER, Vol. 99, 1974, pp. 377-384.

7 Gau, C., and Viskanta, R., "Melting and Solidification of a Metal System in a Rectangular Cavity," *International Journal of Heat and Mass Transfer*, Vol. 27, 1984, pp. 113-123.

8 Ostrach, S., "Fluid Mechanics in Crystal Growth—The 1982 Freeman Scholar Lecture," ASME *Journal of Fluids Engineering*, Vol. 105, 1983, pp. 5-20.

9 Cubberley, W. H., *Metal Handbook—Properties and Selection: Nonferrous Alloys and Pure Metals*, 9th edn., American Society of Metals, Metals Park, OH, 1979, pp. 736-737.

10 Carslaw, S. H., and Jaeger, J. C., *Conduction of Heat in Solids*, 2nd edn., Clarendon Press, Oxford, 1959, Chap. 11.

11 Okada, M., "Melting From a Vertical Plate Between Insulated Top and Bottom Surfaces," in: *Proceedings of the ASME/JSME Thermal Engineering Joint Conference*, ASME, New York, 1983, Vol. 1, pp. 281-288.

12 Ho, C.-J., and Viskanta, R., "Heat Transfer During Melting From an Isothermal Vertical Wall," ASME JOURNAL OF HEAT TRANSFER, Vol. 106, 1984, pp. 12-19.

13 Gau, C., "Heat Transfer During Solid-Liquid Phase Transformation of Metals in Rectangular Cavities," Ph.D. Thesis, Purdue University, 1984.

14 Ho, C.-J., and Viskanta, R., "Experimental Study of Melting in a Rectangular Cavity," in: *Heat Transfer-1982*, U. Grigull et al., eds., Hemisphere, Washington, DC, 1982, Vol. 2, pp. 369-374.

15 Hollands, K. G. T., and Raithby, G. D., "Natural Convection," in: *Handbook of Heat Transfer*, W. M. Rohsenow et al., eds., 2nd edn., McGraw-Hill, New York, 1985.

16 Bareiss, M., and Beer, H., "Experimental Investigation of Melting Heat Transfer With Regard to Different Geometrical Arrangements," *International Communications in Heat and Mass Transfer*, Vol. 11, 1984, pp. 323-333.

17 Jackson, K. A., "Interface Structure," in: *Growth and Perfection of Crystals*, Doremus et al., eds., Wiley, New York, 1958, pp. 319-324.

18 Alfintsev, G. A., and Ovsienko, D. E., "Growth Mechanism of Gallium Crystals Grown From Melts," *Soviet Physics—Doklady*, Vol. 9, No. 6, 1964, pp. 489-491.

R. J. Couvillion
Assistant Professor.
Department of Mechanical Engineering,
University of Arkansas,
Fayetteville, AR 72701
Assoc. Mem. ASME

J. G. Hartley
Associate Professor.
School of Mechanical Engineering,
Georgia Institute of Technology,
Atlanta, GA 30332
Mem. ASME

Drying Front Movement Near Low-Intensity, Impermeable Underground Heat Sources

An analytical model of transient, simultaneous heat, water, and air transfer is developed in this paper. The resulting governing differential conservation equations are simplified by dimensional analysis and applied to a semi-infinite moist soil with an impermeable heat source at the boundary. Solutions for moisture and temperature distributions are generated numerically for varying surface heat flux and initial moisture content. Difficulties in using a moving boundary approach are discussed. The solutions predict, without *using a moving boundary analysis, that a narrow zone with a steep moisture gradient moves through the soil at a rate such that the volume of soil dried per unit surface heat input is constant for a given initial moisture content.*

Introduction

Coupled heat and mass transfer in soils is important in a variety of engineering fields. Some examples are heat transfer in ground source heat pumps, sand casting molds, and underground heat sources such as buildings, electric cables, and pipelines.

When an impermeable heat source is activated on the boundary of a large body of moist soil, temperature gradients which induce moisture movement are created. After a time, the soil at the heat source surface can dry completely, causing a drying front to propagate into the soil. The region of dry soil thus created has a much lower thermal conductivity than the original soil and acts as a layer of insulation. For a constant heat flux source, e.g., an underground electric cable, this would cause the surface temperature to rise and the electric cable insulation could eventually fail. For a constant temperature source, e.g., an underground steam line, the heat loss would drop, a beneficial result.

Analysis of the drying front problem requires an understanding of heat and mass transfer in moist soils. Work in this area has been conducted for approximately 75 years. The most widely accepted expressions for moisture flux due to temperature and moisture content gradients are those presented by Philip and DeVries [1] and Taylor and Cary [2], and these two forms are similar in that diffusivities are used to relate the moisture flux to temperature and moisture gradients. Various theories [1-4] exist for analytical determination of these quantities, but an improved, extended version of the method of Philip and DeVries [1] is presented and used in this work. Since the diffusivities are strong functions of moisture content and are also functions of temperature and pressure, the resulting differential conservation equations are highly nonlinear and solvable only by numerical methods.

In this work governing equations derived to describe heat, moisture, and air transfer are presented along with a method for attacking the drying front problem. These governing equations are cast in nondimensional form and simplified by an order of magnitude analysis. Finally, solutions for temperature distribution, moisture distribution, and drying front position are presented.

Conservation Equations

This work can be applied equally well to most soils and other moist porous media. However, the following assumptions are made in the analysis:

1 The soil is isotropic, and its structure remains fixed.

2 The liquid density is assumed to be constant; specific heats of soil, water, vapor, and air are allowed to vary with temperature; and the vapor and air in the pore spaces are assumed to be ideal gases.

3 The mass of water vapor present is negligible compared to the mass of liquid. As shown in [5] this is valid even at moisture contents corresponding to multimolecular layers on the soil surface.

4 Flow of liquid due to gravity is neglected; hysteresis effects are ignored since only drying is considered; and there are no dissolved salts present.

With these assumptions the conservation of water mass and air mass equations can be written as

$$\frac{\partial \theta}{\partial t} = -\nabla \cdot \left[\frac{j_1 + j_2}{\rho_2}\right] = -\nabla \cdot \left[\frac{j_w}{\rho_2}\right] \tag{1}$$

$$\frac{1}{\rho_2}\frac{\partial[\rho_3(\epsilon-\theta)]}{\partial t} = -\nabla \cdot \left[\frac{j_3}{\rho_2}\right] \tag{2}$$

where $\rho_3(\epsilon - \theta)$ is the mass of air per total soil volume. The conservation of energy equation is

$$\frac{\partial (CT)}{\partial t} = -\nabla \cdot q'' \tag{3}$$

where the volumetric heat capacity C and energy flux q'' are

$$C = \rho_0 c_{v0} + \rho_1(\epsilon-\theta)c_{v1} + \rho_2 c_{v2} + \rho_3(\epsilon-\theta)c_{v3} \tag{4}$$

$$\begin{aligned} q'' &= -k_* \nabla T + h_1 j_1 + h_2 j_2 + h_3 j_3 \\ &= -k_* \nabla T + h_{21} j_1 + h_2 j_w + h_3 j_3 \end{aligned} \tag{5}$$

The vapor density ρ_1 and the partial pressure of the vapor P_1 can be expressed using the relative humidity of the vapor ϕ

$$\rho_1 = \phi \rho_s \tag{6a}$$

$$P_1 = \phi P_s \tag{6b}$$

where ϕ is obtained from a relation derived by Edlefsen and Anderson [6]

$$\phi = \exp\left[\frac{\psi_m(T,\theta)}{R_1 T} + \frac{P - P_0}{\rho_2 R_1 T}\right] \tag{7}$$

The matric potential ψ_m is the negative of the soil suction commonly used in soil science and is a function of temperature and moisture content.

Contributed by the Heat Transfer Division for publication in the JOURNAL OF HEAT TRANSFER. Manuscript received by the Heat Transfer Division March 9, 1984. Paper No. 83-HT-4.

Mass Fluxes

Liquid Flux. A modified form of Darcy's law [7] is used to express the flow of liquid in the form of Philip and DeVries [1]

$$\frac{j_2}{\rho_2} = \frac{-K_s}{\mu_2} K_{rl} \nabla \left(\psi_m + \frac{P}{\rho_2}\right) = -(D_{\theta l}\nabla\theta + D_{Tl}\nabla T + D_{Pl}\nabla P) \qquad (8)$$

Bulk Flow of Vapor and Air. The bulk flow of the air-vapor mixture in the pores is obtained from Darcy's law for gases

$$j_{gb} = -\rho_g K_{rg} \frac{K_s}{\mu_g} \nabla P$$

$$j_{1b} = (\rho_1/\rho_g) j_{gb}; \quad j_{3b} = (\rho_3/\rho_g) j_{gb}$$

Diffusion of Vapor and Air. Fick's law is used to describe the flow of air and water vapor by diffusion. The appropriate forms are [8]

$$j_{1d} = -D_{13}\rho_g \nabla\left[\frac{\rho_1}{\rho_g}\right] = -D_{13}\rho_g\left[\frac{\partial}{\partial\theta}(\rho_1/\rho_g)\nabla\theta + \frac{\partial}{\partial T}(\rho_1/\rho_g)\nabla T + \frac{\partial}{\partial P}(\rho_1/\rho_g)\nabla P\right]$$

$$j_{3d} = -j_{1d}$$

Here D_{13} is the molecular diffusivity of water vapor in air, D_a, modified to account for tortuosity and reduction in flow area.

Total Flow of Vapor and Air. The total flow of vapor is the sum of the bulk flow component and the diffusion component, i.e., $j_1 = j_{1d} + j_{1b}$. In the form of Philip and De Vries [1]

$$\frac{j_1}{\rho_2} = -(D_{\theta v}\nabla\theta + D_{Tv}\nabla T + D_{Pv}\nabla P) \qquad (9)$$

Similarly, for the total flow of air

$$\frac{j_3}{\rho_2} = -(D_{\theta a}\nabla\theta + D_{Ta}\nabla T + D_{Pa}\nabla P) \qquad (10)$$

Total Moisture Flow. The total flow of water is the sum of the liquid flow and vapor flow

$$\frac{j_w}{\rho_2} = \frac{j_1 + j_2}{\rho_2} = -(D_{\theta w}\nabla\theta + D_{Tw}\nabla T + D_{Pw}\nabla P) \qquad (11)$$

Inserting the flux equations (6) and (9)-(11) into the conservation equations (1)-(3) yields

$$\frac{\partial\theta}{\partial t} = \nabla\cdot(D_{\theta w}\nabla\theta + D_{Tw}\nabla T + D_{Pw}\nabla P) \qquad (12a)$$

$$A_1\frac{\partial\theta}{\partial t} + A_2\frac{\partial T}{\partial t} + A_3\frac{\partial P}{\partial t} = \nabla\cdot(D_{\theta a}\nabla\theta + D_{Ta}\nabla T + D_{Pa}\nabla P) \qquad (12b)$$

$$E_1\frac{\partial\theta}{\partial t} + E_2\frac{\partial T}{\partial t} + E_3\frac{\partial P}{\partial t} = \nabla\cdot[\rho_2 h_{21} D_{\theta v}\nabla\theta + (k_* + \rho_2 h_{21} D_{Tv})\nabla T + \rho_2 h_{21} D_{Pv}\nabla P] \qquad (12c)$$
$$-[(c_{p2}D_{\theta w} + c_{p3}D_{\theta a})\nabla\theta + (c_{p2}D_{Tw} + c_{p3}D_{Ta})\nabla T + (c_{p2}D_{Pw} + c_{p3}D_{Pa})\nabla P]\cdot\nabla T$$

Expressions for the diffusivities and A_1, A_2, A_3, E_1, E_2, and E_3 are given in the appendix. The term $k_* + \rho_2 h_{21} D_{Tv}$ is often referred to as the effective thermal conductivity since it includes the effect of vapor flow due to a temperature gradient.

Boundary Conditions

The conservation equations were solved for a one-dimensional semi-infinite soil with an impermeable, constant heat flux source at the boundary. The moisture content, temperature, and pressure distributions are initially uniform. Thus, the following boundary and initial conditions apply:

1 The moisture content, temperature, and pressure at a point far removed from the heat source are constant and equal to the initial values, or

$$\theta(x,t) = \theta_i \text{ as } x \to \infty \qquad (13a)$$

$$P(x,t) = P_i \text{ as } x \to \infty \qquad (13b)$$

$$T(x,t) = T_i \text{ as } x \to \infty \qquad (13c)$$

2 The heat source is impermeable to moisture and air so that

$$j_w = -\rho_2\left[D_{\theta w}\frac{\partial\theta}{\partial x} + D_{Tw}\frac{\partial T}{\partial x} + D_{Pw}\frac{\partial P}{\partial x}\right] = 0 \text{ at } x = x_0 \qquad (14a)$$

$$j_a = -\rho_2\left[D_{\theta a}\frac{\partial\theta}{\partial x} + D_{Ta}\frac{\partial T}{\partial x} + D_{Pa}\frac{\partial P}{\partial x}\right] = 0 \text{ at } x = x_0 \qquad (14b)$$

Nomenclature

C = volumetric heat capacity, J/m^3·K

c_p, c_v = specific heats, J/kg·K

D_a = molecular diffusivity of water vapor in air, m^2/s

D_{13} = modified molecular diffusivity of water vapor in air, m^2/s

$D_{\theta a}, D_{\theta l}, D_{\theta v}$ = isothermal air, liquid, vapor diffusivities, m^2/s

$D_{\theta w}$ = isothermal moisture diffusivity = $D_{\theta l} + D_{\theta v}$, m^2/s

D_{Ta}, D_{Tl}, D_{Tv} = thermal air, liquid, vapor diffusivities, m^2/s·K

D_{Tw} = thermal moisture diffusivity = $D_{Tl} + D_{Tv}$, m^2/s·K

D_{Pa}, D_{Pl}, D_{Pv} = pneumatic air, liquid, vapor diffusivities, m^4/s·N

D_{Pw} = pneumatic moisture diffisivity = $D_{Pl} + D_{Pv}$, m^4/s·N

Fo = Fourier number = $\alpha_0 t/x_r^2$

h = enthalpy, J/kg

h_v = enthalpy of vaporization at 100°C, J/kg

h_{21} = enthalpy of vaporization, J/kg

j = mass flux, a vector, kg/m^2·s

k = thermal conductivity, W/m·K

K_{rg}, K_{rl} = relative permeabilities to gas, liquid

K_s = saturated permeability, m^2

Ko = Kossovich number = $h_{21}\rho_2\epsilon\alpha_0/q'$

Le = Lewis number = $\alpha_0/D_{\theta w}$

P = total pressure, N/m^2

Pn = Posnov number = $D_{Tw}q'/D_{\theta w}k_0\epsilon$

Pn$_p$ = Posnov number based on pneumatic diffusivity = $\dfrac{D_{Pw}q'}{D_{\theta w}\epsilon K_s}\left[\dfrac{\mu_1}{\rho_s h_{21}}\right]_{100^\circ\mathrm{C}}$

q'' = energy flux, a vector, W/m^2

q' = $q_0'' x_r$

R = ideal gas constant, J/kg·K

For a plane heat source x_0 is usually zero; for a cylindrical or spherical heat source x_0 is the radius of the heat source.

3 The heat flux at the surface q_0'' is constant, and the source is impermeable, thus

$$q_0'' = -\left[\rho_2 h_{21} D_{\theta v}\frac{\partial \theta}{\partial x} + (k_* + \rho_2 h_{21} D_{Tv})\frac{\partial T}{\partial x} + \rho_2 h_{21} D_{Pv}\frac{\partial P}{\partial x}\right] \text{ at } x = x_0 \qquad (14c)$$

Interface Conditions at Moving Boundary

Moving boundary problems are formulated by writing governing equations, boundary conditions, and initial conditions in both regions separated by the moving boundary and coupling the two sets of equations with interface conditions at the moving boundary. As an example, consider a two-region melting front problem. The heat equation is written in both the solid and liquid region. Three interface conditions can be written. The temperature at the interface x_f is continuous and equal to the melting temperature T_m

$$T(x_f^-, t) = T(x_f^+, t) \text{ at } x = x_f(t) \qquad (15a)$$

$$T(x_f, t) = T_m \text{ at } x = x_f(t) \qquad (15b)$$

Temperature continuity seems obvious, but its importance will be shown when the drying front problem is formulated. The third interface condition is derived from an energy balance at the interface

$$k_{\mathrm{sol}}\left.\frac{\partial T}{\partial x}\right|_{x_f^+} - k_{\mathrm{liq}}\left.\frac{\partial T}{\partial x}\right|_{x_f^-} = \rho h_{sl}\frac{dx_f}{dt} \qquad (15c)$$

where ρ is the density and h_{sl} is the heat of fusion.

In general, for a two-region *moving* boundary problem with governing equations that are second order in x, the number of interface conditions required is $N_c = 1 + E_1 + E_2$ where E_i is the number of equations in region i. In the melting front problem, $E_1 = 1$, $E_2 = 1$, and $N_c = 3$. If there were no moving boundary, equation (15b) would not be a condition; dx_f/dt in equation (15c) would be zero, and the problem would be reduced to that of two adjoining regions. Since the moving boundary position x_f is variable, another condition is required, equation (15b).

With this background, the formulation of the drying front problem could begin in the same manner. The model often used is shown in Fig. 1. The drying front separates a dry region from a moist region. In formulating the problem it is usually assumed that the soil behind the drying front is completely dry so that the conservation of water mass can be eliminated, leaving two second-order equations, equations (12b) and (12c), in the dry region and three equations, (12a)-(12c), in the wet region. Thus, six interface conditions are required. At the interface, pressure and temperature, but not moisture content, continuity exist, allowing one to write two interface conditions. Three more interface conditions can be derived from air, water, and energy balances, giving a total of five conditions. Another one is not available, and the problem is indeterminant without it. Note that the condition $\theta(x_f^-, t) = 0$ is trivial since the conservation of water mass equation was eliminated on the dry side.

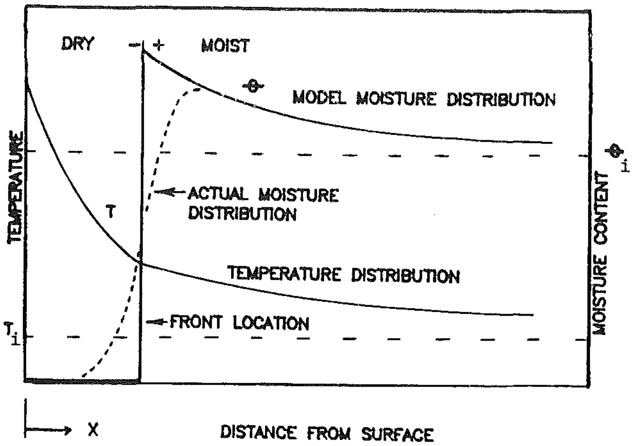

Fig. 1 Possible drying front model

Reconsidering two of the interface conditions from the melting front problem shows why the approach outlined for the drying front problem failed. In the melting front problem the dependent variable T is continuous at the front, and its value at the front T_m is known. A front exists because there is a discontinuity in a property (the internal energy) at T_m. In the attempted formulation of the drying front problem a discontinuity was assumed in a dependent variable θ, rather than a property. The problem could still have been formulated if the moisture content, temperature, or pressure were known at the drying front as the front temperature T_m is known in the melting front problem.

Luikov [9] apparently realized this difficulty and for-

Nomenclature (cont.)

S = saturation = θ/ϵ
t = time, s
T = temperature, K
V_q = volume of soil dried per unit heat input, $\mathrm{m^3/J}$
V_r = reference velocity, m/s
X = dimensionless location
x_r = reference length, m
α = thermal diffusivity, $\mathrm{m^2/s}$
ϵ = porosity, $\mathrm{m^3/m^3}$
θ = volumetric liquid moisture content, $\mathrm{m^3/m^3}$
μ = viscosity, kg/m•s
ρ = density, $\mathrm{kg/m^3}$
ϕ = relative humidity
ψ_m = soil matric potential, J/kg
$\beta_\theta, \beta_p, \beta_T, \delta_1, \delta_2, \delta_3, \delta_4, \delta_5, \eta_1, \eta_2, \eta_3, \gamma_1, \gamma_2, \gamma_3, \nu, \nu_\theta, \nu_p, \nu_T, \tau_1, \tau_2, \tau_3$ = dimensionless coefficients given in appendix

Subscripts

0 = dry, boundary
1, 2, 3 = vapor, liquid, air
b = bulk flow
d = diffusion
f = front
g = air-vapor mixture
i = initial
l = liquid
m = matric, melting
o = reference
r = reference variable
s = saturated vapor
v = vapor
w = water (liquid and vapor)
$_*$ = without mass movement

Superscripts

$+, -$ = ahead, behind front
$*$ = dimensionless

mulated the problem with no moisture content discontinuity. In his earlier works Luikov [4] introduced a quantity called the phase conversion factor ξ. In one-dimensional flow ξ is the ratio of water vapor flux to total water flux. This factor is treated as a property in Luikov's works, and in the drying front formulation it was assumed to undergo a step change at some critical value of the moisture content θ_v. Luikov's formulation included only temperature and moisture content as dependent variables.

The authors have reservations about this formulation from a physical standpoint since it assumes that when the moisture content drops below θ_v all water flow changes instantly from a high liquid fraction to a high vapor fraction. Even if this were acceptable, doubts exist about treating ξ as a property, and the methods used to measure it are not well described. For all of these reasons, the Luikov formulation is not used.

Even if an acceptable moving boundary approach could be formulated a number of serious difficulties would remain. To use the formulation one would solve equations (12*a*)–(12*c*) until the surface moisture content dropped to some arbitrarily selected low moisture content at which the surface would be declared "dry." The moving boundary solution would then be started, and the usual numerical difficulties associated with the initial front velocity would have to be overcome. In addition, as the results of this paper will show, an apparent moist–dry interface moves into the soil well before the surface soil dries. To start the moving boundary solution, the actual moisture distribution, shown as a dashed line in Fig. 1, would be replaced by the discontinuous distribution used in the model, and the moisture content at the front would have to be arbitrarily selected.

In this work a new method which avoids all of the difficulties described above is developed and used. The moisture diffusivities which appear in the governing equations all approach zero smoothly as $\theta \rightarrow 0$. Thus, the rate of drying $\partial\theta/\partial t$ also approaches zero as $\theta \rightarrow 0$, and the soil never completely dries. Drying front movement is predicted by allowing the solution of the governing equations to continue after the soil at the surface of the heat source has reached a near-dry condition. The solutions show that a near-dry zone is separated from a moist zone by a narrow moving region which exhibits a steep moisture content gradient. The front location is taken as the point of maximum slope in the moisture content distribution. Bush [11] reported that a fairly distinct soil color change occurs in the neighborhood of the maximum slope for the sandy silt soil used in this study. The location of this color change is usually recorded as the front location in experimental work.

Order of Magnitude Analysis

In order to evaluate the significance of the individual terms in the governing equations, the equations are nondimensionalized, and an order of magnitude analysis is performed. The moisture content is normalized with respect to the porosity, $S = \theta/\epsilon$, and the temperature is nondimensionalized as

$$T^* = \frac{k_0(T-T_i)}{q'}$$

where $q' = q_0''x_r$, and x_r is a reference length to be described later. The nondimensional pressure is written as

$$P^* = \frac{K_s}{q'}\left[\frac{\rho_s h_{21}}{\mu_1}\right]_{100^\circ\mathrm{C}}(P-P_i)$$

The coordinate x is normalized as $X = x/x_r$, and the dimensionless time is written as a Fourier number

$$\mathrm{Fo} = \frac{\alpha_0 t}{x_r^2}$$

The reference length x_r in cylindrical and spherical coordinates is the radius of the heat source. There is no obvious reference length in rectangular coordinates. If a reference velocity V_r is known, a reference length can be written as $x_r = \alpha_0/V_r$. The reference velocity

$$V_r = \frac{q_0''}{\epsilon\rho_2 h_v}$$

is used in this work for rectangular coordinates, giving a reference length of

$$x_r = \frac{\epsilon\rho_2\alpha_0 h_v}{q_0''}$$

The front position x_f is normalized as

$$X_f^* = \frac{(X_f^{m+1} - X_0^{m+1})}{X_0^m} \bullet \frac{S_i\epsilon\rho_2\alpha_0 h_v}{(m+1)q'}$$

where $m = 0$, 1, 2 for plane, cylindrical, and spherical heat sources, respectively.

After the equations were nondimensionalized, a preliminary order of magnitude analysis was carried out by comparing the magnitudes of the dimensionless coefficients. As a result of these comparisons (see [5] for details), the governing equations can be reduced to

$$\frac{\partial S}{\partial \mathrm{Fo}} = \nabla^*\bullet\left[\frac{1}{\mathrm{Le}}(\nabla^*S + \mathrm{Pn}\nabla^*T^* + \mathrm{Pn}_P\nabla^*P^*)\right] \quad (16a)$$

$$(\tau_2\eta_1+\delta_4)\frac{\partial S}{\partial \mathrm{Fo}} + (\tau_2\eta_2+\delta_5)\frac{\partial T^*}{\partial \mathrm{Fo}} + \tau_2\eta_3\frac{\partial P^*}{\partial \mathrm{Fo}} \quad (16b)$$

$$= \nabla^*\bullet\left[\frac{1}{\mathrm{Le}}(\beta_\theta\nabla^*S + \beta_T\mathrm{Pn}\nabla^*T^* + \beta_P\mathrm{Pn}_P\nabla^*P^*)\right]$$

$$\frac{C}{C_{0o}}\frac{\partial T^*}{\partial \mathrm{Fo}} = \nabla^*\bullet\left[\frac{\mathrm{Ko}\nu_\theta}{\mathrm{Le}}\nabla^*S + \left(\frac{k_*}{k_0} + \frac{\mathrm{KoPn}\nu_T}{\mathrm{Le}}\right)\nabla^*T^* + \frac{\mathrm{Ko}\nu_P\mathrm{Pn}_P}{\mathrm{Le}}\nabla^*P^*\right] \quad (16c)$$

$$+\frac{1}{\mathrm{Le}}[(\gamma_2+\gamma_3\beta_\theta)\nabla^*S + (\gamma_2+\gamma_3\beta_T)\nabla^*T^* + (\gamma_2+\gamma_3\beta_P)\nabla^*P^*]\bullet\nabla^*T^*$$

The boundary conditions become

$$S(X,\mathrm{Fo}) = S_i \text{ as } X\rightarrow\infty \quad (17a)$$

$$P^*(X,\mathrm{Fo}) = 0 \text{ as } X\rightarrow\infty \quad (17b)$$

$$T^*(X,\mathrm{Fo}) = 0 \text{ as } X\rightarrow\infty \quad (17c)$$

$$-\frac{1}{\mathrm{Le}}\left[(\nabla^*S + \mathrm{Pn}\nabla^*T^* + \mathrm{Pn}_P\nabla^*P^*)\right] = 0 \text{ at } X = X_0 \quad (18a)$$

$$-\left[\frac{1}{\mathrm{Le}}(\beta_\theta\nabla^*S + \beta_T\mathrm{Pn}\nabla^*T^* + \beta_P\mathrm{Pn}_P\nabla^*P^*)\right] = 0 \text{ at } X = X_0 \quad (18b)$$

$$-\left[\frac{\mathrm{Ko}\nu_\theta}{\mathrm{Le}}\nabla^*S + \left(\frac{k_*}{k_0} + \frac{\mathrm{KoPn}\nu_T}{\mathrm{Le}}\right)\nabla^*T^* + \frac{\mathrm{Ko}\nu_P\mathrm{Pn}_P}{\mathrm{Le}}\nabla^*P^*\right] = 1 \text{ at } X = X_0 \quad (18c)$$

Expressions for the dimensionless groups in these equations are given either in the nomenclature or the appendix.

Properties

The soil chosen for study was a sandy silt common in the southeastern United States. Undisturbed samples of this soil are typically at a density of 1250 to 1450 kg/m^3, and a density of 1280 kg/m^3 was used in this study. Evaluation of the

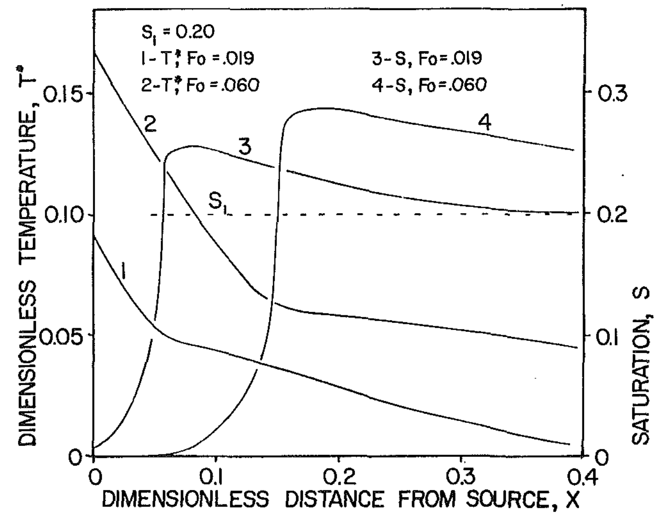

Fig. 2 Dimensionless moisture content and temperature distributions

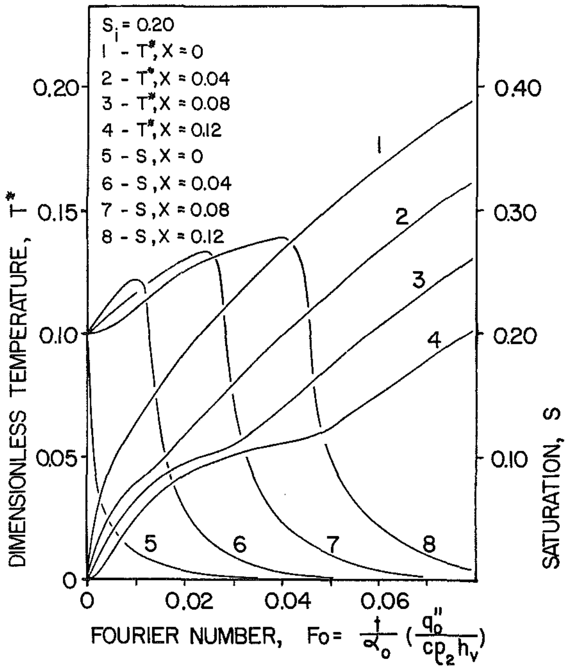

Fig. 3 Dimensionless moisture content and temperature responses

diffusivities and other coefficients which appear in the governing equations requires experimental determination of the saturated permeability and also the thermal conductivity and matric potential over a wide range of moisture contents. These properties were obtained by Drew [12] and Bush [11] and are used here. The relative permeabilities to liquid and gas are also required, and these were calculated using a modified form of the Milington-Quirk method [13] developed in [5]. Details of property calculations can be found in [5].

Results and Discussion

Equations (16*a*)-(16*c*), with the boundary conditions (17*a*)-(18*c*), were solved using an implicit finite difference scheme. The diffusivities which appear in the governing equations are strong functions of moisture content and caused solution stability problems. The problems were eliminated by trying various ΔX and $\Delta \mathrm{Fo}$ combinations until stability was achieved and oscillations were reduced to an acceptable level.

The first numerical solutions indicated that when the initial moisture content and temperature distributions were disturbed only very near the heat source, the pressure disturbance had traveled a great distance into the soil. This indicated that it would be impractical and unnecessary to extend the grid such that the pressure at the last node remained unchanged. For these reasons, the conservation of air mass equation was reduced to $\partial P/\partial t = 0$ and the remaining two conservation equations (16*a*) and (16*c*) were simplified to

$$\frac{\partial S}{\partial \mathrm{Fo}} = \nabla^* \cdot \left[\frac{1}{\mathrm{Le}}\left(\nabla^* S + \mathrm{Pn}\nabla^* T^*\right)\right] \qquad (19a)$$

$$\frac{C}{C_{0o}}\frac{\partial T^*}{\partial \mathrm{Fo}} = \nabla^* \cdot \left[\frac{\mathrm{Ko}\nu_\theta}{\mathrm{Le}}\nabla^* S + \left(\frac{k_*}{k_0} + \frac{\mathrm{KoPn}\nu_T}{\mathrm{Le}}\right)\nabla^* T^*\right]$$

$$+\frac{1}{\mathrm{Le}}\left[(\gamma_2 + \gamma_3\beta_\theta)\nabla^* S + \mathrm{Pn}(\gamma_2 + \gamma_3\beta_T)\nabla^* T^*\right] \cdot \nabla^* T^* \qquad (19b)$$

More numerical simulations were carried out in an effort to further simplify equations (19*a*) and (19*b*). The significance of each term in the equations was evaluated by generating solutions with the coefficient of the term set to zero and then multiplied by 10 for a wide range of heat input–initial saturation combinations. These solutions showed that equation (19*b*) could be simplified to

$$\frac{C}{C_{0o}}\frac{\partial T^*}{\partial \mathrm{Fo}}$$

$$= \nabla^* \cdot \left[\frac{\mathrm{Ko}\nu_\theta}{\mathrm{Le}}\nabla^* S + \frac{\mathrm{KoPn}\nu_T}{\mathrm{Le}}\nabla^* T^* + \frac{k_*}{k_0}\nabla^* T^*\right] \qquad (19c)$$

with little effect on the resulting temperature and moisture content solutions. Equation (19*a*) could not be further simplified.

Hartley [14] concluded that the first term on the right side of equation (19*c*) could also be neglected. This term accounts for the energy flow associated with the water vapor flux due to the moisture content gradient. This vapor flux is opposite in direction to that produced by the temperature gradient. As the moisture content is lowered the drying rate slows and the first two terms on the right side of (19*c*) attain values which are of the same order of magnitude. If low moisture contents are maintained, both of these terms must be retained or an artificially high energy flux results. Hartley did not observe this because he was concerned only with the period of time required for the soil at the heat source surface to dry out. Low moisture contents were not maintained long enough for the effect of eliminating this term to be seen.

Numerical Solutions. Numerical solutions of equations (19*a*) and (19*c*) were carried out for both plane and cylindrical heat sources. Use of the dimensionless variables defined earlier produces solutions which are independent of the surface heat flux for a plane heat source. Typical dimensionless moisture content and temperature distributions resulting from the numerical solutions for a plane source are shown in Fig. 2. As expected, the solutions show that a near-dry region is separated from a moist region by a narrow moving zone which contains a steep moisture gradient. The term near-dry is used because the soil at the surface of the heat source never completely dried under any of the conditions considered, even though surface saturations as low as 2×10^{-6} did result. For convenience, use of the terms "dry" and "dry region" will henceforth refer to soil in the region between the heat source and the drying front location previously defined.

Dimensionless temperature and moisture content responses are shown in Fig. 3 for evenly spaced locations in the soil. The passage of the drying front is indicated by inflections in the temperature response curves at these locations. The inflections in the temperature response curves at the heater surface and interior locations are very useful. By noting the inflections in the responses one can approximately determine the surface drying time and front location.

Plots of normalized front position X_f^* versus Fo are shown in Fig. 4. Before the surface soil dries the value of X_f^* shown merely indicates the location of the maximum slope in the moisture content distribution and probably has no physical significance. After an initial drying period, the drying front moves into the soil at constant velocity, i.e., the soil is dried at a constant rate once the soil at the surface of the heat source is, in effect, dry. The normalized front velocity $dX_f^*/d\mathrm{Fo}$ is given by the slope of the straight-line portion of the curves in Fig. 4. The figure shows that $dX_f^*/d\mathrm{Fo}$ is smaller for higher initial moisture contents. This trend is shown by Fig. 5.

The following equation can be used to describe the results in Figs. 4 and 5

$$\frac{dX_f^*}{d\mathrm{Fo}} = C_1(S_i)$$

where values of C_1 are shown in Fig. 5. Converting this equation back to dimensional form, one can write

$$\frac{1}{q_0''}\frac{dx_f}{dt} = \frac{C_1(S_i)}{S_i \epsilon \rho_2 h_v} = V_q(S_i)$$

In this equation V_q is the volume of soil dried by the passage of the front per unit of heat input at the boundary. Thus, the dimensionless front velocity is a measure of this quantity. Both $dX_f^*/d\mathrm{Fo}$ and V_q decrease as the initial moisture content increases. One expects V_q to decrease as S_i is increased since at higher S_i there is more water per unit volume to be evaporated and moved to the moist side of the front. However, the decrease in $dX_f^*/d\mathrm{Fo}$ is not explained by this effect since it is accounted for in the definition of X_f^*.

Experimental Comparisons. As part of this work a cylindrical soil column was built to simulate one-dimensional linear flow in a semi-infinite moist soil with an impermeable constant flux heat source at the boundary. The sandy silt soil described earlier was used in the experiments. Tests were run with a range of surface heat fluxes and initial moisture contents. Drying front locations were monitored visually while temperatures at evenly spaced locations away from the heat source were also recorded. Despite heavy insulation, radial heat losses which could not be ignored were present; however, these losses were modeled satisfactorily in the numerical solution by applying a fin-type analysis to the soil column.

A typical comparison between temperatures predicted by the numerical solution and the experimental data is shown in Fig. 6. The temperatures from the numerical solution show good agreement with the experimental data at small values of time. However, at larger values of time the surface temperature begins to rise at a faster rate than predicted while temperatures at locations away from the heat source begin to rise at a slower rate. The soil at the heater surface apparently dries sooner than predicted by the numerical solution. The drying front which then begins to move away from the heater surface creates an insulating layer which shields the soil located in the moist region from the heat source, causing the rate of temperature rise to decrease compared to the numerical solution until the front reaches that location. The rate of temperature rise then increases sharply, and an inflection can be seen in the temperature data. The temperature at that location soon rises above that predicted by the numerical solution since the numerical solution predicts that the drying front has not yet reached that location. At a location 12.7 mm from the heat source in Fig. 6 the inflection in the numerical solution for this location does not occur until approximately 180 min. The same type of behavior is exhibited by the data and numerical solution at 25.4 mm from the heat source.

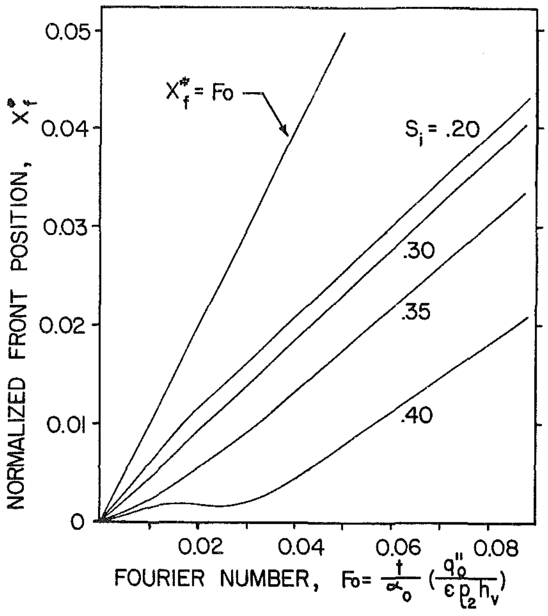

Fig. 4 Normalized front position versus Fourier number

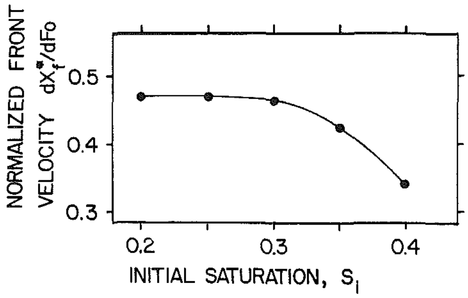

Fig. 5 Normalized front velocity dependence on initial moisture content

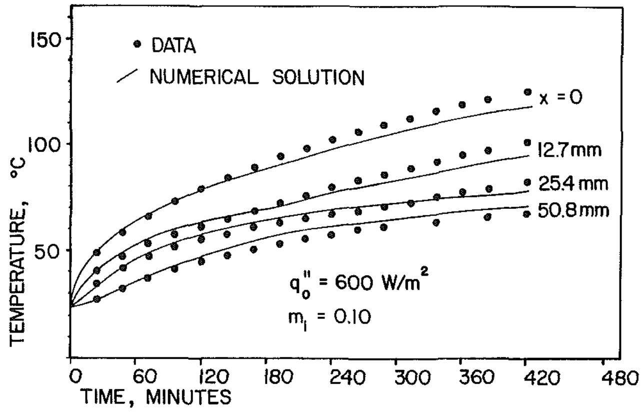

Fig. 6 Comparison of experimental temperature data and numerical solution

The comparison between predicted and observed front location data in Fig. 7 shows clearly the results indicated by the temperature comparisons, i.e., the numerical solution predicts a lower rate of drying front movement than observed experimentally.

From these comparisons one can conclude that the model underestimates the rate of moisture movement somewhat. However, the results are certainly qualitatively correct. The shapes of the experimental and numerical temperature

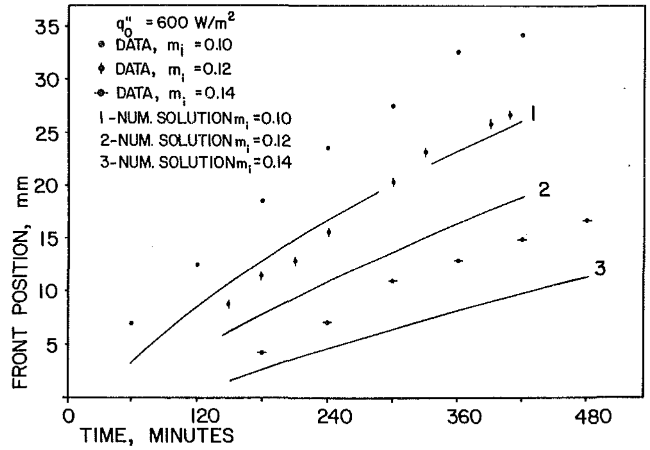

Fig. 7 Comparison of experimental front location data and numerical solution

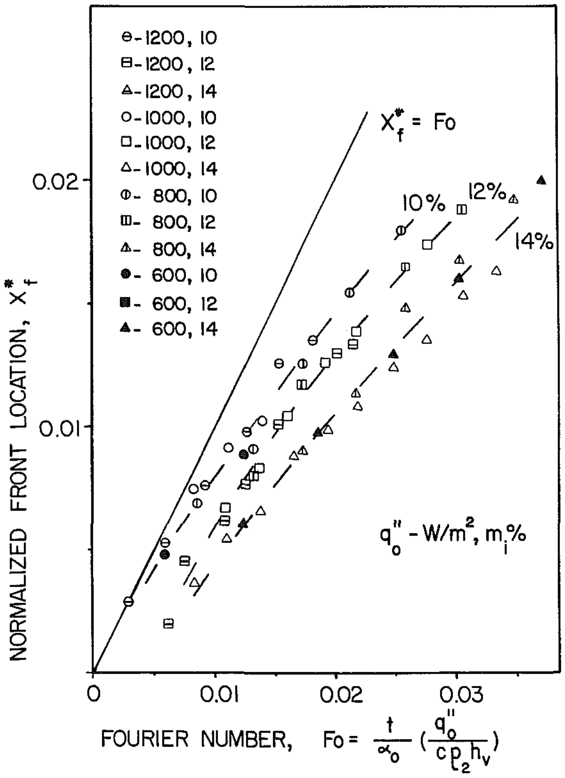

Fig. 8 Normalized experimental front location data

response curves and the plots of front positive versus time are distinctly similar.

More evidence of the qualitative correctness of the model can be seen in Fig. 8. The experimental front location data are normalized in the same manner as the numerical solutions. The moisture contents 10, 12, and 14 percent of dry soil weight plotted in the figure correspond to saturation fractions of 0.25, 0.30, and 0.35, respectively. The figure shows that the normalized front velocity is apparently independent of surface heat flux for rectangular coordinates as indicated by the governing equations. Heat losses from the apparatus cause the data to deviate somewhat from the straight-line relationship predicted by the numerical solutions shown in Fig. 4; otherwise, the two figures exhibit the same trends. In particular, the slope $dX_f^*/d\mathrm{Fo}$ decreases as the moisture content increases as it does in Fig. 4 for saturation fractions in the same range.

Conclusions

As a result of this work, the following conclusions can be made:

1 If the coefficients which relate the flow of liquid water and water vapor to the gradients of moisture content, temperature, and pressure are properly described, solution of the governing equations presented in this paper properly predicts the movement through the soil of a narrow zone with a steep moisture gradient. This narrow zone separates a near-dry region from a moist region. This is done *without* resorting to the usual moving boundary approaches. There are a number of advantages to this new approach over a moving boundary approach:

- The new approach eliminates the need to arbitrarily select some minimum moisture content at which the soil at the surface is declared dry and the change to a moving boundary formulation is made.
- Numerical difficulties with starting a moving boundary solution are eliminated.
- The solutions show that an apparent "moist-dry" interface begins to move into the soil well before soil at the surface of the heat source is normally considered to be dry. Thus, the interface position predicted by the moving boundary solution would be less than that predicted by this approach.

2 In regions of the soil where low moisture contents exist the energy equation cannot be written as simply the heat conduction equation with an effective thermal conductivity which includes a contribution due to vapor movement caused by temperature gradients. Instead, it is necessary to retain the term which represents energy transport due to a vapor movement caused by moisture content gradients.

3 The time at which the drying front begins to move away from the heated surface can be approximately determined by inspection of the surface temperature response curve since a fairly distinct change in slope occurs as the soil dries. The time at which the front passes any position away from the heated surface can also be approximated in this manner since the temperature response curve at such position also exhibits a change in slope when the front passes.

4 For the sandy silt used in this study with a given surface heat flux and initial moisture content the following statements can be made:

After an initial drying period, the drying front, defined as the location of the maximum slope in the moisture content distribution, moves through the soil at a rate such that the volume of soil dried per unit heat input V_q at the boundary is a constant. For a plane heat source V_q is a function of initial moisture content, and it decreases as the initial moisture content is increased.

Acknowledgments

This work was supported by the National Science Foundation and the Electric Power Research Institute on project numbers ENG 78-09244 and RP 78883-1, respectively. The authors are grateful for the support of these organizations.

References

1 Philip, J. R., and DeVries, D. A., "Moisture Movement in Porous Media Under Temperature Gradients," *Trans. Am. Geophysical Union*, Vol. 38, 1957, pp. 222–232.

2 Cary, J. W., and Taylor, S. A., "Thermally Driven Liquid and Vapor Phase Transfer of Water and Energy in Soil," *Soil Sci. Soc. of Am. Proc.*, Vol. 26, 1962, pp. 417–420.

3 Harmathy, T. Z., "Simultaneous Moisture and Heat Transfer in Porous Systems With Particular Reference to Drying," *Ind. and Eng. Chem. Fund.*, Vol. 8, pp. 92–103.

4 Luikov, A. V., "Heat and Mass Transfer in Capillary-Porous Bodies,"

Advances in Heat Transfer, Vol. 1, T. F. Irvine and J. P. Harnett, Eds., Academic Press, New York, 1964, pp. 123–183.

5 Couvillion, R. J., "Heat and Mass Transfer in a Semi-infinite Moist Soil With a Drying Front Present," Ph.D. Thesis, Georgia Institute of Technology, School of Mechanical Engineering, Dec. 1981.

6 Edlefsen, N. E., and Anderson, A. B. C., "Thermodynamics of Soil Moisture," *Hilgardia*, Vol. 15, 1943, pp. 31–298.

7 Childs, E. C., and Collis-George, N., "The Permeability of Porous Materials," *Proc. of the Royal Soc.-A*, Vol. 201, 1950, pp. 392–405.

8 Bird, R. B., Stewart, W. E., and Lightfoot, E. N., *Transport Phenomena*, Wiley, 1960.

9 Luikov, A. V., *Theory of Drying*, Energiya, Moscow, 1968.

10 Mikhailov, M. D., "Exact Solution of Temperature and Moisture Distributions in a Porous Half-Space With Moving Evaporation Front," *Int. J. Heat and Mass Trans.*, Vol. 18, 1975, pp. 797–804.

11 Bush, R. A., "An Empirical Study of the Conditions Leading to Thermal Instability of Soils Used as Cable Backfill," Georgia Power Company Research Report, 1977.

12 Drew, B. C., and Hartley, J. G., "An Experimental Investigation of the Thermal Stability of Soils Subject to a Constant Heat Transfer Rate," presented at the ASME Winter Annual Meeting, Washington, D.C., November 15–20, 1981.

13 Millington, R. J., and Quirk, J. P., "Permeability of Porous Solids," *Trans. Faraday Society*, Vol. 57, 1961, pp. 1200–1207.

14 Hartley, J. G., "An Analysis of the Thermal Stability of the Soil Environment of Underground Electric Cables," Ph.D. Thesis, Georgia Institute of Technology, Aug. 1977.

15 Carslaw, H. S., and Jaeger, J. C., *Conduction of Heat in Solids*, 2nd edn., Oxford University Press, New York, 1959, pp. 283–296.

APPENDIX

Coefficients in Equations (12*a*)–(12*c*)

$$E_1 = P - \phi\rho_s h_{21} + (\epsilon-\theta)\rho_s h_{21}\,\frac{\partial\phi}{\partial\theta}$$

$$E_2 = C + \frac{P(\epsilon-\theta)}{T} + h_{21}(\epsilon-\theta)\left(\frac{\phi d\rho_s}{dT} + \rho_s\,\frac{\partial\phi}{\partial T}\right)$$

$$E_3 = (\epsilon-\theta)\left(\frac{\phi\rho_s h_{21}}{\rho_2 R_1 T} - 1\right)$$

$$A_1 = -\left[(\epsilon-\theta)\frac{R_1}{R_3}\,\frac{\rho_s}{\rho_2}\,\frac{\partial\phi}{\partial\theta} + \frac{P}{\rho_2 R_3 T} - \frac{\phi\rho_s}{\rho_2}\,\frac{R_1}{R_3}\right]$$

$$A_2 = -(\epsilon-\theta)\left[\frac{P}{\rho_2 R_3 T^2} + \frac{R_1}{R_3}\,\frac{\phi}{\rho_2}\,\frac{d\rho_s}{dT} + \frac{R_1}{R_3}\,\frac{\rho_s}{\rho_2}\,\frac{\partial\phi}{\partial T}\right]$$

$$A_3 = \frac{(\epsilon-\theta)}{\rho_2 R_3 T}\left[1 - \frac{\phi\rho_s}{\rho_2}\right]$$

Expressions for Diffusivities

$$D_{\theta v} = \frac{\nu\rho_s}{\rho_2}D_{13}\,\frac{\partial\phi}{\partial\theta} \qquad D_{\theta a} = -D_{\theta v}$$

$$D_{Tv} = \frac{\nu\rho_s}{\rho_2}D_{13}\left(\phi\frac{h_{21}}{R_1 T^2} + \frac{\partial\phi}{\partial T}\right) \qquad D_{Ta} = -D_{Tv}$$

$$D_{Pv} = \frac{\nu\phi\rho_s}{{\rho_2}^2 R_1 T}D_{13}\left(1 - \frac{\rho_2 R_1 T}{P}\right) + \frac{\phi\rho_s}{\rho_2}\,\frac{K_s}{\mu_g}\,K_{rg}$$

$$D_{Pa} = \frac{\nu\phi\rho_s}{{\rho_2}^2 R_1 T}D_{13}\left(\frac{\rho_2 R_1 T}{P} - 1\right) + \frac{(P-\phi P_s)}{\rho_2 R_3 T}\,\frac{K_s}{\mu_g}\,K_{rg}$$

$$D_{\theta l} = \frac{K_s}{\mu_2}\,K_{rl}\frac{\partial\psi_m}{\partial\theta} \qquad D_{Tl} = \frac{K_s}{\mu_2}\,K_{rl}\frac{\partial\psi_m}{\partial T}$$

$$D_{Pl} = \frac{K_s}{\rho_2\mu_2}K_{rl} \qquad \rho_g = \rho_1 + \rho_3 \qquad \rho_3 = \frac{P-P_1}{R_3 T}$$

$$\nu = 1 - \left(1 - \frac{R_1}{R_3}\right)\frac{\rho_1}{\rho_g}$$

Unnamed Dimensionless Groups

$$\nu_\theta = D_{\theta v}/D_{\theta w} \qquad \nu_T = D_{Tv}/D_{Tw} \qquad \nu_P = D_{Pv}/D_{Pw}$$

$$\beta_\theta = D_{\theta a}/D_{\theta w} \qquad \beta_T = D_{Ta}/D_{Tw} \qquad \beta_P = D_{Pa}/D_{Pw}$$

$$\gamma_2 = \epsilon\rho_2 c_{p2}/C_{0o} \qquad \gamma_3 = \epsilon\rho_2 c_{p3}/C_{0o}$$

$$\tau_1 = \phi\rho_s/\rho_2;\ \ \tau_2 = R_1/R_3;\ \ \tau_3 = h_{21}/R_1 T$$

$$\eta_1 = (1-S)\,\frac{\rho_s}{\rho_2}\,\frac{\partial\phi}{\partial S} - \tau_1$$

$$\eta_2 = \frac{q'(1-S)}{k_0 T}\,\tau_1\left[\tau_3 - 1 + \frac{1}{R_1}\left(\frac{\partial\psi}{\partial T} - \frac{\psi}{T}\right)\right]$$

$$\eta_3 = \frac{(1-S)q'}{K_s\rho_2 R_1 T}\bullet\left[\frac{\mu_1}{\rho_s h_{21}}\right]_{100^\circ\mathrm{C}}$$

$$\delta_1 = \frac{P\epsilon\alpha_0}{q'};\ \ \delta_2 = \frac{P(\epsilon-\theta)}{C_{0o}T};\ \ \delta_3 = \frac{(\epsilon-\theta)\alpha_0}{K_s}\bullet\left[\frac{\mu_1}{\rho_s h_{21}}\right]_{100^\circ\mathrm{C}}$$

$$\delta_4 = \frac{P}{\rho_2 R_3 T};\ \ \delta_5 = \frac{(1-S)q'P}{k_0\rho_2 R_3 T^2}$$

Natural Convection Characteristics of Pool Penetration Into a Melting Miscible Substrate

M. Epstein
Mem. ASME

M. A. Grolmes
Mem. ASME

Fauske & Associates, Inc.,
Burr Ridge, IL 60521

Experiments were performed to gain an understanding of the convective heat transfer process occurring in a warm liquid pool as it penetrates into an underlying meltable solid of less dense material, for the case where the molten phase of the solid and pool liquid are mutually miscible. Previous experimental work on downward melting penetration made use of warm aqueous salt solution pools overlying solid polyethylene glycol (PEG) or ice, or pools of heated organic liquids with benzene as the frozen substrate. Owing to the complexity of the melting trends observed in these studies, particularly with PEG substrates, a sufficiently definitive theory of the phenomenon has not yet emerged. As part of the present study, an attempt was made to reproduce the previous experimental results for salt-solution-pool penetration into PEG. An unexpected strong effect of initial solid PEG temperature on melting rate was uncovered for this polymer material. It was found that the unconventional melting trends reported previously at high pool-to-substrate density ratios could be eliminated if careful control of the initial PEG temperature is maintained. These new experimental data indicate that the melting of PEG by an overlying pool of heavier salt solution has much in common with classical, turbulent, thermal convection above a horizontal surface. Additional experiments were conducted which seem to support this conclusion for other pool-substrate material pairs as well.

Introduction

The subject of natural convection flow above a horizontal surface bounded by an extensive body of fluid is an important meteorological problem that has received considerable attention in the past. A comparatively recent development in the field of buoyant convection from a horizontal surface has been the study of the melting of a solid by a heavier overlying hot liquid pool, for the situation in which the molten phase of the solid is miscible with the pool material. Melting of this type is of interest in the design of postaccident core-retention systems for nuclear reactors. A crucible or ladle ("sacrificial bed") of MgO brick is an example of such a system. Following a hypothetical core disruptive accident in a nuclear reactor, molten fuel or fuel-steel mixture may come in contact with the horizontal surface of the sacrificial bed material which, when molten, is miscible with the overlying fuel pool material. The ability to predict the downward rate of penetration of the molten pool into the melting sacrificial material is essential to the design of a core-retention system.

Farhadieh and Baker [1] were apparently the first to experimentally investigate the melting rates and convective motions that can arise within a hot pool above a melting substrate which is miscible with the pool material. These workers used a frozen slab of polyethylene glycol 1500 (PEG 1500) under a heated pool of KI salt solution. Many different effects were observed with this system, the most important of which are illustrated in Fig. 1. A well-defined melt layer of substrate material exists between the melting solid and the liquid pool. The interface between the melt layer and the liquid pool is sharp on the scale of the thickness of the melt layer, indicating that little or no mixing takes place adjacent to the melting surface. Narrow columns or fingers of melt material extend into the overlying heavier solution from discrete sites at the melt film pool interface. These fingers are essentially buoyant plumes that continuously inject melt material into the liquid pool. Large and small convective cells can be seen at the outer edge of the fingers, which produce vigorous mixing between the melt and pool materials so that the pool temperature varies markedly only in a thin "conduction layer" just above the substrate surface.

Based on the visual observations of Farhadieh and Baker, the physical process of heat transfer from a warm pool to a melting horizontal substrate miscible with the pool material would seem to have much in common with high Rayleigh number thermal (natural) convection within a layer of pure fluid above a heated, horizontal surface. Laboratory observations of turbulent thermal convection show clearly that plumes (thermals) of hot fluid are generated from point sources just above the surface [2, 3] and show the existence of a boundary layer close to the surface with an approximately linear temperature drop across it [4]. Over the body of the fluid layer the temperature is found to be essentially constant. It follows that the actual depth of the fluid layer is irrelevant

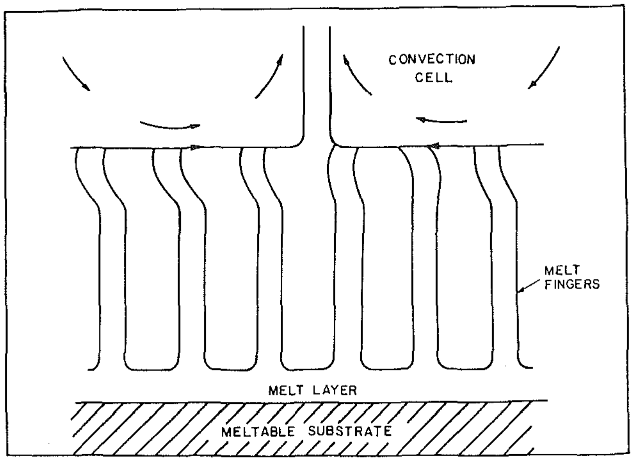

Fig. 1 **Illustration of observed fluid motions within a warm liquid pool overlying a melting miscible substrate**

Contributed by the Heat Transfer Division and presented at the 33rd National Heat Transfer Conference, Denver, CO, August 1985. Manuscript received by the Heat Transfer Division October 22, 1984.

during strong convection conditions, and the heat flux from the plate is proportional to the product of the Rayleigh number (or fractional decrease in fluid density) to the 1/3 power and the temperature difference between the surface and the fluid. It would seem that this result should also be true for the "turbulent downward heat flux" or melting velocity v_m in miscible systems; i.e., $v_m \sim (\Delta\rho/\rho_m)^{1/3} \cdot \Delta T$, where ΔT is the difference between the pool temperature and the substrate melting temperature ("pool superheat") and $\Delta\rho$ is the pool density ρ minus the melt layer density ρ_m. Most of the previous work on melting of a substrate beneath a warm pool, however, suggests that the pool penetration process *cannot* be interpreted in terms of classical natural convection theory.

Farhadieh and Baker [1] observed the melting rate of PEG 1500 to be quite sensitive to the fractional difference in density between the pool and PEG 1500 melt, $\Delta\rho/\rho_m$, which was varied in their experiment by changing the salt concentration in the liquid pool. The variations of v_m with $\Delta\rho/\rho_m$ were observed to occur in stages. For density ratios $\Delta\rho/\rho_m < 0.08$, the observed melting velocities were small and only weakly dependent on $\Delta\rho/\rho_m$ and a laminarlike convection regime was in evidence. At $\Delta\rho/\rho_m \cong 0.08$ there was an abrupt jump in the melting rate, followed by a more gradual increase in the melting rate in accord with $v_m \sim (\Delta\rho/\rho_m)^{1/3}$, i.e., ordinary turbulent natural convection. Above $\Delta\rho/\rho_m = 0.25$, however, the melting velocity was found to increase according to $v_m \sim (\Delta\rho/\rho_m)^{4/3}$, a convection regime which Farhadieh and Baker labeled "upper turbulent." They also examined the effect of variation of the pool temperature on the downward melting rate in the upper turbulent convective regime. The melting rate was found to increase sharply with increasing pool temperature and fits a relation of the form $v_m \sim (\Delta T)^{1.6}$.

Similar work with PEG 1500 substrate material was carried out by Eck and Werle [5], but with aqueous $ZnBr_2$ or NaBr as the pool material. They found a strong variation of the melting velocity with $\Delta\rho/\rho_m$, similar to the trend observed by Farhadieh and Baker, although large quantitative differences between the results of the two studies were noted. The melting velocity was found to increase nearly linearly with ΔT.

The work of Farhadieh and Baker [1] and Eck and Werle [5] is in contrast with the work of Catton et al. [6] who found the melting rate to be independent of the imposed temperature difference between the pool and substrate melting temperature ΔT. Catton et al. used frozen benzene as the meltable substrate material and carbon tetrachloride (CCl_4) or diiodomethane (CH_2I_2) as the liquid pool material to study the effects of ΔT and $\Delta\rho/\rho_m$, respectively. These material pairs allowed their study to focus on the high pool-to-substrate density ratios in the range $0.72 < \Delta\rho/\rho_m < 2.26$.

An extensive laboratory study of the melting of horizontal slabs of ice placed beneath various pools of salt solution (KI, Na, Cl, $MgCl_2$, or $CaCl_2$) was recently reported by Fang et al. [7]. They studied the effects of the density ratio $\Delta\rho/\rho_m$ on the ice melting rate, the pool convection pattern, and the melting interface morphology. While not specifically mentioned in the paper by Fang et al., their observed melting rate dependence on pool density for $\Delta\rho/\rho_m > 0.08$ is well represented by the classical form $v_m \sim (\Delta\rho/\rho_m)^{1/3}$. The upper turbulent regime described by Farhadieh and Baker was not observed.

It is clear from the discussion in the foregoing that several different trends have been reported with these seemingly simple experiments on pool penetration into meltable substrates. Most of the experimental data on ice melting are compatible with what is known for ordinary natural convection induced by a temperature difference. However, most of the trends obtained with PEG 1500 and benzene substrates are difficult to interpret in terms of classical natural convection theory.

The primary goal of this study is to develop, through careful experiments, an understanding of the mechanism by which a warm liquid pool penetrates into an underlying meltable solid of less dense material at large pool-to-substrate density ratios and, therefore, under turbulent convection conditions. As part of the present investigation, an attempt was made to reproduce the results of Farhadieh and Baker [1] for KI salt solution over PEG 1500. An unexpected effect of initial frozen PEG temperature on melting rate was uncovered for this polymer material. It became apparent that the unconventional melting velocity trends reported in [1, 5] in the turbulent flow regime could be eliminated if careful control of the initial PEG temperature is maintained. It was postulated that the experimental results [1, 5] reflect the fact that the latent heat of melting of the polymeric PEG 1500 varies in a nearly exponential (or Arrhenius) manner with its temperature. This idea could not be accepted without careful checking and part of the experimental program was devoted to calorimetry work with PEG 1500. The calorimetry data together with the melting rate data show that the penetration of PEG 1500 substrates by overlying pools of heavier salt solution is largely a matter of the melt-film flow within the boundary layer at the substrate surface; that is, the process appears to be quite similar to the turbulent thermal convection above a horizontal surface. Additional experiments were conducted which seem to support this conclusion for other material pairs.

Experimental Apparatus and Procedures

The experiments were performed with various pool-substrate material pairs: KI salt solution overlying frozen polymeric PEG 1500 and ice, $ZnBr_2$ salt solutions overlying frozen glycerol and ice, and a limited number of experiments involving CCl_4 overlying frozen benzene. The initial density of the salt solution pools was varied by changing the solution concentration. The initial CCl_4 pool density was fixed in all runs at the value for pure CCl_4.

The heart of the experimental apparatus is the test cell in which the melting takes place. In addition to the test cell itself, the apparatus includes auxiliary systems for measuring the initial temperature of the frozen substrate, the temperature of the test cell walls, the instantaneous temperature of the liquid pool, and the instantaneous melt front advance rate.

A schematic diagram of the test cell is presented in Fig. 2. The test section was made up of two parts. The lower "see-through part" consists of two concentric lucite cylinders, between which a vacuum was applied during the experiment to minimize radial heat flow. The lower section is, in actuality, a mold for freezing the lower, substrate material in place prior to an experiment. For this purpose a clean metal plate was used for the bottom of the lower section from which solidification of the substrate material was initiated. The

Nomenclature

v_m = melting velocity
ΔT = temperature difference between pool and melting temperature of substrate (pool superheat)
ΔT_{sub} = temperature difference between melting temperature of substrate and initial substrate (solid subcooling)
$\Delta\rho$ = density difference between the pool and the substrate melt material
ρ = density of pool liquid
ρ_m = density of molten substrate material

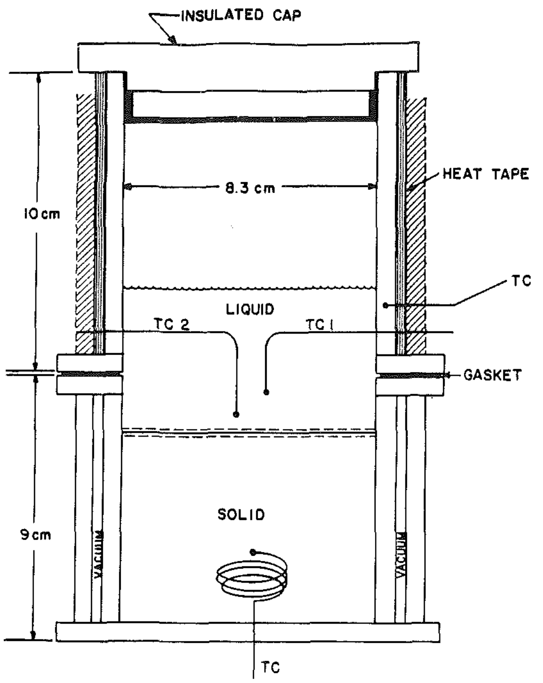

Fig. 2 Test apparatus for melting rate determination

upper part of the test section is a single-walled lucite cylinder which was wrapped with heating tapes and insulating material.

Prior to any experiments, about 250 cm^3 of melted substrate material was poured into the double-walled, lower section. Freezing of this material was then initiated, making use of the lower metal plate to freeze from below. The method of freezing depended very much on the particular substrate material being tested. The details concerning the preparation of the various frozen substrates are given at the end of this section. To insure that the prepared substrate had a uniform initial temperature before the melting experiment, the lower section was placed in a constant-temperature environment maintained at the desired initial temperature. Just before each run, to minimize heat loss from the convecting liquid pool to the side wall of the test section, the upper cylinder was heated with its heat-tape wrapping until its temperature reached the desired pool temperature. The upper cylinder was then placed on top of the double-walled section and the connection of these cylinders was made tight by means of flanges and an intervening gasket. The liquid pool material at the desired density and temperature was poured over the frozen substrate to initiate the melting process. Special care was taken as the pool liquid was poured over the substrate to prevent nonuniform melting of the substrate surface. Two thermocouple wires were passed through the walls of the upper part of the test section and into the liquid pool to monitor its temperature history. The thermocouple measurements always indicated a spatially uniform bulk pool temperature.

Using a video camera with a built-in timer, a movie was taken of the density-driven convective flow field within the lower portion of the pool, which can be viewed through the double-walled part of the test section. A rule with 1.0-mm markings was affixed to the outside of the inner wall of the test section so that the instantaneous position of the melting substrate surface can be determined from the movie. This, together with the video camera's clock, made it possible to compute the instantaneous melt front advance rate.

The procedure for making frozen slabs of PEG 1500 was to pour about 250 g of melted PEG into the lower, double-walled section of the test cell. This section was then placed in an oven within which the temperature was set to a value just below the freezing point of PEG 1500 (T_{mp} = 46.5°C). The PEG was allowed to freeze slowly overnight. After the freezing was completed, the PEG was remelted by raising the oven temperature and then it was refrozen once more. This procedure of repeated solidification was found to result in PEG substrates of reasonably high purity; they were uniform in color and free of bubbles or cracks, with smooth flat surfaces. Finally, the oven containing the frozen PEG was set at the desired initial temperature. A thermocouple was embedded in the PEG to indicate when the frozen PEG reached equilibrium with the oven temperature.

The freezing of glycerol, melting point 18°C, in the double-walled lucite mold was time consuming at first because this substance belongs to the class of organic compounds that are extremely difficult to nucleate. The glycerol was rapidly cooled to a low temperature by placing the mold on top of a slab of dry ice. This did not result in crystallization of the glycerol, but, instead, it hardened into a highly supercooled "glass." The mold was then placed in a freezer maintained at −5°C where the glycerol was allowed to slowly warm and crystallize. Apparently the maximum crystallization velocity of glycerol lies between −5°C and the dry ice temperature of −76°C. At −76°C the crystallization velocity must be extremely low as no glycerol crystals were noted after waiting for about two days. Additional slabs of frozen glycerol were made in the freezer directly, bypassing the "dry-ice step," by using crystals of the glycerol itself as nucleating agents. Glycerol has the virtues of not trapping or dissolving air and of not cracking or funneling during solidification.

In contrast with glycerol, water and benzene showed a strong tendency to trap and dissolve air upon freezing. Preliminary experiments with benzene beneath CCl_4 pools revealed two major difficulties. Large quantities of gas were released from the benzene solid as the melting proceeded. It is very likely that this vigorous gas evolution resulted in stirring of the overlying pool and thus strongly affected the heat transfer rate at the melting benzene surface. The second difficulty was the appearance of a solid deposit along the wall of the test section left behind by the melting benzene interface. Because of this behavior the position of the melt front could not be optically measured with any accuracy. Perhaps this is the reason that in previous work with the CCl_4-benzene system [6] the melt front displacement rate was not measured through optical means and, instead, was inferred from pool heat balance considerations (see the next section). The first measure employed to prevent the entrapment of bubbles of dissolved gas during the freezing process was to scrape the interface with a wooden spoon at frequent intervals. This method was only partially successful. An additional assist in reducing the level of trapped gas within the frozen benzene was provided by periodically replacing the cold, gas-saturated benzene melt within the mold with fresh room-temperature benzene. Not only did this procedure greatly reduce the continuous release of gas at the benzene interface during melting, but, interestingly enough, it also accomplished the objective of eliminating the opaque deposit along the test section wall. Homogeneous, bubble-free ice substrates were also prepared in this manner.

Data Reduction

A typical plot of the melt interface displacement versus time, as determined from the video camera, is shown in Fig. 3. To limit the pool density and temperature change as a result of dilution due to substrate melting, melting penetration measurements were based on experiment run times of no more than a few minutes. After a short initial transient period that can be associated with the pouring of the heated pool material, the interface displacement curve is seen to be linear with time for about 150 s from the start of the run, indicating

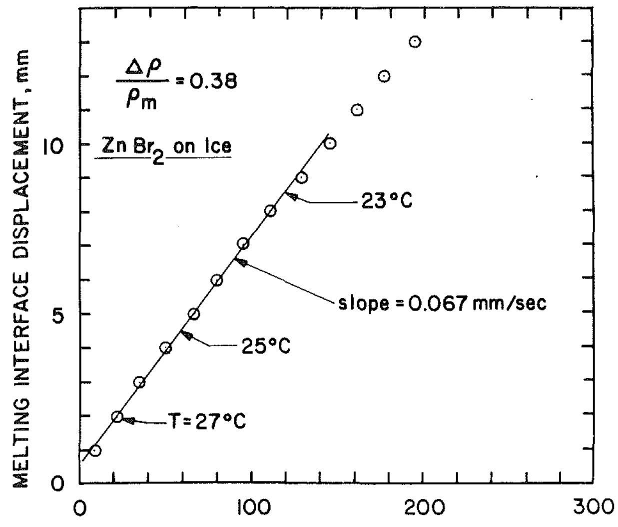

Fig. 3 Typical melting interface displacement history, indicating the pool temperature variation with time

that a quasi-steady melting regime is established. A best fit slope was superimposed upon this linear portion of the interface displacement-time plot, and the downward melting velocity was thus calculated.

It may also be observed from Fig. 3 that there is a change in slope in the interface displacement-time plot at a later time. This change in slope can be related to the fact that the pool temperature is changing during the course of a run. The pool temperature at various times is indicated on the interface location curve in Fig. 3. As will be illustrated shortly, the melting rate is relatively insensitive to changes in pool density, but varies linearly with pool temperature. Experiments of relatively long duration or with shallow pools show that the interface displacement-time plot is, in actuality, a continuous curve of gradually decreasing slope. However, over a narrow range of pool temperatures, the curves display a linear trend from which a melting velocity can be inferred. It is noted in Fig. 3, for example, that a melting velocity of $v_m = 0.067$ mm/s is associated with a pool temperature range 23–27°C. In the actual reporting of the data, this melting velocity was identified with the average pool temperature over the linear portion of the interface displacement curve, i.e., $T = (27 + 23)/2 = 25$°C.

In some experiments, particularly with relatively shallow pools (~ 7 cm in height), the melting interface displacement-time curve could be divided up into several linear segments from which a corresponding number of melting velocity-pool temperature data points were obtained. The specification of the beginning and the end of a linear segment may seem somewhat arbitrary. However, for a given pool-substrate material pair and fixed experiment run time, the melting velocity-pool temperature data point taken from a deep pool (~ 14 cm in height) was very consistent with the data points obtained from a smaller pool. With decreasing pool size, the decrease in the bulk pool temperature during the course of a run is larger and, therefore, the smaller pool generally produces an interface displacement curve which can be approximated by several linear segments, as opposed to just one for a larger pool. The fact that the data from both large and small pools were found to lie on the same melting velocity versus pool temperature curve affirms the insensitivity of the melting rate data to the manner in which the linear slopes are assigned to the melting interface displacement curve. This also indicates that the melting rate response to changing pool conditions is best characterized as "quasi-steady."

As mentioned previously, an alternative way of determining the downward melting rate was employed by Catton et al. [6] in their study of benzene melting. The benzene melting rate was determined by measuring the time rate of change of pool temperature dT/dt. The value of dT/dt was obtained by a linear fit to the pool temperature-time data. The substrate melting rate for a well-insulated system can be related to dT/dt by an energy balance applied to the convecting pool. In the work of Catton et al., the heat released (or absorbed) in the mixing of the substrate and pool materials was not considered in the data reduction process. Because an anomalously low time rate of change (decrease) of pool temperature was obtained in preliminary experiments with KI over PEG and with ZnBr$_2$ over ice, presumably caused by strong heat of mixing effects within the bulk of the pools, it was decided to measure the movement of the melting interface directly. In the opinion of the present authors, this volumetric evolution of heat does not affect the melting process in a major way, since the heat is not released in the immediate neighborhood of the melting interface. Recall that the melt fingers are observed to rise some distance above the melting surface before they mix with the convecting pool. Furthermore, all the substrate-pool material pairs examined in the present study exhibited the same melting rate versus pool temperature trend, despite the fact that the volumetric evolution of heat is very large for some of these pairs and rather small for others. As already mentioned, the pool temperature-time data exhibit a rather strong heat of mixing effect for the KI pool-PEG substrate and the ZnBr$_2$ pool-ice substrate pairs. The data show a moderate heat of solution effect for the ZnBr$_2$ pool-glycerol substrate pair. The heat of solution effect for the KI pool-ice substrate and the CCl$_4$ pool-benzene substrate pairs can be regarded as negligible, in that the melting velocities determined from the energy balance method are in reasonable agreement with those obtained visually for these two material pairs.

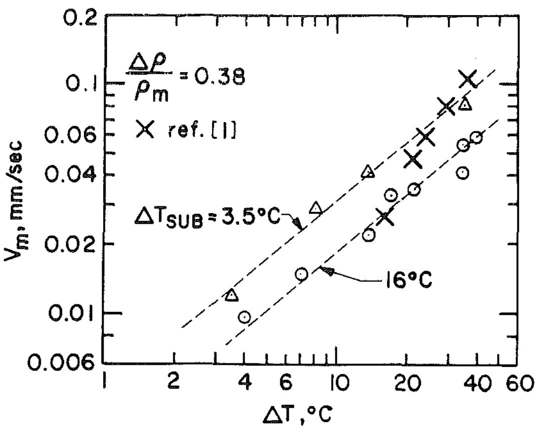

Fig. 4 Measured penetration rate of KI solution pools into polyethylene glycol 1500 substrates as a function of pool superheat; the subcooling of the substrate is a constant parameter in the data (△, ○) of this study

Experimental Results and Discussion

As in the experimental studies of Farhadieh and Baker [1], Catton et al. [6], and Fang et al. [7], the movies made in this study indicated a very thin layer of melted substrate between the melting substrate surface and the warm overlying pool. As in the work cited in these references, narrow columns or fingers of melt material were observed to extend into the overlying heavier pool from sites at the melt film-pool interface.

The Effects of Pool Temperature and Solid Subcooling on the Melting Rate of PEG 1500. Twenty-three experiments on the penetration of aqueous KI solution into melting PEG 1500 were performed covering a variety of initial PEG tem-

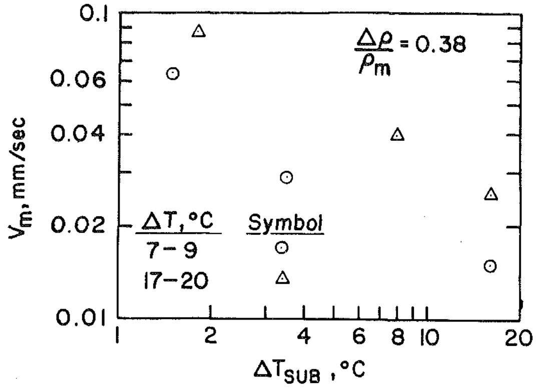

Fig. 5 Measured penetration rate of KI solution pools into polyethylene glycol 1500 substrates as a function of solid subcooling; the pool superheat is a parameter

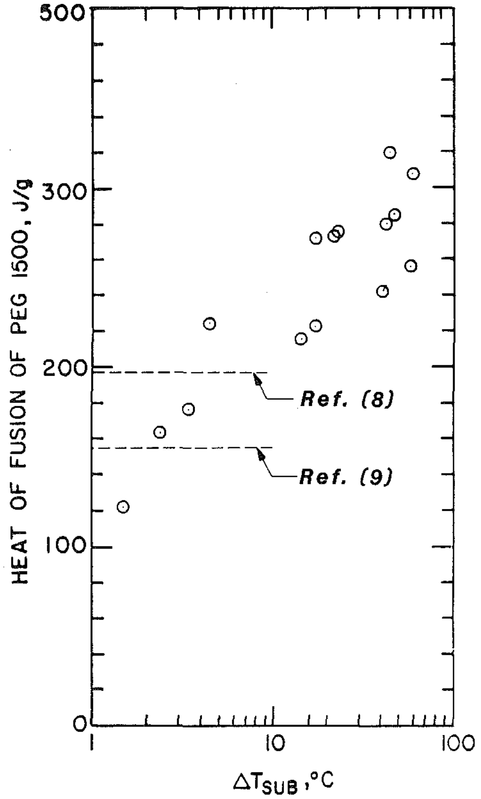

Fig. 6 Measured heat of fusion as a function of solid subcooling for polyethylene glycol 1500

peratures, pool solution temperatures, and pool densities. The pool penetration velocities are plotted in Fig. 4 on logarithmic coordinates as a function of the pool fluid temperature minus the solid melting temperature, i.e., the pool "superheat" ΔT. The data are parametrized by the initial solid subcoolings $\Delta T_{\text{sub}} = 3.5$ and 16°C. The pool fluid to substrate melt density ratio is fixed at $\Delta\rho/\rho_m = 0.38$. Aside from a slight scatter, the melting velocities for these two subcoolings can be regarded as lying on parallel straight lines. The nearly linear relationship between PEG melting velocity and pool superheat ΔT fits very well with the notion that the natural convection melting process of interest here is largely controlled by the melt layer that accumulates at the substrate surface, much like the control exerted by the thermal boundary layer in turbulent natural convection from a horizontal surface. This issue will be revisited later.

Inspection of Fig. 4 reveals that the pool penetration velocity increases sharply with decreasing solid subcooling ΔT_{sub}. From a pure heat transfer point of view, one would expect the effect of the initial PEG temperature (or subcooling) on the melting rate to be small for subcoolings less than about 20°C. At solid subcoolings of 3.5 and 16°C the sensible heat required to raise the PEG solid temperature to its melting point is only 6 and 25 percent, respectively, of the heat of fusion value given in the literature [8] (see below for a more detailed discussion of the PEG heat of fusion). Thus it would seem entirely adequate to ignore the solid subcooling. Of course, this conclusion is not consistent with the evidence in Fig. 4 which shows that the melting velocity is almost doubled by decreasing the solid subcooling from 16 to 3.5°C.

Additional experimental information on the significant temperature dependence of the PEG 1500 melting rate is conveyed in Fig. 5. The melting rate is seen to increase even as the solid subcooling approaches zero. Again, this behavior cannot be explained by heat transfer considerations. It is now appropriate to attempt to rationalize the observed sensitivity of the PEG melting rate to its temperature.

Material Characteristics and the "Heat of Melting" of PEG 1500. Experiments with PEG 1500 revealed that the characteristics of the solid phase of this material change radically with temperature. At room temperature, the properties of the solid seem to correspond to those of a hard waxlike material with a crystalline character. At about 30°C the PEG begins to soften. Above 40°C and up to its melting point of 46.5°C, the PEG "solid" is best described as a substance with a moderate rigidity, much like gelatin or cold cream; it is easily penetrated with a solid probe (pencil, screw driver, etc.).

The fact that the mechanical properties of PEG 1500 are markedly influenced by temperature conditions is not too surprising considering that it is a polymer material. Several polymeric solids lose almost all of their crystalline character at high temperatures. Moreover, the properties of such solids often change dramatically with temperature. Accordingly, it was decided that measurements of the latent heat of melting of PEG 1500 as a function of PEG temperature might be very helpful in rationalizing the melting velocity versus solid subcooling trend displayed in Figs. 4 and 5.

The method of mixtures was used to measure the heat of fusion (or melting) of PEG 1500. Briefly, a weighed sample of solid PEG at a known temperature was dropped into a calorimeter containing a measured amount of molten PEG. By observing the temperature of the molten PEG before and after the addition and melting of the solid sample, the latent heat of melting was determined as a function of the initial temperature of the sample. Values of the liquid and solid phase heat capacities of PEG 1500 are reported in [8]. These were used in the reduction of the calorimetry data. Reference [8] also provides the value of 197 J/g for the latent heat of fusion of PEG 1500. Interestingly enough, a value of 155 J/g for the latent heat is reported in [9].

The results of the present calorimetry work with PEG 1500 are presented in Fig. 6 where the latent heat is plotted against solid subcooling. Thirty-nine calorimetry experiments were performed with PEG 1500. For the sake of clarity, most of the data points in the figure represent average values of the measured latent heat for the same solid temperature. Also shown in the figure are the two literature values for the latent heat. The scatter in the data shows that the heat of melting of PEG 1500 is not exactly reproducible. The scatter, however, is *not* due to technique. The present calorimeter technique was tested with water and benzene and the measured latent heats were within 2 and 22 percent, respectively, of the literature values for these materials. Repeat attempts with water and benzene did not indicate more than 4 percent scatter. Even after fixing the PEG 1500 solid temperature, a range of latent heat values much larger than any possible experimental error was found.

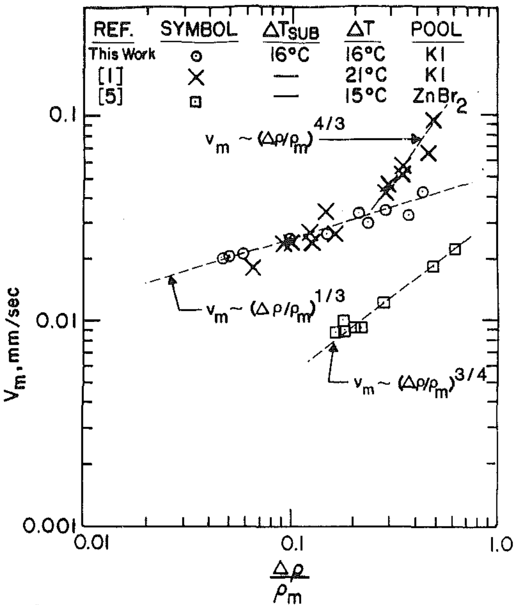

Fig. 7 Measured penetration rate of KI solution pools into polyethylene glycol 1500 substrates as a function of the density ratio; comparison of the present results with previous work

Despite the scatter in the calorimetry data, it is clear that the heat of melting is a rapidly increasing function of the solid subcooling. This trend, together with the experimental results displayed in Figs. 4 and 5, clearly indicates that the melting velocity of PEG 1500 is a function of the heat of melting and, in fact, varies inversely with the heat of melting. This observation, in itself, provides important additional insights into the mechanism controlling the melting process; it suggests that the rate of PEG 1500 melting is controlled to a large extent by the flow within the melt layer that clings to the horizontal surface of the PEG 1500 substrate.

The reason(s) for scatter and the increase in latent heat is not clear. One can only speculate that perhaps the mechanism at work is a variation in the degree of crystallization in polymeric PEG 1500. In this regard sample temperature (solid subcooling) is probably only one contributing variable. Time at a fixed temperature and prior temperature-time history may also play an important role.

Previous Experimental Work With PEG 1500 and the Effects of Pool Density on the Melting Rate of PEG 1500. As mentioned in the introduction, PEG 1500 has been used as the meltable substrate material in two previous experimental studies of the downward penetration of a hot liquid pool [1, 5]. The experimental technique in both of these studies involved the gradual heating of the pool region by passing electric current through the pool liquid or with a fixed arrangement of electrically heated wires or plates submerged within the pool. A heatup phase of about 1/2 h in duration prior to the onset of melting of the PEG substrate was common to the results reported in [1, 5]. It follows that an unknown temperature distribution (or solid subcooling) within the PEG substrate was present at the end of the heatup phase, just prior to the attainment of PEG melting. Because the PEG 1500 melting rate is so sensitive to solid subcooling, the presence of a heatup phase makes it very difficult to interpret the results of [1, 5] quantitatively; in fact, some of the reported trends may prove to be misleading.

A comparison of the measured PEG melting rate dependence on pool superheat with that of [1] is given in Fig. 4. In the present study, where special care was taken to control the PEG temperature, the melting velocity v_m was found to increase nearly linearly with the pool superheat ΔT. The results of [1] reveal a much stronger dependence, with $v_m \simeq (\Delta T)^{1.6}$.

The comparison in Fig. 4 suggests that in the data runs of [1] the subcooling within the solid PEG substrate decreased as the pool temperature increased. Perhaps longer heatup phases were required to attain higher pool temperatures, which, in turn, resulted in higher temperatures within the PEG substrate at the onset of melting.

Experimental data obtained from the present study on the variation of the PEG melting velocity with the pool-to-substrate density ratio $\Delta\rho/\rho_m$ are shown together with previously published data in Fig. 7. The data from [1, 5] displayed in Fig. 7 correspond to those measurements reported for turbulent pool convection conditions only. The results of this study do not show the same sensitivity to density ratio as those of [5] but vary relatively slowly with $\Delta\rho/\rho_m$ in a trend consistent with classical turbulent natural convection. In contrast with the measurements reported in [1] there is no discontinuity in the present data. The upper turbulent regime reported in [1], where $v_m \sim (\Delta\rho/\rho_m)^{4/3}$, is not supported by the present data. The reason(s) for the marked difference between the data sets are not immediately obvious. As was already noted, however, careful control of the substrate temperature is crucial when working with the polymer PEG 1500. Such control is an important feature of the present work. The existence of a heatup phase in the experiments of [1, 5] does introduce uncertainty into the results. Presumably the polymeric behavior of the PEG substrate in the slow heating experiments of [1] just happened to closely match that of the present experiments over the density ratio range 0.1–0.2, where the data are in agreement. We can only conclude from the present investigation of PEG behavior that, in the work of [1], the properties (subcooling) of the substrate changed or "drifted" from experiment to experiment in the very high density ratio regime (> 0.2), thereby producing the so-called "upper turbulent" melting trend. It should be noted that the upper turbulent regime was not observed directly in [1] in the sense that a different convection pattern was noted, but was postulated because the measured melting rate versus density ratio trend changed abruptly for $\Delta\rho/\rho_m \gtrsim 0.2$. Given the sensitivity of the PEG melting rate to its subcooling, PEG melting rate trends obtained from experiments involving the heating of the pool, and, therefore, the slow heating of the solid PEG through an unknown effective temperature (subcooling) range, should be regarded with caution.

Melting Studies With Ice and Common Organic Materials. Attention will now be turned to additional experimental evidence with nonpolymeric materials for the dominance of ordinary natural convection as a transport vehicle in the pool penetration problem. The measured melting rates of ice and glycerol substrates beneath pools of $ZnBr_2$ salt solutions are shown plotted against pool superheat in Fig. 8. Note that the pool-to-substrate density ratio is 0.38 for both material pairs. The density of glycerol melt is 1.26 g cm^{-3} while that of water is 1.0 g cm^{-3}. Thus the ice substrate required a less dense overlying $ZnBr_2$ solution than the glycerol substrate to achieve the fixed value of $\Delta\rho/\rho_m$. It is important to note that the transport properties of aqueous $ZnBr_2$ solutions change with concentration (pool density), such that the viscosity of the $ZnBr_2$ pool over ice is only half that of the $ZnBr_2$ pool over glycerol. Since the viscosity of molten glycerol is about one thousand times that of water, it seems reasonable for the melting rate data of glycerol to fall well below those of ice.

In Fig. 8 the melting velocity data are plotted for solid subcoolings of 3 and 15°C. The negligible difference between the data taken at $\Delta T_{\text{sub}} = 3°\text{C}$ and the data taken at $\Delta T_{\text{sub}} = 15°\text{C}$ can readily be rationalized by comparing the latent heat "absorbed" by the ice or glycerol melting process to the sensible heat absorbed by the subcooling of their solid phases. The latter is found to be less than 15 percent of the former.

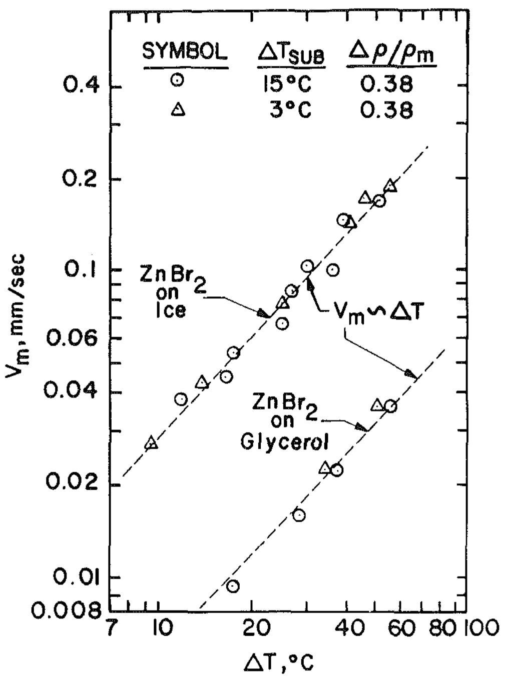

Fig. 8 Measured penetration rate of $ZnBr_2$ solution pools into ice and glycerol substrates as a function of pool superheat

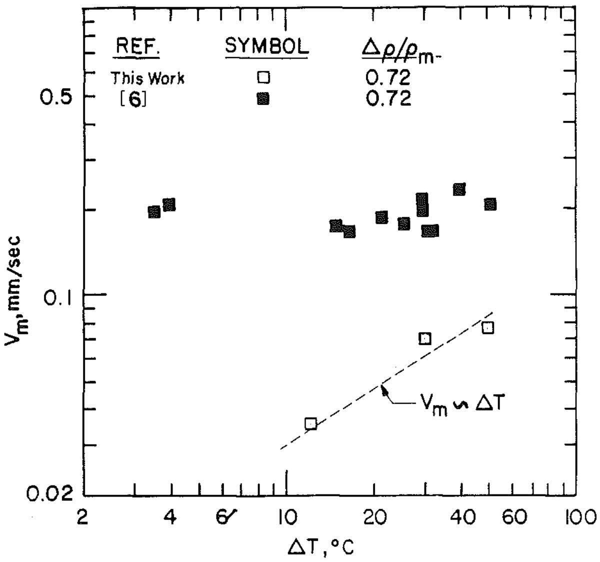

Fig. 9 Measured penetration rate of carbon tetrachloride pools into benzene substrates as a function of pool superheat; comparison of the present results with previous work

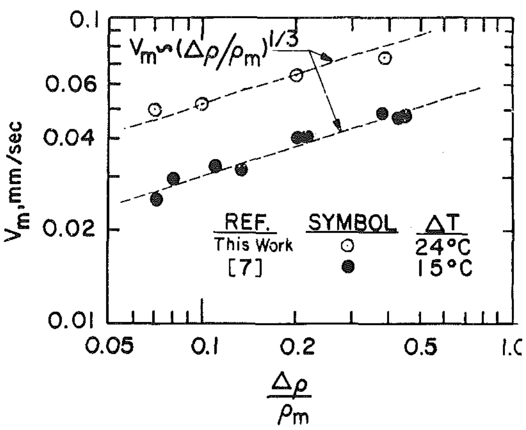

Fig. 10 Measured penetration rate of KI solution pools into ice substrates as a function of the density ratio; comparison of the present results with previous work

This calculated difference is well within the scatter of the data. Recall that the effect of solid PEG 1500 subcooling in the range 1-16°C was found to be very important (see Figs. 4 and 5). Clearly, the ice and glycerol melting data are free of the polymeric behavior exhibited by PEG 1500.

Inspection of Fig. 8 reveals that the ice and glycerol melting rates have the same, nearly linear, ΔT dependence. This implies that pool penetration into substrates with low or high viscosity melts is controlled by heat transfer through the melt or boundary layer just above the substrate surface. This result is in contrast with the experimental work presented in [6], where the rates of penetration of CCl_4 pools into benzene were reported to be independent of ΔT. As part of the present investigation, a few experiments were run with CCl_4 pools overlying solid benzene. Since the preparation of benzene substrates of reasonable high purity proved to be very time consuming, only three experiments were performed with this material. Figure 9 compares the present experimental data on CCl_4 pools overlying solid benzene with those of [6]. The melting velocity results of [6] are much higher than those of the present study. Also, the present data seem to show an increase in the melting velocity with increasing pool temperature, whereas the results of [6] are seen to be essentially independent of pool temperature. Of course, a warning should be given against too hasty acceptance of the present v_m versus ΔT trend for benzene, since it is based on the results of only three melting experiments. However, the much higher benzene melting velocities reported by Catton et al. [6] are disconcerting. It is tempting to ascribe this disagreement to differences in the amount of absorbed gas within the benzene test materials used in the two studies. However, clarification of the CCl_4 penetration behavior into melting benzene must await future experimental work aimed at strengthening the data base for this material pair.

As a check on the experimental work reported here, a few experiments were performed to determine the variation of the melting velocity with the density ratio $\Delta\rho/\rho_m$ for KI salt solution pools overlying ice substrates. This material pair was one of the pairs used in the study of [7], and the experiments of [7] and the present study are similar in technique. Figure 10 shows the present experimental results and the results reported in [7]. The v_m versus $\Delta\rho/\rho_m$ trends from both studies can be represented fairly well with the classical 1/3 power law. The fact that the melting rates reported in this work at $\Delta T = 24°C$ are about 60 percent higher than the rates reported in [7] at $\Delta T = 15°C$ is consistent with the nearly linear relation between melting velocity and pool superheat that has been observed throughout the present study.

Conclusions

The experimental results presented here have conveyed strong evidence that the melting of a solid by an overlying pool of warm, more dense material, miscible with the molten phase of the solid, has much in common with turbulent, thermal natural convection above a heated surface. There are two distinct aspects of the results which contribute testimony to the similarity of the two processes: The melting velocity was found to be a linear function of the temperature difference between the pool and the melting point of the solid and the melting velocity was found to be proportional to the density difference between the pool and the substrate melt to approximately the 1/3 power. These relationships indicate that the resistance to melting is provided by the melt layer and probably a boundary layer that is superposed on the melt layer at the bottom of the pool.

The foregoing observations do not agree with the results of previous experimental studies [1, 5, 6]. Farhadieh and Baker [1] and Eck and Werle [5], in their studies of the melting of polyethylene glycol (PEG) by overlying pools of aqueous salt solution, indicated that the melting velocity versus density difference relation at high pool-to-substrate density ratios does not resemble the relation measured for turbulent thermal natural convection. The experiments performed as part of this study, however, suggest that care must be exercised in using polymeric PEG as a solid substrate material, since its heat of melting is strongly dependent on its initial temperature. In this study careful control of the initial PEG temperature was maintained and the PEG melting rate was found to increase with the pool-to-substrate density difference in perfect accord with classical, turbulent natural convection theory. Catton et al. [6] found the melting rate of benzene to be independent of the imposed temperature difference between the warm pool and the benzene substrate. This is in contrast with the present work where the melting rates of ice, glycerol, and PEG were found to be nearly linear functions of the temperature difference.

Acknowledgments

This material is based on work supported by the National Science Foundation under Grant No. MEA-8360199. Thanks are due to Mr. J. K. Basco and to Mr. V. R. Fletcher for their valuable contributions in the preparation and performance of the experiments. The authors are grateful to Professor S. G. Bankoff of Northwestern University for useful discussions.

References

1 Farhadieh, R., and Baker, L., Jr., "Heat Transfer Phenomenology of a Hydrodynamically Unstable Melting System," ASME JOURNAL OF HEAT TRANSFER, Vol. 100, 1978, pp. 305-310.

2 Sparrow, E. M., Husar, R. B., and Goldstein, R. J., "Observations and Other Characteristics of Thermals," *J. Fluid Mechanics*, Vol. 41, 1970, pp. 793-800.

3 Onat, K., and Grigull, V., "The Onset of Convection in a Horizontal Fluid Layer Heated From Below," *Wärme- and Stoffübertragung*, Vol. 3, 1970, pp. 103-113.

4 Somerscales, E. F. C., and Gazda, I. W., "Thermal Convection in High Prandtl Number Liquids at High Rayleigh Numbers," *Int. J. Heat Mass Transfer*, Vol. 12, 1969, pp. 1491-1511.

5 Eck, G., and Werle, H., "Experimental Studies of Penetration of a Hot Liquid Pool Into a Melting Miscible Substrate," *Nuclear Technology*, Vol. 64, 1984, pp. 275-289.

6 Catton, I., Brinsfield, W. A., and Ghiaasiaan, S. M., "Heat Transfer From a Heated Pool to a Melting Miscible Substrate," ASME JOURNAL OF HEAT TRANSFER, Vol. 105, 1983, pp. 447-543.

7 Fang, L. J., Cheung, F. B., Linehan, J. H., and Pedersen, D. R., "An Experimental Study of Natural Convection Melting of Ice in Salt Solutions," presented at ASME Winter Annual Meeting, New Orleans, LA, Dec. 9-14, 1984.

8 Gaur, U., and Wunderlich, B., "Heat Capacity and Other Thermodynamic Properties of Linear Macromolecules. III. Polyoxides," *J. Phys. Chem. Ref. Data*, Vol. 10, No. 4, 1981, pp. 1001-1049.

9 Union Carbide Carbowax Polyethylene Glycols, Products Bulletin F-47722-EODD, 10/81-20M.

J. H. Lienhard, V[1]

I. Catton[2]

School of Engineering and Applied Science,
University of California,
Los Angeles, CA 90024

Heat Transfer Across a Two-Fluid-Layer Region

Heat transfer across a two-fluid-layer region is calculated for Rayleigh numbers in excess of the critical value. The method of solution is based on Landau's comments regarding the onset of turbulence, following Malkus and others. The linear stability problem is solved for its eigenvalues and eigenfunctions, and the eigenfunctions are used to calculate the contribution of secondary motion to heat transfer. Results are obtained in terms of an overall Nusselt number as a function of Rayleigh number, midlayer thickness, and midlayer thermal conductivity.

Introduction

A major problem in the design of flat-plate solar collectors is the reduction of upper surface heat loss, usually accomplished by the addition of one or more transparent cover plates. A similar geometry sometimes occurs when roofing is insulated with layered material. Heat loss may still occur through these layered systems by conduction or natural convection. Catton and Lienhard [1] in an earlier paper established conditions under which there will be no convection in a two-layer system. In other circumstances, convective contributions may be tolerable, and allowing them to occur may save a great deal of money. There is, then, a need to know what the heat transfer will be. Here we idealize the engineering problem as one of determining the heat transfer across two plane layers of fluid separated by a finite conductance midlayer and bounded by isothermal outer surfaces, the lower heated, the upper cooled (Fig. 1).

Heat transfer across a fluid layer heated from below results first by conduction and then by convection as the bounding temperature difference is increased. The temperature difference is a direct measure of the potential energy available to drive the convection process. In situations where the controlling parameter forms a direct measure of potential and does not change as a result of the onset of convection, the Landau method of predicting convective transport yields exceptionally good results.

The Landau method, based on general ideas developed by Landau in 1944 [10], was applied almost simultaneously by Malkus and Veronis [2] and Stuart [3] to the Benard problem (thermal convection between isothermal parallel plates) and the Taylor problem (momentum transfer between rotating cylinders), respectively. Malkus and Veronis were discouraged by their results but, as pointed out by Catton [4], had made a poor assumption that led to a compounding error as the convection grew more vigorous. Since then a number of applications of the method have been shown to yield successful predictions [5, 6, 9]. In essence, one solves the stability problem, the onset of convection, then uses the eigenvalues and eigenfunctions to calculate convective contributions to heat transfer. By using the so-called Stuart shape assumption certain nonlinearities vanish and a simple expression for the heat transfer results.

In this work, we use the Landau method to calculate the convective heat transfer across the layered system (thermal radiation is not included). The results of an earlier work [1] yield the needed eigenvalues and eigenfunctions. The results are presented in terms of the Nusselt number (ratio of effective to molecular thermal conductivity) and Rayleigh number (dimensionless temperature difference) for a range of midlayer thicknesses and conductivities.

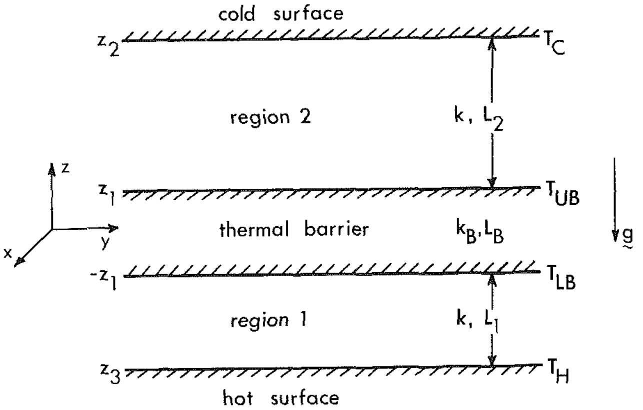

Fig. 1 The physical model

Governing Equations and Eigens of the Linear Stability Problem

The physical situation to be studied is governed by the steady two-dimensional Oberbeck-Boussinesq equations

$$\nabla \cdot \mathbf{v} = 0 \tag{1}$$

$$\frac{D\mathbf{v}}{Dt} = -\frac{1}{\rho_0}\nabla p - \frac{\rho}{\rho_0} g\mathbf{k} + \nu \nabla^2 \mathbf{v} \tag{2}$$

$$\frac{DT}{Dt} = \alpha \nabla^2 T \tag{3}$$

$$\rho = \rho_0[1-\beta(T-T_0)] \tag{4}$$

Equations (1-4) must be satisfied in both fluid regions, and in the thermal barrier we have

$$\nabla^2 T = 0 \tag{5}$$

The boundary conditions imposed are

$$\begin{gathered} \mathbf{v}(y, z_2) = \mathbf{v}(y, z_1) = \mathbf{v}(y, -z_1) = \mathbf{v}(y, z_3) = 0 \\ T(y, z_2) = T_C,\ T(y, z_3) = T_H \end{gathered} \tag{6}$$

together with matching of temperature and heat flux at the surfaces of the thermal barrier. The fluid layers are of infinite extent so periodicity conditions are imposed, viz.

$$\mathbf{v}(y, z) = \mathbf{v}(y+\lambda, z),\ T(y, z) = T(y+\lambda, z)$$

and the solution proceeds by perturbation of the conductive base state (no motion) solutions as detailed by Catton and Lienhard [1]. After analyzing disturbances into normal modes, the resulting eigenvalue problem is solved by the Galerkin method. Eigenvalues (minimum overall critical Rayleigh numbers) are presented in [1] for the lowest mode over a wide range of the parameters

---

[1] Present address: Department of Applied Mechanics and Engineering Sciences and Project in Nonlinear Science, University of California at San Diego, La Jolla, Ca. 92093; Student Mem. ASME

[2] Mem. ASME

Contributed by the Heat Transfer Division and presented at the 21st National Heat Transfer Conference, Seattle, Washington, 1983. Manuscript received by the Heat Transfer Division June 26, 1984.

$$A=\frac{L_B}{L_1+L_2},\ B=\frac{L_2}{L_1},\text{ and } X=\frac{k}{k_B} \qquad (7)$$

Exchange of stabilities was proven in [11]. In particular, it was found that the highest critical Rayleigh numbers are obtained when the thermal barrier is centered ($B=1$). Since the primary occurrence of this geometry is in problems of convection suppression, we shall present numerical results for the heat transfer only for this most stable case.

Heat Transfer

The Landau method will be used to obtain predictions of the heat transfer across the fluid layers in the form of a Nusselt number. The procedure is based on an averaging of the perturbed equations and, following Stuart [3], evaluates the integral average heat flux using the critical eigenfunctions for Rayleigh numbers in excess of critical. The solution appears in terms of so-called power integrals. We proceed, using the energy equation.

Substituting $T=\bar{T}+T'$ with $\overline{T'}=0$ into the energy equation (3), taking the horizontal average, and integrating once yields

$$-\frac{d\bar{T}_1}{dz}+\frac{1}{\alpha}(\overline{w_1T_1'})=\frac{\bar{q}}{k} \qquad \text{Region 1} \qquad (8)$$

$$-\frac{d\bar{T}_B}{dz}=\frac{\bar{q}}{k_B} \qquad \text{Thermal barrier} \qquad (9)$$

$$-\frac{dT_2}{dz}+\frac{1}{\alpha}(\overline{w_2T_2'})=\frac{\bar{q}}{k} \qquad \text{Region 2} \qquad (10)$$

where the overline denotes the horizontal average defined by

$$\bar{F}=\frac{1}{A}\int_A F dA \qquad (11)$$

Here we have assumed that there are no sources or sinks of heat on the sidewalls at infinity.

Next averaging vertically, we obtain

$$-\left\langle\frac{d\bar{T}}{dz}\right\rangle_i+\frac{1}{\alpha}\langle\overline{w_iT_i'}\rangle=\frac{\bar{q}}{k},\ i=1,2$$

$$-\left\langle\frac{d\bar{T}}{dz}\right\rangle_B=\bar{q}/k_B \qquad (12)$$

with $\langle\quad\rangle_i$ denoting the vertical average over region i

$$\langle F\rangle_i=\frac{1}{L_i}\int_{L_i} F dz \qquad (13)$$

and $\bar{q}=\langle\bar{q}\rangle$ in steady state. Equations (12) are simple statements of energy conservation.

Following Malkus and Veronis [2] or Somerton [7], we relate the Reynold's stress type term to the critical Rayleigh number and the Rayleigh number of interest. First, from the energy equation and a fair amount of algebra, one may obtain the exact relationship

$$\langle\overline{w_iT_i'}\rangle=\alpha N_i\left(\left\langle-\frac{d\bar{T}}{dz}\right\rangle_i+\alpha\frac{\langle\overline{T_i'\nabla^2T_i'}\rangle}{\langle\overline{w_iT_i'}\rangle}\right) \qquad (14)$$

where

$$N_i=\frac{\langle\overline{w_iT_i'}\rangle^2}{\langle\overline{w_iT_i'^2}\rangle-\langle\overline{w_iT_i'}\rangle^2}$$

The crux of the power integral method is then the approximate evaluation of the right-hand side of (14). We may motivate the form of the approximation by observing that, near onset, the temperature disturbance and velocity profiles may reasonably be represented as an amplitude depending on the Rayleigh number times the normalized critical eigenfunctions of the linear stability problem. Upon substitution of such a form into the expression for N_i, the amplitudes cancel cleanly out and N_i may be evaluated using only the critical eigenfunctions. Note that the horizontal averaging introduces the same constant factor in all three terms which will also

Nomenclature

a_c = overall critical wavenumber $=\frac{2\pi}{\lambda}(L_1+L_B+L_2)$
A = midlayer to total fluid height aspect ratio $=L_B/(L_1+L_2)$
B = upper to lower fluid layer aspect ratio $=L_2/L_1$
C_j = modal Nusselt number coefficient, jth mode
g = body force per unit mass
k = fluid thermal conductivity
k_B = thermal conductivity of the thermal barrier
k_{eff} = effective thermal conductivity (equation (28))
$\mathbf{k}$ = unit vector in the z direction
L_i = thickness of the ith layer
N_i = modal coefficient for ith layer (equation (14–15))
Nu = Nusselt number $=\bar{q}/q_{\text{cond}}$
Nu_{corr} = Nusselt number obtained from correlation
Nu_{engr} = engineering estimate for Nu (equation (29))
p = fluid pressure
$\bar{q}$ = horizontal average heat flux
q_{cond} = conductive heat flux
Ra = overall Rayleigh number $=\frac{g\beta(T_H-T_C)(L_1+L_B+L_2)^3}{\nu\alpha}$
Ra_c = overall critical Rayleigh number
Ra_i = Rayleigh number of ith layer $=\frac{g\beta\Delta T_iL^3{}_i}{\nu\alpha}$
T = temperature
T_C = temperature of upper isothermal surface, cold
T_H = temperature of lower isothermal surface, hot
T_{LB} = temperature at lower surface of thermal barrier
T_{UB} = temperature at upper surface of thermal barrier
u, v, w = x, y, and z components of fluid velocity
$\mathbf{v}_i$ = vector fluid velocity in ith layer
W_i = dimensionless amplitude of normal mode velocity disturbance in ith layer
x, y, z = Cartesian coordinates (Fig. 1)
X = fluid to midlayer conductivity ratio $=k/k_B$
α = fluid thermal diffusivity
β = fluid coefficient of volume expansion
ΔT_c = overall temperature difference $=T_H-T_C$
ΔT_i = temperature difference across the ith layer
θ_i = dimensionless amplitude of normal mode temperature disturbance in region i
λ = disturbance wavelength
ν = fluid kinematic viscosity
ρ = fluid density

Superscripts, Subscripts, and Symbols

1, 2, B = a variable or parameter in fluid regions 1 or 2, or the thermal barrier, respectively
c = a variable or parameter at the critical state
$'$ = a disturbance
0 = a reference state quantity for the Boussinesq approximation
$\overline{(\quad)}$ = a horizontal average (equation (11))
$\langle\quad\rangle$ = a vertical average (equation (13))

cancel out, so that a particular planform need not be specified. Hence, N_i may be calculated as

$$N_i = \frac{\langle W_i(z_i)\theta_i(z_i)\,|_{a_c}\rangle_i^2}{\langle (W_i(z)\theta_i(z))^2\,|_{a_c}\rangle_i - \langle W_i(z)\theta_i(z)\,|_{a_c}\rangle_i^2} \tag{15}$$

Likewise, one may show that at onset

$$\left\langle -\frac{d\bar{T}}{dz}\right\rangle_{c_i} \langle \overline{w_i T_i'}\rangle = -\langle \overline{T_i'\nabla^2 T_i'}\rangle$$

A similar averaging of the momentum equation shows that, with the shape assumption the ratio of velocity to temperature amplitude is constant with respect to Rayleigh number. Thus, we may calculate

$$\langle \overline{w_i T_i'}\rangle = \alpha N_i \left(\left\langle -\frac{d\bar{T}}{dz}\right\rangle_i - \left\langle -\frac{d\bar{T}}{dz}\right\rangle_{c_i} \right) \tag{16}$$

with N_i given by (15). The expression for $\langle \overline{w_i T_i'}\rangle$ is then complete once $\bar{T}_{LB}$ and $\bar{T}_{UB}$ (appearing in the averaged gradients) are determined.

Our approximation has well-defined physical meaning only near the critical Rayleigh number. The wavenumber may be expected to change as the Rayleigh number increases, so that one cannot argue that the detailed properties of the flow field have the same "shape" as at onset. However, we are interested in an average property of the flow, viz. the average heat transfer, and for our purposes the specifics of the flow are immaterial. Numerous previous studies [4, 5, 6, 7, 9] have shown that the approximation (15-16) of (14) produces a good estimate of convective transport to Rayleigh (or Taylor) numbers several decades beyond critical (if one sums contributions from successive modes), and accordingly well beyond the point at which the shape assumption loses physical significance. Thus, we abandon the physical interpretation of the shape assumption and state our approximation in a semi-empirical form: "Experience has shown that the shape assumption approximation to the expression (14) yields a good estimate of convective transport to Rayleigh numbers greatly in excess of critical." We emphasize that our approximation should not be viewed as a prediction of the flow field at large Rayleigh number.

For single-layer thermal convection, the power integral approximation holds to $\mathrm{Ra} = \mathrm{O}(10^5)$; the success of the power integral method here may be due in part to the fact that the average heat transfer is only weakly dependent upon the wavenumber.

To complete our derivation, we consider the averaged temperature gradients. Noting that

$$-\left\langle \frac{d\bar{T}}{dz}\right\rangle_1 = \frac{T_H - \bar{T}_{LB}}{L_1}$$

$$-\left\langle \frac{d\bar{T}}{dz}\right\rangle_B = \frac{\bar{T}_{UB} - \bar{T}_{LB}}{L_B} \tag{17}$$

and

$$-\left\langle \frac{d\bar{T}}{dz}\right\rangle_2 = \frac{\bar{T}_{UB} - T_C}{L_2}$$

we can substitute the relationships obtained for $\langle \overline{w_1 T_1'}\rangle$ and $\langle \overline{w_2 T_2'}\rangle$ into equations (12) and solve to obtain

$$\bar{T}_{LB} - \bar{T}_{UB} = \frac{(T_H - T_C) - \frac{N_1 L_1}{1+N_1}\left\langle -\frac{d\bar{T}}{dz}\right\rangle_{1c} - \frac{N_2 L_2}{1+N_2}\left\langle -\frac{d\bar{T}}{dz}\right\rangle_{2c}}{\frac{L_1 k_B}{k L_B}\left[\frac{1}{1+N_1} + \frac{L_2}{L_1}\frac{1}{1+N_2} + \frac{L_B}{k_B}\frac{k}{L_1}\right]} \tag{18}$$

so that the convective heat flux $\bar{q}$ may be expressed as

$$\bar{q} = k_B\left\langle -\frac{d\bar{T}}{dz}\right\rangle_B = k_B\frac{(\bar{T}_{LB} - \bar{T}_{UB})}{L_B} \tag{19}$$

The temperature gradients at the onset on motion may be obtained directly from the conductive state

$$\left\langle -\frac{d\bar{T}}{dz}\right\rangle_{1c} = \frac{(T_H - T_C)_c}{L_1(1+B)(1+AX)} \tag{20}$$

and

$$\left\langle -\frac{d\bar{T}}{dz}\right\rangle_{2c} = \frac{B(T_H - T_C)_c}{L_2(1+B)(1+AX)}$$

Finally, we define the Nusselt number as the ratio of convective to conductive heat flux at a given $T_H - T_c$ and, with the conductive heat flux given by

$$q_{\text{cond}} = \frac{k(T_H - T_C)}{L_1}[1 + B + AX(1+B)]^{-1} \tag{21}$$

obtain the final result

$$\mathrm{Nu} = \frac{q}{q_{\text{cond}}} = 1 + \frac{\left(N_1 + B\frac{N_2(1+N_1)}{(1+N_2)}\right)\left(1 - \frac{\mathrm{Ra}_c}{\mathrm{Ra}}\right)}{\left[1 + B\left(\frac{1+N_1}{1+N_2}\right) + AX(1+B)(1+N_1)\right]} \tag{22}$$

where Ra_c and Ra are the critical and actual values of the overall Rayleigh number.

The second term in the above equation represents the convective contribution from a single disturbance mode (single eigenfunction). Following Malkus and Veronis, we assume that the contributions from successive modes can be linearly summed (a procedure which has been justified empirically) and write

$$\mathrm{Nu} = 1 + \sum_j C_j\left(1 - \frac{\mathrm{Ra}_{cj}}{\mathrm{Ra}}\right)U(\mathrm{Ra} - \mathrm{Ra}_{cj}) \tag{23}$$

where the modal Nusselt number coefficient of the jth mode is

$$C_j = \frac{\left(N_{1j} + B\frac{N_{2j}(1+N_{1j})}{(1+N_{2j})}\right)}{\left[1 + B\left(\frac{1+N_{1j}}{1+N_{2j}}\right) + AX(1+B)(1+N_{1j})\right]} \tag{24}$$

and $U(\mathrm{Ra} - \mathrm{Ra}_{cj})$ is the unit step function. For each eigenvalue Ra_{cj}, the eigenfunctions are used to perform the integrations needed to calculate N_{1j} and N_{2j}. The latter are used to obtain C_j.

This result limits properly in that N_{1j} and N_{2j} go over to the values obtained for a single infinite layer between perfectly conducting plates when $X \to 0$, and in that C_j approaches N_{1j} when $B \to 0$ in the above limit.

The Nusselt number prediction has no Prandtl number dependence under the conditions of our model. Our basic assumptions are best satisfied at high Prandtl number. Other studies, as well as the data given below, show that the approximations hold to $\mathrm{Pr} = \mathrm{O}(1)$. The power integral method has never been tested against data for Pr significantly less than one and the momentum equation even provides some grounds for doubt about this range

$$\frac{1}{\mathrm{Pr}}\frac{D}{Dt}\mathbf{v} = -\nabla p + \nabla^2\mathbf{v} + \mathrm{Ra}T\mathbf{k}$$

When $\mathrm{Pr} \ll 1$, the unsteady and nonlinear advective terms will be considerably more important than for $\mathrm{Pr} > 1$. Since the model assumes that the flow is steady and that, in an integral sense, the nonlinear self-distortion of the disturbances is small, the model may not work well for small Pr.

Table 1 Critical Rayleigh and wavenumbers and modal Nusselt number coefficients (sum only *odd*-numbered modes)

A = 0.01

MODE NUMBER	X	0.2	0.5	1.0	2.0	5.0	10.0
1	$\mathrm{Ra}_c \times 10^{-4}$	2.222	2.189	2.185	2.200	2.260	2.365
	a_c	5.206	5.183	5.177	5.173	5.173	5.171
	C	1.688	1.687	1.669	1.628	1.512	1.350
2	$\mathrm{Ra}_c \times 10^{-4}$	2.802	2.801	2.803	2.810	2.837	2.896
	a_c	6.260	6.252	6.240	6.220	6.167	6.086
	C	1.437	1.429	1.417	1.392	1.320	1.211
3	$\mathrm{Ra}_c \times 10^{-5}$	2.582	2.547	2.544	2.560	2.630	2.755
	a_c	9.833	9.769	9.747	9.738	9.736	9.742
	C	1.733	1.714	1.692	1.653	1.548	1.394
4	$\mathrm{Ra}_c \times 10^{-5}$	2.913	2.917	2.922	2.933	2.971	3.053
	a_c	10.90	10.91	10.91	10.88	10.81	10.70
	C	1.615	1.596	1.578	1.549	1.466	1.337
5	$\mathrm{Ra}_c \times 10^{-6}$	1.160	1.147	1.146	1.154	1.186	1.242
	a_c	14.39	14.30	14.27	14.26	14.26	14.27
	C	1.793	1.778	1.755	1.713	1.596	1.428
6	$\mathrm{Ra}_c \times 10^{-6}$	1.251	1.253	1.256	1.260	1.279	1.320
	a_c	15.35	15.36	15.35	15.32	15.22	15.09
	C	1.709	1.690	1.671	1.637	1.541	1.393
7	$\mathrm{Ra}_c \times 10^{-6}$	3.448	3.415	3.413	3.436	3.531	3.698
	a_c	18.91	18.80	18.76	18.74	18.74	18.75
	C	1.831	1.817	1.793	1.749	1.627	1.452
8	$\mathrm{Ra}_c \times 10^{-6}$	3.636	3.641	3.648	3.664	3.726	3.854
	a_c	19.83	19.84	19.82	19.78	19.66	19.50
	C	1.769	1.751	1.731	1.695	1.590	1.430

A = 0.1

MODE NUMBER	X	0.2	0.5	1.0	2.0	5.0	10.0
1	$\mathrm{Ra}_c \times 10^{-4}$	3.260	3.204	3.229	3.433	4.211	5.572
	a_c	6.120	5.834	5.722	5.672	5.643	5.632
	C	1.502	1.453	1.323	1.102	0.725	0.461
2	$\mathrm{Ra}_c \times 10^{-4}$	3.652	3.683	3.756	3.946	4.650	5.950
	a_c	6.802	6.732	6.637	6.492	6.237	6.037
	C	1.394	1.321	1.210	1.029	0.700	0.452
3	$\mathrm{Ra}_c \times 10^{-5}$	3.665	3.651	3.731	3.995	4.927	6.540
	a_c	11.32	11.02	10.85	10.76	10.74	10.75
	C	1.632	1.543	1.391	1.152	0.754	0.476
4	$\mathrm{Ra}_c \times 10^{-5}$	3.780	3.834	3.946	4.207	5.102	6.685
	a_c	11.74	11.68	11.59	11.44	11.21	11.06
	C	1.592	1.494	1.350	1.127	0.745	0.474
5	$\mathrm{Ra}_c \times 10^{-6}$	1.606	1.619	1.667	1.793	2.215	2.940
	a_c	16.29	16.02	15.84	15.72	15.67	15.66
	C	1.681	1.579	1.418	1.169	0.761	0.480
6	$\mathrm{Ra}_c \times 10^{-6}$	1.628	1.654	1.708	1.833	2.247	2.966
	a_c	16.58	16.48	16.36	16.20	15.98	15.85
	C	1.663	1.556	1.400	1.159	0.758	0.479
7	$\mathrm{Ra}_c \times 10^{-6}$	4.704	4.771	4.933	5.320	6.585	8.745
	a_c	21.22	20.97	20.79	20.66	20.58	20.56
	C	1.719	1.608	1.441	1.185	0.769	0.484
8	$\mathrm{Ra}_c \times 10^{-6}$	4.735	4.822	4.993	5.379	6.632	8.782
	a_c	21.43	21.30	21.16	21.00	20.80	20.69
	C	1.711	1.597	1.432	1.180	0.767	0.484

A = 0.2

MODE NUMBER	X	0.2	0.5	1.0	2.0	5.0	10.0
1	$\mathrm{Ra}_c \times 10^{-4}$	4.569	4.550	4.731	5.314	7.360	10.90
	a_c	6.953	6.590	6.372	6.250	6.175	6.151
	C	1.392	1.271	1.077	0.810	0.459	0.266
2	$\mathrm{Ra}_c \times 10^{-4}$	4.785	4.907	5.159	5.753	7.759	11.27
	a_c	7.380	7.253	7.092	6.881	6.588	6.408
	C	1.343	1.208	1.027	0.783	0.452	0.264
3	$\mathrm{Ra}_c \times 10^{-5}$	4.919	5.061	5.383	6.141	8.601	12.80
	a_c	12.54	12.27	12.05	11.90	11.81	11.79
	C	1.539	1.367	1.139	0.847	0.475	0.274
4	$\mathrm{Ra}_c \times 10^{-5}$	4.968	5.148	5.493	6.257	8.708	12.90
	a_c	12.74	12.60	12.44	12.26	12.05	11.93
	C	1.526	1.351	1.127	0.841	0.474	0.273
5	$\mathrm{Ra}_c \times 10^{-6}$	2.139	2.223	2.384	2.737	3.852	5.741
	a_c	17.91	17.67	17.47	17.31	17.18	17.14
	C	1.590	1.400	1.159	0.857	0.479	0.276
6	$\mathrm{Ra}_c \times 10^{-6}$	2.145	2.233	2.397	2.751	3.865	5.753
	a_c	18.01	17.83	17.66	17.48	17.20	17.21
	C	1.588	1.395	1.156	0.856	0.479	0.276
7	$\mathrm{Ra}_c \times 10^{-6}$	6.246	6.520	7.023	8.094	11.43	17.06
	a_c	23.26	23.03	22.84	22.67	22.53	22.48
	C	1.629	1.427	1.177	0.868	0.483	0.278
8	$\mathrm{Ra}_c \times 10^{-6}$	6.252	6.530	7.036	8.108	11.44	17.07
	a_c	23.30	23.11	22.93	22.75	22.58	22.51
	C	1.628	1.425	1.176	0.867	0.483	0.278

A = 0.3

MODE NUMBER	X	0.2	0.5	1.0	2.0	5.0	10.0
1	$\mathrm{Ra}_c \times 10^{-4}$	6.009	6.176	6.647	7.834	11.78	18.55
	a_c	7.670	7.306	7.030	6.843	6.718	6.677
	C	1.317	1.138	0.910	0.641	0.336	0.187
2	$\mathrm{Ra}_c \times 10^{-4}$	6.157	6.438	6.983	8.203	12.15	18.90
	a_c	7.951	7.774	7.566	7.322	7.023	6.859
	C	1.292	1.107	0.887	0.629	0.333	0.186
3	$\mathrm{Ra}_c \times 10^{-5}$	6.397	6.767	7.464	8.975	13.72	21.74
	a_c	13.66	13.40	13.18	13.00	12.85	12.81
	C	1.463	1.230	0.964	0.669	0.347	0.192
4	$\mathrm{Ra}_c \times 10^{-5}$	6.420	6.808	7.519	9.036	13.78	21.80
	a_c	13.75	13.56	13.37	13.17	12.97	12.88
	C	1.459	1.225	0.961	0.667	0.347	0.192
5	$\mathrm{Ra}_c \times 10^{-6}$	2.775	2.960	3.291	3.985	6.129	9.739
	a_c	19.45	19.21	19.00	18.81	18.65	18.59
	C	1.514	1.261	0.981	0.677	0.350	0.193
6	$\mathrm{Ra}_c \times 10^{-6}$	2.777	2.963	3.295	3.990	6.134	9.744
	a_c	19.48	19.26	19.06	18.87	18.69	18.61
	C	1.513	1.260	0.981	0.677	0.350	0.193
7	$\mathrm{Ra}_c \times 10^{-6}$	8.098	8.673	9.681	11.77	18.17	28.92
	a_c	25.21	24.99	24.78	24.59	24.43	24.36
	C	1.550	1.285	0.996	0.685	0.353	0.195
8	$\mathrm{Ra}_c \times 10^{-6}$	8.099	8.675	9.684	11.77	18.18	28.93
	a_c	25.22	25.00	24.80	24.61	24.44	24.37
	C	1.550	1.284	0.996	0.685	0.353	0.195

Results and Discussion

Heat transfer across two fluid layers separated by a finite thickness, finite thermal conductivity midlayer has been estimated. Results are presented in Table 1, where the overall critical Rayleigh number

$$\mathrm{Ra}_c = \frac{g(T_H - T_C)(L_1 + L_B + L_2)^3}{\nu\alpha} \tag{25}$$

the critical wave number

$$a_c = \frac{2\pi}{\lambda}(L_1 + L_B + L_2) \tag{26}$$

Table 2 Comparison of critical Rayleigh numbers for $A = 0.1$, $X = 1$ from this work to odd modes of rigid boundary Benard problem from Catton's exact solution [4]

Mode #	Ra	Ra_{Benard}, Odd	Ra/Ra_{BO}
1	3.229×10^4	17610	1.83
2	3.756		2.13
3	3.731×10^5	219885	1.70
4	3.946		1.79
5	1.667×10^6	1020509	1.63
6	1.708		1.67
7	4.933×10^6	3085829	1.60
8	4.993		1.62

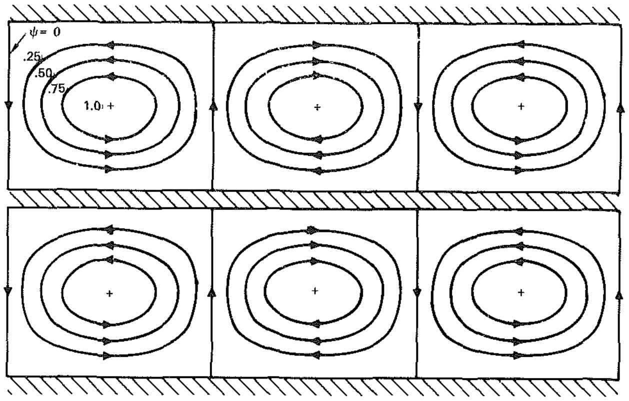

Fig. 2(*a*) Representative convection cells for the first mode: $A = 0.1$, $k/k_B = 0.5$

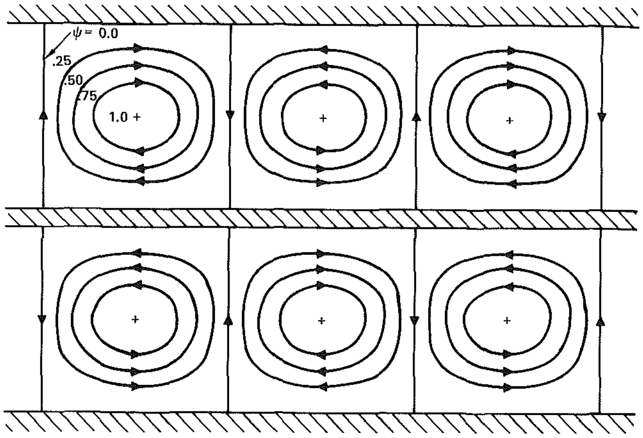

Fig. 2(*b*) Representative convection cells for the second mode: $A = 0.1$, $k/k_B = 0.5$

and the modal Nusselt number coefficients C_j are presented for the first eight modes with

$$0.01 \leq A \leq 0.3,$$

$$0.2 \leq X \leq 10,$$

and

$$B = 1$$

The number of terms in the Galerkin expansion was increased as mode number was increased, from six terms for each layer (modes 1 to 4) to eight terms for each layer (modes 5 to 8). Convergence tests show that the numerical solutions for modes 1 to 4 are accurate to better than 0.05 percent in Ra_c and a_c, and to better than 0.2 percent in C_j. For modes 5 to 8 the values of Ra_c and a_c are accurate to about 0.2 percent while the C_j are accurate to about 1 percent. This degree of convergence is quite adequate in light of the approximate nature of the heat transfer solution.

In order to solve the heat transfer problem the results of [1] have been extended to minimize the Rayleigh number as a function of wavenumber for each of several higher modes. Parametric effects on the critical Rayleigh number of each mode are the same as those discussed previously for the lowest mode; Ra_{ci} increases with increasing midlayer thickness A, and decreases then increases with increasing fluid conductivity X.

The eigenvalues are seen to occur in pairs of values differing by about 20 percent for the lower modes and only a fraction of a percent for the higher modes, with pairs differing by an order of magnitude. Comparison to the eigenvalues for an unpartitioned layer, i.e., the Benard problem with rigid isothermal boundaries, shows (Table 2) that the modal pairs may be loosely characterized by a constant times the eigenvalues of the *odd* disturbance modes of the Benard problem. The odd modes arise due to the zero-velocity condition at the thermal barrier; the constant appears due to more complicated differences between the two problems. The decrease in the constant factor for increasing mode number is expected, since higher modes are generally less sensitive to specific details of the boundary conditions. Similar comments may be made regarding the wavenumber.

Typical mode shapes at onset are shown in Fig. 2. (These are critical eigenfunctions of the stability problem for an assumed planform, not predictions of the flow for finite amplitude convection.) Here the physical reason for the modal pairing is evident. The lowest mode, Fig. 2(*a*), has corresponding convective cells in each layer rotating in the same direction – both clockwise or both counterclockwise. The second mode, Fig. 2(*b*), has corresponding convective cells rotating in opposite directions – one clockwise, the other counterclockwise. This behavior is found in higher modes as well. Thus, the heat transfer mechanism at the thermal barrier may be roughly characterized as countercurrent exchange for the corotating cells and cocurrent exchange for the counterrotating cells. This, again speaking roughly, tends to explain why the countercurrent corotating modes, being somewhat more efficient, occur at a slightly lower Rayleigh number than the less efficient cocurrent counterrotating modes.

Evidently, the corotating/counterrotating pairs represent two possible means of onset for a single flow instability. For the purposes of the Landau method, the modal contributions to heat transfer are summed only for those modes which are physically allowable. Since coroting and counterrotating modes cannot occur simultaneously, and since the corotating modes initiate and develop before incipience of counterrotating modes, we shall only sum contributions from the corotating modes in calculation of heat transfer beyond instability.

Modal Nusselt number coefficients C_j are presented in Table 1. Values of C_j are included for both the corotating (mode numbers 1, 3, 5, 7) and counterrotating modes (2, 4, 6, 8) although *only* the *odd*-numbered (corotating) modes are to be used in calculating the heat transfer beyond instability. The behavior of the C_j with changes in the parameters A and X is entirely predictable. For a given mode, C_j is smaller for less conductive midlayers (X increasing) and for thicker midlayers (A increasing). Similarly, C_j increases with increasing Ra_c to values approaching the theoretical upper bound of 2.0 (which is the free isothermal surface solution). Limiting values for small A and X are as follow:

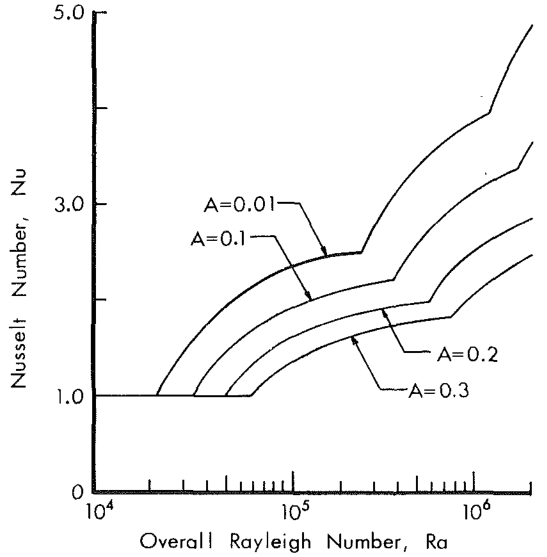

Fig. 3 Effect of midlayer thickness on heat transfer: $k/k_B = 1$

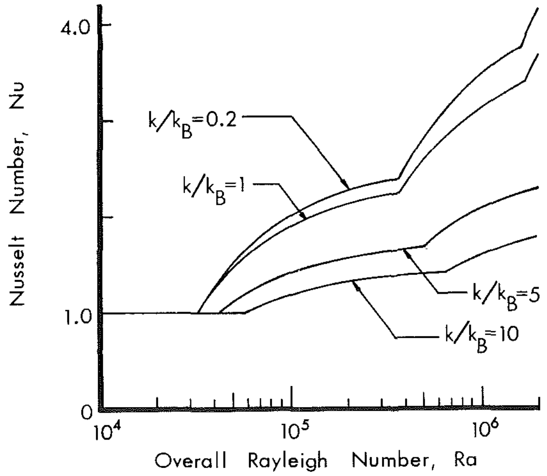

Fig. 4 Effect of midlayer conductivity on heat transfer: $A = 0.1$

$$C_j\Big|_{B=1} = \frac{N_j}{1+AX(1+N_j)}$$

$$C_j\Big|_{B=1} \rightarrow N_j\Big|_{A=0} = 1.72, A\rightarrow 0$$

$$C_j\Big|_{B=1} \rightarrow N_j\Big|_{X=0} = 1.446, X\rightarrow 0$$

where the first constant comes from extrapolation of our results (see below) and the second is a well-known result for the Benard problem.

The effects of A, X, and Rayleigh number are illustrated in Figs. 3 and 4. Figure 3 shows that as the midlayer becomes thicker (A increasing) the heat transfer decreases and the modal transitions (Malkus transitions) shift to higher Rayleigh numbers. Figure 4 shows that the same behavior occurs as the midlayer is made less conductive (X increasing). The curves for $A = 0$ and $X = 0$ will be quite close to those shown for small A and X.

As discussed by Catton and Lienhard, the effects of midlayer conduction upon individual fluid layer stability are most pronounced for thin midlayers of low conductivity. For thick midlayers of high conductivity, the stability problem for each layer approaches the ordinary Benard problem, and one expects that the heat transfer across the system may be adequately described using experimental correlations for ordinary Benard convection such as the three region correlation [8]

$$\mathrm{Nu}_{\mathrm{corr}} = \begin{cases} 1+1.446\left(1-\dfrac{1708}{\mathrm{Ra}}\right), & 1708<\mathrm{Ra}<5900 \\ 0.229\mathrm{Ra}^{0.252}, & 5900<\mathrm{Ra}<9.23\times10^4 \\ 0.157\mathrm{Ra}^{0.285}, & 9.23\times10^4<\mathrm{Ra}<10^6 \end{cases} \tag{27}$$

Taking this approach, one may define an effective conductivity for the fluid layers as

$$k_{\mathrm{eff}} = k\cdot\mathrm{Nu}_{\mathrm{corr}} \tag{28}$$

and sum thermal resistances to obtain an "engineering estimate" as

$$\mathrm{Nu}_{\mathrm{engr}} = \frac{\bar{q}}{q_{\mathrm{cond}}} = \left(\frac{1+AX}{\mathrm{Nu}_{\mathrm{corr}}^{-1}+AX}\right) \tag{29}$$

where $\mathrm{Nu}_{\mathrm{corr}}$ is calculated using the individual layer Rayleigh number Ra_i. To find Ra_i, we note the general relationship

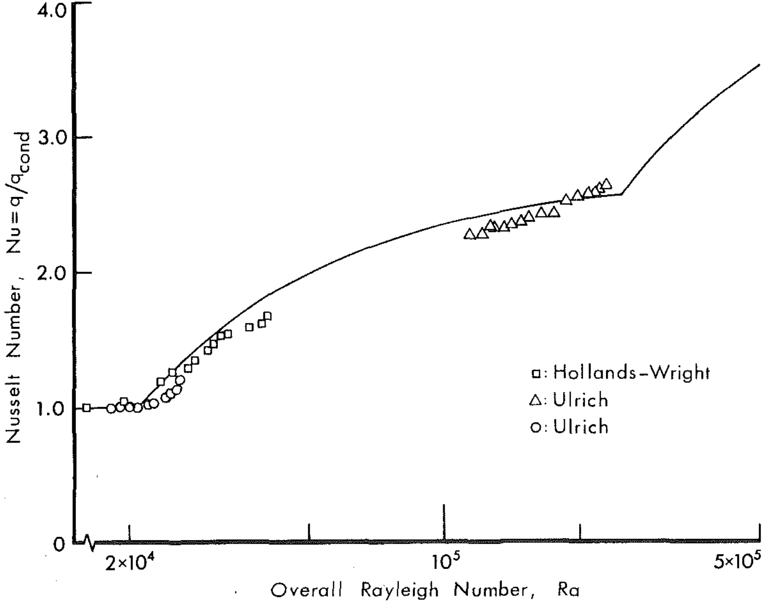

Fig. 5 Comparison of prediction to experiment: $A = 0.001$, $X = 0.05$-0.1

Table 3 Comparison of Nusselt numbers from power integral and estimated solutions

Ra	$\mathrm{Ra_i}$	$\mathrm{Nu_{pwr\ int}}$	$\mathrm{Nu_{engr}}$	$\mathrm{Nu_{Benard}}$
A = 0.3	X = 0.2			
50,000	1,342	1.00	1.00	3.50
70,000	1,866	1.19	1.11	3.81
100,000	2,610	1.53	1.46	4.18
200,000	5,091	1.92	1.86	5.09
500,000	12,393	2.16	2.27	6.61
700,000	17,162	2.33	2.44	7.27
1,000,000	24,213	2.76	2.63	8.05
3,000,000	69,492	3.55	3.28	-
A = 0.01	X = 5.0			
50,000	2,813	1.94	1.53	3.50
70,000	3,894	2.15	1.74	3.81
100,000	5,515	2.31	1.91	4.18
200,000	10,842	2.50	2.23	5.09
500,000	26,399	3.45	2.72	6.61
700,000	36,553	3.73	2.92	7.27
1,000,000	51,569	3.94	3.15	8.05
3,000,000	147,553	5.36	4.67	-

$$\mathrm{Ra}_1 = \mathrm{Ra}[(1+B)^4(1+A)^3(1+AX\mathrm{Nu}_{\mathrm{corr}})]^{-1} \qquad (30)$$

in which $\mathrm{Nu}_{\mathrm{corr}}$ appears as a manifestation of the reduction in ΔT_1 due to convection. Equation (30) must be iterated with equation (27) to find the correct Ra_1 and $\mathrm{Nu}_{\mathrm{corr}}$. For $B=1$, $\mathrm{Ra}_1 = \mathrm{Ra}_2 = \mathrm{Ra}_i$ and (30) is compatible with (29), the latter being particular to a centered midlayer problem.

The results of the engineering solution are compared to the power integral results for two extreme cases in Table 3. The first case, $A=0.3$ and $X=0.2$, shows good agreement, with errors up to 8 percent. The second case, $A=0.01$ and $X=5$, is considerably worse, having errors between 11 and 22 percent and a general trend of underprediction. These comparisons are, however, very encouraging. Firstly, the poor accuracy of the second case was to be expected because the engineering solution is based on an assumption which is strictly valid only for $A\rightarrow\infty$ and $X\rightarrow 0$. Secondly, both estimates were of roughly the same magnitude as our power integral solution. This gives convincing justification of our previous conclusion that only one member of each pair of disturbance modes contributes to the motion beyond modal instability, for if both types of disturbance were to be summed the power integral result would exceed the engineering result by as much as 100 percent. Unfortunately, a look at the C_j shows that the convective contributions from corresponding co- and counterrotating modes would be nearly the same (the counterrotating modes are somewhat less efficient), so that our rough estimate will not allow us to further assess our choice of corotating modes as those physically apparent.

The last column of Table 3 gives Nusselt numbers for the unpartitioned layer at the particular Ra ($\mathrm{Nu}_{\mathrm{Benard}}$). The reduction in heat transfer due to the midlayer is seen to be enormous, amounting to as much as a factor of 3.5. There is no need to point out the importance of this difference to the thermal designer.

Finally, we note that the two-layer power integral solutions may be valid to considerably higher Ra than the power integral solution for the unpartitioned layer, since the Rayleigh number of the individual layers is an order of magnitude lower than the overall Rayleigh number and Ra_i is what actually governs the convective process in each layer. Thus, recalling that comparison to experiment shows the power integral result to be valid to $\mathrm{Ra} = O(10^5)$ for the Benard problem, we anticipated that the two-layer result is valid to $\mathrm{Ra} = O(10^6)$.

Comparison of Predictions to Experiments

Two experimental investigations of two-layer heat transfer are currently available: Hollands and Wright [13], and Ulrich [12]. Both investigate an air layer 2–4 cm thick, centrally partitioned by a one-mil Teflon or Mylar film. Hence, in both studies $A \lesssim 0.001$ and $X \cong 0.05$–0.1.

Power integral calculations have not been made for these specific parameter values, but we may extract appropriate C_j and Ra_c from Table 1 using some facts about the stability problem. Ulrich found that he could parametrize Catton and Lienhard's stability curves with the single parameter X/A when A was small. Lienhard [14] has shown that this parametrization introduces less than 1 percent error in the boundary conditions when $a_iA<0.18$, where a_i is the individual layer wavenumber ($a_c = 2(1+A)a_i$, if $B=1$).

Since Ra_c and N_j, are determined only by the solution of the stability problem for given A and X and the latter is characterized by the ratio X/A, we may find X/A for the experiments and match this value to data for the same X/A in Table 1. In both experiments $X/A \cong 100$ (the stability limit is sensitive only to order of magnitude variations of X/A in this range) and the same ratio X/A occurs for $X=1$ with $A=0.01$. For the first two modes, we have

From Table 1	*Using equations (24) and (30)*
$\mathrm{Ra}_1 = 21850$	$\mathrm{Ra}_{i_1} = 1312.3$
$C_1 = 1.669$	$N_1 = 1.714$
$\mathrm{Ra}_3 = 254400$	$\mathrm{Ra}_{i_3} = 15280$
$C_3 = 1.692$	$N_3 = 1.738$

Substitution of the N_j and Ra_i into (24) and (30) with $A=0.001$ and $X=0.1$ gives

$$\mathrm{Ra}_1 = 21062 \qquad C_1 = 1.714$$
$$\mathrm{Ra}_3 = 245223 \qquad C_3 = 1.738$$

Hence, we have the prediction

$$\mathrm{Nu} = 1 + 1.714\left(1-\frac{21060}{\mathrm{Ra}}\right)U(\mathrm{Ra}-21060)$$
$$+\,1.738\left(1-\frac{245200}{\mathrm{Ra}}\right)U(\mathrm{Ra}-245200)$$

for $\mathrm{Ra} < 1.13\times10^6$ (third transition). To check the validity of the X/A parametrization note

$$a_{c_1} = 5.177 \quad a_{i_1} = 2.563 \quad aA = 0.026 < 0.18$$
$$a_{c_3} = 9.747 \quad a_{i_3} = 4.825 \quad aA = 0.048 < 0.18$$

so the conditions of the approximation are well satisfied. The accuracy of the extrapolation is essentially that of the data in Table 1.

The power integral prediction is compared to the data of Ulrich and of Holland and Wright in Fig. 5. Agreement is seen to be within 10 percent for both sets of data. This level of agreement is consistent with previous power integral results. From the agreement, one may infer that our results give a good estimate of Nusselt number for Prandtl numbers as low as that of air (~0.7) and for gases in general, if the walls are poor emitters of thermal radiation as in these experiments. (Radiation should be no problem in most liquid applications.)

The data extend to overall Rayleigh numbers of 2.4×10^5. At present, no data are available for higher Rayleigh numbers.

We note that Ulrich's data have been corrected for a systematic data reduction error appearing in [12]. The authors have discussed this adjustment with Ulrich [15] and the correction is agreed to be consistent with the experiments as he performed them.

Ulrich's study also includes experiments in which radiative coupling between the layers is significant. While radiative and convective effects are not directly separable therein, indications are that radiation may be very important in establishing the midlayer temperature distribution under high radiation conditions. This could have a significant effect on the thermal convection and may limit the usefulness of the present model under conditions of high radiation. A definitive statement must await further experimentation.

References

1 Catton, I., and Lienhard, J. H., V, "Thermal Stability of Two Fluid Layers Separated by a Solid Interlayer of Finite Thickness and Thermal Conductivity," ASME Journal of Heat Transfer, Vol. 106, Aug. 1984, pp. 605-612.

2 Malkus, W. V. R., and Veronis, G., "Finite Amplitude Cellular Convection," *Journal of Fluid Mechanics*, Vol. 4, Part 3, July 1958, pp. 225-260.

3 Stuart, J. T., "On the Non-Linear Mechanics of Hydrodynamic Stability," *Journal of Fluid Mechanics*, Vol. 4, Part 3, May 1958, pp. 1-24.

4 Catton, I., "Natural Convection in Horizontal Liquid Layers," *The Physics of Fluids*, Vol. 9, No. 2, Dec. 1966, pp. 2521-2522.

5 Catton, I., and Ayyaswamy, P., "Predictions of Momentum Transfer Between Rotating Cylinders: The Narrow Gap Problem," *Journal of Applied Mechanics*, Mar. 1972, pp. 33-35.

6 Sharman, R. D., Catton, I., and Ayyaswamy, P., "Convective Heat Transfer Between Concentric Rotating Cylinders," *AIChE Symposium Series*, Vol. 69, No. 131, pp. 118-125.

7 Somerton, C. W., "Natural Convection and Boiling in Porous Media," Ph.D. Dissertation, University of California at Los Angeles, 1982.

8 Buchberg, H., Catton, I., and Edwards, D. K., "Natural Convection in Enclosed Space—A Review of Application to Solar Energy Collection," ASME Journal of Heat Transfer, Vol. 98, No. 2, May 1976, pp. 182-188.

9 Catton, I., and Suo-Antilla, A. J., "Heat Transfer From a Volumetrically Heated Horizontal Fluid Layer," *Proceedings of the Fifth International Heat Transfer Conference*, Tokyo, Sept. 1974.

10 Landau, L. D., "On the Problem of Turbulence," *Papers of the Academy of Science of the USSR* ("Doklady"), Vol. 44, 1944, p. 339.

11 Lienhard, J. H., V, "Thermal Instability and Heat Transfer in a Singly Partitioned Horizontal Fluid Layer," Master's Thesis in Engineering, UCLA, 1984.

12 Ulrich, T. R., "Heat Transfer Across a Multi-Layered Air Enclosure," Master's Thesis in Engineering, UCI, 1984.

13 Hollands, K. G. T., and Wright, J. L., "Heat Loss Coefficients and Effective Products for Flat-Plate Solar Collectors With Diathermanous Covers," *Solar Energy*, Vol. 30, No. 3, 1983, pp. 211-216.

14 Lienhard, J. H., V, "Thermal Instability in Conductively Coupled Fluid Layer Arrays," presented at AIChE/ASME 23rd National Heat Transfer Conference, Denver, Aug. 4-7, 1985.

15 Ulrich, T. R., personal communication, Nov. 1984.

T. L. Bergman
Assoc. Mem. ASME

F. P. Incropera
Professor.
Fellow ASME

R. Viskanta
Professor.
Fellow ASME

Heat Transfer Laboratory,
School of Mechanical Engineering,
Purdue University,
West Lafayette, IN 47907

Correlation of Mixed Layer Growth in a Double-Diffusive, Salt-Stratified System Heated From Below

Although many mixed layer growth correlations have been developed for stratified solutions which are eroded by mechanically driven mixed layers, little has been done to determine their applicability to solutions for which erosion is thermally driven. In this study entrainment rates have been determined from measurements of mixed layer growth in salt-stratified solutions heated from below. Entrainment data have been obtained for Richardson numbers in the range $80 < Ri < 1000$, and when normalized with respect to the mixed layer convective velocity, the data are well correlated in terms of Ri^{-1}. The correlation also agrees with published data obtained at larger and smaller Richardson numbers for both thermally and salt-stratified solutions heated from below. Predictions based on use of the correlation in a mathematical model of mixed layer development are in excellent agreement with measured mixed layer heights and temperatures.

Introduction

Recent efforts in analyzing engineering systems and processes such as the salt-gradient solar pond, crystal growth, and liquified natural gas storage tanks [1-4] have stimulated interest in double-diffusive convection. In order to reliably design or analyze such systems, a thorough understanding of double-diffusive behavior is imperative.

When the stabilizing component of a double-diffusive system has a molecular diffusivity which is less than that of the destabilizing component, local destabilization may occur even though the density difference across the system is stable. Destabilization causes local convective mixing, which results in formation of a mixed layer whose component concentrations and density are nearly uniform. For example, when an initially isothermal, salt-stratified solution is heated from below, an unstable temperature gradient develops above the heated surface. The gradient may induce local thermal instability and convective motion in a mixed layer which, unlike single-diffusive fluids, is restricted by the stabilizing salt distribution. As heat is continuously supplied to the system, the mixed layer expands at the expense of fluid from the overlying stable region, which is entrained into the mixed layer through an interfacial boundary layer separating the two regions. For large values of the bottom heat flux and/or small stabilizing salt concentration gradients, mixed layer growth may be curtailed when the unstable temperature distribution ahead of the mixed layer destabilizes lower portions of the stable region, leading to formation of a series of thin multiple mixed layers [5]. New layers may continue to form, while existing layers merge in lower regions of the system. In contrast, for smaller heat fluxes and/or larger salinity gradients, slow growth of the mixed layer occurs continuously, without multiple layer formation [6].

Knowledge of the mixed layer growth rate is essential to understanding the behavior of double-diffusive convection, since thermal and salinity conditions are strongly influenced by the growth rate. As mixed layer growth rate data become available, overall system behavior may be predicted from existing mathematical models [7]. Although the mechanism(s) by which overlying stable fluid is entrained into the mixed layer is not well understood, considerable progress has been made in correlating entrainment rates for similar physical systems.

If an initially stratified single diffusive system is destabilized by a turbulence-producing oscillating grid [8] or application of a shear stress [9] at one of its boundaries, steady growth of a mixed layer will occur. Assuming that fluid kinetic energy produced by the applied destabilizing boundary condition is destroyed in the entrainment process, growth rates of the mixed layer may be normalized with the friction velocity of the oscillating grid or applied shear stress and correlated in terms of a bulk Richardson number [8]. That is

$$u_e/u_* = A\,\mathrm{Ri}^n \tag{1}$$

where

$$\mathrm{Ri} \equiv g\Delta\rho\delta_b/(\rho_0 u_*^2) \tag{2}$$

The exponent in equation (1) was initially found to depend on whether the density difference across the interface $\Delta\rho$ was due to a temperature ($n = -1$) or salt concentration ($n = -3/2$) difference [8]. However, subsequent studies [9] have indicated that a value of $n = -1$ is also appropriate for salt stratification. The coefficient A may vary according to whether the friction velocity is defined in terms of length and velocity scales derived from physical features of the oscillating grid [8] or the applied shear stress [9].

The notion that fluid motion within the mixed layer is responsible for entrainment at a density interface has been extended to situations for which motion is induced by bottom heating and the density interface is an interfacial boundary layer separating a bottom mixed layer from an overlying stable, thermally stratified fluid [10]. Rather than normalizing the entrainment rate with a friction velocity, the following convective velocity was used

$$u_* \equiv (g\beta_{T,b}q_b\delta_b/\rho_b c_{v,b})^{1/3} \tag{3}$$

Preferred values of the exponent and correlation coefficient in equation (1) were reported as $n = -1$ and $A = 0.25$ [10]. Since density differences across the interfacial boundary layer are very small for the thermally stratified case, Richardson numbers were restricted to values less than 80.

Entrainment rates across the interfacial boundary layer of double-diffusive, salt-stratified systems heated from below

---

Contributed by the Heat Transfer Division for publication in the JOURNAL OF HEAT TRANSFER. Manuscript received by the Heat Transfer Division June 7, 1984.

have also been normalized with respect to the convective velocity of equation (3) and have been correlated by equation (1), with values of $n=-1$ and $A=0.20$ [11]. Due to the stratifying salinity distribution, density differences across the interfacial boundary layer are large and are due primarily to a large salinity difference. As such, Richardson numbers for the double-diffusive system are in the range $10^3 < \mathrm{Ri} < 10^4$.

Although mixed layer growth rates in salt-stratified solutions heated from below have been correlated with the Richardson number [11], an alternative entrainment mechanism has been hypothesized and used to explain mixed layer growth [12, 13]. This mechanism is assumed to occur due to the coexistence of salinity and temperature gradients at the interfacial boundary layer. Because the Lewis number of salt water solutions is much greater than unity, destabilizing temperature gradients penetrate further from the diffusive region into the bottom mixed layer than the stabilizing salinity gradients. As such, at some point during this double-diffusive process, a local thermal instability will occur causing a cool thermal plume to fall from the interfacial boundary layer into the bottom mixed layer [12]. The plume is assumed to enhance heat and salt transport at the interfacial boundary layer and to result in growth of the bottom mixed layer [13]. Since the double-diffusive driven entrainment mechanism is independent of convective conditions within the mixed layer, correlation of normalized mixed layer growth rates with a Richardson number may not be possible if the mechanism is dominant.

Although several entrainment correlations have been developed for single species stratified solutions which are eroded by mechanically driven mixed layers [14], limited data exist for single or double-diffusive systems with thermally driven mixed layers [10, 11]. Due to the limited data, it is uncertain whether the double-diffusive driven entrainment mechanism is important. Moreover, there are no data for thermally driven mixed layers with Richardson numbers in the range $80 < \mathrm{Ri} < 1000$. Hence a major objective of this study is to obtain data for single mixed layer growth in double-diffusive, salt-stratified systems heated from below in the range $80 < \mathrm{Ri} < 1000$ and to attempt to correlate the results in terms of the convective velocity and the bulk Richardson number. An additional objective is to use the correlation in a mathematical model for predicting mixed layer heights, temperatures, and salt concentrations and to compare predictions with available data.

Experimental Methods

Experiments were performed in a test cell with a square base (305 mm × 305 mm × 200 mm) and 25-mm-thick acrylic side walls. The base of the test cell consisted of an electronic patch heater sandwiched between a 1.6-mm copper plate, which served as the bottom of the test cell, and a 25-mm sheet of styrofoam. A second patch heater was placed between the styrofoam and additional insulation and served as a thermal guard. A control circuit monitored the output of thermistors placed on both sides of the styrofoam and operated the power supply to the guard heater. Temperature differences across the styrofoam were controlled to within ± 0.1°C, thereby minimizing heat losses through the bottom of the test cell. The walls of the test cell were insulated with 50-mm styrofoam sheets. Analysis of the measured temperature distributions within the salt-stratified fluid indicated that increases of the internal energy within the system accounted for approximately 90 percent of the applied bottom heat flux. As such, wall heat losses were generally less than 10 percent of the heat input to the system.

Vertical temperature distributions near the center of the test cell were measured with a thermocouple rake consisting of 29 calibrated copper-constantan thermocouples mounted at 6.4-mm intervals. The heated surface temperature was measured with a thermocouple installed beneath the copper plate. Temperature differences across the copper plate are negligible for the range of heat fluxes used in the experiments. Vertical temperature distributions were automatically recorded with a Hewlett-Packard 3054A data aquisition system. Mixed layer heights were determined by the shadowgraph technique [6]. The shadowgraph was obtained by removing insulation panels from the test cell walls.

The test cell was filled by successively adding six layers of salt solution of different salinity. The test cell was then tightly covered to minimize the development of an evaporatively driven mixed layer at the surface and was allowed to remain undisturbed for two days. The transient, one-dimensional mass diffusion equation was solved for the two-day period to obtain an initial salinity profile corresponding to the start of heating. The predicted profile was nearly linear, except within approximately 10 mm of the bottom and top impermeable boundaries, where a gradual transition to a uniform distribution occurred. The predicted salinity distribution near the top surface is less accurate, however, due to the existence of a thin (≈ 30 mm) evaporatively driven top mixed layer at the outset of each experiment.

As mixed layer growth occurs in response to bottom heating, the vertical distribution of salt concentration within the stable region is known to experience little change [11]. In addition the temperature difference across the interfacial boundary layer is known to be small and to have a negligible effect on the density difference. As such, the density difference is attributed only to the salinity difference Δm_s and is expressed as

$$\Delta\rho = \Delta m_s\, \partial\rho/\partial m_s|_T \tag{4}$$

The salinity difference across the interfacial boundary layer is

Nomenclature

A = coefficient of Richardson number correlation
c_v = specific heat
g = gravitational acceleration
k = thermal conductivity
L = arbitrary length
m_s = salt mass fraction
n = exponent of Richardson number correlation
q_b = bottom heat flux
Ra_T^* = modified thermal Rayleigh number = $g\beta_T q_b L^4/k\alpha\nu$
Ra_S = solutal Rayleigh number = $g\beta_s(\partial m_s/\partial z)_i L^4/\alpha\nu$

Ri = Richardson number = $g\Delta\rho\delta/\rho_0 \cdot u_*^2$
t = time
T = temperature
u_e = entrainment velocity = $d\delta_b/dt$
u_* = convective (friction) velocity
z = vertical space coordinate measured from bottom
α = thermal diffusivity
β_s = saline expansion coefficient
β_T = thermal expansion coefficient
δ_b = mixed layer hieght
δ_p = thermal penetration height

Δm_s = salt mass fraction difference across the interfacial boundary layer
$\Delta\rho$ = mass density difference across the interfacial boundary layer
ν = kinematic viscosity
ρ = mass density

Subscripts

b = bottom mixed layer
d = diffusive region
i = initial
0 = reference

Table 1 Experimental conditions

Experiment	q_b (W/m^2)	$\partial m_s/\partial z\|_i$ (percent/m)	$\mathrm{Ra}_T^*/\mathrm{Ra}_S$
1	40	30.4	0.071
2	40	19.1	0.112
3	90	28.1	0.172
4	90	18.7	0.258
5	40	5.8	0.369
6	90	6.1	0.790
7	450	29.3	0.825
8	450	18.2	1.326
9	450	5.9	4.080

$$\Delta m_s = \frac{1}{\delta_b}\int_{z=0}^{\delta_b} m_{s,i}(z)\,dz - m_{s,i}\ (z=\delta_b) \qquad (5)$$

where the first term on the right-hand side of (5) is the average salinity within the bottom mixed layer and $m_{s,i}(z)$ is the initial salinity distribution within the system.

From knowledge of the mixed layer height as a function of time and the bottom heat flux, initial salinity profile, and thermophysical properties of saline solutions [15], the entrainment and convective velocities may be determined from $u_e = d\delta_b/dt$ and (3), respectively. The salinity difference across the interfacial boundary layer may be determined from (5), allowing for calculation of the corresponding density difference from (4) and the bulk Richardson number from (2).

A total of nine experiments, which were characterized by three different initial salinity distributions and bottom heat fluxes, were performed. The stability of an experiment may be described by the ratio of the modified thermal Rayleigh number to the solutal Rayleigh number

$$\mathrm{Ra}_T^*/\mathrm{Ra}_S = \beta_T q_b / k\beta_s (\partial m_s/\partial z)_i \qquad (6)$$

where Ra_T^* and Ra_S are the modified thermal and solutal Rayleigh numbers, respectively.

The Rayleigh number ratio increases as the system becomes less stable. Values of the initial salinity gradient, the applied heat flux, and the Rayleigh number ratio for the experiments are shown in Table 1.

Theoretical Methods

The experimental mixed layer growth correlation may be used in a multilayer model to predict mixed layer temperature and salt concentration, as well as mixed layer height. The multilayer model is formulated by applying conservation principles to the two-layer system of Fig. 1. The system consists of a bottom mixed layer, whose height and temperature increase with time, and an overlying stable region characterized by an upward propagating temperature distribution. Solution of the model is terminated when thermal effects penetrate to the top of the stable region ($t \approx 5$ h). A detailed discussion of the model, which consists of a system of coupled differential equations describing the mixed layer height (δ_b), temperature (T_b), and thermal penetration depth within the stable diffusive region (δ_p), is available elsewhere [7].

Results

Typical measured vertical temperature distributions are shown in Fig. 2 for Experiment 7. Temperature inversions above the heated surface drive a bottom mixed layer which grows at the expense of the overlying stable region. Thermal effects propagate to the top of the test cell, which is characterized by a thin, slightly cooled mixed layer. Removal of the cover placed on the test cell at the beginning of the experiment increases evaporative losses from the surface. These losses initially decrease surface temperatures until they are offset by heat addition from the underlying diffusive region as thermal effects propagate to the top of the system. Significant temperature differences across the interfacial boundary layer are not evident.

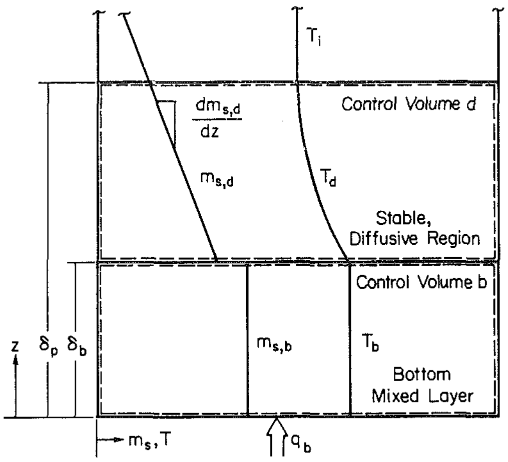

Fig. 1 Two-layer system for response of a salt-stratified solution to heating from below

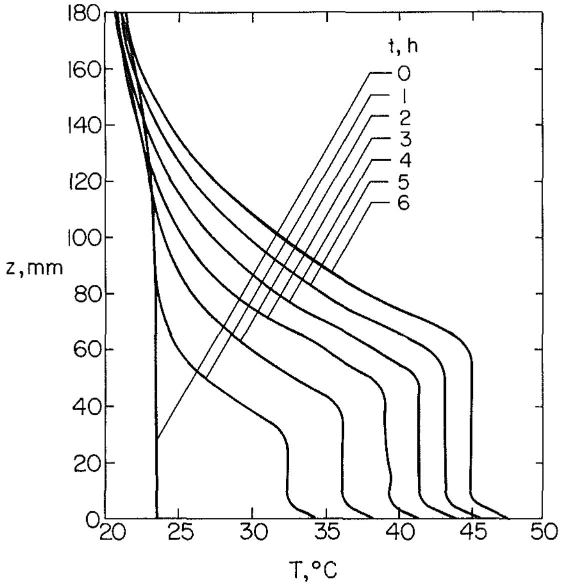

Fig. 2 Typical vertical temperature distributions of Experiment 7

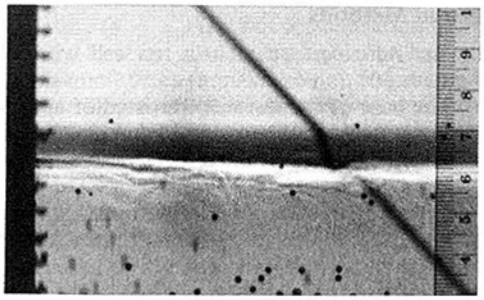

Fig. 3 Shadowgraph of the interfacial boundary layer separating the bottom mixed layer and the stable region of Experiment 7 ($t = 6$ h)

Although the transient temperature profiles in Fig. 2 are typical of system behavior, not all of the experiments exhibited similar trends. For example, Experiment 1, which was characterized by a small Rayleigh number ratio, never experienced mixed layer development, since unstable temperature gradients above the heated surface were too small to overcome the stabilizing salinity distribution. Conversely, for large Rayleigh number ratios (Experiments 8 and 9), con-

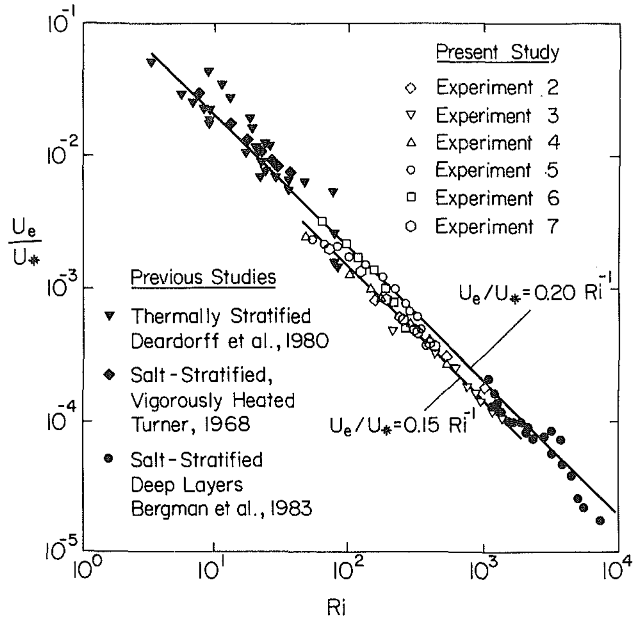

Fig. 4 Mixed layer growth data and correlation

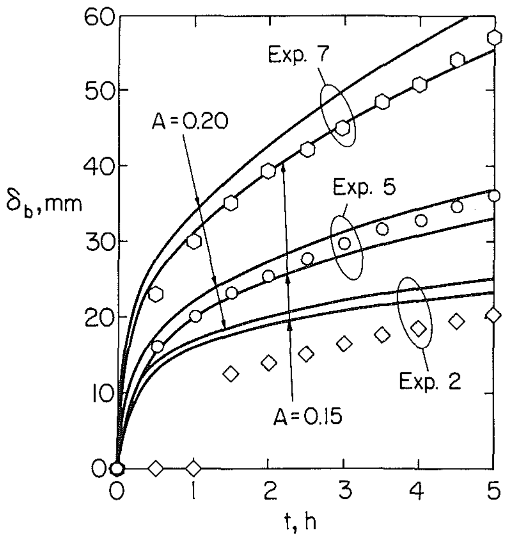

Fig. 5 Measured and predicted mixed layer heights

ditions were characterized by the onset and development of a series of multiple mixed layers above the bottom mixed layer.

Although the intermediate experiments (2–7) were characterized by continuous growth of a single bottom mixed layer, growth rates varied significantly. For example, Experiment 2 attained a mixed layer height of 50 mm after 35 h, while Experiment 7 reached a similar height after only 4 h. In Experiments 2 and 3, the onset of thermal instability was delayed. Only after temperatures near the heated surface had risen by several degrees which, in turn, increased the local value of β_T, did the onset of convection occur at $t = 70$ min for Experiment 2 and $t = 20$ min for Experiment 3.

Although temperature differences across the interfacial boundary layer were negligible, density variations were significant, as is evident in the shadowgraph (Experiment 7, $t = 6$ h) of Fig. 3. The horizontal dark and light bands indicate a large variation in the density across the interfacial boundary layer. Moreover, a straight slanted wire, which is stretched across the collimated light beam on the opposite side of the test cell, casts a shadow which is highly distorted at the interfacial boundary layer, again suggesting significant density variation. Since temperature differences across the interfacial boundary layer are negligible, the sharp density variation at the interfacial layer is, as previously noted, due mainly to salinity variations.

Entrainment rates for the bottom mixed layer were determined from shadowgraph data, normalized with the convective velocity, and plotted against the bulk Richardson number in Fig. 4. In addition, data reduced from the experimental results of Turner [16] for salt-stratified fluids heated vigorously ($q_b \approx 2500$ W/m^2) from below have been included. Due to the vigorous heating, convective velocities are large resulting in small values of the Richardson number. Also shown are large Ri data for salt-stratified systems heated from below in larger test cells with deep mixed layers [11]. Finally, data reported for thermally stratified systems heated from below [10], which are characterized by small stabilizing density differences across the interfacial boundary layer and hence small Ri, are presented.

It is clear that all data are well correlated by the expression

$$u_e/u_* = 0.20\,\mathrm{Ri}^{-1} \qquad (7)$$

For the Richardson number range of the present study, it is also evident that the data are bracketed by equation (7) and the same correlation with $A = 0.15$. The correlation spans three orders of magnitude in Ri and appears to be valid for both salt and thermally stratified systems destabilized by bottom heating. Moreover, the correlation applies regardless of test cell size or configuration.

Since the correlation of equation (7) appears to be valid for single-diffusive systems, as well as double-diffusive systems destabilized by bottom heating, the double-diffusive driven entrainment mechanism may not be dominant in the present study. However, failure to account for this mechanism in the Richardson number correlation may be responsible for some, if not all, of the data scatter evident in Fig. 4.

Several limitations and features of equation (7) and Fig. 4 should be noted. Since the viscosity of the fluid is not included in the correlation, it may, in fact, be limited to water-based solutions [17]. In addition, although the reduced data of Turner [16] are in good agreement with equation (7), correlation of the data is not consistent with Turner's assumption that the growth rate of the mixed layer exceeded the rate of propagation of thermal effects in the stable diffusion region. As such, Turner assumed the existence of large temperature differences across the interfacial boundary layer which offset any density variation due to a salinity difference. Hence, density differences across the interfacial boundary layer were presumed to be zero, precluding applicability of a Richardson number correlation. This premise is in sharp contrast to the assumption inherent in equation (4). However, the fact that Turner noted the eventual formation of multiple mixed layers above the bottom mixed layer indicates that the growth rate of the mixed layer was not large enough to justify neglecting the existence of a propagating temperature profile in the overlying stable region. Rather than being discontinuous at the interfacial boundary layer, the temperature profiles of Turner's experiments must exhibit characteristics similar to those shown in Fig. 2, with small temperature and large density differences across the interfacial boundary layer. This behavior suggests that a Richardson number correlation is, in fact, applicable to his data.

The entrainment correlation of equation (7) may be used in the multilayer model to predict mixed layer heights, temperatures, and salt concentrations. Actual and predicted mixed layer heights are presented in Fig. 5 for experiments 2, 5, and 7, which correspond to small, intermediate, and large values of the Rayleigh number ratio. Predicted results are shown for two values of the Richardson number correlation coefficient, $A = 0.20$ and $A = 0.15$.

Agreement between the actual and predicted mixed layer

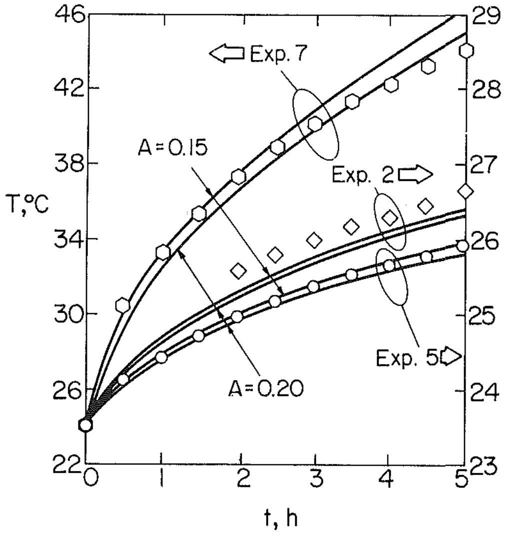

Fig. 6 Measured and predicted mixed layer temperatures

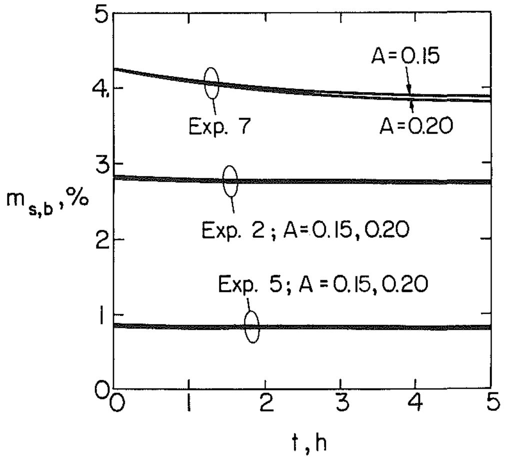

Fig 7 Predicted mixed layer salt concentrations

heights is very good for Experiments 5 and 7, with better corroboration obtained if a value of $A = 0.15$ is used in Experiment 7. This result is expected since inspection of Fig. 4 reveals that the entrainment data of Experiment 7 are better represented by a correlation coefficient of 0.15. Alternatively, Fig. 4 reveals entrainment data for Experiment 5 which are below the correlation for $A = 0.20$ at early times (small values of Ri) and rise to meet the curve at later times (larger Ri). This trend is revealed in Fig. 5 by the good agreement between actual and predicted mixed layer heights for Experiment 5 if a value of $A = 0.15$ is used at early times and $A = 0.20$ is used at later times.

Agreement between predicted and measured mixed layer heights is poor for Experiment 2. The discrepancy is due to failure of the model to account for the delayed onset of convection in the marginally unstable experiments. However, subsequent growth rates predicted by the model are close to those suggested by the data. Agreement between the predicted and actual mixed layer heights for Experiments 4 and 6 is excellent if values of $A = 0.15$ and 0.20, respectively, are chosen.

Predicted and measured mixed layer temperatures are shown in Fig. 6. Once again, agreement between the results is good for Experiments 5 and 7. Good agreement is obtained for Experiment 5, regardless of the correlation coefficient although, as expected, a decrease in the mixed layer growth rate ($A = 0.15$) results in slightly increased layer temperatures. For Experiment 7, mixed layer temperatures are well predicted at early times with $A = 0.15$, but at later times predicted temperatures are slightly larger than the measured values. This discrepancy is attributed to neglecting side wall heat losses in the model. For the relatively high temperatures of Experiment 7, wall losses may be significant and would act to decrease the mixed layer temperature.

Agreement between measured and predicted mixed layer temperatures is poor for Experiment 2, and the discrepancy is again attributed to failure of the model to account for the delayed onset of convection. As mixed layer heights are overpredicted for Experiment 2, mixed layer temperatures are significantly underpredicted. Agreement between the predicted and measured mixed layer temperatures for Experiments 4 and 6 is excellent, regardless of the value of A.

Predicted mixed layer salt concentrations are shown in Fig. 7. There is only a small variation in concentration over the time interval of the experiments, and the trend is one of decreasing concentration with increasing mixed layer height. Weight analysis of a limited number of samples extracted from the bottom mixed layer also indicated a small variation in the mixed layer salinity.

Summary

An experimental correlation has been determined for thermally driven mixed layer growth in a salt-stratified, double-diffusive system. Data span the Richardson number range $80 < \mathrm{Ri} < 1000$ and, when normalized with respect to a convective velocity, are well correlated by the expression $u_e/u_* = A/\mathrm{Ri}$, where A is in the range $0.15 < a < 0.20$. The correlation also agrees well with data for smaller and larger values of Ri, for both thermally and salt-stratified systems, and for a range of test cell configurations. Use of the correlation in a multilayer model results in good agreement with mixed layer height and temperature data if conditions are characterized by immediate mixed layer growth. The model is unable to account for any delay in the onset of convection.

The mixed layer growth correlation is limited to water solutions, since the effects of viscosity are not included, and the multilayer model is limited to short-term (days) experiments, since salt diffusion is neglected. Although the correlation is valid for a range of test cell sizes and configurations, its extension to much larger (solar pond) or much smaller (crystal growth) systems may be limited.

Acknowledgments

Support of this work by the National Science Foundation under Grant No. MEA-8316580 and the Solar Energy Research Institute under Grant No. XP-3030471 is gratefully acknowledged.

References

1 Tabor, H., "Solar Ponds," *Solar Energy*, Vol. 27, 1981, pp. 181-194.

2 Ostrach, S., "Fluid Mechanics of Crystal Growth—The 1982 Freeman Scholar Lecture," ASME *Journal of Fluids Engineering*, Vol. 105, 1983, pp. 5-20.

3 Morioka, M., and Enya, S., "Natural Convection of Density-Stratified Layers in a Vessel I: Observation of Flow Patterns," *Heat Transfer, Japanese Research*, Vol. 12, 1983, pp. 48-69.

4 Viskanta, R., Bergman, T. L., and Incropera, F. P., "Double-Diffusive Convection," in: *Natural Convection: Fundamentals and Applications*, S. Kakac et al., eds., Hemisphere, Washington D.C. (in press).

5 Huppert, H. E., and Linden, P. F., "On Heating a Stable Salinity Gradient From Below," *Journal of Fluid Mechanics*, Vol. 95, 1979, pp. 431-464.

6 Poplawsky, C. J., Incropera, F. P., and Viskanta, R., "Mixed Layer Development in a Double-Diffusive Thermohaline System," ASME *Journal of Solar Energy Engineering*, Vol. 103, 1981, pp. 351-359.

7 Bergman, T. L., Incropera, F. P., and Viskanta, R., "A Multi-Layer

Model for Mixing Layer Development in a Double-Diffusive Thermohaline System Heated From Below," *International Journal of Heat and Mass Transfer*, Vol. 25, 1982, pp. 1411-1418.

8 Turner, J. S., "The Influence of Molecular Diffusivity on Turbulent Entrainment Across a Density Interface," *Journal of Fluid Mechanics*, Vol. 33, 1968, pp. 639-656.

9 Kato, H., and Phillips, O. M., "On the Penetration of a Turbulent Layer Into Stratified Fluid," *Journal of Fluid Mechanics*, Vol. 37, 1969, pp. 643-655.

10 Deardorff, J. W., Willis, G. E., and Stockton, B. H., "Laboratory Studies of the Entrainment Zone of a Convectively Mixed Layer," *Journal of Fluid Mechanics*, Vol. 100, 1980, pp. 41-64.

11 Bergman, T. L., Munoz, D. R., Incropera, F. P., and Viskanta, R., "Correlation for Entrainment of Salt-Stratified Fluid by a Thermally Driven Mixed Layer," ASME Paper No. 83-WA/HT-76.

12 Linden, P. F., and Shirtcliffe, T. G. L., "The Diffusive Interface in Double-Diffusive Convection," *Journal of Fluid Mechanics*, Vol. 87, 1978, pp. 417-432.

13 Meyer, K. A., "A Numerical Model to Describe the Layer Behavior in Salt-Gradient Solar Ponds," ASME *Journal of Solar Energy Engineering*, Vol. 105, 1983, pp. 341-347.

14 Turner, J. S., *Buoyancy Effects in Fluids*, Cambridge University Press, 1979.

15 United States Office of Saline Water, Technical Data Book, 1964.

16 Turner, J. S., "The Behavior of a Stable Salinity Gradient Heated From Below," *Journal of Fluid Mechanics*, Vol. 33, 1968, pp. 183-200.

17 Kantha, L. H., "A Note on the Effect of Viscosity on Double-Diffusive Processes," *Journal of Geophysical Research*, Vol. 85, No. B8, 1980, pp. 4398-4404.

Journal of Heat Transfer
Technical Notes

This section contains shorter technical papers. These shorter papers will be subjected to the same review process as that for full papers.

Turbulent Flow and Heat Transfer in Bends of Circular Cross Section: II – Pressure Distribution Experiments

G. M. Chrysler[1] **and E. M. Sparrow**[2]

Nomenclature

A = cross-sectional area
C_p = pressure coefficient, equation (1)
D = diameter of bend cross section
p = local pressure
p^* = reference pressure, p_∞ for sharp-edged inlet and $p(-10)$ for tube-fed inlet
$p(-10)$ = pressure at $X/D = -10$
p_∞ = ambient pressure
R = radius of bend cross section
R_c = radius of curvature of bend
Re = Reynolds number $= 4\dot{w}/\mu\pi D$
V = mean velocity
$\dot{w}$ = mass flow rate
X = axial coordinate in delivery tube
θ = turning angle of bend
μ = viscosity
ρ = density
ϕ = angular coordinate

Introduction

This paper conveys the results of detailed pressure distribution measurements in bends of circular cross section in the presence of different hydrodynamic conditions at the bend inlet. This information is intended to complement and enhance the heat transfer results presented in [1], which correspond to the same bend geometries (i.e., same circular cross section, radius of curvature, and turning angles), hydrodynamic inlet conditions, and Reynolds number range.

For one of the investigated hydrodynamic conditions, air was conveyed to the bend inlet by a straight circular tube which served as a development length. For the other, air from a very large upstream plenum chamber was drawn into the bend through a sharp-edged inlet. For each of these cases, streamwise and circumferential pressure measurements were made in bends having turning angles of 30, 60, and 90 deg for Reynolds numbers between 5000 and 100,000. Measurements were also made in the hydrodynamic development tube in order to determine whether the circumferential pressure variations in the bend propagate upstream.

In reviewing the literature, attention will be focused on bends and curved tubes of circular cross section. Although the fluid flow in such passages has been extensively investigated, the case of the plenum-fed, sharp-edged inlet appears not to have been previously considered. In-bend pressure distributions are only sparsely reported in the published literature [2, 3] and, as will be elaborated later, the available information is characterized by uncertainties.

Other literature, relevant as background, will be mentioned briefly and representative references cited. Flow field experiments in bends have been performed by laser-Doppler velocimetry in [3–5] and by total pressure and yaw probes [6], while numerical solutions for turbulent and laminar flow are respectively reported in [7, 8] and in [9]. The laminar case was also analyzed using a perturbation method [10]. Curved pipes of sufficient length to allow attainment of fully developed flow were analyzed in [11, 12] for laminar conditions and in [13] for turbulent conditions. Experimentally determined, fully developed friction factors for curved pipes and helical coils are reported for laminar flow in [14] and for turbulent flow in [14–16]. Broad-ranging reviews of flow in bends are contained in the monographs of Ward-Smith [17, 18] and in the survey article of Berger, Talbot, and Yao [19].

Apparatus

The bends used in the pressure distribution experiments were fabricated from plexiglass as described in detail in [20]. Each bend was made up of identical but separate upper and lower walls. A curved troughlike channel of semicircular cross section was machined into each wall so that, when the walls were assembled, they formed a bend of circular cross section. The radius R of the cross section was 1.5875 cm (0.625 in.), and the radius of curvature R_c of the bend centerline was characterized by $R_c/R = 9$. As noted earlier, bends having turning angles $\theta = 30$, 60, and 90 deg were used in the experiments.

In each bend, three pressure taps were installed around the circumference of the cross section at a succession of streamwise stations. The circumferential locations are designated inner wall, midwall, and outer wall and are illustrated in the upper part of Fig. 1. There are 30 taps in the 90 deg bend, 18 in the 60 deg bend, and 12 in the 30 deg bend.

In one of the test setups, air was fed to the bend by a straight circular tube (radius = 1.5875 cm = 0.625 in.) whose centerline was tangent to that of the bend at their point of intersection. The tube was 30 diameters long – sufficiently long so that a linear pressure distribution existed over an appreciable portion of its length, as will be documented shortly. In the other setup, the inlet cross section of the bend was framed by a large circular disk, 50.8 cm (20 in.) in

---

[1] Department of Mechanical Engineering, University of Minnesota, Minneapolis, MN 55455; Assoc. Mem. ASME

[2] Department of Mechanical Engineering, University of Minnesota, Minneapolis, MN 55455; Fellow ASME

Contributed by the Heat Transfer Division for publication in the JOURNAL OF HEAT TRANSFER. Manuscript received by the Heat Transfer Division December 5, 1984.

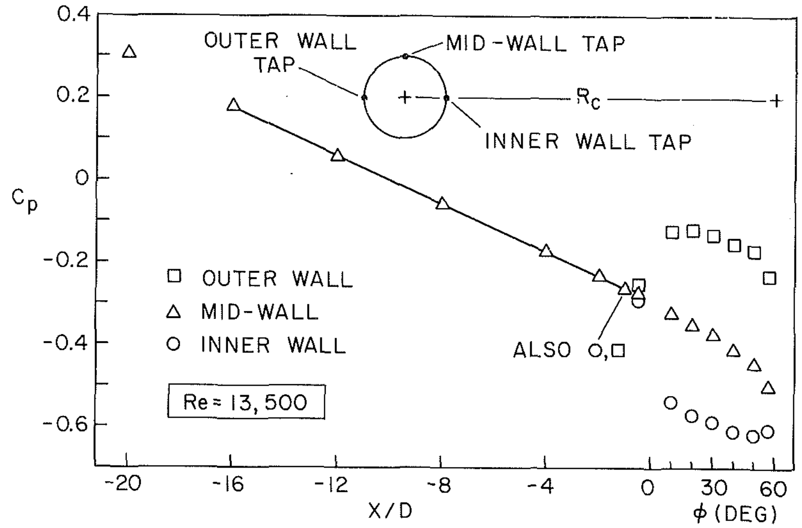

Fig. 1 Representative pressure distributions in the hydrodynamic development tube and the bend

diameter. In effect, the disk served as the downstream wall of a large plenum chamber (i.e., the laboratory room) from which air was drawn into the bend through a sharp-edged inlet. In both setups, the airflow exiting the bend passed into an exhaust tube whose length and diameter were identical to those of the delivery tube in the first setup.

The apparatus was operated in the open-circuit mode and in suction, with the exhaust from the downstream-positioned blower being vented outdoors. The signals from the pressure taps were detected by a Baratron solid-state pressure meter equipped with three sensing heads having respective capacities of 1, 10, and 100 Torr and corresponding resolutions of 0.0001, 0.001, and 0.01 Torr. At each pressure tap, ten consecutive pressure readings were made and subsequently averaged.

Results and Discussion

Data Reduction. The measured pressure distributions will be presented in dimensionless form via the pressure coefficient C_p defined as

$$C_p = (p - p^*)/(\tfrac{1}{2}\rho V^2)^*, \quad (\rho V^2)^* = (\dot{w}/A)^2/\rho^* \tag{1}$$

where p is the local static pressure and p^* is a reference pressure (ρ^* corresponds to p^* and to the known temperature). For the case of the sharp-edged inlet, p^* will be taken as the pressure p_∞ in the plenum from which the air is drawn (i.e., the pressure in the laboratory room). For the bend fed by a hydrodynamic development tube, it is inappropriate to take $p^* = p_\infty$ since, for such a choice, C_p would depend on the length of the development tube and the geometry of its entrance. It appears best to evaluate p^* at a station in the development tube where pressure linearity prevails and which is situated at a designated distance upstream of the bend. Here, the station at $X/D = -10$ is used as the reference location, i.e., $p^* = p(-10)$. The Reynolds number is that for a conventional circular tube, $\mathrm{Re} = \rho VD/\mu = 4\dot{w}/\mu\pi D$.

Upstream Propagation of Bend Pressure Field. Before presenting the pressure distributions in the bend, it is relevant to display the precursive effect of the bend on the pressure field in the delivery tube. Figure 1 shows the streamwise variation of C_p in both the delivery tube and the bend for a representative case – $\mathrm{Re} = 13{,}500$ and $\theta = 60$ deg. The abscissa range $X/D < 0$ corresponds to the delivery tube ($X = 0$ at the bend inlet), while ϕ is the streamwise coordinate in the bend, measured along the centerline.

Table 1 Measured pressure distributions

$\mathrm{Re} \times 10^{-3}$	5	8.2	13.5	22	37	61	100
Plotted in	Fig. 2	[20]	Fig. 3	[20]	[20]	[20]	Fig. 4

In the portion of the tube between $X/D = -16$ and -1, the pressure distribution in the delivery tube is strictly linear and is represented with high precision by the least-squares fit

$$C_p = -0.2916 - 0.02916(X/D) \tag{2}$$

with a corresponding friction factor f of 0.02916 which differs by only 0.7 percent from the Blasius value.

At $X/D = -1$, the outer, inner, and midwall taps yielded identical pressures. However, at $X/D = -0.5$, there is a cross-stream pressure variation whose presence shows that secondary flow exists in the delivery tube upstream of the bend – thereby testifying to the precursive effect of the bend. The existence of such a precursive effect has been omitted in various numerical approaches to the fluid flow problem in the bend. The precursive cross-stream pressure variation in the delivery tube is, however, moderate compared with that which develops in the bend, just downstream of the inlet.

Bend Pressure Distributions. Measurements of the pressure distributions in both the tube-fed bends and in bends with sharp-edged inlets have been made for seven values of the Reynolds number between 5000 and 100,000. The Reynolds numbers are listed in Table 1. As indicated there, C_p versus ϕ distributions for Re = 5000, 13,500, and 100,000 are respectively presented in Figs. 2-4, while the remainder of the distributions are available in [20]. The Re values used to parameterize Figs. 2-4 were selected to illustrate the evolution of the C_p distributions with the Reynolds number. The data are believed to be accurate to 2 percent or better.

Each figure consists of two graphs. The one at the left is for a tube-fed bend, while that at the right is for a bend with a sharp-edged inlet. Each graph conveys results for three turning angles $\theta = 30$, 60, and 90 deg (see the right-hand graph of Fig. 2 for symbol definitions). The data in each graph naturally separate themselves into three tiers which, bottom to top, correspond to the inner-wall, midwall, and outer-wall pressure-tap locations, as indicated in the left-hand graph of Fig. 2.

The pressure distributions for the two bend inlet configurations are distinctively different. For the case of the sharp-edged inlet, the distributions have a general shape that is common to the outer, inner, and midwall tap locations. Starting with a very low value immediately downstream of the

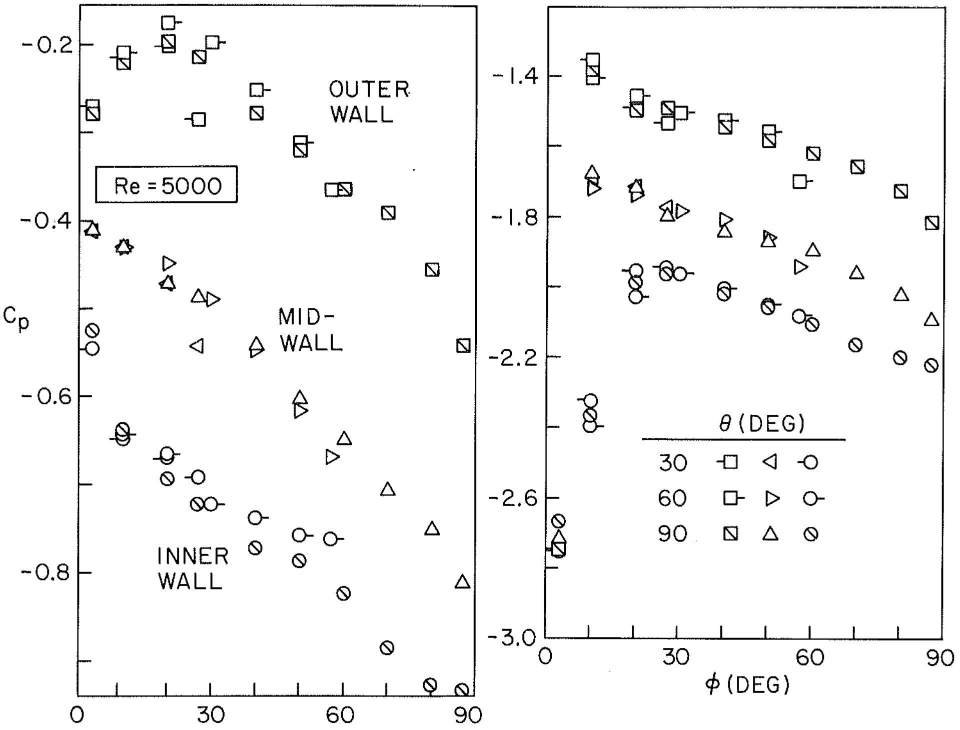

Fig. 2 In-bend pressure distributions for Re = 5000 (left: tube-fed inlet; right: sharp-edged inlet)

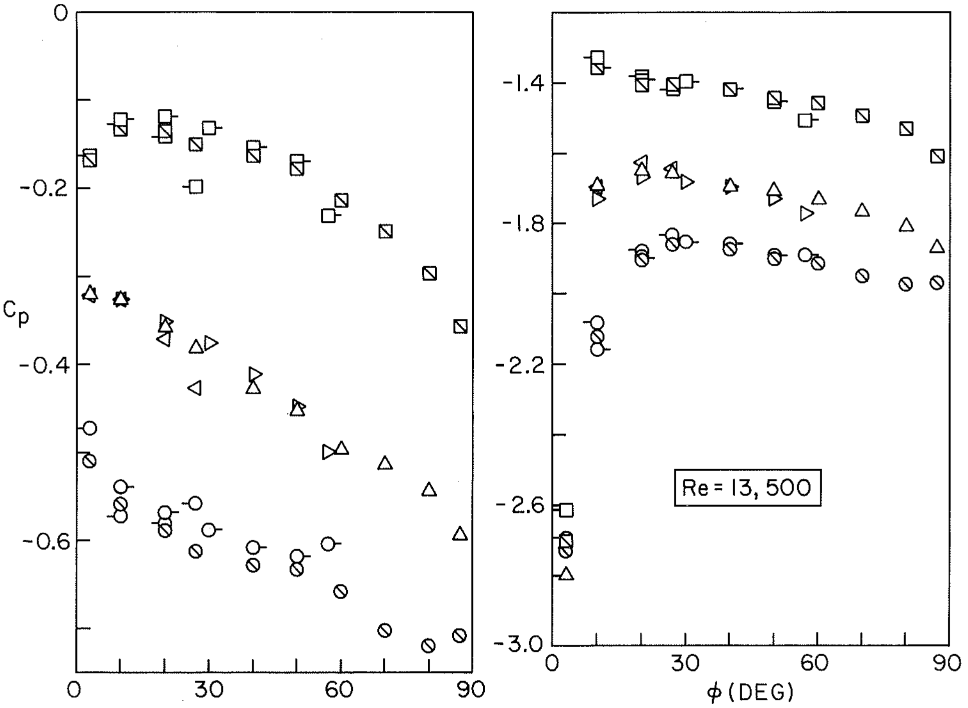

Fig. 3 In-bend pressure distributions for Re = 13,500 (left: tube-fed inlet; right: sharp-edged inlet)

bend inlet, the pressure rises sharply, attains a maximum, and then gradually decreases with increasing downstream distance (this pattern is similar to that in a straight tube with a sharp-edged inlet). In contrast, for a tube-fed bend, the outer, inner, and midwall distributions do not possess a common pattern. At the outer wall, the pressure displays an initial rise, a maximum, and a subsequent decrease, but the initial rise is relatively gradual compared with the very rapid rise exhibited by the outer-wall pressure distributions for the case of the sharp-edged inlet. At both the midwall and inner wall taps, the pressure decreases monotonically in the streamwise direction.

For both inlet configurations, there is a circumferential pressure distribution, as expected. In general, the pressure is highest at the outer wall, lowest at the inner wall, and intermediate at the midwall. Only in the complex recirculation

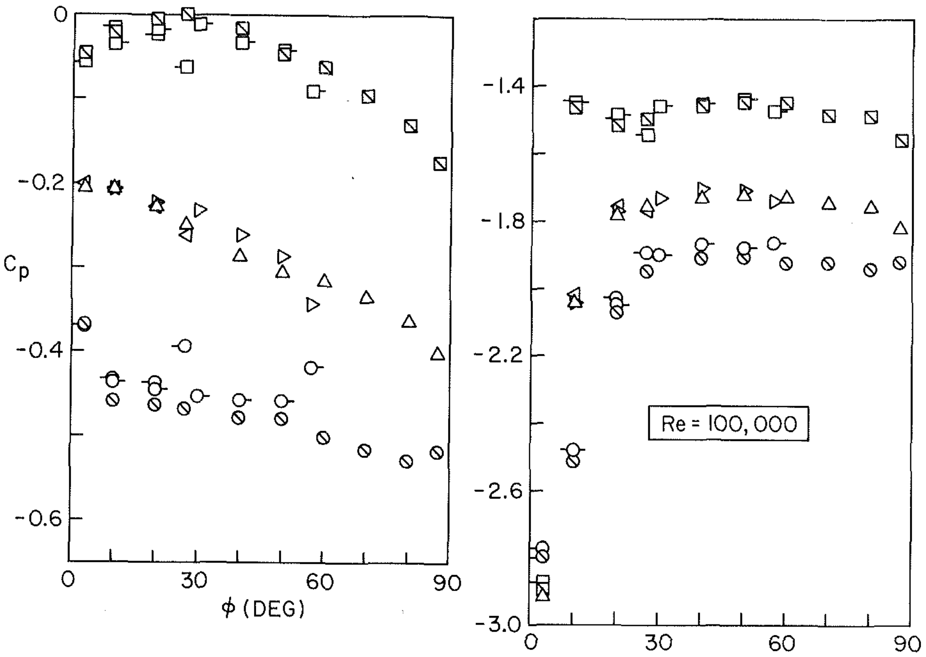

Fig. 4 In-bend pressure distributions for Re = 100,000 (left: tube-fed inlet; right: sharp-edged inlet)

zone immediately downstream of the sharp-edged inlet is this ordering violated.

Considering now the case of the sharp-edged inlet, it may be noted that the low pressure adjacent to the inlet is due to the separation-related contraction of the flow. It is also noteworthy that the pressure coefficient $C_p = 2.778$, which corresponds to an axisymmetric contraction with a contraction coefficient of 0.6, falls squarely among the C_p data at the first measurement station ($\phi = 3$ deg), despite the nonsymmetric nature of the flow. The recovery of the pressure occurs as the contracted flow expands to fill the cross section.

The postrecovery pressure maximum at the outer wall occurred at $\phi = 10$ deg at all Reynolds numbers. This is consistent with the observation, made during complementary flow visualization experiments [1], that the position of the reattachment spot on the outer wall did not change with the Reynolds number. The dropoff of the pressure which normally occurs after the reattachment of the flow is modified by the curvature of the wall. By starting with Re = 5000 and examining the successive outer-wall pressure distributions with increasing Reynolds number, it is seen that in the post-reattachment region, the pressure distributions tend to flatten at higher Reynolds numbers, and a hardly perceptible second maximum appears.

At the inner wall, the pressure maximum occurs downstream of that at the outer wall and is less sharply defined. It is also less strongly locked in place and tends to migrate downstream with increasing Reynolds number. The pressure maximum at the midwall tap location tends both to broaden and to move downstream with increasing Reynolds number.

Downstream of $\phi = 30$ deg, the C_p distributions for the sharp-edged inlet are relatively independent of both the Reynolds number and of ϕ for Re ≥ 22,000.

Attention will next be turned to the case of the tube-fed inlet. Although the initial rise of the outer-wall pressure distributions corresponds to an unfavorable pressure gradient, no evidence of flow separation was revealed by the complementary flow visualizations [1]. At the lower Reynolds numbers, the pressure maximum occurs in the neighborhood of $\phi = 20$ deg, while at higher Reynolds numbers, the maximum both broadens and shifts to the neighborhood of $\phi = 30$ deg.

At the midwall taps, the monotonic pressure decrease is characterized by a slight concave downward curvature, indicating a modest streamwise increase in the pressure drop per unit length. The pressure decrease at the inner wall taps is of a somewhat different character from the pressure decrease at the midwall. First of all, at the inner wall, there is a rapid dropoff just downstream of the inlet, which contrasts with the initial gradual dropoff at the midwall. Second, just before the exit of the 90 deg bend, the inner wall pressure tends to attain a shallow minimum, a feature not in evidence at the midwall. It may be noted that this inner-wall pressure minimum is positioned well downstream of the outer-wall pressure maximum.

With increasing Reynolds number, the C_p distributions for the tube-fed inlet tend both to flatten and to draw together (i.e., smaller gap between the inner-wall and outer-wall pressure distributions).

It may be noted that with certain exceptions, the pressure distributions in the first 30 deg of a 60 or 90 deg bend coincide with the pressure distribution in a 30 deg bend. Similarly, the pressure distribution throughout a 60 deg bend and for the first 60 deg of a 90 deg bend are virtually the same. The exceptions occur adjacent to the respective exits of the 30 and 60 deg bends, where the outer and midwall pressures tend to fall low, and the inner wall pressure falls high. These deviations may result from the precursive effect of the exhaust tube. Support for this hypothesis is provided by the exit-adjacent pressure rise at the inner wall of the 90 deg bend as well as the relatively large exit-adjacent pressure drops at the outer wall and midwall taps.

There do not appear to be either analytical or numerical predictions in the literature with which to compare the measured pressure distributions. The only published circular tube experiments in which in-bend pressure distributions were measured are those of [2] and [3]. In [2], a tube-fed 90 deg bend with a R_c/R ratio of 3.7 was used (the present R_c/R ratio is 9), and pressure data were reported only at Re = 200,000. The only in-bend pressure taps were at 45 deg, which is too little instrumentation to provide definitive pressure distributions. In [3], pressure distributions are reported at Re = 43,000 for a 90 deg bend with $R_c/R = 5.6$. The bend was fed by a straight tube having a length equal to five diameters. Such a tube length delivers a partially developed flow to the inlet of the bend, making the inlet condition uncertain.

References

1 Sparrow, E. M., and Chrysler, G. M., "Turbulent Flow and Heat Transfer in Bends of Circular Cross Section: I—Heat Transfer Experiments," ASME JOURNAL OF HEAT TRANSFER, this issue.

2 Ito, H., "Pressure Losses in Smooth Pipe Bends," *Journal of Basic Engineering*, Vol. 82, 1960, pp. 131-143.

3 Enayet, M. M., Gibson, M. M., Taylor, A. M. K. P., and Yianneskis, M., "Laser-Doppler Measurements of Laminar and Turbulent Flow in a Pipe Bend," *International Journal of Heat and Fluid Flow*, Vol. 3, 1982, pp. 211-217.

4 Agrawal, Y., Talbot, L., and Gong, K., "Laser Anemometer Study of Flow Development in Curved Circular Pipes," *Journal of Fluid Mechanics*, Vol. 85, 1978, pp. 497-518.

5 Azzola, J., and Humphrey, J. A. C., "Developing Turbulent Flow in a 180° Curved Pipe and Its Downstream Tangent," *Proceedings, Second International Symposium on Applications of Laser Anemometry to Fluid Mechanics*, Lisbon, Portugal, July 2-4, 1984.

6 Rowe, M., "Measurements and Computations of Flow in Pipe Bends," *Journal of Fluid Mechanics*, Vol. 43, 1970, pp. 771-783.

7 Patankar, S. V., Pratap, V. S., and Spalding, D. B., "Prediction of Turbulent Flow in Curved Pipes," *Journal of Fluid Mechanics*, Vol. 67, 1975, pp. 583-595.

8 Iacovides, H., and Launder, B. E., "The Computation of Momentum and Heat Transport in Turbulent Flow Around Pipe Bends," *Institution of Chemical Engineers Symposium Series*, No. 86, 1984, pp. 1097-1113.

9 Humphrey, J. A. C., "Numerical Calculation of Developing Laminar Flow in Pipes of Arbitrary Curvature Radius," *Canadian Journal of Chemical Engineering*, Vol. 56, 1978, pp. 151-164.

10 Yao, L. S., "Heat Convection in a Horizontal Curved Pipe," ASME JOURNAL OF HEAT TRANSFER, Vol. 106, 1984, pp. 71-77.

11 Mori, Y., and Nakayama, W., "Study on Forced Convective Heat Transfer in Curved Pipes (1st Report, Laminar Region)," *International Journal of Heat and Mass Transfer*, Vol. 8, 1965, pp. 67-82.

12 Kalb, C. E., and Seader, T. D., "Fully Developed Viscous-Flow Heat Transfer in Curved Circular Tubes With Uniform Wall Temperature," *AIChE Journal*, Vol. 20, 1974, pp. 340-346.

13 Mori, Y., and Nakayama, W., "Study on Forced Convective Heat Transfer in Curved Pipes (2nd Report, Turbulent Region)," *International Journal of Heat and Mass Transfer*, Vol. 10, 1967, pp. 37-59.

14 Seban, R. A., and McLaughlin, E. F., "Heat Transfer in Tube Coils With Laminar and Turbulent Flow," *International Journal of Heat and Mass Transfer*, Vol. 6, 1963, pp. 387-395.

15 Ito, H., "Friction Factors for Turbulent Flow in Curved Pipes," *Journal of Basic Engineering*, Vol. 81, 1959, pp. 123-134.

16 Rogers, G. F. C., and Mayhew, Y. R., "Heat Transfer and Pressure Loss in Helically Coiled Tubes With Turbulent Flow," *International Journal of Heat and Mass Transfer*, Vol. 7, 1964, pp. 1207-1216.

17 Ward-Smith, A. J., *Pressure Losses in Ducted Flows*, Butterworths, London, 1971.

18 Ward-Smith, A. J., *Internal Fluid Flow*, Oxford University Press, Oxford, 1980.

19 Berger, S. A., Talbot, L., and Yao, L. S., "Flow in Curved Pipes," in: *Annual Review of Fluid Mechanics*, Vol. 15, 1983, pp. 461-512.

20 Chrysler, G. M., "Convective Heat Transfer Coefficients for Pipe Flow With Curvature-Induced Secondary Motion," Ph.D. Thesis, Department of Mechanical Engineering, University of Minnesota, Minneapolis, MN, 1984.

Measurements in Turbulent Liquid Flow Through a Vertical Concentric Annular Channel

R. P. Roy,[1,2] V. S. Krishnan,[1] and A. Raman[1]

Introduction

There appears to be a scarcity of experimental studies on turbulent liquid flow through annular channels, either heated or unheated. A few experimental studies have been reported for turbulent air flow through unheated annuli, e.g., Brighton and Jones [1], Heikal et al. [2], and Wilson [3]. Heikal et al. [2] also reported some results on the overall heat transfer rate to air in the entrance region of a heated annulus.

The present experimental work was comprised of (*a*) a study of the fully developed velocity field in turbulent liquid flow through an unheated vertical concentric annulus, and (*b*) a study of the fully developed temperature field and the mean velocity profile in turbulent liquid flow through the same annulus but now with the inner wall heated and the outer wall insulated.

Experimental System

The experimental rig which used liquid Refrigerant-113 [4] as the working fluid has been described elsewhere [5]. Only the annular test section wil be briefly described here.

A. The Test Section. The annular test section was comprised of an outer pipe of 38.1 mm i.d., and an inner section consisting of a thin-walled (1.25 mm wall) seamless stainless steel tube of 15.9 mm o.d. The annulus radius ratio ξ_R was thus 0.417. The vertical test section was 3.66 m long of which heat could be added to the upper 2.75 m by resistively heating (by d-c) the stainless steel inner tube. Concentricity of the test section was maintained by four support vane assemblies, each assembly consisting of three 9 mm long and 1 mm thick vanes in a **Y** configuration, carefully welded to the inner tube at approximately equal axial spacings. The closest vane assembly upstream of the measurement plane was about 32 hydraulic diameters away.

B. Velocity and Temperature Measurement Instrumentation. For velocity measurements under unheated conditions, a three-channel constant temperature anemometer system (TSI Model 1050) was used. This system included a polynomial linearizer (TSI Model 1052) for each anemometer channel. For velocity and temperature measurements under heated conditions, two channels of the anemometer system and a temperature module (TSI Model 1040) were used.

Two types of hot-film anemometer probes were utilized:

1 miniature, single-sensor, quartz-coated hot-film probe, TSI Model 1262 AE-10W: the sensor length (l_s) and diameter (d_s) were 0.51 mm and 25 μm (not including coating) respectively;

2 standard, three-sensor, quartz-coated hot-film probe, TSI Model 1295AC-20W, with a 90 deg bend in the stem; each sensor was 1 mm long and 55 μm in diameter (including coating).

A temperature compensation circuit similar in principle to the one reported by Chevray and Tutu [6] was designed and built to allow on-line temperature compensation of the constant temperature anemometer outputs.

A four-channel data acquisition system (Data Precision 6000) was used to acquire, store, and analyze time series data.

C. Calibration of the Hot-Film Probes. All sensors were calibrated for velocity and/or temperature in a "calibration section" which was a 304 stainless steel pipe of 22.2 mm i.d. and 0.53 m length located just upstream of the test section.

Velocity Calibration. Before calibrating any sensor, it is necessary to determine its directional sensitivity as embodied in the parameter k in the well-known "effective cooling velocity" relation [7]

$$U_{\rm eff}^2(\alpha) = U^2(0)[\cos^2 \alpha + k^2 \sin^2 \alpha] \qquad (1)$$

This part of our work has been reported elsewhere [8]. The best-estimate value of k for the sensors used in the present study (all with l_s/d_s ratio ≈ 19) in the Reynolds number range of interest was found to be 0.30 ± 0.04. Extensive velocity calibrations were subsequently carried out for the three sensors of the three-sensor probe and the sensor of the

---

[1] Department of Mechanical and Aerospace Engineering, Arizona State University, Tempe, AZ 85287

[2] Mem. ASME

Contributed by the Heat Transfer Division for publication in the JOURNAL OF HEAT TRANSFER. Manuscript received by the Heat Transfer Division October 15, 1984.

five diameters. Such a tube length delivers a partially developed flow to the inlet of the bend, making the inlet condition uncertain.

References

1 Sparrow, E. M., and Chrysler, G. M., "Turbulent Flow and Heat Transfer in Bends of Circular Cross Section: I—Heat Transfer Experiments," ASME Journal of Heat Transfer, this issue.

2 Ito, H., "Pressure Losses in Smooth Pipe Bends," *Journal of Basic Engineering*, Vol. 82, 1960, pp. 131-143.

3 Enayet, M. M., Gibson, M. M., Taylor, A. M. K. P., and Yianneskis, M., "Laser-Doppler Measurements of Laminar and Turbulent Flow in a Pipe Bend," *International Journal of Heat and Fluid Flow*, Vol. 3, 1982, pp. 211-217.

4 Agrawal, Y., Talbot, L., and Gong, K., "Laser Anemometer Study of Flow Development in Curved Circular Pipes," *Journal of Fluid Mechanics*, Vol. 85, 1978, pp. 497-518.

5 Azzola, J., and Humphrey, J. A. C., "Developing Turbulent Flow in a 180° Curved Pipe and Its Downstream Tangent," *Proceedings, Second International Symposium on Applications of Laser Anemometry to Fluid Mechanics*, Lisbon, Portugal, July 2-4, 1984.

6 Rowe, M., "Measurements and Computations of Flow in Pipe Bends," *Journal of Fluid Mechanics*, Vol. 43, 1970, pp. 771-783.

7 Patankar, S. V., Pratap, V. S., and Spalding, D. B., "Prediction of Turbulent Flow in Curved Pipes," *Journal of Fluid Mechanics*, Vol. 67, 1975, pp. 583-595.

8 Iacovides, H., and Launder, B. E., "The Computation of Momentum and Heat Transport in Turbulent Flow Around Pipe Bends," *Institution of Chemical Engineers Symposium Series*, No. 86, 1984, pp. 1097-1113.

9 Humphrey, J. A. C., "Numerical Calculation of Developing Laminar Flow in Pipes of Arbitrary Curvature Radius," *Canadian Journal of Chemical Engineering*, Vol. 56, 1978, pp. 151-164.

10 Yao, L. S., "Heat Convection in a Horizontal Curved Pipe," ASME Journal of Heat Transfer, Vol. 106, 1984, pp. 71-77.

11 Mori, Y., and Nakayama, W., "Study on Forced Convective Heat Transfer in Curved Pipes (1st Report, Laminar Region)," *International Journal of Heat and Mass Transfer*, Vol. 8, 1965, pp. 67-82.

12 Kalb, C. E., and Seader, T. D., "Fully Developed Viscous-Flow Heat Transfer in Curved Circular Tubes With Uniform Wall Temperature," *AIChE Journal*, Vol. 20, 1974, pp. 340-346.

13 Mori, Y., and Nakayama, W., "Study on Forced Convective Heat Transfer in Curved Pipes (2nd Report, Turbulent Region)," *International Journal of Heat and Mass Transfer*, Vol. 10, 1967, pp. 37-59.

14 Seban, R. A., and McLaughlin, E. F., "Heat Transfer in Tube Coils With Laminar and Turbulent Flow," *International Journal of Heat and Mass Transfer*, Vol. 6, 1963, pp. 387-395.

15 Ito, H., "Friction Factors for Turbulent Flow in Curved Pipes," *Journal of Basic Engineering*, Vol. 81, 1959, pp. 123-134.

16 Rogers, G. F. C., and Mayhew, Y. R., "Heat Transfer and Pressure Loss in Helically Coiled Tubes With Turbulent Flow," *International Journal of Heat and Mass Transfer*, Vol. 7, 1964, pp. 1207-1216.

17 Ward-Smith, A. J., *Pressure Losses in Ducted Flows*, Butterworths, London, 1971.

18 Ward-Smith, A. J., *Internal Fluid Flow*, Oxford University Press, Oxford, 1980.

19 Berger, S. A., Talbot, L., and Yao, L. S., "Flow in Curved Pipes," in: *Annual Review of Fluid Mechanics*, Vol. 15, 1983, pp. 461-512.

20 Chrysler, G. M., "Convective Heat Transfer Coefficients for Pipe Flow With Curvature-Induced Secondary Motion," Ph.D. Thesis, Department of Mechanical Engineering, University of Minnesota, Minneapolis, MN, 1984.

Measurements in Turbulent Liquid Flow Through a Vertical Concentric Annular Channel

R. P. Roy,[1,2] V. S. Krishnan,[1] and A. Raman[1]

Introduction

There appears to be a scarcity of experimental studies on turbulent liquid flow through annular channels, either heated or unheated. A few experimental studies have been reported for turbulent air flow through unheated annuli, e.g., Brighton and Jones [1], Heikal et al. [2], and Wilson [3]. Heikal et al. [2] also reported some results on the overall heat transfer rate to air in the entrance region of a heated annulus.

The present experimental work was comprised of (*a*) a study of the fully developed velocity field in turbulent liquid flow through an unheated vertical concentric annulus, and (*b*) a study of the fully developed temperature field and the mean velocity profile in turbulent liquid flow through the same annulus but now with the inner wall heated and the outer wall insulated.

Experimental System

The experimental rig which used liquid Refrigerant-113 [4] as the working fluid has been described elsewhere [5]. Only the annular test section wil be briefly described here.

A. The Test Section. The annular test section was comprised of an outer pipe of 38.1 mm i.d., and an inner section consisting of a thin-walled (1.25 mm wall) seamless stainless steel tube of 15.9 mm o.d. The annulus radius ratio ξ_R was thus 0.417. The vertical test section was 3.66 m long of which heat could be added to the upper 2.75 m by resistively heating (by d-c) the stainless steel inner tube. Concentricity of the test section was maintained by four support vane assemblies, each assembly consisting of three 9 mm long and 1 mm thick vanes in a **Y** configuration, carefully welded to the inner tube at approximately equal axial spacings. The closest vane assembly upstream of the measurement plane was about 32 hydraulic diameters away.

B. Velocity and Temperature Measurement Instrumentation. For velocity measurements under unheated conditions, a three-channel constant temperature anemometer system (TSI Model 1050) was used. This system included a polynomial linearizer (TSI Model 1052) for each anemometer channel. For velocity and temperature measurements under heated conditions, two channels of the anemometer system and a temperature module (TSI Model 1040) were used.

Two types of hot-film anemometer probes were utilized:

1 miniature, single-sensor, quartz-coated hot-film probe, TSI Model 1262 AE-10W: the sensor length (l_s) and diameter (d_s) were 0.51 mm and 25 μm (not including coating) respectively;

2 standard, three-sensor, quartz-coated hot-film probe, TSI Model 1295AC-20W, with a 90 deg bend in the stem; each sensor was 1 mm long and 55 μm in diameter (including coating).

A temperature compensation circuit similar in principle to the one reported by Chevray and Tutu [6] was designed and built to allow on-line temperature compensation of the constant temperature anemometer outputs.

A four-channel data acquisition system (Data Precision 6000) was used to acquire, store, and analyze time series data.

C. Calibration of the Hot-Film Probes. All sensors were calibrated for velocity and/or temperature in a "calibration section" which was a 304 stainless steel pipe of 22.2 mm i.d. and 0.53 m length located just upstream of the test section.

Velocity Calibration. Before calibrating any sensor, it is necessary to determine its directional sensitivity as embodied in the parameter k in the well-known "effective cooling velocity" relation [7]

$$U^2_{\text{eff}}(\alpha) = U^2(0)[\cos^2 \alpha + k^2 \sin^2 \alpha] \qquad (1)$$

This part of our work has been reported elsewhere [8]. The best-estimate value of k for the sensors used in the present study (all with l_s/d_s ratio $\approx$ 19) in the Reynolds number range of interest was found to be 0.30 ± 0.04. Extensive velocity calibrations were subsequently carried out for the three sensors of the three-sensor probe and the sensor of the

---

[1] Department of Mechanical and Aerospace Engineering, Arizona State University, Tempe, AZ 85287

[2] Mem. ASME

Contributed by the Heat Transfer Division for publication in the Journal of Heat Transfer. Manuscript received by the Heat Transfer Division October 15, 1984.

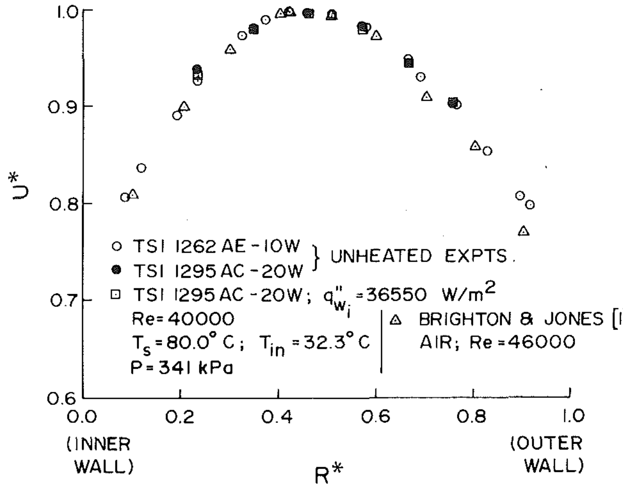

Fig. 1 Mean axial velocity profiles at Reynolds number of 40,000

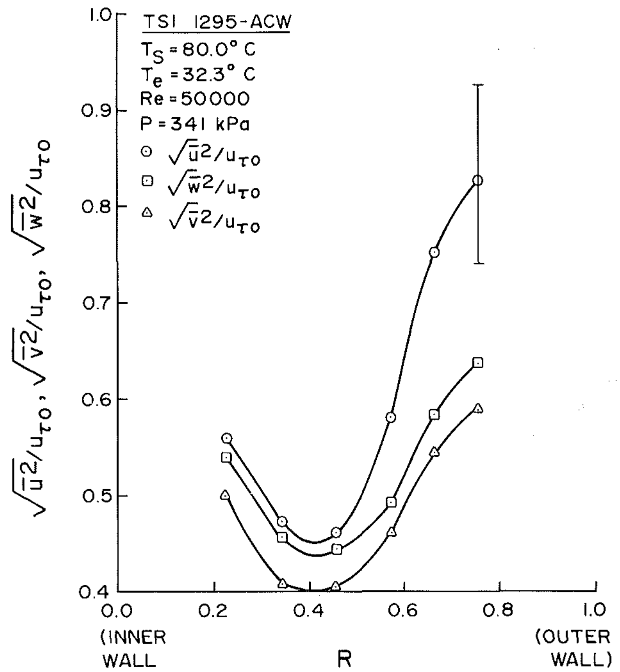

Fig. 2 Turbulence intensity profiles at Reynolds number of 50,000

miniature single-sensor probe. The invariance of the velocity calibrations for several ambient liquid temperatures with the temperature compensation circuit in operation was verified.

Temperature Calibration. The sensor of the miniature single-sensor probe and sensor No. 3 of the three-sensor probe (Nos. 1 and 2 being the x sensors) were calibrated for temperature in conjunction with the temperature module. A linear variation of the module output voltage over the liquid temperature range of interest was obtained.

Results and Discussion

A. Velocity Measurements

(*i*) *Mean Axial Velocity Profiles.* Figure 1 is a plot of nondimensional mean axial velocity U^*, defined as $U/U_{\max}$, versus the nondimensional radial distance from the inner wall R^*, defined as $(r-R_i)/(R_o-R_i)$, for Reynolds number of 40,000. Data obtained from both probe types are shown. The miniature single-sensor probe permitted a closer approach to the walls. Data from unheated as well as heated liquid experiments are shown as are the data of Brighton and Jones at a Reynolds number of 46,000 [1] for comparison. Similar measurements were also made at Reynolds numbers of 35,000 and 50,000, and with other inner wall heat fluxes.

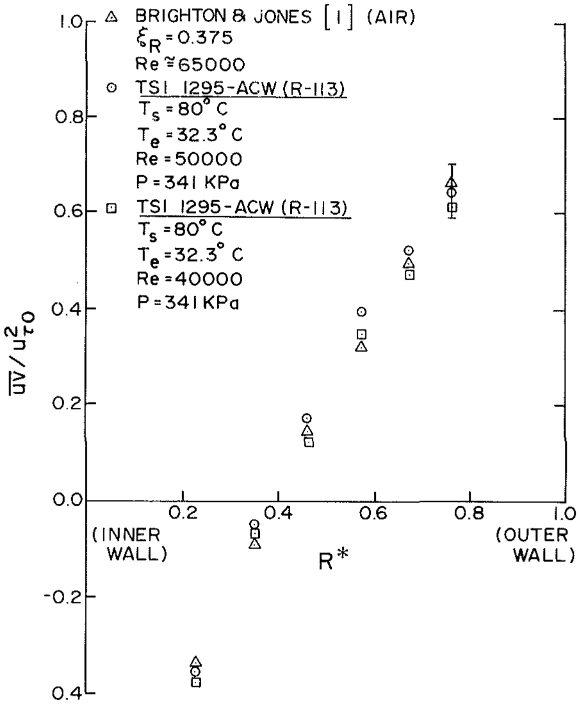

Fig. 3 Reynolds shear stress profiles

A noteworthy feature of these profiles is that the maximum velocity occurs at $R^* \approx 0.41$. This is in agreement with the air experiment results of Brighton and Jones [1], Heikal et al. [2], and Wilson [3].

(*ii*) *Turbulence Intensity Profiles.* Figure 2 shows the radial profiles of the three turbulence intensities $(\bar{u}^2)^{0.5}$, $(\bar{v}^2)^{0.5}$, and $(\bar{w}^2)^{0.5}$, at a Reynolds number of 50,000, measured by means of the three-sensor probe. The intensities have been nondimensionalized with respect to u_{τ_0}, the friction velocity at the outer wall. u_{τ_0} was estimated by extrapolating to the outer wall the best-fit curve through our Reynolds shear stress $(\overline{uv})$ data reported later. The intensity profiles were also measured at Reynolds number of 40,000 and found to be similar to the ones shown in Fig. 2. It can be seen from the figure that the $(\bar{w}^2)^{0.5}$ profile lies between those of $(\bar{u}^2)^{0.5}$ and $(\bar{v}^2)^{0.5}$. Furthermore, the magnitude of $(\bar{w}^2)^{0.5}$ is closer to that of $\bar{u}^2)^{0.5}$ for $R^* \leq 0.41$, and closer to that of $(\bar{v}^2)^{0.5}$ for $R^* > 0.41$. These trends are in agreement with those of Brighton and Jones [1]. Unlike [1] however, small increases in the intensities nondimensionalized with respect to u_{τ_0} were observed with increase in Reynolds number.

We note here that the analysis of the three-sensor probe signals was based upon the assumption that correlations of third and higher orders are small compared to those of the second order. Error estimates revealed that measurements of $\bar{u}^2$ were subject to the largest uncertainty. A typical uncertainty estimate is shown in Fig. 2.

(*iii*) *Reynolds Shear Stress Profiles.* Figure 3 shows plots of the Reynolds shear stress $\overline{uv}$, nondimensionalized with respect to $u_{\tau_0}^2$, at Reynolds numbers of 40,000 and 50,000. Data of Brighton and Jones [1] for air flow at a Reynolds number of 65,000 through an annulus of radius ratio 0.375 are also shown in Fig. 3 for comparison. The $\overline{uv}$ measurements were estimated to have the smallest amount of uncertainty (compared, for example, to the intensity measurements).

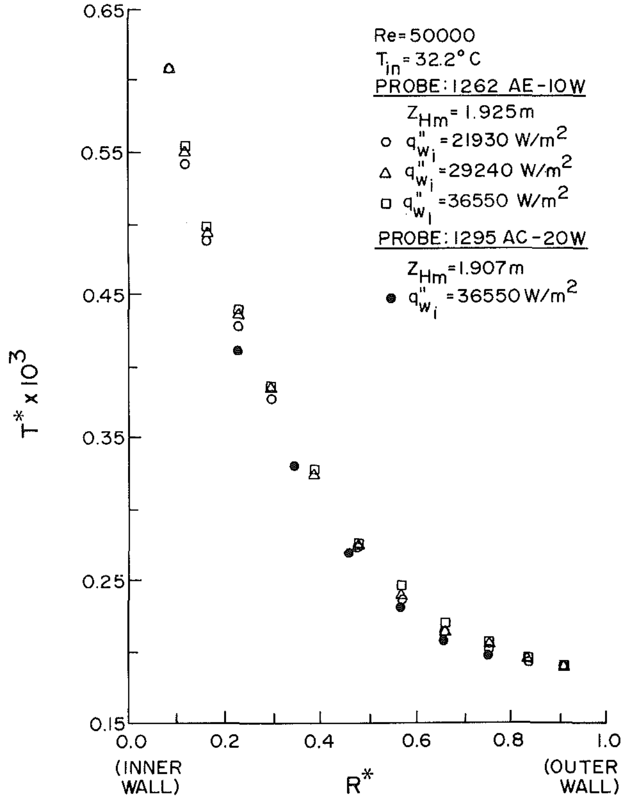

Fig. 4 Mean temperature profiles at Reynolds number of 50,000

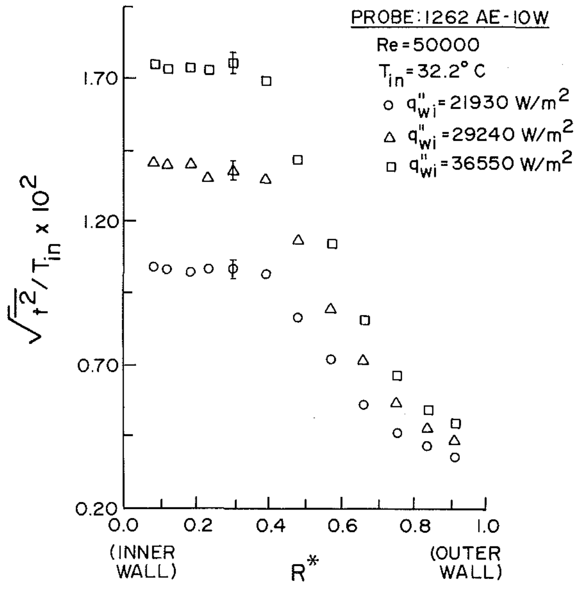

Fig. 5 Temperature fluctuation intensity profiles at Reynolds number of 50,000

B. Temperature Measurements

(*i*) *Mean Temperature Profiles.* Figure 4 shows plots of the mean liquid temperature data T^*, defined as $(T-T_{in})k_f/q''_{w_i}D_h$, for three different inner wall heat fluxes and at a Reynolds number of 50,000, as measured by the miniature single-sensor probe. Also included in the plot are data for one of the heat fluxes obtained by means of the temperature sensor of the three-sensor probe. Mean temperature profile measurements were also made at Reynolds numbers of 35,000 and 40,000 with the data exhibiting the same general trends.

(*ii*) *Temperature Fluctuation Intensity Profiles.* Figure 5 shows three typical liquid temperature fluctuation intensity profiles corresponding to three different inner wall heat fluxes and a Reynolds number of 50,000. While these profiles do not exhibit appreciable dependence on the heat flux magnitude in regions well away from the heated wall, there is a marked increase in the magnitude of the intensity in the wall proximity with increase in wall heat flux. An as yet unexplainable feature of these profiles is the flattening trend as the inner wall is approached, at least in the radial range $0.1<R^*<0.3$. Measurements performed at two other Reynolds numbers, 35,000 and 40,000, exhibited the same feature. Considering that the Prandtl number of liquid Refrigerant-113 at the experiment condition was about seven, one would expect a monotonic increase in the intensity magnitude until closer to the heated wall. Whether electromagnetic field due to the several hundred amperes of heating current flowing through the heated wall influenced these measurements needs to be investigated.

(*iii*) *Spectral Composition of Liquid Temperature Fluctuations.* Measured autopower spectral density functions (not shown here for brevity) show a reduction in the magnitude of the turbulent temperature fluctuation energy by a factor of approximately 10^5 over the frequency range of 1 to 400 Hz.

Concluding Remarks

Accurate velocity field measurements in turbulent liquid flow by constant temperature anemometry are difficult since generally only low sensor overheats can be used. This is because incipience of boiling at the sensor must be prevented. This also makes temperature compensation of the anemometer output signal all the more important.

The relatively large sensing region of the standard three-sensor probe leads to some spatial averaging. This was a problem in our experiments especially in regions where large gradients existed. Large spanwise separation between the x sensors ($\approx$ 1 mm) could have been a problem also. Further measurements including single-point cross-correlation between the radial velocity fluctuations and temperature fluctuations $(\overline{vt})$ by miniature three-sensor probes are presently in progress.

Acknowledgments

This research was supported by National Science Foundation, Heat Transfer Program, grant MEA-8302659.

References

1 Brighton, J. A., and Jones, J. B., "Fully Developed Turbulent Flow in Annuli," ASME *Journal of Basic Engineering*, Vol. 86, 1964, pp. 835–844.

2 Heikal, M. R. F., Walklate, P. J., and Hatton, A. P., "The Effect of Free Stream Turbulence Level on the Flow and Heat Transfer in the Entrance Region of an Annulus," *International Journal of Heat and Mass Transfer*, Vol. 20, 1976, pp. 763–771.

3 Wilson, R. J., "Correlation and Spectral Measurements of Fluctuating Pressure and Velocities in Annular Turbulent Flow," Ph.D. thesis, University of Illinois, Urbana–Champaign, 1979.

4 E. I. Dupont De Nemours and Co., Bulletins FST-11, -1, E-113, 1976–1979.

5 Jain, P. K., and Roy, R. P., "Stochastic Characteristics of Vapor Fraction and Wall Pressure Fluctuations in Boiling Flow," *International Journal of Multiphase Flow*, Vol. 9, No. 5, 1983, pp. 463–489.

6 Chevray, R., and Tutu, N. K., "Simultaneous Measurements of Temperature and Velocity in Heated Flows," *The Review of Scientific Instruments*, Vol. 43, No. 10, 1972, pp. 1417–1421.

7 Hinze, J. O., *Turbulence*, McGraw-Hill, 2 edn., 1975.

8 Raman, A., Krishnan, V. S., and Roy, R. P., "Directional Sensitivity of Cylindrical Hot-Film Velocity Sensors," ASME *Journal of Applied Mechanics*, Vol. 52, No. 1, 1985, pp. 199–202.

Liquid-Solid Contact State in Subcooled Pool Transition Boiling System

S. Inada,[1,2] Y. Miyasaka,[1,3] S. Sakumoto,[4] and G. R. Chandratilleke[1,5]

Introduction

In recent years, it has become desirable in a number of applications to have a high heat transfer coefficient for boiling. A higher heat flux can be attained in subcooled boiling than in saturated boiling. It is therefore required to understand the heat transfer mechanism in subcooled boiling from the bubble-coalescent regime up to the transitional boiling regime. In an earlier report [1], the boiling curves from the discrete-bubble regime in nucleate boiling up to a second burnout point were obtained for various locations on a 10 or 15 mm diameter horizontal surface facing upward for 0-85 K of subcooling. It was confirmed that a number of minute vapor bubbles were rapidly emitted from the heated surface and that the heat flux increased rapidly beyond the burnout value in partial film boiling regime. Furthermore, it has become clear from the measurement of surface temperature variation [2] that the thin vapor film once covering the heated surface breaks down to make liquid–solid contact at the beginning of the transformation of the transition boiling regime into the minute vapor bubble regime. It was possible to explain the mechanism by which liquid is supplied to the heated surface. The rate of variation of the heated surface drying was estimated by a mathematical model based on a mass transfer mechanism [3, 4]. However, the liquid–solid contact in the partial film boiling has yet to be fully clarified. The purpose of this paper is to investigate this contact in more detail by means of a direct technique. Iida et al. [5] studied vapor bubble generation in saturated pool transition boiling by a void probe that uses a series-resonance circuit, and pointed out that the heated surface was covered with a thin vapor film in the minimum heat flux regime. This finding was very helpful to our present subcooled boiling study. However the description of liquid–solid contact behavior based on a void probe signal in the unstable film boiling regime has been ambiguous. Using the same void probe method, but with equipment to enable the probe to approach the heated surface within two to three micrometers, revealed the nature of the liquid–solid contact in partial film boiling.

Experimental Apparatus and Procedure

Figure 1 gives a schematic view of the pool boiling apparatus, described in detail in the previous paper [1]. The pool vessel was 320 mm by 320 mm by 300 mm and its upper side was exposed to the atmosphere. The test liquid was water which had been purified, distilled, and degassed at its saturation temperature for 30 min. The liquid level was maintained at about 160 mm above the heated surface. The temperature of the water was regulated within ±0.5 K by use of the indicated heater and cooler. The heat transfer surface was a conical copper block with a cylindrical tip whose surface was 10 or 15 mm in diameter and horizontal. A 0.05-mm-thick platinum foil was attached to this heating surface by a diffusion-bonding method. Before starting the experiment, the platinum boiling surface was polished by a 6/0 emery paper to obtain a uniform initial surface roughness. The conical copper block with a 65-70 mm diameter was heated by radiation from a molybdenum plate heater. The temperatures of the heat transfer surface were measured with thermocouples welded to the center of the copper cylindrical tip. Four holes of 0.5 mm diameter were drilled up to the center line with a spacing of 1 mm in the vertical direction. The hot junction of the thermocouples consisted of the copper block itself and a 0.05 mm constantan wire spot-welded to the bottom of each hole. The temperature was recorded after the thermocouple indicated steady-state condition. The temperature of the surface was determined by extrapolation of the measured values and the heat flux was deduced from the temperature gradients. A 16-mm high-speed camera was used for observing the phenomena.

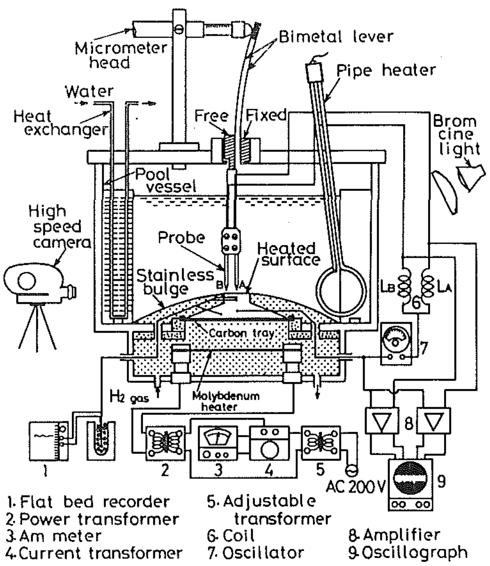

Fig. 1 Pool boiling apparatus

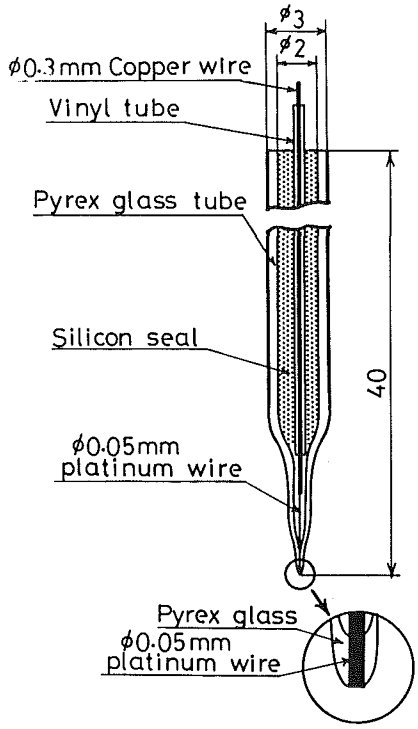

Fig. 2 Structure of the probe

The detecting circuit for the void signal from the series-resonance circuit is shown in Fig. 1. The circuit consists of an oscillator, a coil having self-inductance L, and a condenser

---

[1] Department of Mechanical Engineering, Gunma University, 1-5-1, Tenjincho, Kiryu, 376, Japan

[2] Dr. Assistant Professor

[3] Dr. Professor

[4] Engineer, Ishikawajima Harima Heavy Industries Co., 3-1-15, Toyosu, Kootoku, Tokyo, Japan

[5] Master's student

Contributed by the Heat Transfer Division for publication in the JOURNAL OF HEAT TRANSFER. Manuscript received by the Heat Transfer Division December 2, 1983.

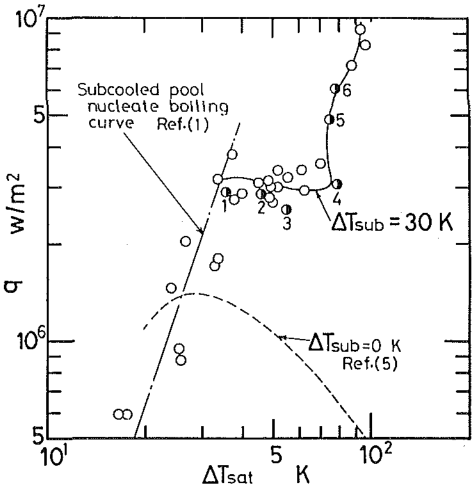

Fig. 3 Boiling curve and the measured boiling regime

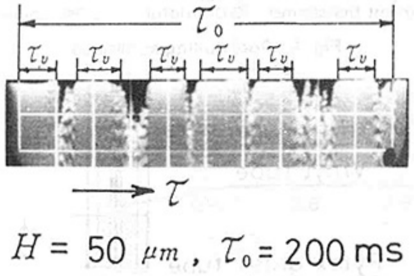

Fig. 4 Distinction of liquid and vapor phases based on void signals

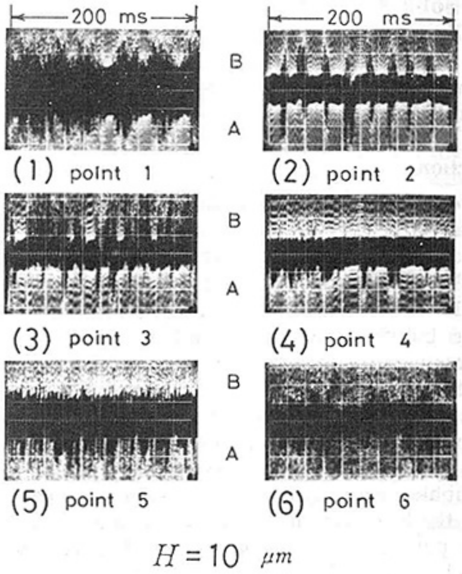

Fig. 5 An example of void signals measured for each point of Fig. 3 at constant height $H = 0.010$ mm

composed of two conductors, one being a probe and the other the heated surface. The resonance frequency and the self-inductance of the coil are in the range of 3000 to 5000 Hz and about five Henry, respectively. If there is a vapor bubble between the probe and the heated surface, the output voltage of the condenser varies sensitively because of the large difference between vapor and liquid permittivities. The fluctuation of the output is amplified further and is indicated on an oscillograph through the d-c restoration and clipper circuits. The frequency response of the amplifier is flat from 0 to 5 kHz.

In this experiment, a double probe was used in order to examine the differences of the void signals with regard to location. One was set up on the vertical line *A* above the central part of the heated surface and another on line *B* 3 mm away above the peripheral part.

Figure 2 shows the structure of the probe. This probe was made of a platinum wire 0.05 mm in diameter which was molded in a pyrex glass tube for electrical insulation such that only its leading edge was exposed. The probe had a needlelike sharp tip. A copper wire of 0.3 mm diameter was joined to the platinum wire at the middle of the probe by soldering.

The probe can be moved up and down in a vertical line and can be brought to within 2-3 μm of the heated surface by a magnifying device that uses a bimetal-type cantilever as shown in Fig. 1. The displacement of the micrometer required to move the probe by 1 μm is 0.11 mm and its minimum displacement is 0.01 mm.

Boiling Curve and Its Measured Regime

In Fig. 3, data marked by the symbol ○ and connected by a solid line are for the location *A* at a subcooling of 30 K. Numbered and marked by the symbol ◑ are the data where liquid–solid contact was detected by a double probe. This boiling curve was obtained for a contaminated surface with scale deposit after the first run, which required 8 h of boiling. In the boiling regime from 1 to 4, the heat flux remains nearly constant even if the wall temperature rises, and therefore, this regime is called transition-type boiling regime in this report. When the wall temperature is increased by a few degrees above 4, the heat flux increases abruptly and a number of minute vapor bubbles are rapidly emitted from the heated surface. Thus the boiling regime above 4 is called the minute bubble emission regime. A chain line in Fig. 3 is a nucleate boiling curve which is obtained by summing-up of data of subcooled pool nucleate boiling. A broken line, which is the saturated boiling curve obtained by Iida et al. [5], represents the conventional transition boiling curve.

Distinction of Liquid and Vapor Phases Based on Void Signals

Figure 4 shows an example of a void signal detected at a height of 0.05 mm from the heated surface at point 1 in Fig. 3. Several wide-band signals of τ_v as shown in Fig. 4 indicate the vapor phase in a sampling time τ_0, implying coalescent vapor bubbles formed successively on the heated surface. Two to three signals with a short period standing up sharply indicate liquid–solid contact. This means that active nucleate boiling occurs in the superheated liquid film that existed under the coalescent bubbles. The dips of the void signal show the presence of the liquid phase.

Void Signals in the Neighborhood of the Heated Surface

Figure 5 shows the void signals detected for each point of Fig. 3 by keeping the height of the probe *H* constant. Two signals on the vertical lines *A* and *B* in Fig. 1 are recorded upward from the bottom and downward from the top, respectively, on the oscillograph so that they are facing each other. For point 1 in Fig. 3 which belongs to the burnout regime, Fig. 5 shows that the active nucleate boiling always appears on the peripheral part of the heated surface. For point 2 of Fig. 5, the wide-band signals appear clearly at a constant period, but the active nucleate boiling signals don't appear appreciably at both *A* and *B*. This can be explained as follows. The entire heated surface must have been covered with a thin vapor film of 0.001-0.002 mm in thickness at the moment when a coalescent bubble departs from the heated surface. It no sooner leaves than the probe will be exposed to the subcooled liquid that now occupies the space above the thin vapor film. After a short time, the edge of the heated surface is furnished with the subcooled liquid and a number of vapor bubbles are generated there and instantly they combine into a single vapor bubble covering the entire heated surface. Again the probe will be exposed to vapor phase. For point 3 of Fig. 5, no liquid-solid contact signals are recognized on A, but the durations of liquid-solid contact on B increase rapidly. This means that the peripheral part of the heated surface was being furnished with the liquid required for the growth of the vapor bubbles. For point 4 of Fig. 5, the vapor phase always comes into appearance on B. On the contrary, liquid-solid contact signal comes into appearance on A intermittently, and at that moment a number of minute bubbles are rapidly emitted from the heated surface. This means that on the central part of the heated surface subcooled liquid has come directly in contact with the dried-up spot through a thin vapor film. When the wall superheat was increased by a few degrees above point 4, only liquid-solid contact signals are detected as shown by points 5 and 6 in Fig. 5. Comparing point 5 with point 6 in Fig. 5, it is clear that the period of the liquid-solid contact becomes short with increase of heat flux. A factor shortening the liquid-solid contact period is rapid liquid-vapor exchanging action induced by the minute bubble emission.

Conclusions

The noteworthy points from the experiment described above are:

1 There is a certain boiling regime where the heated surface is covered with a thin vapor film of micrometer thickness. In this regime, no liquid-solid contact signals occur.

2 If subcooling exceeds 30 K and the heated surface is contaminated by a scale deposit, subcooled liquid readily makes contact with the surface through the thin vapor film, and minute vapor bubbles are rapidly emitted.

3 The period of the liquid-solid contact becomes short with increase of heat flux.

References

1 Miyasaka, Y., Inada, S., and Izumi, R., "Study of Boiling-Characteristic Curves in Subcooled Pool-Boiling of Water," *International Chemical Engineering*, Vol. 23, No. 1, Jan. 1983, pp. 48-55.

2 Inada, S., Miyasaka, Y., and Izumi, R., "Behaviour of Vapor Bubbles and Surface Temperature Variations in Transitional Pool Boiling," *Heat Transfer Japanese Research*, Vol. 11, No. 2, 1982, pp. 42-69.

3 Inada, S., Miyasaka, Y., Izumi, R., and Kobayashi, M., "The Mechanism of Heat Transfer in Transition Boiling," *Bulletin of the JSME*, Vol. 25, No. 205, July 1982, pp. 1085-1092.

4 Inada, S., Miyasaka, Y., Sakumoto, S., Mogi, I., and Izumi, R., "Heat Transfer Mechanism of Liquid-Solid Contact in Pool Transition Boiling of Subcooled Water," *Proc. 2nd World Congress of Chemical Engineering*, Vol. V, 1981, pp. 143-147.

5 Iida, Y., and Kobayashi, K., "On the Behavior of Generating Vapor Bubbles in Saturated Pool Boiling: Part 2—The Behavior Near the Burn-Out Point and in Transition Boiling," *Journal of JSME*, Vol. 36, No. 283, Mar. 1970, pp. 446-453 (in Japanese).

Binary Fluid Convection and Double-Diffusive Convection in a Porous Medium

M. E. Taslim[1,2] and U. Narusawa[1]

Nomenclature

D_s = diffusivity of S component
D_T = diffusivity of T component
D_{TD} = coefficient of cross diffusion for T component induced by S gradient
D_{ss} = coefficient of cross-diffusion for S component induced by T gradient
h = distance between the two horizontal boundaries
H = heat flux per heat capacity in double diffusion
Hs = solute flux in double diffusion
K = permeability
Nu = Nusselt number in cross diffusion (see equation (16a))
Nu′ = Nusselt number in double diffusion (see equation (14))
Nu_s' = solute Nusselt number in double diffusion (see equation (15))
Pr = ν/D_T = Prandtl number
$R_T = \dfrac{g\alpha_T \Delta T_R K h}{\nu D_T}$ = Rayleigh number with respect to ΔT_R
$R_s = \dfrac{S\alpha_s \Delta S_R K h}{\nu D_T} = \beta R_T$ = Rayleigh number with respect to ΔS_R
$R_T' = \dfrac{BR_T + R_s}{(1+\tau b)(B-b)a}$
$R_s' = \dfrac{bR_T + R_s}{(i+\tau b)(B-b)A}$
$\bar{S} = S/\Delta S_R$
$\Delta S_R = (D_{ss}/D_s)\Delta T_0$
$t_1 = (1+\tau b)t$
$T_0 = T(z=0)$
$T_1 = T(z=1)$
$\bar{T} = (T-T_1)/\Delta T_R$
$\Delta T_R = \Delta T_0 = T_0 - T_1$
$\mathbf{V}_1 = \mathbf{V}/(1+\tau b)$
α = expansion coefficient
$\beta = (\alpha_s D_{ss})/(\alpha_T D_s)$
$\eta = (D_{TD} D_{ss})/(D_T D_s)$
$\lambda = K/h^2$
$\lambda' = \lambda(1+\tau b)$
$\tau = D_s/D_T$
$\tau' = (1+\tau B)/(1+\tau b)$
$\omega_1 = \omega/(1+\tau b)$

Subscripts

R = reference scale
S = S component
T = T component

Introduction

This paper is concerned with two transport mechanisms in particular, the first being cross diffusion, a term describing the diffusion of one property along the gradient of another. The well-known effects of cross diffusion are the Soret and the Dufour effects in convection of binary fluids [1]. The other transport mechanism of interest is double diffusion, which occurs in the presence of opposing gradients of two properties [2].

Knobloch [3] demonstrated a close relationship between cross-diffusion problems and double-diffusion problems for viscous fluids. An examination of his paper reveals that the mathematical identity of the two problems also holds for a fluid-saturated porous medium, the study of which has important applications in relation to fossil/geothermal reservoirs and disposal of nuclear waste in geological media.

Formulation and Transformation

The problem of interest here deals with the Rayleigh-Benard geometry, i.e., a horizontal layer of fluid between two boundaries. First, the cross-diffusion problem will be formulated and then it will be transformed into the

---

[1] Department of Mechanical Engineering, Northeastern University, Boston, MA 02115

[2] Assoc. Mem. ASME

Contributed by the Heat Transfer Division for publication in the JOURNAL OF HEAT TRANSFER. Manuscript received by the Heat Transfer Division February 10, 1984.

surface. Again the probe will be exposed to vapor phase. For point 3 of Fig. 5, no liquid-solid contact signals are recognized on A, but the durations of liquid-solid contact on B increase rapidly. This means that the peripheral part of the heated surface was being furnished with the liquid required for the growth of the vapor bubbles. For point 4 of Fig. 5, the vapor phase always comes into appearance on B. On the contrary, liquid-solid contact signal comes into appearance on A intermittently, and at that moment a number of minute bubbles are rapidly emitted from the heated surface. This means that on the central part of the heated surface subcooled liquid has come directly in contact with the dried-up spot through a thin vapor film. When the wall superheat was increased by a few degrees above point 4, only liquid-solid contact signals are detected as shown by points 5 and 6 in Fig. 5. Comparing point 5 with point 6 in Fig. 5, it is clear that the period of the liquid-solid contact becomes short with increase of heat flux. A factor shortening the liquid-solid contact period is rapid liquid-vapor exchanging action induced by the minute bubble emission.

Conclusions

The noteworthy points from the experiment described above are:

1 There is a certain boiling regime where the heated surface is covered with a thin vapor film of micrometer thickness. In this regime, no liquid-solid contact signals occur.

2 If subcooling exceeds 30 K and the heated surface is contaminated by a scale deposit, subcooled liquid readily makes contact with the surface through the thin vapor film, and minute vapor bubbles are rapidly emitted.

3 The period of the liquid-solid contact becomes short with increase of heat flux.

References

1 Miyasaka, Y., Inada, S., and Izumi, R., "Study of Boiling-Characteristic Curves in Subcooled Pool-Boiling of Water," *International Chemical Engineering*, Vol. 23, No. 1, Jan. 1983, pp. 48-55.

2 Inada, S., Miyasaka, Y., and Izumi, R., "Behaviour of Vapor Bubbles and Surface Temperature Variations in Transitional Pool Boiling," *Heat Transfer Japanese Research*, Vol. 11, No. 2, 1982, pp. 42-69.

3 Inada, S., Miyasaka, Y., Izumi, R., and Kobayashi, M., "The Mechanism of Heat Transfer in Transition Boiling," *Bulletin of the JSME*, Vol. 25, No. 205, July 1982, pp. 1085-1092.

4 Inada, S., Miyasaka, Y., Sakumoto, S., Mogi, I., and Izumi, R., "Heat Transfer Mechanism of Liquid-Solid Contact in Pool Transition Boiling of Subcooled Water," *Proc. 2nd World Congress of Chemical Engineering*, Vol. V, 1981, pp. 143-147.

5 Iida, Y., and Kobayashi, K., "On the Behavior of Generating Vapor Bubbles in Saturated Pool Boiling: Part 2—The Behavior Near the Burn-Out Point and in Transition Boiling," *Journal of JSME*, Vol. 36, No. 283, Mar. 1970, pp. 446-453 (in Japanese).

Binary Fluid Convection and Double-Diffusive Convection in a Porous Medium

M. E. Taslim[1,2] **and U. Narusawa**[1]

Nomenclature

D_s = diffusivity of S component

D_T = diffusivity of T component

D_{TD} = coefficient of cross diffusion for T component induced by S gradient

D_{ss} = coefficient of cross-diffusion for S component induced by T gradient

h = distance between the two horizontal boundaries

H = heat flux per heat capacity in double diffusion

Hs = solute flux in double diffusion

K = permeability

Nu = Nusselt number in cross diffusion (see equation (16a))

Nu$'$ = Nusselt number in double diffusion (see equation (14))

Nu$_s'$ = solute Nusselt number in double diffusion (see equation (15))

Pr = ν/D_T = Prandtl number

$R_T = \dfrac{g\alpha_T \Delta T_R K h}{\nu D_T}$ = Rayleigh number with respect to ΔT_R

$R_s = \dfrac{S\alpha_s \Delta S_R K h}{\nu D_T} = \beta R_T$ = Rayleigh number with respect to ΔS_R

$R_T' = \dfrac{BR_T + R_s}{(1+\tau b)(B-b)a}$

$R_s' = \dfrac{bR_T + R_s}{(i+\tau b)(B-b)A}$

$\bar{S} = S/\Delta S_R$

$\Delta S_R = (D_{ss}/D_s)\Delta T_0$

$t_1 = (1+\tau b)t$

$T_0 = T(z=0)$

$T_1 = T(z=1)$

$\bar{T} = (T-T_1)/\Delta T_R$

$\Delta T_R = \Delta T_0 = T_0 - T_1$

$\mathbf{V}_1 = \mathbf{V}/(1+\tau b)$

α = expansion coefficient

$\beta = (\alpha_s D_{ss})/(\alpha_T D_s)$

$\eta = (D_{TD} D_{ss})/(D_T D_s)$

$\lambda = K/h^2$

$\lambda' = \lambda(1+\tau b)$

$\tau = D_s/D_T$

$\tau' = (1+\tau B)/(1+\tau b)$

$\omega_1 = \omega/(1+\tau b)$

Subscripts

R = reference scale

S = S component

T = T component

Introduction

This paper is concerned with two transport mechanisms in particular, the first being cross diffusion, a term describing the diffusion of one property along the gradient of another. The well-known effects of cross diffusion are the Soret and the Dufour effects in convection of binary fluids [1]. The other transport mechanism of interest is double diffusion, which occurs in the presence of opposing gradients of two properties [2].

Knobloch [3] demonstrated a close relationship between cross-diffusion problems and double-diffusion problems for viscous fluids. An examination of his paper reveals that the mathematical identity of the two problems also holds for a fluid-saturated porous medium, the study of which has important applications in relation to fossil/geothermal reservoirs and disposal of nuclear waste in geological media.

Formulation and Transformation

The problem of interest here deals with the Rayleigh-Benard geometry, i.e., a horizontal layer of fluid between two boundaries. First, the cross-diffusion problem will be formulated and then it will be transformed into the

---

[1] Department of Mechanical Engineering, Northeastern University, Boston, MA 02115

[2] Assoc. Mem. ASME

Contributed by the Heat Transfer Division for publication in the JOURNAL OF HEAT TRANSFER. Manuscript received by the Heat Transfer Division February 10, 1984.

corresponding double-diffusive problem. Suppose a binary fluid with a diffusing component S is placed between top and bottom boundaries, across which there exists a "concentration" difference of a second diffusing component T. Utilizing the Boussinesq approximation and the linearized equation of state of the form

$$\frac{\rho-\rho_R}{\rho_R}=-\alpha_T(T-T_R)+\alpha_s(S-S_R) \tag{1}$$

the nondimensional conservation equations with z axis directed upward can be written in the following manner

$$\nabla \cdot \mathbf{V}=0 \tag{2}$$

$$\frac{\lambda}{\Pr}\left[\frac{\partial\omega}{\partial t}+\nabla\times(\omega\times\mathbf{v})\right]=(R_T\nabla\bar{T}-R_S\nabla\bar{S})\times\hat{k}-\omega \tag{3}$$

$$D\bar{T}/Dt=\nabla^2\bar{T}+\frac{D_{TD}\Delta S_R}{D_T\Delta T_R}\nabla^2\bar{S} \tag{4}$$

$$D\bar{S}/Dt=\frac{D_S}{D_T}\nabla^2\bar{S}+\frac{D_{SS}\Delta T_R}{D_T\Delta S_R}\nabla^2\bar{T} \tag{5}$$

where $\mathbf{V}$, ω, $\bar{T}$, and $\bar{S}$ (all nondimensional quantities) are the velocity, the vorticity, the T and S components, respectively, and space coordinates, time, velocity, and the T and S components were normalized with respect to layer depth $(=h)$, h^2/D_T, D_T/h, ΔT_R, and ΔS_R, respectively. As the boundary conditions for the T and S components, we specify the T component at the top $(=T_1)$ and at the bottom $(=T_0)$ boundaries, along with free boundary conditions for the S component. Then, we can define the reference quantities, ΔT_R and ΔS_R, as shown below

$$\begin{gathered}T-T_1=\Delta T_R\bar{T},\quad \Delta T_R=T_0-T_1=\Delta T_0\\ S=\Delta S_R\bar{S},\quad \Delta S_R=(D_{ss}/D_s)\Delta T_0\end{gathered} \tag{6}$$

with the boundary conditions described by the equations below

$$\bar{T}(z=0)=1,\quad \bar{T}(z=1)=0 \tag{7}$$

$$\bar{S}+\bar{T}=\text{const at } z=0 \text{ and } 1 \tag{8}$$

ΔS_R is the concentration difference of the S component induced by the cross-diffusion effect of the T component [4]. Under the definitions of ΔT_R and ΔS_R given by equations (6), the following conservation equations along with equation (2) and the boundary conditions of equations (7) and (8) constitute the formulation for convection of a binary mixture

$$\frac{\lambda}{\Pr}\left[\frac{\partial\omega}{\partial t}+\nabla\times(\omega\times\mathbf{v})\right]=R_T(\nabla\bar{T}-\beta\nabla\bar{S})\times\hat{k}-\omega \tag{3a}$$

$$\frac{D\bar{T}}{Dt}=\nabla^2\bar{T}+\eta\nabla^2\bar{S} \tag{4a}$$

$$\frac{DS}{Dt}=\tau(\nabla^2\bar{S}+\nabla^2\bar{T}) \tag{5a}$$

The transformation of the problem of binary fluid convection into that of double-diffusive convection closely parallels that given by Knobloch [3]. First, we introduce the following new principal variables P and Q

$$P=a(\bar{T}+b\bar{S}+e),\quad Q=A(\bar{T}+B\bar{S}+E) \tag{9}$$

Then, equations (2), (3a), (4a), (5a), written in terms of P and Q, become

$$\nabla\cdot\mathbf{V}_1=0 \tag{2b}$$

$$\frac{\lambda'}{\Pr}\left[\frac{\partial\omega_1}{\partial t_1}+\nabla\times(\omega_1\times\mathbf{V}_1)\right]=(R_T'\nabla P-R_S'\nabla Q)\times\hat{k}-\omega_1 \tag{3b}$$

$$\frac{\partial P}{\partial t_1}+\mathbf{V}_1\cdot\nabla P=\nabla^2 P \tag{4b}$$

$$\frac{\partial Q}{\partial t_1}+\mathbf{V}_1\cdot\nabla Q=\tau'\nabla^2 Q \tag{5b}$$

where

$$R_T'=\frac{BR_T+R_s}{(1+\tau b)(B-b)a},\quad R_s'=\frac{bR_T+R_s}{(1+\tau b)(B-b)A},$$
$$\lambda'=\lambda(1+\tau b),\quad \tau'=(1+\tau B)/(1+\tau b),$$
$$t_1=(1+\tau b)t,\quad \mathbf{V}_1=\mathbf{V}/(1+\tau b),$$

and

$$\omega_1=\omega/(1+\tau b),$$

with b and B being the two roots of the following equation

$$\tau x^2+(1-\tau)x-\eta=0 \tag{10}$$

Finally, by setting

$$e=-b,\quad E=-B,\quad a=1/(1-b),\quad A=1/(1-B) \tag{11}$$

the boundary conditions for P and Q, corresponding to equations (7), (8), will become

$$P(z=0)=Q(z=0)=1 \tag{7b}$$

$$P(z=1)=Q(z=1)=0 \tag{8b}$$

The set of equations (2b) – (5b) along with the boundary conditions of equations (7b) and (8b) is identical to the formulation describing double-diffusive convection in the Rayleigh–Benard geometry with P and Q specified at the top and bottom boundaries.

Discussion

Past studies of a fluid-saturated porous medium for the Rayleigh–Benard geometry are mainly concerned with cases in which temperature difference and solute concentration are the T and S (and P and Q) components, respectively. Then, the cross-diffusion terms in equations (4a) and (5a) correspond to the Dufour and the Soret effects. The former effect being negligible for liquids (i.e., $\eta=0$), the solution to equation (10) becomes $b=0$, $B=1-1/\tau$ with the range of diffusivity ratio τ of $\sim 1/10 - \sim 1/100$ for thermosolutal systems. (It should be mentioned here that when both T and S components are solutes, then both cross-diffusion effects are equally important.)

(*a*) *Linear Stability Analysis.* Nield [5] performed a linear stability analysis of the double-diffusive Rayleigh–Benard problem. For the fixed values of temperature and solute concentration at the rigid top and bottom boundaries, his analysis for the case of $\lambda << 1$ yielded

$$R_T'-R_s'/\tau=4\pi^2 \tag{12a}$$

for direct (monotonic) instability, and

$$R_T'-R_s'=4\pi^2(1+\tau) \tag{12b}$$

for overstable (oscillatory) instability, with the transition from the direct mode to the overstable mode occurring at

$$R_s'=\frac{4\pi^2\tau^2}{(1-\tau)},\quad R_T'=\frac{4\pi^2}{(1-\tau)}.$$

The corresponding stability criteria of a binary fluid with the Soret effect can be deduced from the above result through the transformation yielding

$$R_T=4\pi^2/[1+\beta(1+1/\tau)] \tag{13a}$$

for the direct mode, and

$$R_T=4\pi^2(1+\tau)/(1+\beta) \tag{13b}$$

for the overstable mode, with the transition occurring at $\beta=-(1+1/\tau+1/\tau^2)^{-1}$. This result agrees completely with that obtained by Brand and Steinberg [6]. Nield [5] also studied marginal (direct mode) stability conditions of ther-

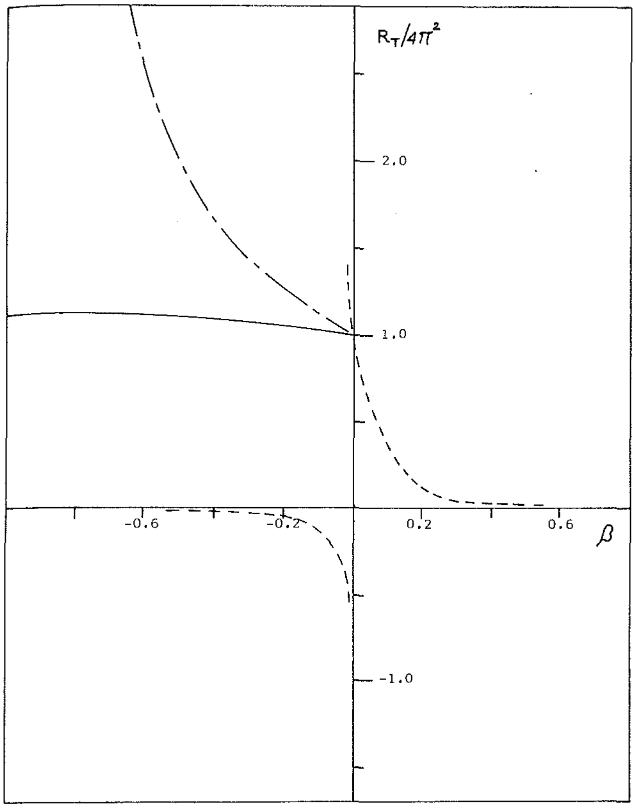

Fig. 1 $R_T/4\pi^2$ versus β for $\tau = 1/100$: ········ = stationary instability of equation (13*a*), — · — = oscillatory instability of equation (13*b*), = steady finite amplitude instability of equation (13*d*)

mosolutal problem for various types of boundary conditions, other than those discussed above, resulting in the following general equation

$$R_T' - R_s'/\tau = C \qquad (12c)$$

Upon transformation, the corresponding stability condition for a binary fluid becomes

$$R_T = \frac{C}{1 + \beta(1 + 1/\tau)} \qquad (13c)$$

The values of C are tabulated in Table 1. It should be noted that for the boundary condition of constant flux, T and S (and P and Q) should be scaled in terms of the applied fluxes. The cases, discussed by Nield but not listed in Table 1, result in boundary conditions of a mixed (or third) kind for the corresponding binary fluid problem.

(*b*) *Finite Amplitude Analyses.* According to the study by Rudraiah, Srimani, and Friedrich [7] for double-diffusive convection in a porous medium with rigid boundaries of specified T and S values, steady finite amplitude instabilities can occur, for $2\pi^2\tau^3/(1-\tau^2) < R_s'$ and $\tau < 1$, at

$$R_T' = [(\tau R_s')^{1/2} + 2\pi(1-\tau^2)^{1/2}]^2 \qquad (12d)$$

The above equation shows that for a sufficiently large value of R_s' in the diffusive regime (i.e., $R_T' > 0$, $R_s' > 0$), subcritical instability is a possibility. The equation can be transformed into the following form for the threshold of steady, finite amplitude instability of a binary mixture with the Soret effect

$$R_T = \frac{4\pi^2(1-\tau^2)}{\left(1 - \dfrac{\beta\tau}{1-\tau}\right)^{1/2} - \left(-\dfrac{\beta\tau}{1-\tau}\right)^{1/2}} \qquad (13d)$$

for $(-\beta)R_T > 2\pi^2\tau^2/(1+\tau)$ and $\tau < 1$. As can be seen, finite amplitude instability occurs only for positive values of R_T (i.e., bottom heating) and a negative value of β. (It should be noted that both α_s (solute expansion coefficient) and D_{ss} (Soret coefficient) could have either sign. For example, for the methanol-water mixture α_s is negative and the sign of D_{ss} changes at ~26 percent methanol by weight [8].) Figure 1 shows the stability curves, described by equations (13*a*, *b*, *d*) for $\tau = 1/100$. The curve for the onset of steady finite amplitude instability does not extend all the way to $\beta = 0$ because of the restriction imposed on equation (13*d*), although the point at which the curve ends is very close to $\beta = 0$. It should also be noted that, for a negative value of β, steady finite amplitude instability could occur slightly above the marginal value of natural convection without the Soret effect (i.e., $R_T = 4\pi^2$ at $\beta = 0$).

(*c*) *Heat and Mass Transfer Near Marginal Conditions.* Heat and solute transports near marginal stability conditions have been studied by Rudraiah, Srimani, and Friedrich [7] (henceforth to be referred to as RSF) for the double-diffusive problem near the threshold of steady finite amplitude instability, and by Brand and Steinberg [9] for a binary mixture with the Soret effect near critical conditions (for both the direct and overstable modes). In the double-diffusive problem, discussed by RSF, the Nusselt number Nu′ and the solute Nusselt number Nu_s' are evaluated in relation to the heat flux at the bottom boundary. In our symbols, they are

$$\mathrm{Nu}'\left(= \frac{Hh}{D_T\Delta T_0}\right) = \left\langle \frac{\partial P}{\partial z} \right\rangle_{z=0} = 1 - 2\pi\bar{C} \qquad (14)$$

$$\mathrm{Nu}_s' = \left(= \frac{H_s h}{D_s \Delta S_0}\right) = \left\langle \frac{\partial Q}{\partial z} \right\rangle_{z=0} = 1 - 2\pi\bar{E} \qquad (15)$$

with the bracket, ⟨ ⟩, indicating a horizontal average, and H and H_s being heat flux per heat capacity and solute flux, respectively. RSF evaluated the values of C and E numerically, based on their truncated forms of finite amplitude motion. For a small value of τ, their results can be approximated by the following forms

$$\mathrm{Nu}' = \begin{cases} 1 + \dfrac{2\Lambda}{\Lambda + 2} & \text{for } \Lambda \geq 0 \\ 1 & \text{for } \Lambda < 0 \end{cases} \qquad (16)$$

$$\mathrm{Nu}_s' = 1 + \frac{2\Lambda}{\Lambda + 2\tau^2}\,. \qquad (17)$$

where

$$\Lambda = \frac{1}{4\pi^2}\left\{ -\theta + [\theta^2 + 8\pi^2\tau^2\lambda(R_T' - R_s'/\tau - 4\pi^2)]^{1/2}\right.,$$

$$\theta = \tau R_s' - R_T' + 4\pi^2(1+\tau^2).$$

The numerical values of Nu′ and Nu_s' calculated from equations (16) and (17) for $\tau = 10^{-1/2}$, $R_s' = 10^2$, and $\lambda = 10^{-5}$ for $40 < R_T' < 300$ agree exactly with those obtained by RSF and shown in the first column ($R_s' = 100$) and the third column ($R_s' = 0$) of Table 1 in their paper. However, for $\tau = 2^{-1/2}$, *equations (16) and (17) fail to agree with the correct values* listed in the second column in their table. With this restriction in mind, equations (16) and (17) can be expressed in terms of $\bar{T}$ and $\bar{S}$, which describe the corresponding binary fluid problem, and they are

$$\mathrm{Nu} = \left\langle \frac{\partial \bar{T}}{\partial z} \right\rangle_{z=0} = 1 + \frac{2\Lambda_1}{\Lambda_1 + 2} \qquad (16a)$$

$$\tau\left\langle \frac{\partial \bar{T}}{\partial z} \right\rangle_{z=0} + (\tau - 1)\left\langle \frac{\partial \bar{S}}{\partial z} \right\rangle_{z=0} = 1 + \frac{2\Lambda_1}{\Lambda_1 + 2\tau^2} \qquad (17a)$$

with

Table 1 Values of *C* in equations (12*c*) and (13*c*) for various boundary conditions

Boundary conditions for T & S components in double-diffusive problem	Corresponding boundary conditions for T & S components in binary fluid problem with the Soret effect	Boundary conditions for velocity field, common to both problems		Value of C
		top	bottom	
constant values for T & S	constant T values and free boundaries for S	rigid	rigid	39.48 ($4\pi^2$)
constant values for T & S	constant T values and free boundaries for S	rigid	free	27.10
constant T- & S-fluxes	constant T flux and rigid boundaries for S	rigid	rigid	12.00
constant T- & S-fluxes	constant T flux and rigid boundaries for S	rigid	free	3.00

$$\Lambda_1 = \frac{1}{4\pi^2}\Big\{-\theta_1 + \Big[\theta_1^2 + 8\pi^2\tau^2\lambda\Big(R_T\Big(1+\frac{\beta(1+\tau)}{\tau}\Big)-4\pi^2\Big)\Big]^{1/2}\Big\}$$

$\theta_1 = 4\pi^2(\tau^2+1) - R_T$, where the Nusselt number is now defined based on the temperature difference across the fluid layer in the binary fluid problem. Subtracting equation (17*a*) from equation (16*a*) one obtains

$$\left\langle \frac{\partial \bar{T}}{\partial z} \right\rangle_{z=0} + \left\langle \frac{\partial \bar{S}}{\partial z} \right\rangle_{z=0} = -\frac{(\mathrm{Nu}-1)(3-\mathrm{Nu})(1+\tau)}{\mathrm{Nu}-1+\tau^2(3-\mathrm{Nu})} \qquad (18)$$

From the free boundary condition for the *S* component of equation (8), the right-hand side of the above equation should be zero. In other words, when the steady finite amplitude study of RSF on the double-diffusive problem, which is based on a truncated form of a convective field, is transformed into the corresponding binary fluid problem, the free boundary condition for the *S* component is satisfied approximately; the error of the approximation to be represented by equation (18). It can be shown easily that the maximum deviation of the right-hand side of equation (18) from zero is $-2\tau(1-\tau)/(1+\tau)$ at $\mathrm{Nu} = 3 - 2/(1+\tau)$. Equation (16*a*) shows that for small values of both τ (thermosolutal case) and λ (a porous medium with low permeability), the Nusselt number is practically independent of the value of β, which means that, once instability sets in, the Soret effect on heat transfer quickly disappears.

References

1 Gutkowicz-Krusin, D., Collins, M. A., and Ross, J., "Rayleigh-Benard Instability in Nonreactive Binary Fluids. I. Theory," *Phys. Fluids*, Vol. 22, 1979, pp. 1443-1450.

2 Turner, J. S., *Buoyancy Effects in Fluids*, Cambridge University Press, 1973.

3 Knobloch, E., "Convection in Binary Fluids," *Phys. Fluids*, Vol. 23, 1980, pp. 1918-1920.

4 Schecter, R. S., Prigogine, I., and Hamm, J. R., "Thermal Diffusion and Convective Stability," *Phys. Fluids*, Vol. 15, 1972, pp. 379-386.

5 Nield, D. A., "Onset of Thermohaline Convection in a Porous Medium," *Water Resources Res.*, Vol. 4, 1968, pp. 553-560.

6 Brand, H., and Steinberg, V., "Convective Instabilities in Binary Mixtures in a Porous Medium," *Physica*, Vol. 119A, 1983, pp. 327-338.

7 Rudraiah, N., Srimani, P. K., and Friedrich, R., "Finite Amplitude Convection in a Two-Component Fluid Saturated Porous Layer," *Int. J. Heat Mass Transfer*, Vol. 25, 1982, pp. 715-722.

8 Hurle, D. T. J., and Jakeman, E., "Soret-Driven Thermosolutal Convection," *J. Fluid Mech.*, Vol. 47, 1971, pp. 667-687.

9 Brand, H., and Steinberg, V., "Nonlinear Effects in the Convective Instability of a Binary Mixture in a Porous Medium Near Threshold," *Phys. Letters*, Vol. 93A, 1983, pp. 333-336.

Heat Transfer Characteristics for a Plate Fin

V. K. Garg[1,2] **and K. Velusamy**[1]

Introduction

Conventionally the heat transfer characteristics of fins are determined by solving the fin conduction equation with a convective heat transfer coefficient assumed uniform all along the fin surface. This approach leads to uncertain results because, in general, the heat transfer coefficient varies along the fin surface. The correct way is to solve the conduction problem for the fin and the convective heat transfer problem for the flowing fluid simultaneously.

Herein we describe a method for such a simultaneous solution for a plate fin that is washed by a laminar forced convection boundary layer flow. The motivation for the present work came from [1] where an analysis was carried out for a particular Prandtl number (Pr = 0.7) employing the Patankar-Spalding method [2]. This is quite an involved method for this rather simple problem; in addition, Sparrow and Chyu [1] doubt that their observations are applicable to Prandtl numbers much different from 0.7. Herein, we present results for a wide range of Prandtl numbers ($0.01 \leq \mathrm{Pr} \leq 100$) using a method that is very simple and inexpensive compared to the Patankar-Spalding method. The results are presented for both the complete and the conventional (simple) models.

Analysis

Let a uniform free stream with velocity u_∞, temperature T_∞, kinematic viscosity ν, and thermal conductivity K_f approach a plate fin that is aligned parallel to the oncoming flow (see inset of Fig. 3). The length of the fin is L, its thickness is $2t$, and its thermal conductivity is K_w. This is attached to a base surface whose temperature is T_0. The temperature of the fin T_w varies along its length.

For a thin fin the energy balance yields

---

[1] Department of Mechanical Engineering, Indian Institute of Technology, Kanpur 208016, U.P., India

[2] Mem. ASME

Contributed by the Heat Transfer Division for publication in the JOURNAL OF HEAT TRANSFER. Manuscript received by the Heat Transfer Division October 30, 1984.

Table 1 Values of *C* in equations (12*c*) and (13*c*) for various boundary conditions

Boundary conditions for T & S components in double-diffusive problem	Corresponding boundary conditions for T & S components in binary fluid problem with the Soret effect	Boundary conditions for velocity field, common to both problems		Value of C
		top	bottom	
constant values for T & S	constant T values and free boundaries for S	rigid	rigid	39.48 ($4\pi^2$)
constant values for T & S	constant T values and free boundaries for S	rigid	free	27.10
constant T- & S-fluxes	constant T flux and rigid boundaries for S	rigid	rigid	12.00
constant T- & S-fluxes	constant T flux and rigid boundaries for S	rigid	free	3.00

$$\Lambda_1 = \frac{1}{4\pi^2}\Big\{-\theta_1 + \Big[\theta_1^2 + 8\pi^2\tau^2\lambda\Big(R_T\Big(1+\frac{\beta(1+\tau)}{\tau}\Big)-4\pi^2\Big)\Big]^{1/2}\Big\}$$

$\theta_1 = 4\pi^2(\tau^2+1) - R_T$, where the Nusselt number is now defined based on the temperature difference across the fluid layer in the binary fluid problem. Subtracting equation (17*a*) from equation (16*a*) one obtains

$$\left\langle \frac{\partial \bar{T}}{\partial z} \right\rangle_{z=0} + \left\langle \frac{\partial \bar{S}}{\partial z} \right\rangle_{z=0} = -\frac{(\mathrm{Nu}-1)(3-\mathrm{Nu})(1+\tau)}{\mathrm{Nu}-1+\tau^2(3-\mathrm{Nu})} \qquad (18)$$

From the free boundary condition for the *S* component of equation (8), the right-hand side of the above equation should be zero. In other words, when the steady finite amplitude study of RSF on the double-diffusive problem, which is based on a truncated form of a convective field, is transformed into the corresponding binary fluid problem, the free boundary condition for the *S* component is satisfied approximately; the error of the approximation to be represented by equation (18). It can be shown easily that the maximum deviation of the right-hand side of equation (18) from zero is $-2\tau(1-\tau)/(1+\tau)$ at $\mathrm{Nu} = 3 - 2/(1+\tau)$. Equation (16*a*) shows that for small values of both τ (thermosolutal case) and λ (a porous medium with low permeability), the Nusselt number is practically independent of the value of β, which means that, once instability sets in, the Soret effect on heat transfer quickly disappears.

References

1 Gutkowicz-Krusin, D., Collins, M. A., and Ross, J., "Rayleigh-Benard Instability in Nonreactive Binary Fluids. I. Theory," *Phys. Fluids*, Vol. 22, 1979, pp. 1443-1450.

2 Turner, J. S., *Buoyancy Effects in Fluids*, Cambridge University Press, 1973.

3 Knobloch, E., "Convection in Binary Fluids," *Phys. Fluids*, Vol. 23, 1980, pp. 1918-1920.

4 Schecter, R. S., Prigogine, I., and Hamm, J. R., "Thermal Diffusion and Convective Stability," *Phys. Fluids*, Vol. 15, 1972, pp. 379-386.

5 Nield, D. A., "Onset of Thermohaline Convection in a Porous Medium," *Water Resources Res.*, Vol. 4, 1968, pp. 553-560.

6 Brand, H., and Steinberg, V., "Convective Instabilities in Binary Mixtures in a Porous Medium," *Physica*, Vol. 119A, 1983, pp. 327-338.

7 Rudraiah, N., Srimani, P. K., and Friedrich, R., "Finite Amplitude Convection in a Two-Component Fluid Saturated Porous Layer," *Int. J. Heat Mass Transfer*, Vol. 25, 1982, pp. 715-722.

8 Hurle, D. T. J., and Jakeman, E., "Soret-Driven Thermosolutal Convection," *J. Fluid Mech.*, Vol. 47, 1971, pp. 667-687.

9 Brand, H., and Steinberg, V., "Nonlinear Effects in the Convective Instability of a Binary Mixture in a Porous Medium Near Threshold," *Phys. Letters*, Vol. 93A, 1983, pp. 333-336.

Heat Transfer Characteristics for a Plate Fin

V. K. Garg[1,2] and K. Velusamy[1]

Introduction

Conventionally the heat transfer characteristics of fins are determined by solving the fin conduction equation with a convective heat transfer coefficient assumed uniform all along the fin surface. This approach leads to uncertain results because, in general, the heat transfer coefficient varies along the fin surface. The correct way is to solve the conduction problem for the fin and the convective heat transfer problem for the flowing fluid simultaneously.

Herein we describe a method for such a simultaneous solution for a plate fin that is washed by a laminar forced convection boundary layer flow. The motivation for the present work came from [1] where an analysis was carried out for a particular Prandtl number (Pr = 0.7) employing the Patankar-Spalding method [2]. This is quite an involved method for this rather simple problem; in addition, Sparrow and Chyu [1] doubt that their observations are applicable to Prandtl numbers much different from 0.7. Herein, we present results for a wide range of Prandtl numbers ($0.01 \leq \mathrm{Pr} \leq 100$) using a method that is very simple and inexpensive compared to the Patankar-Spalding method. The results are presented for both the complete and the conventional (simple) models.

Analysis

Let a uniform free stream with velocity u_∞, temperature T_∞, kinematic viscosity ν, and thermal conductivity K_f approach a plate fin that is aligned parallel to the oncoming flow (see inset of Fig. 3). The length of the fin is L, its thickness is $2t$, and its thermal conductivity is K_w. This is attached to a base surface whose temperature is T_0. The temperature of the fin T_w varies along its length.

For a thin fin the energy balance yields

---

[1] Department of Mechanical Engineering, Indian Institute of Technology, Kanpur 208016, U.P., India

[2] Mem. ASME

Contributed by the Heat Transfer Division for publication in the JOURNAL OF HEAT TRANSFER. Manuscript received by the Heat Transfer Division October 30, 1984.

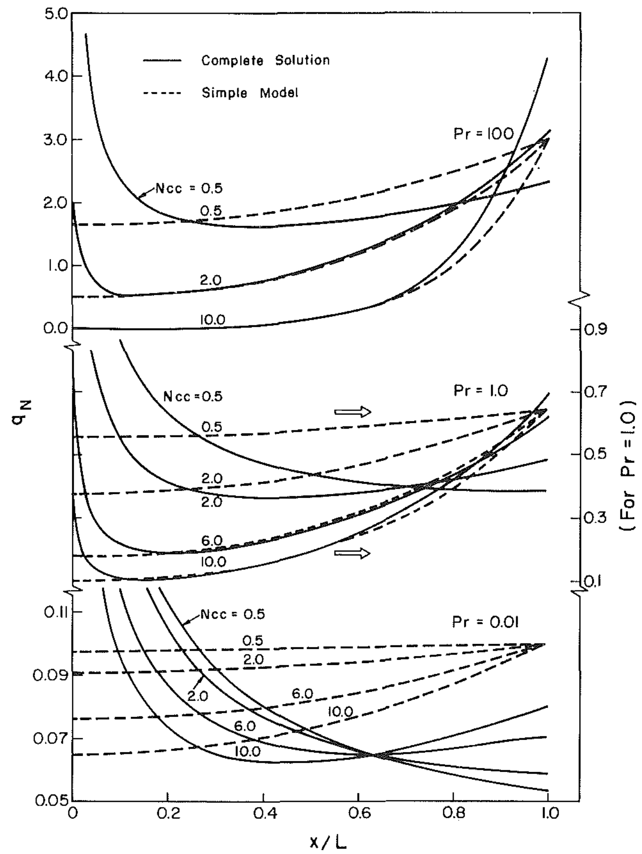

Fig. 1 Local heat flux at the fin surface

$$d^2\theta_w(X)/dX^2 = N_{cc}h_N(X)\theta_w(X) \tag{1}$$

with boundary conditions $d\theta_w(0)/dX = 0$ and $\theta_w(1) = 1$, where $X = x/L$, $\theta_w(X) = (T_w(X) - T_\infty)/(T_0 - T_\infty)$, $h_N(X) = (h(X)L/K_f)R_{eL}^{-1/2}$, $N_{cc} = (K_fL/K_wt)R_{eL}^{1/2}$, $R_{eL} = U_\infty L/\nu$, and $h(X)$ = local heat transfer coefficient.

Since the flow situation is similar to a laminar boundary layer flow over a flat plate, the well-known Blasius solution is applicable. For the fluid temperature T_f, the flat plate boundary layer energy equation with the wall temperature varying as some monomial of X in the form $(T_w(X) - T_\infty) = CX^n$ yields, for negligible viscous dissipation [3],

$$\theta_f'' + \frac{1}{2}\mathrm{Pr}f\theta_f' - n\mathrm{Pr}f'\theta_f = 0 \tag{2a}$$

with boundary conditions

$$\theta_f(0) = CX^n \text{ and } \theta_f(\infty) = 0 \tag{2b}$$

where $\theta_f(\eta) = (T_f(X, y) - T_\infty)/(T_0 - T_\infty)$, f is the Blasius function, and the primes denote differentiation with respect to $\eta = (yX^{-1/2}/L)/R_{eL}^{1/2}$.

Equations (1) and (2) are coupled through

$$-K_f\partial T_f/\partial y = h(X)(T_w(X) - T_\infty) \text{ at } y = 0$$

Both (1) and (2) are solved easily by the Runge-Kutta method utilizing their linearity. A fifth-order polynomial

$$\theta_w(X) = \sum_{i=0}^{5} C_iX^i \tag{3}$$

is fitted to the fin temperature distribution to take care of the fact that equation (2) holds only for the fin temperature varying as some monomial of X. Numerical experimentation confirmed that a fifth-order polynomial provided the best fit to the fin temperature distribution over the range $0.01 \leq \mathrm{Pr} \leq 100$. In fact, for Pr = 0.7 even a third-order polynomial resulted in exactly the same results as those reported by Sparrow and Chyu [1]. The solution of equation (2) consists of two independent orthogonal solutions for each index i. These two solutions are found by integrating equation (2) with appropriate initial conditions using the Runge-Kutta method. The boundary conditions (2*b*) provide the relations for proper linear combination of the two solutions.

The boundary condition at infinity is assumed to hold at $\eta_{\max}$, where $\eta_{\max}$ is found for each Prandtl number such that $\theta_f'(\eta_{\max}) \leq 10^{-10}$ for the results presented here. It may be noted that

$$h_N(X) = -(\theta_f'(0)/\theta_f(0))X^{-1/2} \tag{4}$$

The conduction equation (1) is also solved in a similar manner but from the base ($X = 1$) to the tip ($X = 0$) of the fin using equation (4). This yields the coefficients C_i of (3).

The following iterative procedure is followed for the solution:

1 Solve the Blasius equation for f and f'.
2 Assume a uniform fin temperature distribution, such as $\theta_w(X) = 1$ for $0 \leq X \leq 1$.
3 Solve (2) for $\theta_f(\eta)$ and compute $h_N(X)$ from (4).
4 Solve (1) for $\theta_w(X)$ using the above $h_N(X)$.
5 Repeat steps 3 and 4 until convergence.

Results and Discussion

For Prandtl numbers ranging from 0.01 to 100 and N_{cc} ranging from 0.0 to 10 for each Prandtl number, dimensionless values of the local heat transfer coefficient h_N, the local heat flux q_N, the overall heat transfer rate per unit width of the fin Q_N, the fin temperature distribution θ_w, and the effectiveness φ based on an isothermal fin were determined from the relations

$$q_N = (qL/K_f)(T_0 - T_\infty)^{-1}R_{eL}^{-1/2} = h_N\theta_w$$

$$Q_N = (Q/K_f)(T_0 - T_\infty)^{-1}R_{eL}^{-1/2} = -(2/N_{cc})d\theta_w(1)/dX$$

and

$$\varphi = -(N_{cc}\bar{h}_N)^{-1}d\theta_w(1)/dX = (1/2)Q_N/\bar{h}_N \tag{5}$$

where q and Q are the dimensional counterparts of q_N and Q_N, respectively. The relations for q_N, Q_N, φ, and the uniform heat transfer coefficient $\bar{h}_N$ for the conventional (simple) model are well known [4, 5].

It may be noted that $N_{cc} = 0$ implies an infinite fin conductance (K_wt) or an isothermal fin, and higher values of N_{cc} imply higher R_{eL} and K_f, longer fin length L, and/or smaller fin conductance.

The local heat transfer coefficient is found to decrease from the tip to the base of the fin. However, it increases with either N_{cc} or Pr. Equation (4) shows that $h_N \rightarrow \infty$ as $X \rightarrow 0$. In fact the present model, being one dimensional, ceases to be valid for such a high h_N. A two-dimensional model must be considered near $X = 0$.

The local heat flux variation q_N for both the models is shown in Fig. 1. Note the different ordinate scales for different Pr. The difference between the results for the two models decreases as N_{cc} and/or Pr increases. The variation of this difference with Pr, although evident in Fig. 1, could not be foreseen in [1] since there results for only one Pr (= 0.7) are available. We may mention that we also computed results for Pr = 0.7 but are unable to show graphic comparison since our results are in perfect agreement with those of [1].

The fin temperature distribution predicted by both the models is shown in Fig. 2. It is shown only for the lowest and the highest Prandtl number values, since its variation is similar for other Pr values. The difference between the base and the tip temperatures of the fin increases with either N_{cc} or Pr. Simple model always predicts less base-tip temperature difference than that which really prevails. Also, while the

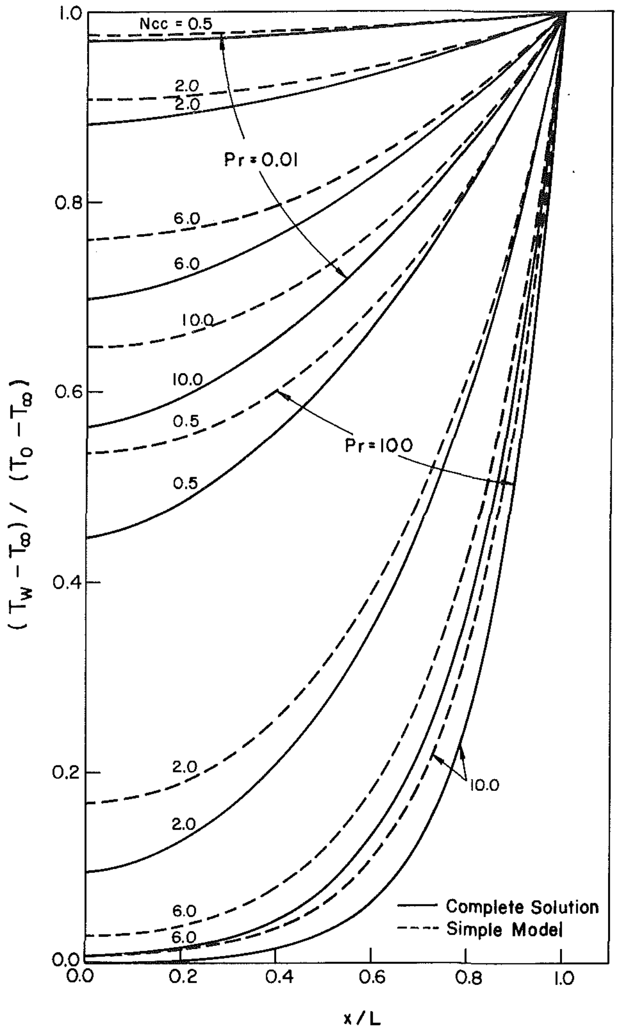

Fig. 2 Fin temperature distributions

Table 1 $\eta_{\max}$ and the ratio φ/Q_N for various Pr

Pr	$\eta_{\max}$	$\varphi/Q_N = 0.5/\bar{h}_N$
0.01	91.8	4.99550
0.1	30.3	1.83513
1.0	11.1	0.77055
10.0	4.6	0.35105
60.0	2.3	0.19303
100.0	2.0	0.16323

difference between the temperature distributions for the two models increases with N_{cc} at Pr = 0.01, it decreases with N_{cc} at Pr = 100. It should be noted that the fin becomes less and less isothermal as N_{cc} increases.

The overall heat transfer rate Q_N predicted by both the models is shown in Fig. 3. Note again the different ordinate scales for different Pr. Q_N decreases as N_{cc} increases for a fixed Pr but it increases as Pr increases for a fixed N_{cc}. From the fact that Q_N for both models is nearly the same it appears as if the simple model is sufficient for the overall fin heat transfer rate. However, the local prediction would be substantially in error.

The fin effectiveness φ has exactly the same variation as Q_N in Fig. 3 as is clear from equation (5). Values of φ/Q_N and $\eta_{\max}$ are listed in Table 1 for various Pr values.

References

1 Sparrow, E. M., and Chyu, M. K., "Conjugate Forced Convection-Conduction Analysis of Heat Transfer in a Plate Fin," ASME Journal of Heat Transfer, Vol. 104, 1982, pp. 204–206.

2 Patankar, S. V., and Spalding, D. B., *Heat and Mass Transfer in Boundary Layers*, 2nd edn., Intertext, London, 1970.

3 Schlichting, H., *Boundary Layer Theory*, 7th edn., McGraw-Hill, New York, 1979, pp. 136, 301.

4 Eckert, E. R. G., and Drake, R. M., *Analysis of Heat and Mass Transfer*, McGraw-Hill, Tokyo, 1972, pp. 75–84.

5 Kays, W. M., *Convective Heat and Mass Transfer*, McGraw-Hill, New York, 1966, p. 207.

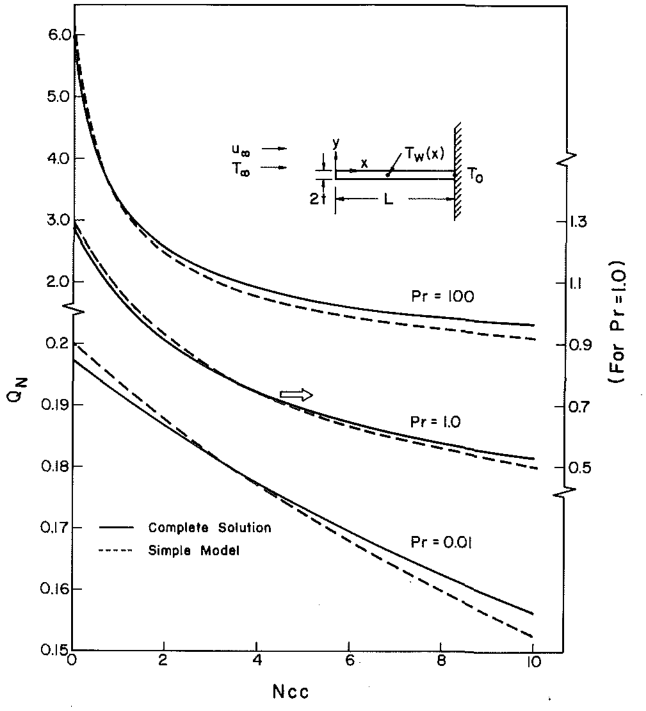

Fig. 3 Overall rate of fin heat transfer

Temperature and Heat-Flux Distributions in a Strip-Heated Composite Slab

G. F. Jones[1]

Nomenclature

Bi = hD/k_s
d = fin thickness, m
D = substrate thickness, m
h = heat transfer coefficient, W/m^2-K
k = thermal conductivity, W/m-K
l = half-spacing between strip heaters, m
m = $\sqrt{ht^2/k_f d/(1+\mathrm{Bi})}$
Q = one-half heat flow rate per unit length of strip heater, W/m
$\hat{q}$ = heat flux
T = temperature, K
t = half-width of strip heater, m

---

[1] Solar Energy Section, Advanced Engineering Technology, Los Alamos National Laboratory, Los Alamos, NM 87545; Mem. ASME

Contributed by the Heat Transfer Division for publication in the Journal of Heat Transfer. Manuscript received by the Heat Transfer Division November 5, 1984.

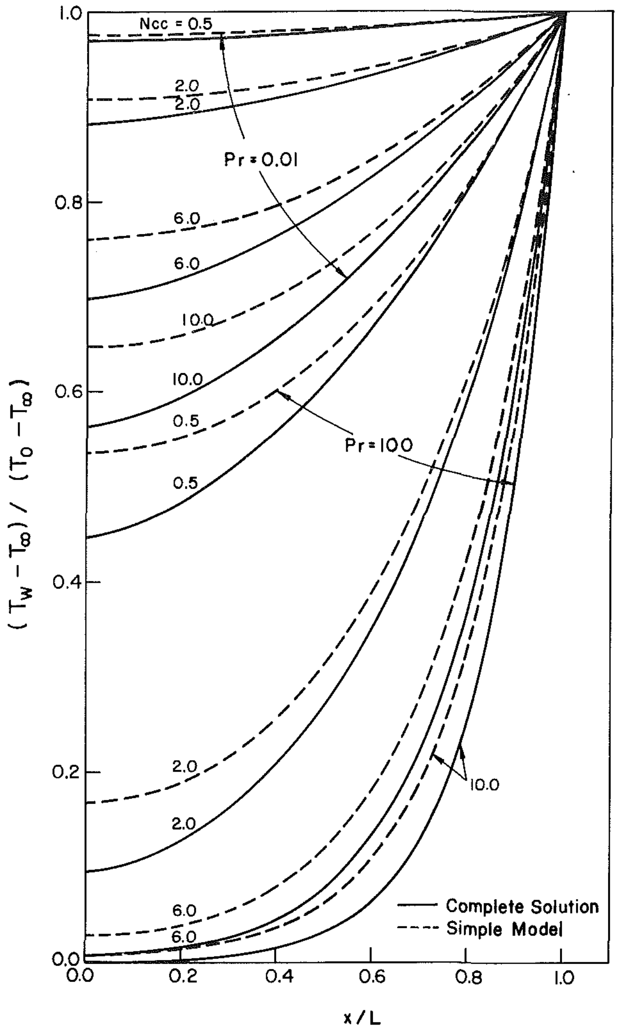

Fig. 2 Fin temperature distributions

Table 1 $\eta_{\max}$ **and the ratio** φ/Q_N **for various Pr**

Pr	$\eta_{\max}$	$\varphi/Q_N = 0.5/\bar{h}_N$
0.01	91.8	4.99550
0.1	30.3	1.83513
1.0	11.1	0.77055
10.0	4.6	0.35105
60.0	2.3	0.19303
100.0	2.0	0.16323

difference between the temperature distributions for the two models increases with N_{cc} at Pr = 0.01, it decreases with N_{cc} at Pr = 100. It should be noted that the fin becomes less and less isothermal as N_{cc} increases.

The overall heat transfer rate Q_N predicted by both the models is shown in Fig. 3. Note again the different ordinate scales for different Pr. Q_N decreases as N_{cc} increases for a fixed Pr but it increases as Pr increases for a fixed N_{cc}. From the fact that Q_N for both models is nearly the same it appears as if the simple model is sufficient for the overall fin heat transfer rate. However, the local prediction would be substantially in error.

The fin effectiveness φ has exactly the same variation as Q_N in Fig. 3 as is clear from equation (5). Values of φ/Q_N and $\eta_{\max}$ are listed in Table 1 for various Pr values.

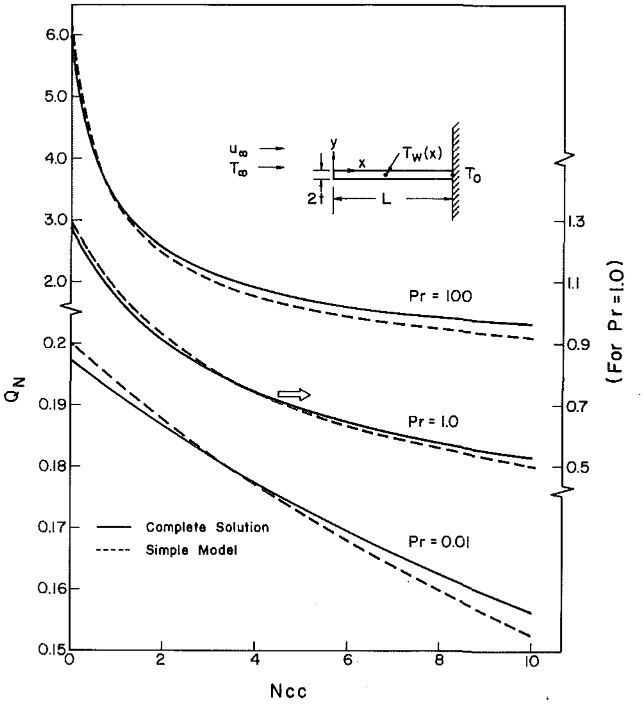

Fig. 3 Overall rate of fin heat transfer

References

1 Sparrow, E. M., and Chyu, M. K., "Conjugate Forced Convection-Conduction Analysis of Heat Transfer in a Plate Fin," ASME JOURNAL OF HEAT TRANSFER, Vol. 104, 1982, pp. 204-206.

2 Patankar, S. V., and Spalding, D. B., *Heat and Mass Transfer in Boundary Layers*, 2nd edn., Intertext, London, 1970.

3 Schlichting, H., *Boundary Layer Theory*, 7th edn., McGraw-Hill, New York, 1979, pp. 136, 301.

4 Eckert, E. R. G., and Drake, R. M., *Analysis of Heat and Mass Transfer*, McGraw-Hill, Tokyo, 1972, pp. 75-84.

5 Kays, W. M., *Convective Heat and Mass Transfer*, McGraw-Hill, New York, 1966, p. 207.

Temperature and Heat-Flux Distributions in a Strip-Heated Composite Slab

G. F. Jones[1]

Nomenclature

Bi = hD/k_s
d = fin thickness, m
D = substrate thickness, m
h = heat transfer coefficient, W/m^2-K
k = thermal conductivity, W/m-K
l = half-spacing between strip heaters, m
m = $\sqrt{ht^2/k_f d/(1+\text{Bi})}$
Q = one-half heat flow rate per unit length of strip heater, W/m
$\hat{q}$ = heat flux
T = temperature, K
t = half-width of strip heater, m

---

[1] Solar Energy Section, Advanced Engineering Technology, Los Alamos National Laboratory, Los Alamos, NM 87545; Mem. ASME

Contributed by the Heat Transfer Division for publication in the JOURNAL OF HEAT TRANSFER. Manuscript received by the Heat Transfer Division November 5, 1984.

x = coordinate, m
y = coordinate, m
γ = t/l
ϵ = figure-of-merit variable defined by equation (6)
η = x/l
λ = k_s/k_f
μ = D/l
ν = d/l
ξ = y/D
ϕ = $T-T_\infty/(Q/k_f)$

Subscripts

e = exact
f = fin
qD = quasi-two-dimensional
$2D$ = two-dimensional
s = substrate
∞ = fluid

Introduction

This note considers the steady temperature and heat-flux distributions in a composite slab consisting of two dissimilar materials in intimate contact with each other. One material, of large thermal conductivity, is heated on one side by equally spaced strip heaters, and the other material, which has small conductivity, is cooled on the opposite side by convection to a fluid whose temperature is constant over the distance between the strips. The materials of large and small conductivity are referred to as the fin and the substrate, respectively. Such a problem applies to the strip heating of process equipment or laboratory experiments where uniform or near-uniform temperatures or heat fluxes are required.[2] Because the conductivity of the substrate is small, a large number of closely spaced strip heaters would be necessary to achieve uniformity. To reduce both the number of and cost for such heaters, a thin sheet of a good conductor (the fin) is placed between the heat sources and the substrate to distribute heat flow evenly between coarsely spaced strips.

The problem of heat flow through a strip-heated single-material slab has been solved previously by Van Sant [2] for the case where the slab is convectively cooled and for constant-heat-flux and constant-temperature strips and by Schmitz [3] for a slab that is maintained at a constant temperature at its cooled side and the strip heater temperature is uniform.

In this note, an analytical solution is obtained by simultaneously solving the steady energy equations for both constituents of the composite medium. Although expressions for local temperature and heat flux are obtained, primary focus is on the heat-flux distribution at the convectively cooled side of the slab, this being the side over which uniformity is desired. Based on an approximate analytical solution, a design procedure to determine the strip heater spacing necessary for a prescribed maximum variation in heat flux at this surface is developed. Expressions for the steady temperature and heat flux are also obtained for the limiting cases of infinite heat transfer coefficient and zero-thickness substrate.

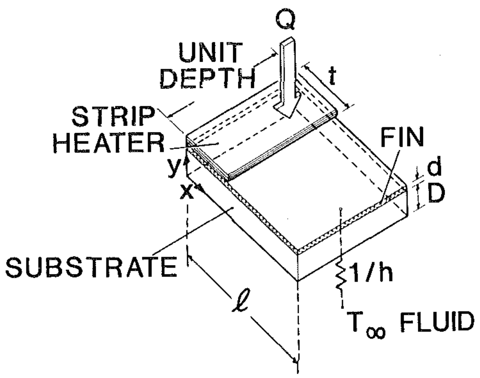

Fig. 1 Problem geometry

Exact Solution

The geometry for the problem at hand is shown in Fig. 1. The strip heater is positioned above the fin in the region $0 \le x \le t$. The heat-flow rate over this area per unit length of the heater is Q. In the region $t \le x \le l$, the fin is insulated on top. The side boundaries at $x=0$ and $x=l$ are lines of symmetry, thus making the spacing between strip heater centers $2l$. We impose the usual condition that $d/l << 1$ so that conduction in the fin in the y direction may be lumped. The steady, constant-property energy equations and boundary conditions in dimensionless form for the fin and substrate become

Fin:

$$\phi_f'' - \frac{\lambda}{\mu\nu}\phi_{s,\xi}(\eta,\ \xi=1) = \begin{bmatrix} -1/\nu\gamma \\ 0 \end{bmatrix} \text{ for } \begin{bmatrix} 0 \le \eta < \gamma \\ \gamma < \eta \le 1 \end{bmatrix} \tag{1a}$$

$$\phi_f'(\eta=0) = \phi_f'(\eta=1) = 0 \tag{1b}$$

$$\phi_f(\eta=\gamma_+) = \phi_f(\eta=\gamma_-) \tag{1c}$$

$$\phi_f'(\eta=\gamma_+) = \phi_f'(\eta=\gamma_-) \tag{1d}$$

Substrate:

$$\mu^2\phi_{s,\eta\eta} + \phi_{s,\xi\xi} = 0 \tag{2a}$$

$$\phi_{s,\eta}(\eta=0,\xi) = \phi_{s,\eta}(\eta=1,\xi) = 0 \tag{2b}$$

$$\phi_{s,\xi}(\eta,\xi=0) - \mathrm{Bi}\phi_s(\eta,\xi=0) = 0 \tag{2c}$$

$$\phi_s(\eta,\xi=1) = \phi_f(\eta) \tag{2d}$$

The boundary conditions (1c) and (1d) satisfy temperature and heat flux continuity in the fin at the point separating its heated and unheated regions. In equation (2a) μ is much less than one for all practical purposes.

Using classical methods, we obtain the substrate temperature distribution

$$\phi_s(\eta,\ \xi) = \frac{\mu}{\lambda}\left\{\frac{1}{\mathrm{Bi}} + \xi\right\} + \sum_{n=1}^{\bar{n}} b_n \left\{\frac{1}{\mathrm{Bi}}\cosh(n\pi\mu\xi) + \frac{1}{n\pi\mu}\sinh(n\pi\mu\xi)\right\}\cos(n\pi\eta) \tag{3a}$$

where

$$b_n = \frac{2\bar{n}\sin(n\pi\gamma)\sin(n\pi/\bar{n})/\lambda\gamma(n\pi)^2}{\nu(n\pi)^2\{\cosh(n\pi\mu)/\mathrm{Bi} + \sinh(n\pi\mu)/n\pi\mu\}/\lambda + n\pi\sinh(n\pi\mu)/\mathrm{Bi} + \cosh(n\pi\mu)/\mu} \tag{3b}$$

The temperature distribution in the fin is obtained from equation (3a) by setting $\xi = 1$ according to equation (2d). In equation (3b) the term $\sin(n\pi/\bar{n})/(n\pi/\bar{n})$ is included to smooth out disturbances in the solution that result from discontinuous heating at $\xi = 1$ [4]. A value for $\bar{n} = 20$ en-

---

[2] Processes involving natural convection, for instance, are sensitive to the imposed thermal-boundary conditions and may necessitate uniform boundary heat fluxes or temperatures [1].

sures convergence of equation (3a) to better than 10^{-6} for all cases considered here.

A dimensionless heat flux is defined by

$$\hat{q}(\eta,\ \xi)=\lambda\phi_{s,\xi}(\eta,\ \xi)/\mu \tag{4}$$

so that the integral of $\hat{q}(\eta,\ \xi)$ over any surface in the η direction is one.

With equations (3a) and (4), the dimensionless heat flux at the convectively cooled surface is

$$\hat{q}_e(\eta)=1+\frac{\lambda}{\mu}\sum_{n=1}^{\hat{n}}b_n\cos(n\pi\eta) \tag{5}$$

To assess the degree of uniformity of heat flux at this surface, we define a figure-of-merit variable ϵ as

$$\epsilon\equiv1-\hat{q}(\eta=1)/\hat{q}(\eta=0) \tag{6}$$

In equation (6), ϵ represents the ratio of the difference in heat flux at the $\eta=0$ and $\eta=1$ locations to that at $\eta=0$. Defined in this manner, $\epsilon=0$ corresponds to uniform heat flux distribution and $\epsilon>0$ to a maldistribution of heat flux at the convectively cooled surface. With equation (5), ϵ becomes

$$\epsilon_e=\frac{\lambda}{\mu}\sum_{n=1}^{\hat{n}}b_n[1-(-1)^n]\Big/\left(1+\frac{\lambda}{\mu}\sum_{n=1}^{\hat{n}}b_n\right) \tag{7}$$

For the case of a uniform temperature at the cooled surface, the substrate temperature, heat flux, and ϵ_e are obtained from the same equations above with the term $1/\mathrm{Bi}=0$ in equations (3). In the limit $\lambda\rightarrow1$ and $\nu\rightarrow0$, the above solution reduces to that obtained by Schmitz for a single-material slab.

By inspecting equations (7) and (3b), we note that ϵ_e depends upon the dimensionless groups λ/ν, Bi, μ, and γ, several of which contain the dimensional variable l. We now consider the case of practical interest where l is desired from equation (7) for a fixed value of ϵ_e and note that l cannot be obtained very easily from it. Rather than attempting to solve equation (7) for l, we seek an alternative solution to the problem. We propose a perturbation method, using even powers of μ as expansion parameters to obtain an approximate analytical solution valid for small μ. The zeroth-order term accounts only for conduction in the ξ direction and, upon solution, provides a zeroth-order estimate of l directly. The second-order term includes the effect of conduction in the η direction and, with this term, an improved estimate of l is obtained by a simple trial-and-error procedure.

Approximate Solution

We seek a solution in the form

$$\phi_s(\eta,\ \xi)=\phi_{s0}(\eta,\ \xi)+\mu^2\phi_{s2}(\eta,\ \xi)+0(\mu^4) \tag{8}$$

The solutions for ϕ_{s0} and ϕ_{s2} are obtained in the usual way [5] to give

$$\phi_s(\eta,\ \xi)=\frac{\gamma}{m^2\nu}\left\{f(\xi)\begin{bmatrix}1\\0\end{bmatrix}+[f(\xi)-(\mu p)^2g(\xi)]\right.$$
$$\left.\sinh\left\{p\left(\gamma-\begin{bmatrix}1\\0\end{bmatrix}\right)\right\}\cosh\left\{p\left(\eta-\begin{bmatrix}0\\1\end{bmatrix}\right)\right\}\Big/\sinh(p)\right\}$$
$$\text{for}\begin{bmatrix}0\le\eta<\gamma\\ \gamma<\eta\le1\end{bmatrix} \tag{9}$$

where

$$f(\xi)=(1+\mathrm{Bi}\,\xi)/(1+\mathrm{Bi}) \tag{10a}$$

$$g(\xi)=\mathrm{Bi}[\xi^3(1+\mathrm{Bi})-1-\mathrm{Bi}\xi]/6(1+\mathrm{Bi})^2$$
$$+[\xi^2(1+\mathrm{Bi})-1-\mathrm{Bi}\xi]/2(1+\mathrm{Bi})^2 \tag{10b}$$

$$p^2=[\mu^2\Lambda+(\gamma/m)^2]^{-1} \tag{11}$$

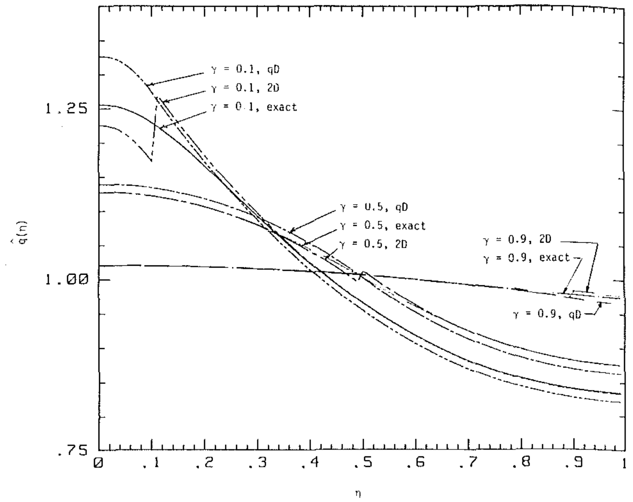

Fig. 2 Dimensionless heat flux from the exact solution and two-dimensional and quasi-two-dimensional approximate solutions; $\mu=0.2$, $\lambda/\nu=0.3$, Bi $=5$

$$\Lambda=(\mathrm{Bi}^2+3\mathrm{Bi}+3)/3\mathrm{Bi}(\mathrm{Bi}+1) \tag{12}$$

$$m^2=\gamma^2\lambda\mathrm{Bi}/\mu\nu(1+\mathrm{Bi})=(ht^2/kd)/(1+hD/k_s) \tag{13}$$

Expressions for dimensionless heat flux at $\xi=0$ and ϵ are obtained from these.

$$\hat{q}_{2D}(\eta)=\frac{1}{\gamma}\left\{\begin{bmatrix}1\\0\end{bmatrix}\right.$$
$$+G\sinh\left\{p\left(\gamma-\begin{bmatrix}1\\0\end{bmatrix}\right)\right\}\cosh\left\{p\left(\eta-\begin{bmatrix}0\\1\end{bmatrix}\right)\right\}\Big/$$
$$\left.\sinh(p)\right\}\text{for}\begin{bmatrix}0\le\eta<\gamma\\ \gamma<\eta\le1\end{bmatrix} \tag{14}$$

$$G=1+(3+\mathrm{Bi})(\mu p)^2/6(1+\mathrm{Bi}) \tag{15}$$

and

$$\epsilon_{2D}=1-G\sinh(p\gamma)/\{\sinh(p)+G\sinh[p(\gamma-1)]\} \tag{16}$$

It is also of interest to obtain the zeroth-order heat flux at $\xi=0$ and ϵ. In the limit $\mu\rightarrow0$, from equations (9) and (11) we obtain

$$\hat{q}_{qD}(\eta)=\frac{1}{\gamma}\left\{\begin{bmatrix}1\\0\end{bmatrix}\right.$$
$$+\sinh\left\{m\left(1-\begin{bmatrix}\gamma^{-1}\\0\end{bmatrix}\right)\right\}\cosh\left\{m\gamma^{-1}\left(\eta-\begin{bmatrix}1\\0\end{bmatrix}\right)\right\}$$
$$\left.\Big/\sinh(m\gamma^{-1})\right\}\text{for}\begin{bmatrix}0\le\eta\le\gamma\\ \gamma\le\eta\le1\end{bmatrix} \tag{17}$$

$$\epsilon_{qD}=1-\sinh(m)/\{\sinh(m\gamma^{-1})+\sinh[m(1-\gamma^{-1})]\} \tag{18}$$

In this limit, the effect of heat conduction in the η direction within the substrate is neglected and the analysis becomes quasi-two-dimensional. Because this component of conduction tends to make the temperature more uniform at the convectively cooled surface, the quasi-two-dimensional case thus represents an upper bound on the nonuniformity of heat flux at that surface.

For constant temperature at the cooled surface, the above equations are used with the following changes: $f(\xi)=\xi$; $g(\xi)=(\xi^3-\xi)/6$; $\Lambda=1/3$; $m^2=\gamma^2\lambda/\mu\nu=k_st^2/k_fDd$; and $G=1+(\mu p)^2/6$. For the case of a zero-thickness substrate, equations (9), (17), and (18) are used to determine fin temperature, heat flux, and ϵ, respectively. Here $p=m\gamma^{-1}$, $m^2=ht^2/k_fd$, $f(\xi)=1$, and $g(\xi)=0$. If the fin is of zero thickness, only the two-dimensional solution applies wherein $p^2=1/\mu^2\Lambda$.

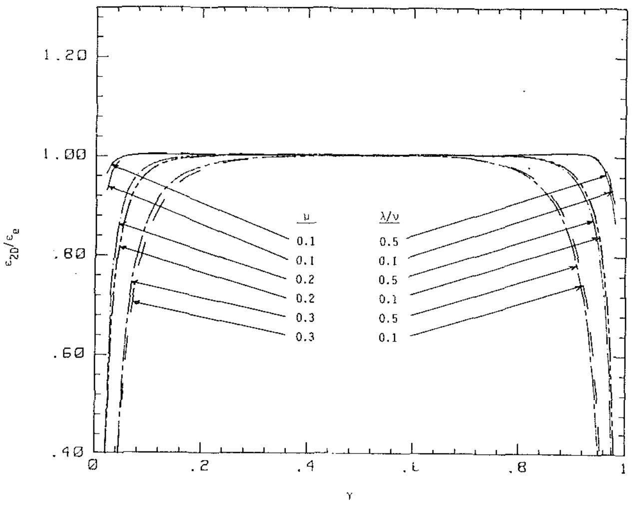

Fig. 3 Ratio of ϵ_{2D} to ϵ_e for Bi = ∞

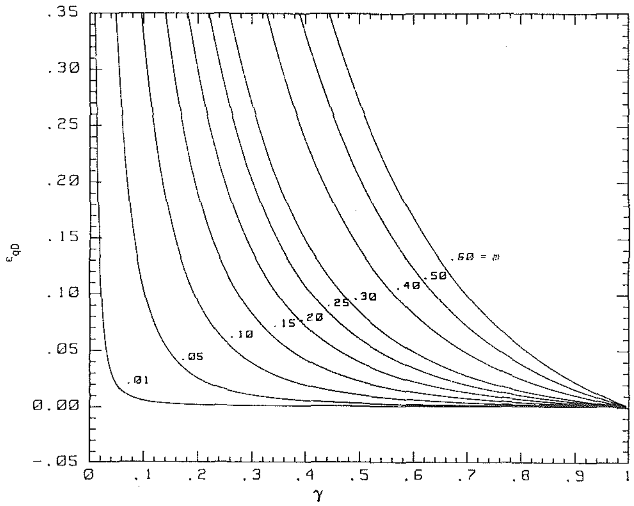

Fig. 5 Figure-of-merit variable ϵ_{qD} versus γ with m as parameter

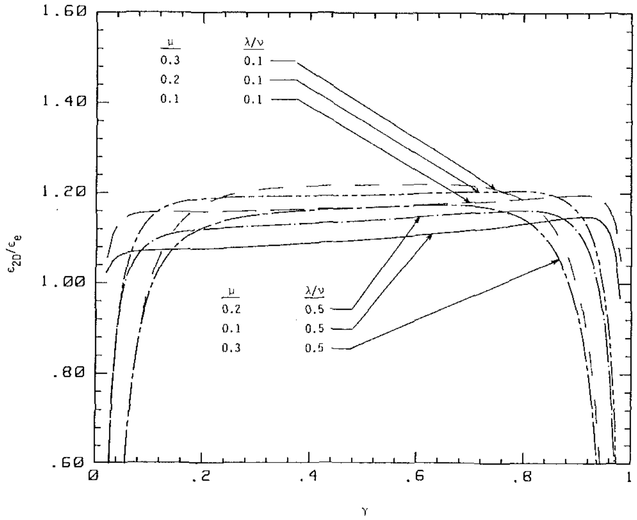

Fig. 4 Ratio of ϵ_{2D} to ϵ_e for Bi = 5

Results

The dimensionless heat flux is shown in Fig. 2 from the exact solution, and the two-dimensional and quasi-two-dimensional approximate solutions. In Fig. 2, $\mu = 0.2$, $\lambda/\nu = 0.3$, and Bi = 5. Here we note that agreement between the exact and two-dimensional approximate solutions is excellent except in the neighborhood of $\eta = \gamma$. At $\eta = \gamma$, a discontinuity in the heat flux and temperature from the approximate two-dimensional model occurs for all $\xi < 1$. This is explained by considering the developments leading to equation (9) where $\phi_s(\eta, \xi)$ depends on ϕ_f and ϕ_f''. From equations (1*a*) and (1*c*), ϕ_f continuity at $\eta = \gamma$ is ensured, whereas ϕ_f'' is discontinuous there. The discontinuity is imposed on the substrate through equation (9). We note, however, that the two-dimensional approximate solution is in better overall agreement with the exact solution than the quasi-two-dimensional one.

The ratio of ϵ_{2D} to ϵ_e is shown for a range of μ and λ/ν values in Fig. 3 for infinite Bi and in Fig. 4 for Bi = 5. Excellent agreement between the exact and approximate two-dimensional solutions for the range $0.2 \leq \gamma \leq 0.8$ for the infinite Bi case is noted. For the Bi = 5 case, agreement is within 20 percent for the range $0.1 \leq \gamma \leq 0.9$ with the value of ϵ_{2D} overestimated here. For Bi < 5 and $\mu > 0.3$, heat conduction in the η direction in the substrate becomes large and the perturbation solution is no longer valid. The exact solution [equations (3), (5), and (7)] should be used in this case. An inconsistency that exists in Figs. 3 and 4 that causes $\epsilon_{2D}/\epsilon_e \rightarrow -\infty$ as $\gamma \rightarrow 1$ instead of $\epsilon_{2D}/\epsilon_e \rightarrow 1$ results from the approximate nature of ϵ_{2D}. At $\gamma = 1$, ϵ_{2D} undershoots zero by about 1 or 2 percent for the cases shown, while $\epsilon_e = 0$.

The figure-of-merit variable ϵ_{qD} is shown in Fig. 5 for a wide range of m values. Referring to equation (13), m^2 is proportional to the ratio of the conductive resistance in the fin in the η direction to the conductive plus convective resistance in the substrate in the ξ direction. Thus, a reduction in the value of m for a fixed γ is expected to increase the uniformity of heating at the cooled surface. We note that Fig. 5 shows this behavior explicitly. Because m is not a function of l, Fig. 5 may be used to obtain zeroth-order estimates of l directly, given a prescribed ϵ_{qD} value. Second-order corrections to l may then be determined by using the results from the approximate two-dimensional analysis given above.

Design Procedure

The following step-by-step procedure may be used to estimate strip heater spacing for a prescribed ϵ value:

1 From specified values of k_f, k_s, h, D, d, and t calculate m using equation (13).

2 Prescribe ϵ_{qD} and, using m and Fig. 5, estimate γ. Estimate $l = t/\gamma$ to zeroth order.

3 Obtain estimates of Λ, p, and G from equations (12), (11), and (15), respectively. Solve for ϵ_{2D} from equation (16). If ϵ_{2D} is much smaller than ϵ_{qD}, recalculate ϵ_{2D} using a slightly larger value of l than that obtained in Step 2. Repeat this step until the desired value of ϵ_{2D} is obtained.

In addition, Figs. 3 and 4 may be used to correct ϵ_{2D} values obtained from Step 3 to ϵ_e. ϵ_e is the value that would be obtained from equation (7) for the last value of l from Step 3 above.

References

1 Lior, N., Jones, G. F., Ozoe, H., Chao, P., and Churchill, S. W., *Heat Transfer Considerations in the Use of New Energy Resources*, T. Mizushina and W. J. Yang, eds., Hemisphere, Washington, D.C., 1983.

2 Van Sant, J. H., "Temperature Variations on the Surface of a Strip-Heated Flat Plate," ASME JOURNAL OF HEAT TRANSFER, Vol. 89, 1967, pp. 372–373.

3 Schmitz, R. A., "Heat Flux Through a Strip-Heated Flat Plate," ASME JOURNAL OF HEAT TRANSFER, Vol. 92, 1970, pp. 201–202.

4 Lanczos, C., *Discourse on Fourier Series*, Hafner, New York, 1966, pp. 61–75.

5 Nayfeh, A. H., *Perturbation Methods*, Wiley, New York, 1973, p. 31.

Boundary Perturbation Method for Free Boundary Problem in Convectively Cooled Continuous Casting

R. Siegel[1]

Nomenclature

A = dimensionless parameter and dimensionless length = $a\bar{u}\rho\lambda/k(t_f - t_c) = a/\gamma$
a = half-width of slab ingot
b = vertical distance from center of solidification interface to bottom edge of mold
h = convective heat transfer coefficient at sides of ingot; $H = h(t_f - t_c)/\bar{u}\rho\lambda = (1/A)(ha/k)$
k = thermal conductivity of solidified material
n = summation index in series; $m = 2n - 1$
n = normal to interface; $N = n/\gamma$
S = dimensionless coordinate along solidification interface
t = temperature
u = casting velocity of ingot
W = potential plane = $\Psi + i\Phi$
x, y = coordinates in physical plane; $X = x/\gamma$, $Y = y/\gamma$
X_0, X_1 = zeroth and first-order terms in expansion of $X(\Psi, \Phi)$
Y_0, Y_1 = zeroth and first-order terms in expansion of $Y(\Psi, \Phi)$

Greek symbols

γ = length scale parameter = $k(t_f - t_c)/\bar{u}\rho\lambda$
θ = angle between interface normal and ingot centerplane
λ = latent heat of fusion per unit mass of solid
ρ = density of solidified material
Φ = potential function = $(t_f - t)/(t_f - t_c)$
Ψ = heat flow function orthogonal to Φ

Subscripts

c = coolant temperature
f = solidification temperature
s = soldification interface
w = cooled boundary of ingot
$1, 2, 3, \ldots$ = locations around ingot boundary

Introduction

An important metal fabrication technique is the continuous casting of an ingot by withdrawal from a mold. The solidification interface is an unknown "free boundary" governed by the heat transfer conditions. As pointed out in [1] the "precise understanding of the physics that controls the shape of the phase boundary separating melt and solid during steady solidification is becoming increasingly important." This is true with regard to various crystal growth processes, and the casting of metal with desired structural characteristics. The phase transformation boundary is influenced by the casting rate and how strongly the sides of the ingot are cooled. The complicated heat transfer process that determines the interface shape has been analyzed by using various mathematical approximations and numerical methods, as given for example in [1–7].

In the present paper some new mathematical techniques are used to deal with a more general boundary condition than in the author's previous work [6, 7]. In the previous work the sides of the ingot were assumed to be very strongly cooled as the ingot left the mold, so that the ingot sides were assumed to be at the coolant temperature. In this analysis a constant convective heat transfer coefficient is applied at the ingot sides; hence the temperature distribution along the sides is unknown. The analysis is for a pure or eutectic substance where there is a well-defined interface between liquid and solid regions.

To deal with the convective cooling condition, the problem is first inverted to treat the physical coordinates as dependent variables of temperature and heat flow. This maps the ingot into a region that is almost rectangular. A boundary perturbation method (small k/ha) is then used to obtain an analytical solution in the almost rectangular region. The solidification interface shapes are shown to depend on two dimensionless parameters, one being a function of the casting velocity and the other depending on the convective heat transfer coefficient at the cooled wall.

Analysis

Problem Description. Figure 1 shows a slab ingot being formed by continuous casting at velocity $\bar{u}$. The mold walls are of insulating material, and due to metal contraction there is often poor contact of these walls with the ingot. Hence the heat flow resulting from liquid-to-solid phase change at the solidification interface is conducted to the ingot sides, which are cooled by forced convection with heat transfer coefficient h. The boundary condition at the sides is

$$h[t_w(y) - t_c] = \mp k \left.\frac{\partial t}{\partial x}\right|_w \qquad (x = \pm a, y < b) \tag{1}$$

As shown in [6], the boundary conditions at the solidification interface are

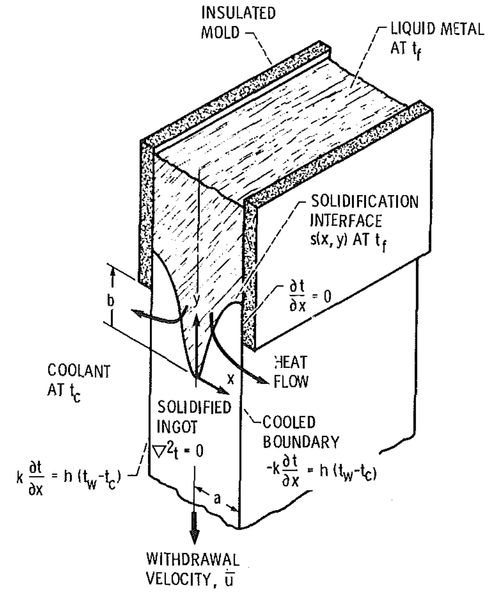

Fig. 1 Convectively cooled slab ingot being withdrawn from mold in continuous casting

---

[1] NASA Lewis Research Center, Cleveland, OH 44135; Fellow ASME.

Contributed by the Heat Transfer Division for publication in the JOURNAL OF HEAT TRANSFER. Manuscript received by the Heat Transfer Division January 21, 1985.

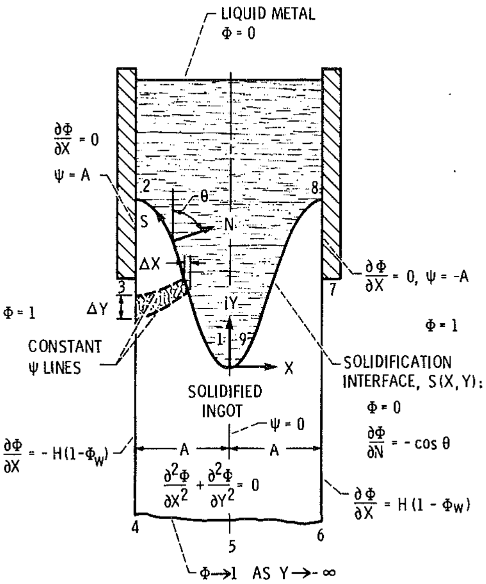

Fig. 2 Ingot cross section and boundary conditions in dimensionless physical plane

$$t(x_s, y_s) = t_f \tag{2}$$

$$k\frac{\partial t}{\partial n}\bigg|_s = \rho\lambda\bar{u}\cos\theta \tag{3}$$

Along the portions of the ingot sides that are within the insulated mold

$$\frac{\partial t}{\partial x} = 0 \quad (x = \pm a, y > b) \tag{4}$$

As discussed by the limitations in [6], there are conditions where the energy transported by the motion of the ingot is small compared with heat conduction within the ingot. The ingot temperature distribution is then governed by

$$\frac{\partial^2 t}{\partial x^2} + \frac{\partial^2 t}{\partial y^2} = 0 \tag{5}$$

When solving equation (5), the temperature or temperature derivative is usually specified along each portion of the boundary. In the present situation both the temperature and its normal derivative are specified along the solidification interface; it is the unknown interface shape that must be found. The convective boundary condition (1) introduces the complexity that the boundary temperature is unknown along the cooled ingot sides. Dealing with this condition in the presence of the unknown solidification boundary is the subject of this paper, as compared with [6, 7] wherein the ingot sides were at a specified uniform temperature. An analytical solution will be obtained for the unknown solidification interface shape.

Region in Potential Plane. The analysis begins by representing the ingot in a potential plane. A potential function Φ is defined as $\Phi = (t_f - t)/(t_f - t_c)$, and from equation (5) the conduction equation within the ingot is then

$$\frac{\partial^2 \Phi}{\partial X^2} + \frac{\partial^2 \Phi}{\partial Y^2} = 0 \tag{6}$$

Along the solidification interface at t_f

$$\Phi = 0 \tag{7}$$

and along the insulated boundaries in the mold

$$\frac{\partial \Phi}{\partial X} = 0 \tag{8}$$

Equation (3) at the solidification interface transforms to

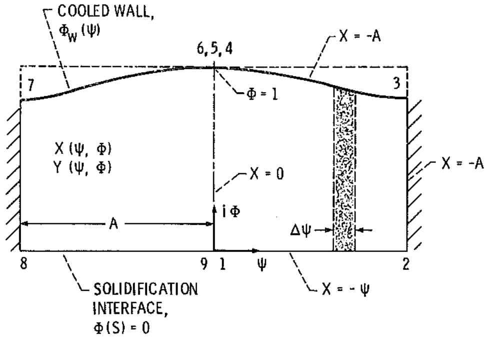

Fig. 3 Ingot in potential plane, $W = \Psi + i\Phi$

$$\frac{\partial \Phi}{\partial N} = -\cos\theta \tag{9}$$

and along the convectively cooled sides equation (1) becomes

$$\frac{\partial \Phi}{\partial X} = \pm H(1 - \Phi_W) \tag{10}$$

where the minus sign applies at the left side of the ingot (Fig. 2).

A heat flow function Ψ is now defined, where constant Ψ lines bound a fixed amount of heat flow. Since heat flow is normal to lines of constant temperature, the constant Ψ and Φ lines form an orthogonal coordinate system. At the solidification interface the Cauchy–Riemann equations give $\partial\Phi/\partial N|_s = -\partial\Psi/\partial S|_s$. Then by use of equation (9) (since $\partial\Psi/\partial N|_s = \partial\Phi/\partial S|_s = 0$)

$$\frac{\partial \Psi}{\partial X}\bigg|_s = \frac{\partial \Psi}{\partial S}\bigg|_s \frac{\partial S}{\partial X} = -\frac{\partial \Phi}{\partial N}\bigg|_s \left(-\frac{1}{\cos\theta}\right) = -1$$

Integrating along the interface, and letting $\Psi = 0$ along $X = 0$, yields

$$\Psi = -X \text{ along } \widehat{12} \text{ and } \widehat{89} \tag{11}$$

The insulated boundaries $\widehat{23}$ and $\widehat{78}$ are normal to the Φ lines and hence are lines of constant Ψ. Since these boundaries join the interface at $\Psi = A$ and $-A$ it follows that

$$\Psi = A \text{ along } \widehat{23}, \quad \Psi = -A \text{ along } \widehat{78} \tag{12}$$

The boundary conditions in terms of Ψ and Φ are summarized in Fig. 2. The ingot boundaries are lines of constant Ψ or Φ, with the exception of the cooled sides $\widehat{34}$ and $\widehat{67}$. Along these sides the variation of Ψ and Φ with Y is unknown; however Φ will be between 0 and 1, and will approach 1 along $\widehat{456}$ where $Y \to -\infty$. Using these conditions the ingot maps into the complex potential plane to form the region in Fig. 3. The solidification interface is along $\Phi = 0$, and the upper boundary $\Phi_w(\Psi)$ has an unknown shape. In the W plane, the X, Y are dependent variables of Ψ, Φ. Since Ψ, Φ are analytic functions of X, Y, the X, Y are conjugate harmonic functions of Ψ, Φ and satisfy

$$\frac{\partial^2 X}{\partial \Psi^2} + \frac{\partial^2 X}{\partial \Phi^2} = 0 \tag{13a}$$

$$\frac{\partial^2 Y}{\partial \Psi^2} + \frac{\partial^2 Y}{\partial \Phi^2} = 0 \tag{13b}$$

Perturbation Analysis. The geometry in Fig. 3 is symmetric; hence, only the right side will be considered. From the geometry and the boundary condition (11), X is known along all portions of the boundary as shown on the right side of Fig. 3; hence the solution for $X(\Psi, \Phi)$ would be governed by a conventional Dirichlet problem if the boundary $\widehat{34}$ were known. The shape of this boundary depends on the convective boundary condition (10), but this contains the unknown Φ_w.

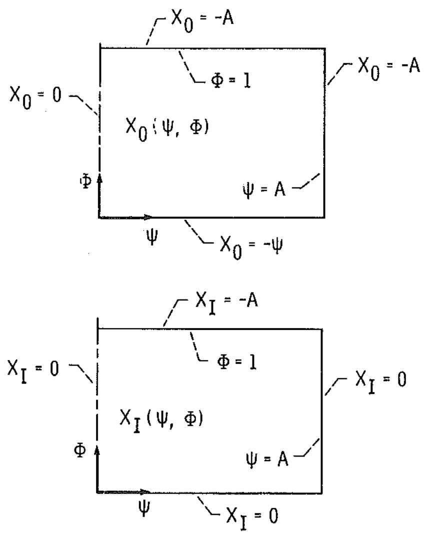

Fig. 4 Dirichlet boundary conditions for $X_0(\Psi, \Phi)$ and $X_I(\Psi, \Phi)$

An analytical solution will be obtained by a boundary perturbation technique.

The $X(\Psi, \Phi)$ will be expanded in terms of the quantity $ha/k = HA$. When $h \to \infty$ the cooled boundary is all at t_c ($\Phi = 1$). Generally the ingot is strongly cooled, so the conductance h would be greater than the conductance k/a through the ingot half-width. Hence the quantity $(ha/k)^{-1}$ is small and is used as a perturbation parameter. Then let

$$X(\Psi, \Phi) = X_0(\Psi, \Phi) + \frac{1}{HA} X_I(\Psi, \Phi) + \frac{1}{(HA)^2} X_{II}(\Psi, \Phi) + \ldots \qquad (14)$$

Since ha/k is large, the $\Phi_w(\Psi)$ curve in Fig. 3 is assumed to be not far below the $\Phi = 1$ line (the upper limit as $ha/k \to \infty$); the validity of this approximation will be examined later. Then the values of $X(\Psi, 1)$ on the upper dashed line in Fig. 3 can be expressed in terms of a Taylor series expansion upward from $\widehat{34}$,

$$X(\Psi, 1) = X(\Psi, \Phi_w) + (1 - \Phi_w) \left.\frac{\partial X}{\partial \Phi}\right|_w + \ldots \qquad (15)$$

Now use equation (14) on the left side, and $X(\Psi, \Phi_w) = -A$ on the right to obtain

$$X_0(\Psi, 1) + \frac{1}{HA} X_I(\Psi, 1) + \ldots = -A + (1 - \Phi_w) \left.\frac{\partial X}{\partial \Phi}\right|_w + \ldots \qquad (16)$$

To deal with the last term on the right side, consider the shaded heat flow channel bounded by constant Ψ lines in Fig. 2. Equating the solidification energy in ΔX to the heat flow out of ΔY on the cooled side gives $\rho \lambda \bar{u} |\Delta x|_s = h |\Delta y|_w (t_w - t_c)$, or in dimensionless form

$$|\Delta X|_s = H |\Delta Y|_w (1 - \Phi_w) \qquad (17)$$

Along S, $|\Delta X| = \Delta \Psi$ from equation (11), and along w both Ψ and Φ are variable. Then equation (17) can be written as

$$\Delta \Psi \Big|_s = H(1 - \Phi_w) \left(\frac{\Delta Y}{\Delta \Psi} \Delta \Psi + \frac{\Delta Y}{\Delta \Phi} \Delta \Phi \right)_w \qquad (18)$$

From Fig. 3 it is evident from the shaded strip that $\Delta \Psi|_s = \Delta \Psi|_w$. Then by using the Cauchy-Riemann equations and letting the finite differences shrink to differential size, equation (18) becomes

$$\frac{1}{H} = (1 - \Phi_w) \left(-\frac{\partial X}{\partial \Phi} + \frac{\partial X}{\partial \Psi} \frac{d\Phi}{d\Psi} \right)_w \qquad (19)$$

Along w, $X = -A$ so that $\partial X/\partial \Phi|_w d\Phi + \partial X/\partial \Psi|_w d\Psi = 0$. This is used to eliminate $\partial X/\partial \Psi$ from equation (19) to yield

$$\frac{1}{H} = -(1 - \Phi_w) \left\{ \frac{\partial X}{\partial \Phi} \left[1 + \left(\frac{d\Phi}{d\Psi} \right)^2 \right] \right\}_w \qquad (20)$$

As will be evident later, the cases of physical interest have A values that are 1 or larger; then along $\widehat{34}$ (as indicated by Fig. 3) the Φ will be changing much more slowly than Ψ. Hence $(d\Phi/d\Psi)^2 << 1$ in equation (20) and can be neglected in the perturbation method. The remaining part of equation (20) is then substituted into equation (16) to obtain

$$X_0(\Psi, 1) + \frac{1}{HA} X_I(\Psi, 1) = -A - \frac{A}{HA}$$

By collecting zeroth and first-order terms, the boundary conditions for X_0 and X_I are found that apply along the dashed upper boundary in Fig. 3

$$X_0(\Psi, 1) = -A \qquad (21a)$$

$$X_I(\Psi, 1) = -A \qquad (21b)$$

The solution for $X(\Psi, \Phi)$ to satisfy all the boundary conditions can thus be obtained by solving the two Dirichlet problems for $X_0(\Psi, \Phi)$ and $X_I(\Psi, \Phi)$ in Fig. 4, and using the results in equation (14) to first order.

Solutions for X_0 and X_I. The solutions for X_0 and its conjugate harmonic function Y_0 have already been obtained in [7] as

$$X_0(\Psi, \Phi) = -\Psi - \frac{2A}{\pi} \sum_{n=1}^{\infty} \frac{1}{n} \sin \frac{n\pi\Psi}{A} \frac{\sinh(n\pi\Phi/A)}{\sinh(n\pi/A)} \qquad (22a)$$

$$Y_0(\Psi, \Phi) = -\Phi - \frac{2A}{\pi} \sum_{n=1}^{\infty} \frac{1}{n} \frac{1}{\sinh(n\pi/A)} \times \left(\cos \frac{n\pi\Psi}{A} \cosh \frac{n\pi\Phi}{A} - 1 \right) \qquad (22b)$$

The solution for X_I is found from the results in [8], which yields

$$X_I = -\frac{4A}{\pi} \sum_{n=1}^{\infty} \frac{1}{m} \sin \frac{m\pi\Psi}{A} \frac{\sinh(m\pi\Phi/A)}{\sinh(m\pi/A)} \qquad (23a)$$

$$Y_I = -\frac{4A}{\pi} \sum_{n=1}^{\infty} \frac{1}{m} \cos \frac{m\pi\Psi}{A} \frac{\cosh(m\pi\Phi/A)}{\sinh(m\pi/A)} \qquad (23b)$$

The series in equations (22) and (23) converge slowly, but much more rapidly converging forms can be obtained. An example of how this was done is shown for X_0 in the Appendix; the other series were treated in a similar manner. The results are as follows, where for convenience the Y values have been made relative to $Y_2 = Y(A, 0)$ at the upper edge of the solidification interface.

$$X_0(\Psi, \Phi) = -\Psi - \frac{2A}{\pi} \tan^{-1} \left[\frac{e^{-\frac{\pi}{A}(1-\Phi)} \sin(\pi\Psi/A)}{1 - e^{-\frac{\pi}{A}(1-\Phi)} \cos(\pi\Psi/A)} \right] + \frac{4A}{\pi} \sum_{n=1}^{\infty} \frac{1}{n} \frac{\sinh \frac{n\pi}{A}(1-\Phi)}{e^{\frac{2n\pi}{A}} - 1} \sin \frac{n\pi\Psi}{A} \qquad (24a)$$

Table 1 Values of dimensionless wall temperature at lower edge of mold, Φ_3

ha/k	A			
	1	2	4	6
5	0.72721	0.54975		
10	.80376	.66718	0.54260	
20	.85999	.75917	.66085	0.59450
40	.90054	.82770	.75413	.70260
∞	1.00000	1.00000	1.00000	1.00000

$$Y_0(\Psi,\Phi)-Y_{0,2}=-\Phi-\frac{4A}{\pi}\ln(1+e^{-\pi/A})$$

$$+\frac{A}{\pi}\ln\left[1-2e^{-\frac{\pi}{A}(1-\Phi)}\cos(\pi\Psi/A)+e^{-\frac{2\pi}{A}(1-\Phi)}\right]$$

$$+\frac{2A}{\pi}\sum_{n=1}^{\infty}\frac{(-1)^n}{n}\frac{1}{e^{\frac{2n\pi}{A}}\sinh(n\pi/A)}$$

$$-\frac{4A}{\pi}\sum_{n=1}^{\infty}\frac{\cos(n\pi\Psi/A)}{n}\frac{\cosh\frac{n\pi}{A}(1-\Phi)}{e^{\frac{2n\pi}{A}}-1} \qquad (24b)$$

$$X_1(\Psi,\Phi)=-\frac{2A}{\pi}\tan^{-1}\left[\frac{2e^{-\frac{\pi}{A}(1-\Phi)}\sin(\pi\Psi/A)}{1-e^{-\frac{2\pi}{A}(1-\Phi)}}\right]$$

$$+\frac{8A}{\pi}\sum_{n=1}^{\infty}\frac{1}{m}\frac{\sinh\frac{m\pi}{A}(1-\Phi)}{e^{\frac{2m\pi}{A}}-1}\sin\frac{m\pi\Psi}{A} \qquad (25a)$$

$$Y_1(\Psi,\Phi)-Y_{1,2}=-\frac{8A}{\pi}\tanh^{-1}e^{-\frac{\pi}{A}}$$

$$-\frac{A}{\pi}\ln\left[\frac{1+2e^{-\frac{\pi}{A}(1-\Phi)}\cos(\pi\Psi/A)+e^{-\frac{2\pi}{A}(1-\Phi)}}{1-2e^{-\frac{\pi}{A}(1-\Phi)}\cos(\pi\Psi/A)+e^{-\frac{2\pi}{A}(1-\Phi)}}\right]$$

$$-\frac{4A}{\pi}\sum_{n=1}^{\infty}\frac{1}{m}\frac{1}{e^{\frac{2m\pi}{A}}\sinh(m\pi/A)}$$

$$-\frac{8A}{\pi}\sum_{n=1}^{\infty}\frac{1}{m}\frac{\cosh\frac{m\pi}{A}(1-\Phi)}{e^{\frac{2m\pi}{A}}-1}\cos\frac{m\pi\Psi}{A} \qquad (25b)$$

Solidification Interface Shape. The coordinates of the solidification interface, which are along $\Phi = 0$, can then be obtained from

$$\frac{X_s(\Psi)}{A}=-\frac{\Psi}{A} \qquad (26a)$$

$$\frac{Y_s(\Psi)-Y_2}{A}=\frac{Y_0(\Psi,0)-Y_{0,2}}{A}+\frac{1}{HA}\frac{Y_1(\Psi,0)-Y_{1,2}}{A} \qquad (26b)$$

Although equations (26) give the shape of the interface, they do not give its vertical location in the mold. For this the quantity $Y_2 - Y_3$ is given by

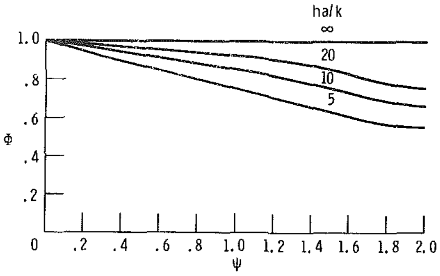

Fig. 5 Shape of ingot in potential plane for various *ha/k* and $A = 2$

$$\frac{Y_2-Y_3}{A}=-\frac{Y_0(A,\Phi_3)-Y_{0,2}}{A}-\frac{1}{HA}\frac{Y_1(A,\Phi_3)-Y_{1,2}}{A} \qquad (27)$$

The quantities on the right can be obtained from equations (24*b*) and (25*b*). Then to evaluate equation (27) the value of Φ_3 is needed. Along the side of the ingot $\widehat{34}$, $X = -A$ and $\Phi = \Phi_w(\Psi)$, where $\Phi_w(\Psi)$ is unknown. Inserting these relations into equation (14) gives

$$-A=X_0(\Psi,\Phi_w)+\frac{1}{HA}X_1(\Psi,\Phi_w) \qquad (28)$$

where the quantities on the right side are found from equations (24*a*) and (25*a*). The Φ_w at any Ψ can then be found by solving equation (28) by trial and error or by iteration. The Φ_3 is the specific value of Φ_w that is at $\Psi = A$, but if this value of Ψ is inserted directly into equation (28) an identity, $-A = -A$, is obtained. The Φ_3 can be found by using a Ψ very slightly less than A or by taking the limit $\Psi \rightarrow A$, which yields

$$1=\frac{2}{e^{\frac{\pi}{A}(1-\Phi_3)}+1}+4\sum_{n=1}^{\infty}(-1)^n\frac{\sinh\frac{n\pi}{A}(1-\Phi_3)}{e^{\frac{2n\pi}{A}}-1}$$

$$+\frac{4}{HA}\left[\frac{1}{2\sinh\frac{\pi}{A}(1-\Phi_3)}-2\sum_{n=1}^{\infty}\frac{\sinh\frac{m\pi}{A}(1-\Phi_3)}{e^{\frac{2m\pi}{A}}-1}\right] \qquad (29)$$

The Φ_3 can thus be found for various A and HA (Table 1).

Results and Discussion

In the analysis it was assumed that the ingot in the potential plane would have an upper boundary shape such as in Fig. 3. Since this upper boundary was *a priori* unknown, its shape was evaluated from the solution, equation (28), to see whether it was consistent with the perturbation solution. Results were obtained for $A = 1$, 2, 4, and 6, and since they were similar for each A, typical results are shown in Fig. 4 for $A = 2$. Since in the solution, the boundary condition was extrapolated from the curved upper boundary to the straight $\Phi = 1$ line, the upper boundary cannot be "too far" from $\Phi = 1$. From Fig. 5 this is consistent with the perturbation parameter $HA = ha/k$ not being "too small" for the perturbation solution to be valid within the first-order terms given here. Since part of the curve for $ha/k = 5$ is rather far from $\Phi = 1$, it is desirable to check the validity of the solution as follows.

All the Dirichlet boundary conditions in Fig. 3 have been satisfied, as well as the conditions of heat flow and temperature along the solidification interface. The only boundary

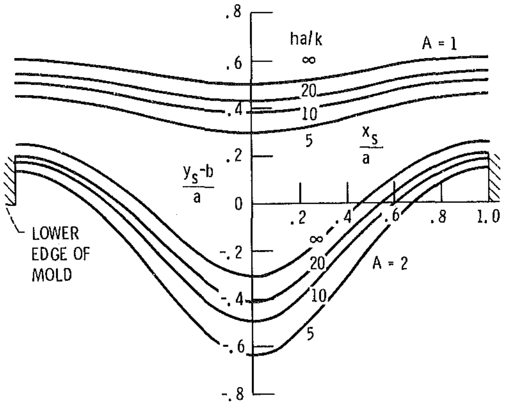

(a) A = 1, 2.

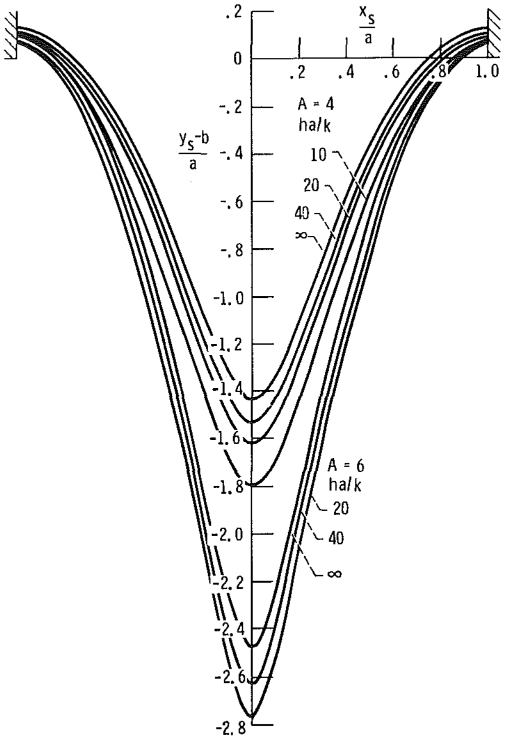

(b) A = 4, 6.

Fig. 6 Shape of solidification interface for various values of *A* and *ha/k*

condition that is not satisfied exactly is equation (10). Using the Cauchy-Riemann equations this can be written as $-\partial\Psi/\partial Y = \pm H(1 - \Phi_W)$. From equation (28) the $\Phi_w(\Psi)$ can be found along side 34 of the ingot. Then from equation (26*b*) used with equations (24*b*) and (25*b*) the $Y(\Psi)$ can also be found along 34. It is then straightforward to numerically obtain $-\partial\Psi/\partial Y$ and check its agreement with $-H(1 - \Phi_w)$ along the left side of the ingot. Agreement within better than 5 percent was obtained for the parameters used here except for a region very close (within $Y/A < 0.04$) to the lower edge (point 3) of the mold. The lack of good agreement in this small region is not surprising because the heat flow lines curve rapidly in the vicinity of the mold edge, and the simplification made with regard to equation (20) is not accurate. However, this small region adjacent to the lower edge of the mold accounts for only a small portion of the total heat flow and hence should not appreciably affect the predicted shapes of the solidification interfaces.

The solidification interfaces as evaluated from equations (26*a*) and (26*b*) are given in Figs. 6(*a*) and (*b*). For each A a set of curves is given for various values of ha/k. For $ha/k \rightarrow \infty$ there is infinite convective cooling ability at the ingot sides, and the sides are at the coolant temperature. These curves are the same as in [6] where the solution was obtained by a different method of analysis. As the A is increased, corresponding to an increased casting velocity, the interface is pulled down further in the center of the ingot. This increases the heat flow paths from the interface to the ingot sides to accommodate the greater amount of solidification energy that must be removed.

When h is finite, the cooling ability at the wall is reduced and the interface is pulled down an increased amount in much the same manner as for an increased casting rate. This change of geometry shortens the heat conduction paths to the sides of the ingot to compensate for the increased convective resistance, and to still enable the heat of solidification to be removed.

References

1 Ettouney, H. M., and Brown, R. A., "Finite-Element Methods for Steady Solidification Problems," *Journal of Computational Physics*, Vol. 49, No. 1, Jan. 1983, pp. 118-150.

2 Yao, L. S., "Natural Convection Effects in the Continuous Casting of a Horizontal Cylinder," *International Journal of Heat and Mass Transfer*, Vol. 27, No. 5, May 1984, pp. 697-704.

3 Adenis, D. J.-P., Coats, K. H., and Ragone, D. V., "An Analysis of the Direct-Chill-Casting Process by Numerical Methods," *Institute of Metals Journal*, Vol. 91, 1962-63, pp. 395-403.

4 Sfeir, A. A., and Clumpner, J. A., "Continuous Casting of Cylindrical Ingots," ASME JOURNAL OF HEAT TRANSFER, Vol. 99, No. 1, Feb. 1977, pp. 29-34.

5 Mizikar, E. A., "Mathematical Heat Transfer Model for Solidification of Continuously Cast Steel Slabs," *Metallurgical Society of AIME, Transactions*, Vol. 239, Nov. 1967, pp. 1747-1753.

6 Siegel, R., "Analysis of Solidification Interface Shape During Continuous Casting of a Slab," *International Journal of Heat and Mass Transfer*, Vol. 21, No. 11, Nov. 1978, pp. 1421-1430.

7 Siegel, R., "Cauchy Method for Soldification Interface Shape During Continuous Casting," ASME JOURNAL OF HEAT TRANSFER, Vol. 105, No. 3, Aug. 1983, pp. 667-671.

8 Hildebrand, F. B., *Advanced Calculus for Engineers*, Prentice-Hall, New York, 1949, pp. 420-422.

APPENDIX

Improved Convergence for X_0

The solution for $X_0(\Psi, \Phi)$, equation (22*a*), can be written as

$$X_0(\Psi, \Phi) = -\Psi - \frac{2A}{\pi} \sum_{n=1}^{\infty} \frac{1}{n} \sin\frac{n\pi\Psi}{A} \frac{e^{\frac{n\pi\Phi}{A}} - e^{-\frac{n\pi\Phi}{A}}}{e^{\frac{n\pi}{A}} - e^{-\frac{n\pi}{A}}} \qquad \text{(A1)}$$

For large n the ratio of the exponential terms goes to the limit $e^{-(n\pi/A)(1-\Phi)}$. The limiting term of the series is subtracted and added to obtain

$$X_0 = -\Psi - \frac{2A}{\pi} \sum_{n=1}^{\infty} \frac{1}{n} \sin\frac{n\pi\Psi}{A} e^{-\frac{n\pi}{A}(1-\Phi)}$$

$$-\frac{2A}{\pi} \sum_{n=1}^{\infty} \frac{1}{n} \sin\frac{n\pi\Psi}{A} \left[\frac{e^{\frac{n\pi\Phi}{A}} - e^{-\frac{n\pi\Phi}{A}}}{e^{\frac{n\pi}{A}} - e^{-\frac{n\pi}{A}}} - e^{-\frac{n\pi}{A}(1-\Phi)} \right] \qquad \text{(A2)}$$

The first summation is carried out analytically, and the second one converges much more rapidly than the summation in equation (A1). Equation (A2) can be written as

$$X_0 = -\Psi - \frac{2A}{\pi} \sum_{n=1}^{\infty} \frac{1}{n} Im\, e^{\frac{in\pi}{A}[\Psi + i(1-\Phi)]}$$

$$+ \frac{4A}{\pi} \sum_{n=1}^{\infty} \frac{1}{n} \frac{\sinh \frac{n\pi}{A}(1-\Phi)}{e^{\frac{2n\pi}{A}} - 1} \sin \frac{n\pi\Psi}{A} \qquad \text{(A3)}$$

Let $\xi = e^{i(\pi/A)[\Psi + i(1-\Phi)]}$ so that,

$$\sum_{n=1}^{\infty} \frac{1}{n} Im\, e^{\frac{in\pi}{A}[\Psi + i(1-\Phi)]}$$

$$= Im \sum_{n=1}^{\infty} \frac{\xi^n}{n} = Im[-\ln(1-\xi)]$$

$$= -\tan^{-1}\left[\frac{-e^{-\frac{\pi}{A}(1-\Phi)} \sin(\pi\Psi/A)}{1 - e^{-\frac{\pi}{A}(1-\Phi)} \cos(\pi\Psi/A)}\right]$$

This is substituted for the first series in equation (A3) to obtain the form for X_0 in equation (24a) which converges rapidly. For $A = 1$ only about three terms are required; for $A = 6$, about 15 terms were used.

Predicting Two-Dimensional Steady-State Soil Freezing Fronts Using the CVBEM

T. V. Hromadka II[1]

Nomenclature

K_f, K_t = frozen and thawed conductivities
ϕ_f, ϕ_t = frozen and thawed temperatures
C = freezing front in domain Ω
Ω_f, Ω_t = frozen and thawed domains
ω = exact solution (analytic)
ϕ, ψ = function $\omega = \phi + i\psi$, $i = \sqrt{-1}$
S, n = tangential and normal coordinates
$\hat{\omega}_f$, $\hat{\omega}_t$ = frozen and thawed region CVBEM approximations

Introduction

In previous papers, Hromadka and Guymon [1] applied the complex variable boundary element method (CVBEM) to the problem of predicting freezing fronts in two-dimensional soil systems. Hromadka et al. [2] subsequently compare the CVBEM solution to a domain solution method and prototype data for the Deadhorse Airport runway at Prudhoe Bay, Alaska. In another work, the model is further extended to include an approximation of soil water flow [3]. An example in using domain methods to model a moving interface in heat transfer problems is given in Yoo and Rubinsky [4].

An example in the use of real variable boundary element methods [5] in the approximation of such moving boundary phase change problems and a review of the pertinent literature is given in O'Niell [6]. It is noted that although the CVBEM moving boundary phase change model of Hromadka and Guymon [1] will determine the steady-state location of the freezing front, the modeling process must evolve through a time history of the freezing front movement from a prescribed initial location. In contrast, this paper presents an alternative approach which directly focuses upon the steady-state freezing front location.

Consequently for problems where such steady-state freezing front locations are needed, the technique presented herein will significantly reduce the computational effort over that required in solving a time evolution problem.

Hromadka and Guymon [7] develop a relative error estimation scheme which exactly evaluates the relative error distribution on the problem boundary that results from the CVBEM approximator matching the known boundary conditions. This relative error determination is used to add or delete boundary nodes to improve accuracy. Thus, the CVBEM permits a direct and immediate determination of the approximation error involved in solution of an assumed Laplacian system.

The CVBEM is used instead of a real variable boundary element method due to the available modeling error evaluation techniques developed. The modeling accuracy is evaluated by the model-user in the determination of an approximative boundary upon which the CVBEM provides an exact solution. Although inhomogeneity (and anisotropy) can be included in the CVBEM model, the resulting fully populated matrix system quickly becomes large. Therefore in this paper, the domain is assumed homogeneous and isotropic except for differences in frozen and thawed conduction parameters on either side of the freezing front. The example problems presented were obtained by use of a popular 64K microcomputer (the current version of the program used in this study has the capacity to accommodate 30 nodal points).

Governing Equations and Assumptions

For steady-state conditions, the governing heat flow equations reduce to the Laplace equation (the transient heat capacitance term is omitted). The following assumptions are utilized (Fig. 1):

1 The two-dimensional soil system is rigid with negligible deformations due to frost heave. (Deformations could easily be included in a general purpose model by including an appropriate frost heave approximation procedure.)

2 The soil system is completely frozen above the freezing front and completely thawed below the freezing front (for the considered examples, frozen and thawed conductivities have a ratio of less than 10).

3 The soil-water flow is assumed negligible.

4 All boundary conditions are assumed constant for all time (mixed boundary conditions are currently neglected).

5 The soil system is homogeneous and isotropic (or the system is rescaled such that the modified domain is homogeneous and isotropic).

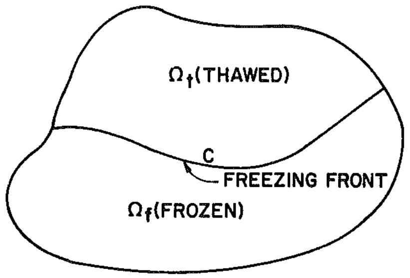

Fig. 1 Problem definition

---

[1] U.S. Geological Survey, Laguna Niguel, CA

Contributed by the Heat Transfer Division for publication in the JOURNAL OF HEAT TRANSFER. Manuscript received by the Heat Transfer Division October 22, 1984.

$$X_0 = -\Psi - \frac{2A}{\pi} \sum_{n=1}^{\infty} \frac{1}{n} Im\, e^{\frac{in\pi}{A}[\Psi + i(1-\Phi)]}$$

$$+ \frac{4A}{\pi} \sum_{n=1}^{\infty} \frac{1}{n} \frac{\sinh \frac{n\pi}{A}(1-\Phi)}{e^{\frac{2n\pi}{A}} - 1} \sin \frac{n\pi\Psi}{A} \qquad \text{(A3)}$$

Let $\xi = e^{i(\pi/A)[\Psi + i(1-\Phi)]}$ so that,

$$\sum_{n=1}^{\infty} \frac{1}{n} Im\, e^{\frac{in\pi}{A}[\Psi + i(1-\Phi)]}$$

$$= Im \sum_{n=1}^{\infty} \frac{\xi^n}{n} = Im[-\ln(1-\xi)]$$

$$= -\tan^{-1}\left[\frac{-e^{-\frac{\pi}{A}(1-\Phi)} \sin(\pi\Psi/A)}{1 - e^{-\frac{\pi}{A}(1-\Phi)} \cos(\pi\Psi/A)} \right]$$

This is substituted for the first series in equation (A3) to obtain the form for X_0 in equation (24*a*) which converges rapidly. For $A = 1$ only about three terms are required; for $A = 6$, about 15 terms were used.

Predicting Two-Dimensional Steady-State Soil Freezing Fronts Using the CVBEM

T. V. Hromadka II[1]

Nomenclature

K_f, K_t = frozen and thawed conductivities
ϕ_f, ϕ_t = frozen and thawed temperatures
C = freezing front in domain Ω
Ω_f, Ω_t = frozen and thawed domains
ω = exact solution (analytic)
ϕ, ψ = function $\omega = \phi + i\psi$, $i = \sqrt{-1}$
S, n = tangential and normal coordinates
$\hat{\omega}_f$, $\hat{\omega}_t$ = frozen and thawed region CVBEM approximations

Introduction

In previous papers, Hromadka and Guymon [1] applied the complex variable boundary element method (CVBEM) to the problem of predicting freezing fronts in two-dimensional soil systems. Hromadka et al. [2] subsequently compare the CVBEM solution to a domain solution method and prototype data for the Deadhorse Airport runway at Prudhoe Bay, Alaska. In another work, the model is further extended to include an approximation of soil water flow [3]. An example in using domain methods to model a moving interface in heat transfer problems is given in Yoo and Rubinsky [4].

An example in the use of real variable boundary element methods [5] in the approximation of such moving boundary phase change problems and a review of the pertinent literature is given in O'Niell [6]. It is noted that although the CVBEM moving boundary phase change model of Hromadka and Guymon [1] will determine the steady-state location of the freezing front, the modeling process must evolve through a time history of the freezing front movement from a prescribed initial location. In contrast, this paper presents an alternative approach which directly focuses upon the steady-state freezing front location.

Consequently for problems where such steady-state freezing front locations are needed, the technique presented herein will significantly reduce the computational effort over that required in solving a time evolution problem.

Hromadka and Guymon [7] develop a relative error estimation scheme which exactly evaluates the relative error distribution on the problem boundary that results from the CVBEM approximator matching the known boundary conditions. This relative error determination is used to add or delete boundary nodes to improve accuracy. Thus, the CVBEM permits a direct and immediate determination of the approximation error involved in solution of an assumed Laplacian system.

The CVBEM is used instead of a real variable boundary element method due to the available modeling error evaluation techniques developed. The modeling accuracy is evaluated by the model-user in the determination of an approximative boundary upon which the CVBEM provides an exact solution. Although inhomogeneity (and anisotropy) can be included in the CVBEM model, the resulting fully populated matrix system quickly becomes large. Therefore in this paper, the domain is assumed homogeneous and isotropic except for differences in frozen and thawed conduction parameters on either side of the freezing front. The example problems presented were obtained by use of a popular 64K microcomputer (the current version of the program used in this study has the capacity to accommodate 30 nodal points).

Governing Equations and Assumptions

For steady-state conditions, the governing heat flow equations reduce to the Laplace equation (the transient heat capacitance term is omitted). The following assumptions are utilized (Fig. 1):

1 The two-dimensional soil system is rigid with negligible deformations due to frost heave. (Deformations could easily be included in a general purpose model by including an appropriate frost heave approximation procedure.)

2 The soil system is completely frozen above the freezing front and completely thawed below the freezing front (for the considered examples, frozen and thawed conductivities have a ratio of less than 10).

3 The soil–water flow is assumed negligible.

4 All boundary conditions are assumed constant for all time (mixed boundary conditions are currently neglected).

5 The soil system is homogeneous and isotropic (or the system is rescaled such that the modified domain is homogeneous and isotropic).

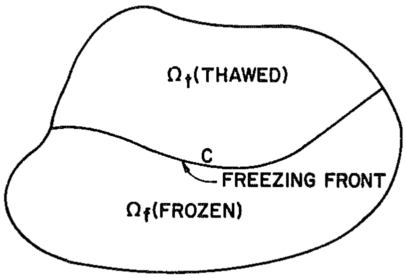

Fig. 1 Problem definition

---

[1] U.S. Geological Survey, Laguna Niguel, CA

Contributed by the Heat Transfer Division for publication in the JOURNAL OF HEAT TRANSFER. Manuscript received by the Heat Transfer Division October 22, 1984.

6 The effects of ice-lensing at the freezing front are ignored.

7 The steady-state heat conduction processes are modeled by the two-dimensional Laplace equation.

8 There is a single freezing front interior of the domain.

The steady-state conditions are evaluated by solving simultaneously

$$\begin{aligned} K_f \nabla^2 \phi_f &= 0, \quad \text{in } \Omega_f \\ K_t \nabla^2 \phi_t &= 0, \quad \text{in } \Omega_t \end{aligned} \tag{1}$$

where ϕ is the potential temperature function and (K_f, K_t) are the frozen and thawed thermal conductivities corresponding to the respective domains (Ω_f, Ω_t). On the freezing front (assumed 0°C isotherm) the conditions required are

$$\phi_f = \phi_t = 0, \quad (x, y) \epsilon C \tag{2}$$

and for $\partial\phi/\partial n = \partial\psi/\partial S$ by the Cauchy-Riemann relationship

$$K_f \frac{d\psi}{dS} = -K_t \frac{d\psi}{dS} \tag{3}$$

where (ϕ_f, ϕ_t) are the frozen and thawed temperatures on the freezing front contour C; ψ is the stream function which is conjugate to the potential ϕ; and S is a tangential coordinate on C, in a counterclockwise direction.

Modeling Approach (Simultaneous Potential Problem Solutions)

The modeling approach initiates by developing a CVBEM approximator $\hat{\omega}_f(z)$ and $\hat{\omega}_t(z)$ for the frozen and thawed domains, respectively. Hromadka and Guymon [8] give the details for developing such CVBEM approximators. The numerical technique determines the analytic function $\hat{\omega}(z)$ which satisfies the boundary conditions of either normal flux or temperature specified at nodal points located on the problem boundary Γ. Because $\hat{\omega}(z)$ is analytic throughout the interior domain Ω which is enclosed by Γ, then the real and imaginary parts of $\hat{\omega}(z) = \hat{\phi}(z) + i\hat{\psi}(z)$ both exactly satisfy the Laplace equation over Ω. (This property afforded by the CVBEM is not guaranteed by any of the domain methods such as finite elements on finite differences.)

For the steady-state condition, the governing heat flow equations reduce to the Laplace equations shown in (1). Consequently, an $\hat{\omega}(z)$ determined for both the frozen and thawed regions satisfies the Laplace equations exactly, leaving only errors in satisfying the boundary conditions. To develop a CVBEM steady-state solution, an $\hat{\omega}(z)$ is developed for each of the separate regions. Initially, both $\hat{\omega}_f(z)$ and $\hat{\omega}_t(z)$ are defined by

$$\begin{aligned} \hat{\omega}_f(z) &= \hat{\omega}_f^1, \quad z\epsilon\Omega \\ \hat{\omega}_t(z) &= \hat{\omega}_t^1, \quad z\epsilon\Omega \end{aligned} \tag{4}$$

where in equation (4) $\Omega = \Omega_t \cup \Omega_f$ is the global domain, and the first-order CVBEM approximators are based on the entire domain. This procedure results in simply estimating the 0°C isotherm location for the homogeneous problem of Ω being entirely frozen or thawed. Let C^1 be the contour corresponding to this 0°C isotherm (e.g., located by a y-coordinate trial-and-error iteration such as bisection).

The second iteration step begins by defining Ω_f^2 and Ω_t^2 based on the mutual boundary of C^1. CVBEM approximators $\hat{\omega}_f^2$ and $\hat{\omega}_t^2$ are then defined for Ω_f^2 and Ω_t^2, respectively.

Examining the stream functions $\hat{\psi}_f^2$ and $\hat{\psi}_t^2$, estimates of the discrepancy in meeting equation (3) are evaluated. The $\hat{\omega}_f^2$ function is now used to determine the next location of the 0°C isotherm. This is accomplished by determining a new $\hat{\omega}_f^*$ with the stream function values of $\hat{\omega}_t^2$ (and modified to include the thawed or frozen conductivity) superimposed at the nodal values of C^1. Next, a new 0°C isotherm C^* is located for $\hat{\omega}_f^*$. The next estimated location for the 0°C isotherm, C^2, is located by averaging the y coordinates of the nodal points between C^1 and C^*. Figure 2 illustrates this procedure.

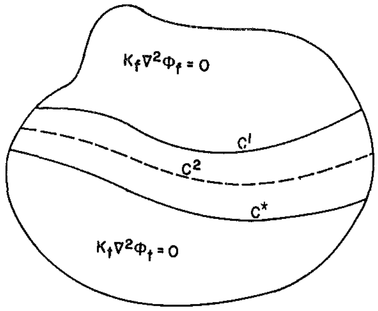

Fig. 2 Redefining the freezing front location

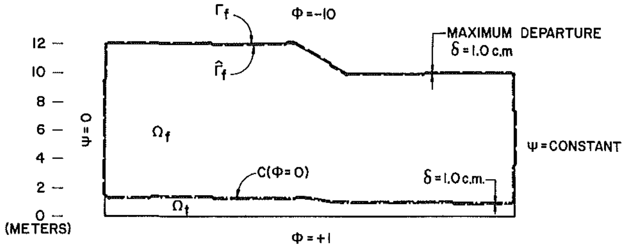

Fig. 3 The approximative boundary $\hat{\Gamma}_f$ and the goodness of fit to the problem boundary, Γ_f

The third iteration step proceeds by defining Ω_f^3 and Ω_t^3 based on the mutual boundary of C^2 and the above procedure is repeated.

The iteration process continues until the final estimates of Ω_f and Ω_t are determined with corresponding $\hat{\omega}_f$ and $\hat{\omega}_t$ approximators such that

$$|K_f d\hat{\psi}_f/ds - K_t d\hat{\psi}_t/ds| < \epsilon, \quad z\epsilon C \tag{5}$$

The Approximative Boundary

As discussed previously, the subject problem reduces to finding a solution to the Laplace equation in Ω_f and Ω_t where Ω_f and Ω_t coincide along the steady-state freezing front location C. The CVBEM develops approximators $\hat{\omega}_f$ and $\hat{\omega}_t$ which exactly satisfy the Laplace equation over Ω_f and Ω_t, respectively. Consequently, the only numerical error occurs in matching the boundary conditions continuously on Γ_f, Γ_t, and C.

To evaluate the precision in predicting the freezing front location, an approximative boundary is determined for each subproblem domain of Ω_f, Ω_t. The approximative boundary results from plotting the level curves of each CVBEM approximator (i.e., $\hat{\omega}_f$, $\hat{\omega}_t$) which correspond to the boundary conditions of the problem.

For example, in Ω_f the thermal boundary conditions for a roadway embankment (Fig. 3) are defined on the problem boundary Γ_f by

ϕ = −10°C, $z \in$ top surface
ϕ = 0°C, $z \in$ freezing front
ψ = 0, $z \in$ left side (symmetry)
ψ = const, $z \in$ right side (zero flux)

After developing an $\hat{\omega}_f$ for Ω_f from the CVBEM, the approximative boundary $\hat{\Gamma}_f$ is determined by plotting the prescribed level curves. Figure 3 also includes Γ_f superimposed with Γ_f. Because $\hat{\omega}_f$ is analytic within the interior of the approximative boundary and satisfies the prescribed boundary conditions on the boundary $\hat{\Gamma}_f$, then $\hat{\omega}_f$ is the exact solution of the boundary value problem redefined on $\hat{\Gamma}_f$ and its interior $\hat{\Omega}_f$. Should $\hat{\Gamma}_f$ completely cover Γ_f, then $\hat{\omega}_f$ is the exact solution to the subject problem.

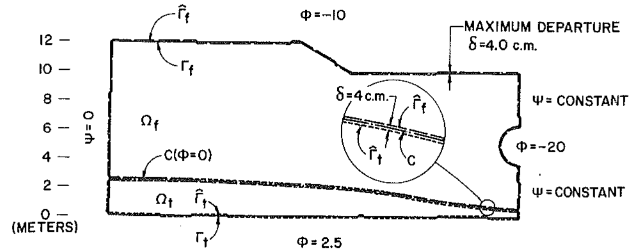

Fig. 4 Application of the CVBEM geothermal model to predict steady-state conditions

Thus, the CVBEM modeling error is directly evaluated by the closeness-of-fit between $\hat{\Gamma}_f$ and Γ_f. Hromadka and Guymon [7] successfully use this approximate boundary concept in the evaluation of approximation error resulting from the application of the CVBEM to the solution of several homogeneous potential boundary value problems. However, in this paper, the approximative boundary concept is used not only to examine the closeness-of-fit to the boundary conditions, but possibly more crucial, the closeness-of-fit of matching the estimated freezing front location between Ω_f and Ω_t along the contour C. Should Ω_f and Ω_t match C continuously, then $\hat{\omega}_f$ and $\hat{\omega}_t$ equate thermal flux continuously along C.

Applications

In order to demonstrate the use of the CVBEM approach and the approximative boundary, two applications are considered.

Figure 3 depicts an application of the geothermal model for a roadway embankment problem and the use of the approximative boundary. Figure 4 illustrates the two-dimensional steady-state freezing front location for a geothermal problem involving a buried subfreezing 3-m-dia pipeline. An examination of the approximation boundaries indicates that a good CVBEM approximator was determined by use of a 26-node CVBEM model. The maximum departure δ between the approximative boundaries and the problem boundary Γ occurred along the top of the pipeline and had a value of approximately 3.5 cm. The average departure $\bar{\delta}$ is estimated at less than 1 cm. The freezing front maximum departure is approximately 4 cm and occurred at the right-hand side. Average departure on C is less than 2 cm. (In the examples, thermal properties of a Fairbanks silt are used.)

The example problems presented illustrate the usefulness of the CVBEM in predicting the steady-state freezing front location for two-dimensional problems. Possibly the most important result is the accurate determination of the approximation error involved in using the CVBEM. The usual procedure for estimating the freezing front is to use a finite element or finite difference numerical analog. A hybrid of these domain methods is to include a variable mesh in order to better accommodate the interface. However, none of these methods provide the error of approximation. In comparison, the CVBEM model provides the approximation error not only in matching the boundary conditions, but in predicting the interface location between Ω_f and Ω_t. This error is simple to interpret as an approximative boundary displacement from the true problem boundary, and the displacement between Ω_f and Ω_t along the freezing front contour C.

Another significant result of this research is the development of the CVBEM computer code to run on many FORTRAN 64K microcomputers.

Conclusions

The CVBEM is used to develop a two-dimensional model for predicting the steady-state freezing front location. The model provides for an accurate and simple-to-use error analysis of the predicted results by use of the approximative boundary technique. The model is adaptable for many currently available microcomputers which accommodate FORTRAN.

References

1 Hromadka, T. V., II, and Guymon, G. L., "Application of a Boundary Integral Equation to Prediction of Freezing Fronts in Soils," *CRST*, Vol. 6, 1982, pp. 115–121.

2 Hromadka, T. V., II, Guymon, G. L., and Berg, R. L., "Comparison of Two-Dimensional Domain and Boundary Integral Geothermal Models to Embankment Freeze-Thaw Field Data," *Permafrost, Fourth International Conference, Proceedings*, National Academy Press, 1983.

3 Hromadka, T. V., II, "The Complex Variable Boundary Element Method," Springer-Verlag, 1984.

4 Yoo, J., and Rubinsky, B., "Numerical Computation Using Finite Elements for the Moving Interface in Heat Transfer Problems With Phase Transformation," *Numerical Heat Transfer*, Vol. 6, 1983.

5 Brebbia, C. A., and Walker, S., *Boundary Element Techniques in Engineering*, Butterworths, London, 1979.

6 O'Niell, K., "Boundary Integral Solution Equation Solution of Moving Boundary Phase Change Problems," *Int. J. Num. Mech. Engg.*

7 Hromadka, T. V., II, and Guymon, G. L., "An Algorithm to Reduce Approximation Error From the CVBEM," *Numerical Heat Transfer* (in press), 1984.

8 Hromadka, T. V., II, Guymon, G. L., and Yen, C. C., "The Complex Variable Boundary Element Method: Development," *Int. Journal of Num. Methods in Eng.*, 1984.

9 Outcalt, S., "A Simple Energy Balance Model of Ice Segregation," *Cold Regions Science and Technology*, Vol. 3, 1980, pp. 145–151.

The Plating Algorithm for Radiation Script-F Transfer Factor

D. K. Edwards[1]

Introduction

Calculation of the script-F transfer factor is the goal of a conventional engineering radiation heat transfer analysis of an enclosure. As described in the literature, e.g., [1–7], the procedure for doing so is to use a standard matrix inversion routine followed by some matrix multiplications. An alternative view of the procedure is offered here. Here the following question is answered: How are the script-F transfer factors for an enclosure changed by "plating" a black surface, that is, changing its emissivity from 1 to its actual value? The answer is a set of recursion relations that allows the transfer factors to be found from the shape factors in N plating steps. The merits of advancing this view are thought to be as follows: (1) The recursion equations clearly display important properties that permit comparisons to be made to assess roundoff errors introduced during computation and to give added insight into the radiative transfer process. (2) The algorithm is easily coded if a personal computer at hand has no matrix inversion in its library. (3) The algorithm saves computer time in executing parametric studies.

Analysis

Transfer factors denoted here as $\bar{F}_{i,j}$ are defined conventionally so that the net flux out of an area A_i on the wall of an enclosure of N surfaces is

---

[1] Department of Mechanical Engineering, University of California—Irvine, Irvine, CA 92717; Fellow ASME

Contributed by the Heat Transfer Division for publication in the JOURNAL OF HEAT TRANSFER. Manuscript received by the Heat Transfer Division November 27, 1984.

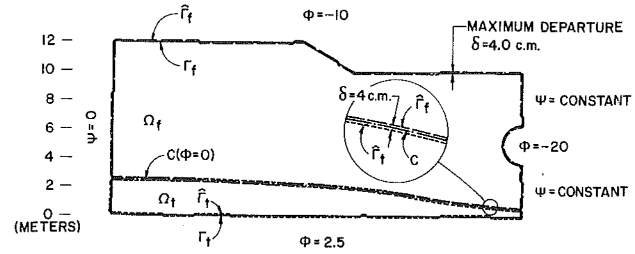

Fig. 4 Application of the CVBEM geothermal model to predict steady-state conditions

Thus, the CVBEM modeling error is directly evaluated by the closeness-of-fit between $\hat{\Gamma}_f$ and Γ_f. Hromadka and Guymon [7] successfully use this approximate boundary concept in the evaluation of approximation error resulting from the application of the CVBEM to the solution of several homogeneous potential boundary value problems. However, in this paper, the approximative boundary concept is used not only to examine the closeness-of-fit to the boundary conditions, but possibly more crucial, the closeness-of-fit of matching the estimated freezing front location between Ω_f and Ω_t along the contour C. Should Ω_f and Ω_t match C continuously, then $\hat{\omega}_f$ and $\hat{\omega}_t$ equate thermal flux continuously along C.

Applications

In order to demonstrate the use of the CVBEM approach and the approximative boundary, two applications are considered.

Figure 3 depicts an application of the geothermal model for a roadway embankment problem and the use of the approximative boundary. Figure 4 illustrates the two-dimensional steady-state freezing front location for a geothermal problem involving a buried subfreezing 3-m-dia pipeline. An examination of the approximation boundaries indicates that a good CVBEM approximator was determined by use of a 26-node CVBEM model. The maximum departure δ between the approximative boundaries and the problem boundary Γ occurred along the top of the pipeline and had a value of approximately 3.5 cm. The average departure $\bar{\delta}$ is estimated at less than 1 cm. The freezing front maximum departure is approximately 4 cm and occurred at the right-hand side. Average departure on C is less than 2 cm. (In the examples, thermal properties of a Fairbanks silt are used.)

The example problems presented illustrate the usefulness of the CVBEM in predicting the steady-state freezing front location for two-dimensional problems. Possibly the most important result is the accurate determination of the approximation error involved in using the CVBEM. The usual procedure for estimating the freezing front is to use a finite element or finite difference numerical analog. A hybrid of these domain methods is to include a variable mesh in order to better accommodate the interface. However, none of these methods provide the error of approximation. In comparison, the CVBEM model provides the approximation error not only in matching the boundary conditions, but in predicting the interface location between Ω_f and Ω_t. This error is simple to interpret as an approximative boundary displacement from the true problem boundary, and the displacement between Ω_f and Ω_t along the freezing front contour C.

Another significant result of this research is the development of the CVBEM computer code to run on many FORTRAN 64K microcomputers.

Conclusions

The CVBEM is used to develop a two-dimensional model for predicting the steady-state freezing front location. The model provides for an accurate and simple-to-use error analysis of the predicted results by use of the approximative boundary technique. The model is adaptable for many currently available microcomputers which accommodate FORTRAN.

References

1 Hromadka, T. V., II, and Guymon, G. L., "Application of a Boundary Integral Equation to Prediction of Freezing Fronts in Soils," *CRST*, Vol. 6, 1982, pp. 115–121.

2 Hromadka, T. V., II, Guymon, G. L., and Berg, R. L., "Comparison of Two-Dimensional Domain and Boundary Integral Geothermal Models to Embankment Freeze-Thaw Field Data," *Permafrost, Fourth International Conference, Proceedings*, National Academy Press, 1983.

3 Hromadka, T. V., II, "The Complex Variable Boundary Element Method," Springer-Verlag, 1984.

4 Yoo, J., and Rubinsky, B., "Numerical Computation Using Finite Elements for the Moving Interface in Heat Transfer Problems With Phase Transformation," *Numerical Heat Transfer*, Vol. 6, 1983.

5 Brebbia, C. A., and Walker, S., *Boundary Element Techniques in Engineering*, Butterworths, London, 1979.

6 O'Niell, K., "Boundary Integral Solution Equation Solution of Moving Boundary Phase Change Problems," *Int. J. Num. Mech. Engg.*

7 Hromadka, T. V., II, and Guymon, G. L., "An Algorithm to Reduce Approximation Error From the CVBEM," *Numerical Heat Transfer* (in press), 1984.

8 Hromadka, T. V., II, Guymon, G. L., and Yen, C. C., "The Complex Variable Boundary Element Method: Development," *Int. Journal of Num. Methods in Eng.*, 1984.

9 Outcalt, S., "A Simple Energy Balance Model of Ice Segregation," *Cold Regions Science and Technology*, Vol. 3, 1980, pp. 145–151.

The Plating Algorithm for Radiation Script-F Transfer Factor

D. K. Edwards[1]

Introduction

Calculation of the script-F transfer factor is the goal of a conventional engineering radiation heat transfer analysis of an enclosure. As described in the literature, e.g., [1–7], the procedure for doing so is to use a standard matrix inversion routine followed by some matrix multiplications. An alternative view of the procedure is offered here. Here the following question is answered: How are the script-F transfer factors for an enclosure changed by "plating" a black surface, that is, changing its emissivity from 1 to its actual value? The answer is a set of recursion relations that allows the transfer factors to be found from the shape factors in N plating steps. The merits of advancing this view are thought to be as follows: (1) The recursion equations clearly display important properties that permit comparisons to be made to assess roundoff errors introduced during computation and to give added insight into the radiative transfer process. (2) The algorithm is easily coded if a personal computer at hand has no matrix inversion in its library. (3) The algorithm saves computer time in executing parametric studies.

Analysis

Transfer factors denoted here as $\bar{F}_{i,j}$ are defined conventionally so that the net flux out of an area A_i on the wall of an enclosure of N surfaces is

---

[1] Department of Mechanical Engineering, University of California—Irvine, Irvine, CA 92717; Fellow ASME

Contributed by the Heat Transfer Division for publication in the JOURNAL OF HEAT TRANSFER. Manuscript received by the Heat Transfer Division November 27, 1984.

$$q_i = \sum_{j=1}^{N} \bar{F}_{i,j}(B_i - B_j) \tag{1}$$

where B_j denotes the black-body radiosity, σT_j^4 for the grey-walled enclosure. For an enclosure with all surfaces black, the transfer factors are the ordinary shape or angle factors $F_{i,j}$. The method here used to find $\bar{F}_{i,j}$ is to begin with $F_{i,j}$ and change the emissivity of one surface at a time from 1 to its actual value ϵ_k.

Let the absorption by the ith surface be a_i, the product of the emissivity-absorptivity ϵ_i and the irradiation q_i^-.

$$a_i = \epsilon_i q_i^- = \sum_j \bar{F}_{i,j} B_j \tag{2}$$

When surface k is black prior to plating, the emissivity is 1; thus for any black surface equation (2) indicates that

$$q_k^- = \sum_j \bar{F}_{k,j} B_j \tag{3}$$

Upon the plating of k the radiosity is converted from B_k to q_k^+, the sum of the emitted and reflected fluxes.

$$q_k^+ = \epsilon_k B_k + (1-\epsilon_k)(q_k^-)^* \tag{4}$$

Here the asterisk denotes the new value after plating. From equation (3), by replacing B_k with q_k^+, there is found

$$(q_k^-)^* = \sum_{j \neq k} \bar{F}_{k,j} B_j + \bar{F}_{k,k} q_k^+ \tag{5}$$

Combining equations (4) and (5) gives the new radiosity

$$q_k^+ = \frac{1}{D}\epsilon_k B_k + \frac{1}{D}(1-\epsilon_k)\sum_{j \neq k} \bar{F}_{k,j} B_j \tag{6}$$

where the denominator D is

$$D = 1 - (1-\epsilon_k)\bar{F}_{k,k} \tag{7}$$

The absorption at the ith surface is changed by B_k being replaced by q_k^+. Accordingly for any $i \neq k$ it holds that

$$a_i^* = \sum_{j \neq k} \bar{F}_{i,j} B_j + \bar{F}_{i,k} q_k^+$$

$$a_i^* = \sum_{j \neq k}\left[\bar{F}_{i,j} + \frac{1}{D}(1-\epsilon_k)\bar{F}_{i,k}\bar{F}_{k,j}\right]B_j + \frac{1}{D}\epsilon_k \bar{F}_{i,k} B_k \tag{8}$$

The absorption by k itself is affected by both the change in ϵ_k and q_k^+.

$$a_k^* = \epsilon_k \sum_{j \neq k} \bar{F}_{k,j} B_j + \epsilon_k \bar{F}_{k,k} q_k^+$$

$$a_k^* = \epsilon_k \sum_{j \neq k}\left[\bar{F}_{k,j} + \frac{1}{D}(1-\epsilon_k)\bar{F}_{k,k}\bar{F}_{k,j}\right]B_j + \frac{1}{D}\epsilon_k^2 \bar{F}_{k,k} B_k \tag{9}$$

Comparison of equation (8) or equation (9) with equation (2) written in the form

$$a_i^* = \sum_j \bar{F}_{i,j}^* B_j$$

shows that four cases exist:

Case 1. $(i \neq k,\ j \neq k)$

$$\bar{F}_{i,j}^* = \bar{F}_{i,j} + \frac{1}{D}(1-\epsilon_k)\bar{F}_{i,k}\bar{F}_{k,j} \tag{10}$$

Case 2. $(i \neq k,\ j \neq k)$

$$\bar{F}_{i,k}^* = \frac{1}{D}\epsilon_k \bar{F}_{i,k} \tag{11}$$

Case 3. $(i = k,\ j \neq k)$

$$\bar{F}_{k,j}^* = \epsilon_k\left[\bar{F}_{k,j} + \frac{1}{D}(1-\epsilon_k)\bar{F}_{k,k}\bar{F}_{k,j}\right] = \frac{1}{D}\epsilon_k \bar{F}_{k,j} \tag{12}$$

Case 4. $(i = k,\ j = k)$

$$\bar{F}_{k,k}^* = \frac{1}{D}\epsilon_k^2 \bar{F}_{k,k} \tag{13}$$

The simplification of equation (12) follows from equation (7).

With this formulation important properties are readily seen. They follow from the shape factor properties prior to any plating

$$A_i F_{i,j} = A_j F_{j,i} \quad \text{(all unplated)} \tag{14}$$

$$\sum_j F_{i,j} = 1 \quad \text{(all unplated)} \tag{15}$$

Upon any subsequent plating reciprocity expressed by equation (14) is conserved. Multiply equation (10) by area A_i. Use reciprocity once in the first term on the right and twice for the second term. The result is

$$A_i \bar{F}_{i,j}^* = A_j \bar{F}_{j,i}^* \tag{16}$$

Similarly equation (11) can be multiplied by A_i and equation (12) by A_k to achieve an identical result. Also upon any plating, equations (10) and (11) show that for any $i \neq k$

$$\sum_j \bar{F}_{i,j}^* = \sum_j \bar{F}_{i,j} \quad i \neq k \tag{17}$$

For $i = k$, equations (12) and (13) show that

$$\sum_j \bar{F}_{k,j}^* = \epsilon_k \tag{18}$$

Thus before plating the transfer factors sum to unity; upon plating they sum to the emissivity; and upon subsequent platings of other surfaces the sum remains invariant.

Application

To accomplish the conversion of the shape factor matrix to the transfer factor matrix, equations (10-13) are applied recursively. First with $k=1$, the matrix is converted; then again with $k=2$, and so on until $k=N$. Any black surface is simply skipped when its k number comes up. Refractory surfaces (surfaces in radiative equilibrium) are treated as having $\epsilon_k = 0$. These are best numbered so as to be done first, so that zero rows and columns are grouped to permit easy reduction of the transfer factor matrix. Parametric calculations in which ϵ_k is varied for a given surface are best done last, saving the $\bar{F}_{i,j}$ values prior to plating that surface as well as the $\bar{F}_{i,j}^*$ values found, so that $\bar{F}_{i,j}$ serves as the start of a single final step per new ϵ_k value.

References

1 Hottel, H. C., "Radiant Heat Transmission," in: *Heat Transmission*, W. H. McAdams, ed., McGraw-Hill, New York, 1954.

2 Gebhart, B., *Heat Transfer*, McGraw-Hill, New York, 1961.

3 Ishimoto, T., and Bevans, J. T., "Method of Evaluating Script-F for Radiant Exchange Within an Enclosure," *AIAA Journal*, Vol. 1, 1963, pp. 1428-1429.

4 Sparrow, E. M., "On the Calculation of Radiant Interchange Between Surfaces," in: *Modern Developments in Heat Transfer*, W. Ibele, ed., Academic Press, New York, 1963.

5 Bobco, R. P., "Radiation Heat Transfer in Semigray Enclosures With Specularly and Diffusely Reflecting Surfaces," ASME JOURNAL OF HEAT TRANSFER, Vol. 86, 1964, pp. 123-130.

6 Wiebelt, J. A., *Engineering Radiation Heat Transfer*, Holt, Rinehart, and Winston, New York, 1966.

7 Siegel, R., and Howell, J. R., *Thermal Radiation Heat Transfer*, Hemisphere/McGraw-Hill, New York, 1981.

Least-Squares Smoothing of Direct-Exchange Areas in Zonal Analysis[1]

M. E. Larsen[2] and J. R. Howell[3]

Nomenclature

a = absorptivity of gas, m^{-1}
A_i = area of ith surface zone, m^2
E = emissive power, W/m^2
$g_\gamma g_\mu$ = direct-exchange area from volume γ to volume μ, m^2
$g_\gamma s_i$ = direct-exchange area from γth volume to ith surface, m^2
H = object function, arbitrary units
M = number of zones = $N + \Gamma$
N = number of enclosure surfaces
$[R]$ = weighting matrix [equation (11)], arbitrary units
q'' = heat flux, W/m^2
q''' = volumetric heating rate, W/m^3
S = path length, m
$s_i g_\gamma$ = direct-exchange area from ith surface to γth gas volume, m^2
$s_i s_j$ = direct-exchange area from ith to jth surface, m^2
V = volume of individual volume element, m^3
w_{ij} = arbitrary weights of object function
x_{ij} = an element of $[X]$ [equation (4)], m^2
$[X]$ = matrix of all direct-exchange areas, m^2
Γ = number of volume elements
δ_i = area deficit of ith conservation constraint, m^2
θ_i = angle measured from A_i surface normal
λ_i = ith Lagrange multiplier of equation (6), m^2
τ = transmittance

Subscripts

i, j = quantities related to surface elements
γ, μ = quantities related to volume elements

Superscripts

$'$ (prime) = adjusted direct-exchange area
$p, p+1$ = successive iterations of λ_i in equation (15)
$*$ = exact direct-exchange areas

Introduction

A powerful and practical approach to estimating radiant heat transfer rates and temperatures in radiating enclosures is the zone method [1-3]. The fundamental representation of an enclosure's optical and geometric properties is given by its direct-exchange areas. As described in [1, 3] direct-exchange areas may be converted to total-exchange areas which embody the enclosing surface's properties. Finally, treatment of enclosures containing nongrey media may be effected by use of directed-flux areas. Directed-flux areas are formed by taking temperature-dependent weighted averages of total-exchange areas for two or more grey gases (one of which may be transparent).

The starting point in zonal analysis is the division of the system into finite area and volume elements. The direct-exchange areas relating radiant exchange between the area elements (A_i, A_j) and volume elements (V_γ, V_μ) for an enclosure containing a grey medium are defined by

$$s_i s_j = \frac{1}{\pi}\int_{A_j}\int_{A_i}\frac{\tau(S_{ij})\cos(\theta_i)\cos(\theta_j)}{S_{ij}^2}\,dA_i dA_j \tag{1a}$$

$$s_i g_\gamma = \frac{a}{\pi}\int_{V_\gamma}\int_{A_i}\frac{\tau(S_{i\gamma})\cos(\theta_i)}{S_{i\gamma}^2}\,dA_i dV_\gamma \tag{1b}$$

and

$$g_\mu g_\gamma = \frac{a^2}{\pi}\int_{V_\mu}\int_{V_\gamma}\frac{\tau(S_{\mu\gamma})}{S_{\mu\gamma}^2}\,dV_\gamma dV_\mu \tag{1c}$$

where

$$\tau = \exp(-aS)$$

Equations (1) have the physical dimension of area. Reciprocity requires

$$s_i s_j = s_j s_i \tag{2a}$$

$$s_i g_\gamma = g_\gamma s_i \tag{2b}$$

$$g_\gamma g_\mu = g_\mu g_\gamma \tag{2c}$$

For an enclosure of N surface elements and Γ volume elements, conservation of energy dictates

$$(4aV)_\gamma = \sum_{i=1}^{N} g_\gamma s_i + \sum_{\mu=1}^{\Gamma} g_\gamma g_\mu \tag{3a}$$

$$A_i = \sum_{j=1}^{N} s_i s_j + \sum_{\gamma=1}^{\Gamma} s_i g_\gamma \tag{3b}$$

Equations (3a) and (3b) may be considered to be energy balances (divided by emissive power) for A_i and V_γ in an isothermal, black-walled enclosure.

Evaluation of Direct-Exchange Areas

The complexities of enclosure analysis which arise from geometry must be dealt with in the evaluation of direct-exchange areas. Graphic representation of direct-exchange areas is given in [3] for rectangular enclosures composed of cube-shaped volume elements. Direct-exchange areas for cylindrical enclosures are tabulated in [1]. Becker [4] gives a simplified technique for evaluating equation (1b) for rectangular parallelepiped enclosures. Edwards and Balakrishnan [5] have reported simplified expressions for direct-exchange areas between cube-shaped volume elements.

When zonal analysis is performed on enclosures with many surface and volume elements, entering the required exchange areas from existing (tabulated or graphic) sources is tedious. We have analyzed two- and three-dimensional enclosures containing grey media (with up to 285 surface and volume elements) and performed the integrations indicated by equations (1) as described in [6].

In practice, none of the preceding techniques will yield a complete set of direct-exchange areas which identically meet the constraints of equations (3) (due to the accumulation of error). Here we present a technique for "smoothing" direct-exchange area estimates so that equations (3) will be satisfied.

---

[1] A portion of this work was completed at Sandia National Laboratories supported by the U.S. Department of Energy under contract number DE-AC04-76DP00789.

[2] Fluid Mechanics and Heat Transfer Division III, Sandia National Laboratories, Albuquerque, NM 87185

[3] Mechanical Engineering Department, The University of Texas at Austin, Austin, TX 78712; Fellow ASME

Contributed by the Heat Transfer Division for publication in the JOURNAL OF HEAT TRANSFER. Manuscript received by the Heat Transfer Division November 16, 1984.

We will first consider alternate adjustment techniques already reported in the literature.

Alternate Means of Adjusting Direct-Exchange Areas

In general, after exploiting reciprocity, equations (2), there may be as many as $M(M+1)/2$ ($M=N+\Gamma$) unique direct-exchange areas to evaluate. For most geometries symmetry considerations will further reduce the number of unique direct-exchange areas. Equations (3) may be used to evaluate M exchange areas, leaving $M(M-1)/2$ independent estimates to be made. Sowell and O'Brien [7] have given a concise methodology for using equations (3) to evaluate M exchange areas (without violating the constraints of equations (2)). The development in [7] is given for conventional, transparent-enclosure view factors, but the method is easily generalized to direct-exchange areas of zonal analysis. This technique is particularly useful when M is small. For a system with many surface and volume elements a serious drawback of using the conservation constraints directly to obtain M exchange areas is that the cumulative error of $(M-1)$ other estimates is "lumped into" each of these (M) exchange areas. The first $M(M-1)/2$ estimates may be systematically small or large resulting in significant error in the evaluation of the last M direct-exchange areas.

Vercammen and Froment [8] developed a regression technique which they used to smooth configuration factors obtained by the Monte Carlo technique. The technique reported in this paper accomplishes essentially the same result. However, the technique presented here is more readily adapted to general application in zonal analysis computer codes. The technique of [8] operates on only the nonzero-valued and unique factors. This requires the zero-valued and repeating-valued factors to be identified.

Least-Squares Smoothing Using Lagrange Multipliers

Consider an enclosure consisting of N surface elements and Γ volume elements for which a complete set of direct-exchange areas has been estimated. In general this will involve $M(M+1)/2$ estimates when reciprocity, equations (2), is exploited. The direct-exchange areas may be assembled to form an $M \times M$ matrix $[X]$

$$[X]=\begin{bmatrix}[ss] & [sg]\\ [sg]^T & [gg]\end{bmatrix} \qquad (4)$$

Reciprocity requires that $[X]$ be symmetric. Further, conservation (equations (3)) requires the ith row (or column) to sum to c_i, where

$$\sum_{j=1}^{M} x_{ij}=c_i$$

$$c_i=A_i \qquad i\le N$$

$$c_i=(4aV)_\gamma \quad \gamma=i-N, \qquad i>N$$

Assume that an estimate of $[X]$ has been made which obeys the symmetry (reciprocity) constraints but the conservation constraints (equations (3)) are not quite satisfied. We wish to adjust $[X]$ to meet these constraints while minimizing the disturbance to the original estimates of $[X]$. We define

$$H=\sum_{i=1}^{M}\sum_{j=1}^{M}\frac{1}{2w_{ij}}(x'_{ij}-x_{ij})^2 \qquad (5)$$

where x_{ij} is the original estimate of an element of $[X]$ and x'_{ij} is the adjusted value. We wish to find x'_{ij} to meet the conservation constraints, while minimizing H. The weights w_{ij} will allow us to arbitrarily assign relative penalties to adjustments of certain factors. The method of Lagrange multipliers will be used and the Lagrangian L is

$$L=H+\sum_{i=1}^{M}\lambda_i(g_i+g_i^*) \qquad (6)$$

where λ_i are the Lagrange multipliers and g_i and g_i^* are, respectively, the row- and column-sum constraints

$$g_i=c_i-\sum_{j=1}^{M}x'_{ij} \quad i=1,2...M \qquad (7a)$$

$$g_i^*=c_i-\sum_{j=1}^{M}x'_{ji} \quad i=1,2...M \qquad (7b)$$

The Lagrangian is formed with $2M$ constraints, but only M Lagrange multipliers. Due to symmetry, there are only M *independent* constraints.

Differentiating L with respect to x'_{ij} and equating to zero gives

$$\frac{\partial L}{\partial x'_{ij}}=0=\frac{1}{w_{ij}}(x'_{ij}-x_{ij})-\lambda_i-\lambda_j \qquad (8)$$

λ_i and λ_j both appear in equation (8) because x'_{ij} participates in both the ith and jth constraints (due to symmetry). Then

$$x'_{ij}-x_{ij}=w_{ij}(\lambda_i+\lambda_j) \qquad (9)$$

Notice that we must require $w_{ij}=w_{ji}$ to preserve symmetry. Equation (9) may be written for each of M elements and these may be summed on the j index

$$\sum_{j=1}^{M}[x'_{ij}=x_{ij}+w_{ij}(\lambda_i+\lambda_j)]$$

Further, we require the adjusted factors (x'_{ij}) to meet the constraints of equation (7), yielding

$$c_i-\sum_{j=1}^{M}x_{ij}=\lambda_i\sum_{j=1}^{M}w_{ij}+\sum_{j=1}^{M}\lambda_j w_{ij} \qquad (10)$$

M of these equations (equation (10)) may be written and the resulting set of equations may be written

$$[R]\bar{\lambda}=\bar{\delta} \qquad (11)$$

where

$$r_{ij}=w_{ij} \qquad i\neq j$$

$$r_{ii}=w_{ii}+\sum_{j=1}^{M}w_{ij}$$

$$\delta_i=c_i-\sum_{j=1}^{M}x_{ij}$$

Equation (11) may be solved for $\bar{\lambda}$ and the adjusted value x'_{ij} is given by

$$x'_{ij}=x_{ij}+w_{ij}(\lambda_i+\lambda_j) \qquad (12)$$

Solving for the Lagrange multipliers from equation (11) and adjusting x_{ij} per equation (12) results in the minimization of H. For a system of many elements equation (11) represents a large set of equations. However, if most of the w_{ij} are about the same size, the system becomes increasingly well-conditioned as M becomes large. Notice that no problems arise if some of the w_{ij} are made to be zero to require the corresponding x_{ij} to remain undisturbed in the smoothing process.

An orderly means of assigning w_{ij} is required if the method is to be convenient for large systems. Smoothing with $w_{ij}=x_{ij}^2$ will be demonstrated in the following section. For the case in which $w_{ij}=1$ (all i and j) the solution to equation (11) is simply:

$$\lambda_i = \frac{\delta_i}{M} - \frac{1}{2M^2} \sum_{j=1}^{M} \delta_j \tag{13}$$

An undesirable consequence of using all equal weights (w_{ij}) is that all of the x_{ij} will be adjusted equally (to the extent allowed by the reciprocity constraint). Zero-valued x_{ij} (for example, $s_i s_j = x_{ij} = 0$, where A_i and A_j are surface area elements on the same planar surface) will be disturbed and "negative areas" can result.

As discussed in reference [6], w_{ij} may be assigned such that one weight applies to [*ss*], another to [*sg*], and a third to [*gg*]. For this case the solution of equation (11) can be simplified to the solution of a set of three linear algebraic equations. That weighting scheme will not be discussed here in deference to the scheme presented in the following section.

Results

The procedure outlined in the preceding section was conveniently integrated into existing zonal analysis codes [6] which analyze two- and three-dimensional enclosures. No provision needs to be made for zero-valued and repeated x_{ij} (as in [8]). The corrections required to meet the conservation constraints are distributed among all the exchange areas in proportion to their original magnitude. Obviously the impact of the smoothing process on final analysis results depends on the quality of initial estimates of the direct-exchange areas. As the number of elements in the system is increased, the details of what happens to an individual direct-exchange area in the adjustment process become less important. The current method was tested using the two-dimensional code to analyze an enclosure of square cross section. A detailed example illustrating the use of the current technique for this enclosure, with four surface elements and a single gas volume element, is presented in [9]. The same enclosure was also analyzed with 15 surface elements per side and 225 volume elements (M = 285). Although equation (13) represents a large system of equations, including the smoothing technique did little to increase the storage requirements of the zonal analysis code. The direct-exchange areas for a system [X] may be stored using one storage element for each x_{ij} on or above the diagonal, or $M(M+1)/2$ storage elements. In the present case ($w_{ij} = x_{ij}^2$)-weighting was used and the same storage space was used for x_{ij} and w_{ij} (since [X] and [R] are not required at the same time in the smoothing process). Using single-precision accuracy, equation (11) (M = 285) was solved by successive-overrelaxation with a relaxation factor of 1.25. Convergence was achieved such that

$$\sum_{i=1}^{M} (\lambda_i^{p+1} - \lambda_i^{p})^2 < 10^{-10} \tag{15}$$

in 11 iterations. After smoothing, the conservation constraints were met to six significant figures. The increase in processing time to run the zonal analysis due to the inclusion of the smoothing process is, of course, dependent on computer hardware and compiler/code optimization. In the present case running the code on a CDC 170 model 855 computer, using an FTN5 compiler, 4-10 s of additional execution time was required to perform the smoothing process, depending on the level of optimization selected when the code was compiled.

It should be apparent that the present technique does not invoke additional physical insight in causing the direct-exchange areas to obey conservation. As a result, it will not always be beneficial to use such a smoothing technique. Generally, if desired analysis results are dependent on a large number of factors, the smoothing will improve the analysis. For the uninteresting case of a gray medium in radiative equilibrium with an isothermal boundary, a set of direct-exchange areas that obey conservation will yield the correct (isothermal) temperature distribution in the medium (regardless whether *any* of the individual exchange areas are correct). To further examine the errors that can be *introduced* by smoothing let us consider a detailed example. The current technique is to be applied to the configuration factors of an infinitely long enclosure of square cross section which contains a transparent medium. The four sides of the enclosure are the four surfaces considered in the analysis. The actual matrix of configuration factors, computed analytically, is

$$[X^*] = \begin{bmatrix} 0.0 & f_1 & f_2 & f_1 \\ f_1 & 0.0 & f_1 & f_2 \\ f_2 & f_1 & 0.0 & f_1 \\ f_1 & f_2 & f_1 & 0.0 \end{bmatrix} \quad \begin{matrix} f_1 = 1 - 1/\sqrt{2} & = 0.2929 \\ f_2 = \sqrt{2} - 1 & = 0.4142 \end{matrix}$$

An initial estimate (provided by one of the reviewers of this paper) of this matrix which was made using the Monte Carlo technique yields

$$[X] = \begin{bmatrix} 0.0000 & 0.2948 & 0.4132 & 0.2920 \\ 0.2948 & 0.0000 & 0.2982 & 0.4070 \\ 0.4132 & 0.2982 & 0.0000 & 0.2950 \\ 0.2920 & 0.4070 & 0.2950 & 0.0000 \end{bmatrix}$$

When the foregoing smoothing technique is applied with ($w_{ij} = x_{ij}^2$)-weighting, the following matrix is obtained

$$[X'] = \begin{bmatrix} 0.0000 & 0.2949 & 0.4101 & 0.2950 \\ 0.2949 & 0.0000 & 0.2950 & 0.4101 \\ 0.4101 & 0.2950 & 0.0000 & 0.2949 \\ 0.2950 & 0.4101 & 0.2949 & 0.0000 \end{bmatrix}$$

Let us define the following measure of closeness in comparing two matrices

$$H([X], [X^*]) = \sqrt{\sum_{i=1}^{M} \sum_{j=1}^{M} \left(\frac{x_{ij}^* - x_{ij}}{x_{ij}^*} \right)^2} \tag{16}$$

Using equation (16) as the measure of quality, the adjustment results in only a very modest improvement in the matrix, $H([X], [X^*]) = 0.010$ while $H([X'], [X^*]) = 0.007$. The rows and columns of [X'] sum to unity. Looking at the elements individually, six of the nonzero elements of [X] were improved and six were assigned values less accurate than the original estimate. Consider the enclosure for the simple case in which it is black-walled, and the ith wall has unit emissive power while the other walls are relatively cold. Then the configuration factor x_{ij} is the heat flux imposed on the jth wall. If our purpose is to estimate the heat flux on one of the cold walls, the desired result has been compromised by the adjustment if the particular x_{ij} was unfavorably adjusted. However, if the aim of the analysis is to estimate the heat that must be supplied to the hot wall, the smoothing process has been wholly successful. The desirability of performing the smoothing process clearly depends on what quantities are to be predicted and on the system boundary conditions. In short, there can be no guarantees that smoothing will improve the analysis if there is no knowledge a priori regarding the accuracy of the factors to be smoothed. Analyses particularly at risk are those in which the important results are heavily dependent on one or a few of the quantities being smoothed. For systems with large M the probability of the smoothing process enhancing the analysis is increased. The techniques of

[7] and [8] may be more appropriate for systems with a small number of elements.

Conclusion

A simple solution has been presented which allows a set of direct-exchange areas to be smoothed to meet conservation constraints while minimizing the disturbance of the original estimates. The method is particularly well suited for large systems for which the exact nature of the deficiencies of the direct-exchange areas is unknown. Smoothing with $w_{ij} = x_{ij}^2$ is readily incorporated into codes performing zonal analysis and has been demonstrated to be effective and efficient. The tendency of this smoothing technique is to adjust each x_{ij} in proportion to its original size. Conservation of energy is invoked through the adjustment without additional physical insight. As a result, reasonable accuracy of the original estimates of the direct-exchange areas must be assumed and this limitation should be considered. The method should not be applied unless reasonable faith in the "shape" of the original estimates is justified.

Acknowledgments

The authors acknowledge J. R. Wilson for recommending the use of the method Lagrange multipliers in this minimization process.

References

1 Hottel, H. C., and Sarofim, A. F., *Radiative Transfer*, McGraw-Hill, New York, 1967.

2 Hottel, H. C., "Radiant Heat Transmission," in: *Heat Transmission*, W. H. McAdams, ed., 3rd ed., McGraw-Hill, 1954, Ch. 4.

3 Hottel, H. C., and Cohen, E. S., "Radiant Heat Exchange in a Gas-Filled Enclosure: Allowance for Non-Uniformity in Temperature," *AIChE Journal*, Vol. 4, No. 1, 1958, pp. 3-14.

4 Becker, H. B., "A Mathematical Solution for Gas-to-Surface Radiative Exchange Area for a Rectangular Parallelepiped Enclosure Containing a Gray Medium," ASME JOURNAL OF HEAT TRANSFER, Vol. 99, May 1977, pp. 203-207.

5 Edwards, D. K., and Balakrishnan, A., "Volume Interchange Factors for Nonhomogeneous Gases," ASME JOURNAL OF HEAT TRANSFER, Vol. 94, May 1972, pp. 181-187.

6 Larsen, M. E., "The Exchange Factor Method: An Alternative Zonal Formulation for Analysis of Radiating Enclosures Containing Participating Media," Ph.D. Dissertation, The University of Texas at Austin, 1983.

7 Sowell, E. F., and O'Brien, R. F., "Efficient Computation of Radiant-Interchange Configuration Factors Within the Enclosure," ASME JOURNAL OF HEAT TRANSFER, Vol. 94, Aug. 1972, pp. 326-328.

8 Vercammen, H. A. J., and Froment, G. F., "An Improved Zone Method Using Monte Carlo Techniques for the Simulation of Radiation in Industrial Furnaces," *International Journal of Heat and Mass Transfer*, Vol. 23, No. 3, Mar. 1980, pp. 329-336.

9 Larsen, M. E., and Howell, J. R., "Least-Squares Smoothing of Direct-Exchange Areas in Zonal Analysis," ASME Paper No. 84-HT-40.

Laser Reflection in a Scattering Medium With a White Diffusively Reflecting Substrate

D. C. Look, Jr.[1,2] and M. Vijayan[1]

Introduction

This experimental study concerns the loss of visibility of a pattern that is formed on the substrate when a planar scattering medium is subjected to a finite sized collimated light. The pattern is in the form of a bright spot surrounded by a dark circular area surrounded by a bright outer area. Figure 1 is a photograph of the pattern as seen through double-distilled water when viewing the white substrate. To obtain this pattern, the beam must be incident normal to the smooth front surface of the medium and to the white diffusely reflecting substrate. Look and Nelson [1] also dealt with this phenomenon. In [1] a discussion is presented on the effect of the reflection of laser radiation in a transparent, nonscattering medium for identical geometric and detection conditions as reported here. Good agreement between theory and experiment was demonstrated in this reference.

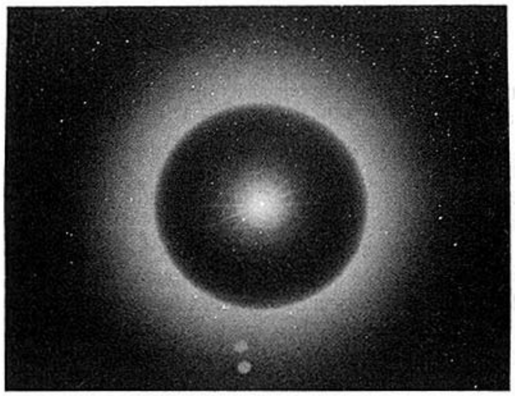

Fig. 1 Photograph of the effect of a white diffusely reflecting substrate in a finite medium

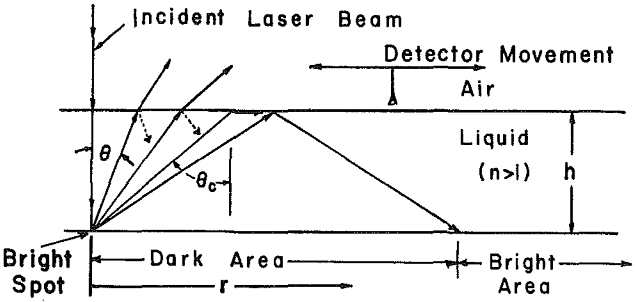

Fig. 2 Schematic of the outside reflection effect in a transparent slab

The purpose of this presentation is to extend the study as reported in [1] to the effects of pure scattering. In other words, it was found experimentally that as the optical thickness of the medium increases, this pattern starts to disappear and finally vanishes from view on the air side. The result of this experimental study is a statement of conditions required to obscure this pattern. The method used to accomplish this task is to direct a detector probe with a small angular field of view normal to the front surface. A jump in the detector readings occurs when the detector probe aperture crosses from the region of the dark area into the bright outer area. The size of this jump decreases as the optical thickness increases until for a certain optical thickness (called the flex point) the jump ceases to occur.

Theoretical Analysis

A theory of the formation of this pattern is described in [1]. Figure 2 illustrates the phenomena when a laser beam is incident normal to a parallel nonscattering medium ($n > 1$) with a white diffuse substrate. The radiation diffusely reflected from this substrate returns to the front surface of the medium where it is reflected and transmitted to varying degrees dependent upon its angle of incidence on this front surface (as depicted in Fig. 2). The bright spot is due to an inside effect which is discussed in [1]; it will not be a subject of discussion here.

---

[1] Thermal Radiative Transfer Group, Mechanical and Aerospace Engineering Department, University of Missouri—Rolla, Rolla, MO 65401

[2] Mem. ASME

Contributed by the Heat Transfer Division for publication in the JOURNAL OF HEAT TRANSFER. Manuscript received by the Heat Transfer Division November 1, 1984.

[7] and [8] may be more appropriate for systems with a small number of elements.

Conclusion

A simple solution has been presented which allows a set of direct-exchange areas to be smoothed to meet conservation constraints while minimizing the disturbance of the original estimates. The method is particularly well suited for large systems for which the exact nature of the deficiencies of the direct-exchange areas is unknown. Smoothing with $w_{ij} = x_{ij}^2$ is readily incorporated into codes performing zonal analysis and has been demonstrated to be effective and efficient. The tendency of this smoothing technique is to adjust each x_{ij} in proportion to its original size. Conservation of energy is invoked through the adjustment without additional physical insight. As a result, reasonable accuracy of the original estimates of the direct-exchange areas must be assumed and this limitation should be considered. The method should not be applied unless reasonable faith in the "shape" of the original estimates is justified.

Acknowledgments

The authors acknowledge J. R. Wilson for recommending the use of the method Lagrange multipliers in this minimization process.

References

1 Hottel, H. C., and Sarofim, A. F., *Radiative Transfer*, McGraw-Hill, New York, 1967.

2 Hottel, H. C., "Radiant Heat Transmission," in: *Heat Transmission*, W. H. McAdams, ed., 3rd ed., McGraw-Hill, 1954, Ch. 4.

3 Hottel, H. C., and Cohen, E. S., "Radiant Heat Exchange in a Gas-Filled Enclosure: Allowance for Non-Uniformity in Temperature," *AIChE Journal*, Vol. 4, No. 1, 1958, pp. 3–14.

4 Becker, H. B., "A Mathematical Solution for Gas-to-Surface Radiative Exchange Area for a Rectangular Parallelepiped Enclosure Containing a Gray Medium," ASME JOURNAL OF HEAT TRANSFER, Vol. 99, May 1977, pp. 203–207.

5 Edwards, D. K., and Balakrishnan, A., "Volume Interchange Factors for Nonhomogeneous Gases," ASME JOURNAL OF HEAT TRANSFER, Vol. 94, May 1972, pp. 181–187.

6 Larsen, M. E., "The Exchange Factor Method: An Alternative Zonal Formulation for Analysis of Radiating Enclosures Containing Participating Media," Ph.D. Dissertation, The University of Texas at Austin, 1983.

7 Sowell, E. F., and O'Brien, R. F., "Efficient Computation of Radiant-Interchange Configuration Factors Within the Enclosure," ASME JOURNAL OF HEAT TRANSFER, Vol. 94, Aug. 1972, pp. 326–328.

8 Vercammen, H. A. J., and Froment, G. F., "An Improved Zone Method Using Monte Carlo Techniques for the Simulation of Radiation in Industrial Furnaces," *International Journal of Heat and Mass Transfer*, Vol. 23, No. 3, Mar. 1980, pp. 329–336.

9 Larsen, M. E., and Howell, J. R., "Least-Squares Smoothing of Direct-Exchange Areas in Zonal Analysis," ASME Paper No. 84-HT-40.

Laser Reflection in a Scattering Medium With a White Diffusively Reflecting Substrate

D. C. Look, Jr.[1,2] **and M. Vijayan**[1]

Introduction

This experimental study concerns the loss of visibility of a pattern that is formed on the substrate when a planar scattering medium is subjected to a finite sized collimated light. The pattern is in the form of a bright spot surrounded by a dark circular area surrounded by a bright outer area. Figure 1 is a photograph of the pattern as seen through double-distilled water when viewing the white substrate. To obtain this pattern, the beam must be incident normal to the smooth front surface of the medium and to the white diffusely reflecting substrate. Look and Nelson [1] also dealt with this phenomenon. In [1] a discussion is presented on the effect of the reflection of laser radiation in a transparent, nonscattering medium for identical geometric and detection conditions as reported here. Good agreement between theory and experiment was demonstrated in this reference.

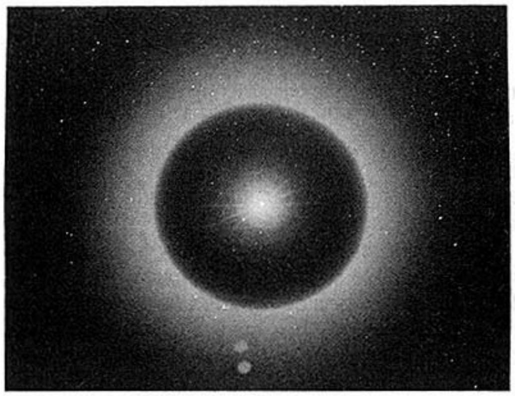

Fig. 1 Photograph of the effect of a white diffusely reflecting substrate in a finite medium

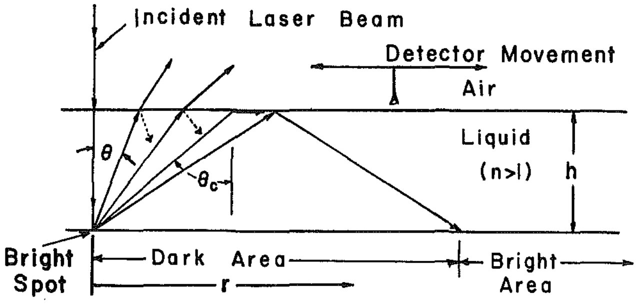

Fig. 2 Schematic of the outside reflection effect in a transparent slab

The purpose of this presentation is to extend the study as reported in [1] to the effects of pure scattering. In other words, it was found experimentally that as the optical thickness of the medium increases, this pattern starts to disappear and finally vanishes from view on the air side. The result of this experimental study is a statement of conditions required to obscure this pattern. The method used to accomplish this task is to direct a detector probe with a small angular field of view normal to the front surface. A jump in the detector readings occurs when the detector probe aperture crosses from the region of the dark area into the bright outer area. The size of this jump decreases as the optical thickness increases until for a certain optical thickness (called the flex point) the jump ceases to occur.

Theoretical Analysis

A theory of the formation of this pattern is described in [1]. Figure 2 illustrates the phenomena when a laser beam is incident normal to a parallel nonscattering medium ($n > 1$) with a white diffuse substrate. The radiation diffusely reflected from this substrate returns to the front surface of the medium where it is reflected and transmitted to varying degrees dependent upon its angle of incidence on this front surface (as depicted in Fig. 2). The bright spot is due to an inside effect which is discussed in [1]; it will not be a subject of discussion here.

---

[1] Thermal Radiative Transfer Group, Mechanical and Aerospace Engineering Department, University of Missouri—Rolla, Rolla, MO 65401

[2] Mem. ASME

Contributed by the Heat Transfer Division for publication in the JOURNAL OF HEAT TRANSFER. Manuscript received by the Heat Transfer Division November 1, 1984.

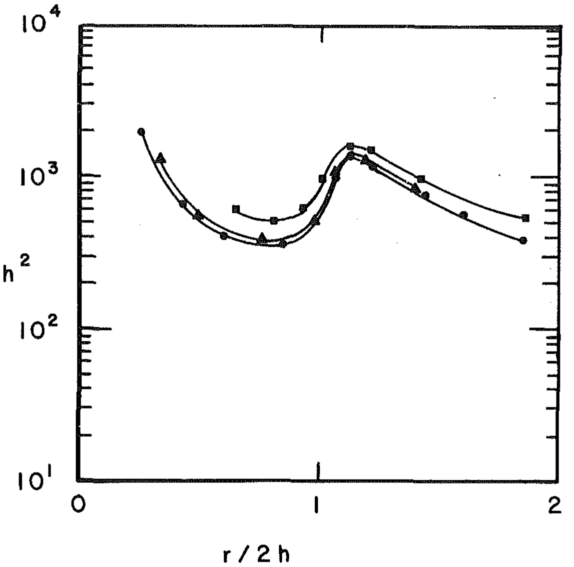

Fig. 3 Product of the adjusted voltage and adjusted depth squared (Vh^2) versus $r/2h$ with no particles: h = 1.23 cm; h = 2.34 cm; h = 3.00 cm

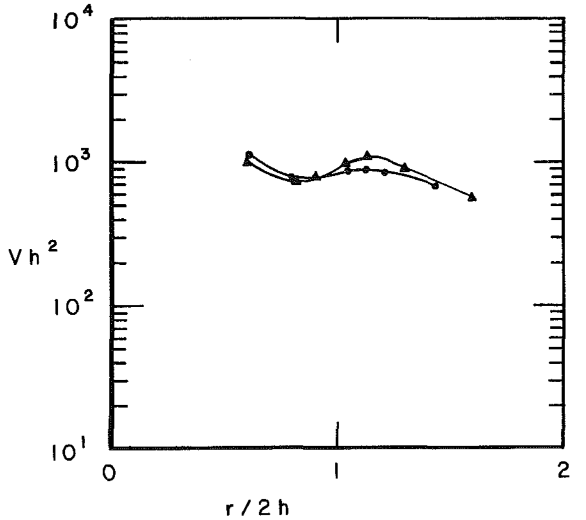

Fig. 4 Product of the adjusted voltage and adjusted depth squared (Vh^2) versus $r/2h$ with 1.5 cm^3 of 10 percent solution of 0.481 μm particles: h = 1.59 cm; h = 2.38 cm

In [1] it was demonstrated that the flux detected on the air side is a function of $r/2h$ such that

$$\Delta F \propto \frac{\rho}{h^2}\,[1+(r/2h)^2]^{-3/2} \tag{1}$$

where ρ is the reflectance on the water side of the liquid-air interface and h is the liquid depth. This expression exhibits a large discontinuity when $r/2h = r_c/2h = 1.134$ because of ρ

$$\rho \simeq (n-1)^2/(n+1)^2 \quad \text{for } \theta<\theta_c \text{ or } r<r_c$$
$$=1 \quad \text{for } \theta>\theta_c \text{ or } r>r_c \tag{2}$$

The critical radius r_c is defined as the radial position where the detector encounters the large intensity change (the outer edge of the darker area).

The addition of scattering particles to the medium tends to obscure or reduce the contrast between the dark and bright areas. The determination of the conditions needed to make this difference disappear was the goal of this study.

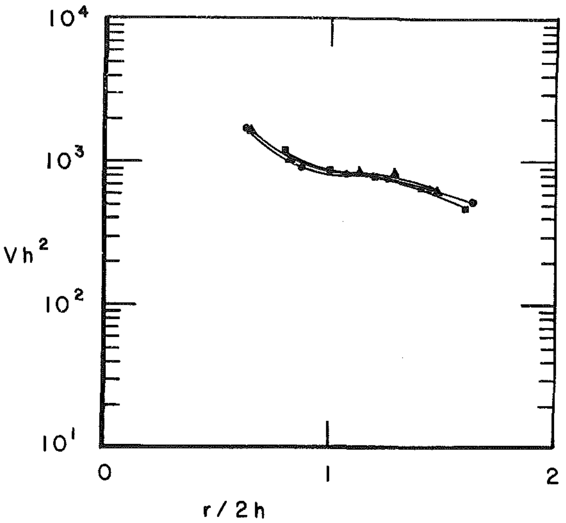

Fig. 5 Product of the adjusted voltage and adjusted depth squared (Vh^2) versus $r/2h$; flex points; 0.481 μm particles: h = 1 cm; h = 1.76 cm; h = 2.64 cm

Experimental

The experimental setup, also illustrated by Fig. 2, consisted primarily of a source, a large tank, and a detector. The source was a He-Ne laser. The scattering medium was contained in a glass tank. A 3M White Velvet® painted plate served as the diffusely reflecting substrate. The detector probe was a fiber optics bundle which transmitted the received power to a photomultiplier. Thus, the experimental data consisted of radial position-voltage reading pairs for a given depth, particle size, and volume of particles dispersed in the water.

After filling the tank with distilled water and positioning it, the white painted plate was lowered into the water and adjusted to depths of 1 cm, 2 cm, and 3 cm. Starting with clear water at each depth, data were collected for various optical thicknesses. These optical thicknesses (resulting from scattering) were obtained by adding known quantities of uniformly sized spherical latex particles to the distilled water. Particles of two different sizes (0.481 μm and 0.091 μm diameter) were dispersed (one at a time) into the water. Data were acquired until the detector probe crossed over the ring pattern ($r>r_c$). For the data reduction, (1) the detector dark level voltage was subtracted from the voltage measurements, and (2) the differences between the center of incident laser beam and detector probe positions were determined. These data were then plotted for graphic interpretation.

Results and Discussion

Examples of the graphs are shown in Figs. 3-5. A similar set resulted for 0.091-μm-dia particles. In these figures the vertical axis is Vh^2 (note ΔF is proportional to V) while the horizontal axis is $r/2h$. Note that the discontinuity at the dark area boundary is smoothed because of the finite aperture of the detector system but still clearly visible (see Fig. 3). The pattern starts losing its characteristic S shape as the scattering particle volume is increased (e.g., Fig. 4) until a point where the water became so optically thick that the contrast between the formally dark and bright areas is completely wiped out (Fig. 5).

For the data presented in these figures, the water depth has been corrected because of an experimental measurement error due to parallax and the meniscus. The corrected values of h are in the legend of each figure.

Figure 5 presents the approximate flex points of the data for 0.481 μm particles. This flex point is defined as existing

Table 1 Conditions of limiting visibility

PARTICLE SIZE (D - μm)	MEDIUM DEPTH (h - cm)	N	$h^{2/3}ND^{1.6}$
0.481	1.0	36	11.16
	1.76	25	11.30
	2.64	19	11.25
0.091	.667	675	11.13
	1.722	360	11.20
	2.67	270	11.22

when the identity of the end of the dark circular area and the beginning of the bright outer area can not be ascertained from the data (i.e., there was no intensity increase as $r/2h$ increased). Table 1 presents the corrected medium depths, particle sizes, and N, the approximate number per 0.1 cm^3 of 10 percent solution of the uniformly sized spherical latex particles added to the water which produced this obscuring of the contrast. A simple mathematical expression relating these three parameters was found to be

$$h^{2/3} N D^{1.6} \simeq 11.21 \tag{3}$$

This expression may be cast in a more convenient form using the optical depth τ, as defined in [2]

$$\tau = \frac{\epsilon V_j}{V_j + V_w} CH \tag{4}$$

where C is the scattering cross section, $\bar{C}$, per scattering particle volume; V_j is the total volume of solution containing particles (ϵ is the fraction of V_j which is particles), and V_w is the volume of water in the tank. Manipulation of equation (4) for these data yielded the following expression

$$\tau D^{4.6}/h^{1/3}\bar{C} = 1.427(10^{-5}) \tag{5}$$

where D is the scattering particle diameter.

Conclusion

The experimental results obtained were reasonably consistent. The expression relating the condition of the visibility limit and the medium characteristics was found. This expression, equation (5), appears to be applicable to both isotropic and anisotropic cases since the asymmetry factor g has a value of 0.071 for the 0.091 μm particles and 0.81 for the 0.481 μm particles.

Acknowledgments

The authors wish to acknowledge the National Science Foundation Grant MEA-81-21430 for partial support of this research.

References

1 Look, D. C., Jr., and Nelson, H. F., "Reflection of Laser Radiation From Transparent Media (n > 1) With a Diffusely Reflecting Substrate," *Optical Engineering* (in press).

2 Look, D. C., Jr., Nelson, H. F., and Crosbie, A. L., "Anisotropic Two-Dimensional Scattering: Comparison of Experiment With Theory," ASME JOURNAL OF HEAT TRANSFER, Vol. 103, No. 1, Feb. 1981, pp. 127–134.